A geochemical history of Tabon Cave (Palawan, Philippines) : environment, climate, and early modern humans in the Philippine archipelago

Omar Choa

MUSÉUM NATIONAL D'HISTOIRE NATURELLE

École doctorale « Sciences de la Nature et de l'Homme » – ED 227

Année 2018

N° attribué par la bibliothèque
|_|_|_|_|_|_|_|_|_|_|_|_|

THÈSE

Pour obtenir le grade de

DOCTEUR DU MUSÉUM NATIONAL D'HISTOIRE NATURELLE

Spécialité : PRÉHISTOIRE

Présentée et soutenue publiquement par

Omar Choa

Le 30 avril 2018

A geochemical history of Tabon Cave (Palawan, Philippines): environment, climate, and early modern humans in the Philippine archipelago

---

Directeur : Sémah, François / Co-directeur : Lebon, Matthieu

JURY :

Mme Lewis, Helen	**Associate Professor, University College Dublin (Irlande)**	**Rapporteure**
M. Sifeddine, Abdelfettah	**Directeur de recherche 1, Institut de recherche pour le développement (Mexique)**	**Rapporteur**
M. Asrat, Asfawossen	**Associate Professor, Addis Ababa University (Éthiopie)**	**Examinateur**
M. Dizon, Eusebio	**Scientist III, National Museum of the Philippines (Philippines) ; Lecturer, University of the Philippines (Philippines)**	**Examinateur**
M. Ghaleb, Bassam	**Directeur du Laboratoire de radiochronologie, Geotop, Université du Québec à Montréal (Canada)**	**Examinateur**
M. Lebon, Matthieu	**Maître de conférences, Muséum national d'histoire naturelle (France)**	**Co-directeur**
M. Sémah, François	**Professeur, Muséum national d'histoire naturelle (France)**	**Directeur**

A geochemical history

of

Tabon Cave

(Palawan, Philippines)

Environment, climate,
and early modern humans
in the Philippine archipelago

Omar Choa

MUSÉUM NATIONAL D'HISTOIRE NATURELLE

PARIS

ABSTRACT

Tabon Cave (Palawan, Philippines) is a key prehistoric site in Southeast Asia, one of the few to have yielded *Homo sapiens* fossils from the Late Pleistocene. Its history remains poorly understood: heavy physical and chemical alterations have greatly complicated its stratigraphy, and contextually isolated archaeological finds hamper the construction of a clear chronology. This study reexamines Tabon Cave using a multi-pronged geosciences approach to explore environment, climate, and early modern human presence in the region. The results reveal a major period in the cave's history between 40 and 33 ka BP, when drier climates, more open landscapes, and active human use of the cave were briefly spaced by a wet episode that left an extensive, gypsiferous speleothem. Future innovative research approaches spurred by the unique constraints of the site will undoubtedly further highlight the unique scientific and heritage value of Tabon Cave, a window into the earliest odysseys of our species across the archipelagos of Southeast Asia.

RÉSUMÉ

La grotte de Tabon (Palawan, Philippines) est un site préhistorique majeur en Asie du Sud-Est. Elle a livré des fossiles d'*Homo sapiens* datant du Pléistocène supérieur, rares dans la région. Pourtant, son histoire demeure mal connue : d'importantes altérations physiques et chimiques compliquent la lecture de sa stratigraphie, tandis que des objets archéologiques sans contexte clair entravent l'élaboration d'une chronologie fiable. Cette étude jette un nouveau regard sur la grotte de Tabon à travers une approche pluridisciplinaire des sciences de la Terre. Elle explore notamment l'environnement et le climat des premiers hommes anatomiquement modernes dans la région. Les résultats mettent en lumière une période clef entre 40 et 33 ka BP, caractérisée par des climats plus secs, des paysages plus ouverts et une empreinte humaine marquée dans la grotte. Cette période a également été ponctuée par un court épisode d'humidité qui a laissé un spéléothème gypsifère étendu en guise de témoin. Dans l'avenir, de nouvelles approches, prenant en compte les contraintes particulières du site, pourraient permettre de souligner davantage la valeur scientifique et patrimoniale unique de la grotte de Tabon, une fenêtre sur les premiers périples de notre espèce à travers les archipels d'Asie du Sud-Est.

A C K N O W L E D G E M E N T S

First of all, I would like to express my heartfelt gratitude to all the wonderful people at the National Museum of the Philippines for believing in and supporting this project: Director Barns, Dr Labrador, Sir Angel, Ma'am Owis, Sir Leo, Clyde, Ate Ame, Ate Nids, and Taj. A big thank you to Ma'am Sweepea for the faunal survey data. Doc, your thrust for the continuation of research at Tabon and Lipuun has played an essential role in the birth of this thesis.

To Ma'am Nida and Kuya Larry of the Quezon branch of the NM, as well as Ma'am Maribel and the rest of the Quezon LGU, your invaluable presence, warm hospitality, and generous assistance have been instrumental in the success of the various field missions to Tabon these past years.

A big shout-out goes to the faculty, staff, and students of ASP—thank you for introducing me to the world of archaeology, and for all the amazing and unforgettable experiences that we shared. Thank you, Sir Mandy, Sir Vic, Ma'am Grace, Alfred, Leee, Ate Aidz, Ate Digs, Ate Tess, and Kuya Cads. Emil, thanks for your help and advice on palaeoenvironment and palaeoclimate. To my fellow 2010 San Juan field schoolers—Noel, Tash, Ric, Kate, Ate A—look where we are now!

Julien, thank you so much for patiently responding to my endless questions about Tabon over e-mail and in person—your thesis has been my second bible, alongside Fox's monograph! Maïlys, thanks for carving out time to help me with ESR tests. Hermine and Aude, thank you for the discussions, advice, and company. Thanks also go out to all the former and current PhD students on the second floor of the Musée de l'Homme, especially the people in Bureau 207!

Nicole, thank you for the generous donation of your priceless archives on Fox, Tabon, Lipuun, and Palawan—a treasure trove in the truest sense of the word. Thank you for the amazing work that you did and continue to do in Palawan.

Thank you so much to the PREHsea Project for making my research possible. I am especially indebted to all the people who participated in the 2014 field school at Tabon Cave for helping me with sample collection—the PSU students, our Indonesian colleagues, Boss Archie, and our amazing logistical support team, especially Kuya Bak-Bak and Kuya Philip.

Olivier and Mehdi, thank you for your precious help in setting up the organic matter extraction protocol. Marie Balasse, Denis, and the Service de Spectrométrie de Masse Isotopique du Muséum et la Région Île-de-France, thank you for helping me with stable isotope analysis. Thank you as well to Jean-Pascal Dumoulin at the LMC14 for your generous assistance with radiocarbon dating. To everyone in my research group, UMR 7194, thank you for the various ways in which you have contributed to this project.

ACKNOWLEDGEMENTS

Bassam, thank you so much for embarking with me on this adventure. Your patience, guidance, and dedication have helped me navigate the technical maze that is uranium-series dating. My gratitude also goes to André Poirier, Nicole Turcot, and everyone else at Geotop, both for your technical support and for making me feel at home in Montréal.

François and Matthieu, thank you so much for believing in me and for being with me every step of this long, arduous journey. Your faith and perseverance in the face of the scientific challenges posed by this project have been instrumental in bringing it to fruition.

Last, but certainly not the least, thank you to my wonderful family in France and in the Philippines for all your love and support.

Omar Choa
Paris, France

TABLE OF CONTENTS

LIST OF FIGURES

LIST OF TABLES

PREFACE

On the southwestern coast of the Philippine island of Palawan, a cave yawns out on to the South China Sea. Its numerous sister caves honeycomb the vast karstic landscape all around, and for thousands of years, humans in the region have been continuously drawn to their siren call. From the first *Homo sapiens* to walk on Palawan, to mysterious practitioners of elaborate jar burial rites and, more recently, archaeologists and other scientists, the Tabon Caves Complex continues to attract, charm, and intrigue humans to this day.

Given its strategic location on Palawan, a key geographical zone for understanding migration between the Sunda Shelf and the Philippine archipelago, the Tabon Caves Complex has been the subject of much scientific attention. The first researcher to have conducted extensive work on the complex is the late Dr. Robert Fox, former Chief Anthropologist of the National Museum of the Philippines. His pioneering work in the 1960s put the complex on the map of Southeast Asian prehistory, due in large part to the discovery of several Late Pleistocene human fossils in one of the major sites of the complex, Tabon Cave. The notable rarity of comparable specimens in Island Southeast Asia, in the light of many unresolved questions concerning the settlement of the region's archipelagos, makes the Tabon Cave finds especially important. Aside from archaeological and anthropological significance, the Tabon Caves Complex and its surrounding area, Lipuun Point, play host to a rich diversity of flora and fauna. Together, they constitute a remarkable natural and cultural landscape whose need for protection has been recognized by various stakeholders—local, national, and international. Finally, the complex is endowed with singular heritage value, not just for Filipinos nor Southeast Asians, but for all of humankind, as it bears witness to our species' earliest encounters with island environments.

In recognition of the complex's importance, several research programmes were conducted in the 1990s and beyond, with a particular focus on Tabon Cave. However, work at this site has been hampered by numerous difficulties. Among these is the lack of secure stratigraphic context for many key finds, notably the human fossils. While they have been heavily studied from a palaeoanthropological point of view, their lack of contextual information has made it difficult to describe their world in terms of environment, climate, and time. The paucity of conserved animal and plant remains from the cave also means that 'classic' approaches cannot

be used to study the said themes. Finally, the spatial heterogeneity of the stratigraphy and the rarity of datable materials have entailed difficulties in the construction of a coherent chronology. These barriers have 'isolated' the fossils and restricted substantiated discussions of their role in early dispersals of, and environmental adaptations by, anatomically modern humans in Island Southeast Asia.

To re-contextualize the fossils and make concrete contributions to the discussions just cited, it became clear that it would be necessary to work around the site's numerous obstacles. A response was first crafted in the author's master's thesis and is greatly expanded in this dissertation: a geoscience approach based on an important element of the Tabon Cave stratigraphy, guano. Present in many parts of the cave, this dark, organic-rich deposit, consisting of bird/bat droppings and often sandwiched within weathering sequences, was hypothesized to be the missing link between the different areas of the cave. Aside from potentially resolving questions concerning the cave's stratigraphy, guano can also provide environmental information through stable isotope geochemistry. Furthermore, the study of its diagenesis through characterization of derivative authigenic minerals can reveal clues to past climatic changes. Finally, guano and its associated minerals are some of the few datable materials in the cave, with radiocarbon dating being applicable on the former and uranium-series dating appearing to show promise for the latter. This study therefore combines these methods and applies them to the Tabon Cave guano deposits and diagenetic mineral products. In doing so, it aims to reconstruct the environmental and climatic contexts of the earliest human occupations of the site, and eventually contribute to the wider debate on the first settlement of the Southeast Asian archipelagos by our species, *Homo sapiens*.

Chapter I

Introduction

1.1. Tabon Cave: a prominent site for *Homo sapiens* dispersals in Island Southeast Asia

Tabon Cave, located on the island of Palawan in the southwestern Philippines, is a key piece of the puzzle that is the prehistory of Southeast Asia. It is one of the few sites to have yielded *Homo sapiens* fossils dating back to the Late Pleistocene (the geological age ranging from 126 to 12 ka; Subcommission on Quaternary Stratigraphy, 2016). Over this span of time, the fossil record for anatomically modern humans in the region is still very limited.

The oldest known specimens are teeth from Fuyan Cave (Daoxian, southern China), with 47 specimens dating between 120 and 80 ka (Liu *et al.*, 2015); teeth from Lida Ajer (Sumatra, western Indonesia), placed between 73 and 63 ka (Westaway *et al.*, 2017); and various skeletal fragments from Tam Pà Ling (Huà Pan, northern Laos), ranging from 70 to 44 ka (Demeter *et al.*, 2017). At Callao Cave (Cagayan Valley, northern Philippines), a metatarsal belonging to the genus *Homo* and dated to 67 ka can be considered contemporaneous with the two aforementioned sites, but the attribution to *Homo sapiens* is provisional due to morphological and size proximity to *Homo habilis* and *Homo floresiensis* (Mijares *et al.*, 2010). The isolation of the Cagayan Valley region, surrounded by open sea on the northern tip of the Philippine archipelago, suggests that the Callao hominins were already capable of making long maritime voyages.

After these earliest examples come two sites that are very similar in many aspects: Niah Cave (Sarawak, Malaysian Borneo), and Tabon Cave (Palawan, southwestern Philippines). Aside from having been excavated around the same period (from the 1950s to the 1960s), the earliest occupation of the caves by anatomically modern humans are also comparable: 46 (to 34) ka for Niah Cave, and 47 (to 16.5) ka for Tabon Cave (Détroit *et al.*, 2004; Barker *et al.*, 2007).

These important finds remain, unfortunately, rare, leaving many gaps in understanding concerning the arrival, dispersal, and adaptation of *Homo sapiens* in this part of the world. Much is still unknown about *Homo sapiens*'s presence in Australia by at least 40 ka and potentially as early as 65 ka (Bowler *et al.*, 2003; Clarkson *et al.*, 2017), despite the fact that this period in the region represents a pivotal chapter in the global story of human evolution and migration.

The island of Palawan, on which Tabon Cave is found, is strategically situated on the northeastern end of the Sunda Shelf and borders the rest of the Philippines (Figure 1). It thus very likely played a key role in the settlement of the archipelago, being the easiest point of entry from mainland Southeast Asia. During periods of low sea level in particular, the distance between Palawan and Borneo could shrink to a mere 2.5 km from its present-day value of 140 km (over MIS 6 [191–130 ka] and 8 [300–243 ka], for example), making for a short sea crossing (Robles *et al.*, 2015). This would have been an easy feat for the first modern humans in the archipelagos, already capable of extended sea voyages as suggested by their early presence in Australia. More generally, the island plays a central role in the study of human dispersals in Island Southeast Asia during the Late Pleistocene: it is surrounded in all directions by important human fossil regions, with Luzon to the north, Java, Borneo, and Flores to the south, and Thailand and Laos to the west. Palawan is thus essential to understanding the timeline of anatomically modern human dispersals in the region.

1.2. Brief background of research in Tabon Cave

1.2.1. The 1960s

Tabon Cave was first excavated in the 1960s under the supervision of Dr. Robert Fox, then Chief Anthropologist of the National Museum of the Philippines. This opening chapter in the archaeological study of the site culminated in the publication of a monograph, which remains to this day the authoritative reference on Tabon Cave (Fox, 1970).

Fox identified six widely dispersed archaeological horizons characterized by stone artefact associations, to which he gave the designation 'Flake Assemblages'. Radiocarbon dating placed four of the six assemblages between 30.5 ± 1.1 and 9.25 ± 0.25 ka BP, while the oldest and youngest were respectively estimated at 45–50 and 8.5–9.5 ka (Fox, 1970: 24).

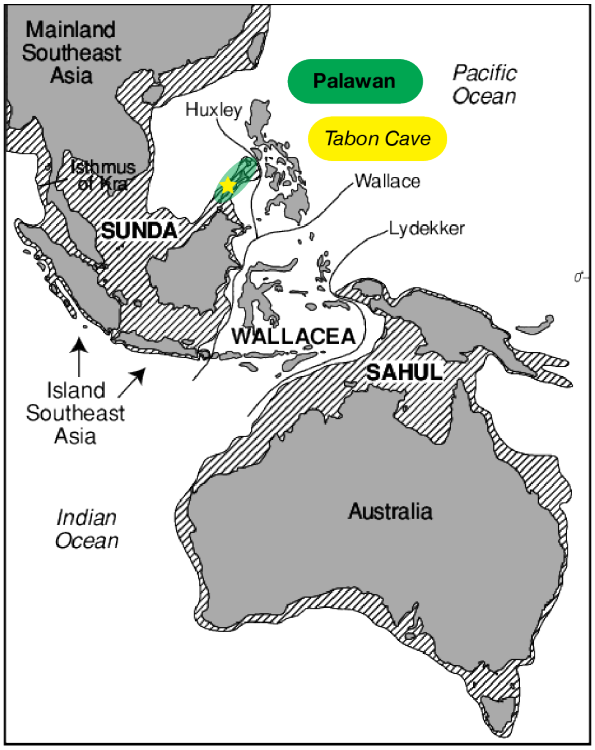

Figure 1. Tabon Cave and the island of Palawan are located on the Sunda Shelf. Together with Wallacea and Sahul, they constitute the three main biogeographical regions that span Southeast Asia and Australia (modified from Harrison *et al.*, 2006).

Dating was performed by Ferguson and Libby (1963) and Berger and Libby (1966) at the Institute of Geophysics of the University of California, Los Angeles, during the early days of the method. The assemblages were found intercalated with various geological features. Flake Assemblages I-A (ca. 8.5–9.5 ka) and III (22–24.2 ka BP) were separated by a hard floor that Fox described as "calcareous" (Fox, 1970: 26–27). Flake Assemblage II, situated above the same hard floor, was found buried underneath a stalactite near the cave mouth. The presence of many ancient floors, suggested by Fox to have been formed by dripping water, was also observed; however, their contours did not match those of the archaeological horizons nor the cave floor at the time of excavation.

The assemblage elements were determined to have been produced by direct percussion and come in assorted forms and sizes (Figure 2). They reflect the expected debris from the various steps of the lithic *chaîne opératoire*, suggesting that stone tool manufacture was one of the activities that took place in Tabon Cave (Jago-on, 2006).

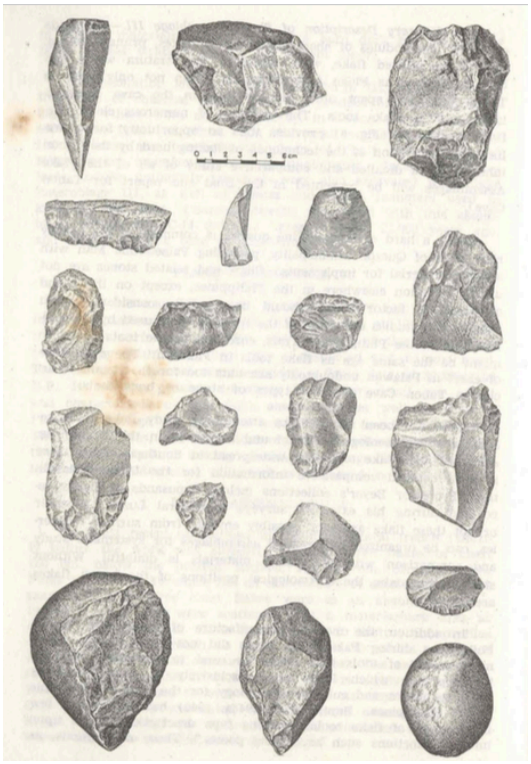

Figure 2. Assortment of lithic artefacts from Tabon Cave (Fox, 1970: 30).

Various animal remains were found in association with the lithic assemblages. Most of the excavated bones belonged to small birds, bats, and other microfauna; unfortunately, these were most likely discarded, given the discrepancy between their presence in the reports and their near-absence in the collections (Corny, 2008). The few macrofaunal remains recovered were identified to be from pig and deer. However, not a single marine shell was found; Fox takes this to indicate that occupation of Tabon Cave took place during periods of low sea stand, when the shore would have been 30 to 35 km further out (Fox, 1970: 38).

Bits of charcoal also accompanied most of the assemblages. Flake Assemblage III, in particular, was associated with numerous fragments that were thought to be the result of scattered cooking activities.

Several human remains were unearthed in the cave, notably a frontal bone (Figure 3). Its owner was given the moniker 'Tabon Man', and it has become the most iconic human fossil from the site thus far. Fox associated the frontal bone with Flake Assemblage III, estimated to date to between 22 and 24 ka ago (Fox, 1970: 40).

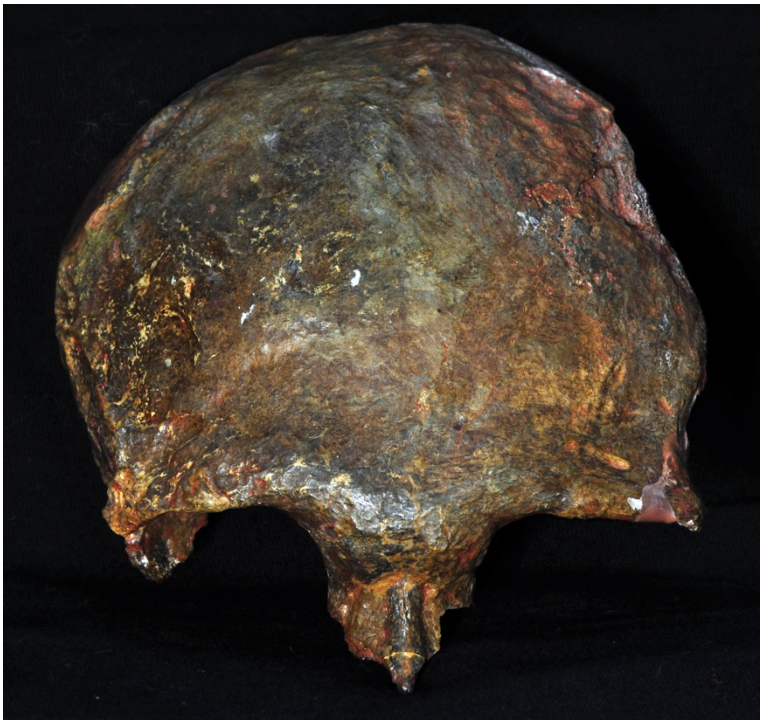

Figure 3. The Tabon Cave frontal bone. Photo by Florent Détroit.

Use of Tabon Cave during the Philippine Early Metal Age (defined by Fox as ranging from 500 to 200 BC) was also documented, this time as burial grounds. Large pottery fragments from funeral jars and other vessels were found strewn across the cave floor when the site was first discovered. Burial goods recovered include ornaments made from jade (Figure 4), stone, and glass, as well as iron artefacts (Fox, 1970: 44).

These findings attest to the archaeological richness of Tabon Cave, the fruit of its long history of human occupation. It is one of the few sites that can shed light on the dynamics of human migrations and adaptations in Island Southeast Asia during the Late Pleistocene and the Holocene.

However, in the decade that followed, the discovery of numerous archaeological caves and rock shelters in the Peñablanca limestone formation, on the northernmost fringes of the Philippine archipelago, shifted interest away from Palawan and put Tabon Cave research on pause (Ronquillo, 1985; Ronquillo, 1995). The documents and artefacts produced from the excavations were divided between the National Museum in Manila and Fox's home in Baguio (around 250 km north of Manila), where they would remain unstudied until the 2000s (Dizon, 2000; Corny, 2008).

Figure 4. A jade artefact called *lingling-o* found in Tabon Cave. Photo by Archie Tiauzon.

1.2.2. The 1990s to present

In the 1990s, the first foundations were laid for the future collaboration on Tabon Cave research between the National Museum of the Philippines and the Muséum national d'histoire naturelle of France. The fossils underwent anthropometric analysis, imaging, and for the first time, direct dating, all at the Institut de paléontologie humaine in Paris (Dizon, 2000). The frontal bone, in particular, was again attributed a Late Pleistocene age at 16.5 ± 2 ka, albeit younger than initially estimated by Fox (Dizon *et al.*, 2002).

Alongside the renewed interest in Tabon Cave driven mainly by the new studies on the human fossils, a series of reinvestigative excavations was carried out in the early 2000s by the National Museum of the Philippines (Orogo, 2000a; Orogo, 2000b; Orogo, 2001a; Orogo, 2001b). These campaigns yielded new fossil discoveries, notably a human tibia fragment dated via uranium-series to 47 +11/–10 ka (Figure 5) (Dizon, 2003; Détroit *et al.*, 2004). Unfortunately, the fossils were recovered in disturbed contexts, making stratigraphical correlation difficult. Nevertheless, taking into account the occasionally significant error margins, they can be considered to confirm the presence of *Homo sapiens* in Tabon Cave during at least the latter part of the Late Pleistocene, more than 30,000 years ago (Détroit *et al.*, 2004).

Figure 5. The tibia fragment dated to 47 +11/–10 ka (Détroit *et al.*, 2004).

A significant quantity of lithic artefacts was also recovered during the excavations and formed the basis of study for several theses (Patole-Édoumba, 2002; Jago-on, 2006; Schmidt, 2008; Xhauflair, 2009). These newer studies employed typo-technological analysis, use-wear analysis, ethnography, and geochemistry to study various aspects of stone tool production, such as knapping techniques, contact material, retouch, and sourcing.

An important excavation followed in 2007 with the organization of a field school in Tabon Cave as part of the Human Origins Patrimony in South East Asia (HOPsea) Project. Geoscientific sampling for soil micromorphology and isotope studies was also conducted around the same time by the Palawan Island Pre- and Proto-historical Research Project (PIPPRP), resulting in two published papers (Lewis, 2007; Lewis *et al.*, 2008) and one forthcoming (Johnston and Hernandez, *in prep.*).

Finally, research picked up in the succeeding decade under the Managing Prehistoric Heritage in Southeast Asia (PREHsea) Project. The project combined field research, collections rehabilitation, government synergies, science communication, and heritage management. The fieldwork consisted of sampling and excavation within both small-scale missions and larger-scale field schools, with the 2014 campaign in particular (Figure 6) providing the material for this study.

Figure 6. The 2014 excavations conducted under the auspices of the PREHsea Project.

1.3. A complex site

The study of Tabon Cave, an extremely complex archaeological site, presents particular challenges due to several factors.

1.3.1. A puzzling stratigraphy

One of these challenges is the *nature* of the stratigraphy itself: the site is composed of numerous sub-sequences that are not always easy to correlate.

A major source of this complexity is diagenesis caused by the alteration of guano. The term *guano* designates both bat and bird excrement, rich in carbon and nitrogen. Initially composed of uric acid for birds and urea for bats, it also contains undigested insect remains (in the case of insectivorous taxa) and other waste products (Bird *et al.*, 2007). Guano undergoes biological and chemical transformations over time through the action of microbial communities and changes in the local environment. One of the consequences of the ensuing loss of chemical equilibrium is dissolution of existing mineral assemblages and precipitation of new ones (with phosphates, abundant in guano, playing a major role); these diagenetic processes can have a significant influence on the archaeological and sedimentary records of a site (Karkanas *et al.*, 1999; Quattropani *et al.*, 1999; Karkanas *et al.*, 2000; Karkanas *et al.*, 2002; Shahack-Gross *et al.*, 2004). In Hayonim Cave (Israel), for example, the heterogeneity of preservation conditions, attributed to phosphates, was found to be related to the spatial distribution of bones (Stiner *et al.*, 2001). Phosphates generated by bat colonization and human occupation were also identified to be responsible for the development of a 'decarbonated pocket' in the Caune de l'Arago (France). This sedimentary feature, resulting from dissolution of clays and carbonates and precipitation of authigenic phosphate minerals, cut and altered the original deposits (Quattropani *et al.*, 1999).

In Tabon Cave, guano is present in varying quantities, distributed both horizontally and vertically throughout the site (Figures 7 and 8). At the time of the first excavations in the 1960s, Fox estimated its thickness to reach 6 m or more (Fox, 1970: 21). Differential weathering in space and time suggests that equivalent layers may have undergone divergent paths of geochemical evolution, making it difficult to establish visual and mineralogical parallels between the various zones of the cave. In particular, localized and discontinuous formation of phosphatic and sulphatic speleothems complicate correlation of stratigraphic profiles across the cave. Lewis (2007) was the first to investigate the guano deposits and their associated authigenic minerals, notably identifying potential diagenesis of wood ash. Lewis *et al.*, (2008) also brought to light the true nature of certain hard deposits in the cave, thought up to that point to be composed of calcium carbonate (and, until then, called 'travertine'), as actually consisting of re-precipitated gypsum. Gallet (2012) dug deeper into the issue of authigenic mineral formation by conducting preliminary spectroscopic analysis on a series of layers. His work provided a wider preview of the rich mineralogical diversity in the cave first suggested by Lewis (2007) based on her soil micromorphological observations. Finally, Choa (2014; 2016) applied a targeted, interdisciplinary approach on specific guano weathering sequences to obtain a higher-resolution understanding of the diagenetic processes at work in Tabon Cave.

Figure 7. Example of a guano weathering sequence in Tabon Cave, with the 'parent' layer at the base (in dark blackish brown). Note the thick, white alteration layer. Photo by Florent Détroit.

Figure 8. Another guano weathering sequence, situated very near the one in Figure 7, but differing notably by the absence of the white alteration layer. Photo by Anne-Marie Sémah.

Aside from guano diagenesis, another factor that complicates the stratigraphy is disturbances by fauna. The Philippine megapode (*Megapodius cumingii tabon*; also known as the Philippine scrubfowl or the Tabon scrubfowl) was found to be responsible for several holes observed in the cave prior to the first excavations, some measuring as deep as 1.3 m (Fox, 1970). The eggs that it would lay in these holes attracted monitor lizards, who would in turn also dig through the holes, further reworking sediments.

Humans also contributed to disturbing the cave deposits at various points in time. Refitting of bone remains by Corny and Détroit (2010) showed that some fragments were separated by at least 12 m when they were collected during the first excavations in the 1960s. This observation is supported by taphonomic analysis and, along with the presence of burnt

human bones, suggest ancient human activity as a source of disturbance. More recently, treasure hunter pits have been observed in the cave (Figure 9). In the Philippine context, this phenomenon is often associated with quests for 'Yamashita's treasure', war loot said to have been amassed by Japanese soldiers across Southeast Asia during World War II and then buried in various sites in the Philippines, including caves (Seagrave and Seagrave, 2003). The activity further complicates stratigraphical reconstruction and highlights the necessity of better heritage management practices for the site. Finally, the hostile preservation conditions inside the cave act on the fragile deposits, leading to the collapse of certain profiles and baulks (Figure 10).

Figure 9. A treasure hunter pit in Tabon Cave.

Figure 10. A particularly fragile profile composed of extremely loose sediments toward the base that readily give way.

1.3.2. Discontinuities in data

The diversity of the personnel who worked on the site over the long stretch of time for which it has been under study contributes its own measure of difficulty. Whereas the various teams individually applied rigour in their excavation methodology and data gathering, less effort was exerted toward maintaining continuity across the different field campaigns. As a result, for example, there is no unified system of nomenclature for the stratigraphy—each layer has ended up with three or four different names, and despite recent advances, correspondences between layers described by different teams are not always clear (Lewis, 2007; Gallet, 2012).

This has complicated data synthesis and blurs the big picture of the current state of knowledge on Tabon Cave. Additionally, the excavations carried out in the 1960s were intensive and removed much of the original cave floor, making it difficult to correlate drawn profiles with their equivalents in the field.

Nevertheless, several initiatives were carried out to address the situation, starting in the 2000s. Site visits and painstaking analysis of the Fox documentary archives and artefact collections curated by the University of the Philippines in Baguio eventually bore fruit. The horizontal grid originally employed by Fox was successfully reconstructed and updated, greatly facilitating the work of future researchers. Corny (2008) produced a major contribution to the study of the site by reconstituting the spatial distribution of recorded artefacts. Finally, Gallet (2012) made advances in the synthesis of the cave's stratigraphy.

1.4. The present work's contribution

Despite the challenges just cited, the study of Tabon Cave remains an essential stepping stone toward understanding the settlement of the Philippine archipelago in particular and human dispersals in Island Southeast Asia in general. To this day, the cave remains one of the rare sites to have yielded Late Pleistocene *Homo sapiens* remains. Its geographical position as a possible gate into the Philippine islands for early humans secures its important place in the prehistory of the region. Additionally, as just one of the over 200 cavities and rock shelters in the Tabon Caves Complex (the vast majority of which remain unexplored), it is potentially a mere window into the full archaeological richness of the karstic network. The complex itself serves as the centrepiece of Lipuun Point, the surrounding area that is characterized by varied environments—towering limestone cliffs, extensive coastal landscapes, and luxuriant tropical vegetation—all teeming with incredible biodiversity and serving as the backdrop of early human presence in Palawan.

Aside from its scientific and natural value, Tabon Cave is also endowed with unique historical and heritage value. Since research efforts began almost six decades ago, it remains to this day one of the most studied sites in the Philippines, holding an important place in Southeast Asian archaeology and in Philippine history. For many Filipinos, and not just the local communities in the municipality of Quezon where the site is located, 'Tabon' *is* synonymous with 'prehistory'.

The complexity of the site's stratigraphy deserves to be acknowledged, but it should in no way hinder further study, particularly from other methodological angles. Many questions remain concerning the formation and evolution of the cave's deposits—their age, nature, and palaeoenvironmental significance. It will be difficult to answer these without further, focused work on the stratigraphy. Nevertheless, the application of a multi-disciplinary approach to targeted areas and layers makes it possible to tackle specific research questions concerning the cave and its surrounding landscape, of which much is still unknown despite their importance for understanding past human adaptations and lifeways in the region.

The goal of this work, then, is not to present a detailed, continuous, high-resolution history of Tabon Cave. Rather, it aims to focus on two key aspects of the site—namely, the physical and chemical transformations that unfolded within the cave, and what they reveal about the environment and climate surrounding the earliest human occupations of the site. Particular attention is given to certain deposits that link these twin aspects and hold great potential for palaeoenvironmental and palaeoclimatic research in Southeast Asia: guano, and its derivative authigenic minerals. Previous work on these deposits in the region has focused on the application of various geoarchaeological approaches, including soil micromorphology, geomorphology, isotope geochemistry, mineralogy, and others (Gilbertson *et al.*, 2005; Stephens *et al.*, 2005; Bird *et al.*, 2007; Dykes 2007; Lewis 2007; Lewis *et al.*, 2008; Barker 2013; Wurster *et al.*, 2015; Barker and Farr, 2016; Marwick *et al.*, 2017; Morley, 2017; Morley and Goldberg, 2017; Morley *et al.*, 2017; O'Connor *et al.*, 2017; Stephens *et al.*, 2017; McFarlane and Lundberg, 2018; Johnston and Hernandez, *in prep.*). The present thesis builds upon this body of literature through the creative blend of select approaches, namely, sedimentology, mineralogy, stable isotope geochemistry, and radioisotope geochemistry. At the same time, it goes beyond by applying them to a remarkable site with 40,000 years of human occupation and rare scientific, natural, historical, and heritage value worthy of protection for future generations, all in hopes of elucidating the earliest adventures of our species across the islands of Southeast Asia.

Chapter II

The site

2.1. Geographical context

Tabon Cave is one of the approximately 215 caves and rock shelters that constitute the Tabon Caves Complex (Fox, 1970; National Museum of the Philippines, 2014). This karstic network, situated at latitude 9°16'N and longitude 117°58'E, forms part of a limestone promontory called Lipuun Point located on the southwestern coast of the island of Palawan, in the southwestern part of the Philippine archipelago (Figure 11).

Figure 11. The location of the Tabon Caves Complex within the Philippine archipelago.

2.1.1. Palawan

Palawan is a slender island measuring about 425 km long, with a width varying between 8.5 and 40 km (Provincial Government of Palawan, 2017). It runs from southwest to northeast, tracing a diagonal from Malaysian Borneo to Mindoro in the Philippines. To its west lies the South China Sea, while to the east is the Sulu Sea.

Palawan experiences a tropical wet climate that interacts dynamically with its geography. The northwest experiences a dry season for half of the year (from November to May), followed by a wet season for the other half (from June to October). The rest of the island is characterized by a dry season that lasts from one to three months, but the east coast is wetter up north than down south (Wikramanayake *et al.*, 2002).

Palawan is a tropical and subtropical moist broadleaf forest biome composed of various vegetation types. Around a third of the island (31%) is covered by lowland evergreen dipterocarp rainforest, with *Casuarina* being particularly dominant in the south. In the east, moist semi-deciduous forests flourish under a rain shadow, alongside a large region of ultramafic forest in the south-central part of the island. Montane forests take over at higher elevations (between 800 and 1,500 m). Coastal areas are characterized by beach forest, notably featuring mangrove species. Finally, wide areas of the south are covered in limestone forest (Wikramanayake *et al.*, 2002).

As mentioned in Section 1.1, Palawan is located at the northeastern corner of the Sunda Shelf, representing a southeastern extension of the Asian continent and hosting one of the three main biogeographical zones of the region, along with Wallacea and Sahul (Figure 12). During the Pleistocene, sea-level changes (mainly due to the alternation between glacial and interglacial periods) continuously transformed the contours of the Sunda Shelf, hiding and revealing landmasses. Today, the principal, visible portions correspond to mainland Southeast Asia and the continental islands of Sumatra, Java, Bali, Borneo, and Palawan. The same phenomenon operated on the Sahul Shelf, whose visible modern-day portions include New Guinea, Australia, and Tasmania. However, the oceanic islands between the two shelves, corresponding to the Wallacea biogeographical zone, have always been surrounded by water.

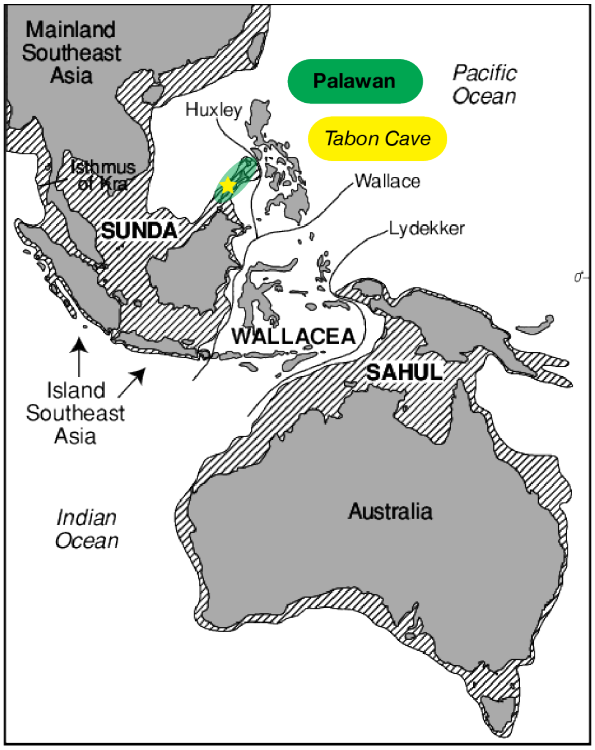

Figure 12. Tabon Cave and Palawan with respect to Sunda, Wallacea, and Sahul (modified from Harrison *et al.*, 2006).

The Huxley line separates Palawan from the rest of the Philippine archipelago, attributing the former to the Sunda biogeographical zone and the latter to Wallacea. While Palawan has never been connected to the rest of the Philippines, there is less certainty concerning possible terrestrial connections to Borneo, its closest neighbour on the Sunda Shelf. The two islands are currently separated by a channel of 140 km in width and 145 m in depth, but bathymetric simulations suggest that these dimensions could have been greatly reduced during glacial periods. In particular, Robles *et al.* (2015) propose that Palawan and Borneo could have been connected during the Middle Pleistocene (either ca. 440 ka, during MIS 12, or ca. 630 ka, during MIS 16). In terms of biodiversity, Palawan is thus expected to share more affinities with Borneo and other regions on the Sunda Shelf than with the rest of the Philippines. While Palawan does harbour some fauna similar to that of Borneo, a significant proportion of its numerous endemic animal species are actually phylogenetically closer to those in the oceanic part of the Philippine archipelago; its zoological biodiversity appears to be a potpourri of ancient dispersals from neighbouring Philippine islands, other old taxa, recent [mammal] dispersals from Borneo, and local endemism (Brown and Diesmos, 2009; Corlett, 2014). Palawan's highly diverse flora is also more similar to that of the Philippines than to that of Borneo (van Welzen *et al.*, 2011).

Today, the diversity of Palawan's flora and fauna extends beyond its terrestrial ecosystems to its coasts and waters. The Province of Palawan, composed of the main island plus smaller clusters of neighbouring islands along with the surrounding waters, is notably home to 44,500 ha of mangrove forests that count 31 species—the widest such cover in the Philippines. Numerous species of coral, birds, freshwater fish, amphibians, and reptiles, as well as several marine mammals, populate the province. Additionally, Palawan is home to at least 57 ethnolinguistic groups of which several are indigenous, like the Batak, the Cuyunon, the Tagbanwa, and the Pala'wan (including the Tau't Batu, some of whom still live in caves today). This richness has led to the declaration of the province as a Man and Biosphere Reserve by UNESCO in 1990 (UNESCO, 2013).

2.1.2. Lipuun Point

Lipuun Point is part of the southwestern Palawan municipality of Quezon, whose centre (*poblacion*) is situated across Malanut Bay to the southeast (Figure 13). It is bounded on the north by the South China Sea, on the east by Nakoda Bay, and on the west by Malanut Bay. To the south and southwest, thick mangrove forests border an isthmus that forms a bridge to the Palawan mainland.

Lipuun Point is composed of mid-Miocene limestone domes, reaching as high as 210 m above sea level and flanked by steep ravines. The entire area is blanketed in lush tropical forest that often conceals cave mouths (Figure 14). Among those that have been explored, many have yielded numerous archaeological remains, including human fossils, stone tools, ceramics, and mortuary objects (in shell, jade, bronze, iron, copper, glass, gold, and carnelian). This rich diversity of materials covers various periods from the Late Pleistocene to the earliest contacts with ancient China during the Song Dynasty and indicates a long history of human presence in the area. Additionally, the mosaic of environments that compose Lipuun Point is home to thriving biodiversity. Its caves, jungles, coasts, and waters host unique and fragile flora and fauna, in part due to the confluence of contrasting ecosystems.

In recognition of its outstanding prehistoric and natural value, authorities took various measures to protect the area. Together with the Tabon Caves Complex, Lipuun Point and its environs, covering 138 ha, were declared a 'Site Museum Reservation' on 11 April 1972 by virtue of Presidential Proclamation No. 996 (Office of the President of the Philippines, 1972).

Additionally, since 2006, they have been on the UNESCO Tentative List of the Republic of the Philippines for future nomination to the World Heritage List (UNESCO World Heritage Centre, 2018).

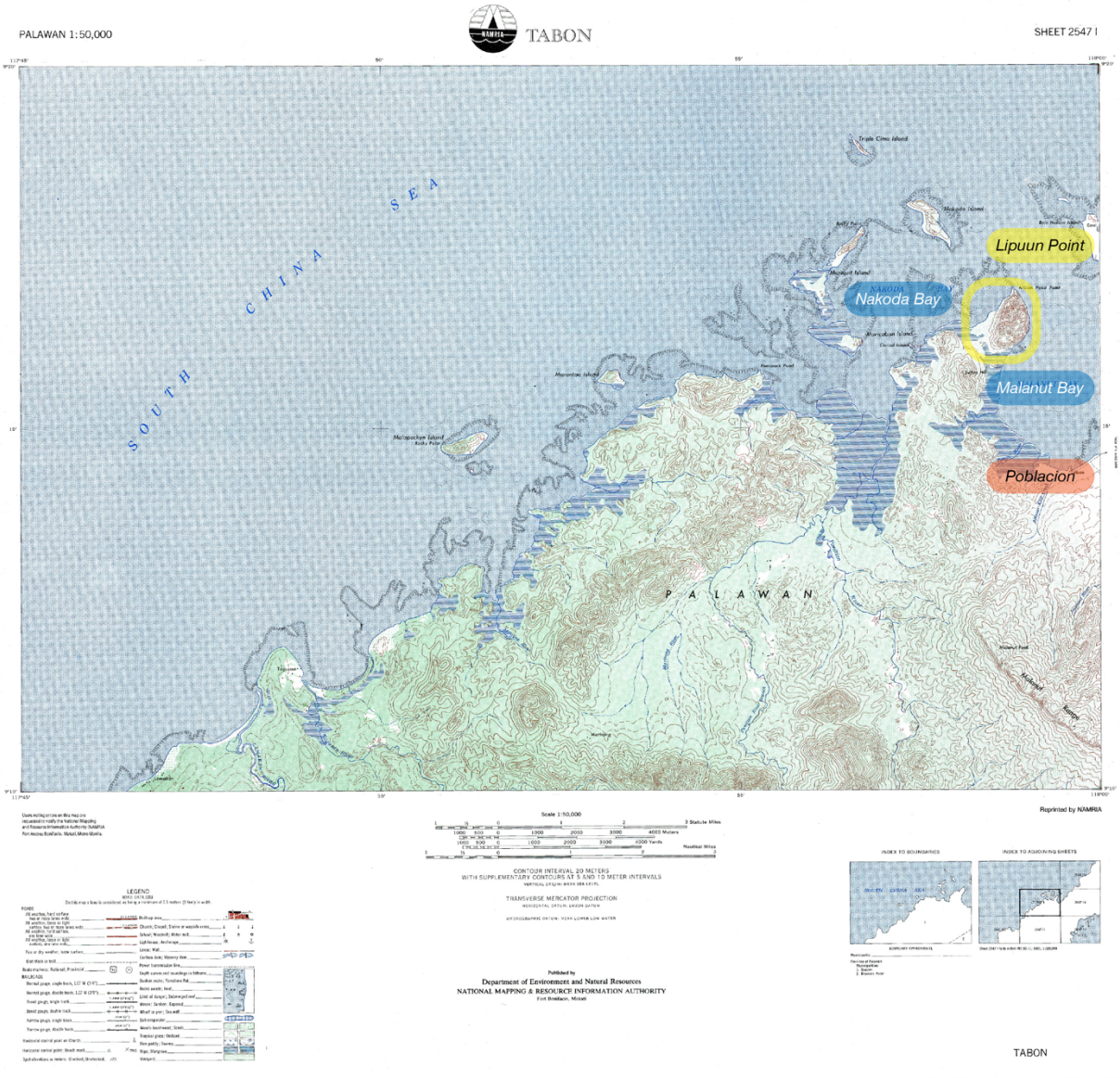

Figure 13. A topographical map of the Quezon area showing the location of Lipuun Point (formerly indicated as 'Albion Head Point'). Annotations added by the author to the original map prepared by the National Mapping and Resource Information Authority (NAMRIA), Department of Environment and Natural Resources (DENR), Republic of the Philippines.

Figure 14. Lipuun Point as seen from the South China Sea. Many of the cave openings are veiled in vegetation. Photo by Yōsuke Kaifu.

2.1.3. Archaeology

The area around Lipuun Point and Quezon is relatively rich in archaeological sites, a phenomenon that Fox attributes to several factors. First, the topography facilitates movement from the east coast of Palawan to the west (and vice versa), elsewhere complicated by the mountain range that runs along the spine of the island. Around Quezon, the mountains give way to hills and lowlands that are easier to cross (Fox, 1970: 11). Additionally, the landscape is favourable to hunting and gathering. Concerning aquatic resources in particular, the rivers that criss-cross the area and the bays shielded by reefs and islands represent relatively accessible sources of food, notably shellfish (Fox, 1970: 11–13). Finally, the caves and rock shelters that honeycomb the limestone formations of the area lend themselves naturally to habitation, while at the same time finding later [re]use as burial sites. The bats (and other cave fauna) that populate them also serve as another important food resource: their consumption in Tabon Cave was documented by Fox and continues in contemporary times among mountain groups in the area (Fox, 1970: 13).

Of the approximately 215 caves and rock shelters that compose the Tabon Caves Complex, there are 38 that have been explored and recognized to have archaeological and anthropological significance (National Museum of the Philippines, 2014); several of these are presented in Figure 15.

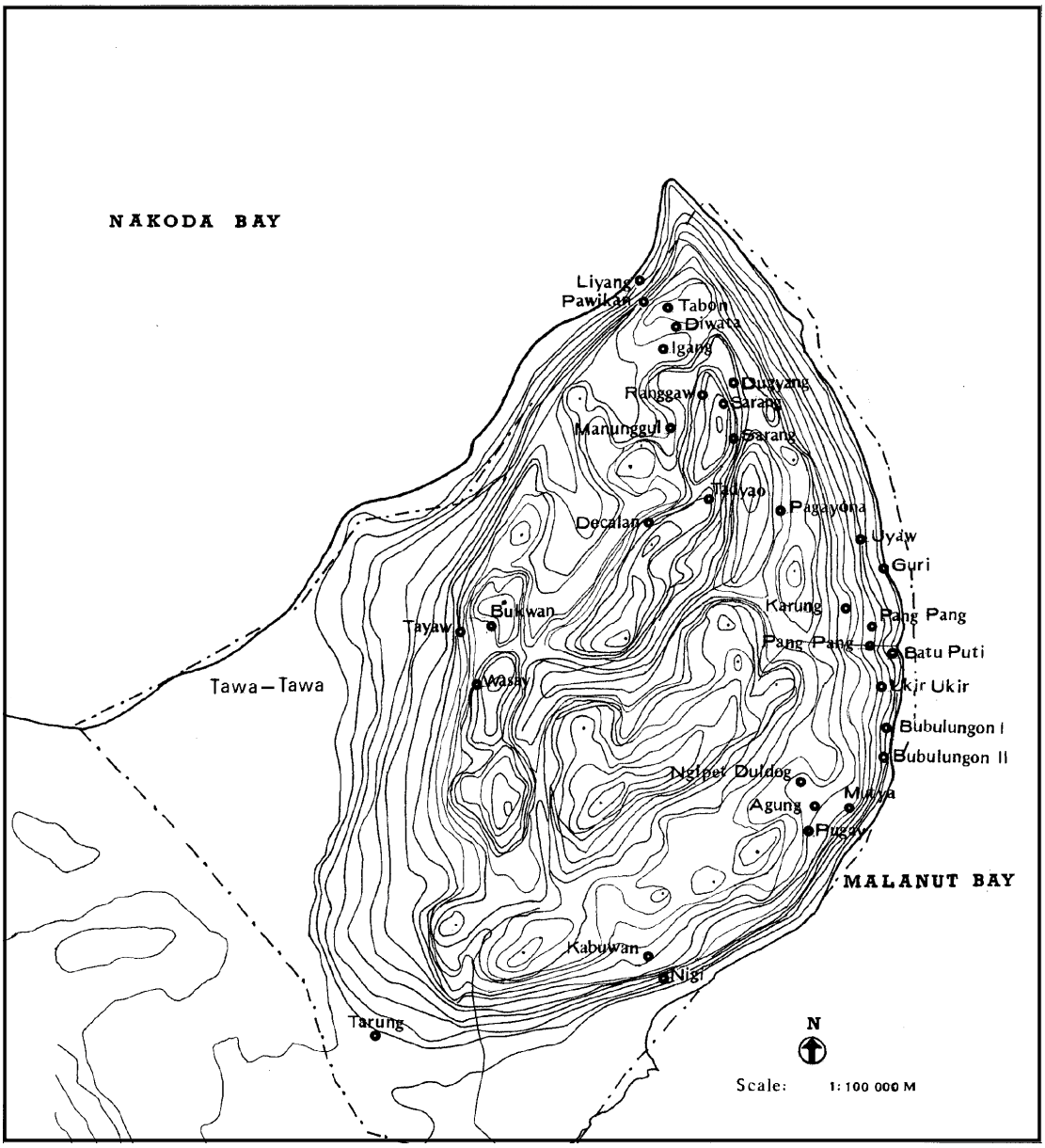

Figure 15. A simplified topographic map of Lipuun Point showing some of the caves identified to have archaeological/anthropological value (Bautista, 2000).

Aside from Tabon, some of the caves where efforts were more concentrated include Diwata (containing Metal Age jar burials), Guri (containing flake and blade tools, as well as Early Metal Age jar burials), and Manunggul (containing Neolithic and Metal Age jar burials). Manunggul Cave is particularly renowned for the eponymous decorated burial jar, declared a

'National Cultural Treasure' by the National Museum of the Philippines, that embodies the prehistory of the archipelago in the Filipino imagination (Figure 16). The imagery of the jar lid, representing two anthropomorphic figures in a boat, is so striking that Fox chose it as the cover for the Tabon Caves monograph.

Figure 16. The Manunggul Jar on display at the National Museum of the Philippines. Photo by Jun Anteola.

The caves of the complex were, at various points in time, used for habitation and burial. The earliest traces of human presence are represented by flake tools, as well as human and faunal remains. These are followed by jar burials, dominant in the complex, then by Chinese tradeware ceramics (Fox, 1970: 8).

Zooming out of Lipuun Point, at least 35 archaeological caves and rock shelters were identified in eastern Quezon, where limestone formations can be found over an area of 30,000 ha (Fox, 1970: 9–10). Figure 17 illustrates some of these sites. Specific attention has been given to Duyong and Pilanduk Caves, near the mouth of the Iwahig River, around 11 km northeast of Lipuun Point by water. Duyong Cave contained a small flake-and-blade assemblage associated with marine and brackish-water shellfish, a Neolithic burial with various shell artefacts (including adzes-axes made from giant clam, *Tridacna gigas*), and over 5,000 bones of sea cow (order Sirenia; possibly *Dugong dugon*) (Fox, 1970: 54–62). Neighbouring Pilanduk Cave

also yielded flake tools associated with shells, a Neolithic axe, and burial jars (Fox, 1970: 65). In the general area, some of the more marked differences with Lipuun Point concerning archaeology include the presence of boat and log coffin burials, as well as evidence of more recent use by ancestors of the modern-day Pala'wan people (Fox, 1970: 11). Zooarchaeological research is currently being undertaken at Pilanduk Cave (J. Ochoa, *pers. comm.*).

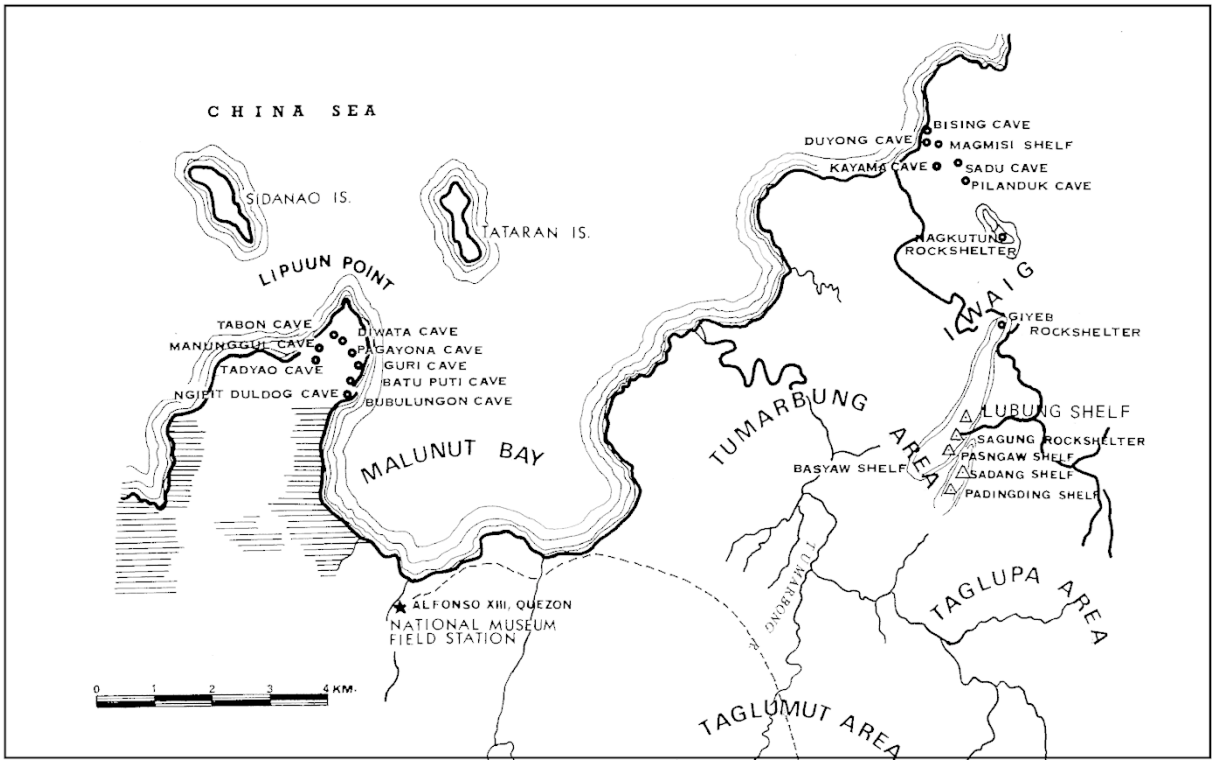

Figure 17. A simplified topographic map of Quezon showing some of the caves and rock shelters identified to have archaeological/anthropological value (Bautista, 2000).

2.2. Tabon Cave

2.2.1. Description and layout

Tabon Cave is tucked into a limestone cliff in the northeastern part of Lipuun Point, opening out on to the South China Sea. Situated at 34 m above sea level, its mouth measures 8 m tall by 16 m wide. The cave consists of a spacious main chamber, measuring 40 m long by 20 m wide and oriented at 45° counterclockwise from geographic north (Figure 18). A smaller auxiliary chamber, informally called the 'diverticulum' and measuring 16 m long by 4 m wide, is situated in the southwestern corner of the cave.

Figure 18. The main chamber of Tabon Cave. Photo by Maria Rebecca Ferras.

The main chamber features a number of stalactites and stalagmitic pillars, concentrated along the northeastern and southwestern walls. The front part of the cave is dry and well-lit; however, the back, including the diverticulum, is damp in certain areas. Several guano mounds are present in the main chamber, situated right under swiftlet roosts. The diverticulum, however, is currently populated by a bat colony.

The original excavation grid developed by Fox was simplified and updated in the 2000s (Figure 19). The grid divides the cave into a network of squares, each measuring 2 m by 2 m. Using the primary datum point that had been defined midway across the cave entrance (DP1),

a reference longitudinal line (in red) was drawn across the entire length of the cave. Vertical transects at intervals of 2 m were then laid to the left and to the right, respectively labelled E*n* and W*n*, where *n* starts from 1 and increases away from the reference longitudinal line. A reference latitudinal line was also drawn horizontally through DP1, followed by horizontal transects at intervals of 2 m: these were labelled N*n* and S*n*, with *n* solely equivalent to 1 for N*n* and reaching up to 21 for S*n*.

2.2.2. Stratigraphy

As mentioned in Section 1.3.1, Tabon Cave is characterized by a rather complex stratigraphy, composed of numerous sub-sequences that do not always seem to be related. This section presents an overview of the profiles that were sampled for the present study. For simplicity, they are organized according to the following artificial division of the cave into three:

- the North Zone, covering transects S1 to S4;
- the Central Zone, covering transects S6 to S10; and
- the South Zone, covering transects S14 to S18.

These zones are illustrated in Figure 19.

For each profile, the different layers that were identified in the field are labelled downward from 1 to *n* and are discussed briefly. Since this presentation is purely descriptive, no attempts are made to establish links between layers across different profiles, whether or not they share the same number and/or description; the numbering is considered to be independent for each profile.

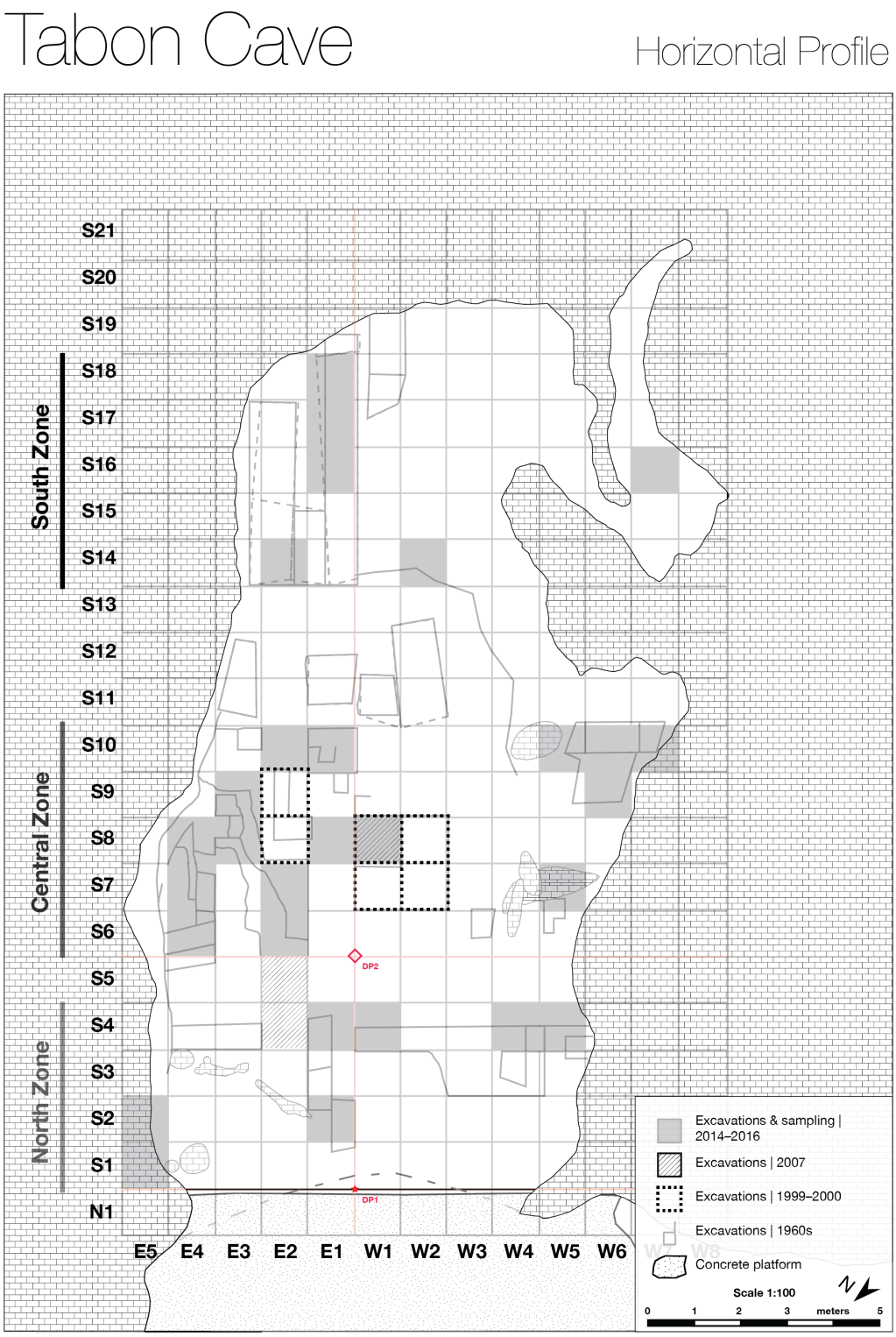

Figure 19. The updated excavation grid of Tabon Cave and the three zones defined for this study.

The North Zone: transects S1 to S4

Square S4E1

Figure 20 shows the vertical profile for the South Wall of Square S4E1. The sequence is composed of ten layers.

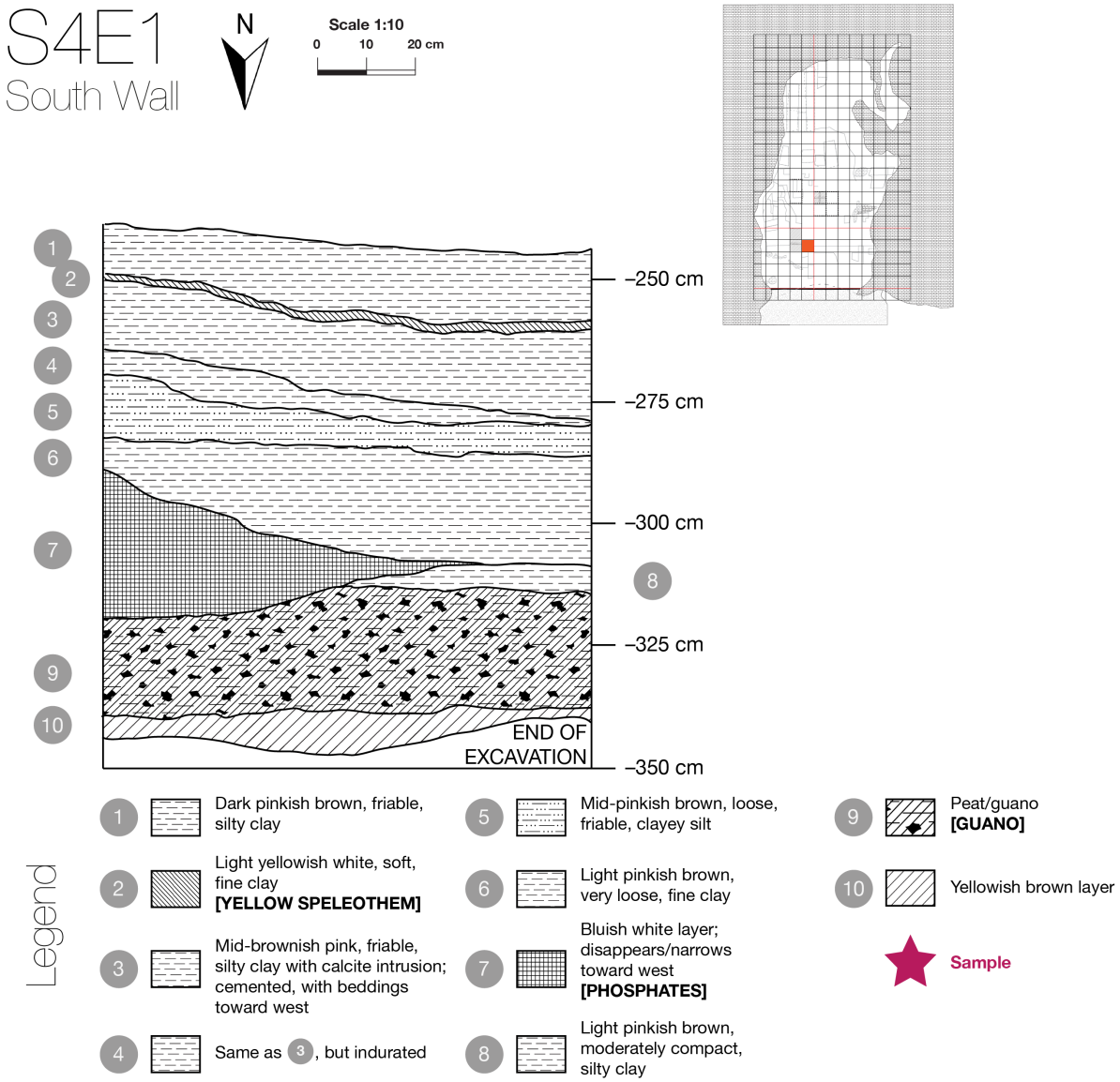

Figure 20. South Wall vertical profile for Square S4E1.

Layer 10, at the bottom, is a yellowish brown level. It is overlain by Layer 9, a guano deposit of consistently significant thickness (between 20 and 25 cm throughout). Layer 8 follows, a silty clay level of light pinkish brown colour that is moderately compact and is only visible on the western half of the profile. Above is Layer 7, a bluish white deposit that is likely composed of phosphates. It is more prominent on the east end of the profile this time (measuring up to

30 cm thick), narrowing out to disappear completely before reaching the west end. Up next, Layer 6 consists of fine, light pinkish brown clay that has a loose texture. Layer 5, composed of clayey silt, is also loose and friable, but is of mid-pinkish brown colour this time. In Layer 4, indurated silty clay of mid-brownish pink colour is cemented in certain areas, and beddings can be seen toward the western part. Calcite intrusions are also present. Layer 3 is similar to Layer 4 but is more friable. A soft, fine clay level of light yellowish white colour forms Layer 2, noteworthy for measuring only 3 cm thick. Finally, Layer 1 is a friable, silty clay deposit similar to Layer 3, but of dark pinkish brown colour this time.

Square S4W1

Figure 21 shows the vertical profile for the East Wall of Square S4W1. The sequence is composed of thirteen layers.

At the bottom, the very compact, white/grey level representing Layer 13 is characterized by laminations, which are present throughout the sequence. Atop Layer 13, very fine gravels of light pinkish brown colour form the very compact Layer 12. Some calcite may have been deposited in the layer. Just above, the similarly compact, pinkish fine sand of Layer 11 has an appearance suggestive of laminar deposition. Layer 10 is also very compact, but it is composed of relatively wet silt with a dark brown colour instead and is possibly composed of, or may contain, calcite. Layer 9 recalls Layer 11 with its very compact, laminated sediments of pinkish white colour, measuring between 20 to 30 cm thick. Less compact sediments form Layer 8, of brownish grey colour. Layer 7 follows, a thick (25 to 30 cm) and compact grey-white deposit pockmarked by lenses of fine sand. Next is Layer 6, a transition level composed of dark brown clay that is possibly influenced by percolation from Layer 5 above, which is a significant (20 cm) guano accumulation of a very dark black colour. Layer 4 is another thick (20 to 25 cm) level whose compact texture seems to be due to the aggregation of very fine sand into very fine gravel. It also appears to be moist. Layer 3 shares similarities with Layer 4, but the very fine sand of yellowish white colour that constitutes it is loose and dry instead. Layer 2, of possible sulphatic origin, is also principally yellowish white in colour, although it contains some very fine pinkish sand. Finally, Layer 1 at the top is a thick (30 cm) mix of compact, laminated soil and very fine pink sand, recalling Layers 9 and 11.

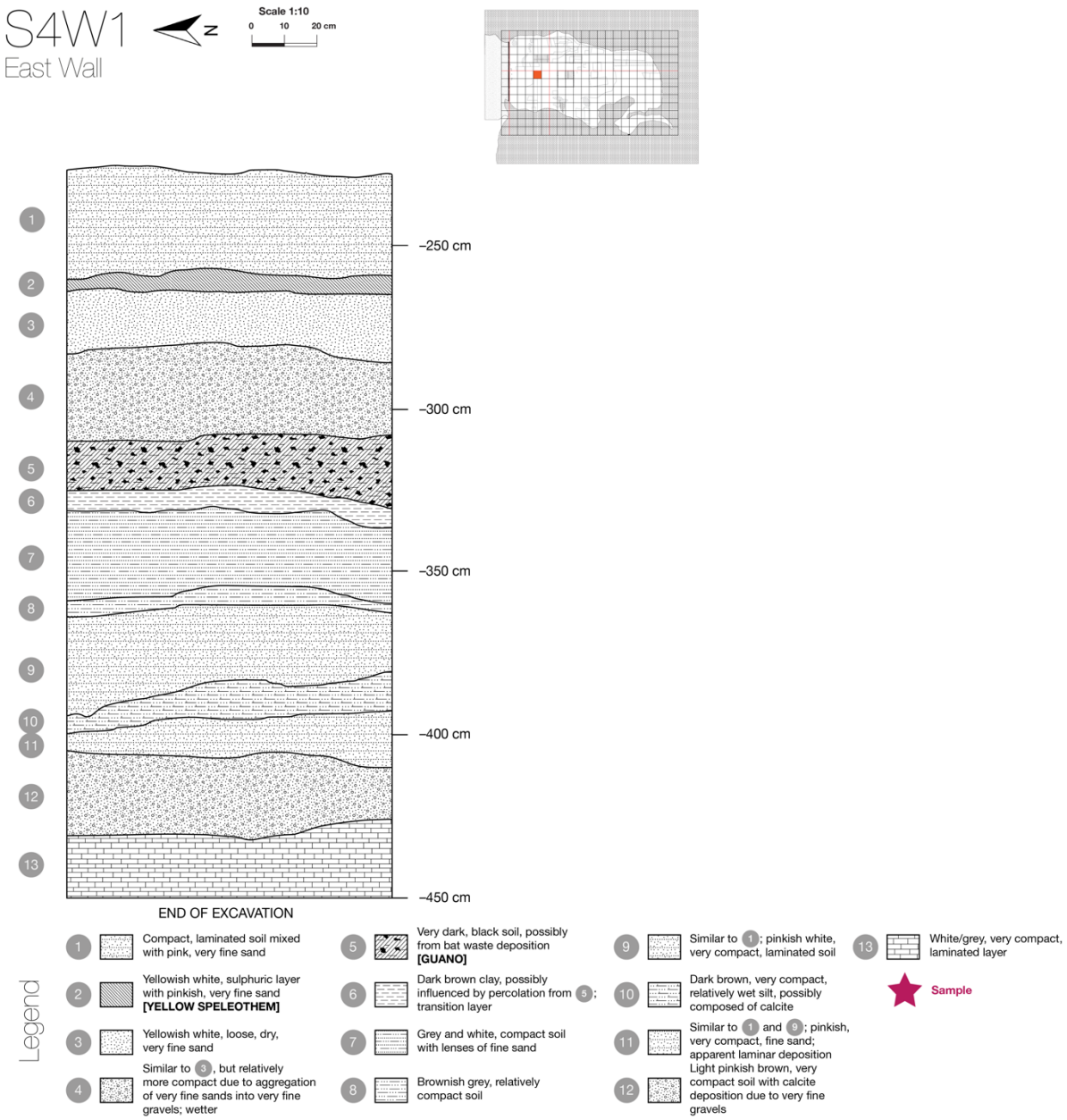

Figure 21. East Wall vertical profile for Square S4W1.

Squares S4W3 to S4W4

Figure 22 shows the vertical profile for the South Wall of Squares S4W3 to S4W4. The sequence is composed of eight layers.

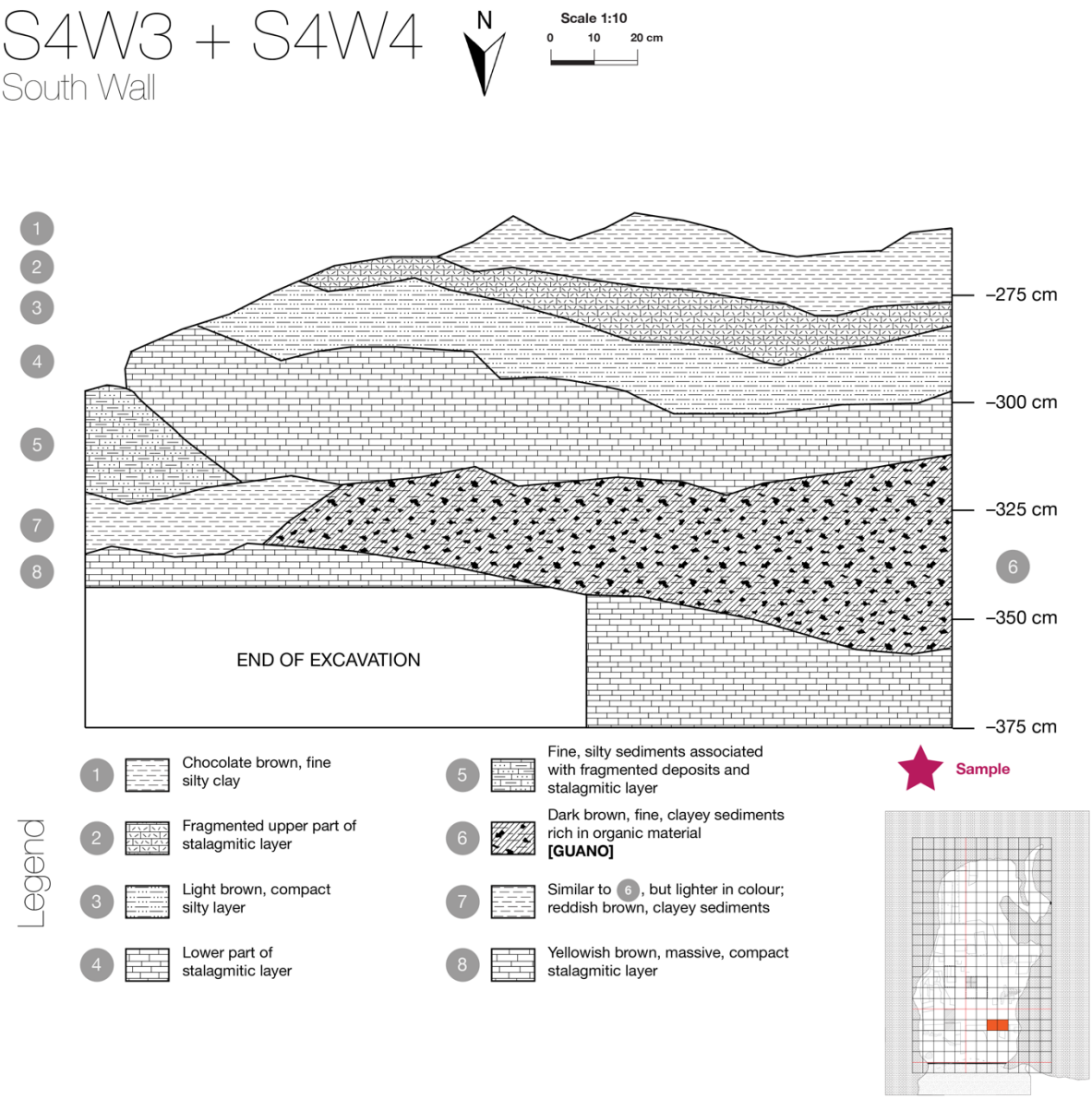

Figure 22. South Wall vertical profile for Squares S4W3 to S4W4.

The deepest excavated level is Layer 8, a massive and compact stalagmitic floor of yellowish brown colour. On top are clayey sediments that are light reddish brown toward the east (Layer 7) while being dark brown, very fine, and rich in organic matter in the greater western half—likely a guano deposit (Layer 6). It is particularly thick on the west end of the profile, measuring almost 50 cm. Above Layer 7 is Layer 5, consisting of fine, silty sediments and fragmented material that mesh into another stalagmitic floor to the west, Layer 4. The stalagmitic floor is covered by the compact, light brown silt of Layer 3. This is in turn covered by yet another stalagmitic floor, Layer 2, which is nevertheless more fragmented than Layer 4. The sequence is capped off by fine, silty clay of a chocolate brown colour forming Layer 1.

Square S4W5

Figure 23 shows the vertical profile for the West Wall of Square S4W5. The sequence is only composed of two layers: Layer 2 consists of fine, white gravel, whereas Layer 1 is a very wet silt level of dark brown colour that contains some microfaunal remains.

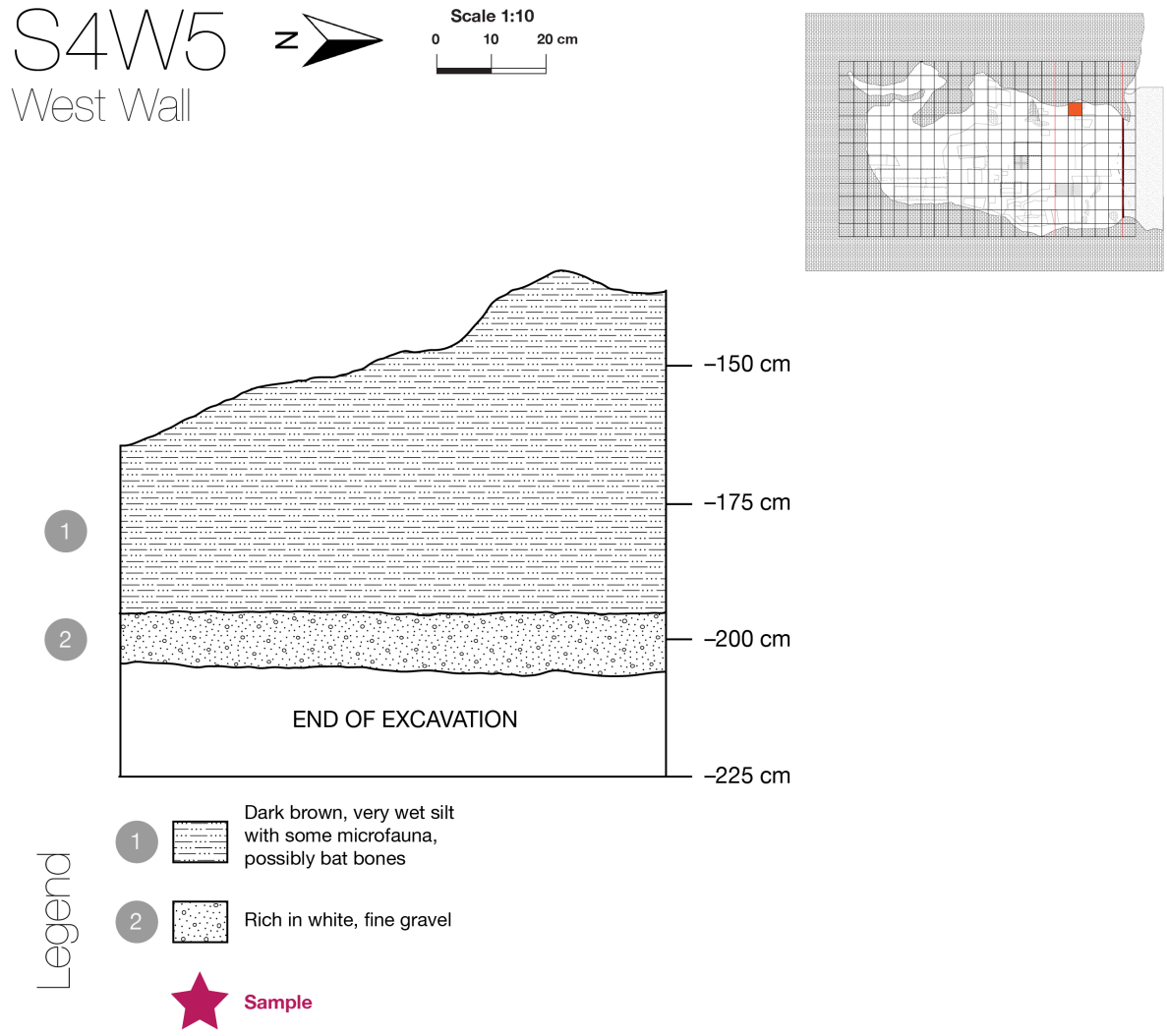

Figure 23. West Wall vertical profile for Square S4W5.

The Central Zone: transects S6 to S10

Squares S6E2 to S7E2

Figure 24 shows the vertical profile for the East Wall of Squares S6E2 to S7E2. The sequence is composed of eleven layers.

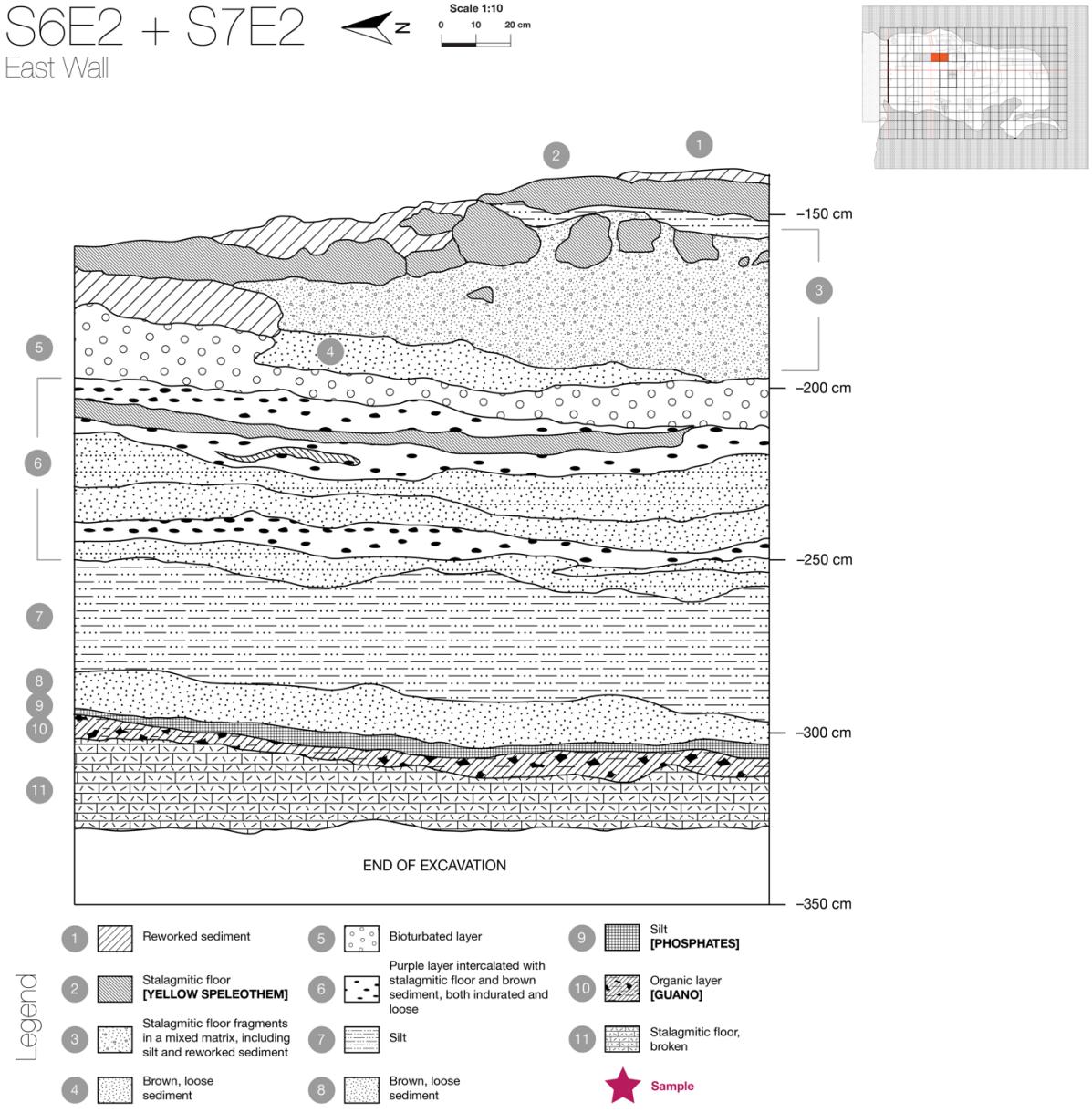

Figure 24. East Wall vertical profile for Squares S6E2 to S7E2.

At the bottom of the excavated profile is Layer 11, a broken stalagmitic floor. It is overlain by a layer of apparent organic nature interpreted to be guano, Layer 10. Immediately above is a white, phosphatic layer of silty texture, Layer 9. Next is Layer 8, consisting of brown, loose sediment, while the thicker Layer 7 is composed of silt. Layer 6 is an extremely complex layer

with multiple facies: it is essentially an intercalation of purple sub-layers with a yellowish stalagmitic floor, combined with variably indurated and loose brown sediment. On top of Layer 6 is Layer 5, characterized by visible traces of bioturbation. The brown, loose sediment of Layer 4, recalling Layer 8, overlies Layer 5. The top of the sequence is characterized by a certain degree of interweaving between Layers 3, 2, and 1: Layer 3 is a mix of fragments from the yellowish stalagmitic floor Layer 2 (similar to that seen in Layer 6), reworked sediment from Layer 1, and silt.

Square S6E4

Figure 25 shows the vertical profile for the North Wall of Square S6E4. The sequence is composed of twelve layers.

Layer 12, at the bottom, is a very compact, grey-coloured level, possibly consisting of rock or the cave structure itself, given the proximity of the square to the cave walls. Layer 11 is composed of pinkish white sediment with very fine gravel and mineral inclusions. Particle size is smaller in Layer 10, composed of very fine, light brown silt, but apparent mineral inclusions are still present. The yellowish brown, similarly very fine silt of Layer 9 comes on top. Like the two layers below it, Layer 8 is also characterized by very fine silt, but is of dark brown colour and corresponds to a guano deposit. Layer 7 above is, again, composed of very fine silt which nevertheless consist of white phosphates this time. Interlaced with it is the relatively loose, pinkish brown clay of Layer 6. Layer 5 is also pinkish in hue but yellow in colour, and in contrast with Layer 6, it is very compact and features laminations. Layer 4 is the first level in the sequence with heterogeneous particle sizes—very fine silt and soil gravels are mixed, forming a pinkish white deposit. Somewhat recalling Layer 5, Layer 3 is also very compact and laminated, although it is pinkish brown rather than pinkish yellow. The texture alternation continues, with Layer 2 consisting of relatively loose and very fine sand-/silt-sized particles of yellowish brown colour. Finally, the top of the sequence is represented by the grey and compact Layer 1, characterized by very fine gravel peppered with ‘pores’ that probably reflect bioturbation.

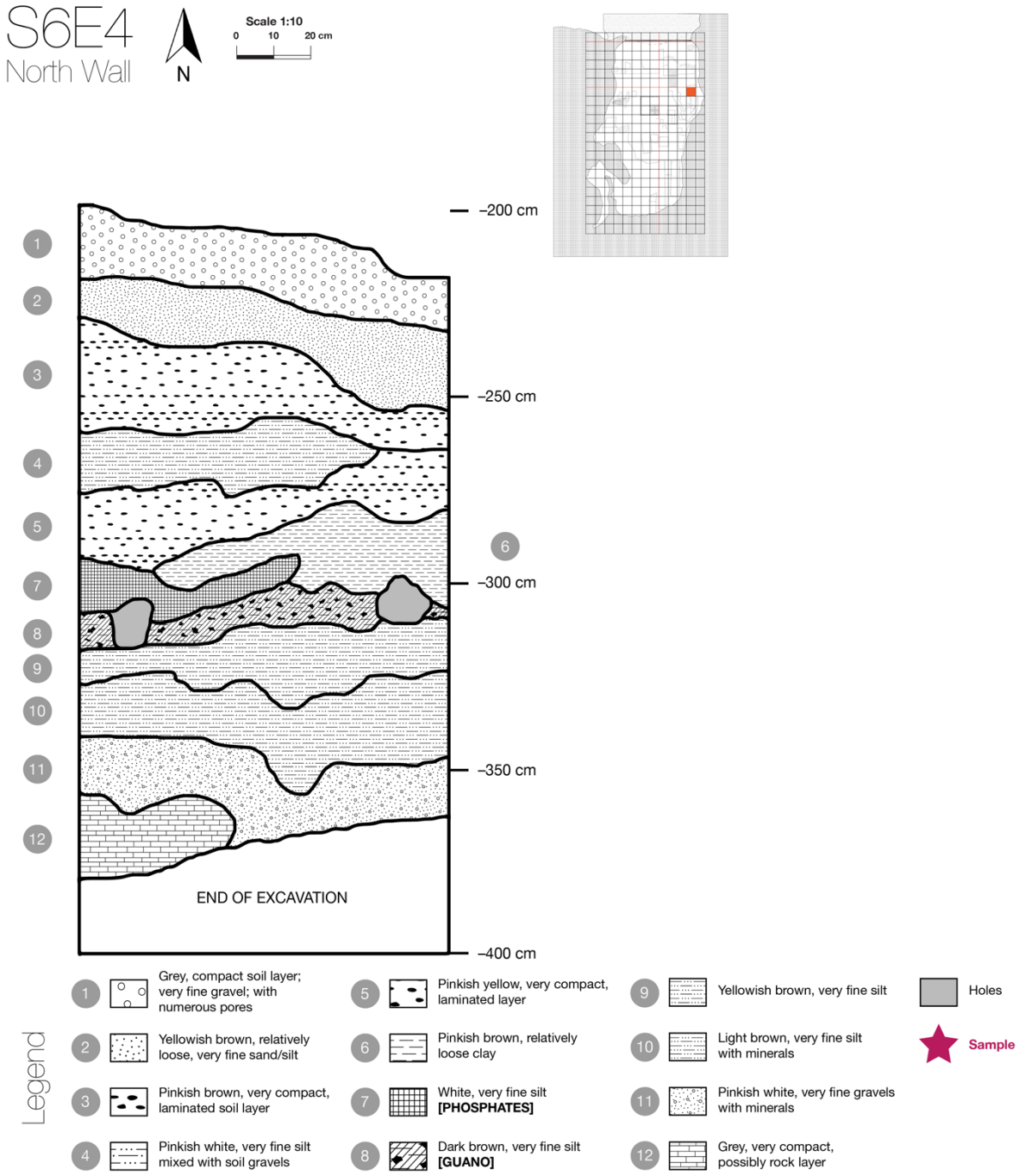

Figure 25. North Wall vertical profile for Square S6E4.

Squares S7E4 to S8E4

Figure 26 shows the vertical profile for the East Wall of Squares S7E4 to S8E4. The sequence is composed of nine layers.

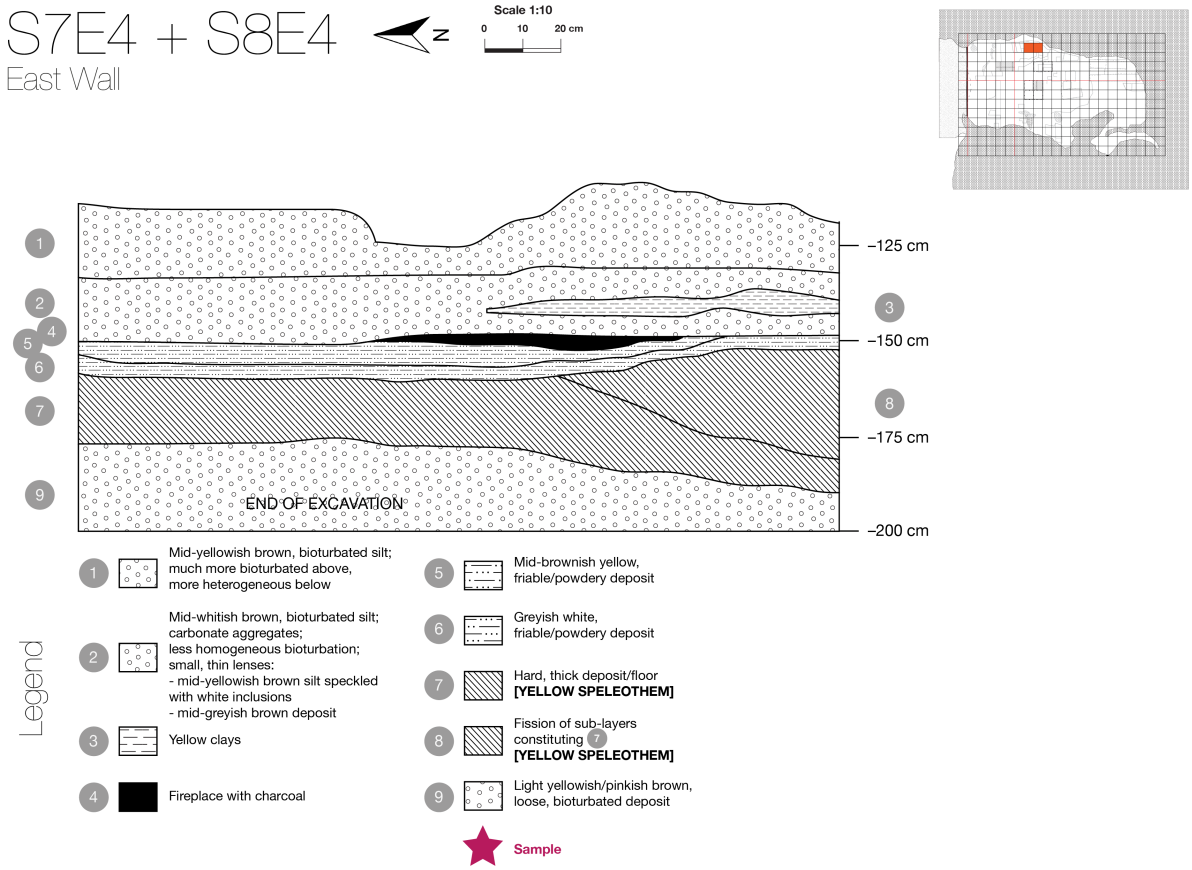

Figure 26. East Wall vertical profile for Squares S7E4 to S8E4.

The base of the currently visible profile, Layer 9, is a loose, light yellowish/pinkish brown deposit with traces of bioturbation. It is overlain by Layers 8 and 7, which form a hard, thick floor; Layer 8 represents the fission of Layer 7 into numerous sub-layers. Above this floor are Layers 6 and 5, friable deposits with a powdery texture that only differ in colour (greyish white for Layer 6, and mid-brownish yellow for Layer 5). In the centre of the profile and just atop Layer 5 is Layer 4, a charcoal-bearing fireplace that is one of the rare, stratigraphically-intact archaeological features in the cave. Layer 3 is a yellow clay lens that pierces Layer 2, a mid-whitish brown deposit of heterogeneously bioturbated silt. Layer 2 contains apparent carbonate aggregates and other smaller, thinner lenses: one of mid-yellowish brown silt speckled with white inclusions, and another of mid-greyish brown colour. Finally, mid-yellowish brown Layer 1 also consists of bioturbated silt, with bioturbation being particularly pronounced toward the top.

Squares S8E1 to S9E1

Figure 27 shows the vertical profile for the West Wall of Square S8E1 to S9E1. The sequence is composed of ten layers. A hard, stalagmitic floor, Layer 10, forms the base of the excavated sequence. It is overlain by Layer 9, a black, organic guano layer. Layer 8 consists of brown clay and covers the greater northern half of Layer 9. Just above are the loose, white phosphatic sediments of Layer 7. Layer 6, next on top, is another brown clay level that recalls Layer 8. The remaining layers are, for the most part, stalagmitic floors of varying colours and textures. Layer 5 consists of pink sediments and resembles an altered floor. Layer 4 is another stalagmitic floor, but it is notably hard and laminated, while Layer 3 above is again loose and altered. The brown sediments of Layer 2 are also loose and vary in hue from yellowish to pinkish. They interrupt the sequence of floors before it ends with another hard, laminated deposit in the form of Layer 1.

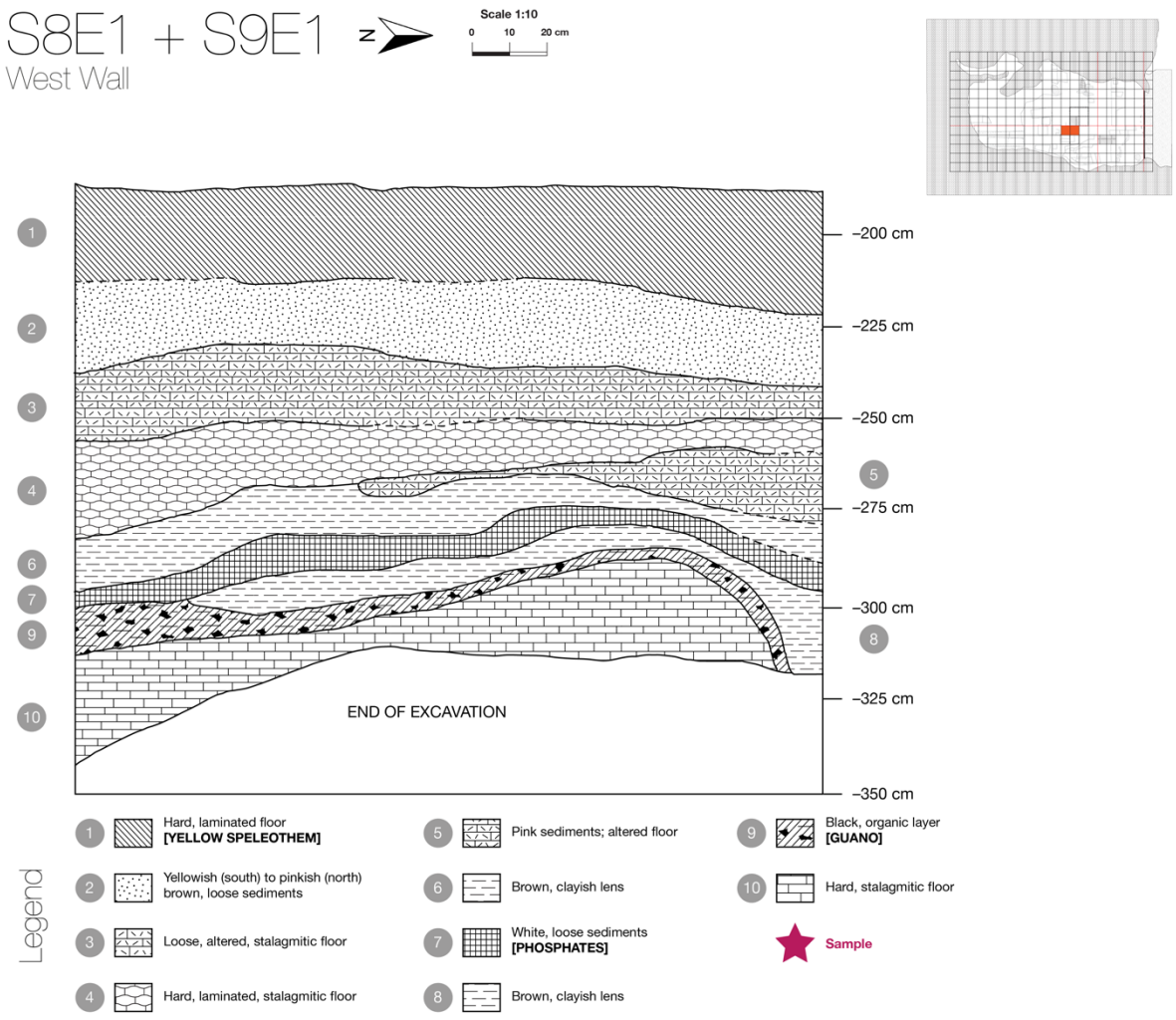

Figure 27. West Wall vertical profile for Square S8E1 to S9E1.

Square S9E3

Figure 28 shows the vertical profile for the East Wall of Square S9E3. The sequence is composed of twelve layers.

Layer 12, a loose, dark brown guano deposit of silty texture, is nearly invisible at the bottom of the profile. It is covered by the loose, light brown silt of Layer 11. This deposit is in turn overlain by the white (almost chalk-like) and very loose phosphatic, sandy silt of Layer 10. Just above, Layer 9 provides a sharp contrast with its compact silty gravel of pinkish yellow colour. Layer 8 brings back the loose textures seen in the lower part of the profile with its light yellowish brown sediment composed of dry, sandy silt. However, compactness returns in Layer 7, characterized by a thick (almost 50 cm in places), pinkish white, floor-like deposit that could be calcareous. Layer 6 above is again composed of dry, very loose silt recalling Layer 8, but it has a finer, more powdery texture. Layer 5 is a moderately thick (around 30 cm), yellowish white speleothem deposit. Layer 4 on top is similar, but is more compact and has characteristic, alternating blackish grey and yellow bands laminated together. Layer 3 brings a change in texture, with loose and dry fine sand bearing white calcitic inclusions. The two deposits that complete the sequence, Layers 2 and 1, are both characterized by a mid-purplish brown colour and consist of compact, sandy silt; however, Layer 1 has 'pores' that are most likely due to bioturbation.

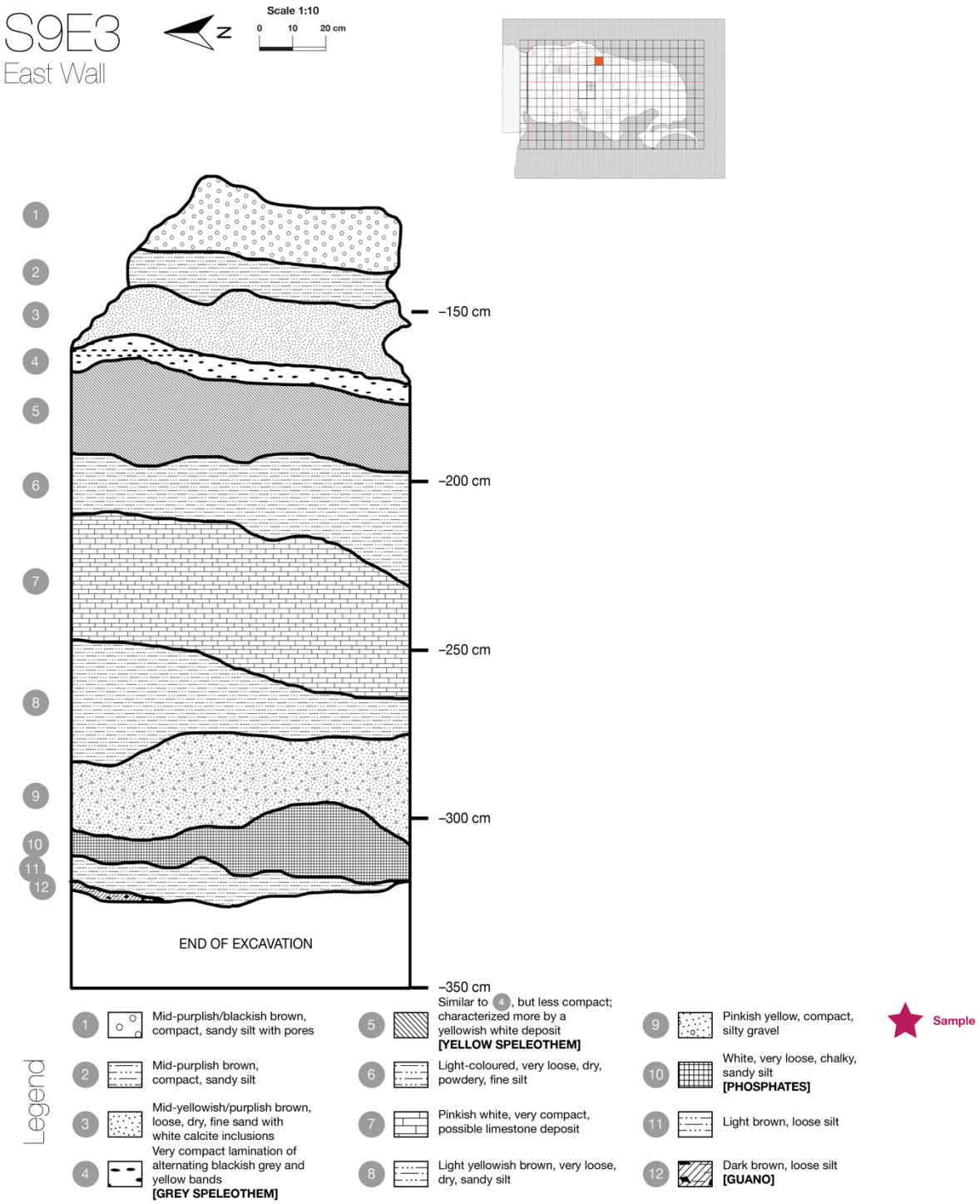

Figure 28. East Wall vertical profile for Square S9E3.

Square S10E1

Figure 29 shows the vertical profile for the South Wall of Square S10E1. The sequence is composed of sixteen layers.

No description is currently available for the deepest level of the sequence, Layer 16. Layers 15 and 13 consist of yellowish brown clay, separated by a lamination/concretion in the form of Layer 14. Layers 12 and 11 are thick (each measuring approximately 50 cm), indurated guano deposits, with Layer 12 featuring a green patina. Layer 10 is a thinner and looser guano deposit of brownish black colour, overlain by the white phosphates of Layer 9. The upper half of the sequence features several stalagmitic deposits, starting with the weathered limestone of Layer 8 (of significant thickness, at around 30 cm). This is overlain by a pinkish, altered guano deposit in the form of Layer 7. Another limestone layer takes over as Layer 6. Layer 5 is somewhat similar to Layer 7, consisting of pinkish brown clay mixed with guano. Layer 4 is yet another weathered limestone deposit, not unlike Layer 8. On top of it is Layer 3, a yellowish brown silty clay deposit. Layers 2 and 1 top off the sequence, with Layer 2 composed of laminated silt and Layer 1 being another weathered limestone deposit.

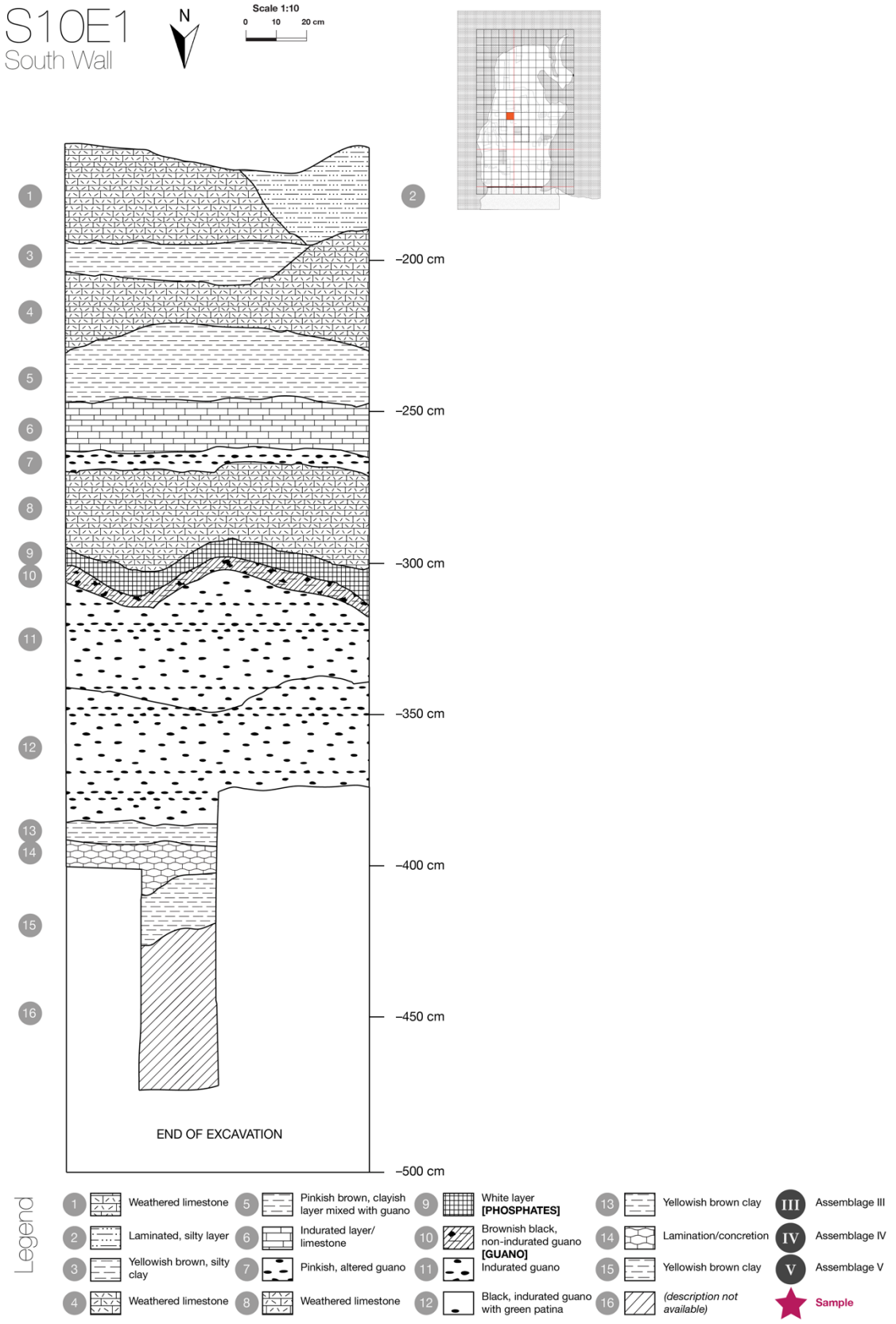

Figure 29. South Wall vertical profile for Square S10E1.

The South Zone: transects S14 to S18

In the South Zone, working names exist for two study areas and are used here for simplicity. These two areas refer to Squares S16E1 to S18E1, collectively known as the South Trench; and Square S16W7, located in the small southwestern chamber known as the diverticulum.

The South Trench

The South Trench is an excavation pit located at the very back of Tabon Cave and oriented along its longitudinal axis. It was originally excavated by Fox and forms part of the main longitudinal profile of the cave, which ran all the way down the centre line from the back to the entrance. (The profile is called 'Longitudinal L C' and conserved in the Fox documentary archives at the University of the Philippines in Baguio (Corny 2008).) The trench measures almost four meters deep and is characterized by a relatively straightforward vertical profile, in stark opposition to the central zones of the cave. The profile, as represented by the south wall of the trench, is presented in Figure 30 below. Previous descriptive work on this profile was conducted by X. Gallet (2012), in conjunction with J. Corny and F. Sémah, within the broader framework of the present study. Twelve layers were identified in the stratigraphic sequence and are labelled accordingly in the profile.

Layer 12, at the very bottom of the sequence, is the hard, partially weathered, and occasionally cavernous bedrock. Its exposed thickness varies from 20 to 50 cm. Concretions are present both atop and within the carbonate elements of the layer.

Layer 11 consists of light brown/ochre-coloured sediments that appear to be composed of particles in the silty clay textural class. It measures between 10 and 40 cm in thickness. The west part features zones in various shades of pink. The layer is primarily characterized by the presence of a very solid stalagmitic floor that is in direct contact with the bedrock. The floor is composed of several sub-layers that can be easily differentiated in certain areas.

Layer 10 is a thick (40 to 60 cm), compact level composed of fine black sediments that are likely to be guano. The lower part of the layer has a much darker hue than the upper part. Traces of bioturbation from the top going down are also visible (e.g. roots, burrows, wasp nests). Organic matter is abundant in the layer.

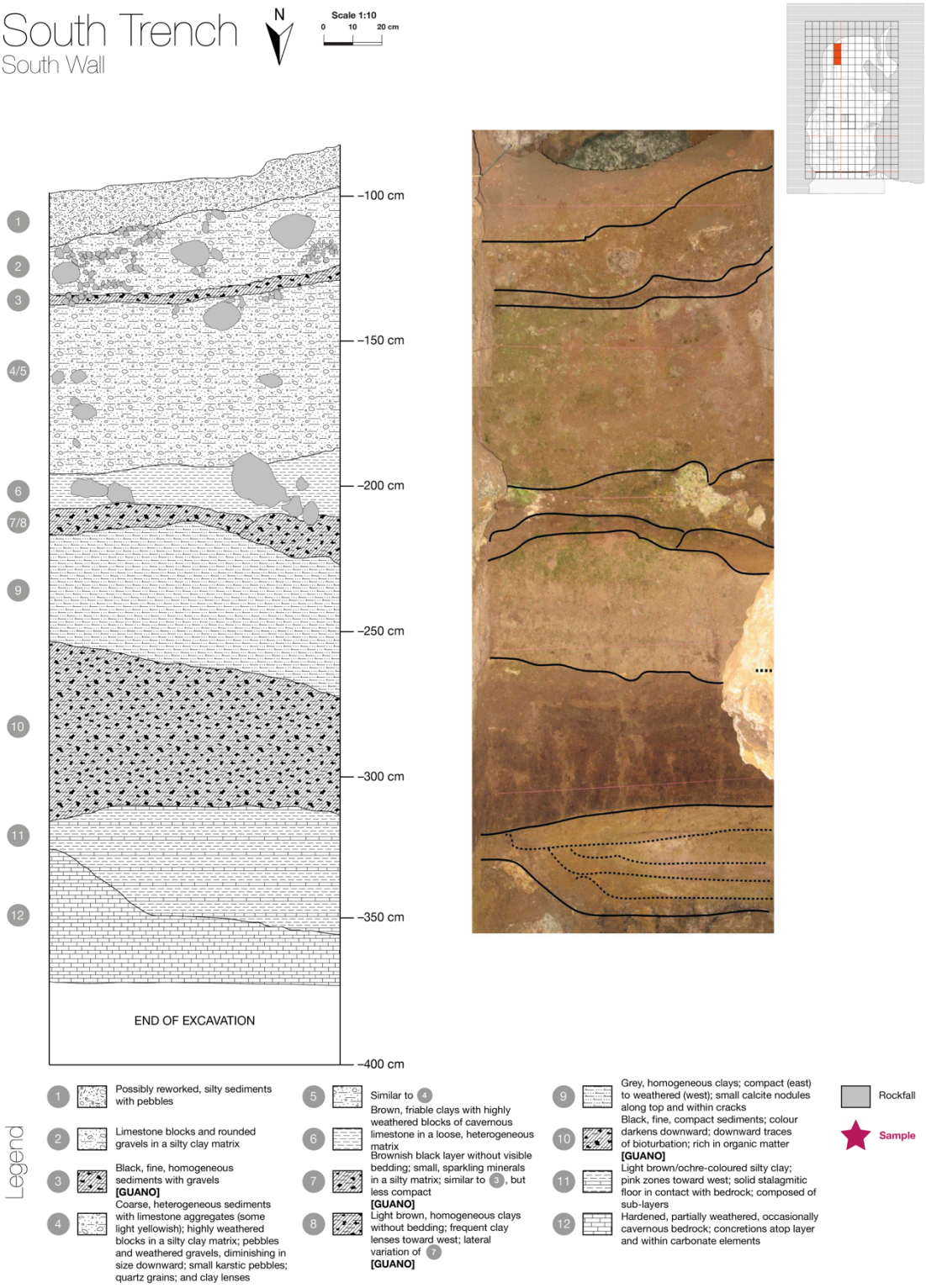

Figure 30. Vertical profile of the South Trench in Tabon Cave. The layer numbers are indicated on the left-hand side of the profile and are accompanied by their corresponding descriptions in the legend underneath. Photo from Gallet (2012).

Layer 9 corresponds to another thick level (40 to 50 cm), this time comprising grey and homogeneous clay-sized particles. Significant lateral variation is present: the clays appear more compact on the east wall, and more weathered on the west. Small calcite nodules are distributed across the top of the layer and within cracks.

Layer 8 is a thin level (10 to 20 cm) composed of light brown clays that are unbedded and homogeneous. Nevertheless, discoloured clay lenses increase in frequency toward the west wall of the trench.

Layer 7 is a brown-black level without visible bedding and appears to be another guano deposit. It measures about 10 cm in thickness. It consists of a silty matrix embedded with small, sparkling minerals, likely to be authigenic phosphates. Layer 8 seems to be a lateral variation of this layer.

Layer 6 is a loose, heterogeneous matrix measuring between 10 and 25 cm in thickness. It mixes friable, brown clays with highly weathered blocks of cavernous limestone.

Layers 4/5 form a thick (approximately 60 cm) level of coarse, heterogeneous sediments. The silty clay matrix features highly weathered blocks and limestone aggregates (some of which are light yellow in colour). Pebbles and weathered gravels (whose size diminishes progressively toward the top), small karstic pebbles, quartz grains, and some clay lenses are also present.

Layer 3 is composed of fine, homogeneous black sediments—a third guano level. It only spans a thickness of around 5 cm. It seems to be more compact than, but is otherwise similar to, Layer 7. Some gravel-sized elements are present.

Layer 2 is defined by a silty clay matrix featuring limestone blocks and rounded gravels. Its thickness runs between 15 and 25 cm.

Finally, Layer 1, at the top of the sequence, consists of reworked silty sediments with pebbles. The measured thickness at the time of vertical profile preparation varies from 15 to 20 cm.

The diverticulum

The diverticulum is a small chamber in the southwestern corner of the cave (Figure 31), accessible by crawling up through a narrow passage. No excavations have ever been conducted inside, and no profiles are available. The floor is wet and slippery, and like the general back area of the cave, the chamber is extremely humid. It is currently occupied by a bat colony (of unknown species).

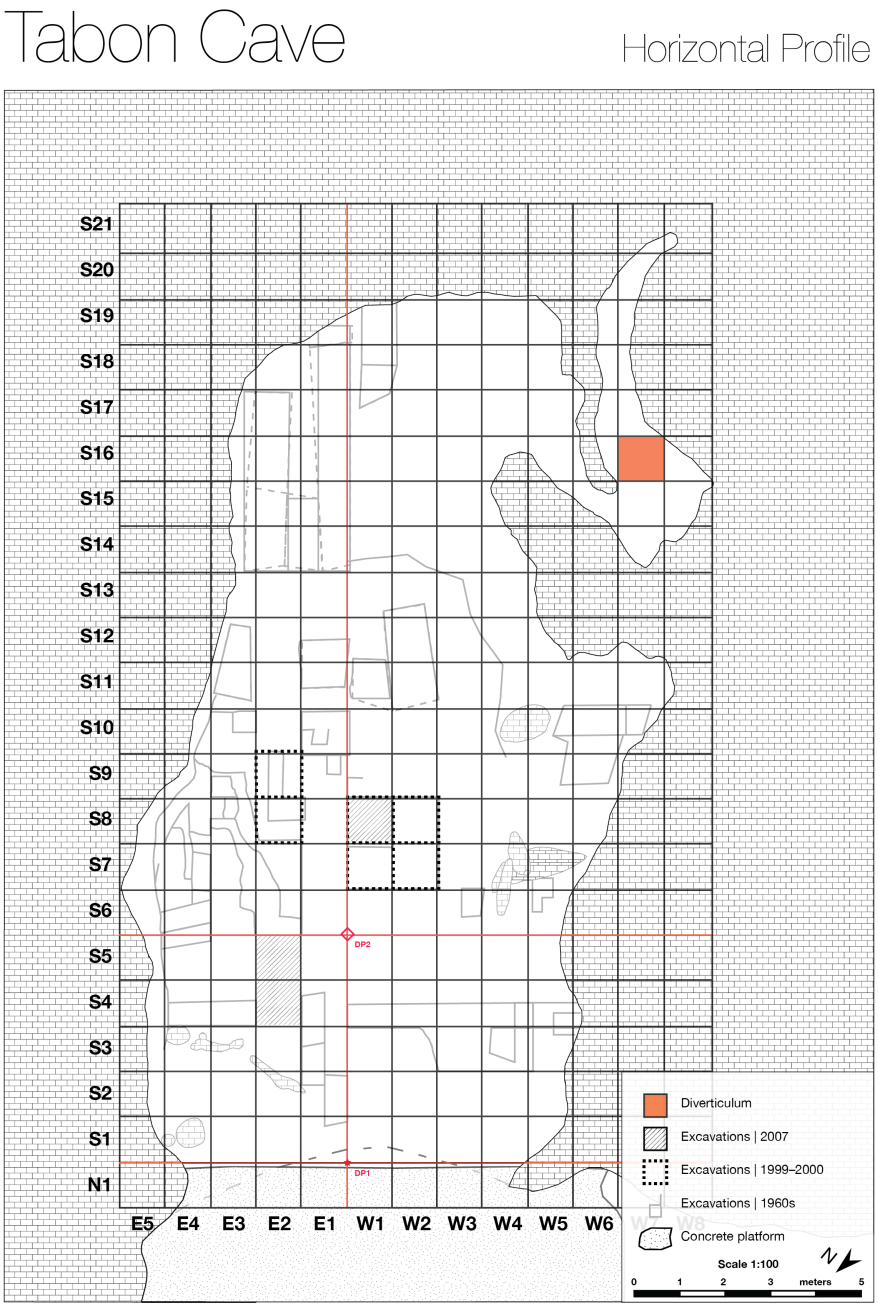

Figure 31. Location of the diverticulum in Tabon Cave.

2.2.3. Archaeology

Palaeoanthropology

Several studies have been conducted on the human fossils from Tabon Cave. Macintosh took the lead with his palaeoanthropological analysis of an almost complete mandible, with Barker providing dental analysis (Macintosh *et al.*, 1978); the study links the owner of the mandible to Australian aborigines, but doubts have since been cast on this finding (Dizon *et al.*, 2002). Additionally, collaboration between the National Museum of the Philippines and the Muséum national d'histoire naturelle in Paris, France have made possible further analyses and dating of both the original fossils, notably the frontal bone and several mandibular elements, as well as new ones (Dizon *et al.*, 2002; Dizon, 2003; Détroit *et al.*, 2004). One of these, a left mandibular fragment, has strange morphology: its shares many overall similarities with *Pongo*, but the third molar (M_3) and the socket of the fourth premolar (P_4) actually point to a large and remarkably robust *Homo* (notwithstanding the doubts surrounding the origin of the third molar) (Figure 32; Dizon *et al.*, 2002). Another one, a right mandibular fragment this time (identified by its accession number P-XIII-T-436 Sg19), has been more confidently attributed to modern *Homo sapiens* based on its morphology and dimensions (Figure 33; Dizon *et al.*, 2002). These studies provide the latest ages for the specimens while noting their considerable morphological variability and placing them in the context of the pre-Holocene human occupation of insular Southeast Asia.

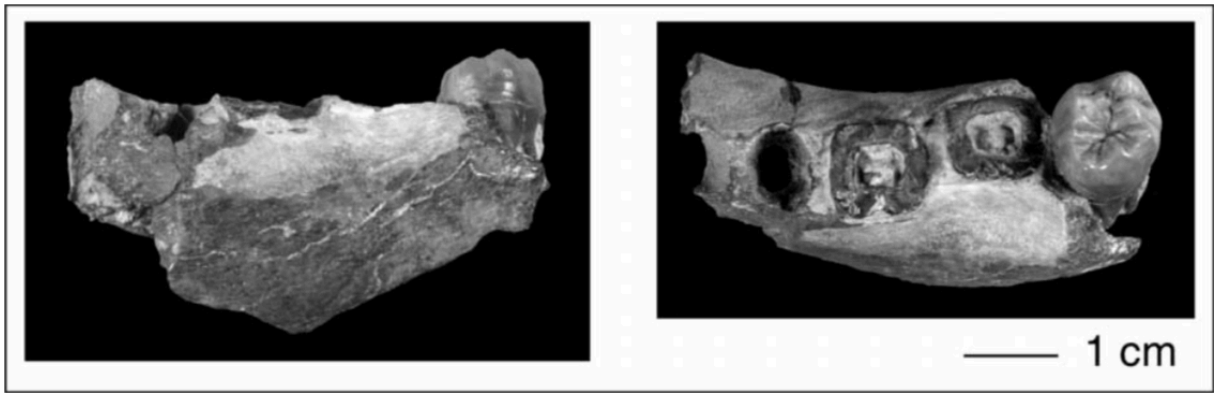

Figure 32. External and occlusal views of the left mandibular fragment with the third molar in wrong anatomical position (Dizon *et al.*, 2012).

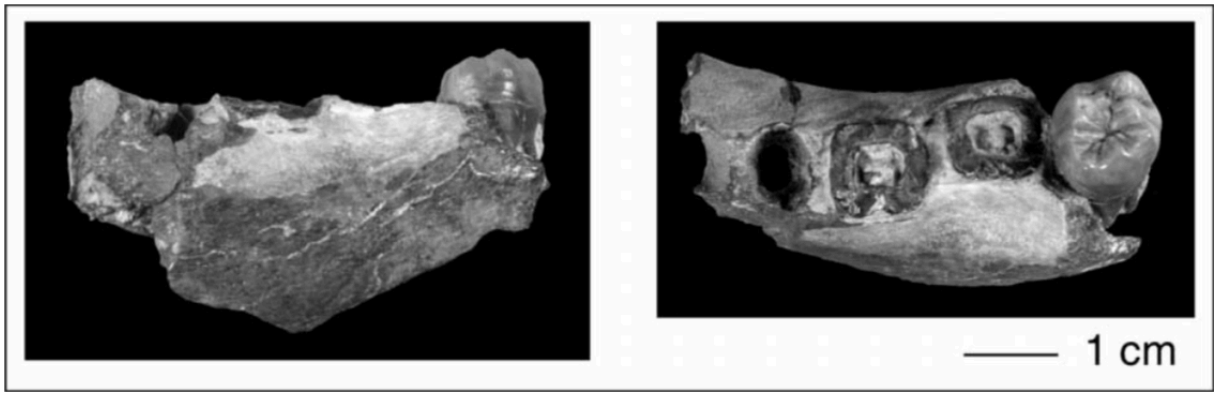

Figure 33. Internal and occlusal views of the right mandibular fragment (P-XIII-T-436 Sg19) (Dizon *et al.*, 2012).

Corny (2008) built on the abovementioned studies in carrying out GIS analysis of the entire collection of 3,857 archaeological materials excavated by Fox in the 1960s and applying this to 204 human bone remains representing a Minimum Number of Individuals (MNI) equivalent to 6 that feature wide morphological variability; these specimens were found in the reserves of the National Museum of the Philippines in 2002 and had heretofore been unstudied. He found that many of the bones were originally discovered in disturbed concentrations surrounded by potsherds, so to discriminate jar burial bones from older ones, he performed visual analysis based on criteria used by Fox, including colour and mineralisation. He places his conclusions in the context of the human occupation of the cave, which he describes as spanning three periods from the terminal Pleistocene to the late Holocene. In continuing analysis of the human remains from the National Museum reserves, it appeared that there were at least twice as many bones as previously thought (483 specimens; Corny, *et al.*, 2017). Study of this expanded collection, in particular through refitting, confirmed the initial finding that ancient human activity had an important taphonomic impact on the assemblage. Additionally, comparative morphometric analysis that includes 339 permanent first upper molars (UM1) confirmed previously cited results pointing to significant morphological variability. Specifically, two morphotypes appeared to surface from the assemblage: one characterized by large UM1 dimensions that exceed variability for submodern Southeast Asians, and another that is closer to the Philippine Negritos, a group with phenotypic similarities to African pygmy populations and who are present across the archipelago (Corny, *et al.*, 2017). One of the most exciting things about the collection is that, based on archival documents, a large part of it is likely to date to the Pleistocene, making it a valuable addition to the scant modern human fossil record for this period in Southeast Asia.

Finally, Cosalan (2017) revisited the frontal bone, this time in a comparative regional study using 3D geometric morphometrics. She concluded that the fossil is not only closely related to other Late Pleistocene specimens from the region (namely, China, South Asia, Australia, and Melanesia) and more recent Indonesian ones, but also shares certain morphological characteristics with some Manobo individuals, an Austronesian ethnolinguistic group in the southeastern Philippines with genetic ties to the Denisovans.

Lithics

Given the scarcity of faunal remains in Tabon Cave, its lithic industry plays an even greater role in understanding human behaviour for the site, and it has attracted the attention of a number of researchers. Fox himself (1970) identified and did preliminary description of the six flake assemblages briefly presented in Section 1.2.1, calling them I-A, I-B, II, III, IV, and V. Each of these assemblages was deemed to correspond to a distinct archaeological horizon. By noting their stratigraphical positions and obtaining ^{14}C ages on charcoal remains that most of them were associated with, Fox established the first tentative chronostratigraphy for Tabon Cave, thus cementing the key role that these assemblages play in the understanding of the cave's archaeology. This topic was later picked up by Corny (2008) who, as part of his study, localized and identified the flake assemblages defined by Fox. This enabled him to place them in his GIS analysis of Tabon Cave and use them as chrono-cultural indicators for the rest of the archaeological materials, thereby refining understanding of the cave's chronostratigraphy.

Later studies on the Tabon Cave lithic materials focused more on technology and use-wear, picking up on Fox's interpretation of the flakes as having been produced through direct percussion (Fox, 1970). Patole-Edoumba (2002; 2009), for example, carried out a typo-technological analysis of the artefacts from the upper layers (Flake Assemblages I-A and I-B). She concluded the use of a specific knapping technique rather than the lack altogether thereof, as previous studies had asserted based solely on morphological analyses. Aside from studying how the tools were made, researchers also broached the subject of the possible kinds of material that the tools were used on. Mijares (2004) analysed the chert flakes from the 2000-2001 archaeological excavations and concluded that they were used on hard material. Having also noted edge retouch, he suggested that it was due to use rather than intention application. His study was carried forward by Jago-on (2006; 2007; 2008), who analysed the same collection and added the one from the 2007 excavation. The subject of contact material, first explored by

Mijares, received further attention from Xhauflair (2009) and Pawlik (Xhauflair and Pawlik, 2010), who applied a functional approach through use-wear and residue analysis. Xhauflair and colleagues expanded and combined this with ethnography to study plant processing among the Pala'wan, one of the modern-day ethnolinguistic communities in Palawan (Xhauflair and Pawlik, 2010; Xhauflair *et al.*, 2017). This focus on the relationship between man and environment in Palawan is echoed in the work of Schmidt (2008; 2009). Using a variety of geochemical techniques, he looked at the characterisation and sourcing of the red jasper used as raw material and found that it was collected from the Panitian and Malatgao Rivers located some 8 km to 9 km from the site; this enabled him to address the issue of human mobility within the local landscape at Tabon Cave.

Geoarchaeology

Another relatively little-explored perspective from which Tabon Cave has been viewed is geoarchaeology. Lewis (2005; 2007) conducted soil micromorphological analyses to study human occupation, depositional processes, and environmental change relating to Tabon Cave. She was the first to identify the potential presence of authigenic minerals in the cave and to suggest a link between them and post-depositional alteration of the archaeological materials (Lewis, 2007). She has also contributed to longstanding attempts at dating the cave in publishing uranium-series dates on a gypsum speleothem that features prominently in the cave stratigraphy (Lewis *et al.*, 2008). Corny (2008), in analysing the spatial distribution of all the 3,857 artefacts from Tabon Cave, found evidence for large-scale reworking of the cave deposits that he interpreted as anthropogenic. Finally, the current Tabon Cave research team synthesized existing knowledge on the stratigraphy and conducted preliminary sedimentological and geochemical analyses on the various sequences (Gallet, 2012).

Chapter III

Materials and methods

3.1. Methods

As laid out in Section 1.4, the present study focuses on the physical and chemical transformations in Tabon Cave and their implications for past environmental changes in the region. Accordingly, a previously developed multi-disciplinary approach (Choa, 2014) was expanded and enhanced to produce higher-resolution data in space and in time.

3.1.1. Grain-size analysis

One of the biggest mysteries concerning Tabon Cave is its highly complex stratigraphy, as detailed in Section 1.3. Various factors, primarily diagenesis and disturbances, contribute to this intricacy. Nevertheless, one of the running hypotheses concerning the stratigraphy holds that the back part of the cave is better preserved than the front part. This hypothesis is based on two observations:

- There are much less deposits of visible chemical origin in the back than in the front.
- Except for the South Trench, the back part of the cave has been preserved from excavation and other physical disturbances (e.g. treasure hunting, faunal reworking).

Thus, the back part may provide a clearer picture of the geological history of the cave by eliminating diagenesis and disturbances from the equation.

To translate the stratigraphy of the back part of the cave into concrete, sedimentological data, basic grain-size analysis through laser diffraction was applied to the South Trench, the only open excavation in the area. The goal is not to produce a high-resolution description of the cave's sedimentological dynamics, but rather to provide a broad framework that can serve as a reference in interpreting the physicochemical transformations in the cave and past environmental changes in the region.

3.1.2. Mineralogical characterization

The physical and chemical transformations in the cave, due primarily to diagenesis of its guano deposits, can be studied through characterization of *authigenic* (formed in situ) minerals that result from the said diagenesis. The minerals consist principally of phosphates and sulphates. This part of the study was addressed using mineralogical characterization techniques to identify these minerals.

In particular, Fourier-transform infrared spectroscopy (FTIR) was employed, with supplementary analyses through X-ray diffraction (XRD) to obtain more precise data. FTIR's ability to detect both crystalline and amorphous materials makes it suitable for Tabon Cave, where poorly crystallized authigenic minerals are abundant based on previous analyses (Choa, 2014). The recourse to XRD was motivated by its capability to countercheck and refine identifications made in FTIR, particularly of materials with crystalline phases.

The nature of the authigenic minerals across a given stratigraphical sequence also gives indirect information about the general climatic (and to a certain extent, environmental) context surrounding their formation.

3.1.3. Stable isotope analysis

Tackling palaeoenvironmental reconstruction more directly, previous work has shown the potential of stable isotope analysis on guano from Tabon Cave (Choa *et al.*, 2016). (Its viability is further discussed in Section 3.5.2.) Data from other proxies such as pollen and microfauna remain insufficient, unavailable, or absent, continuing to make stable isotope analysis on guano one of the few methods capable of providing palaeoenvironmental data for Tabon Cave. The approach was expanded in this study through application to a much greater number of samples from all over the cave, as well as refined through a more elaborate pre-treatment protocol designed to yield more robust data.

3.1.4. Radioisotope dating

Finally, radioisotope dating was included in this study because of the absolute necessity of obtaining chronological points of reference for the interpretation of the other data, most especially from stable isotope analysis: chronology is the missing link that will bridge the geological history, palaeoenvironmental reconstruction, and human occupation of Tabon Cave.

Two techniques were employed: radiocarbon dating of guano, and uranium-series dating of authigenic mineral layers. Radiocarbon dating was applied to easily identifiable, stratigraphically constrained guano layers in hopes of finally obtaining secure chronological data. Uranium-series dating was also carried out on targeted phosphate layers that suggested promise for the technique, again with the goal of pinning additional chronological markers onto the cave's stratigraphy.

Both of these techniques have been applied to the site in the past, with mixed results. Although radiocarbon dating has generally yielded reliable ages, some of its most important target materials (all of the human fossils, notably) are from reworked contexts. The technique's success has so far hinged on charcoal fragments that have been stratigraphically situated with success (presented in Section 5.3.2). Meanwhile, uranium-series dating has been conducted on the human fossils with the aim of obtaining direct ages (Dizon *et al.*, 2002; Détroit *et al.*, 2004), as well as on various guano and authigenic mineral deposits in hopes of finally building a clear chronostratigraphy (Lewis *et al.*, 2008; Ghaleb *et al.*, 2012). The ages on the fossils, some of which have large error margins, are often treated with precaution because of the strong geochemical activity observed in the cave, and their lack of context limits their usefulness for chronostratigraphical [re]construction. The guano and authigenic mineral deposits provided globally inconclusive results, ranging from clearly delimited ages in Lewis (2008) to stratigraphically incoherent ones attributed to the influence of uranium mobility in Ghaleb (2012).

3.2. Materials

General sampling was conducted in Tabon Cave during the 2014 field campaign, supplemented by specific sampling in 2016.

A total of 86 bulk sediment samples were collected in 2014, whereas 8 bulk sediment samples were gathered in 2016.

The sampling areas are presented in Figure 34. The complete list of samples with their context information and a short description is presented in Appendix A.

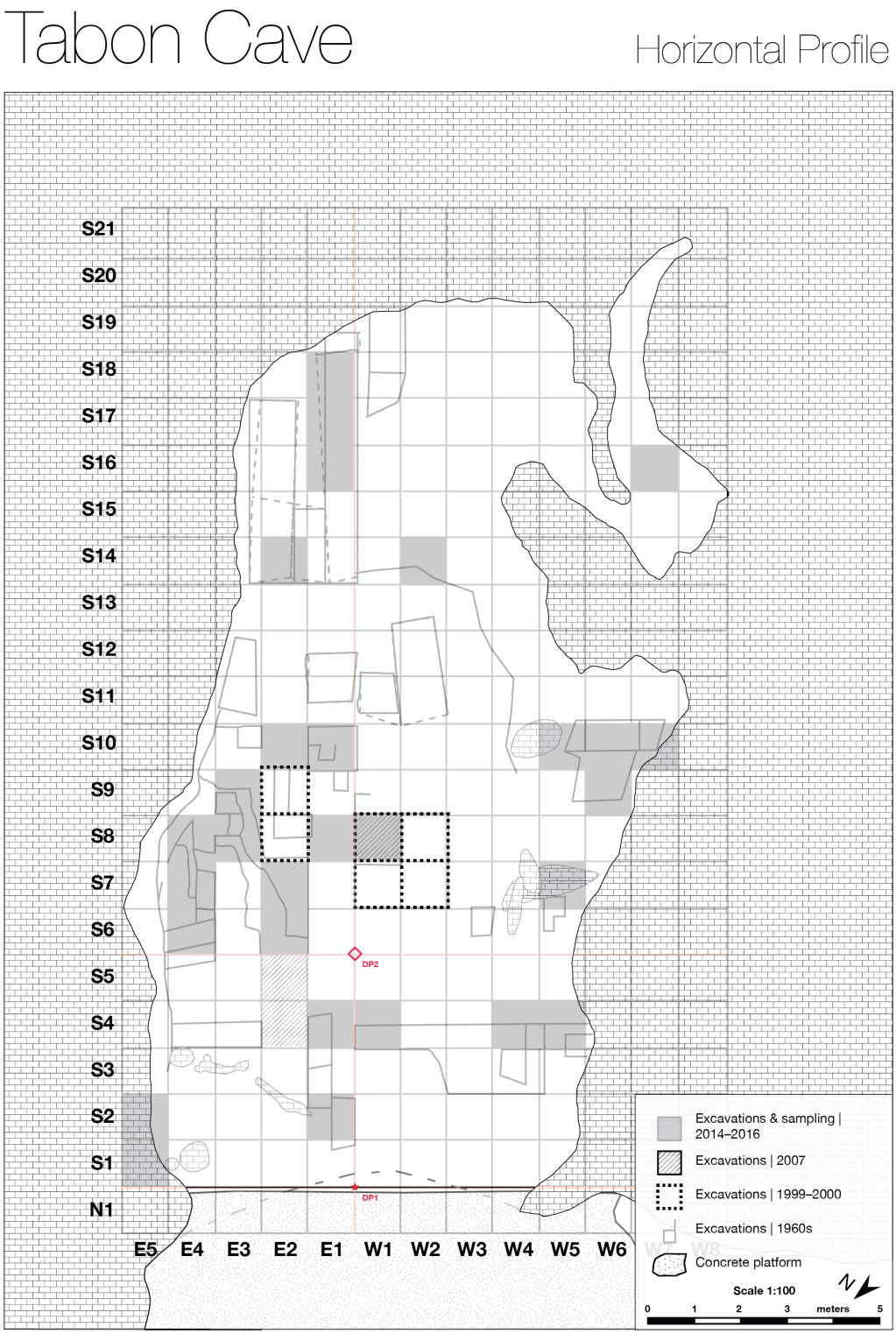

Figure 34. Sampling areas for the present study.

3.3. Grain-size analysis

3.3.1. Sample selection

Samples for grain-size analysis all come from the South Trench and are given in Table 1 below.

Table 1. Samples for grain-size analysis.

Sample	Layer	Depth (cm below DP)	Description
G	1	113	From capping speleothem
MM4	3	135-140	From Layer 3 on profile
F	3	142	Dark reddish brown
E	4/5	162	Mid-yellowish brown
D	9	220	Mid-reddish brown
MM3	9	223-228	At interface of Layers 7/8 and 9 on profile
C	9	238	Mid-greyish brown
MM2	10	265-270	At interface of Layers 9 and 10 on profile
B	10	285	Dark reddish black
MM1	11	316-321	At interface of Layers 10 and 11 on profile
A	11	333	Dark yellowish brown; clayey

Samples A, B, C, D, E, F, and G were collected as bulk sediment. Upon identification of the layers to be sampled, nails were inserted into the vertical profile to mark sampling locations. Plastic-wrapped labels containing the same information were left on the nails in the samples' original locations. Photographs were taken for documentation purposes.

Samples MM1, MM2, MM3, and MM4 were originally collected for soil micromorphology (hence the 'MM' in the sample names), using tin columns measuring 12.5 cm × 4 cm × 5 cm. Unfortunately, they did not survive transport from Quezon to Paris intact, and so were instead recycled as bulk sediment samples for particle size analysis.

No samples were collected from Layers 2, 6, and 7/8.

3.3.2. Sample analysis

Sample preparation and data acquisition

For each sample, approximately 30 mg of sediment were measured. Aggregates were crushed by hand, then ground using a porcelain mortar and pestle. The sediment was then transferred into a beaker, with just enough water added to submerge it and facilitate further disintegration of aggregates. The mixture was left to sit under a fume hood.

Samples were analyzed using a Malvern Instruments Mastersizer 2000 particle size analyzer at the Plateau de caractérisation des Archéomatériaux et des Archives sédimentaires du Musée de l'Homme (UMR 7194 – MNHN). A 1-L glass beaker filled with 800 ml of distilled water served as the sample tank.

Measurement parameters were configured manually, with laser intensity in particular set to above 70%. The background was measured and, laser obscuration was calibrated to 0%. Samples continuously underwent magnetic agitation throughout data acquisition.

For each sample, sediment in suspension was gradually added into the sample tank using a pipette until laser obscuration reached approximately 10%. Three measurements were then taken, and their mean was calculated. Both frequency and cumulative distribution data points were generated.

Between samples, the analyzer cell and dispersion unit were rinsed, and the sample tank emptied and refilled with distilled water. The dispersion unit was also rinsed with distilled water.

Upon completion of data acquisition, samples were transferred into a drying oven for water evaporation and subsequent sediment recovery.

Data analysis

Particle size data was analyzed using a suite of statistical indices described below. Sorting indices are defined following Miskovsky (2002), whereas particle size means use definitions by Rawle (2000) and Folk and Ward (1957). These parameters reflect degree of sorting and sorting bias, as well as enabling succinct description of particle size distributions. They are thus correlated with conditions of sediment transport and deposition, complementing field observations and other sources of sedimentological data (Syvitski, 2007).

Sorting indices

Trask's sorting index (So) is calculated in millimeters and defined as

$$So = \sqrt{\frac{Q_1}{Q_2}}, \text{ (Equation 1)}$$

where Q_1 represents the first quartile and Q_2 the second. For a given sample, the first quartile corresponds to the diameter below which 75% of grains fall. The second quartile is the diameter at which 50% of grains are coarser and 50% finer, making it equivalent to the median.

So is interpreted as follows:

Table 2. So values and corresponding sorting descriptions.

So value	Sorting
$So < 2.5$	Very well-sorted
$2.5 < So < 3.5$	Normally sorted
$3.5 < So < 4.5$	Fairly sorted
$4.5 < So$	Poorly sorted

The standard deviation (σ_0) is an alternative index for describing sorting. Inman (1952) calculates it in ϕ units as follows:

$$\sigma_0 = \frac{P_{84} - P_{16}}{2}. \text{ (Equation 2)}$$

P_{84} and P_{16} correspond to the 84th and 16th percentiles, respectively. For a given sample, the 84th percentile corresponds to the diameter below which 84% of grains fall; the 16th percentile is analogously defined.

σ_0 is interpreted as follows:

Table 3. σ_0 values and corresponding sorting descriptions.

σ_0 value	Sorting
$\sigma_0 = 0.35$	Very well-sorted
$0.35 < \sigma_0 < 0.50$	Well-sorted
$0.50 < \sigma_0 < 1$	Poorly sorted
$1 < \sigma_0$	Very poorly sorted

Folk and Ward offer a more nuanced calculation of the standard deviation, again using ϕ units:

$$\sigma_1 = \frac{P_{84}-P_{16}}{4} + \frac{P_{95}-P_5}{6.6}. \text{ (Equation 3)}$$

P_{84}, P_{16}, P_{95}, and P_5 correspond to the 84th, 16th, 95th, and fifth percentiles, respectively. P_{84} is defined just above, under σ_0; P_{16}, P_{95}, and P_5 follow parallel definitions.

The corresponding interpretation table for σ_1 follows:

Table 4. σ_1 values and corresponding sorting descriptions.

σ_1 value	Sorting
$\sigma_1 < 0.35$	Very well-sorted
$0.35 < \sigma_1 < 0.50$	Well-sorted
$0.50 < \sigma_1 < 1$	Moderately sorted
$1 < \sigma_1 < 2$	Poorly sorted
$2 < \sigma_1 < 4$	Very poorly sorted
$4 < \sigma_1$	Extremely poorly sorted

Trask's skewness (*Sk*) reflects the sorting bias of a given frequency distribution, indicating whether fine or coarse grains are better-sorted. It is calculated in millimeters as follows:

$$Sk = \sqrt{\frac{Q_1 - Q_3}{Md^2}}$$. (Equation 4)

Q_1 represents the first quartile, Q_3 the third, and Md the median, equivalent to Q_2.
For a given sample, Q_3 corresponds to the diameter below which 25% of grains fall.

Sk is interpreted as follows:

Table 5. *Sk* values and corresponding descriptions of sorting bias.

Sk value	Sorting bias
Sk = 1	None
Sk > 1	Fine grains are better-sorted
Sk < 1	Coarse grains are better-sorted

Pettijohn (1957) proposed a similar asymmetry coefficient (*Asq*) that also describes sorting bias, calculated this time in ϕ units:

$$Asq = \frac{Q_1 + Q_3 - 2Md}{2}$$. (Equation 5)

Q_1 represents the first quartile, Q_3 the third, and Md the median, also equivalent to Q_2.

Asq is interpreted as follows:

Table 6. *Asq* values and corresponding descriptions of sorting bias.

Asq value	Sorting bias
Asq = 0	None
Asq < 0	Fine grains are better-sorted
Asq > 0	Coarse grains are better-sorted

Folk and Ward's (1957) kurtosis (K) is another index for describing the shape of a grain-size frequency distribution, based in particular on the relative proportions of the component grain-size classes. It is calculated in ϕ units and is given as:

$$K = \frac{P_{95} - P_5}{2.44(Q_3 - Q_1)}. \text{ (Equation 6)}$$

P_{95} represents the 95th percentile, P_5 the fifth, Q_3 the third quartile, and Q_1 the first.

K is interpreted as follows:

Table 7. K values and corresponding descriptions of kurtosis.

K value	Kurtosis
$K < 0.67$	Very platykurtic
$0.67 < K < 0.90$	Platykurtic
$0.90 < K < 1.11$	Mesokurtic
$1.11 < K < 1.50$	Leptokurtic
$1.50 < K$	Very leptokurtic

In a distribution composed of multiple populations, equivalent proportions produce a *platykurtic* curve, whereas the dominance of one gives a *leptokurtic* curve.

Grain-size means

The volume moment mean is a diameter that corresponds to the centre of gravity of a given grain-size distribution (Rawle, 2000). It enables computation of mean grain size in large distributions, where grain counting is impractical or impossible. It is calculated as

$$D[4,3] = \frac{\sum d^4}{\sum d^3}, \text{ (Equation 7)}$$

where d stands for grain diameter.

Folk and Ward's mean grain size was originally proposed as a more accurate index for mean size calculation in bimodal and skewed frequency distributions (Folk and Ward, 1957). It is given by

$$M_Z = \frac{\phi 16 + \phi 50 + \phi 84}{3}, \text{ (Equation 8)}$$

where $\phi 16$ indicates, on the Krumbein phi scale, the 16th percentile, or the diameter below which 16% of the grains in the distribution under consideration fall. (The Krumbein phi scale is a transformation derived from the Wentworth scale introduced by Krumbein and Aberdeen [1937].) This definition can be transposed to calculate $\phi 50$, then equivalent to the median, and $\phi 84$.

To enable comparison with the volume moment mean, the mean grain size was converted to the metric scale before being plotted, using the following equation:

$$D = D_0 \times 2^{-\phi}, \text{ (Equation 9)}$$

where D stands for the grain diameter (in millimeters) and D_0 is a reference diameter (set to 1 mm).

This equation is derived from the definition of the Krumbein phi scale,

$$\phi = -\log_2 \frac{D}{D_0}. \text{ (Equation 10)}$$

3.4. Mineralogical characterization

3.4.1. Fourier-transform infrared spectroscopy (FTIR)

Theoretical background

Fourier-transform infrared spectroscopy (FTIR) is an analytical technique from chemistry that has found application in archaeology, specifically in materials characterization. It is capable of identifying and quantifying crystalline, amorphous, and organic materials (Fröhlich, 1981; Fröhlich, 1989; Weiner, 2010). A given sample submitted to infrared radiation registers an absorption spectrum that describes correspondences between two parameters: the frequency of the radiation, and the energy associated with the specific vibration modes of the sample material's constituent molecular groups (Pollard *et al.*, 2007). The most useful region of this spectrum corresponds to wave numbers 4000 to 400 cm^{-1}, called the mid-infrared range, as it is here that organic and mineral compounds produce characteristic absorption spectra (Pollard and Heron, 2008). The technique presents major advantages: a relatively small amount of sample (less than 0.5 mg) is sufficient, and analysis is rapid (Weiner, 2010). However, interpreting the resulting spectra can be challenging.

Different methods of sample preparation for FTIR analysis exist. Fine grinding using an agate mortar and pestle is sufficient for measurement via *attenuated total reflectance* (ATR). ATR-FTIR generates absorption spectra by capitalizing on the phenomenon of total internal reflection (Stuart, 2002). The ground sample is directly applied onto the ATR accessory platform crystal for subsequent infrared irradiation. Advantages include ease-of-use and good general characterization quality.

For higher-resolution results, the *potassium bromide* (KBr) pellet method is preferred, with the disadvantage of requiring more elaborate preparation (Milosevic 2012). The sample is mixed with powdered KBr to obtain a very precise weight and then pressed into a pellet under high pressure. The invisibility of KBr itself to infrared radiation (down to 400 cm^{-1}; Pavia *et al.*, 2015) and the exclusion of external factors during irradiation (the sample being well-sealed in the KBr matrix) results in generally clearer spectra.

Sample selection and analysis

All samples collected for this study underwent FTIR analysis for basic characterization.

FTIR analysis was performed at the Plateau de spectrométrie infrarouge du MNHN, a division of the Plateau de caractérisation des Archéomatériaux et des Archives sédimentaires du Musée de l'Homme (UMR 7194 – MNHN). Grinding was performed for spectrum acquisition via ATR to improve contact between the sample (in powder form) and the ATR diamond crystal. This preparation method has the advantage of delivering efficient qualitative analysis for general characterization of a considerable number of samples all while being time- and labour-efficient, making it ideal for the current study.

For each sample, approximately 15 g of material were ground to fine powder form for approximately 3 minutes using agate mortars and pestles for homogenization.

Infrared spectra were acquired in Bruker OPUS Spectroscopy Software using a Bruker VERTEX 70 FTIR spectrometer coupled with a Specac Quest ATR Diamond Accessory. Scanning was performed at a resolution of 4 cm^{-1} with 128 scans for samples and 256 scans for the background over the range 6000–70 cm^{-1}, subsequently cropped to 4000–100 cm^{-1}.

Spectral identification through peak comparison was performed over the range 4 000–400 cm^{-1} with the aid of bibliographic information, the infrared spectrum database of the *Plateau de caractérisation des Archéomatériaux et des Archives sédimentaires du Musée de l'Homme (UMR 7194 – MNHN)*, and the Infrared Standards Library of the Kimmel Center for Archaeological Science (Weizmann Institute of Science).

3.4.2. X-ray diffraction (XRD)

Theoretical background

X-ray diffraction (XRD) is an analytical technique used for characterization of crystalline materials. It functions according to Bragg's law, which states that (Robinson *et al.*, 1995):

$$n\lambda = 2d \sin\varphi \text{ , (Equation 11)}$$

where

n : the order of wavelengths,
λ : the wavelength,
d : the interatomic distance, and
φ : the diffraction angle of the departing X-ray.

The technique involves focusing monoenergetic collimated X-rays on a given sample and studying the diffracted portion, which depends on the crystal structure of the sample (Garrison, 2016). Diffraction requires the distance between the scattering points to be of the same magnitude as the wavelength of the incident X-ray. Because the structure of a crystalline material is the repetition of a unit cell specific to it, meaning that the interatomic distance is unique, identification is generally accurate, making it a valuable tool for characterization of crystalline minerals and archaeological materials (e.g. clay minerals in pottery, corrosion products on metal; (Pollard *et al.*, 2007)).

Sample selection and analysis

Due to resource limitations, it was not possible to perform XRD analysis on all the samples, necessitating the creation of a smaller sample set. The FTIR analysis revealed close similarities between several samples based on their infrared spectra. These samples were grouped together, and at least one representative was chosen per group. Given that the samples were already in powder form after being prepared for FTIR, they were sent directly for XRD without further processing.

XRD analysis was performed with the help of X. Gallet and M.-M. Blanc-Valleron at the Centre de recherche sur la Paléobiodiversité et les Paléoenvironnements (UMR 7207 – MNHN) using a Bruker D2 Phaser with a LYNXEYE detector. Diffractograms were run through the PDF-2 2003 database using DIFFRAC.EVA V3.2 XRD Software.

3.5. Stable isotope analysis

3.5.1. Theoretical background

Isotopes refer to atoms that differ in their number of neutrons, but otherwise share the same number of protons. Generally speaking, they can either be unstable and undergo radioactive decay, as in the case of carbon-14 (^{14}C), or be relatively stable over time, as in the case of carbon-13 (^{13}C) and carbon-12 (^{12}C), the three isotopes of carbon.

Isotopes are studied through *isotope-ratio mass spectrometry*. This method consists of three main phases (Kienitz, 1968):

1. ionization of a given sample, resulting in electrically charged isotopes as ions;
2. separation of the ions according to their mass-to-charge ratio (m/z) using electromagnetic fields; and
3. detection of the individual ions through their abundance and m/z values.

Concretely speaking, the sample is first vaporized through the application of heat, and the resulting gas phase ionized through electron bombardment. Accelerators then propel the ions into a field generated by a magnetic sector, which deflects them along varying paths according to their m/z values. A detector registers the arrival of the ions at specific spots corresponding to the deflection paths, producing a mass spectrum that plots the m/z values against the relative abundance of the ions (OpenStax, 2017). A schematic diagram illustrating the method is shown in Figure 35.

Various techniques for isotope-ratio mass spectrometry exist, differing based on the isotopes to be studied (stable or radiogenic) as well as ionization, ion transport and separation (mass analysis), and ion detection methods. These include inductively-coupled plasma mass spectrometry (ICP-MS), thermal ionization mass spectrometry (TIMS), and accelerator mass spectrometry (AMS), among others (Gross, 2017). In ICP-MS, the sample (in solid, liquid, or slurry form) is ionized using a plasma, generated through inductive heating of a gas using an electromagnetic coil to make it electrically conductive. TIMS ionizes [solid] samples through contact with a metal filament that is heated, triggering spontaneous ionization of sample material at elevated temperatures. Finally, with AMS, the specificity of this sensitive technique

lies not in ionization, but in separation: the powerful acceleration applied on the ions enables better differentiation, particularly of low-abundance isotopes.

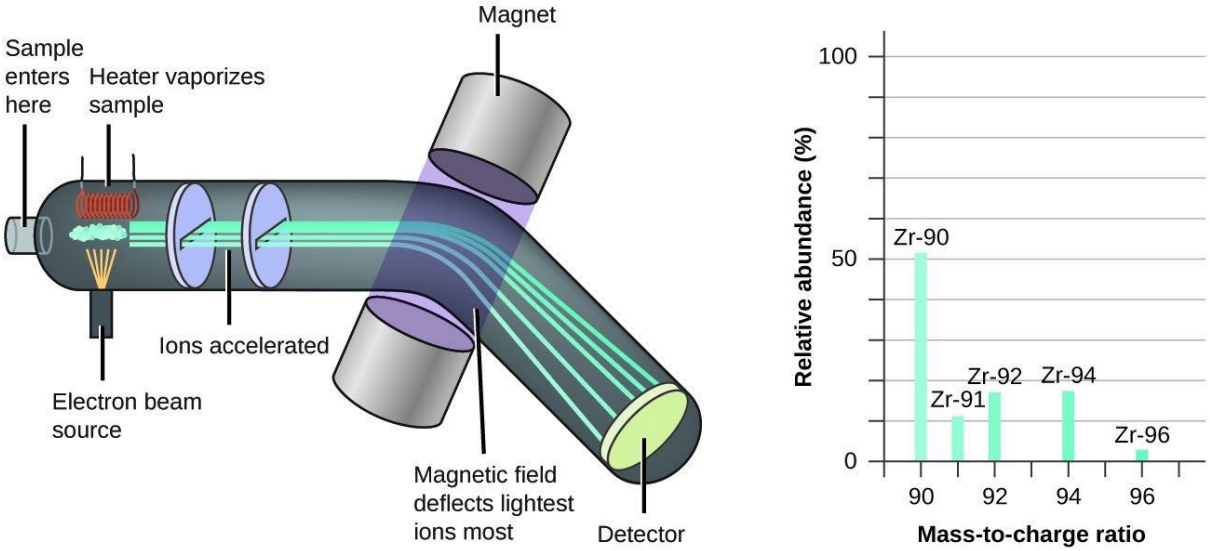

Figure 35. Schematic diagram of a mass spectrometer set-up for zirconium (Zr) analysis, with the resulting mass spectrum of Zr isotopes (OpenStax, 2017).

3.5.2. Applications to archaeology

Stable isotope analysis is an approach that, in recent years, has been finding increasing applications in archaeology. In certain materials (e.g. bone, shell), the ratio of two non-radioactive isotopes of the same element (e.g. ^{13}C and ^{12}C) can provide information about formation and evolution of biomineral, organic, and geological matter (Malainey, 2011). Examples of subjects on which it can shed light on are diet, migration, provenance, palaeoenvironment, and palaeoclimate (Brown and Brown, 2011; Malainey, 2011; Reitz and Shackley, 2012). In this study, stable isotope analysis is conducted on fossil guano from Tabon Cave (previously presented in Section 1.3.1) to recover broad data on local vegetation around the site at the time of guano deposition.

History of the approach

The application of stable isotope analysis to guano was pioneered by Des Marais *et al.* (1980), who related ^{13}C data from 40-year-old guano in Carlsbad (New Mexico, USA) to plant photosynthesis, insects, and bat populations at the local scale. Mizutani *et al.* (1992) later applied the same approach to a stratified guano deposit spanning 25 years in Eagle Creek Cave (Arizona, USA), adding information from ^{15}N.

Similar studies with greater time depth followed in the 2000s. Wurster *et al.* (2008) used isotopic signatures of ^{13}C and D (deuterium; ^{2}H) to highlight climate change over the Pleistocene-Holocene transition in Bat Cave, Grand Canyon (Arizona, USA). Campbell *et al.* (2017) combined ^{13}C and ^{15}N data with pollen and soil nutrient information to obtain a more complete picture of the ancient environments around Fern Cave (Alabama, USA), a site with Woodland Indian occupation dated to ca. 2.8 cal ka BP and thus of archaeological importance.

In Europe, applications of the approach have thus far focused on Romanian caves. Onac *et al.* (2014) were able to observe the Medieval Warm Period (AD 950–1250) and describe high-resolution climate shifts using ^{13}C isotopic signatures in guano from Gaura cu Muscă Cave (southwestern Romania). They corroborated their findings using clay colour and quantity, peat bog pollen and microcharcoal, and speleothem ^{13}C and ^{18}O data from other sites (Onac et al. 2014). In Zidită Cave (western Romania), Forray *et al.* (2015) studied environmental change and human activity over the past 900 years by analyzing stable isotopes, pollen, and microcharcoal, all from the same guano deposit this time.

In the three decades that followed the work of Des Marais *et al.* (1980), the approach was applied to sites situated in varying geographical regions and spanning different (albeit still relatively restricted) time scales. Its development through innovation and corroboration with other sources of data have consolidated the principles underlying the approach and have arguably resolved the question of its feasibility. This would pave the way for its application to tropical guano and to time scales stretching into the Late Pleistocene, enabling examination of long-term environmental change through this specific marker.

The first such investigation was pioneered by Bird *et al.* in their 2007 study of Makangit Cave (northern Palawan, Philippines) (Bird *et al.*, 2007). This landmark work established the presence of grassland in northern Palawan during the LGM (Last Glacial Maximum; ca. 18 ka ago), replaced by closed tropical forest by the mid-Holocene (5 ka ago). This study was expanded by Wurster *et al.* across the region to include sites in southern Palawan, northern Borneo, and peninsular Malaysia (Wurster *et al.*, 2010). They concluded that, over the Last Glacial Period (125–10 ka ago) and particularly during the LGM, forest contraction occurred in Palawan and peninsular Malaysia while rainforest persisted in Borneo, lending weight to the hypothesized past existence of rainforest refugia in the region (Gathorne-Hardy *et al.*, 2002).

This was later confirmed for eastern Borneo (at least for the past 15 ka), although local variation was noted (Wurster *et al.*, 2017).

Stable isotope analysis of guano for palaeoenvironmental reconstruction has also been successfully applied to other tropical regions beyond Southeast Asia. In the Caribbean, Royer *et al.* (2015) innovated on the approach by applying it to modern phytophagous bat guano from two sites in Guadeloupe (Leeward Islands, Lesser Antilles), and by investigating the effect of seasonal variations on the corresponding stable isotope (^{13}C and ^{15}N) ratios. The team found that seasonality had a perceptible but nevertheless contained effect on guano biogeochemistry, affirming the applicability of the approach for palaeoenvironmental reconstruction in a slightly different context. They went further back in time by looking at a frugivorous bat guano sequence extending to 40 ka BP in Blanchard Cave on the neighbouring island of Marie-Galante. The team's findings suggest that, while overall drier conditions prevailed in the region during the Late Pleistocene, oscillations into wet conditions nevertheless occurred from time to time (Royer *et al.*, 2017). Meanwhile, across the Pacific in New Caledonia, Wirrmann *et al.* (2017) found good covariation between stable isotope data from swiftlet guano (^{13}C and D this time) and yearly mean daily rainfall at Hama Cave (Lifou Island, Loyalty Islands), concluding that guano could provide high-resolution palaeoclimatic data.

The marriage of stable isotope analysis with complementary approaches allowed it to mature and become more refined. For example, Widga *et al.* (2015) employed palaeontological and ecomorphological analyses of bat remains from Mammoth Cave (Kentucky, USA) to provide a more nuanced interpretation of the palaeoenvironmental data obtained from stable isotope analysis. Cleary *et al.* (2016) took up the challenge of making sense of ^{15}N data from guano, often discounted as nothing more than a trophic level indicator (and an unreliable one at that) with limited use for palaeoenvironmental reconstruction. With help from pollen and ^{13}C isotopic signatures, the team was able to establish the influence of human activity and water availability on ^{15}N data from 300-year-old guano in Zidită Cave (western Romania). Unfortunately, they were less optimistic with regard to fossil guano, citing decomposition and bioturbation as potential hindrances to reliable interpretation (Cleary *et al.*, 2016).

Carbon-13

Carbon-13 isotope analysis relies on the significant presence and central role of carbon in organic matter. Carbon-13 represents 1.07% of all carbon found in nature (carbon-12 representing 98.93%, and carbon-14 one part per trillion) (Brown and Brown, 2011).

In isotope analysis, carbon-13 is represented by its *isotopic signature* $\delta^{13}C$, defined as follows (McSween *et al.*, 2003):

$$\delta^{13}C = 1000 \times \frac{R_{sample} - R_{standard}}{R_{standard}}, \text{ (Equation 12)}$$

where

$$R_{sample} = \left(\frac{^{13}C}{^{12}C}\right)_{sample} \text{ (Equation 13)}$$

and

$$R_{standard} = \left(\frac{^{13}C}{^{12}C}\right)_{VPDB}. \text{ (Equation 14)}$$

Isotopic signatures are reported in per mil (‰), and the quantities R_{sample} and $R_{standard}$ represent the ratio of carbon-13 to carbon-12 isotopes in the sample and in the standard, respectively.

For $\delta^{13}C$, the international standard used by convention is Vienna Pee Dee Belemnite (VPDB), developed after exhaustion of the original standard, Pee Dee Belemnite (PDB). PDB refers to a marine fossil, *Belemnitella*, found in the Cretaceous Pee Dee formation in South Carolina (USA) that is free of carbon-14. The CO_2 obtained from this fossil served as the original standard for carbon (Reitz and Shackley, 2012). As availability of this standard is quite limited, modern geochemistry practice employs internal laboratory standards calibrated to it.

In palaeoenvironmental reconstruction, carbon-13 isotope analysis serves to determine the photosynthetic pathways employed by plants in a given area based on their $\delta^{13}C$ values, with each of these pathways corresponding to different environmental and climatic conditions. Carbon-13 isotopes are transmitted up the food chain from the plants to the dependent insect population (Des Marais *et al.*, 1980). Transmission continues upward to the insects' predators; of these, bats and birds will leave behind insect remains in their guano. Isotope analysis of these remains then allows determination of the photosynthetic pathways used by the plants at the base of the food chain, and by extension, enables reconstruction of the local vegetation at the time the guano was deposited.

The three photosynthetic pathways are C_3, C_4, and CAM (Jones, 2009):

- Plants that use the C_3 pathway fix CO_2 directly via the enzyme RuBisCO (ribulose-1,5-bisphosphate carboxylase/oxygenase) to form PGA (3-phosphoglyceric acid), a 3-carbon compound (hence the name of the pathway). Most plants from cool, humid environments use the C_3 pathway—these include trees (which are exclusively C_3, with rare exceptions), as well as temperate cereals like wheat.
- C_4 plants perform photosynthesis more efficiently through the addition of an initial carboxylation reaction. CO_2 is first concentrated by having the enzyme PEP (phospho*enol*pyruvate) carboxylase fix HCO_3^- in the mesophyll cells. This process produces OAA (oxaloacetate) and various other 4-carbon compounds (giving the pathway its name). The 4-carbon compounds are then transferred to bundle sheath cells and decarboxylated to release CO_2, which then undergoes final carboxylation by RuBisCO. C_4 plants are well-adapted to hot and dry environments—examples include semi-arid as well as tropical species like cogon (*Imperata cylindrica*) and carabao grass (*Paspalum conjugatum*).
- The CAM pathway is similar to the C_4 pathway except that the initial carboxylation (which produces 4-carbon compounds) occurs at night, while the decarboxylation (which produces CO_2) and final carboxylation happen during the day. This pathway is commonly found in succulent plants that live in arid environments, such as cacti.

The three pathways are identifiable through stable isotope analysis because of their separate value ranges for $\delta^{13}C$ (although some overlapping may occur at the range boundaries). C_3 plants fall between –32 and –20‰, C_4 plants fall between –17 and –9‰, and CAM plants fall between the two (Cerling *et al.*, 1997; Bowsher *et al.*, 2008). In tropical contexts, as is the case of the present study, the preponderance of C_3 plants corresponds to a humid environment dominated by tropical forest, whereas C_4 plants point to drier, more arid conditions and the presence of grassland. Thus, determination of $\delta^{13}C$ values in insectivorous bat and bird guano deposited in such contexts could provide a general picture of local vegetation at the time of guano deposition (Bird *et al.*, 2007; Wurster *et al.*, 2010b).

Nitrogen-15

Nitrogen-15 isotope analysis capitalizes on the presence of nitrogen in the biosphere under various oxidation states and matter phases to study variations in its isotopic composition (Hoefs, 2015). Nitrogen-15 represents 0.37% of all nitrogen found in nature, while nitrogen-14 represents 99.63% (Hoefs, 2015).

In isotope analysis, nitrogen-15 is represented by its *isotopic signature* $\delta^{15}N$, defined as follows (McSween *et al.*, 2003):

$$\delta^{15}\mathrm{N} = 1000 \times \frac{R_{\mathrm{sample}} - R_{\mathrm{standard}}}{R_{\mathrm{standard}}}, \text{ (Equation 15)}$$

where

$$R_{\mathrm{sample}} = \left(\frac{^{15}\mathrm{N}}{^{14}\mathrm{N}}\right)_{\mathrm{sample}} \text{ (Equation 16)}$$

and

$$R_{\mathrm{standard}} = \left(\frac{^{15}\mathrm{N}}{^{14}\mathrm{N}}\right)_{\mathrm{AIR}}. \text{ (Equation 17)}$$

Isotopic signatures are reported in per mil (‰), and the quantities R_{sample} and $R_{standard}$ represent the ratio of nitrogen-15 to nitrogen-14 isotopes in the sample and in the standard, respectively.

The standard for $\delta^{15}N$ is air nitrogen (denoted by 'AIR'), as it is both evenly distributed and readily accessible in the atmosphere (constituting 78% of it) (Meier-Augenstein, 2010).

As applied to ecology, nitrogen-15 isotope analysis is generally used to determine trophic levels; a more positive $\delta^{15}N$ value indicates a higher position up the food chain (Reitz and Shackley, 2012). Most values hover between –10 to +20‰ (Hoefs, 2015). In the case of guano, fossilization may be accompanied by extraneous increases in $\delta^{15}N$ values due to certain post-depositional processes, particularly fixation of atmospheric nitrogen by microbes as they break down organic matter—this is the main obstacle to the viability of $\delta^{15}N$ as an ecological marker. Assuming that these increases can be properly corrected for (a challenge that is still wrought with complexities), $\delta^{15}N$ values could aid in characterizing guano producers as either insectivorous or frugivorous.

3.5.3. Protocol development

No unified protocol exists for extracting insect cuticles from guano. The constituent steps and their order vary from author to author. The protocol developed for this study was adapted from Wurster *et al.* (2010b) and Wurster *et al.* (2010c). In the first paper, the authors applied four organic matter recovery procedures with the goal of comparing stable isotope results between the four resulting extracts:

1. *bulk guano* (BG): obtained after simple decarbonation of the bulk sample
2. *guano extract* (GE): obtained after dense medium separation and decarbonation of the bulk sample
3. *solvent-extracted guano* (SEG): obtained after dense medium separation, decarbonation, and delipidation of the bulk sample
4. *solvent extract* (SE): obtained after evaporation of the solvent used for bulk sample delipidation

While the authors found a correlation in $\delta^{13}C$ values across the different procedures, horizontal shifts were observed. GE values were found to be more negative than BG values, suggesting that dense medium separation removed a positive $\delta^{13}C$ contribution from the heavy fraction. SEG values were more positive than GE values though, pointing to a negative $\delta^{13}C$ contribution from lipids. Nevertheless, whatever the procedure used, a basic signal can be obtained (Wurster *et al.*, 2010b).

In terms of $\delta^{15}N$ values, GE samples did not change much over time, whereas older SEG samples were more positive. This indicates that older GE samples incorporated compounds that made a negative $\delta^{15}N$ contribution (Wurster *et al.*, 2010b).

The authors noted that dense medium separation increased carbon and nitrogen concentration in the samples, which is important for reliable stable isotope results.

Finally, concerning elemental ratios, it was noted that lipids artificially increase the C:N ratio in guano from 6.9, the value for *n*-acetyl-*d*-glucosamine (the component polysaccharide of chitin). The authors determined that SEG best represents insect chitin in bat guano, and equally confirmed this through infrared spectroscopy. For palaeoenvironmental reconstruction using $\delta^{13}C$ values, they recommend samples that fall within a narrow C:N range (6 to 8) for increased confidence (Wurster *et al.*, 2010b).

Decarbonation

Cave guano may contain carbonates due to water percolation through the karst system and onto cave deposits, followed by precipitation (Mizutani *et al.*, 1992b). They constitute a source of carbon that is separate from the guano producers' diet and may mask the palaeoenvironmental signal sought. For this reason, carbonate removal or *decarbonation* (essentially through transformation into CO_2) is a necessary step in preparing guano samples for stable isotope analysis. Additionally, decarbonation may increase the carbon content per unit of sample weight (Mizutani *et al.*, 1992a)—ideal for the Tabon Cave guano samples, presumed to be relatively old (at least 30,000 years) and in which organic matter preservation may be highly variable, especially given the aggressive diagenesis at work in the cave. This is important, as low carbon content may translate to lower reliability for stable isotope signatures.

In the author's earlier research (Choa, 2014), decarbonation was done through *acid fumigation*, which involved exposing samples to vapours from 4 small beakers of 12N HCl under a hood for 24 hours. Acid fumigation is efficient, requires less time and labour than wet methods, and preserves acid- and water-soluble organic carbon (Harris *et al.*, 2001; Ramnarine *et al.*, 2011). However, it may change the natural abundance of ^{15}N in the samples (Harris *et al.*, 2001).

A 2 N HCl bath was thus preferred for decarbonation, in line with most protocols in the literature (Mizutani *et al.*, 1992b; Wurster et al. 2007; Wurster et al. 2008; Wurster *et al.*, 2010b; Wurster *et al.*, 2010c).

Delipidation

Aside from carbonates, lipids are another isotopic signal polluant in guano. They also contain carbon that is exogenous with respect to the original carbon in guano producers' diet, since they are synthesized and contributed *a posteriori* by the animals (Wurster *et al.*, 2009). Lipid removal or *delipidation* is done via solvent extraction, either manually through solvent washes or automatically using an accelerated solvent extractor. Aside from eliminating lipids, solvent extraction also removes nitrogen-bearing compounds that are preferentially depleted in nitrogen-15, which may mask the original $\delta^{15}N$ signal (Wurster, McFarlane, *et al.*, 2010).
In the literature's varying guano preparation protocols for stable isotope analysis, only those of Des Marais *et al.* (1980), Wurster *et al.* (2008), and Wurster *et al.* (2010b) include delipidation. Due to the unavailability of an accelerated solvent extractor, Wurster *et al.* (2008)'s delipidation protocol was chosen for the present study. It involves an initial wash in methanol, followed by 3 washes in chloroform/methanol (2:1, v/v). The protocol was slightly simplified for the present study with the removal of the first methanol wash.

Static dense medium separation

Dense medium separation is a technique used to isolate analytes of interest from a matrix through mixture with a heavy liquid adjusted to a specific density (Wurster *et al.*, 2010c). Components that have a lower density than the heavy liquid will float, forming the *light fraction*, whereas those whose density is higher will sink, forming the *heavy fraction*, with the heavy liquid in between. The technique is commonly used in dating approaches that rely on specific minerals (e.g. zircon). Heavy liquids are prepared by mixing certain salts like zinc chloride

($ZnCl_2$) or sodium polytungstate (SPT) with deionized water (DI-H_2O) and adjusting the density until the target value is achieved.

Fraction recovery may be done through the use of either *separatory funnels* or *centrifugation*. With separatory funnels, the mixture is allowed to decant to let the fractions separate. The fractions are then recovered one at a time by controlling the funnel stopcock. With centrifugation, the fractions are separated mechanically, the light one poured off manually. Separatory funnels were initially tested for the present study, but funnel outlets were repeatedly clogged by the heavy fraction. Centrifugation was thus chosen, being easier to implement.

The qualifier 'static' refers to the solidification of the mixture through freezing. Fraction recovery as described above, with the mixture in the liquid phase, typically involves some sample loss, as well as cross-contamination through fraction re-mixing. Freezing makes sample recovery easier, limits sample loss, and minimizes the risk of contamination.

In guano, organic matter may be accompanied by denser material contributed by the depositional environment, notably minerals. Aside from carbonates and silicates, nitrogen-bearing minerals resulting from microbial fractionation and carrying high $\delta^{15}N$ values may also be present (Wurster *et al.*, 2010c). In the literature, previous authors have used a solution of $ZnCl_2$ and 2 N HCl set to a specific gravity of 2.0 to separate the organic and mineral fractions in guano, while at the same time decarbonating samples (Wurster *et al.*, 2008; Wurster *et al.*, 2010b). For the present study, it was decided to separate dense medium separation and decarbonation, use SPT instead of $ZnCl_2$, and work with density rather than specific gravity. Most minerals have a density above 2.0 g/cm^3, while organic matter falls below 1.6 g/cm^3 (Wurster *et al.*, 2010c). Thus, heavy liquid density needed to be set between 1.6 and 2.0 g/cm^3, and 1.87 g/cm^3 was chosen following Wurster *et al.* (2010c).

Recovery of insect cuticles

After recovery of the light fraction, it needed to be purified of the heavy liquid; a filtration unit was deployed for the task. Initial attempts involved the use of cellulose acetate membranes with a 0.45 µm-retention capacity (Thermo Scientific™ Nalgene™) as filters, and a laboratory faucet as a vacuum pump. The laboratory faucet was later replaced with an actual vacuum pump

for greater efficiency, while the cellulose acetate membranes were replaced with glass fibre filters of 0.7 μm-retention capacity (Grade 698; VWR, Pennsylvania, USA).

Many protocols in the literature call for a neutralization step through an NaOH wash at this point; in Wurster, *et al.*'s study (2010b), however, this resulted in significant loss of organic matter. Given that the Tabon Cave samples are, again, assumed to be relatively old and may not have much organic matter to begin with, especially in light of the poor preservation conditions in the site, this step was abandoned.

With sample quantity drastically reduced, decarbonation through an acid bath could be performed with greater efficiency. As with the heavy liquid, the acid also needed to be eliminated from the samples through filtration.

The final step in recovering the samples, now theoretically composed only of insect cuticles, was the elimination of the external phase (distilled H_2O) in which the samples were suspended after the last purification. This was accomplished through freeze-drying, which allowed for easy removal of the external, liquid phase through sublimation while preserving the very small quantity of sample material.

Verification

To verify that the extracted material was indeed composed of insect cuticles, certain samples were tested in infrared microspectroscopy to check whether their spectra corresponded to that of chitin, the principal constituent of insect cuticles (sample quantities were too small for regular infrared spectroscopy).

Peaks characteristic of chitin were successfully observed in most of the verified samples, with reference to Pearson *et al.* (1960), Cardénas *et al.* (2004), Wurster *et al.* (2010b), and Kaya *et al.* (2014). Figure 36 compares 3 spectra from Sample F-2 against reference spectra of chitin from both modern and archaeological contexts. The peaks in modern chitin at 2924 and 2854 cm^{-1}, corresponding to aliphatic compounds, are heavily attenuated but still visible in both the archaeological and the sample chitin. The amide I (1627 cm^{-1}) and amide II peaks (1544 cm^{-1}) are clearly visible. Finally, the saccharide ring peaks (from 1068 to 1012 cm^{-1}) are visible

and have the same general form across the archaeological and sample spectra but are less pronounced in the modern spectrum.

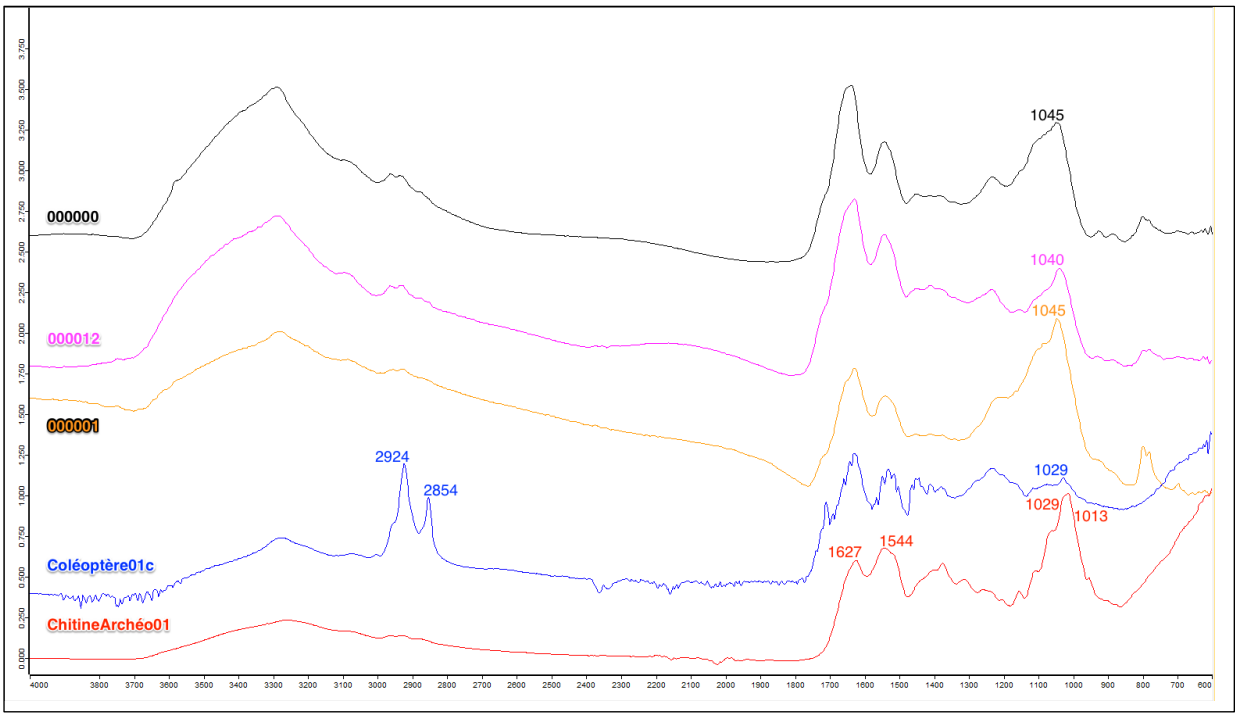

Figure 36. Comparison of FTIR spectra from Sample F-2, a duplicate of Sample F, after protocol application (000000, 000012, and 000001); modern chitin from Coleoptera legs (Coléoptère01c); and archaeological chitin (ChitineArchéo01).

However, additional peaks that do not belong to chitin were also observed in the sample spectra presented, notably the silicate doublet at 800 and 780 cm^{-1}.

3.5.4. Sample selection

From the general sample set, specimens collected from guano layers in different zones of the cave were selected for stable isotope analysis, as these are the only samples expected to yield insect remains for palaeoenvironmental reconstruction. The corresponding sampling zones are presented in Figure 37.

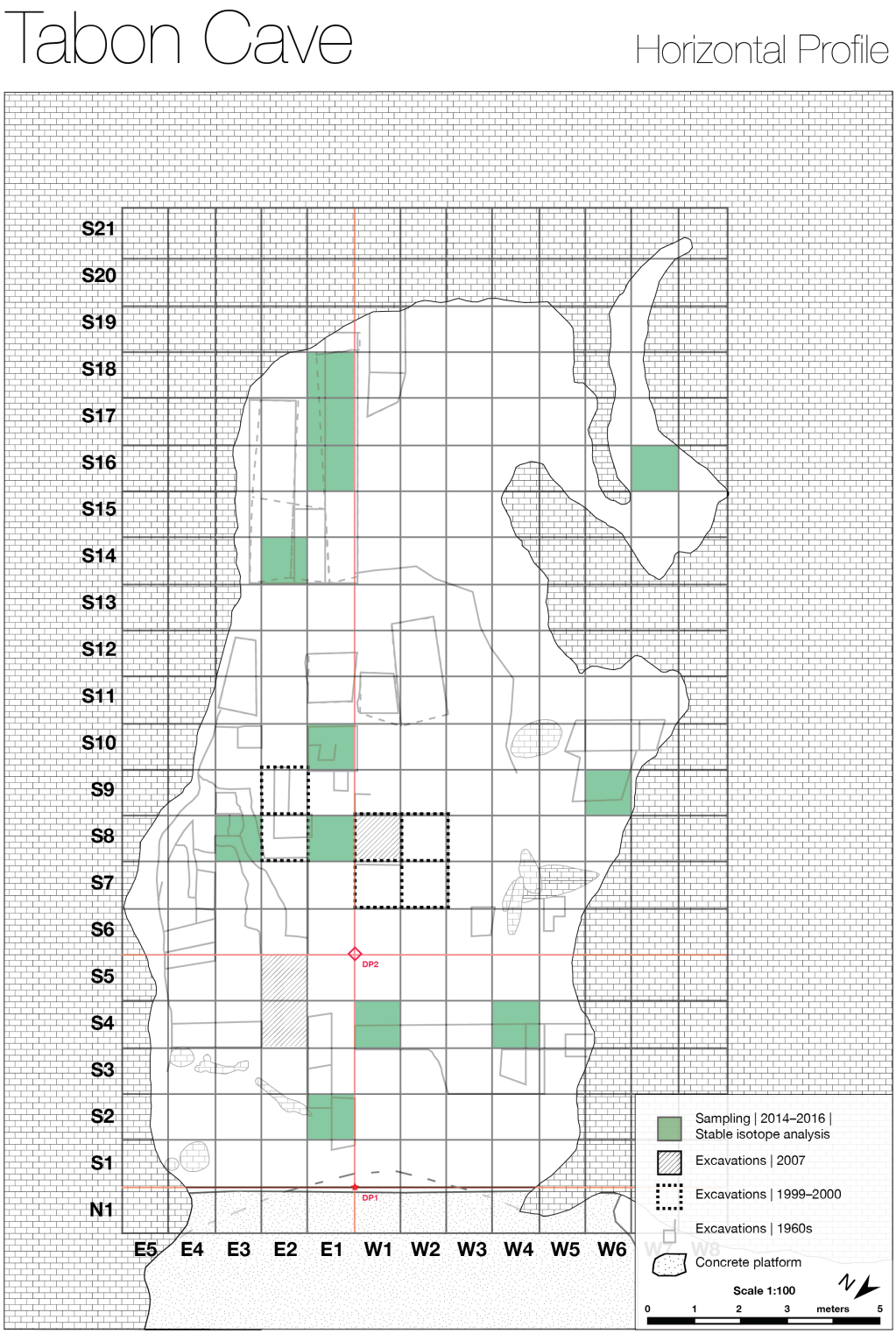

Figure 37. Sampling zones for stable isotope analysis.

For certain squares, multiple samples from the target layer were analyzed to check results repeatability. For the South Trench, however, samples from all layers were analyzed. Due to promising initial results, particular attention was given to Layer 3, from which 4 extra samples (BULK07 to BULK10) were collected during the 2016 field mission to test repeatability.

In order to establish a baseline for comparison, as well as to determine the impact of diagenesis on stable isotope signatures in the fossil guano of Tabon Cave, modern specimens were also collected and analyzed. Two samples from the main chamber of the cave, where swiftlets currently roost, were collected: Sample 52 (Square S14E2), and Sample 53 (Square S9W6). They were each duplicated for repeatability, yielding Samples 52-1, 52-2, 53-1, and 53-2. A final sample, Sample 30, was collected from the diverticulum (Square S16W7) in the southwestern part of the cave, presently occupied by a bat colony.

In all, a total of 36 samples were processed for stable isotope analysis.

Table 8. List of samples for stable isotope analysis.

Sample	Location	Layer (square-specific)	Depth (cm below DP)
2	Square S2E1	Equivalent of Layer 5 in S4W1	292
3	Square S2E1	Equivalent of Layer 5 in S4W1	312
7	Square S2E1	Equivalent of Layer 5 in S4W1	337
BULK03	Square S4W1	5	313
BULK04	Square S4W1	5	313
BULK05	Square S4W1	5	313
BULK06	Square S4W1	5	313
8	Square S4W4	6	302
9	Square S4W4	6	318
10	Square S4W4	6	325
11	Square S4W4	6	332
12	Square S4W4	6	337
13	Square S4W4	Equivalent of Layer 1 in S4W5	145

Sample	Location	Layer (square-specific)	Depth (cm below DP)
21	Square S8E1	10	326
45	Square S8E3	Equivalent of Layer 12 in S9E3	325
53-1	Square S9W6	Surface	(undefined)
53-2	Square S9W6	Surface	(undefined)
X17	Square S10E1	4	318
52-1	Square S14E2	Surface	(undefined)
52-2	Square S14E2	Surface	(undefined)
30	Square S16W7	Surface	(undefined)
A	South Trench	11	333
B	South Trench	10	285
C	South Trench	9	238
D	South Trench	7/8	220
E	South Trench	4/5	162
F	South Trench	3	142
G	South Trench	1	113
MM1	South Trench	10–11	316-321
MM2	South Trench	9–10	265-270
MM3	South Trench	7/8–9	223-228
MM4	South Trench	2–3	135-140
BULK07	South Trench	3	135
BULK08	South Trench	3	135
BULK09	South Trench	3	135
BULK10	South Trench	3	130

3.5.5. Sample analysis

Samples were treated for insect cuticle isolation, consisting of the following steps in order:

1. Delipidation
2. Static dense medium separation
3. Recovery of insect cuticles (including decarbonation)
4. Verification

Sample preparation

Samples were pre-treated following the detailed procedures presented in Appendix B.

Data acquisition

Mass spectrometry was performed at the Service de Spectrométrie de Masse Isotopique du Muséum (SSMIM) at the Muséum national d'histoire naturelle in Paris, France.

Samples were measured into 8 x 5 mm tin capsules, which were then folded up into compact cubes. The cubes were collected in a 96-well plate and run in a Thermo Fisher™ DELTA V Advantage Isotope Ratio Mass Spectrometer (IRMS) coupled with a Thermo Fisher™ FLASH 2000 Organic Elemental Analyzer (OEA) (Thermo Fisher Scientific, Bremen, Germany).

3.6. Radioisotope dating

3.6.1. Carbon-14

Application to Tabon Cave guano

One of the most important issues concerning the various guano layers in Tabon Cave is their age, which is crucial in giving chronological context to whatever palaeoenvironmental data they may provide. Unfortunately, previous attempts to date them, via uranium-series in particular, had been unsatisfactory. The stratigraphically incoherent or improbable ages obtained were attributed to uranium leaching and uptake, as well as the open-system nature of the deposits (Ghaleb *et al.*, 2012).

Thus far, radiocarbon dating had not been attempted on the fossil guano in the cave for two reasons, both based on one deposit in particular: Layer 12 in the front part (Figure 38). First, the stratigraphic position of Layer 12, at more than 1.5 m below the fireplace securely dated to at least 33 ka BP, suggested that its age would at least be close to the technical limits of the method, if not beyond (however, this conjecture is admittedly difficult to substantiate without data on the sedimentation rates in Tabon Cave). Second, in the initial uranium-series dating tests conducted by Ghaleb *et al.* (2012), the most promising sample dated to ca. 110 ka corresponds to Layer 10 in the front part of the cave, which overlies Layer 12 (Figure 38). Entertaining the hypothesis that this age is plausible (the uranium content of the sample being close to that of modern guano), it would the minimum age for Layer 12 and put it well beyond the reach of radiocarbon dating. These ideas gave rise to the hypothesis that Layer 12 is radiocarbon-dead.

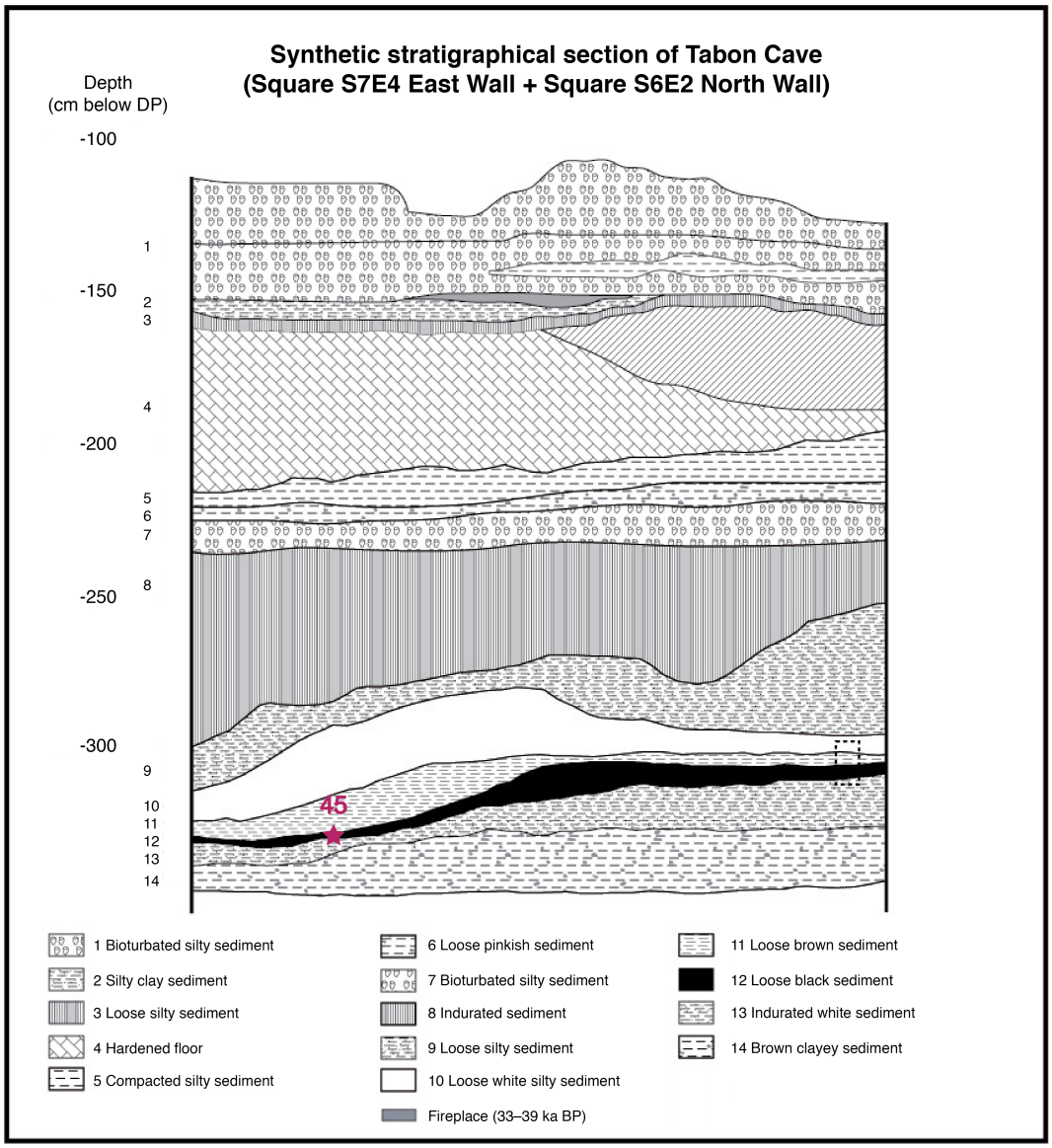

Figure 38. A synthetic stratigraphical section of Tabon Cave, mostly representative of the front part of the site. Layers 12 and 10 are visible toward the bottom of the profile. Layer 12, represented by Sample 45 (projected location), was targeted for radiocarbon dating.

In the back part of the cave, three guano deposits have been identified: Layers 10, 7/8, and 3 (Figure 39). Uranium-series dating had been unsuccessfully attempted on Layers 10 and 7/8, resulting in infinite ages (Ghaleb *et al.*, 2012). Radiocarbon dating has not been tested on any of these deposits so far, and there is no *a priori* indication that they are radiocarbon-dead, especially since their relationship to Layer 12 in the front part of the cave remains unclear.

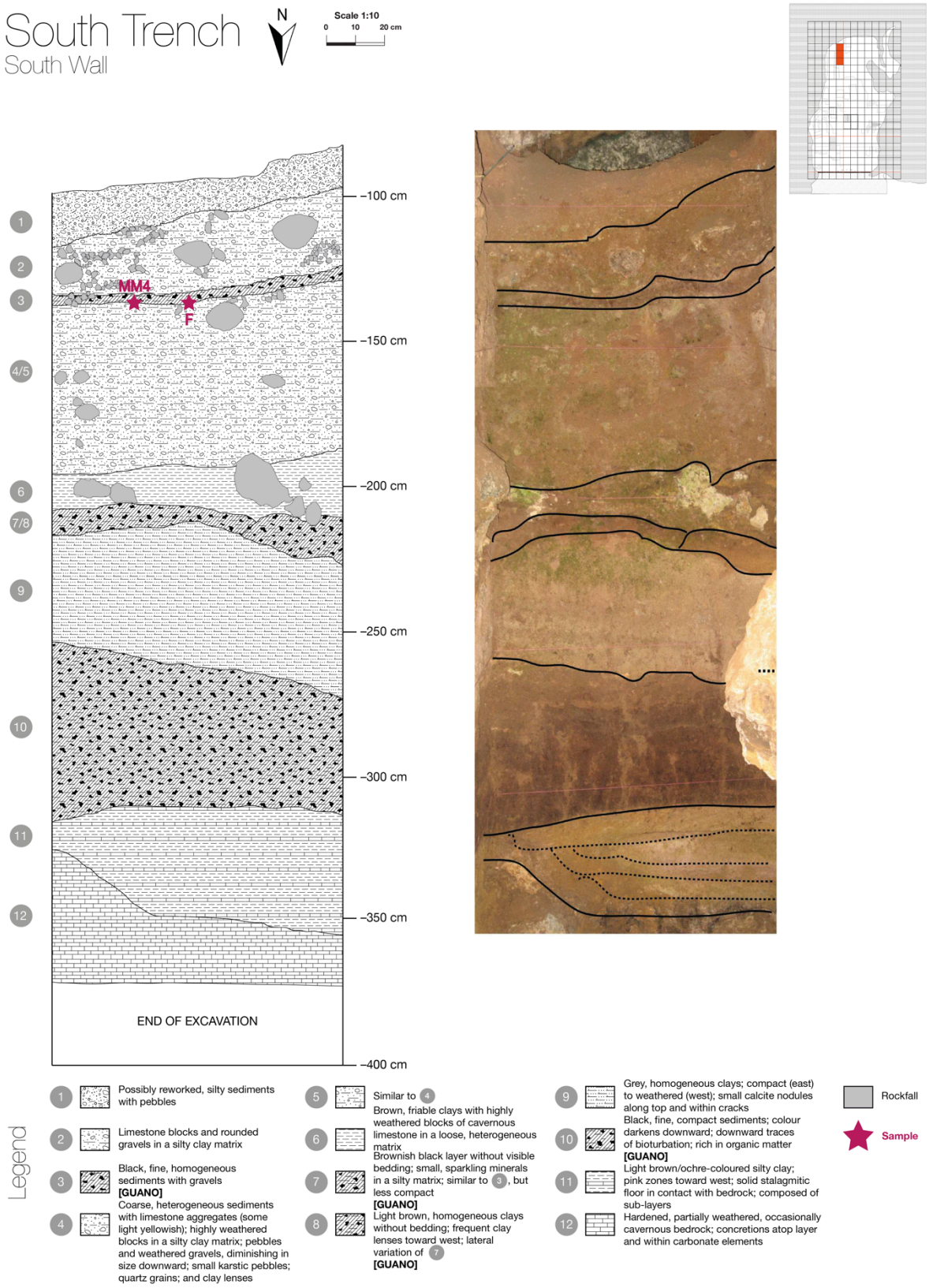

Figure 39. The vertical profile for the south wall of the South Trench, representing the back part of Tabon Cave. The three identified guano deposits are Layers 10, 7/8, and 3. Layer 3, represented by Samples F and MM4, was targeted for radiocarbon dating.

Sample selection

An opportunity arose to have radiocarbon dating performed via accelerator mass spectrometry (AMS) on three samples at the Laboratoire de Mesure du Carbone 14 (LMC14) (Gif-sur-Yvette, France), courtesy of Jean-Pascal Dumoulin. In comparison to conventional radiometric dating, AMS has the advantages of requiring small sample quantities and providing greater precision. The former is particularly useful for Tabon Cave guano: despite certain deposits having organic carbon content of at least 20% (Choa *et al.*, 2016), pre-treatment for organic matter extraction can eliminate much of original sample weight. In Section 4.3.1, which describes sample loss after preparation for stable isotope analysis, it was not always possible to keep rates at the minimum threshold of 87%. While the protocol differs for radiocarbon dating, the objective of organic matter extraction is the same, so loss rates should be comparable.

Of the three samples to be dated, two were collected from Layer 3. Being the youngest fossil guano deposit in the back part of the cave, it was considered to be the one best suited to radiocarbon dating. Two samples, Samples F and MM4, were chosen for repeatability. The third sample, Sample 45, was collected from Layer 12 in the front part of the cave to test the radiocarbon-dead hypothesis. All samples were in bulk sediment form.

Sample analysis

Sample preparation and analysis were performed by the LMC14 staff.

Samples were first examined under a stereomicroscope for removal of possible contaminants (e.g. hairs, fibers, rootlets). A sufficient quantity of each sample was then collected for acid-base-acid (ABA) treatment, consisting of the following steps:

1. The sample was treated in an excess of 0.5 N HCl for several hours at 80 °C to eliminate carbonates, then rinsed with ultrapure H_2O until neutral pH was achieved.
2. Next, the sample was treated with 0.1 N NaOH for one hour at 80 °C to remove humic acids. Another rinsing with ultrapure H_2O followed to re-neutralize the pH.
3. Finally, the sample underwent a last wash in 0.5 N HCl for one hour at 80 °C to eliminate any modern atmospheric CO_2 that the sample may have absorbed during

the base treatment. It was then rinsed with ultrapure H_2O one final time to bring the pH back to neutral.

Taking into account the differing total organic carbon (TOC) content of the samples, as well as the necessity of producing a CO_2 volume containing around 1 mg of carbon upon sample combustion, a suitable quantity of material was further collected from each sample. Combustion was conducted in the presence of around 500 mg of CuO and a silver wire for five hours at 835 °C.

The resulting CO_2 then underwent reduction by hydrogen in the presence of iron powder at 600 °C. The mass of iron is thrice that of carbon, with a minimum value of 1.5 mg and a maximum of 4 mg. The carbon precipitated onto the iron powder, and the result was pressed onto a mount for measurement via accelerator mass spectrometry (AMS).

For each sample, carbon-14 activity was calculated by comparing the consecutively measured intensities of the carbon-14, carbon-13, and carbon-12 beams with those of CO_2 standards prepared from HOxII (Oxalic Acid SRM 4990C). It is denoted in pMC (percent Modern Carbon) and normalized to a $\delta^{13}C$ value of –25‰.

The radiocarbon ages were calculated following Mook and van der Plicht (1999), with fractionation corrected using the $\delta^{13}C$ value calculated from the $^{13}C/^{12}C$ ratio measured by ARTEMIS, the accelerator mass spectrometer.

The $\delta^{13}C$ used takes into account fractionation that may have occurred during sample preparation as well as during AMS measurement. It is also reliant on the transmission of the setup, specifically the $^{13}C/^{12}C$ value measured out of ARTEMIS relative to the $^{13}C/^{12}C$ value measured out of the source. These values depend on the beam at injection, current, and emittance; thus, the $\delta^{13}C$ measured by ARTEMIS cannot be compared to that measured by a mass spectrometer. The $\delta^{13}C$ values are corrected relative to a standard; as such, they do not affect the measurement of the radiocarbon age.

Measurement uncertainty simultaneously takes into consideration statistical error and measurement variability for both sample and subtracted background. Results are indicated without reservoir age correction.

3.6.2. Uranium-234 and thorium-230

All uranium-series analyses were conducted at the Geotop Research Centre on the Dynamics of the Earth System at the Université du Québec à Montréal (UQÀM) in Canada.

Background

In 2012, a field mission to Tabon Cave was organized to investigate several stratigraphical profiles. The focus was on understanding various weathering sequences that had previously been observed in the cave, as well as the sedimentary contrasts between the different zones of the cave (Ghaleb *et al.*, 2012). During the said mission, a number of bulk sediment samples were collected for uranium-series analysis in hopes of clarifying the cave's chronology. The majority of these samples originate from the weathering sequences and were provisionally described as being composed of guano, phosphates (e.g. hydroxylapatite), or sulphates (e.g. gypsum).

The areas where the samples were collected are indicated in Figure 40.

The report indicates that, while some of the ages appear consistent, others are stratigraphically incoherent (i.e. younger ages for deeper layers). Specifically, uranium content was found to be either far above (in the case of fossil guano) or far below (in the case of authigenic minerals) that of the modern guano sample (2.372 ppm), rendering the U/Th ratios unsuitable for chronology reconstruction. It was suggested that interpretation would need to take into account uranium uptake, distribution variability, trapping, and leaching, as well as system behaviour (closed/open). Nevertheless, some of the deposits that were studied and others that were identified appeared to hold promise for further analysis: these are the 'grey speleothem' phosphates, the white hydroxylapatite layers, and the 'yellow speleothem' sulphates.

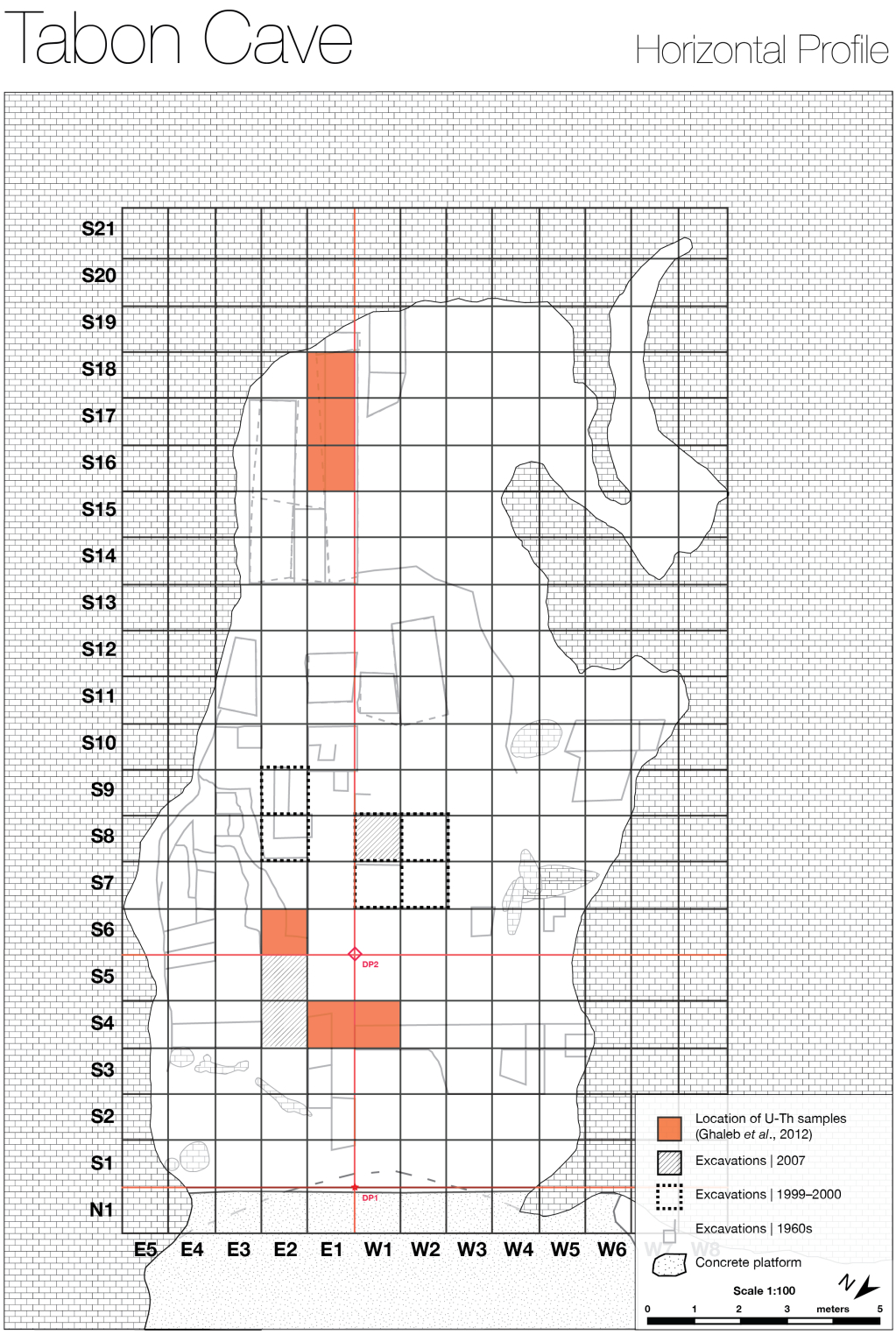

Figure 40. Distribution of samples collected in 2007, 2009, and 2012 and used for uranium-series analysis.

The grey speleothem

The 'grey speleothem' is a highly compact stratigraphical feature visible in the east part of the Central Zone (Squares S8E3 to S9E3, in particular). It consists of blackish grey and yellow bands (Figure 41 and Figure 42). During the 2012 field mission to Tabon Cave, a big, solid block sample (Sample D13; approximate dimensions 9 cm × 6 cm × 2 cm) was collected for future dating.

Figure 41. The grey speleothem, visible on an exposed profile in the east part of the Central Zone.

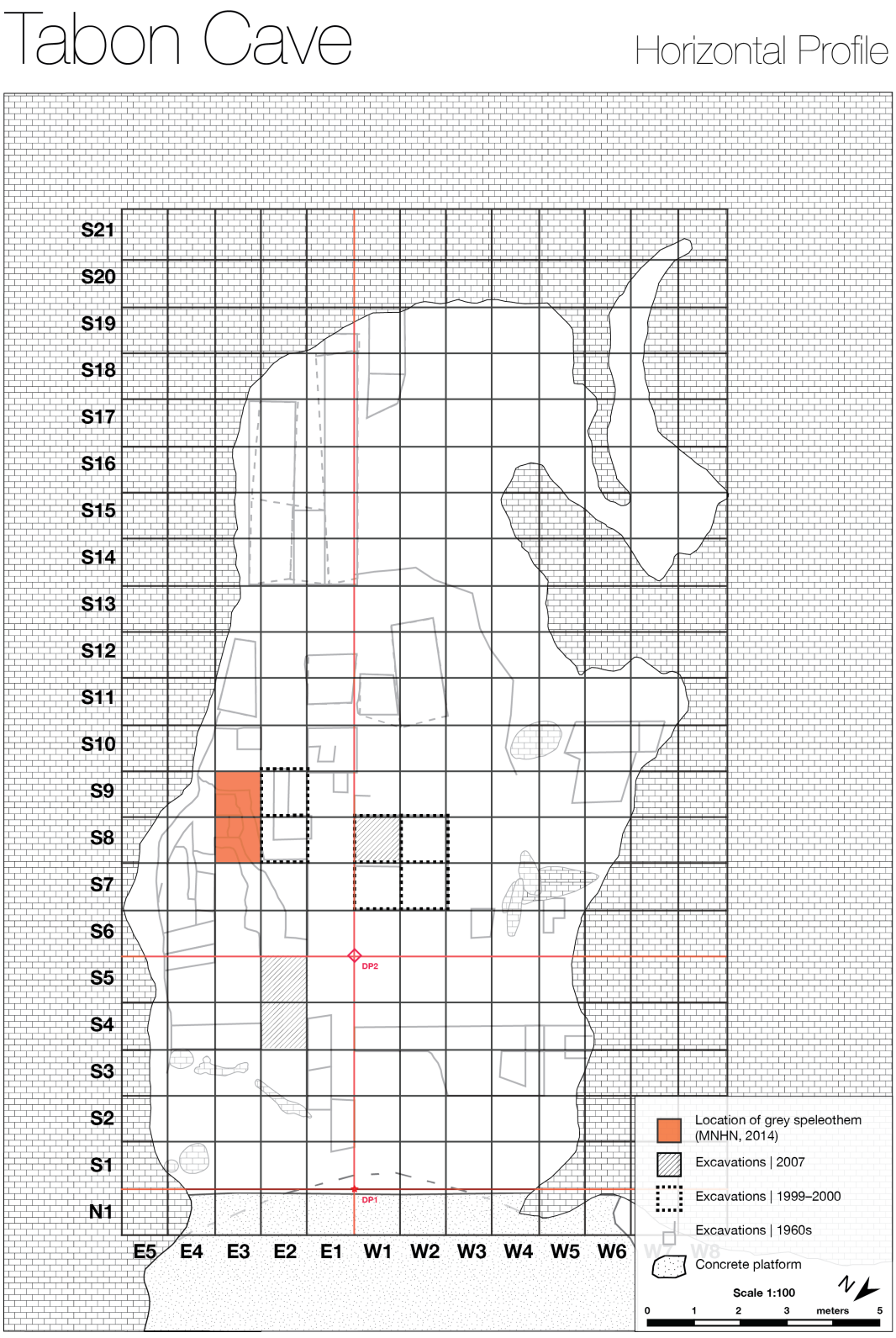

Figure 42. The east part of the Central Zone where the grey speleothem is visible in the stratigraphy.

The compact nature of the grey speleothem suggested that it might constitute a closed system for uranium, and consequently, that it might lend itself to uranium-series dating. More importantly, a preliminary test on the block yielded a uranium-series age of around 50 ka (B. Ghaleb, *pers. comm.*), which would fit nicely into the stratigraphy if verified: the fireplace, located above, falls between 33 and 39 ka BP, while Layer 10 below has been tentatively dated to around 110 ka (Figure 43; Ghaleb *et al.*, 2012). A sampling strategy for the block was thus developed to verify these hypotheses.

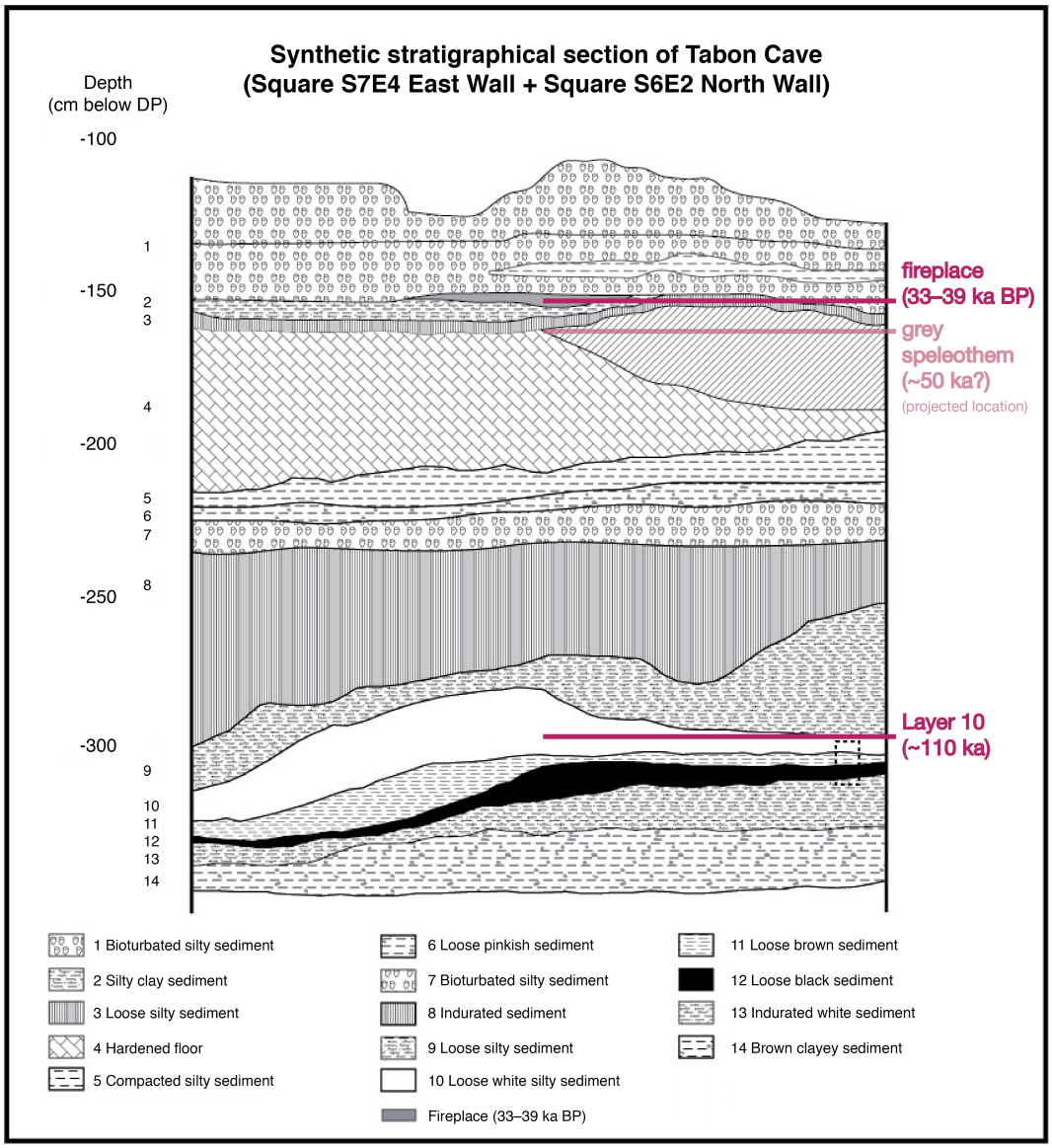

Figure 43. The synthetic stratigraphical section of Tabon Cave. The locations of the fireplace and of Layer 10 are indicated alongside their available chronological data. Sandwiched between the two are the projected location of the grey speleothem and its preliminary age, slightly washed out.

Hydroxylapatite

In the analysis that followed the 2012 field mission, the hydroxylapatite sample Tab-2012-D6 was one of the handful that suggested promise for dating. Its reasonable uranium content pointed to the possible proximity of its calculated and true ages (Ghaleb et al. 2012). The sample was collected from a white, powdery layer, found to be composed of hydroxylapatite.

Hydroxylapatite ($Ca_5(PO_4)_3(OH)$) is one of the first phosphate minerals to form during guano diagenesis (Karkanas and Goldberg, 2010). In karst contexts, it is a direct product of phosphates in guano reacting with calcium in limestone (Onac and Vereş, 2003). However, it can also result from the dissolution of bone or ash (Schiegl *et al.*, 1996; Karkanas *et al.*, 1999; Forbes and Bestland, 2006).

Ghaleb *et al.* (2012) posit that the hydroxylapatite in Tabon Cave is an early product of guano weathering based on two arguments: the relatively limited deviation of its uranium content from that of the modern guano sample analyzed for reference (5.512 ppm vs 2.372 ppm), and the presence of a fossil guano layer immediately underneath, Layer 12 (Figure 44). If this hypothesis is confirmed, then the calculated U/Th age of around 110 ka may indeed closely approach the actual age. As such, similar low-uranium, guano-derived hydroxylapatite samples from the cave could hold promise for the establishment of its chronology. Nevertheless, an important factor to take into account is the extremely high uranium content of the underlying fossil guano layer (90.248 ppm for Tab-2012-D5, collected underneath Tab-2012-D6; Ghaleb *et al.*, 2012). The excess uranium might have come from intensive leaching of the hydroxylapatite layer above, and this increased complexity in the layer's geochemical history would make it much more complicated to date (C. Falguères, *pers. comm.*).

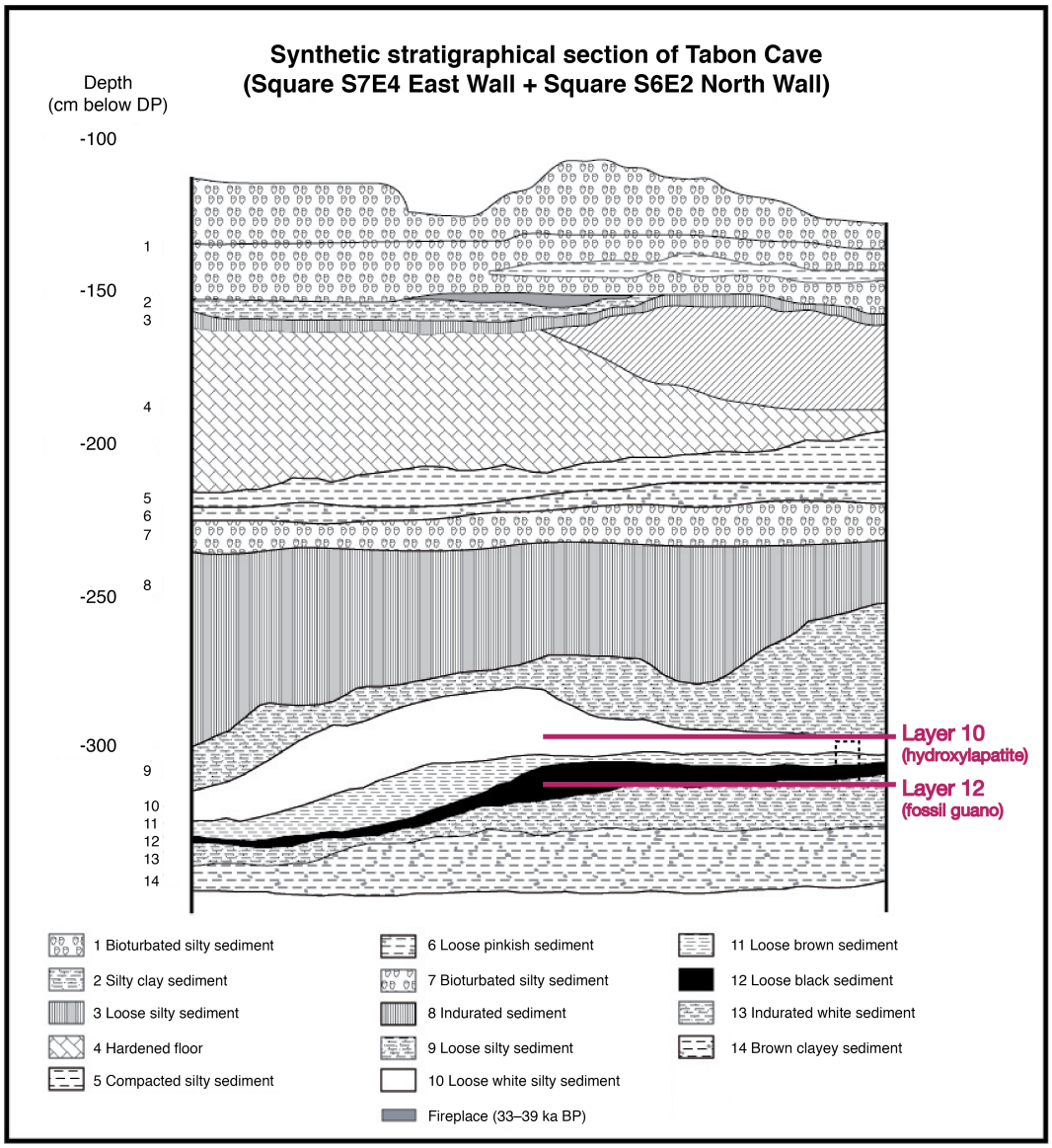

Figure 44. The synthetic stratigraphical section of Tabon Cave highlighting the locations of Layer 10, composed of hydroxylapatite, and Layer 12, composed of fossil guano.

The yellow speleothem

Lewis *et al.* (2008) undertook uranium-series dating of a speleothem sample, TBG1, from Tabon Cave (Figure 45). According to them, TBG1 was collected from a "thick, hard greyish-white layer recorded by Fox and later authors as 'travertine' (Figure 46)... The upper part of this deposit is hard, layered speleothem, while the lower part is soft loose silt... Only the upper hard layers were sampled for U-series study, with a block... collected from an exposed section" (Lewis *et al.*, 2008: 40-41). Characterization revealed TBG1 to be composed of gypsum and not calcite, as the previous appellation of travertine suggested. The team obtained ages of 20.2 ± 0.8 and 19.5 ± 0.8 ka BP on the upper part of the sample. They validated these ages

through correlation with the ^{14}C dates that Fox obtained on the constraining layers just above (> 21 ka BP) and below (23.2 ± 1 ka BP), respectively Layers C and D (Fox, 1970).

Figure 45. Location of speleothem sample TBG1 collected by Lewis *et al.* (2008) for uranium-series dating.

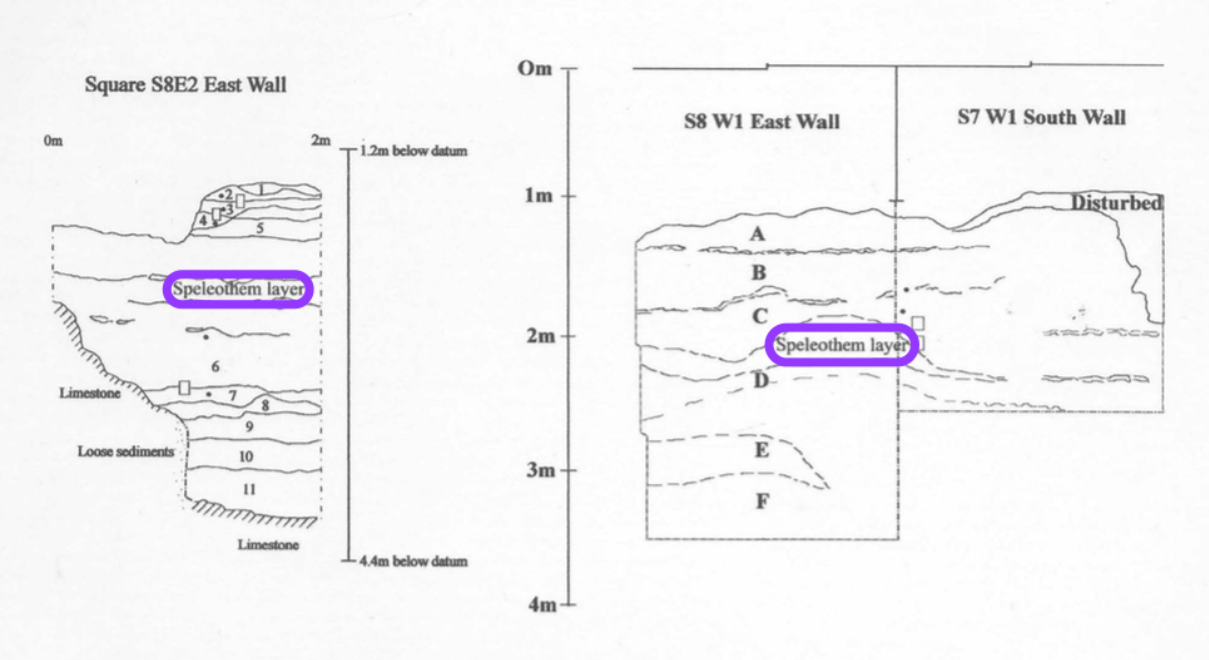

Figure 46. Locations sampled by Lewis and various colleagues in Tabon Cave. The speleothem sample collected for uranium series dating, TBG1, "... came from the uppermost, hard layers immediately under the equivalent of Layer C" (indicated by the annotations) (Lewis *et al.*, 2008: 42).

The speleothem layer sampled by Lewis *et al.* (2008) is located at around 200 cm below DP (Figure 46). According to an earlier profile prepared by Orogo (2001b), the layers that bracket the speleothem, C and D, both consist of soft, fine sediment (Figure 47).

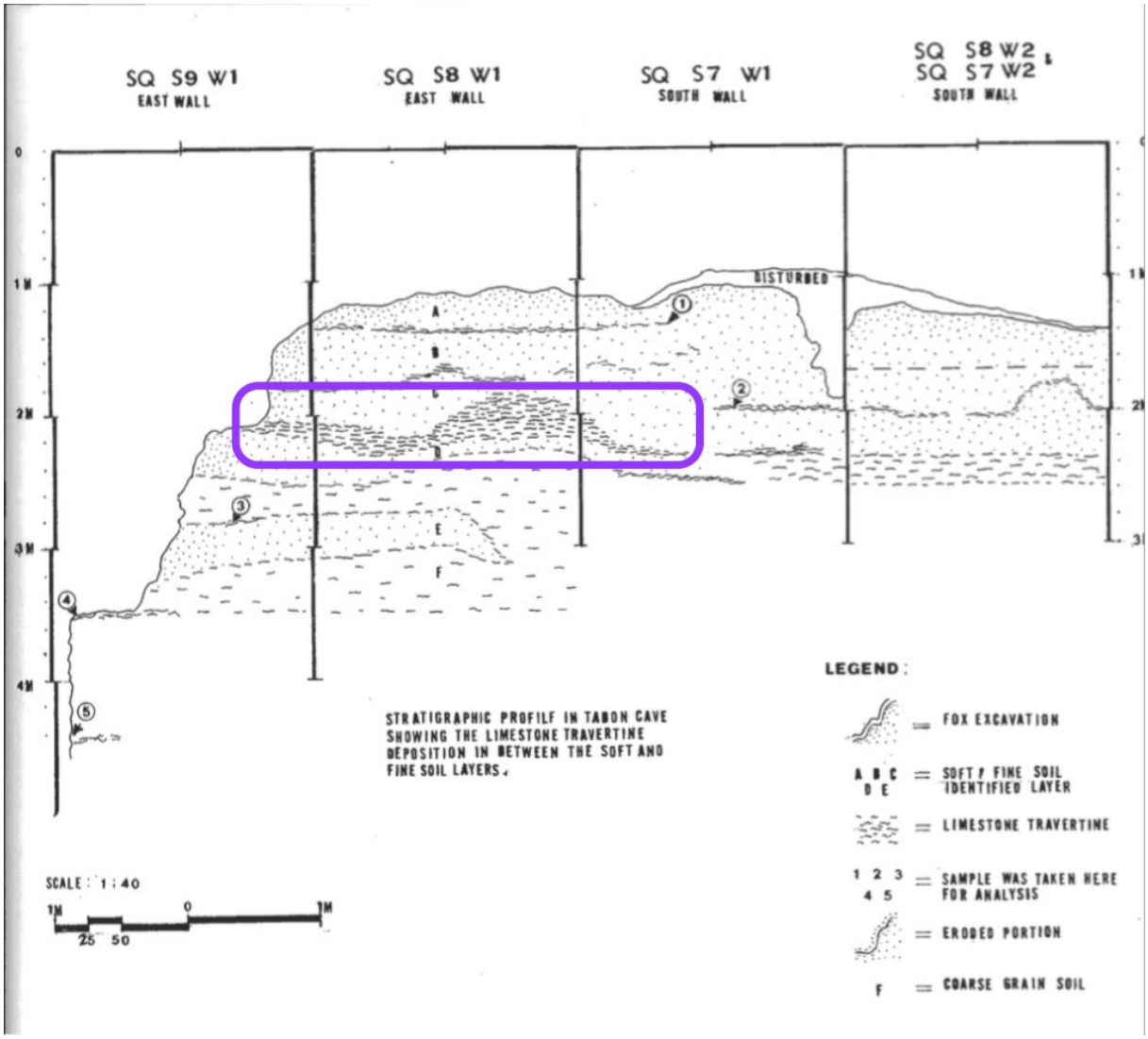

Figure 47. Vertical profiles from the central zone of Tabon Cave (Orogo, 2001b). The speleothem layer, shown by the annotation and indicated as 'limestone travertine' in the legend, is sandwiched between Layers C and D.

Comparing it with the profiles prepared by Fox (1969) for the same zone, in which the depths are offset by around 100 cm with respect to the datum point, the speleothem layer seems to correspond to Layer III, which is situated at around 220 cm below DP (Figure 48).

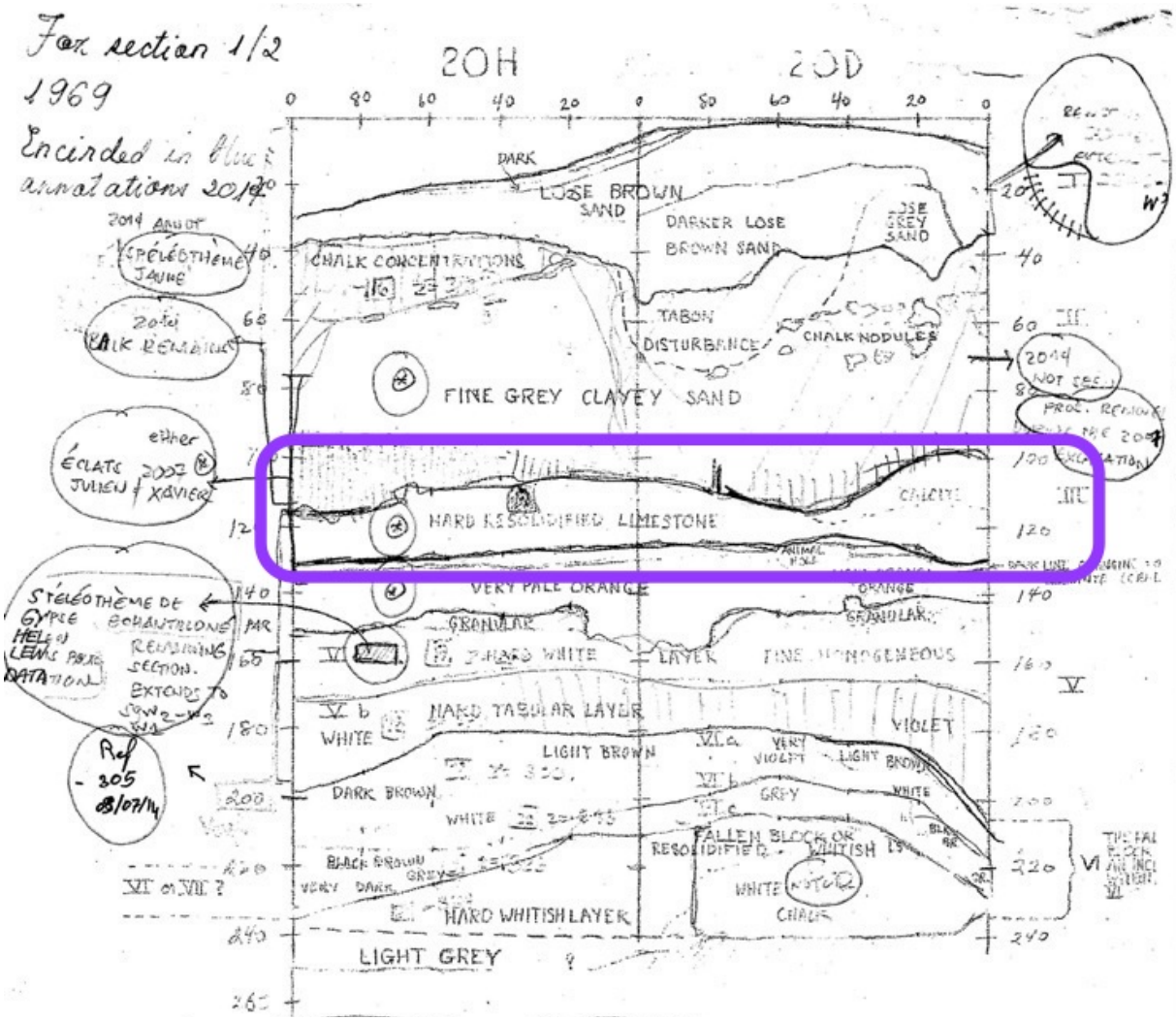

Figure 48. Vertical profiles from the central zone of Tabon Cave (Fox, 1969). The speleothem layer is shown by the annotation and indicated as 'hard resolidified limestone'/'calcite'/'Layer III'.

A speleothem of light yellow colour was observed by the MNHN team in the same area where Lewis *et al.* (2008) collected their gypsum sample for uranium-series dating, TBG1 (Figures Figure 49 and Figure 50). A new sample was collected in 2014 for further analysis, Sample 16.

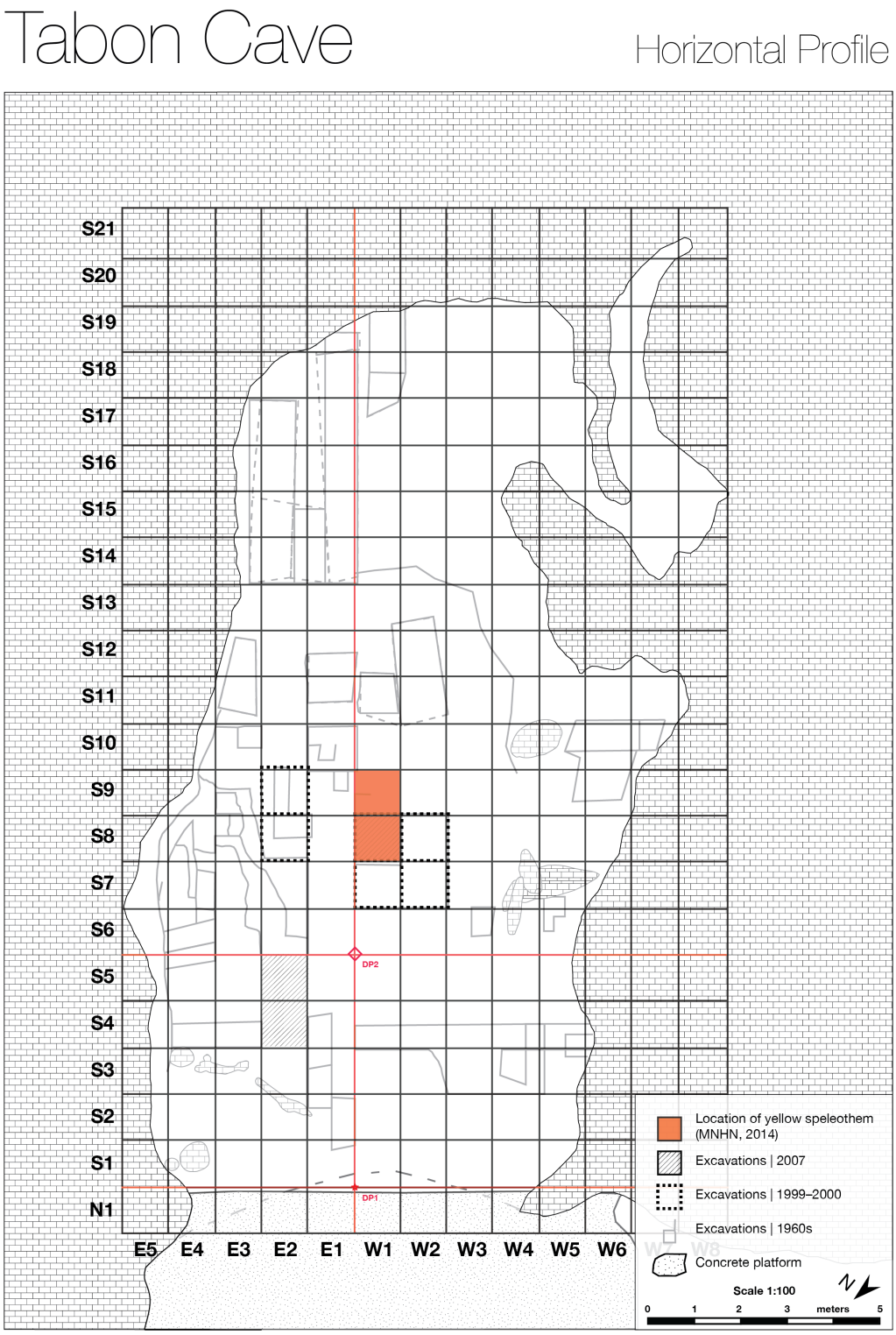

Figure 49. Location of the yellow speleothem sample, Sample 16, collected in 2014 by the MNHN team.

Figure 50. Close-up of the yellow speleothem.

Mineralogical characterisation revealed gypsum and brushite to be the principal phases, with traces of variscite and taranakite (Figure 51). Nitratite and tinsleyite may also be present, albeit representing a very small contribution (Figure 52).

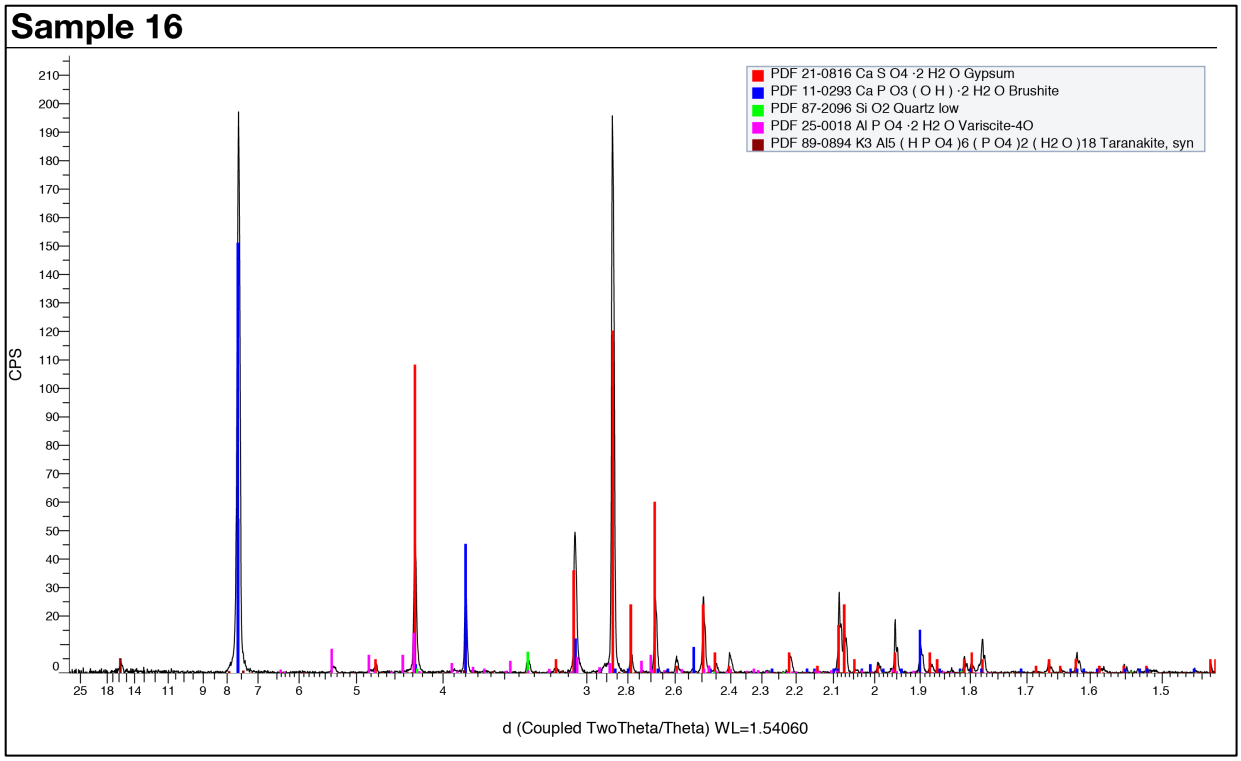

Figure 51. X-ray diffractogram of Sample 16. Identified phases include gypsum, brushite, quartz, variscite, and taranakite.

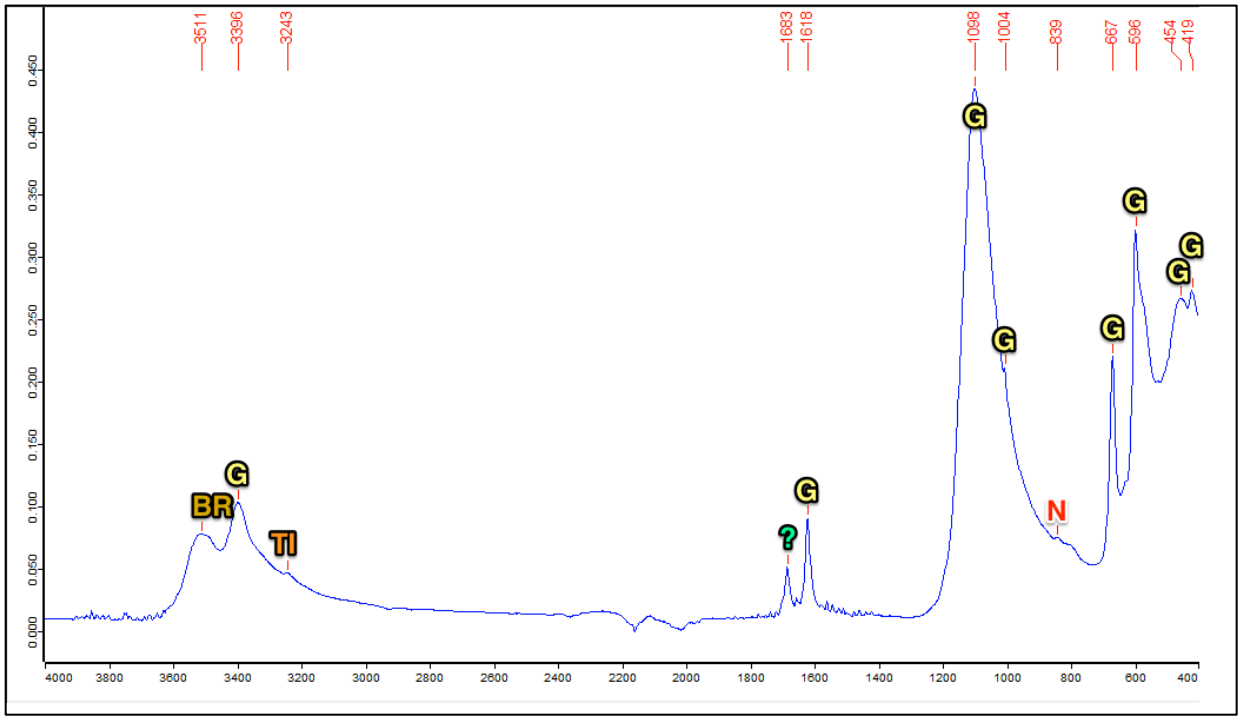

Figure 52. Fourier-transform infrared spectroscopy (FTIR) spectrum of Sample 16 in attenuated total reflection (ATR) mode. Identified phases include gypsum (G), nitratine (N), and tinsleyite (Tl). The brushite (B) identification is uncertain. A strong peak at 1683 cm^{-1} remains unidentified.

Given that:

- Sample 16 was collected in the exact same zone as TBG1; that
- its depth (212 cm below DP) corresponds quite well to that of the Lewis speleothem (200–220 cm below DP); and that
- it is composed primarily of gypsum,

it is highly likely Sample 16's layer of origin, the yellow speleothem, is equivalent to the Lewis speleothem.

It is worth noting that this layer seems to have undergone weathering over the course of only several years, altering its observable characteristics. Lewis *et al.* (2008) describe the layer as hard and greyish white and cite that Fox recorded it as travertine. Gallet (*pers. comm.*) affirms that, during the first excavation of the said layer by the MNHN team, the use of a crowbar was necessary. When Sample 16 was collected in 2014, however, the layer was observed to be friable/powdery and characterised by a yellowish white colour.

Sample selection

For the grey speleothem, a longitudinal section measuring 9 cm × 1 cm × 2 cm was sawn off the original block and polished to remove the crust (Figure 53). Five zones on the section were selected for sampling, after which samples were sawn off and polished (SG-01 to SG-05; Figure 54). A sixth sample, collected during the 2016 field mission, was added to the set (SG-06; Figure 55). The main objective was to cross-validate the numerous radiocarbon dates obtained for the fireplace, given its stratigraphical proximity to the grey speleothem.

Figure 53. Profile view of the original block (above) and the detached longitudinal section (below).

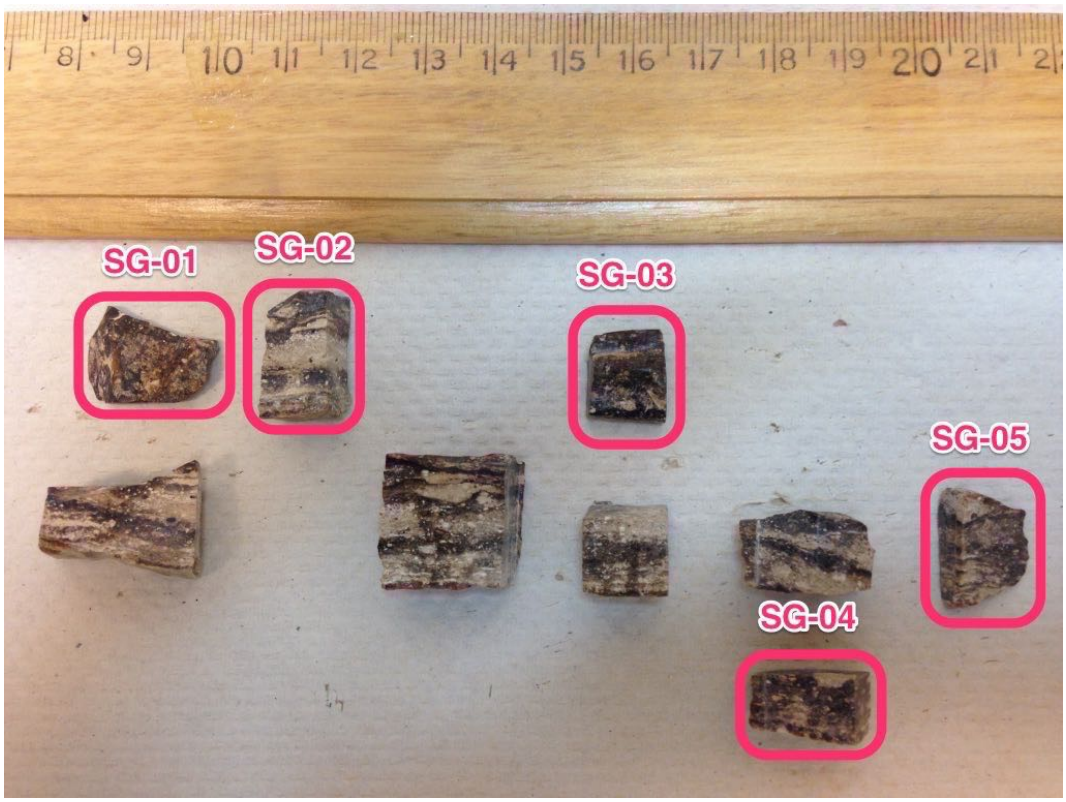

Figure 54. Exploded view of the detached longitudinal section, with the 5 samples SG-01 to SG-05 indicated.

Figure 55. The supplementary sixth element of the grey speleothem sample set, SG-06.

For hydroxylapatite, five samples were processed for uranium-series analysis: Samples 06, 15, 20, 28, and 44. They were selected based on visual appearance (a light greyish/bluish white colour), texture (very fine silt), and mineralogical profile (with hydroxylapatite as the dominant phase, identified in FTIR and/or XRD). The main objective was to try to reproduce the age of 109.8 ± 2.6 ka obtained on Sample D6 by Ghaleb *et al.* (2012), operating on the hypothesis that the samples all belong to the same chronostratigraphical unit given their similar visual aspects, comparable depths, and relatively localized spread within the cave.

Finally, for the yellow speleothem, only one sample was selected for uranium-series dating due to practical limitations. Sample 16 was analyzed with the main objective of reproducing the Lewis *et al.* (2008) ages.

Sample analysis

Characterization

For the grey speleothem phosphates, *energy-dispersive X-ray spectroscopy* (EDS) was carried out for chemical characterization prior to radioisotope analysis, using a Hitachi S-3400N Scanning Electron Microscope (SEM) fitted with a Deben Centaurus SEM Cathodoluminescence (CL) and Back-Scattered Electron (BSE) Detector.

Each sample was mounted on a rectangular aluminium platform at an orientation of 90° counterclockwise from the desired analysis position (this compensates for the preparatory 90° clockwise rotation by the SEM before analysis). The mounted sample and platform were then screwed onto the metal stub, and the combined height (in mm) of the entire assembly was measured using the manufacturer-provided scale. The fixed platform size of 32 mm and the variable assembly height were entered into the SEM software interface, and the stage height was adjusted automatically. After verifying that the top of the sample does not touch the check gauge, the specimen chamber was shut.

Air was evacuated from the chamber until internal pressure decreased to 30 Pa, at which point the electron beam was activated. The parameters of the resulting image—brightness, contrast, focus, magnification—were adjusted to render identified sites of interest more clearly. Their EDS spectra were acquired and plotted for qualitative analysis, then normalized for quantitative analysis, using Oxford Instruments INCA software. After analysis, the electron beam was turned off and air reintroduced before changing samples.

An initial test was performed with all six samples simultaneously mounted (Figure 56). Unfortunately, the significant differences in sample thickness led to difficulties in image adjustment (notably depth-of-field), so samples were analyzed individually instead.

Mineralogical analysis via FTIR and XRD was then performed on the grey speleothem samples to corroborate EDS findings, as well as on the hydroxylapatite and yellow speleothem samples. Protocol details are described in Section 3.4.

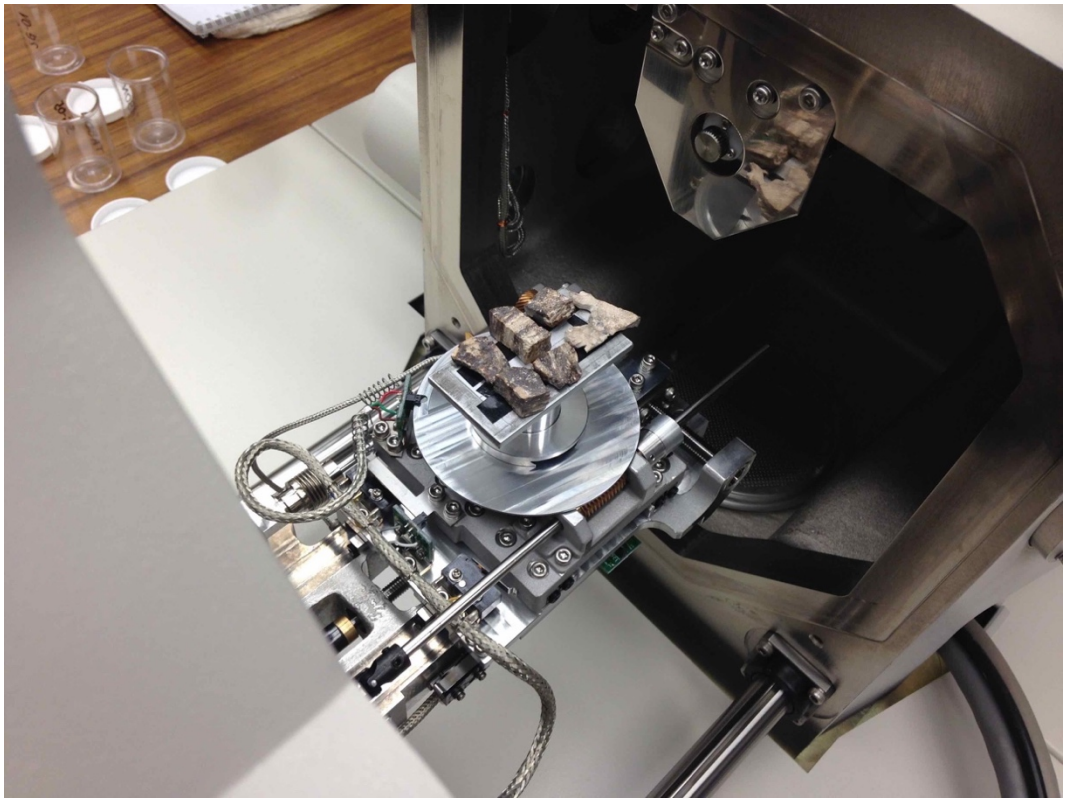

Figure 56. Initial attempt at a single EDS run of all six samples.

Extraction chromatography

This section is composed of three major sub-sections, each describing the uranium and thorium extraction chromatography protocol for:

- the grey speleothem samples;
- the hydroxylapatite samples; and
- the yellow speleothem sample.

A short note on the labware cleaning protocol and a table of weights summarizing the measured sample and spike quantities close the section.

For each sample type analyzed, the main steps are the following:

- sample and spike preparation
- dissolution
- centrifugation
- separation of thorium and uranium fractions
- purification of thorium and uranium fractions

The main idea involves differential percolation of a dissolved sample in a resin matrix to separate its thorium and uranium atoms. By capitalizing on the mutually exclusive solubility of the two elements, it is possible to manipulate the matrix chemically to retain one while extracting the other. (Uranium is soluble in H_2O, while thorium is soluble in HCl.)

The protocol for gypsum was modified to adjust for its low solubility, mainly through the addition of a precipitation step.

Grey speleothem

SAMPLE AND SPIKE PREPARATION

The samples were finely ground using a small agate mortar and pestle. Between 0.3 and 0.4 g of sample were then weighed into aluminium dishes (Figure 57), with the rest set aside for further characterization via infrared spectroscopy. The dishes were placed in a furnace at 500 °C for 1.5 hours to destroy organic matter through ignition.

In the meantime, six 50-ml Teflon-PTFE beakers were prepared in a cleanroom environment. The beakers were labelled with the sample names and purged of static electricity. Between 0.15 and 0.20 g of an isotopic spike solution were then squirted into each beaker and weighed accurately. (The spike consists of pre-determined concentrations of the following isotopes, used here as tracers: uranium-236, uranium-233, and thorium-229.) The beakers were placed on a hot plate at 85 °C for 1 hour, allowing the liquid phase to evaporate and leaving heavy isotopes to stick to the beaker bottoms.

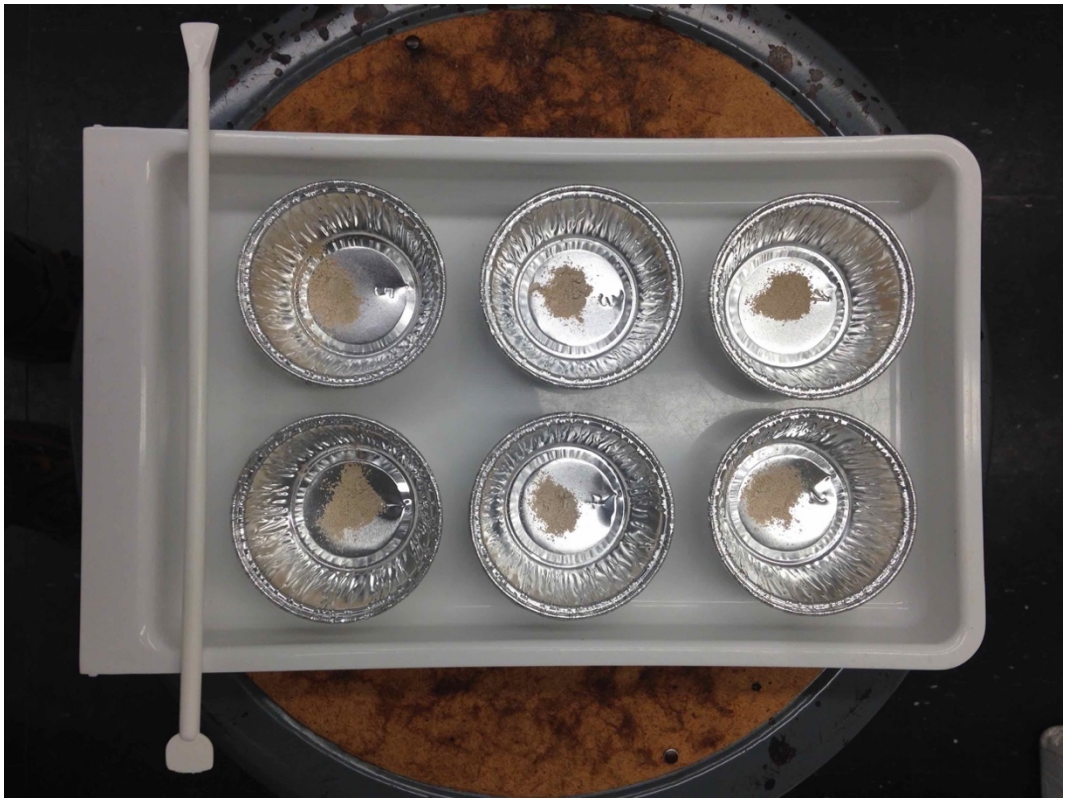

Figure 57. The 6 samples in aluminium dishes after grinding and before organic matter ignition.

Once the samples were ready, they were carefully taken out of the furnace and allowed to cool slightly before being transferred into their respective beakers and entering into contact with the tracer isotopes. The aluminium dishes were rinsed as necessary with Milli-Q® H_2O to recover the maximum amount of sample.

DISSOLUTION

A few millilitres of 6 M HCl were then added to each beaker to dissolve the samples. The resulting mixtures were lightly stirred using sterile inoculation loops and left to sit at 80 °C on a hot plate.

CENTRIFUGATION

After 2 days, the samples were removed from the hot plate and re-dissolved in a few millilitres of 6 M HCl. Brackish material was observed at this point (Figure 58), possibly consisting of either sedimentary particles or residue from the organic matter ignition, so the samples were purified by centrifugation. Using up to 5 ml of 6 M HCl per sample, the samples were rinsed from their beakers into 50-ml conical-base polypropylene centrifuge tubes (Sarstedt AG & Co., Nümbrecht, Germany). The tubes were placed in a Beckman J6 High Capacity (HC)

Centrifuge, which was then set to run for 20 minutes between 2 000 and 2 400 rpm in a temperature range of 22 to 24 °C. In the meantime, the beakers were set aside for later reuse.

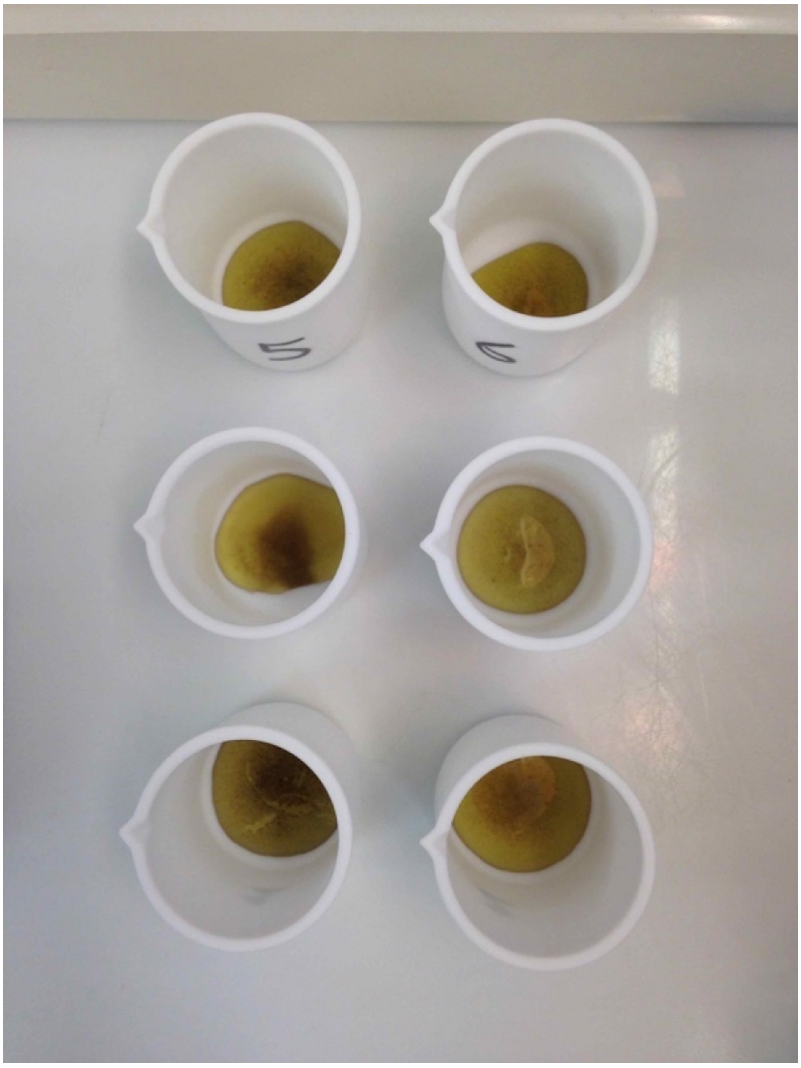

Figure 58. The 6 samples after the initial acid dissolution. Brackish material can be seen in the beakers.

THORIUM AND URANIUM FRACTION SEPARATION

Next, six columns were assembled for the first column array. Each column consisted of a 10-cm plastic tube (capacity: 5 ml) fitted with a plastic cone (capacity: 10 ml) on top. The bottom of the column was obstructed using a polyethylene disc (to serve as a filter), and a funnel was attached. The columns were mounted on a custom 6-slot holder with 30-ml beakers placed underneath for waste collection.

The columns then underwent priming. Each column was flushed with acetone to expel potential residual air from fabrication in the polyethylene disc. The acetone was then rinsed out

with Milli-Q® H_2O. Finally, AG® 1-X8 analytical grade anion exchange resin (200–400 mesh, chloride form) was injected continuously using a Pasteur pipette, allowing the aqueous phase to percolate through the polyethylene disc, until the entire length of the column tube was filled with pure resin.

As a final step before running the samples, the resin underwent conditioning. This refers to expansion and contraction of the resin mesh through successive interstitial substitution of mobile phases (HCl for thorium and H_2O for uranium) to improve retention capacity.

Due to the recurrent use of proportional volumes throughout the extraction chromatography protocol, unit volumes were defined to facilitate execution. For the first column array, this was set to 5 ml.

Conditioning began with 1 volume of 6 M HCl to eliminate any residual initial thorium. Once all the HCl had gone through the columns, two volumes of Milli-Q® H_2O were added, this time to eliminate any residual initial uranium. Finally, four volumes of 6 M HCl were injected to prepare the resin for thorium extraction and remove any remaining interstitial H_2O from the mesh.

The column array undergoing resin conditioning is shown in Figure 59.

The samples were then transferred from the centrifuge tubes back into their original beakers. The tube walls were rinsed with 6 M HCl to recover the maximum amount of sample material while taking care to avoid contamination by the settled solid phase. The centrifuge tubes were subsequently discarded while the samples were re-dissolved in a few millilitres of 6 M HCl in their beakers.

Next, the samples were run through the columns for recovery of the thorium fraction (thorium itself as well as other undesired, non-uranium components), their corresponding beakers placed underneath. Once the columns were completely strained, four volumes of 6 M HCl were added to each to ensure that no thorium remained.

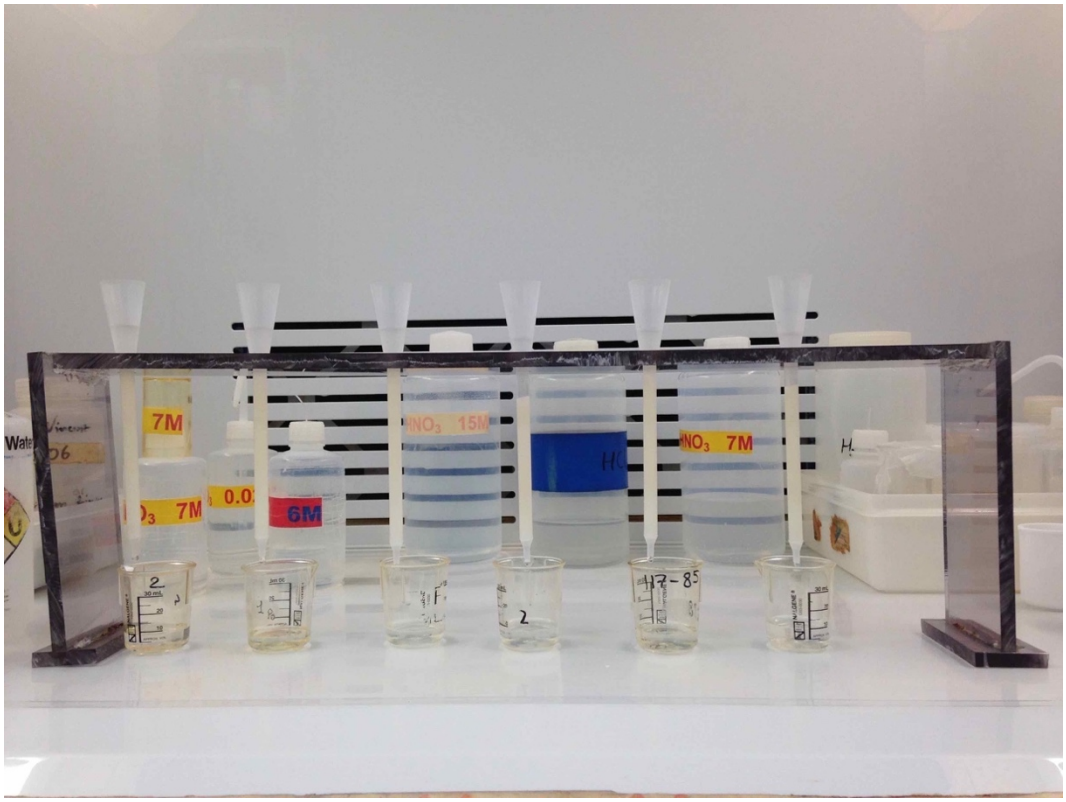

Figure 59. The first column array undergoing resin conditioning.

Once all the thorium fraction solutions had been recovered from the columns, the uranium fraction thus fixed in the resin, the thorium beakers were transferred to a hot plate set to 85 °C and left overnight to let the liquid phase evaporate.

For recovery of the uranium fraction, Teflon-PTFE beakers of 30-ml capacity were placed under the columns. Four volumes of Milli-Q® H_2O were added to flush the uranium fraction into the beakers.

After the columns were completely strained, the beakers were transferred to a hot plate set to 85 °C and left overnight to let the liquid phase evaporate.

Once both the thorium and uranium fraction beakers were dry, the columns were washed with distilled H_2O to flush the resin out for replacement.

URANIUM FRACTION PURIFICATION

A second column array was set up for uranium fraction purification. This time, the columns were assembled from 0.2-ml tubes and fitted with 2-ml cones. The same 30-ml waste collection beakers were placed under the columns.

The columns were primed with acetone and rinsed with Milli-Q® H_2O. This time, UTEVA® resin (100–150 µm, Bulk; Eichrom Technologies, IL, USA) was injected into the columns (Figure 60).

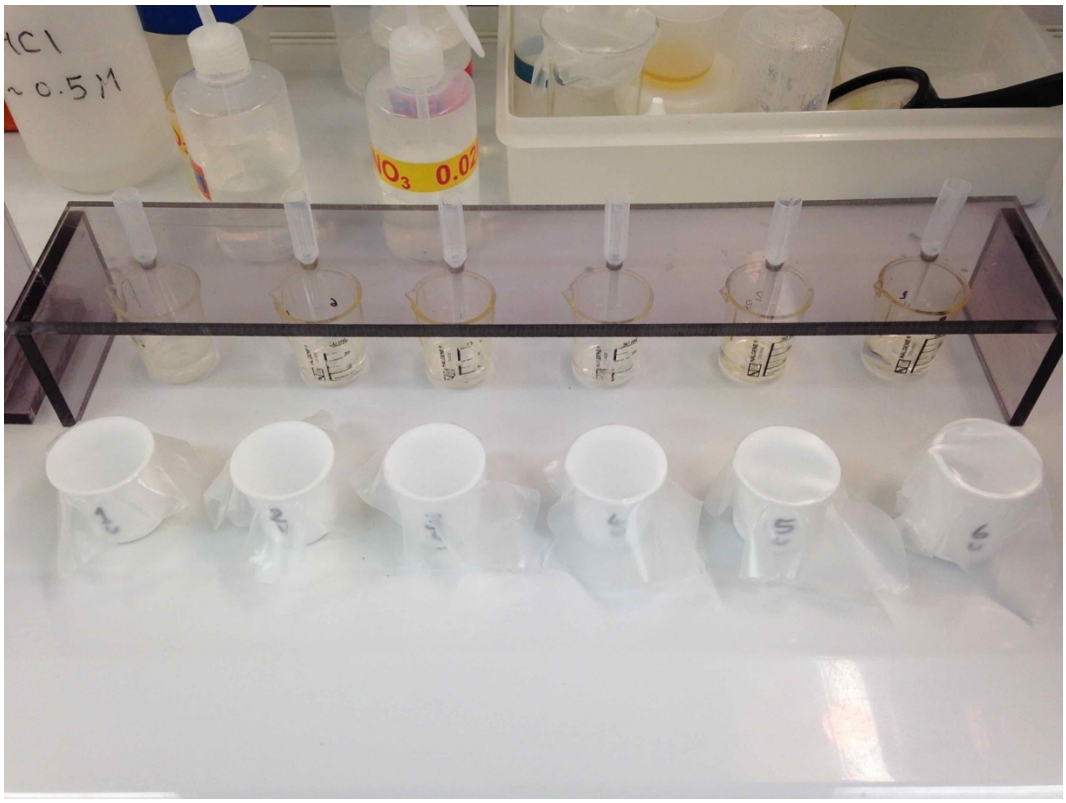

Figure 60. The second column array undergoing resin conditioning.

As with the first column array, a unit volume, this time equivalent to 2 ml (the full capacity of the second column array's cones), was defined to facilitate protocol execution.

Resin conditioning was performed by running the following reagents through the column array in the given order:

- 1 volume of 3 M HNO_3;
- 1 volume of Milli-Q® H_2O;
- 1 volume of 0.02 M HNO_3; and
- 2 volumes of 3 M HNO_3.

The waste collection beakers were emptied at this point.

Next, the uranium fraction samples were dissolved in their 30-ml Teflon-PTFE beakers with 3 M HNO_3. The beakers were covered with cling film and left to sit.

The samples were then run through the columns, the beakers rinsed thrice with 3 M HNO_3 to ensure that all sample material was recovered, then placed under the columns to re-collect the samples. The columns were subsequently flushed with 2 successive half-volumes of 3 M HNO_3 to eliminate iron.

The purified uranium was collected in 15-ml Teflon-PFA vials (Savillex™ Corporation) by flushing the columns with 2 successive half-volumes of 0.02 M HNO_3.

The vials were transferred to a hot plate set between 60 and 85 °C and left overnight to let the liquid phase evaporate.

THORIUM FRACTION PURIFICATION

The first column array was primed again and re-injected with AG® 1-X8 resin.

The unit volume previously defined for the first column array (5 ml) was once again invoked for the purification of the thorium fraction.

Resin conditioning was performed by running the following reagents through the column array in the given order:

- 1 volume of 7 M HNO_3;
- 1 volume of Milli-Q® H_2O;
- 1 volume of 6 M HCl; and
- 4 volumes of 7 M HNO_3.

The waste collection beakers were emptied at this point.

Next, the thorium fraction samples were dissolved in their 50-ml Teflon-PTFE beakers with 7 M HNO_3. The beakers were covered with cling film and left to sit.

The samples were then run through the columns, the beakers rinsed thrice with 7 M HNO_3 to ensure that all sample material was recovered, then placed under the columns to re-collect the samples. The columns were subsequently flushed with 4 volumes of 7 M HNO_3 to eliminate impurities.

The purified thorium was collected in clean beakers by flushing the columns with 4 volumes of 6 M HCl.

The beakers should ideally have been transferred to a hot plate set to 85 °C and left overnight to let the liquid phase evaporate, as in the preceding fraction recovery and purification sub-protocols. However, as column percolation had not yet finished by midnight, it was allowed to continue overnight. Evaporation was postponed to the next day and accelerated at a temperature of 120 °C. (Column percolation has to be completed on the same day as resin conditioning; otherwise, the resin will harden by the next day, and the entire sub-protocol will have to be repeated.)

Once the liquid phase in the beakers had significantly evaporated, it was transferred into 15-ml Teflon-PFA vials (Savillex™ Corporation) accompanied by a few drops of 7 M HNO_3. The vials were heated further at 120 °C on a hot plate. When the vials were almost dry, the temperature was brought down to 90 °C.

Finally, around 4 to 5 drops of 15 M HNO_3 were added to each beaker to facilitate thorium dissolution.

Hydroxylapatite

SAMPLE AND SPIKE PREPARATION

Of the five samples, four were already in very fine powder form ready for weighing, so only Sample 06 was ground using a small agate mortar and pestle. Between 0.3 and 0.4 g of sample were then weighed into aluminium dishes. The dishes were placed in a furnace at 500 °C for 2.5 hours to destroy organic matter through ignition.

Spike preparation was performed in a cleanroom environment. Five 50-ml Teflon-PTFE beakers were prepared, labelled with the sample names, and purged of static electricity. Between 0.15 and 0.20 g of an isotopic spike solution were then squirted into each beaker. The beakers were placed on a hot plate at 80 °C (instead of the previous 85 °C) for 1 hour, allowing the liquid phase to evaporate and leaving heavy isotopes to stick to the beaker bottoms.

Once the samples were ready, they were carefully taken out of the furnace and allowed to cool slightly before being transferred into their respective beakers. The aluminium dishes were rinsed twice with Milli-Q® H_2O to recover the maximum amount of sample.

DISSOLUTION

The samples were dissolved in a few millilitres of 6 M HCl. The resulting mixtures were lightly stirred using sterile inoculation loops and left overnight at 80 °C on a hot plate.

The next day, the samples were re-dissolved in 6 M HCl in preparation for centrifugation.

CENTRIFUGATION

Using 6 M HCl, the samples were rinsed from their beakers into 50-ml conical-base polypropylene centrifuge tubes (Sarstedt AG & Co., Nümbrecht, Germany), with each tube containing 6 ml of mixture. The tubes were placed in a Beckman J6 High Capacity (HC) Centrifuge, which was then set to run for 20 minutes at 2 000 rpm in a temperature range of 22 to 24 °C. In the meantime, the beakers were set aside for later reuse.

THORIUM AND URANIUM FRACTION SEPARATION AND PURIFICATION

Separation and purification of the thorium and uranium fractions were done following the procedures described for the grey speleothem.

Yellow speleothem

The extraction chromatography protocol had to be modified for Sample 16, as its gypsiferous composition translated to very poor solvability.

SAMPLE AND SPIKE PREPARATION

A few solid clumps were first rinsed in H_2O and left to dry overnight, revealing 'clean' and 'dirty' zones; the 'clean' zones correspond to actual sample material, whereas the 'dirty' zones consist of encrusted sedimentary particles (Figure 61). The encrustations were scraped off with a spatula to clean the sample.

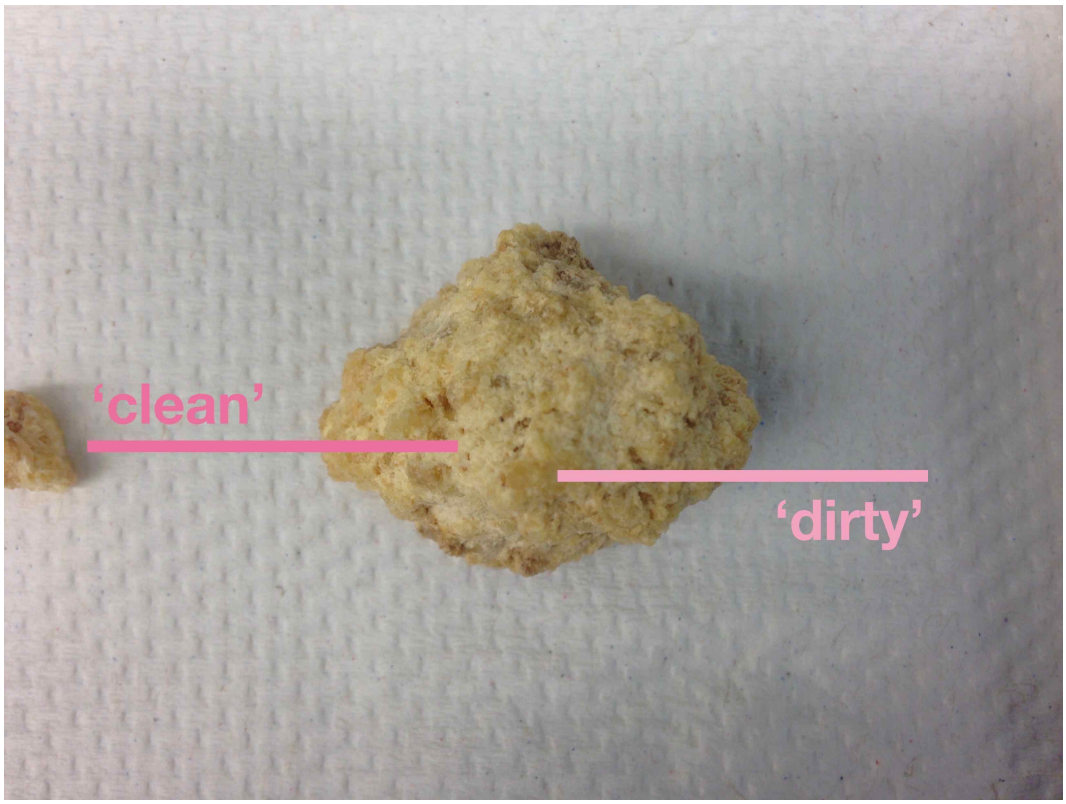

Figure 61. The 'clean' and 'dirty' zones on a gypsum clump from Sample 16.

The sample was then finely ground using a small agate mortar and pestle. It was assumed to have low uranium content based on the data reported by Lewis *et al.* (2008), so the mass range of 0.3 to 0.4 g previously used for the other samples was multiplied by a factor of 10 to obtain 3 to 4 g. This was weighed into an aluminium dish and placed in a furnace at 500 °C for 2.5 hours to destroy organic matter through ignition.

Spike preparation was performed in a cleanroom environment. A 250-ml Teflon-PTFE beaker was prepared, labelled with the sample name, and purged of static electricity. Between 0.15 and 0.20 g of an isotopic spike solution were then squirted into the beaker. It was placed on a hot plate at 80 °C for 1 hour, allowing the liquid phase to evaporate and leaving heavy isotopes to stick to the beaker bottom.

Once the sample was ready, it was carefully taken out of the furnace and allowed to cool slightly before being transferred into its beaker. The aluminium dish was rinsed twice, alternating Milli-Q® H_2O with a few squirts of 6 M HCl to recover the maximum amount of sample.

DISSOLUTION

The sample was dissolved in a few millilitres of 6 M HCl. The resulting mixture was lightly stirred using a sterile inoculation loop and placed on a hot plate set to 135 °C. After several hours, a stir bar was placed in the beaker, which was then transferred onto a magnetic stirrer and left overnight.

The next day, the gypsum was found to be only partially dissolved. A quantity of Milli-Q® H_2O sufficient to submerge the sample was then added into the beaker, followed by 20 to 30 drops of 6 M HCl. The beaker was placed on a hot plate set to 80 °C for 2 to 3 hours. It was stirred by hand, then allowed to decant. The resulting liquid phase was recovered in a separate 250-ml Teflon-PTFE beaker.

The solid phase in the original beaker repeatedly underwent the procedure, with occasional magnetic stirring and heat-assisted decantation. The liquid phase from each cycle was recovered. All in all, three cycles to completely dissolve the gypsum and two 250-ml beakers (including the original one) to hold the liquid phase were necessary. The beakers were placed on a hot plate set to 135 °C for decantation and partial evaporation. A few drops of purified $FeCl_3$ were then added before turning down the temperature and leaving the beakers to sit overnight.

PRECIPITATION

The following day, NH_4OH was added into the beakers to increase the pH to at least 8, creating alkaline conditions (verified using a litmus strip) and triggering precipitation of $FeOH_3$ that would concentrate the uranium and thorium in the sample. $FeCl_3$ was again added

to promote further precipitation. The beakers were then placed on a hot plate set to 135 °C for partial evaporation.

CENTRIFUGATION

The beaker contents were transferred into 50-ml conical-base polypropylene centrifuge tubes (Sarstedt AG & Co., Nümbrecht, Germany). They were placed in a Beckman J6 High Capacity (HC) Centrifuge, which was then set to run for 20 minutes between 2000 and 2400 rpm in a temperature range of 22 to 24 °C.

The supernate was discarded, while the precipitate was rinsed with Milli-Q® H_2O and re-dissolved in 6 M HCl in preparation for extraction chromatography.

COLUMN PREPARATION

A single column was assembled, primed, and conditioned following the procedures described for the grey speleothem phosphates. To keep it moist for the recovery and purification of the thorium and uranium fractions, planned for the next day, it was immersed in a 600-ml Teflon-PTFE beaker filled with Milli-Q® H_2O. The beaker was covered with cling film and set aside.

THORIUM AND URANIUM FRACTION SEPARATION AND PURIFICATION

Separation and purification of the thorium and uranium fractions were done following the procedures described for the grey speleothem.

Labware cleaning

After use, all labware was cleaned following a specific protocol. Preliminary rinsing was first done with distilled H_2O. Wipes soaked in acetone were used to scrub beakers, particularly the inside, followed by another rinsing with distilled H_2O.

The labware was then immersed in a soap solution for 12 hours before undergoing 3 hot baths (soap, HCl, and HNO_3), each lasting 3 hours, in a large-capacity glass beaker on a hot plate set between 130 and 150 °C. Distilled H_2O was used for rinsing after each bath, with an additional rinsing in Milli-Q® H_2O after the last bath (HNO_3) before drying.

Table of weights

Table 9 summarizes the samples for uranium-series analysis.

Table 9. List of uranium-series analysis samples.

Sample	Nature	Sample weight (g)	Spike weight (g)
SG-01	Grey speleothem	0.4034	0.1973
SG-02	Grey speleothem	0.3633	0.2005
SG-03	Grey speleothem	0.3631	0.2106
SG-04	Grey speleothem	0.3495	0.1994
SG-05	Grey speleothem	0.3805	0.1931
SG-06	Grey speleothem	0.3609	0.1892
Sample 06	Hydroxylapatite	0.4048	0.1971
Sample 15	Hydroxylapatite	0.3961	0.1906
Sample 20	Hydroxylapatite	0.3842	0.2064
Sample 28	Hydroxylapatite	0.4051	0.2009
Sample 44	Hydroxylapatite	0.3872	0.2061
Sample 16	Yellow speleothem	3.8175	0.2063

Mass spectrometry

Mass spectrometry was carried out on a Nu Plasma II Multi-Collector ICP-MS (Nu Instruments Ltd., Wrexham, UK). To enable introduction into the mass spectrometer, samples were diluted in around 10 ml of 2% HNO_3, injected into beakers using an Eppendorf Research® plus pipette.

Chapter IV

Results

4.1. Grain-size analysis

Table 10 recapitulates the list of samples for grain-size analysis, all collected from the South Trench.

Table 10. Samples for grain-size analysis.

Sample	Layer	Depth (cm below DP)	Description
G	1	113	From capping speleothem
MM4	3	135-140	From Layer 3 on profile
F	3	142	Dark reddish brown
E	4/5	162	Mid-yellowish brown
D	9	220	Mid-reddish brown
MM3	9	223-228	At interface of Layers 7/8 and 9 on profile
C	9	238	Mid-greyish brown
MM2	10	265-270	At interface of Layers 9 and 10 on profile
B	10	285	Dark reddish black
MM1	11	316-321	At interface of Layers 10 and 11 on profile
A	11	333	Dark yellowish brown; clayey

4.1.1. Overview

Grain-size class analysis shows that the profile consists primarily of fine particles. It is strongly dominated by silt, which constitutes at least 50% by proportion of nearly all samples. Grain sizes dwindle even further in Layers 3 and 9, where clay peaks complement the silt ones. However, mean grain size is actually more influenced by fine sand: the contours of the mean grain size curve heavily resemble those of the fine sand curve. This would be supported by the proximity of the dominant silt to fine sand in terms of grain size. The mean grain size and fine sand curves both contain peaks that correspond to the base of each of the three guano deposits (Layers 3, 7/8, and 10) that are characteristic of the profile. Finally, minor but noteworthy peaks in the coarse sand curve are found at the base of the profile and around the topmost guano level (Layer 3).

In the lower half of the profile (Layers 9, 10, and 11), grain size is very homogeneous overall, with some heterogeneity observed at the ends. Sorting is generally poor, although it improves somewhat at the base of Layer 10 and is excellent in Layer 9 before deteriorating again, moving up. In the upper half (Layers 1, 3, and 4/5), sorting is again poor with a broad distribution of grain diameters. The two samples representing Layer 3, F and MM4, offer contrasting pictures: Sample F appears to be composed of well-sorted silt, while Sample MM4 is characterized by poorly-sorted fine sand. This can be explained by coarse grains from the surrounding rockfall layers (2 and 4/5) having been incorporated into MM4 during sampling, as it was originally collected for soil micromorphology and was thus intentionally made to straddle multiple layers. The sequence ends with fairly sorted silt-sized grains in Layer 1.

Sorting indices confirm that the profile has an overall composition of well-sorted fine grains. Any information about coarser components is probably overshadowed, although positive values for Pettijohn's asymmetry coefficient (Asq) suggest that these are also well-sorted amongst themselves.

Cumulative distribution curves point to changing modes of deposition. At the bottom of the sequence, the base of Layer 11 corresponds to mature transport conditions that reflect equilibrium between existing sediments and incoming waterborne ones. However, toward the top of this layer, preferential deposition of coarser grains points to fast currents. Layer 10 is again characterized by mature transport conditions, while Layer 9 is more delicate to interpret,

represented by parabolic curves (and thus fast currents) but nevertheless composed of fine grains and not coarse ones. Layers 4/5 are similar to Layer 9 in that they are composed of parabolic curves but also have a paradoxically fine composition. Finally, the logarithmic curve of Layer 1 represents mature transport conditions for its fine fraction.

Resemblances between the frequency and cumulative distribution curve contours of certain samples from different layerssuggest similarities in modes of deposition. These layers are sometimes adjacent, as in the cases of Layers 11 and 10 or 10 and 9. However, they can also be apart, as with Layers 11 and 4/5 or, in the starkest example, Layers 9 and 3.

4.1.2. Grain-size classes

The laser diffraction results for the grain-size classes are presented in Figure 62.

The sequence begins with Layer 11 at the bottom, dominated mainly by silt (around 50 to 55%) and fine sand (around 30 to 40%). The lower part of the layer is characterized by the presence, in similar proportions of around 10%, of coarse sand and clay; these decrease to practically negligible levels in the upper sample in Layer 11 and give way to silt and fine sand.

In Layer 10, silt remains the primary particle class represented (around 55 to 65%). Clay increases and reaches its maximum concentration across the entire sequence at the top of this layer (25%). Fine sand declines to just around 10%, whereas coarse sand remains insignificant.

Up next, Layer 9 is composed almost exclusively of silt and clay (82 and 18%, respectively). However, toward the interface with Layers 7/8, there is a sharp increase in fine sand (to almost 30%) that is accompanied by drops in silt and clay content. Coarse sand then makes a small comeback (1.3%) and fine sand retreats, as silt and clay recover slightly.

In Layers 4/5, the matrix is more than ever dominated by silt (around 80 to 85%) despite the presence of cobble and boulder-sized inclusions (50 to 200 mm and 200 to 500 mm, respectively) and visible in the profile. However, at the interface with Layer 3, silt drops dramatically and gives way to peaks of both fine and coarse sand (47 and 13%, respectively). A smaller decrease of around 10% is also observed in the clay content.

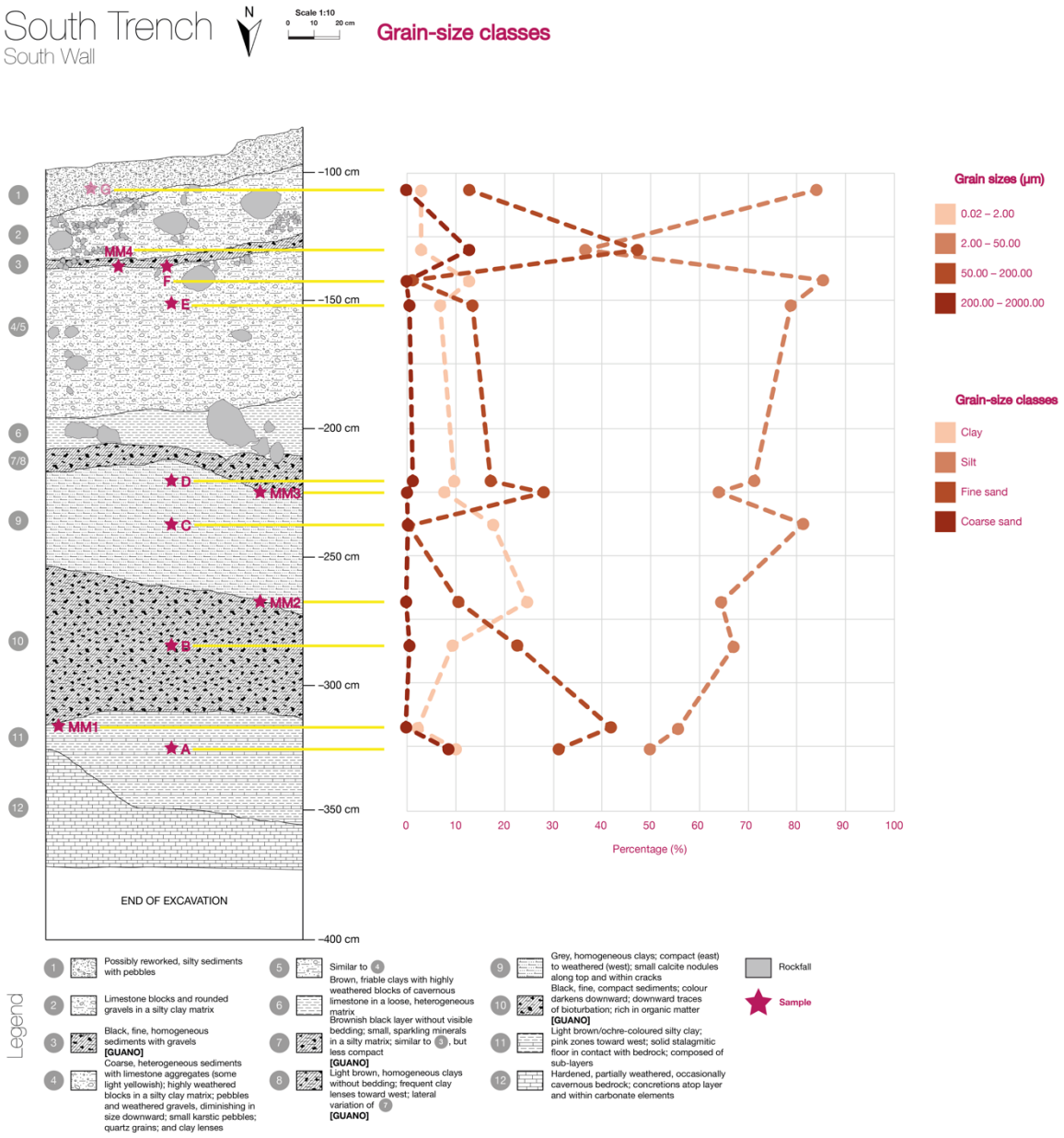

Figure 62. Grain-size classes presented against the south wall profile of the South Trench. Stars indicate the locations of the samples on the profile.

Finally, silt returns in Layer 1 to cap off the profile at 84%, reaffirming its status as the defining particle class of the sequence.

Except for some differences in the lower third of the sequence, the silt curve is almost a mirror image of the fine sand curve.

4.1.3. Mean grain size

Figure 63 shows the evolution of the mean grain size (in µm) across the sequence according to two indices calculated from the laser diffraction results: the volume moment mean (D [4,3]), and Folk and Ward's mean grain size (M_z).

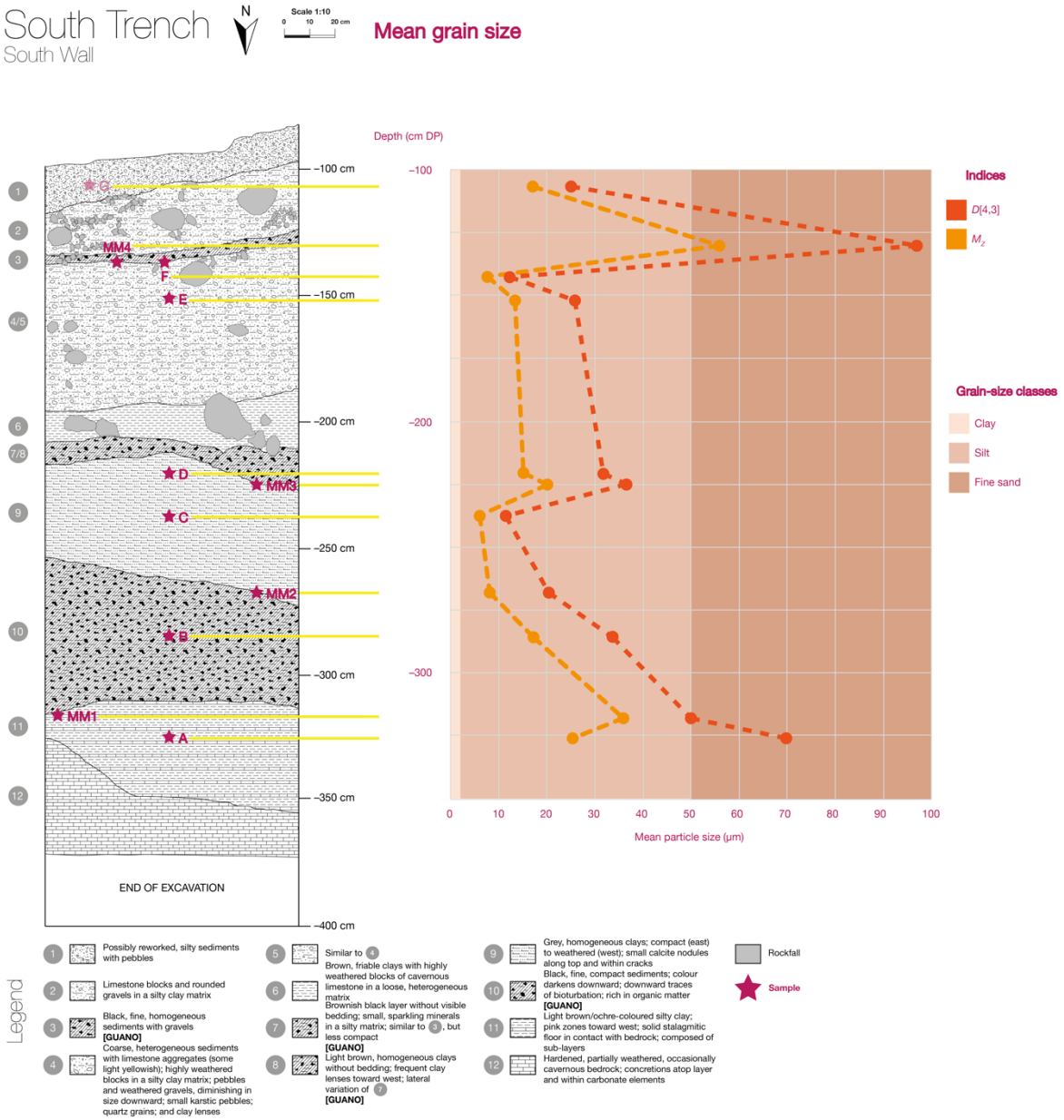

Figure 63. Mean grain size as two indices, presented against the south wall profile of the South Trench. Stars indicate the locations of the samples on the profile.

Like the grain-size class curves, the mean grain size curves affirm the primacy of silt throughout the sequence, staying mostly in the corresponding region of the graph. They start off from the base by converging, but quickly end up following very similar contours. The final shape generated by these contours closely recalls that of the fine sand curve. Another key point is the clear presence of two peaks: a small one toward the top of Layer 9, and a big one toward the top of Layers 4/5. The peaks echo the local maxima that occur at the same depths in the fine sand curve. Taken together, these observations suggest that fine sand strongly influences mean grain size in the South Trench.

4.1.4. Frequency distributions

The frequency distributions generated from the current sample set are plotted on a base-10 logarithmic scale against the profile, as shown in Figure 64.

At the base of the sequence, in Layer 11, grain sizes are primarily spread out across the fine sand and silt classes. The highest grain-size frequency falls within the fine sand interval, albeit on the lower end (74 μm). Some coarse sand is also present while a noticeable segment of silt-sized grains approaches the interface with clay, making for a heterogeneous distribution. Moving up the layer, these differences are flattened out as the mode emerges around 56 μm, very close to the interface between fine sand and silt (50 μm). With the disappearance of the coarse sand and the finer silt grains, the distribution tails collapse.

Figure 65 shows a close-up of the frequency distribution curves for the two samples from Layer 11. The one for Sample A has positive asymmetry and is multimodal. This indicates that while coarser grains are better sorted, overall sorting remains poor, affirming the heterogeneity of the distribution established above. Asymmetry remains positive for Sample MM1, which is nevertheless much better sorted; still, a small population of finer silt grains remains noticeable, making the curve slightly bimodal.

In Layer 10, while the fine sand proportions resemble those in the upper part of Layer 11, silt becomes the dominant grain-size class. Most of the particles are once again centered around the fine sand–silt interface, whereas a portion leans toward clay. The distributions of the two samples from the layer are very similar.

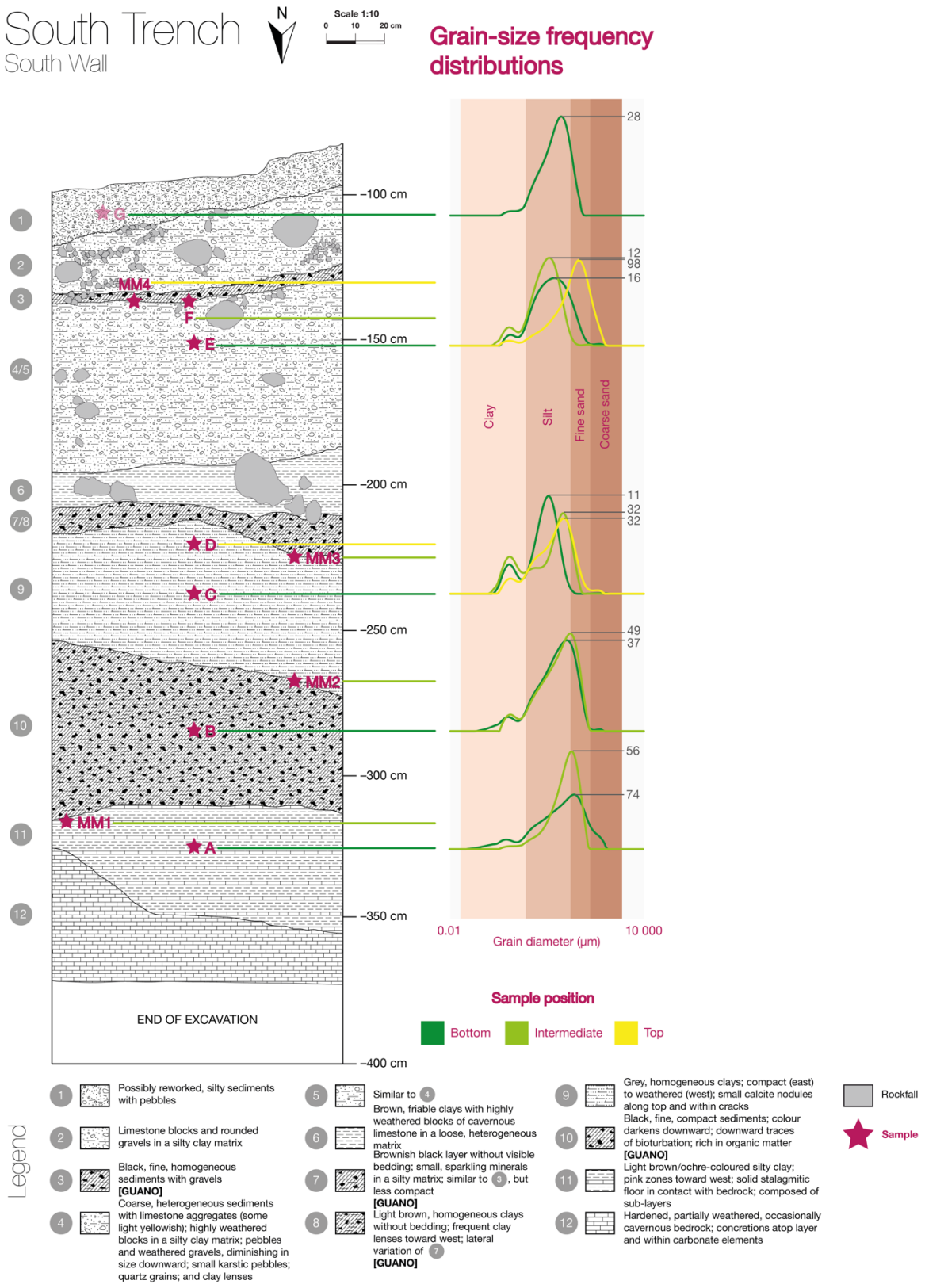

Figure 64. The frequency distributions presented against the south wall profile of the South Trench. Stars indicate the locations of the samples on the profile. Adjacent samples are shown as overlapping curves. For each group of adjacent samples, the bottommost one is indicated in dark green, the intermediate one in light green, and the topmost one in yellow.

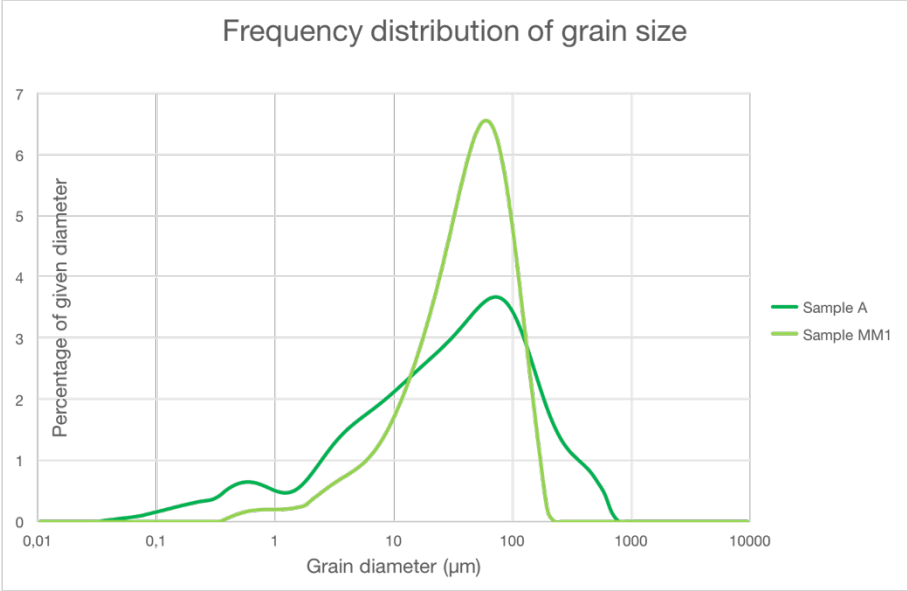

Figure 65. Frequency distribution of grain size for the two samples representing Layer 11: A and MM1.

Figure 66 zooms in on the corresponding curves for Layer 10, again characterized by positive asymmetry—this means that the silt grains that reign over the distribution are actually closer to fine sand in size. As in Layer 11, a segment of the silt population (< 10 µm) has diameters that approach the boundary with clay (2 µm). Both curves are slightly multimodal, having one clear mode and amorphous, ill-defined slopes to the left, again indicating poor sorting.

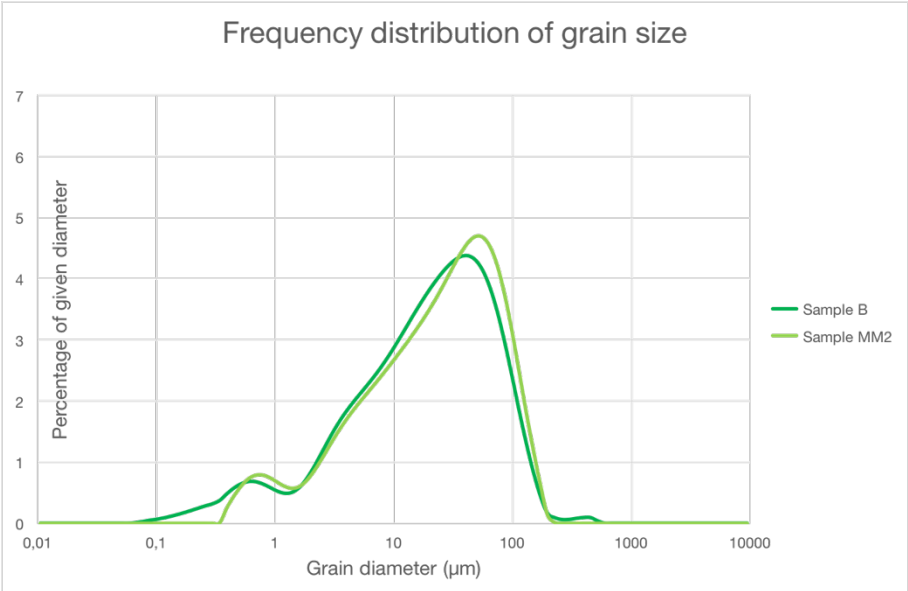

Figure 66. Frequency distribution of grain size for the two samples representing Layer 10: B and MM2.

Layer 9 starts with a highly homogeneous Gaussian distribution of silt-sized grains, with a

well-defined mode at 11 μm. Near the top of the layer, however, the mode shifts toward coarser grains, settling at 32 μm. This is accompanied by a decrease in finer silt, which eventually returns along with a small quantity of coarse sand.

The three curves for Layer 9 are plotted in Figure 67. The Sample C distribution is both highly symmetrical and unimodal, corresponding to excellent sorting within its region, the silt grain-size class. In the distributions for Samples MM3 and D, positive asymmetry shifts sorting to the right in favour of coarser grains while causing it to deteriorate overall, as shown by the multimodality of the curves.

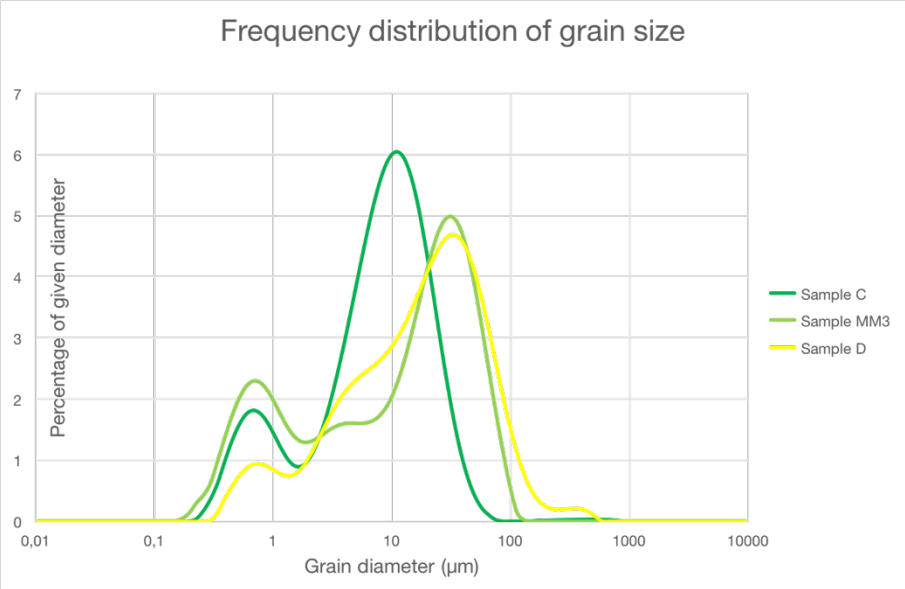

Figure 67. Frequency distribution of grain size for the three samples representing Layer 9: C, MM3, and D.

A broad distribution of silt and fine sand grains with a large continuum of diameters takes over in Layers 4/5 and 3. The fine sand eventually gives way to better-sorted silt, with a more sharply defined mode at 12 μm. At the interface with Layer 3, however, the mode shifts abruptly into the heart of the fine sand region at 98 μm. This is accompanied by a steep drop in silt.

Exhibiting perfect symmetry, the Sample E curve is nevertheless broadly spread with an ill-defined mode (Figure 68). The Sample F curve is better sorted, remaining symmetrical but being more clearly unimodal. In Sample MM4, sorting moves away from silt to fine sand.

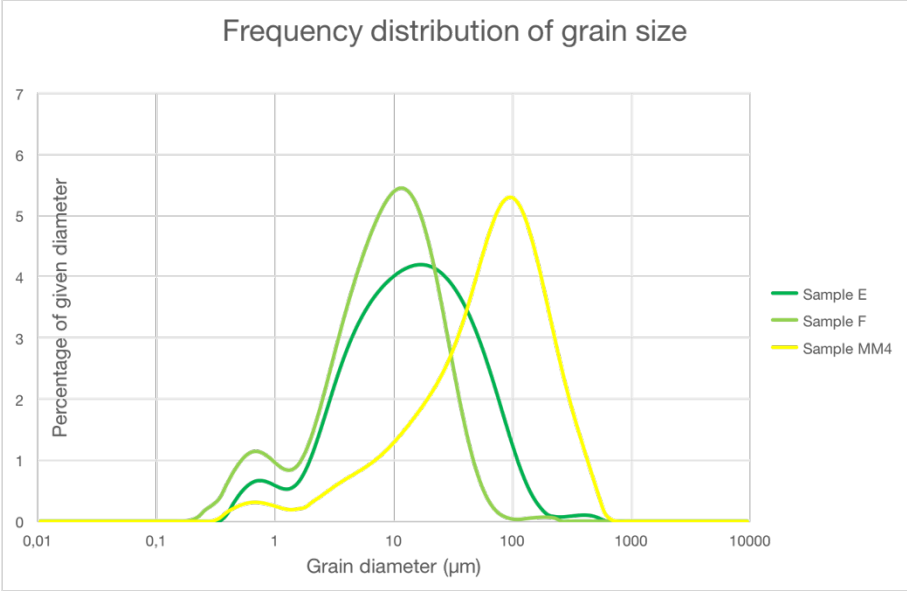

Figure 68. Frequency distribution of grain size for the three samples across Layers 4/5 and 3: E, F, and MM4.

Finally, in Layer 1 at the top of the sequence, silt-sized grains regain dominance of the distribution. As in Layer 10, the majority are closer to the interface with fine sand, while a segment of the population has diameters that approach the boundary with clay. Some fine sand remains present.

The curve is slightly asymmetric in favour of coarser grains, as well as being slightly multimodal (Figure 69). Silt-sized grains are fairly sorted overall, with preference for those that are close to fine sand in size.

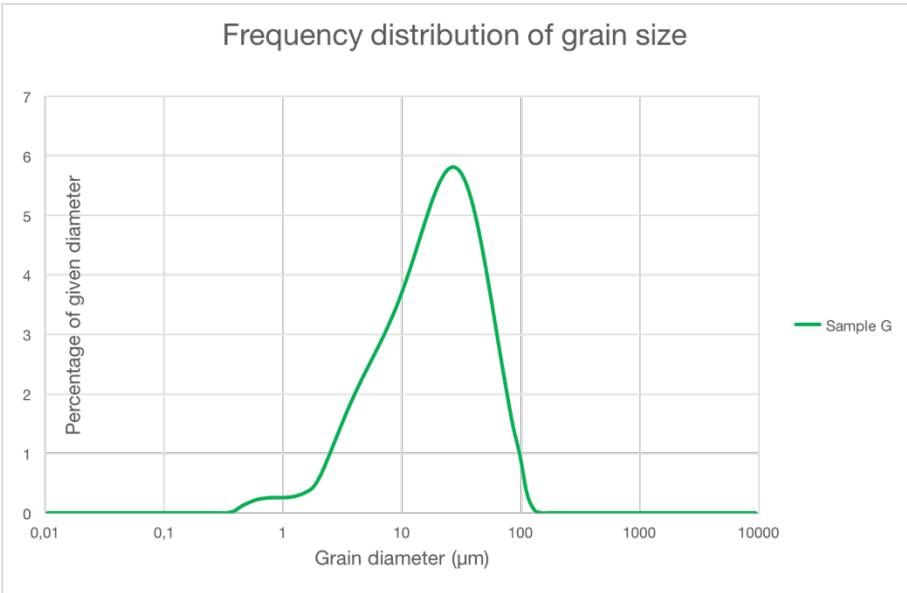

Figure 69. Frequency distribution of grain size for Sample G, representing Layer 1.

Resemblances can be observed between certain samples from different layers. This is starkest in Samples C (Layer 9) and F (Layer 3)—the frequency distribution curves share the same form except for the very minimal presence of coarse sand in Sample F, as well as slight differences in amplitude and width (Figure 70).

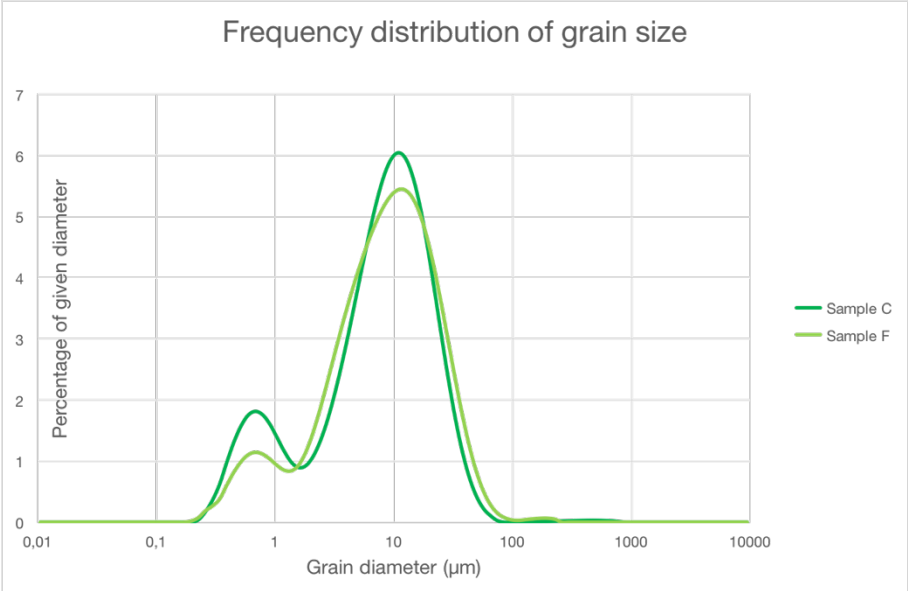

Figure 70. Frequency distribution of grain size for Samples C and F.

Discounting the coarse sand component and the horizontal difference of around 40 µm between the principal modes, the curves for Samples A (Layer 11) and B (Layer 10) also trace analogous contours (Figure 71).

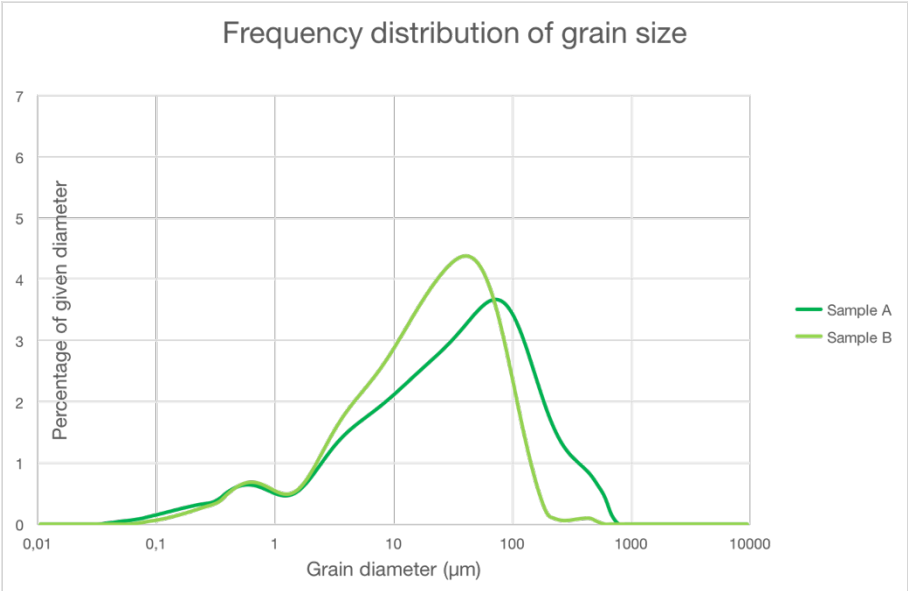

Figure 71. Frequency distribution of grain size for Samples A and B.

Samples MM1 (Layer 11) and MM4 (Layers 4/5) share the same general form as well, although the latter is shifted toward coarser grains, again by approximately 40 µm (Figure 72).

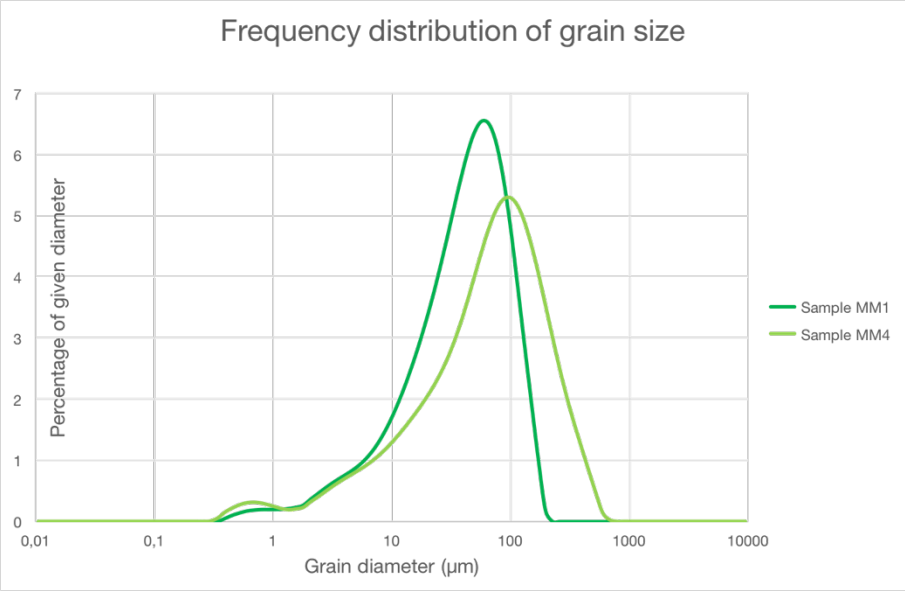

Figure 72. Frequency distribution of grain size for Samples MM1 and MM4.

Finally, Samples MM2 (Layer 10) and D (Layer 9) approximately follow the same shape. Aside once more from the coarse sand component and a minimal horizontal shift (< 10 µm), Sample MM2 would resemble Sample D after smoothening (Figure 73).

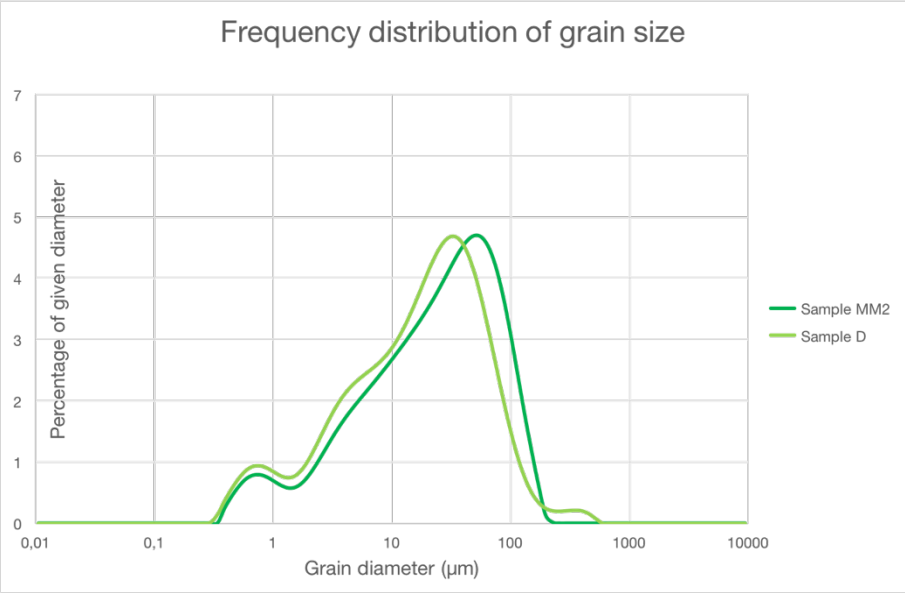

Figure 73. Frequency distribution of grain size for Samples MM2 and D.

The peaks at 0.59 and 0.68 μm are artefacts produced by the application of an artificial index of refraction during data analysis using the laser particle analyser software; they were thus not presented as part of the results.

4.1.5. Indices

Table 11 presents the indices calculated from the current dataset, with the samples arranged in stratigraphical order.

Table 11. Particle size indices for the Tabon Cave South Trench samples.

Depth (cm below DP)	Layer	Sample	*So* (mm)	σ_0 (ϕ)	σ_1 (ϕ)	*Sk* (mm)	*Asq* (ϕ)	*K* (ϕ)
113	1	G	1.354	-1.473	-1.444	8.440	0.126	-0.955
135-140	3	MM4	1.398	-1.809	-1.876	4.779	0.202	-1.126
142	3	F	1.381	-1.534	-1.631	12.931	0.090	-1.144
162	4/5	E	1.524	-1.787	-1.789	11.704	0.031	-0.971
220	9	D	1.469	-1.987	-2.021	9.861	0.261	-1.014
223-228	9	MM3	1.482	-1.979	-2.002	8.645	0.233	-1.001
238	9	C	1.339	-1.804	-1.775	12.830	0.169	-1.166
265-270	10	MM2	1.495	-2.753	-2.457	12.029	0.829	-0.735
285	10	B	1.504	-2.016	-2.103	9.595	0.200	-1.074
316-321	11	MM1	1.310	-1.401	-1.459	5.443	0.147	-1.107
333	11	A	1.646	-2.505	-2.612	8.700	0.277	-1.071

All the *So* values fall below 2.5, corresponding to very good grain sorting. The σ_1 values, being less than 0.35, confirm this. However, the σ_0 computations yielded negative results; given that this index should have a minimum value of 0.35, it is unusable as is for the current dataset. However, it can still be exploited through its definition as half of the difference between the 84th and 16th percentiles (P_{84} and P_{16}, respectively). The negative values indicate that P_{84} is less than P_{16}; in other words, the distribution consists of a vast majority of fine grains.

There is also a conflict between the *Sk* and *Asq* values, both measures of asymmetry. Whereas *Sk* is always greater than 1, corresponding to better sorting for fine grains, the positive values for *Asq* indicate better sorting for coarse grains. It is possible that the values for both indices

are simultaneously valid, even complementary, if the two size classes are equivalently well-sorted.

Finally, the ***K*** values are all below 0.67, corresponding to platykurtic curves for all the samples.

4.1.6. Cumulative distributions

The bottom of the sequence is described by a flattened ***S*** logarithmic curve corresponding to Sample A, with a subtle hyperbolic component that can be observed just below 1 μm. This part of Layer 11 corresponds to mature transport conditions, where equilibrium has been achieved between the sediments in place and the suspended solids in the water entering the system (Miskovsky and Debard, 2002).

Moving up Layer 11, Sample MM1 shows a shift to a parabolic curve, indicated by the pronounced downward concavity at larger diameters. This suggests the presence of fast currents to which the suspended solids have not yet been able to adapt, leading to preferential deposition of coarser grains (up to the size of fine sand, in this case) (Miskovsky and Debard, 2002).

The curves are presented in Figure 74.

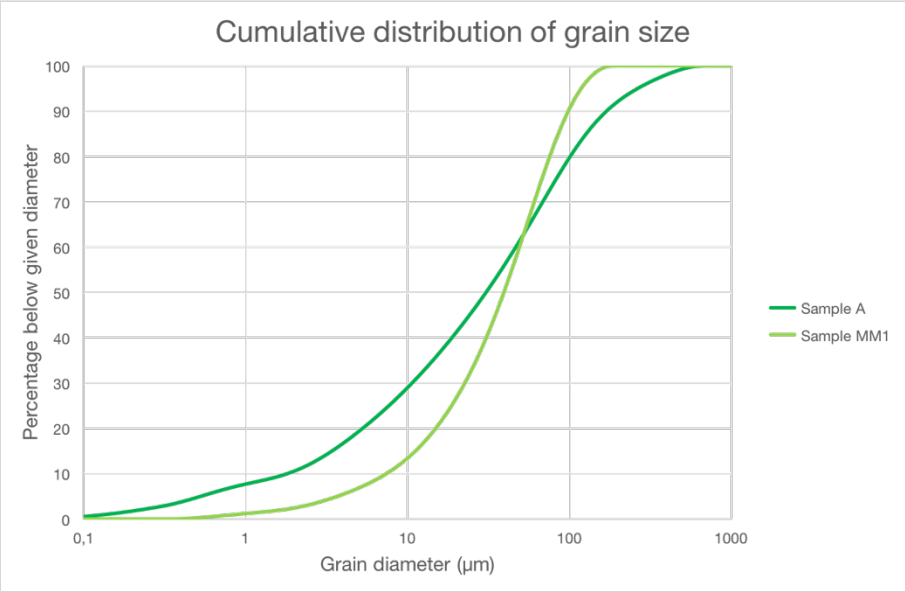

Figure 74. Cumulative distribution of grain size for the two samples representing Layer 11: A and MM1.

In Layer 10, Sample B is also described by a logarithmic curve that recalls that of Sample A in Layer 11. However, Sample B is finer in composition: at the silt–fine sand interface (50 µm), Sample B already counts around 80% of grains, versus only around 60% for Sample A.

Toward the interface with Layer 9, Sample MM2 is represented by a composite curve. Its behaviour after 20 µm follows that of Sample B's logarithmic curve and is thus consistent with the cumulative curve description for Layer 10. However, at smaller diameters, it is characterized by a significant hyperbolic bump, perhaps due to influence from the finer Layer 9.

The curves for the two samples are shown in Figure 75.

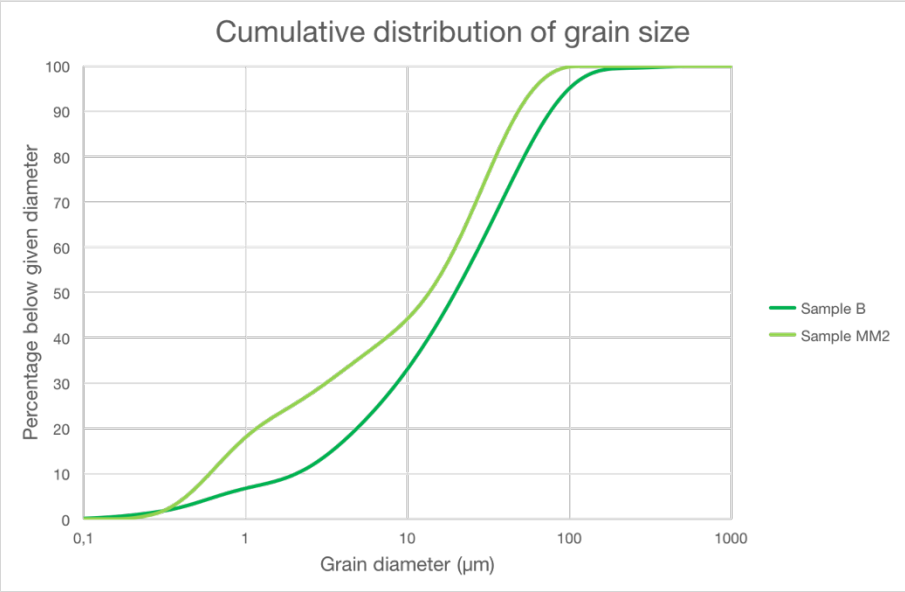

Figure 75. Cumulative distribution of grain size for the two samples representing Layer 10: B and MM2.

Layer 9 is represented by three samples, all of which are described by parabolic curves (Figure 76). As in Layer 11, a small hyperbolic component centered at around 1 µm is visible; however, a notable overall shift toward finer grain sizes distinguishes Layer 9. Within the layer itself, finer grains are more present in the middle than at the top: more than 99% of grains in Sample C, located at the heart of the layer, are smaller than fine sand (< 50 µm), versus only around 75 to 85% for Samples MM3 and D.

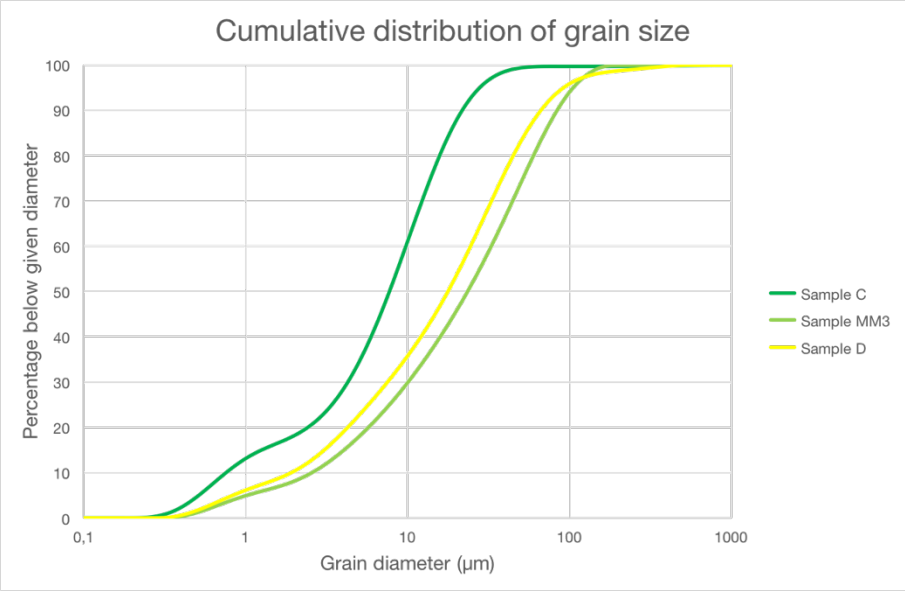

Figure 76. Cumulative distribution of grain size for the three samples representing Layer 9: C, MM3, and D.

A trio of parabolic curves also characterizes Layers 4/5 (Figure 77). The hyperbolic bump around 1 µm, while still present, is now less pronounced. The primary composition remains relatively fine and is given by Sample E, with 87% of grain sizes falling below the silt–fine sand interface at 50 µm. However, the transition to Layer 3 presents two contrasting pictures. On the one hand, Sample F shows a shift toward smaller diameters, with around 99% of grains measuring under 50 µm. On the other hand, Sample MM4 shows a marked increase in coarse particles with a strong right-shift and only around 42% of grains measuring under 50 µm.

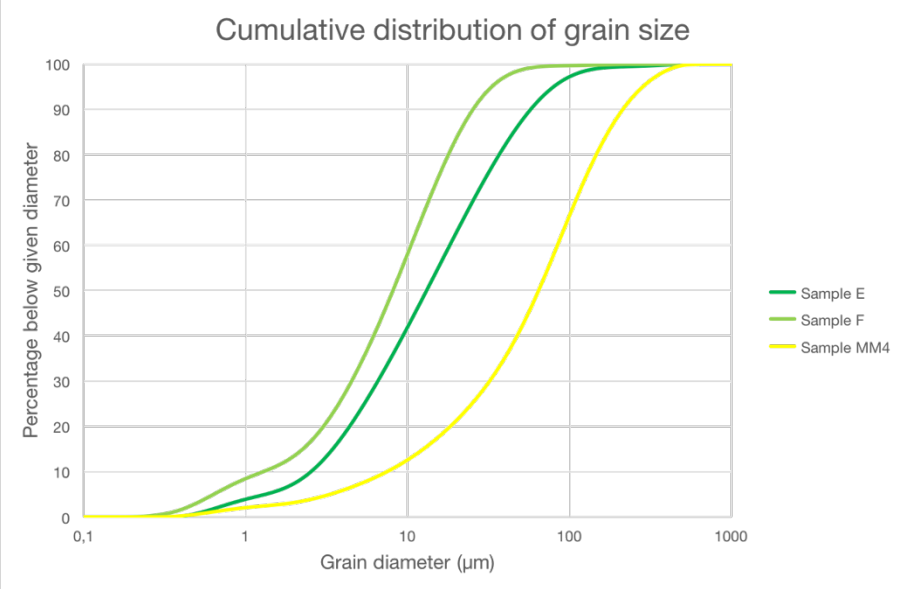

Figure 77. Cumulative distribution of grain size for the three samples across Layers 4/5 and 3: E, F, and MM4.

The sequence is completed by the highly logarithmic curve for Sample G, representing Layer 1 (Figure 78). Grain size returns to being fine, with around 90% of elements falling below 50 µm. Clay and fine sand are both still present, albeit in small quantities.

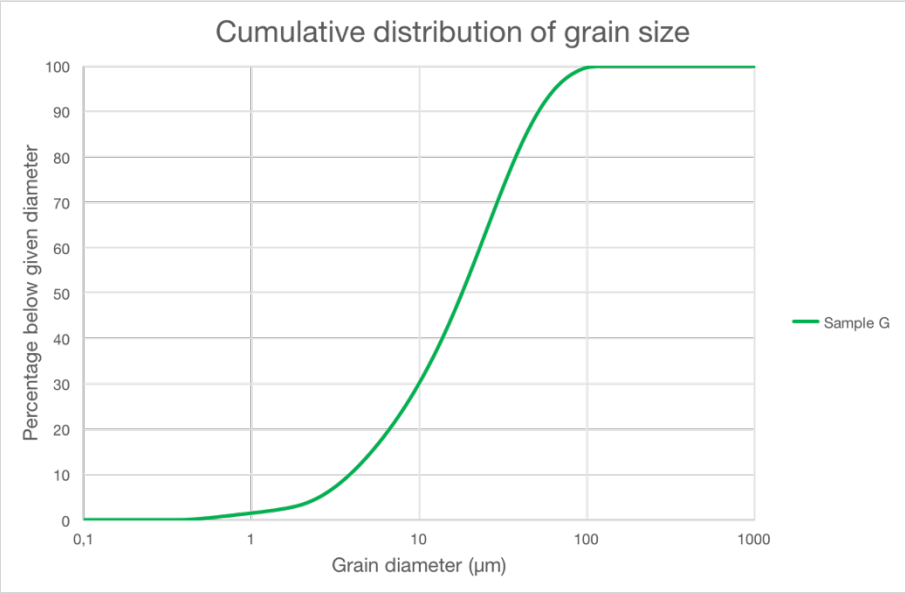

Figure 78. Cumulative distribution of grain size for Sample G, representing Layer 1.

As with the frequency distributions, parallels can be drawn between some of the cumulative distribution curves. The frequency distributions for Samples C (Layer 9) and F (Layers 4/5) are again tightly comparable, except for the slight divergence in the clay category (< 2 µm) that nevertheless disappears quickly as grain size increases (Figure 79).

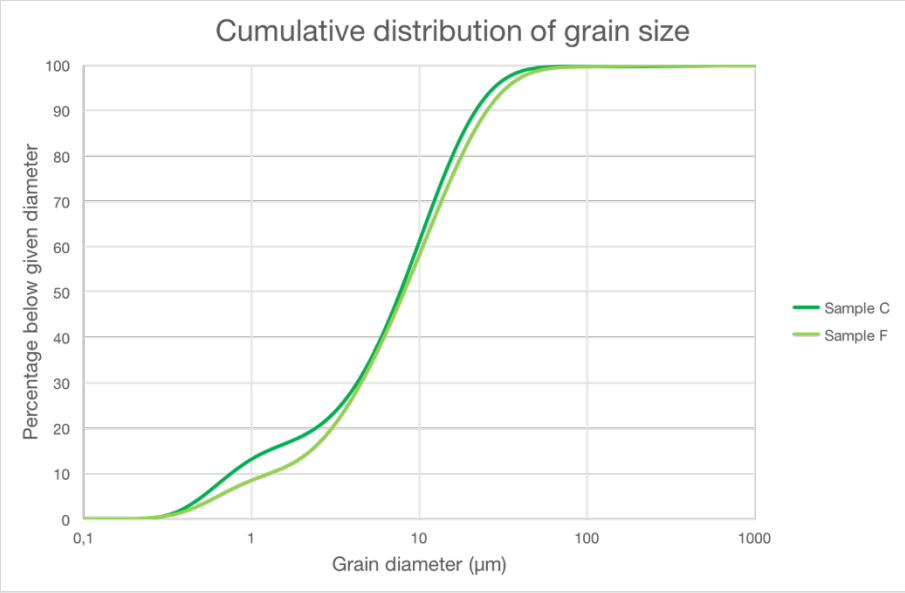

Figure 79. Cumulative distribution of grain size for Samples C and F.

The similarity observed between the curves for Samples A and B are less obvious this time, especially toward larger diameters, where Sample A takes longer to 'saturate'. Another 'couple' that previously emerged among the frequency distribution curves and whose cumulative distribution curves are instead divergent are Samples MM2 and D. However, these two pairs can come together to form a new one, embodied by the tight correlation between Samples B (Layer 10) and D (Layer 9)—their cumulative distribution curves closely hug each other (Figure 80). Finally, the distributions for Samples MM1 (Layer 11) and MM4 (Layers 4/5) again share the same contour, with MM4 diverging from MM1 toward a coarser composition as before (Figure 81).

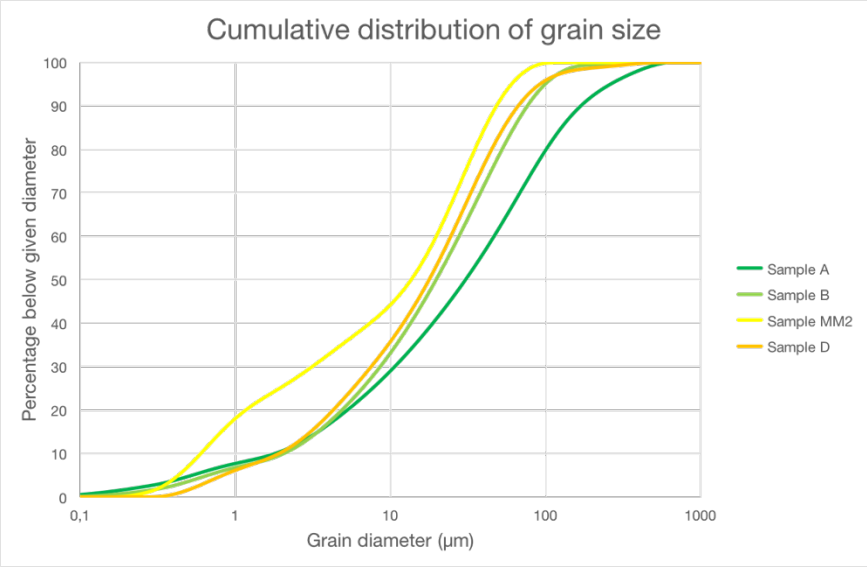

Figure 80. Cumulative distribution of grain size for Samples A, B, MM2, and D.

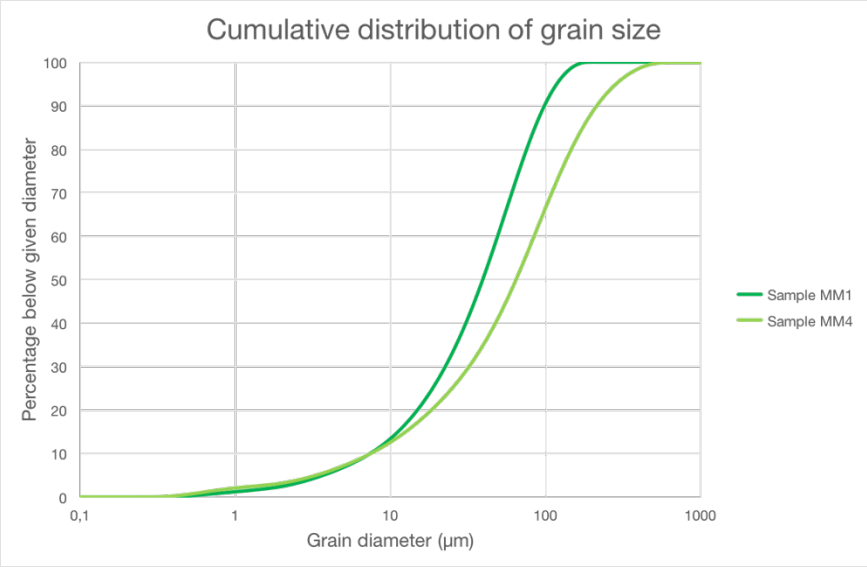

Figure 81. Cumulative distribution of grain size for Samples MM1 and MM4.

4.2. Mineralogical characterization

To facilitate presentation of the mineralogical characterization results, the following threefold division of the cave defined in Section 2.2.2 will be used:

- the North Zone, covering transects S1 to S4;
- the Central Zone, covering transects S6 to S10; and
- the South Zone, covering transects S14 to S18.

These zones and their constituent sampling squares are illustrated in Figure 82.

A total of 32 components were identified through mineralogical characterization. They are presented in Table 12, with each component classified into one of five groups: sulphates, carbonates, phosphates, silicates, and others. This significant degree of mineralogical diversity, mostly due to guano diagenesis, underscores the spatial and temporal heterogeneity of the cave's chemistry, which can eventually be attributed to changes in the climate and/or environment outside.

With the exception of four components, highlighted in grey, names and formulae follow the International Mineralogical Association List of Minerals (September 2017). For conciseness, abbreviations are used for elements, compounds, and identified components: elements and compounds are shortened using standard chemical nomenclature, while a custom system of two capitalized and italicized letters was set up for components to distinguish them from similar combinations in standard chemical nomenclature.

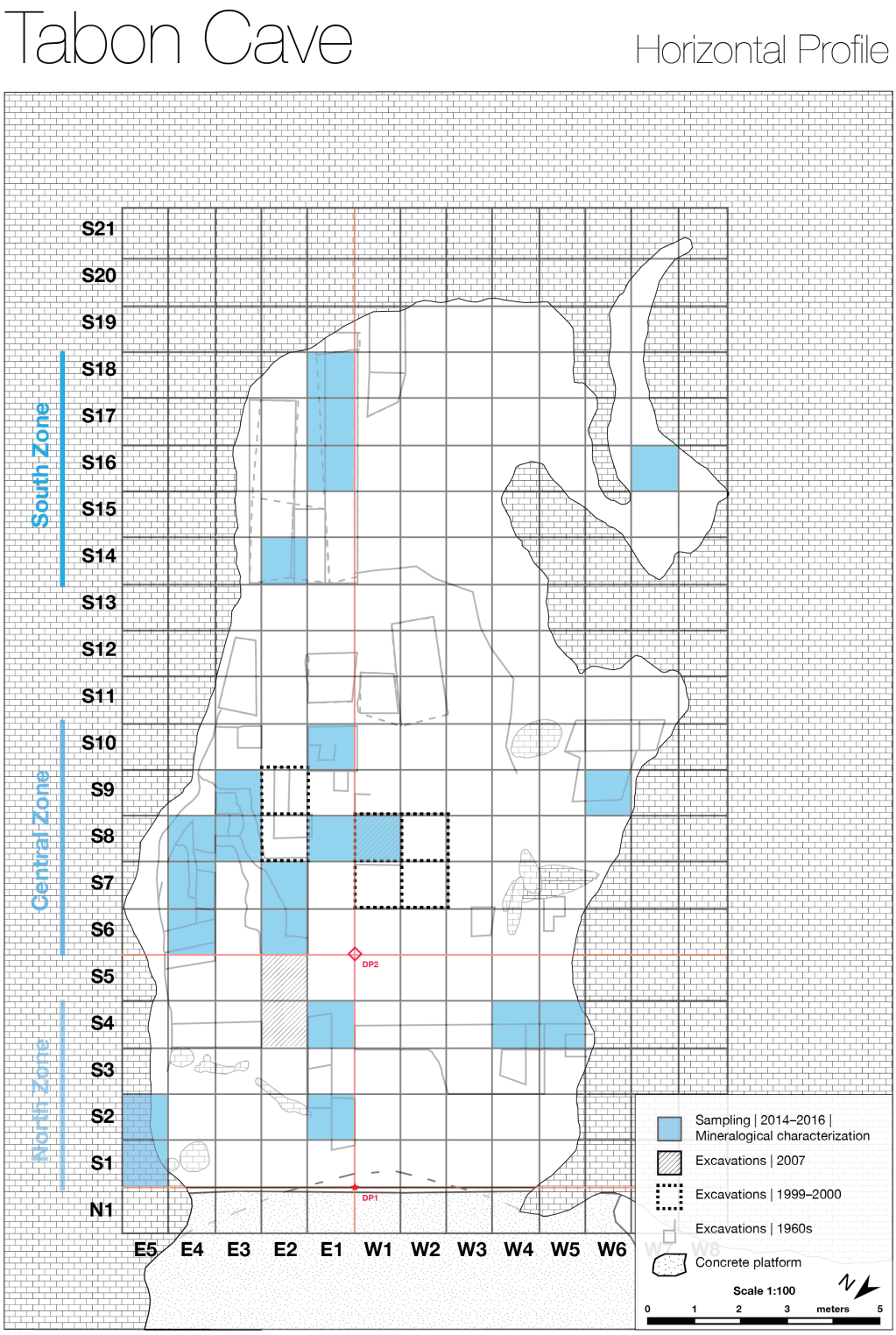

Figure 82. Sampling squares for mineralogical characterization.

Table 12. List of identified components in samples analyzed for mineralogical characterization.

Group	Abbreviation	Name	Formula
Sulphates	RS	rostite	$Al(SO_4)(OH) \cdot 5H_2O$
	AR	ardealite	$Ca_2(PO_3OH)(SO_4) \cdot 4H_2O$
	GY	gypsum	$Ca(SO_4) \cdot 2H_2O$
Carbonates	CC	calcite	$Ca(CO_3)$
Phosphates	CHAP	carbonate-rich hydroxylapatite	$Ca_5(PO_4,CO_3)_3(OH,O)$
	HAP	hydroxylapatite	$Ca_5(PO_4)_3OH$
	BR	brushite	$Ca(PO_3OH) \cdot 2H_2O$
	MN	monetite	$Ca(PO_3OH)$
	WL	whitlockite	$Ca_9Mg(PO_3OH)(PO_4)_6$
	MG	montgomeryite	$Ca_4MgAl_4(PO_4)_6(OH)_4 \cdot 12H_2O$
	CR	crandallite	$CaAl_3(PO_4)(PO_3OH)(OH)_6$
	VR	variscite	$Al(PO_4) \cdot 2H_2O$
	TL	tinsleyite	$KAl_2(PO_4)_2(OH) \cdot 2H_2O$
	TK	taranakite	$K_3Al_5(PO_3OH)_6(PO_4)_2 \cdot 18H_2O$
	LC	leucophosphite	$KFe^{3+}{}_2(PO_4)_2(OH) \cdot 2H_2O$
	SP	spheniscidite	$(NH_4)Fe^{3+}{}_2(PO_4)_2(OH) \cdot 2H_2O$
	VV	vivianite	$Fe^{2+}{}_3(PO_4)_2 \cdot 8H_2O$
	ST	strengite	$Fe^{3+}(PO_4) \cdot 2H_2O$
	TP	triplite	$(Mn^{2+},Fe^{2+})_2(PO_4)F$
	MT	mitridatite	$Ca_2Fe^{3+}{}_3O_2(PO_4)_3 \cdot 3H_2O$
Silicates	SC	sarcolite	$Na_4Ca_{12}Al_8Si_{12}O_{46}(SiO_4,PO_4)(OH,H_2O)_4(CO_3,Cl)$
	MM	montmorillonite	$(Na,Ca)_{0.3}(Al,Mg)_2Si_4O_{10}(OH)_2 \cdot nH_2O$
	IL	illite	$K_{0.65}Al_{2.0}[Al_{0.65}Si_{3.35}O_{10}](OH)_2$
	MC	muscovite	$KAl_2(Si_3Al)O_{10}(OH)_2$
	KL	kaolinite	$Al_2Si_2O_5(OH)_4$
	OP	opal	$SiO_2 \cdot nH_2O$
	QZ	quartz	SiO_2
	CH	chert	SiO_2
	TD	tridymite	SiO_2
Others	CT	chitin	$(C_8H_{13}O_5N)_n$
	NU	natrouranospinite	$Na_2(UO_2)_2(AsO_4)_2 \cdot 5H_2O$
	RK	rokühnite	$FeCl_2 \cdot 2H_2O$

The mineralogical characterization results are compiled in Tables 13 and 14, structured as follows:

Rows

Samples are arranged in rows on two geographical levels: a *broad* categorization, following the threefold latitudinal division of the cave described above (North, Central, and South Zones), and a *specific* categorization, corresponding to the sampling squares. Zones are separated from each other in the table by horizontal dashed lines, while squares are alternately shaded in white and grey for easy differentiation. Within the squares, samples are arranged from top to bottom, in order of increasing depth.

Columns

The columns represent the different mineral and non-mineral components that were identified in the samples. *Major* and *minor* categories were employed to structure the identifications. The major categories correspond to the five component classification groups (sulphates, carbonates, phosphates, silicates, and others), separated from each other in the table by vertical dashed lines. The minor categories correspond to specific elements or compounds that certain components share, sometimes across major categories (e.g. calcium).

Visualization of identifications

For each sample, the concentration of identified components was estimated using the following scale:

- xxx: Strong. The component dominates the sample.
- xx: Average. The component has a balanced presence.
- x: Weak. The component is only detectable in trace amounts.

The technique used to identify a component is given by its cell colour:

- Light yellow: Fourier-transform infrared spectroscopy (FTIR)
- Light orange: X-ray diffraction (XRD)
- Light red: both

In cases where both FTIR and XRD identify a component (light red cells) but the quantifications diverge, the one for FTIR is given first, followed by a slash, then the one for XRD.

Table 13. Summary of mineralogical characterization results, covering sulphates, carbonates, silicates, and miscellany.

Latitudinal division	Square(s)	Sample	Depth (cm DP)	Sulphates			Carbonates	Silicates								Others		
				Al	PO_3OH	Ca	CO_3	Na / Ca		K		Al	H_2O	SiO_2					
								PO_4 / CO_3 / Cl	Mg										
				rostite	*arcdealite*	*gypsum*	*calcite*	*sarcolite*	*montmorillonite*	*illite*	*muscovite*	*kaolinite*	*opal*	*quartz*	*chert*	*tridymite*	*chitin*	*natrouranospinite*	*rokühnite*
North Zone	S1E5	X22	Surface				xx		xxx					xx					
	S2E5	X21	Surface				xxx		xxx					xx / xxx					
	S2E1	1	-260			xxx			x	x									
	S2E1	27	-266										xx	xx					
	S2E1	2	-292			xxx			x	x				x					
	S2E1	5	-300 to -320			xxx			x	x									
	S2E1	3	-312			xx			xx					x / xxx			x		
	S2E1	4	-343											xx					
	S2E1	6	-337					x						x					
	S2E1	7	-367						x					xx			xxx		
	S4E1	15	-300																
	S4W4	13	-145						xx					xx					
	S4W4	8	-302						xx					xx					
	S4W4	9	-318						x					xx			x		
	S4W4	10	-325			xx			xx					xx			xx		
	S4W4	11	-332						xx					xx			x		
	S4W4	12	-337						xx				xx				x		
	S4W5	14	-140							xxx				xxx					
Central Zone	S6E4	28	-307											x					
	S7E4	33	-157			xxx			x	x									
	S8E4	31	-121			xxx			xx					xx					
	S8E4	32	-136		x				xx					xxx					
	S8E4	34	-168		xx	xxx			x		x		x	x / xx	x				
	S8E4	35	-182			xxx			x				x						
	S8E3	44	-305											x					
	S8E3	45	-325										xx	x / xx					
	S9E3	36	-125			xxx			xx					xxx					
	S9E3	37	-144		x				xx					xxx					
	S9E3	38	-157		xx / xxx	xx							xx	xx		x			
	S9E3	39	-167		xxx								xx	xx	xx	x			
	S9E3	39.5	-213										x	xx					
	S9E3	40	-231										xxx	xx					
	S9E3	41	-259										xxx	xx					
	S9E3	42	-276										xx	xx					
	S9E3	43	-299										x	xx					
	S6E2 + S7E2	22	-165		xxx										xx	x			
	S6E2 + S7E2	50	-182		x / xx	xxx			x	x				xx					
	S6E2 + S7E2	49	-199		x	xxx			x				xx						
	S6E2 + S7E2	48	-207		x	xxx			x				xx	xx					
	S6E2 + S7E2	47	-217		x								xx	xx					
	S6E2 + S7E2	46	-222										xx	xx / xxx					
	S6E2 + S7E2	23	-225		x	xxx			x	x									
	S6E2 + S7E2	24	-260										xx	xx					
	S6E2 + S7E2	25	-310										xx	x					
	S8E1	16	-212			xxx			x	x				x					
	S8E1	17	-260										xx						
	S8E1	18	-280				xx				xx		xx	xx					
	S8E1	19	-300											xx					
	S8E1	20	-318											x					
	S8E1	21	-326																
	S8E1	26	-350																
	S8W1	29	-249										xx	xx					
	S10E1	X20	-177										x	xx					
	S10E1	X19	-182										x	xx			x		
	S10E1	X18	-203										x	xx			x		
	S10E1	X17	-218										x	xx			x		
	S10E1	X16	-225		xx									xx					
	S10E1	X15	-240						x						x				
	S10E1	X14	-246						x	x			x						
	S10E1	X13	-247											xx					
	S10E1	X12	-270											xxx					
	S10E1	X11	-280						x	x				x / xxx					
	S10E1	X10	-290											x / xxx					
	S10E1	X9	-300											x					
	S10E1	X8	-320															x	
	S10E1	X7	-345						x					x					
	S10E1	X6	-377						xx					xxx					
	S10E1	X5	*(not available)*						xx					xxx					
	S10E1	X4	-400						xxx					xxx					
	S10E1	X3	-415						xxx					xxx					
	S10E1	X2	-440						xxx					xxx					
	S10E1	X1	-460							xx				xxx					
	S9W6	53	Surface		xx	xxx			xx					x / xx			xx		
South Zone	S14E2	52	Surface		xx	x				x							xx		xxx
	South Trench	G	-113	xx							xx		xx	x / xxx		xx			
	South Trench	MM4	-135 to -140						xx					xx / xxx					
	South Trench	F	-142						xx					xx / xxx					
	South Trench	E	-162							xx				xx / xxx					
	South Trench	D	-220									xx		xx / xxx					
	South Trench	MM3	-223 to -228						xx					xx / xxx					
	South Trench	C	-238						x					xx / xxx					
	South Trench	MM2	-265 to -270						xx					xx / xxx					
	South Trench	B	-285							x			x	x / xx					
	South Trench	MM1	-316 to -321							xx				x / xx					
	South Trench	A	-333							xx			x	x / xxx					
	Diverticulum	30	Surface							xx				x					

Table 14. Summary of mineralogical characterization results, covering phosphates.

Latitudinal division	Square(s)	Sample	Depth (cm DP)	Phosphates																	
				Ca						Al						Fe				Mn	Ca
				CO_3	PO_4	H_2O	PO_3OH	Mg				OH	PO_3OH	K	NH_4						
				carbonate-rich hydroxylapatite	*hydroxylapatite*	*brushite*	*monetite*	*whitlockite*	*montgomeryite*	*crandallite*	*variscite*	*tinsleyite*	*taranakite*	*leucophosphite*	*sphenisicidite*	*vivianite*	*strengite*	*triplite*	*mitridatite*		
North Zone	S1E5	X22	Surface	xx		x															
	S2E5	X21	Surface	xx / x		x				x											
	S2E1	1	-260	x		x					x										
	S2E1	27	-266	xx		xx					xxx										
	S2E1	2	-292	x		x / xx					x	x				x	x				
	S2E1	5	-300 to -320	x		x					x										
	S2E1	3	-312	xx		xx				x	xx				xx						
	S2E1	4	-343	xxx		xx				x	x										
	S2E1	6	-337	xxx		x					x					x					
	S2E1	7	-367	xx		xx					xx										
	S4E1	15	-300	xxx		x					x					x					
	S4W4	13	-145	xx		xx					xx										
	S4W4	8	-302	xx		xx					xx										
	S4W4	9	-318	xx		xx					xx										
	S4W4	10	-325	xx		xx				xx	x			xx							
	S4W4	11	-332	xx		xx					x										
	S4W4	12	-337	xx		xx					x										
	S4W5	14	-140	xx		xx				x	x / xx										xx
Central Zone	S6E4	28	-307	xxx							x										
	S7E4	33	-157	x		x					x										
	S8E4	31	-121	xx		xx					xx										
	S8E4	32	-136	xx		xx					x										
	S8E4	34	-168	xx		x					xx			xx							
	S8E4	35	-182	x		x					xxx										
	S8E3	44	-305	xxx							x										
	S8E3	45	-325		xx						x / xx			xxx							
	S9E3	36	-125	xx		xx					x										
	S9E3	37	-144	xx		xx					x										
	S9E3	38	-157	xx		xx	xx		xx		x		xx								
	S9E3	39	-167	xx	x	xx	x / xx				x		xx								
	S9E3	39.5	-213		xx	x					xxx										
	S9E3	40	-231		xx						xxx										
	S9E3	41	-259		xx						xxx										
	S9E3	42	-276		xx						xxx										
	S9E3	43	-299		xx						xxx										
	S6E2 + S7E2	22	-165	x		xxx / xx	x														
	S6E2 + S7E2	50	-182	x / xx		x / xx					x		xx	x							
	S6E2 + S7E2	49	-199	x		x					xx			xx							
	S6E2 + S7E2	48	-207	x		x / xx					xx			xx							
	S6E2 + S7E2	47	-217	xx		x					xxx										
	S6E2 + S7E2	46	-222	xx		xx					xx / x			xx	xx			x			
	S6E2 + S7E2	23	-225	x		x															
	S6E2 + S7E2	24	-260	xx		x					xxx										
	S6E2 + S7E2	25	-310	xx		xx					xxx			xx							
	S8E1	16	-212			x / xx					xx		x			x	x				
	S8E1	17	-260	x		x / xx	x				x / xx			xx / xxx		xx					
	S8E1	18	-280	x		x					xxx										
	S8E1	19	-300	xx		xx					xxx			xx							
	S8E1	20	-318	xxx		x					x		xx								
	S8E1	21	-326	xxx		xx					x		xx								
	S8E1	26	-350	xxx		xx					x		xx								
	S8W1	29	-249	x		x					xxx										
	S10E1	X20	-177		xx	x					xxx										
	S10E1	X19	-182	xx		xx					xxx										
	S10E1	X18	-203	xx		xx					xxx										
	S10E1	X17	-218	xx		xx					xxx										
	S10E1	X16	-225	xx		xx					xxx										
	S10E1	X15	-240		xx	x				x	xx		xx								
	S10E1	X14	-246	x		x				x	x			xx							
	S10E1	X13	-247	xx		xx					xxx										
	S10E1	X12	-270	x		x					x										
	S10E1	X11	-280	xx		xx				x / xx	xx				xx						
	S10E1	X10	-290	xx		xx				xxx	x			x							
	S10E1	X9	-300	x						xxx	xx			x							xxx
	S10E1	X8	-320	xxx		x															xx
	S10E1	X7	-345	xx		x				x / xx	x		xx			xx					xxx
	S10E1	X6	-377	x		x					x										
	S10E1	X5	*(not available)*		x						x										
	S10E1	X4	-400	x		x					x										
	S10E1	X3	-415	x		x					x										
	S10E1	X2	-440								x										
	S10E1	X1	-460		x						x										
	S9W6	53	Surface	xxx		x					xx										
South Zone	S14E2	52	Surface	x	xx						xx										
	South Trench	G	-113								xx / xxx										
	South Trench	MM4	-135 to -140	x		x					x	x									
	South Trench	F	-142	x		x					x	x									
	South Trench	E	-162	x		x					x	x									
	South Trench	D	-220	x							xx										
	South Trench	MM3	-223 to -228	x	xx						xx / xxx	xx									
	South Trench	C	-238	x						x	xx	x									
	South Trench	MM2	-265 to -270	x	xx						xx / xxx	xxx									
	South Trench	B	-285	xx	xx			xx			x		x								x
	South Trench	MM1	-316 to -321	xx	xxx			xxx	xx		x		x								xx
	South Trench	A	-333	xx	xx					xx	x		x								
	Diverticulum	30	Surface	xxx				x			x										

4.2.1. The North Zone: transects S1 to S4

In the North Zone, the eastern part (Squares S1E5 to S2E5) is represented by surface samples that are primarily composed of calcite and montmorillonite. Although they do contain some carbonate-rich hydroxylapatite in early crystallization alongside other calcium phosphates (brushite, crandallite), they are essentially sedimentary in nature.

In the central part (Squares S2E1 and S4E1), the lower portion of the profile is dominated by highly crystalline carbonate-rich hydroxylapatite, whereas the upper portion appears to be strongly marked by the presence of gypsum, pointing to differing diagenetic mechanisms (calcium bonding with phosphate versus sulphate ions, respectively). Various aluminium phosphates were also identified, chiefly variscite in varying degrees of crystallinity, indicating authigenesis in the presence of aluminium (most likely from clay minerals). Several iron phosphate minerals (spheniscidite, vivianite, strengite) were detected as well, pointing to changes in oxidation conditions that facilitated iron mobility. Silicates have a weak overall presence and appear to have undergone alteration, with quartz occasionally exhibiting poor crystallinity and being accompanied by opal. Finally, chitin peaks were detected in some of the samples from the fossil guano deposit in this area (corresponding to Layer 9 in Square S4E1), suggesting a higher degree of organic matter preservation compared to other parts of the cave.

Finally, in the western part (Squares S4W4 to S4W5), while the fossil guano deposit (Layer 6 in Squares S4W3 to S4W4) is generally characterized by brushite and carbonate-rich hydroxylapatite in early crystallization, it may also contain more intermediate to advanced authigenic minerals than it appears to (as seen in the lone specimen analyzed in XRD, Sample 10). The upper part has more strongly-expressed variscite than the lower part, where chitin peaks were identified. Montmorillonite and quartz appear to be present throughout the layer, except at the bottom where quartz is replaced by opal, again pointing to silicate alteration. In the upper level studied in this area (Layer 1 in Square S4W5), the FTIR profile appears similar to the upper part of Layer 6 in Squares S4W3 to S4W4, but there are again some 'hidden' minerals (i.e. mitridatite and crandallite) seen only in XRD, specifically in Sample 14. XRD also confirms the presence of hydroxylapatite and variscite. Montmorillonite is replaced by illite, strongly present in this sample (although not identified in XRD), while quartz is well-defined.

Squares S1E5 to S2E5

Table 15 presents the results for Squares S1E5 to S2E5, situated in the eastern part of the North Zone.

Table 15. Summary of mineralogical characterization results for Squares S1E5 to S2E5.

Square	Sample	Depth (cm DP)	Carbonates	Phosphates				Silicates	
			Ca					Si_4O_{10}	SiO_2
			CO_3	PO_4	PO_3OH	Al			
			CC	*CHAP*	*HAP*	*BR*	*CR*	*MM*	*QZ*
S1E5	X22	Surface	xx	xx		x		xxx	xx
S2E5	X21	Surface	xxx	xx	x	x	x	xxx	xx / xxx

The two samples from this area were both collected from the present cave surface, between the east wall and some stalagmitic columns.

Calcite (CC) is present in both samples and is particularly dominant in X21. Both samples also have carbonate-rich hydroxylapatite (CHAP); however, X21 has a small FTIR peak at 629 cm^{-1} that is absent in X22 and is indicative of early crystallization (Figure 83; Weiner, 2010: 311–313). This may explain why hydroxylapatite (HAP) was faintly detected in XRD, albeit in its simple, non-carbonate form (Figure 84). (The international XRD database used, PDF-2 2003, did not contain carbonate-rich hydroxylapatite.) A touch of the calcium phosphate mineral brushite (BR) was detected in both samples via FTIR, while XRD suggested the possible presence of the aluminium phosphate crandallite (CR) in Sample X21. The clearly dominant phase in both samples is montmorillonite (MM), and this fine-grained clay mineral was only detected in FTIR. Finally, the presence of quartz (QZ) was noted. Whereas the FTIR doublet peaks (at approximately 800 and 780 cm^{-1}) are rounded and slant downwards in Sample X21, possibly indicating transformation, they are visible in Sample X22 (Figure 85).

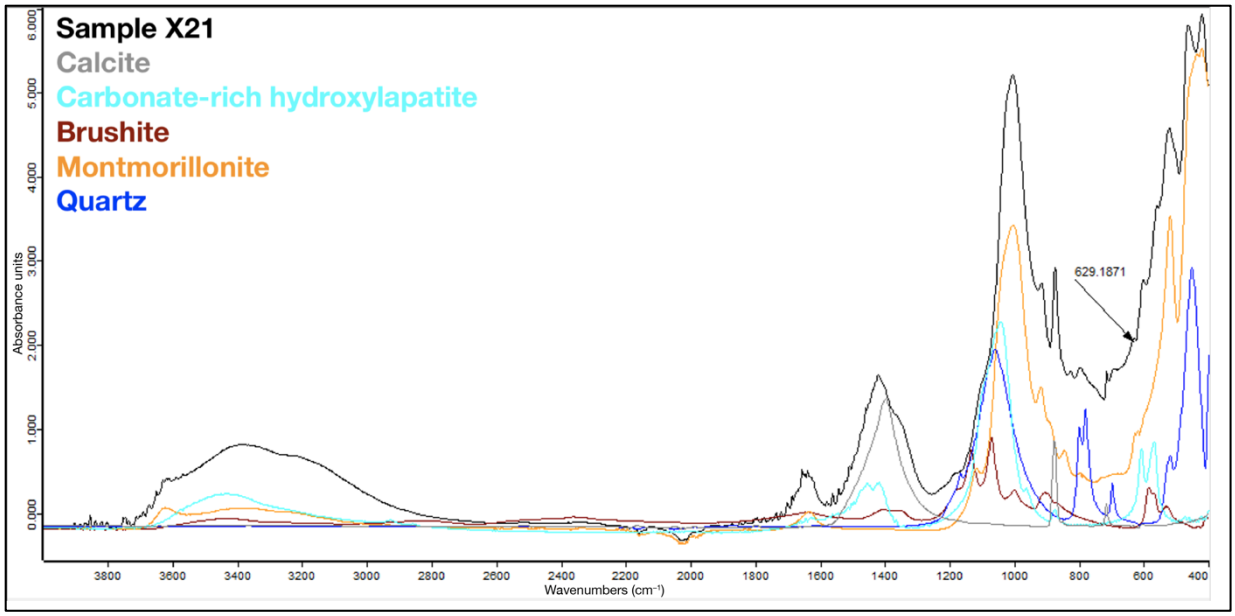

Figure 83. ATR-FTIR spectrum of Sample X21 in absorbance mode.

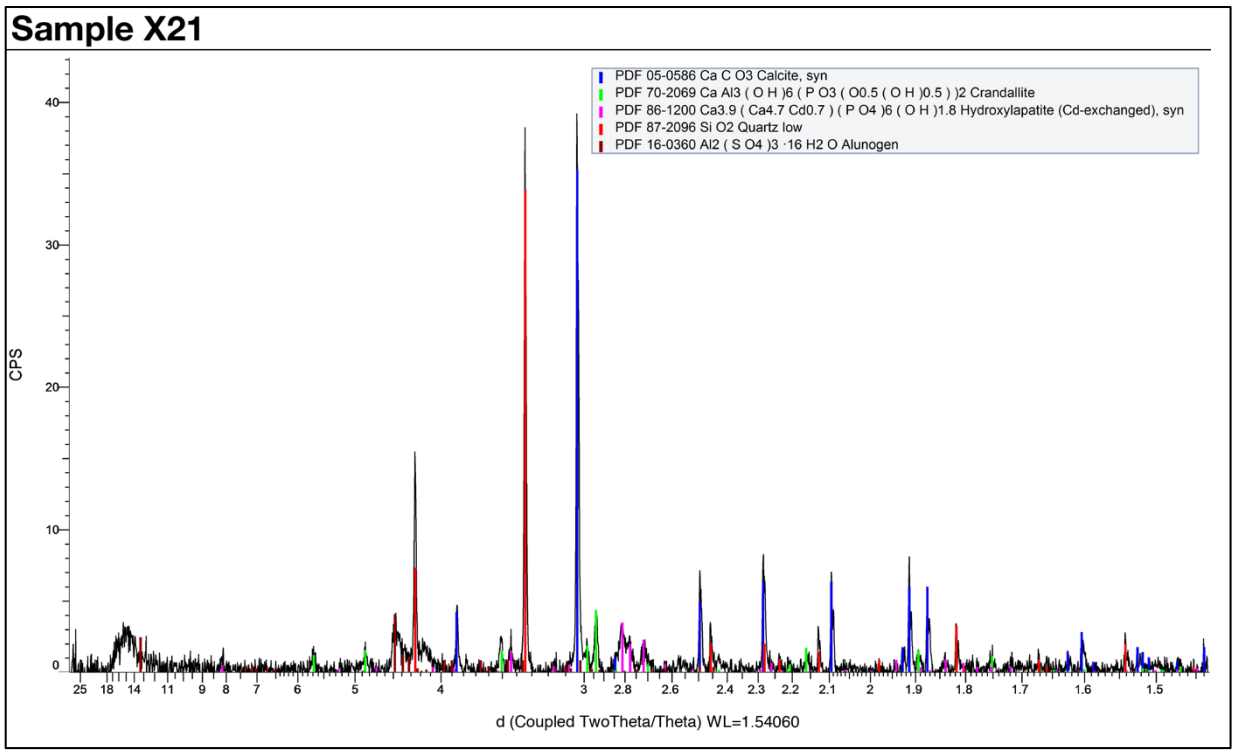

Figure 84. X-ray diffractogram of Sample X21.

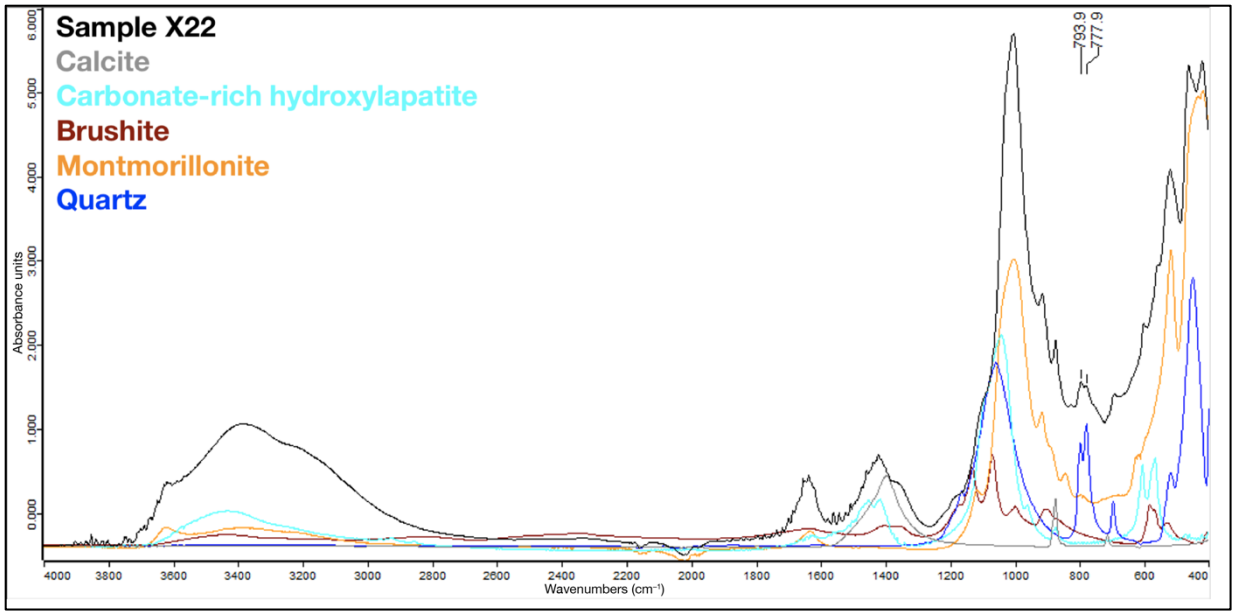

Figure 85. ATR-FTIR spectrum of Sample X22 in absorbance mode.

Squares S2E1 and S4E1

Table 16 presents the results for Squares S2E1 and S4E1, situated in the central part of the North Zone.

Table 16. Summary of mineralogical characterization results for Squares S2E1 and S4E1.

Square	Sample	Depth (cm DP)	Sulphates	Phosphates								Silicates					Others
			Ca	PO_3OH	CO_3	PO_4	Al	K	NH_4	Fe		Al		K	H_2O	SiO_2	
												PO_4 / CO_3 / Cl	Mg				
			GY	BR	CHAP	HAP	CR	VR	TL	SP	VV	ST	SC	MM	IL	OP	QZ	CT
S2E1	1	-260	xxx	x	x			x						x	x			
S2E1	27	-266		xx	xx			xxx								xx	xx	
S2E1	2	-292	xxx	x / xx	x			x	x		x	x		x	x		x	
S2E1	5	-300 to -320	xxx	x	x			x						x	x			
S2E1	3	-312	xx	xx	xx		x	xx		xx				xx			x / xxx	x
S2E1	7	-337		xx	xx			xx						x			xx	xxx
S2E1	4	-343		xx	xxx	xxx	x	x									xx	
S2E1	6	-367		x	xxx	xxx		x			x		x				x	
S4E1	15	-300		x	xxx			x			x							

The majority of samples from this area were collected from Square S2E1; unfortunately, being a treasure hunter's pit, no stratigraphical profile was drawn up for this square.

The strong detection of the calcium sulphate gypsum (GY) in the upper half of the sequence confirms its presence in this area of the cave, between 260 and 320 cm below DP, as seen for example in Sample 2 (Figures 86 and 87).

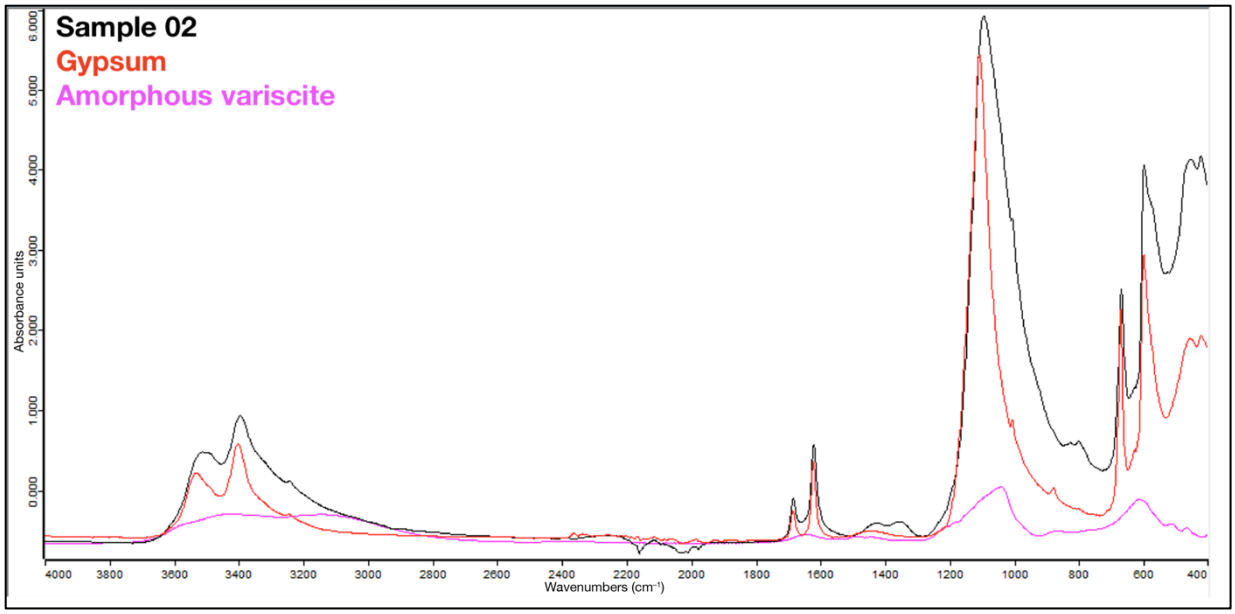

Figure 86. ATR-FTIR spectrum of Sample 2 in absorbance mode.

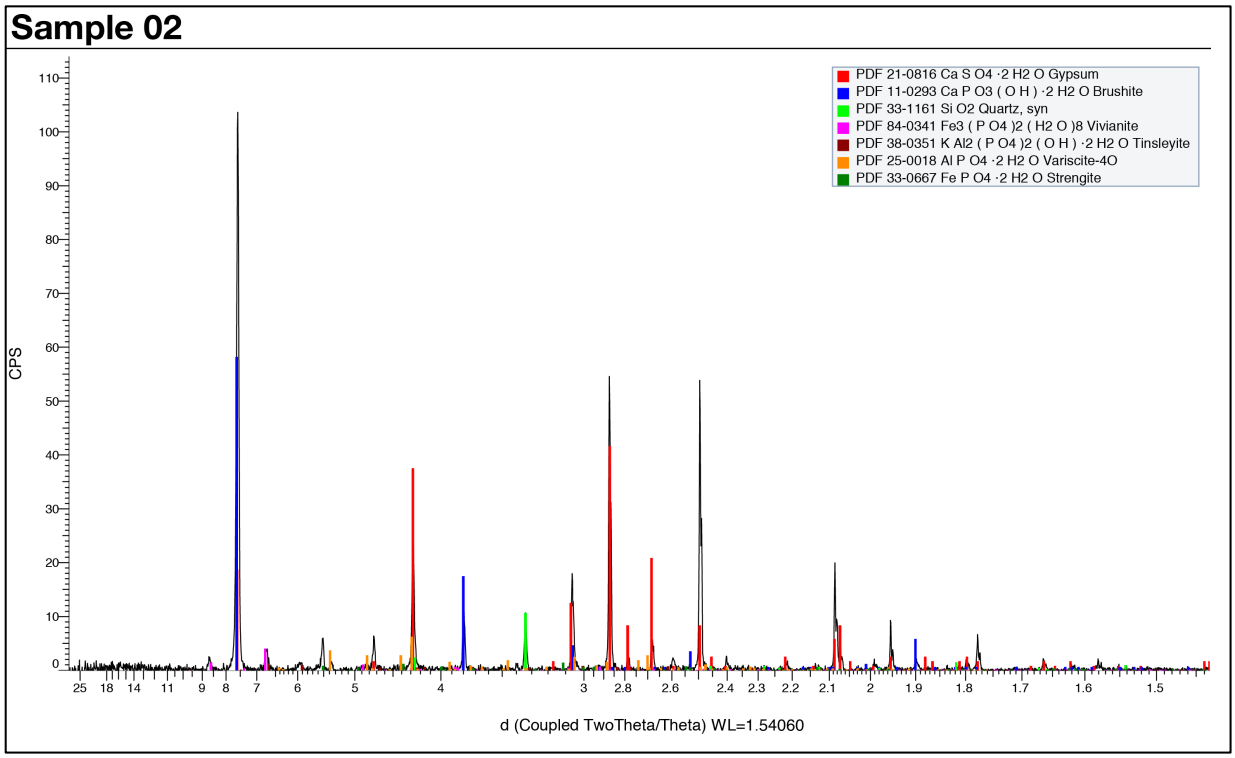

Figure 87. X-ray diffractogram of Sample 2.

Among the calcium phosphates, brushite (BR) is present in varying quantities all throughout. Carbonate-rich hydroxylapatite (CHAP) has about the same degree of presence except at the bottom, where it is very pronounced (Figure 88). XRD confirms the dominance of hydroxylapatite (HAP) here (Figure 89). Additionally, carbonate-rich hydroxylapatite (CHAP) has a pronounced crystallization peak in FTIR at 630 cm^{-1} in this part of the profile, as well as

near the top: for instance, in Sample 27 (Figure 90). In the other samples, the peak is smaller, but nevertheless present.

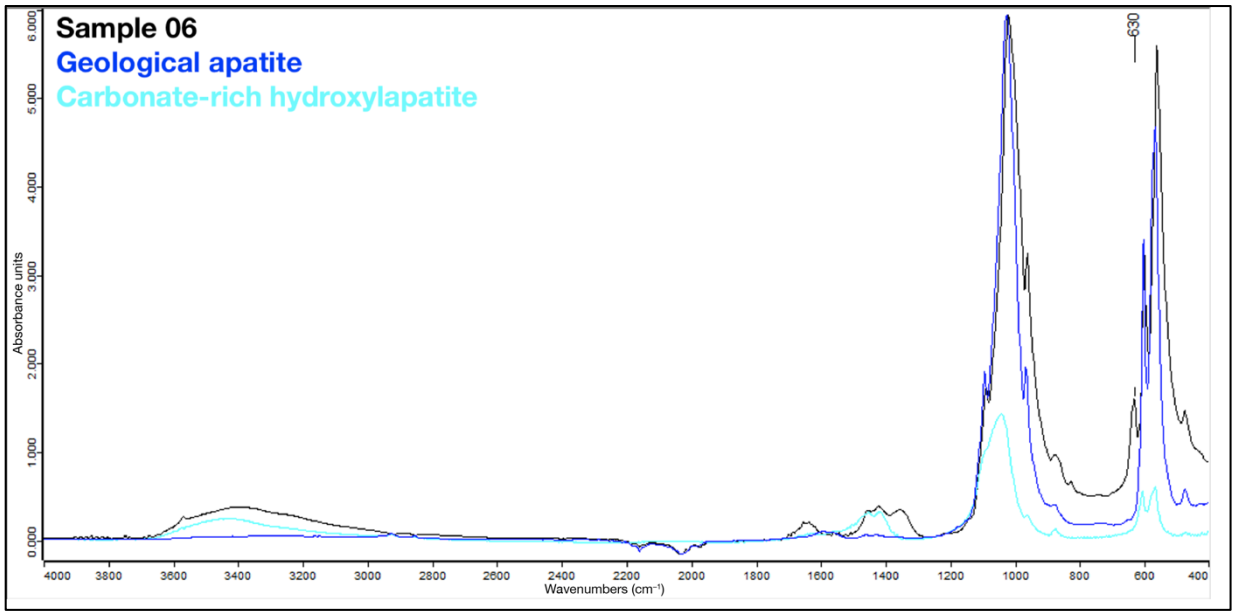

Figure 88. ATR-FTIR spectrum of Sample 6 in absorbance mode.

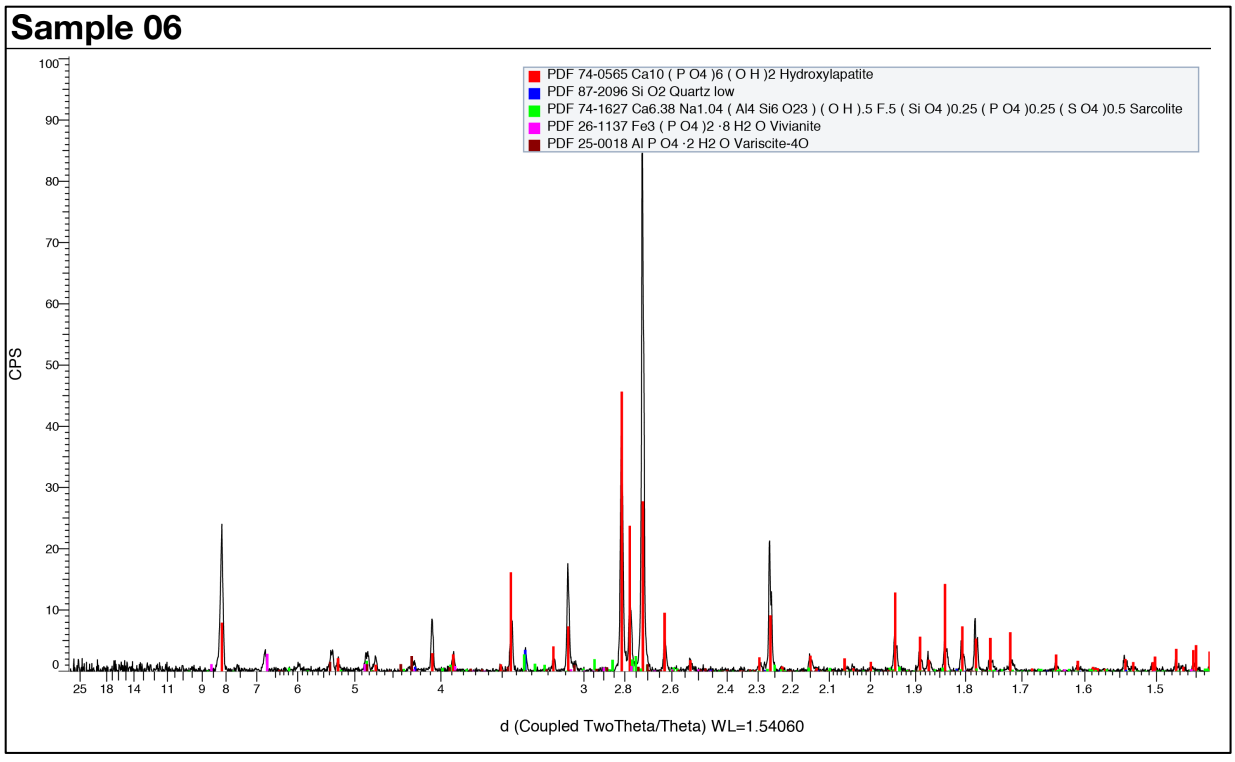

Figure 89. X-ray diffractogram of Sample 6.

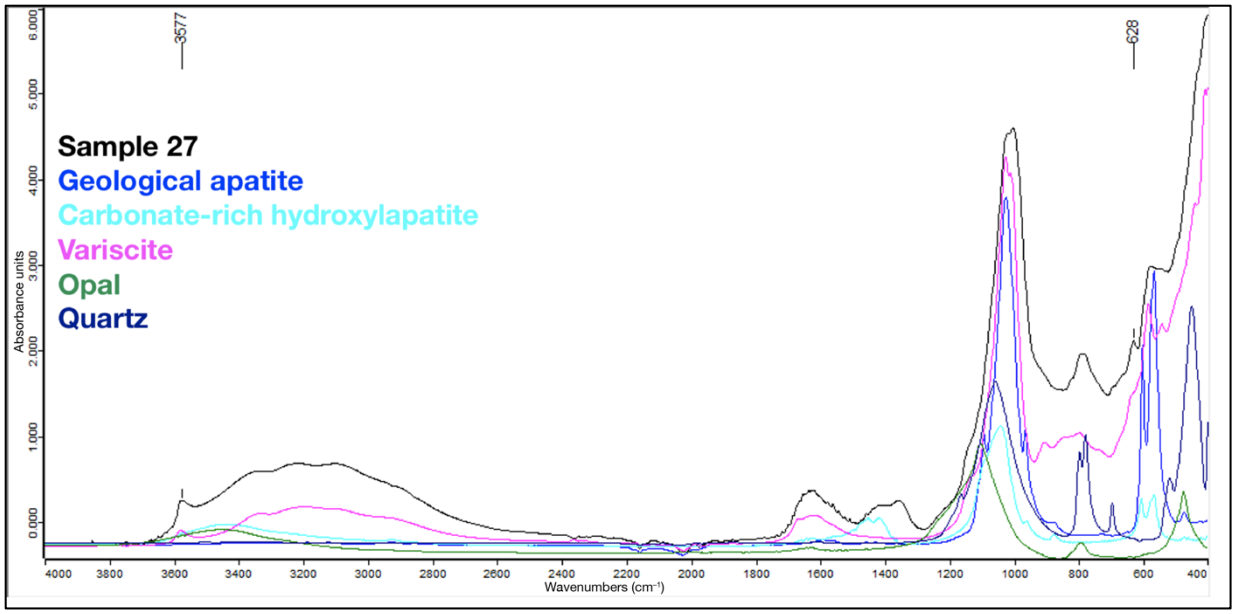

Figure 90. ATR-FTIR spectrum of Sample 27 in absorbance mode.

Crandallite (CR) makes a couple of faint, occasional appearances in the lower half of the sequence, again only in XRD, as in Square S2E5. Variscite (VR), an aluminium phosphate like crandallite (CR) but without calcium, is ubiquitous with a particularly strong presence in Sample 27, usually indicated by an FTIR peak at around 3577 cm^{-1} (Figure 90). This authigenic mineral has varying degrees of crystallization in the sequence: detection in XRD generally indicates a certain degree of crystallinity, but shoulders around 1200 cm^{-1} in FTIR may indicate the presence of an amorphous phase (Figure 86). Another aluminium phosphate, this time containing potassium, tinsleyite (TL), was observed in Sample 2 via XRD.

Several iron phosphate minerals were also identified in Square S2E1. Spheniscidite (SP), characterized by its ammonium (NH_4^+) cation, was detected via XRD in Sample 3 (Figure 91). Traces of vivianite (VV) were identified at the bottom of the profile and again near the top, where it is accompanied by strengite (ST).

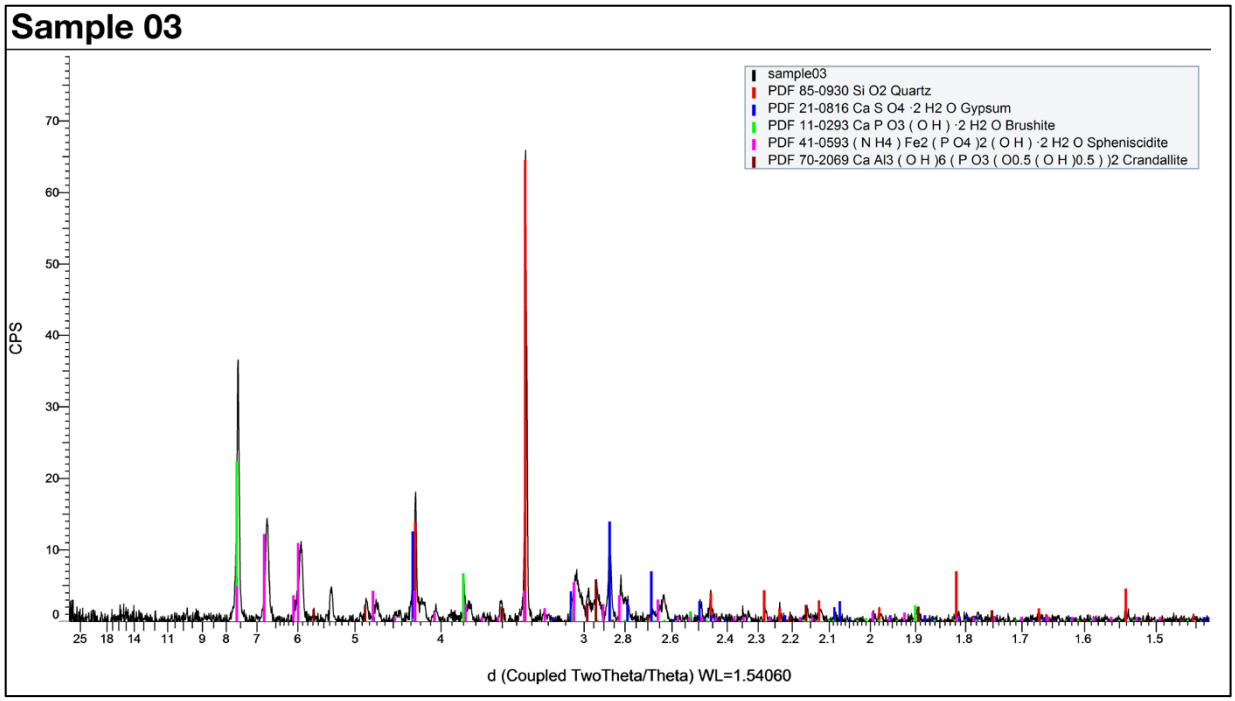

Figure 91. X-ray diffractogram of Sample 3.

Silicate minerals do not have particularly significant visibility in the sequence. Two principal aluminium silicates were identified through FTIR in the greater upper half of the profile, montmorillonite (MM) and illite (IL), and in generally low quantities. A third aluminium silicate, sarcolite (SC), was detected via XRD at the bottom.

For ordinary silicates, quartz (QZ) is generally present throughout the sequence, although only XRD detected it at the very bottom. As with variscite (VR), the degree of crystallinity varies throughout: the doublet peaks at around 800 and 780 cm^{-1} in FTIR are at times visible (Samples 7 and 4), at times barely so (Sample 27), and at times resemble transforming opal (OP) (Sample 3) (Figure 92). In Sample 27, however, the presence of opal (OP) is confirmed alongside quartz (QZ) (Figure 90).

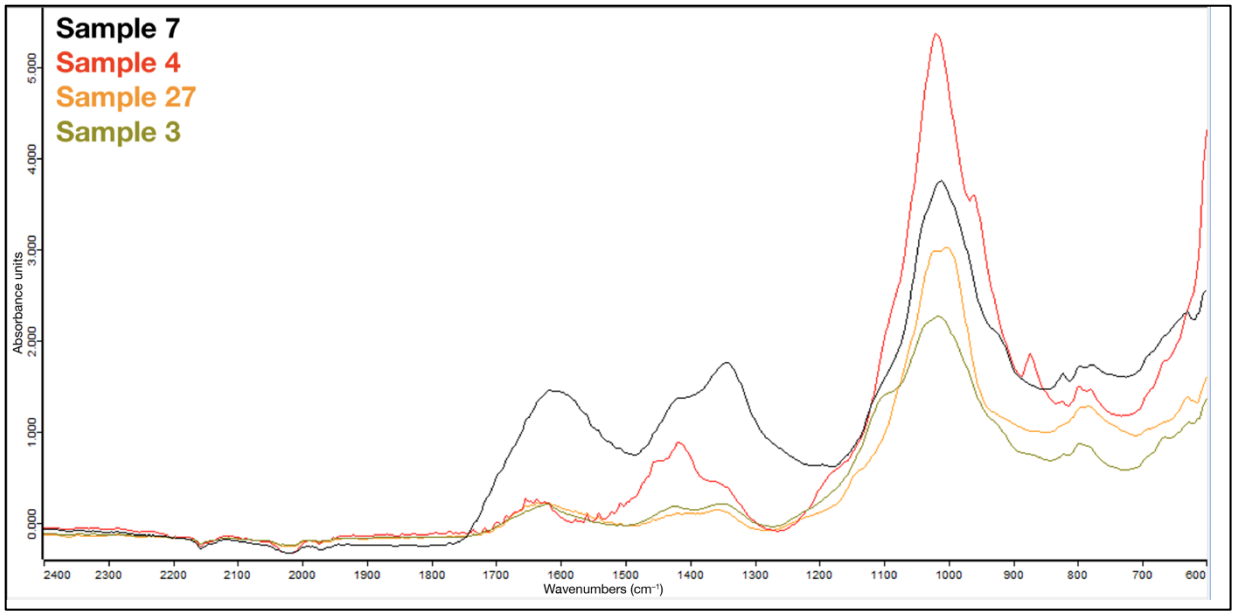

Figure 92. ATR-FTIR spectra of Samples 7, 4, 27, and 3 in absorbance mode.

After identification of mineral components, a couple of samples were left with unresolved peaks in FTIR, mainly between 1800 and 1200 cm^{-1}. Comparison with the modern guano samples 52 and 53 suggested that Sample 7 and, to a lesser extent, Sample 3, contain chitin (CT) (Figure 93). This could indicate preservation of other molecules corresponding to organic matter.

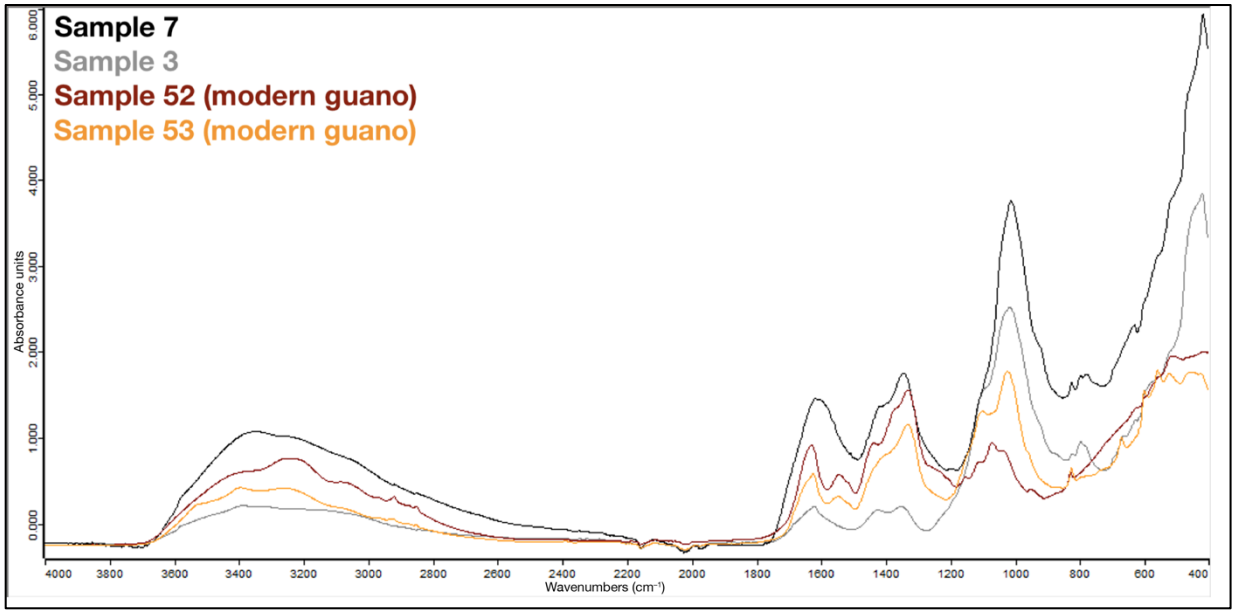

Figure 93. ATR-FTIR spectra of Samples 7, 3, 52, and 53 in absorbance mode.

Moving to the neighbouring square, S4E1, Figure 94 presents the vertical profile. Sample 15 was collected from bluish white Layer 7. Its mineralogy is almost identical that of Sample 6, collected from a white layer overlying a black layer at the very bottom of Square S2E1 (Figure 95). Carbonate-rich hydroxylapatite (CHAP) remains the dominant phase, accompanied by brushite (BR), variscite (VR), and vivianite (VV). As with Sample 6, it was not possible to clearly identify the presence of quartz (QZ) via FTIR in this sample.

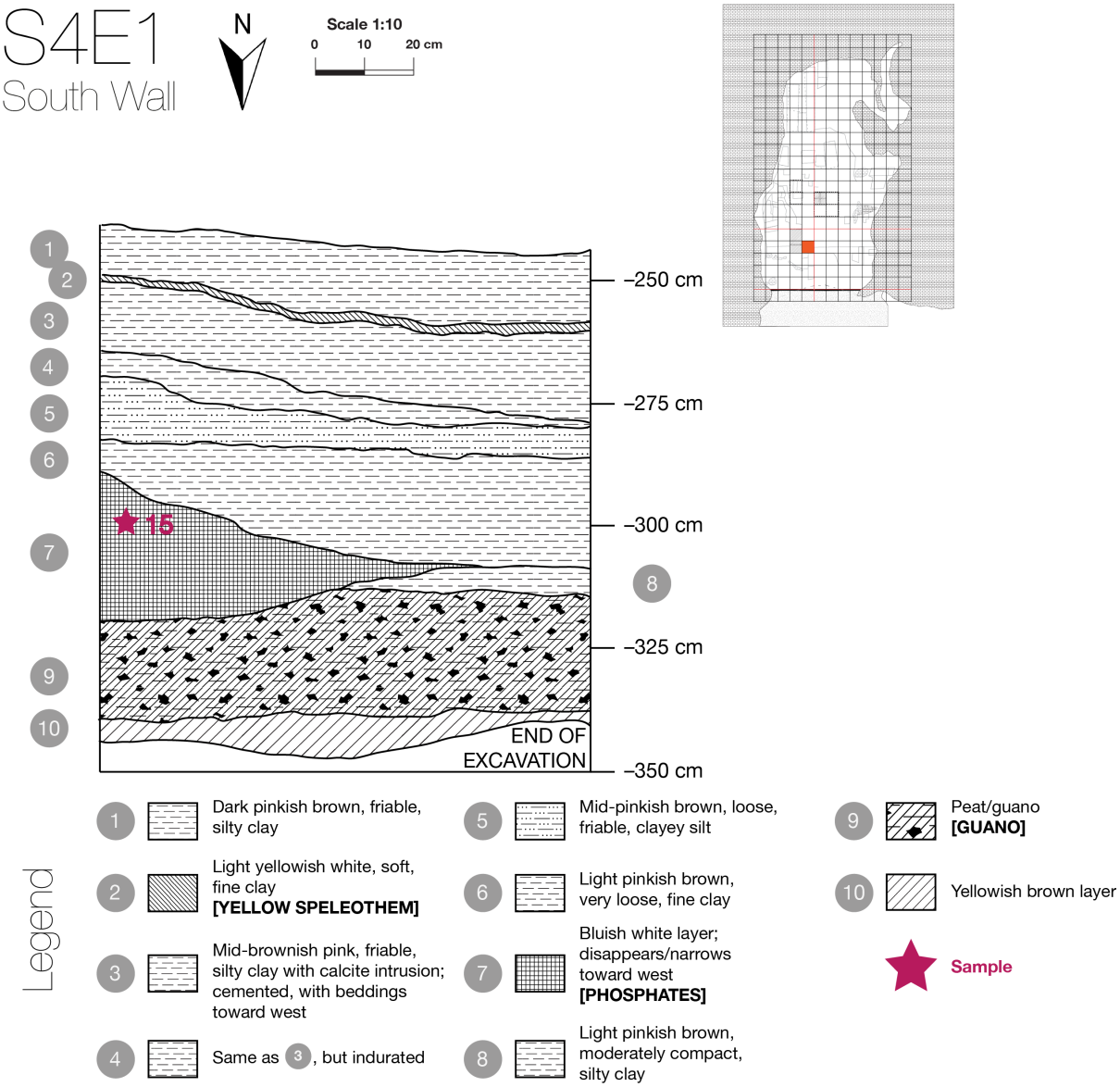

Figure 94. South Wall vertical profile for Square S4E1, with the location of Sample 15 indicated.

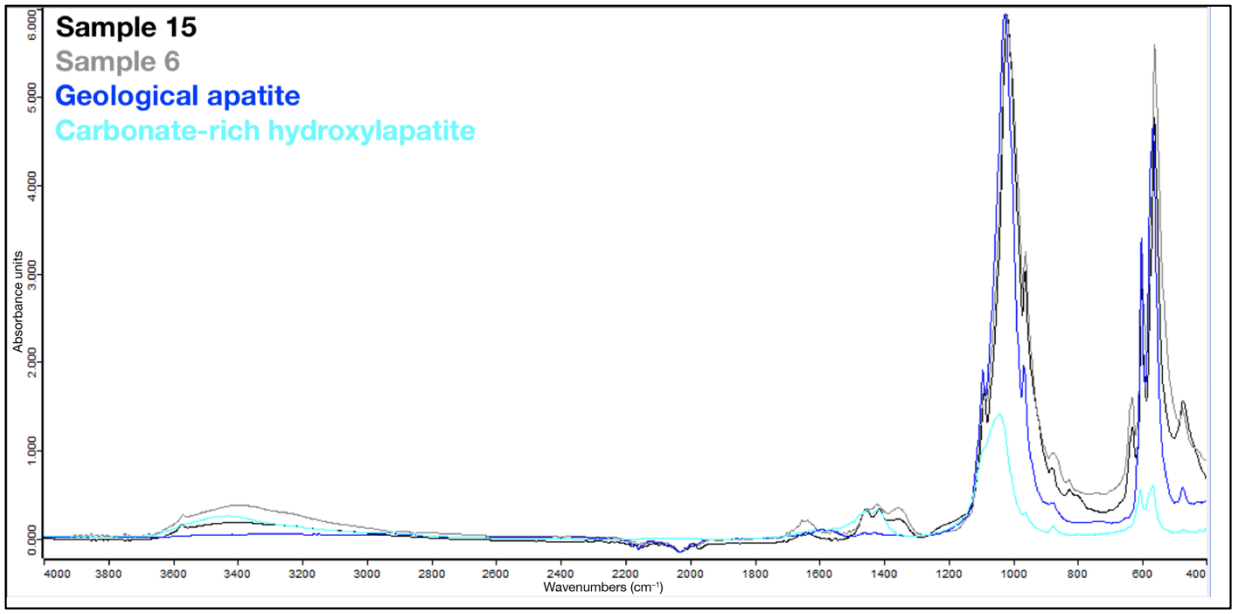

Figure 95. ATR-FTIR spectra of Samples 15 and 6 in absorbance mode.

Squares S4W4 to S4W5

Table 17 presents the results for Squares S4W4 to S4W5, situated in the western part of the North Zone.

Table 17. Summary of mineralogical characterization results for Squares S4W4 to S4W5.

Square	Sample	Depth (cm DP)	Sulphates	Phosphates						Silicates				Others
			Ca	PO_3OH	PO_4		Fe		Al	Ca	K	H_2O	SiO_2	
								K						
			GY	BR	CHAP	HAP	MT	LC	VR	CR	MM	IL	OP	QZ	CT
S4W5	14	-140		xx	xx	xx	xx		x / xx	x		xxx		xxx	
S4W4	13	-145		xx	xx				xx		xx			xx	
S4W4	8	-302		xx	xx				xx		xx			xx	
S4W4	9	-318		xx	xx				xx		x			xx	x
S4W4	10	-325	xx	xx	xx			xx	x	xx	xx			xx	xx
S4W4	11	-332		xx	xx				x		xx			xx	x
S4W4	12	-337		xx	xx				x		xx		xx		x

Figures 96 and 97 present the vertical profiles for Squares S4W4 (attached to that of S4W3) and S4W5.

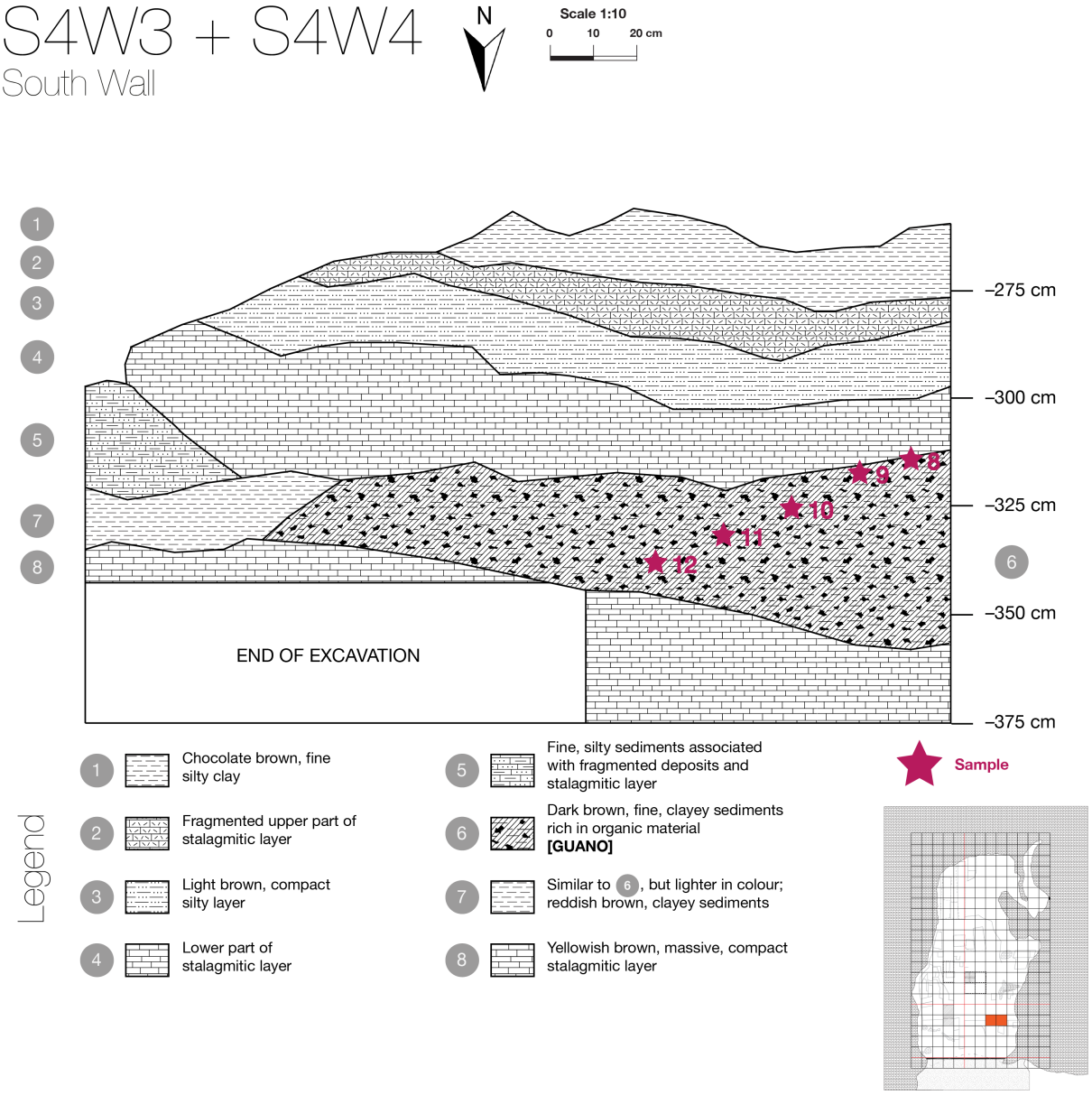

Figure 96. South Wall vertical profile for Squares S4W3 to S4W4, with the location of Samples 8 to 12 indicated.

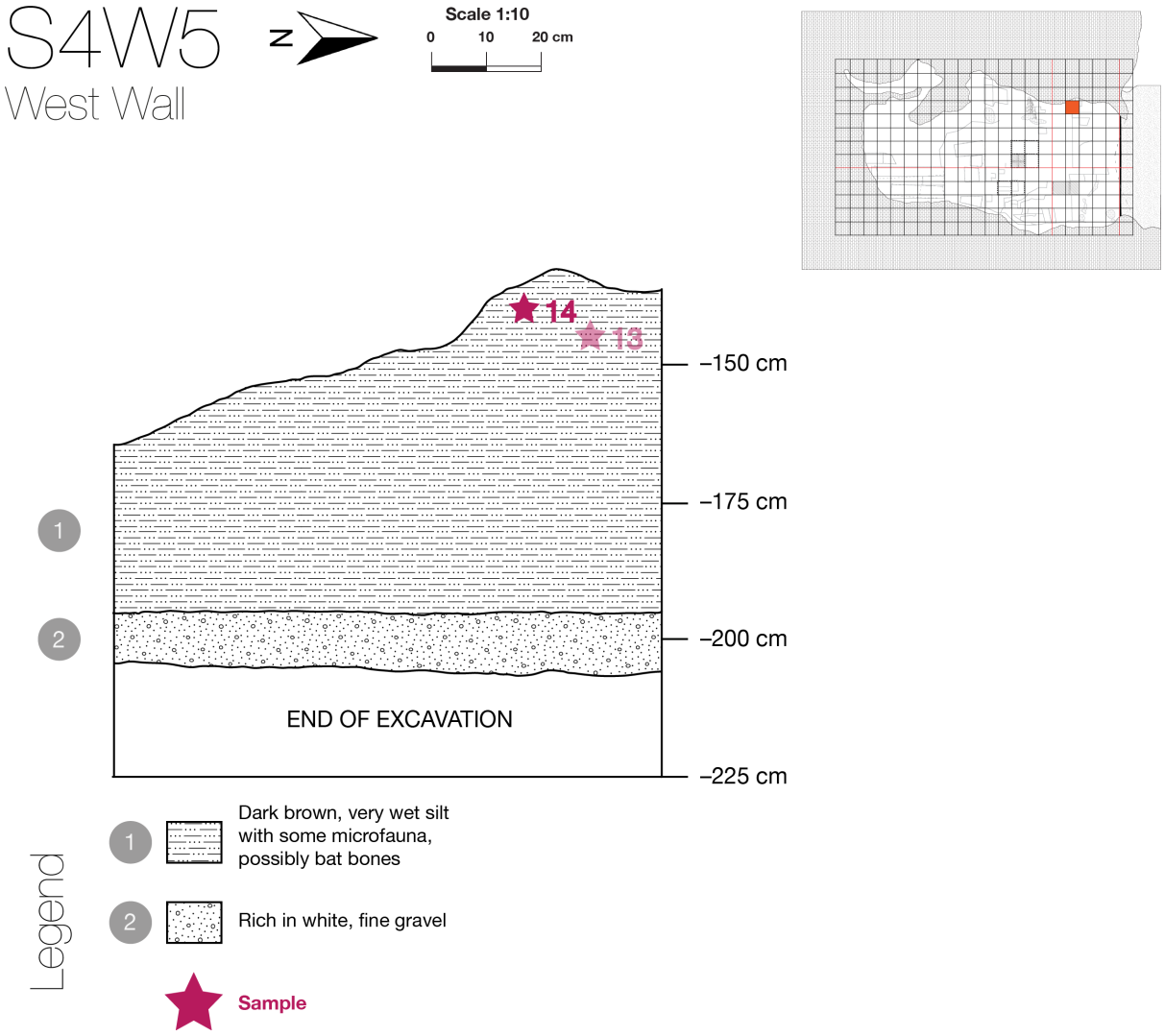

Figure 97. West Wall vertical profile for Square S4W5, with the location of Samples 13 and 14 indicated. Sample 13, projected from Square S4W4, is rendered translucent.

Square S4W4 is where most of the samples in this area come from. Samples 8 to 12 were collected from Layer 6, described as consisting of guano. The mineralogy is relatively homogeneous, with a 'generic' profile consisting of brushite (BR) and carbonate-rich hydroxylapatite (CHAP) in early crystallization (again, due to the small FTIR peak at around 630 cm^{-1}), accompanied by variscite (VR) that is more strongly expressed in the upper part of the layer than below: Sample 10 is given as an example (Figure 98). In terms of silicates, montmorillonite (MM) and quartz (QZ) are generally present except in Sample 12 at the bottom, where quartz (QZ) is replaced by opal (OP). Otherwise, quartz (QZ) is usually well-defined whenever present. Many samples also show characteristics of chitin (CT) in FTIR.

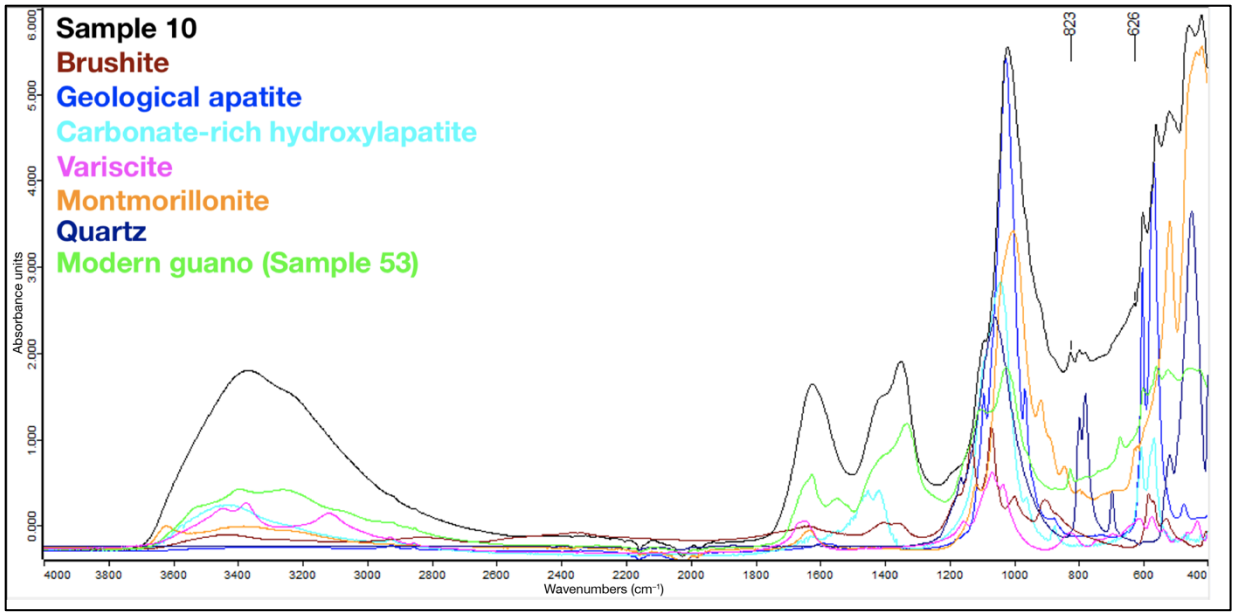

Figure 98. ATR-FTIR spectrum of Sample 10 in absorbance mode.

Only Sample 10 was analyzed in XRD for Square S4W4. The results agree with some of the FTIR identifications (brushite, BR; quartz, QZ), exclude some of them (hydroxylapatite, HAP; variscite, VR; montmorillonite, MM), and include others not detected in FTIR: gypsum (GY), the iron phosphate leucophosphite (LC), and crandallite (CR) (Figure 99). It is possible that the other samples in the square contain these same 'hidden' minerals.

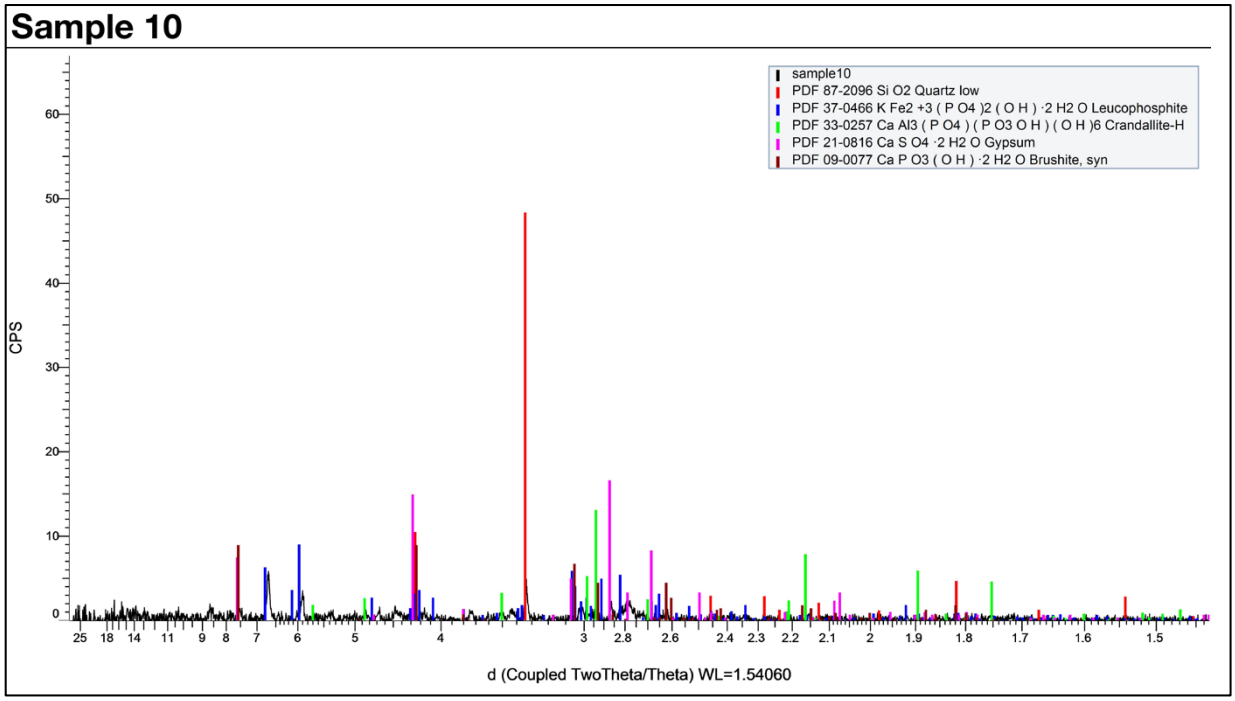

Figure 99. X-ray diffractogram of Sample 10.

In Square S4W5, Samples 13 and 14 were collected from the top of Layer 1. They conform to the generic mineralogical profile previously described for Square S4W4. For Sample 14, however, illite (IL) replaces montmorillonite (MM) (Figure 100). This clay mineral is strongly represented alongside quartz (QZ). XRD confirms the presence of hydroxylapatite (HAP) and variscite (VR) this time, as well as adding mitridatite (MT; a calcium iron phosphate) and crandallite (CR; already present in Square S4W4) (Figure 101). Brushite (BR) and illite (IL) were not among the minerals identified in XRD.

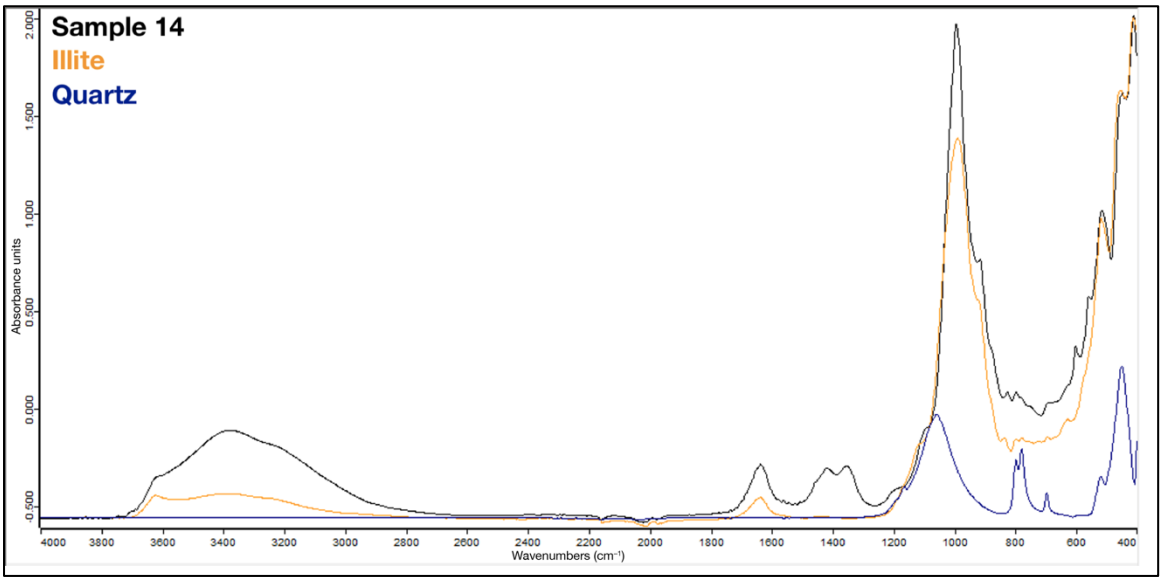

Figure 100. ATR-FTIR spectrum of Sample 14 in absorbance mode.

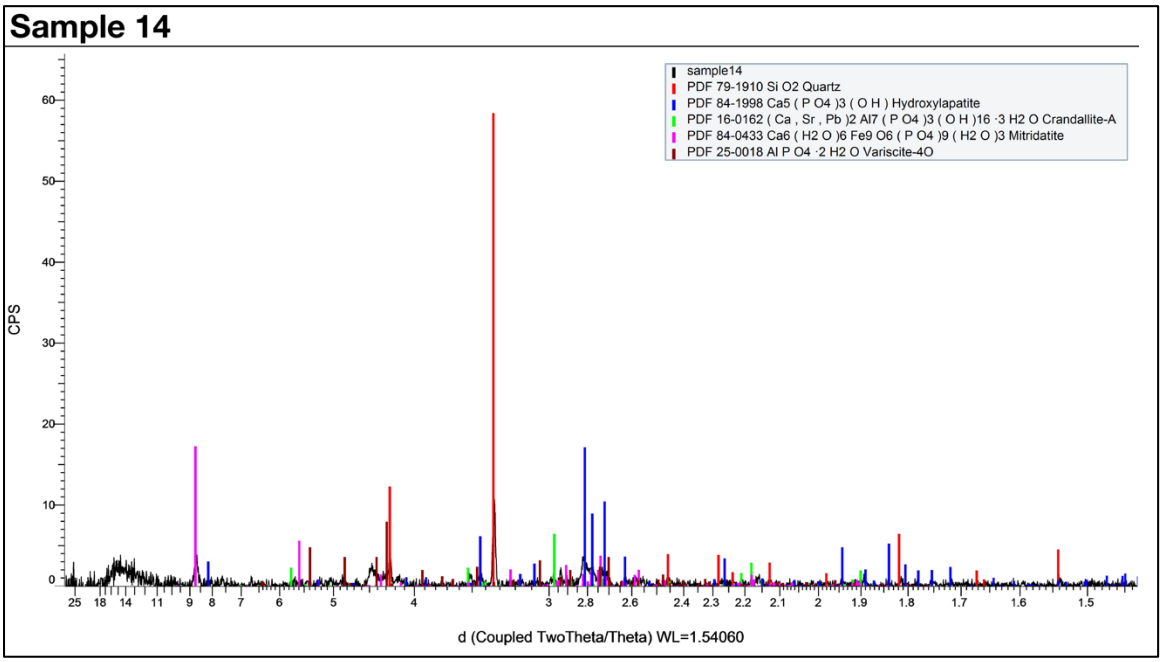

Figure 101. X-ray diffractogram of Sample 14.

4.2.2. The Central Zone: transects S6 to S10

In the Central Zone, two main areas were studied: the eastern part, composed of squares in the vicinity of the fireplace (S6E4 to S8E4; S8E3 to S9E3; and S6E2 to S7E2), and the central part, adjacent to the longitudinal centre line of the cave (S8E1 to S8W1; and S10E1).

The eastern part is composed of highly weathered stratigraphic sequences. One of their most characteristic features is the abundance of 'dry' minerals in the upper layers (immediately above the fireplace), generally above 200 cm below DP: these refer primarily to the calcium sulphates gypsum and ardealite, but the calcium phosphates brushite and monetite (formed when brushite loses its water molecules) are also included.

One particularly recurrent calcium phosphate is hydroxylapatite, exhibiting a certain degree of variation throughout the sequence, from the incorporation or absence of the carbonate ion CO_3^{2-} to differences in crystallinity (and diagenetic advancement) based on the form of the FTIR peak at 629 cm^{-1}. It is particularly prominent in a white layer in the lower part of the sequences, where it is the dominant phase (Layer 7, Square S6E4; Layer 10, Square S9E3).

Minerals indicative of more aggressive weathering like variscite, leucophosphite (and its ammonium analogue, spheniscidite), and taranakite are also present. The aluminium phosphate variscite is particularly well-represented in the layers below the fireplace in a highly crystalline form and is often accompanied by opal, pointing to advanced diagenetic action in this part of the sequences, especially on clay and other silicate minerals. Meanwhile, the proximity of the iron phosphate leucophosphite to the fireplace (via Sample 34) suggests that ash may have provided the iron incorporated into the mineral. Finally, the highly insoluble potassium phosphate taranakite is often in association with the soluble sulphate minerals of the layers around the fireplace.

Montmorillonite, illite, and occasionally muscovite constitute the clay minerals detected in the sequences, although their presence is not remarkably pronounced. As in the North Zone, quartz is not always easy to identify, with the silicate doublet that commonly indicates its presence (around 800 and 780 cm^{-1}) often reduced to a single, amorphous peak (around 800 cm^{-1}), corresponding to opal. Its crystallinity varies, from intermediate stages of transformation (shoulder still detectable around 780 cm^{-1}) to the equivalent of geological opal (well-defined

peak around 800 cm^{-1}). Finally, traces of chert are occasionally present in the sulphatic layers surrounding the fireplace, possibly corresponding to microscopic debris from lithic tool manufacture.

Moving to the central part, the mineralogy can be broadly described as a dichotomy between the lower half, dominated by silicates (mainly montmorillonite and quartz), and the upper half, dominated by diverse authigenic minerals (mainly variscite and calcium phosphates). Iron and potassium phosphates are also occasionally present, while the very top of the sequence is rich in gypsum, linking it to the eastern part.

Squares S6E4 to S8E4: the fireplace

Table 18 presents the results for Squares S6E4 to S8E4, situated in the eastern part of the Central Zone.

Table 18. Summary of mineralogical characterization results for Squares S6E4 to S8E4.

Square	Sample	Depth (cm DP)	Sulphates				Phosphates		Silicates					
			Ca	PO_3OH		CO_3	Fe	Al	Ca	K		H_2O	SiO_2	
			GY	*AR*	*BR*	*CHAP*	*LC*	*VR*	*MM*	*IL*	*MC*	*OP*	*QZ*	*CH*
S8E4	31	-121	xxx		xx	xx		xx	xx				xx	
S8E4	32	-136		x	xx	xx		x	xx				xxx	
S7E4	33	-157	xxx		x	x		x	x	x				
S8E4	34	-168	xxx	xx	x	xx	xx	xx	x		x	x	x / xx	x
S8E4	35	-182	xxx		x	x		xxx	x			x		
S6E4	28	-307				xxx		x					x	

Figures 102 and 103 present the vertical profiles for Squares S6E4 to S8E4.

Looking first at Square S6E4 and Sample 28, collected from Layer 7 consisting of white, very fine silt, the dominant phase is carbonate-rich hydroxylapatite (CHAP) (Figure 104). The pronounced peak at 629 cm^{-1} indicates advanced crystallization. Some variscite (VR) and quartz (QZ) are also present.

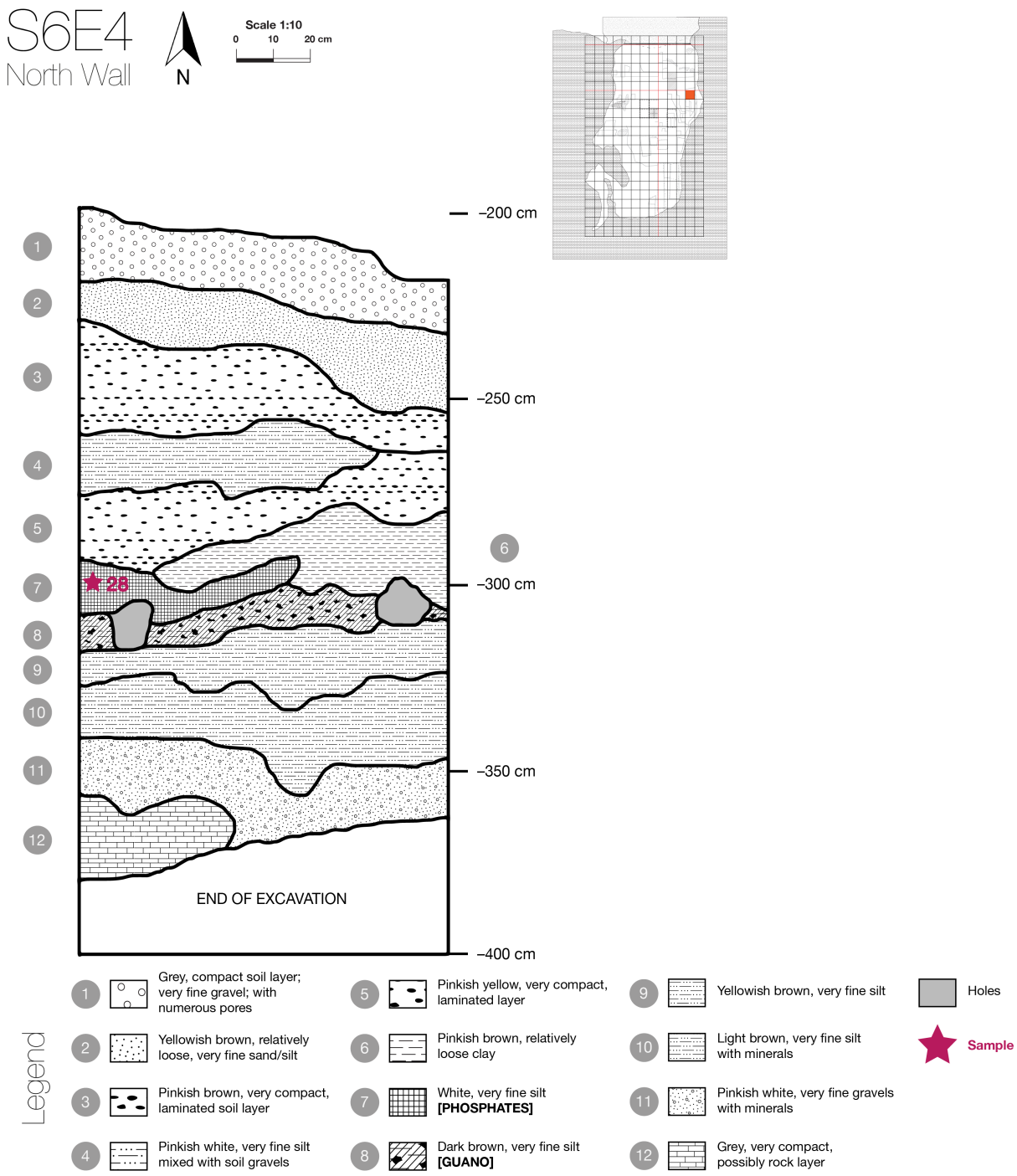

Figure 102. North Wall vertical profile for Square S6E4, with the location of Sample 28 indicated.

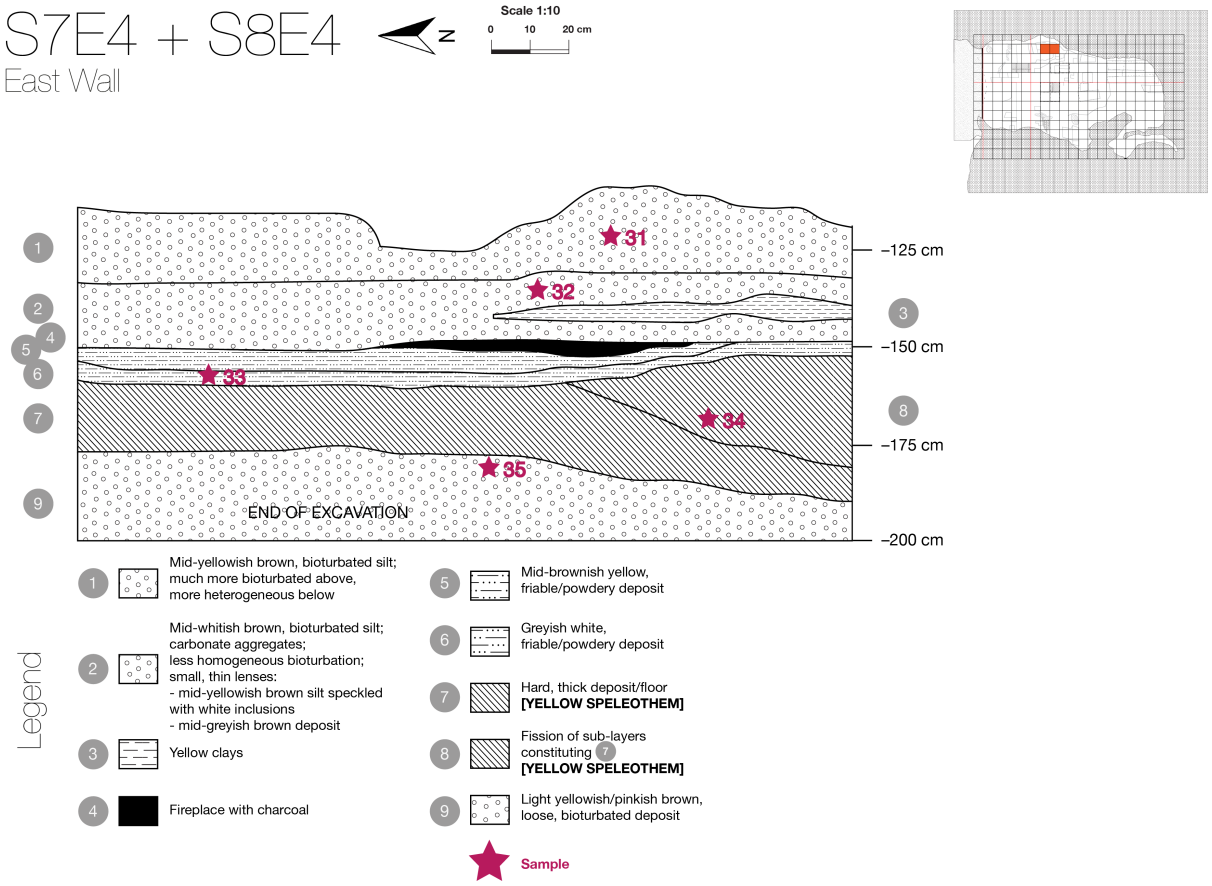

Figure 103. East Wall vertical profile for Squares S7E4 to S8E4, with the location of Samples 31 to 35 indicated.

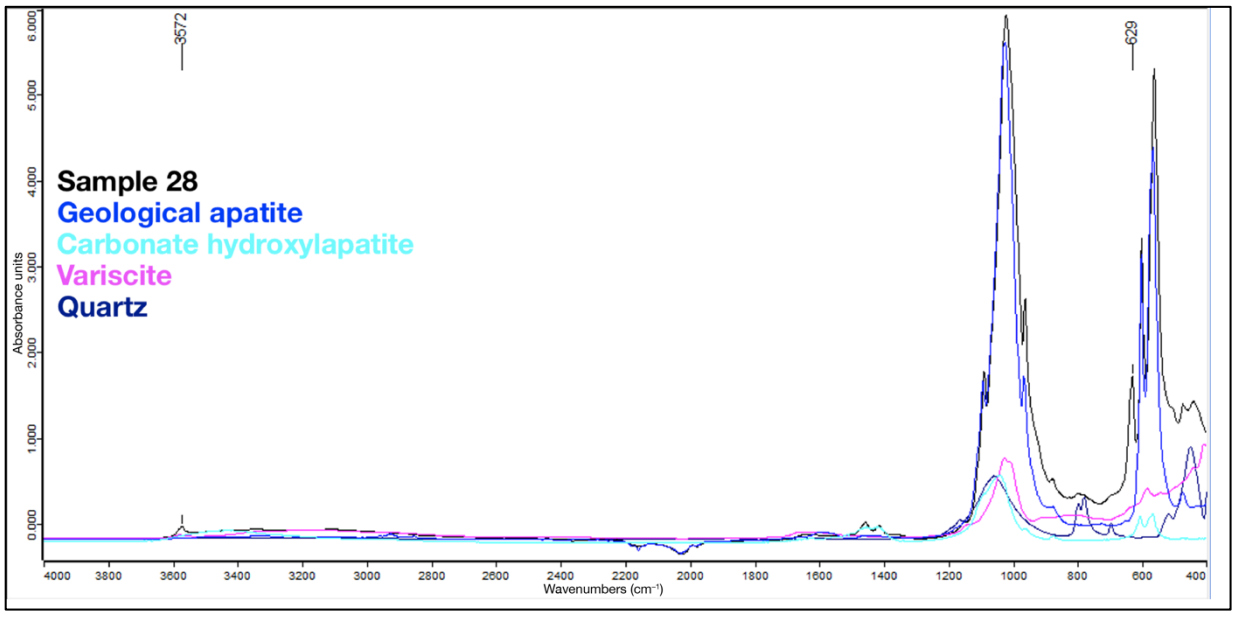

Figure 104. ATR-FTIR spectrum of Sample 28 in absorbance mode.

Moving southward to Squares S7E4 and S8E4, all of the samples except Sample 32 contain a strong gypsum (GY) component (Figure 105). Brushite (BR), carbonate-rich hydroxylapatite (CHAP), and montmorillonite (MM) are also present, although they are less marked in the lower part of the profile than above. Carbonate-rich hydroxylapatite (CHAP) was noted to be highly crystalline at lower depths (visible peak at 629 cm^{-1} in Samples 34 and 35, at the bottom of the sequence; Figure 106). Some traces of illite (IL) possibly accompany montmorillonite (MM) in Sample 33, halfway through the sequence. Variscite (VR) was also identified, but is particularly strong toward the bottom, in Sample 35. Transforming opal (OP) is also present in this part of the profile, as seen in the shape of the silicate peak at around 800 cm^{-1}; however, in the higher samples (32 and 31), the peak is accompanied by another, well-expressed one at 780 cm^{-1}, representing together the silicate doublet that is often characteristic of quartz (QZ) (Figure 105). Finally, in Sample 34, transforming opal (OP) may also be accompanied by chert (CH; peak at 1091 cm^{-1}). These silicate relationships are illustrated in Figure 106.

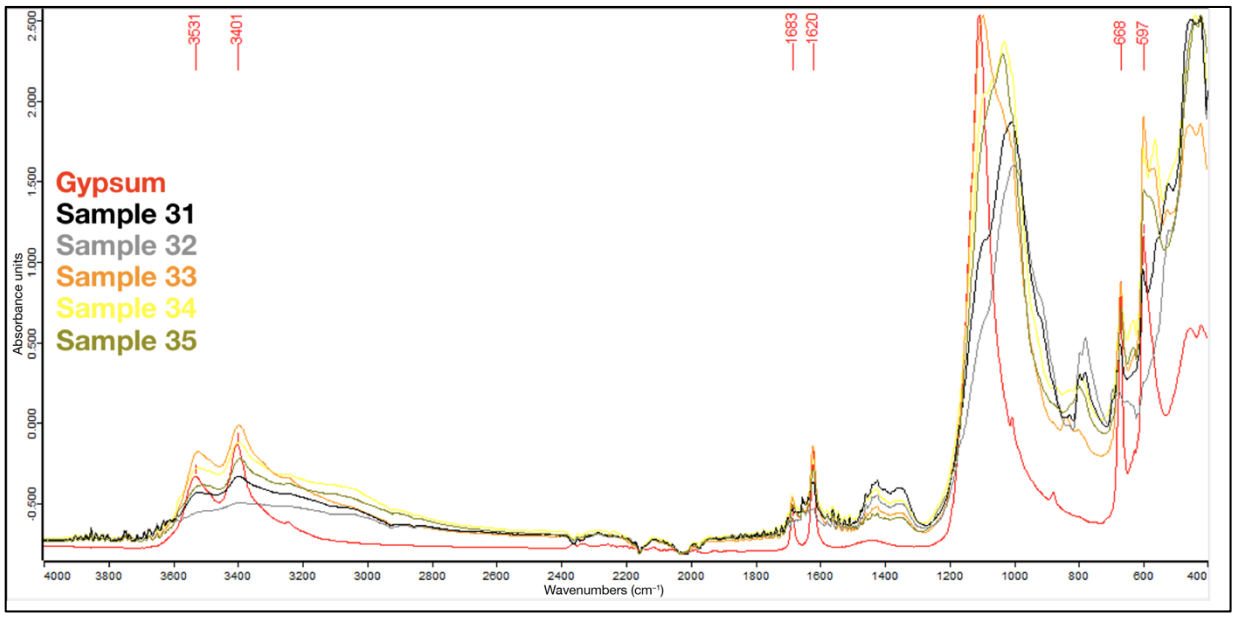

Figure 105. ATR-FTIR spectra of Samples 31 to 35 in absorbance mode.

As in Squares S4W4 to S4W5, XRD analysis of Sample 34 confirms the presence of some minerals identified in FTIR (gypsum, GY; variscite, VR; quartz, QZ), excludes some (brushite, BR; hydroxylapatite, HAP; montmorillonite, MM), and proposes others: ardealite (AR), leucophosphite (LC), muscovite (MC) (Figure 107). With the exception of two cases, FTIR did not find any of these proposed minerals in the other samples. The first case is the detection

of ardealite (AR) in Sample 32, and the second is illite (IL) in Sample 33 (which could be due to potassium depletion and alteration of the muscovite/MC detected in Sample 34 just below). It is impossible to know for sure whether these 'hidden' minerals are present in the other samples unless those are analyzed in XRD. In any case, they are difficult to detect in FTIR, at least for this particular sequence.

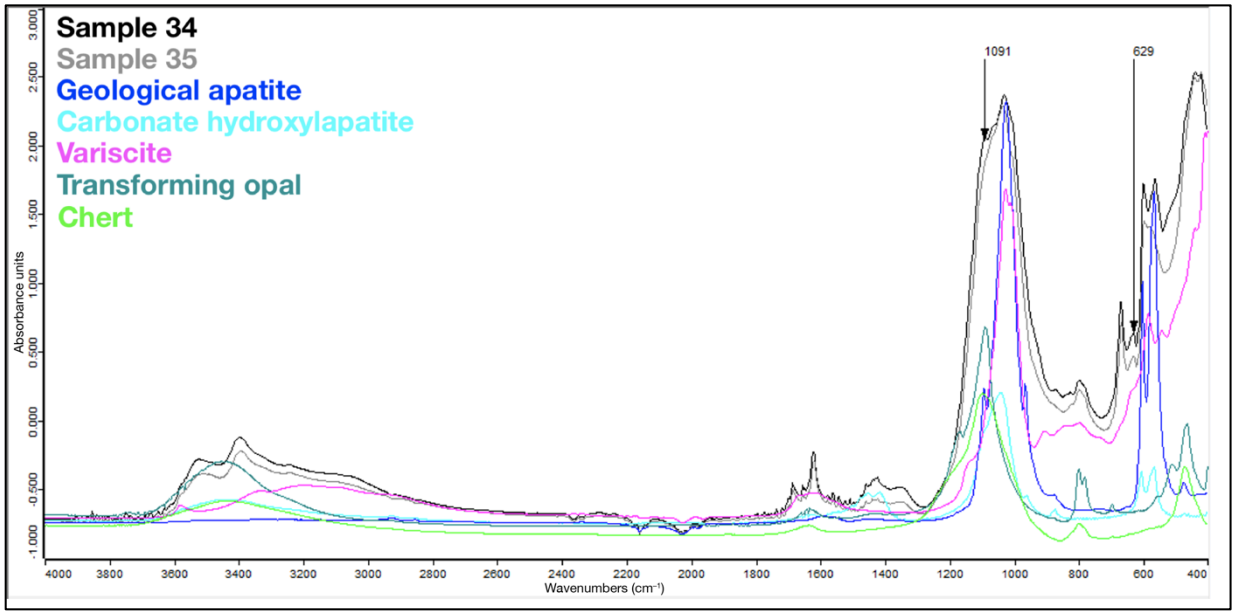

Figure 106. ATR-FTIR spectra of Samples 34 and 35 in absorbance mode.

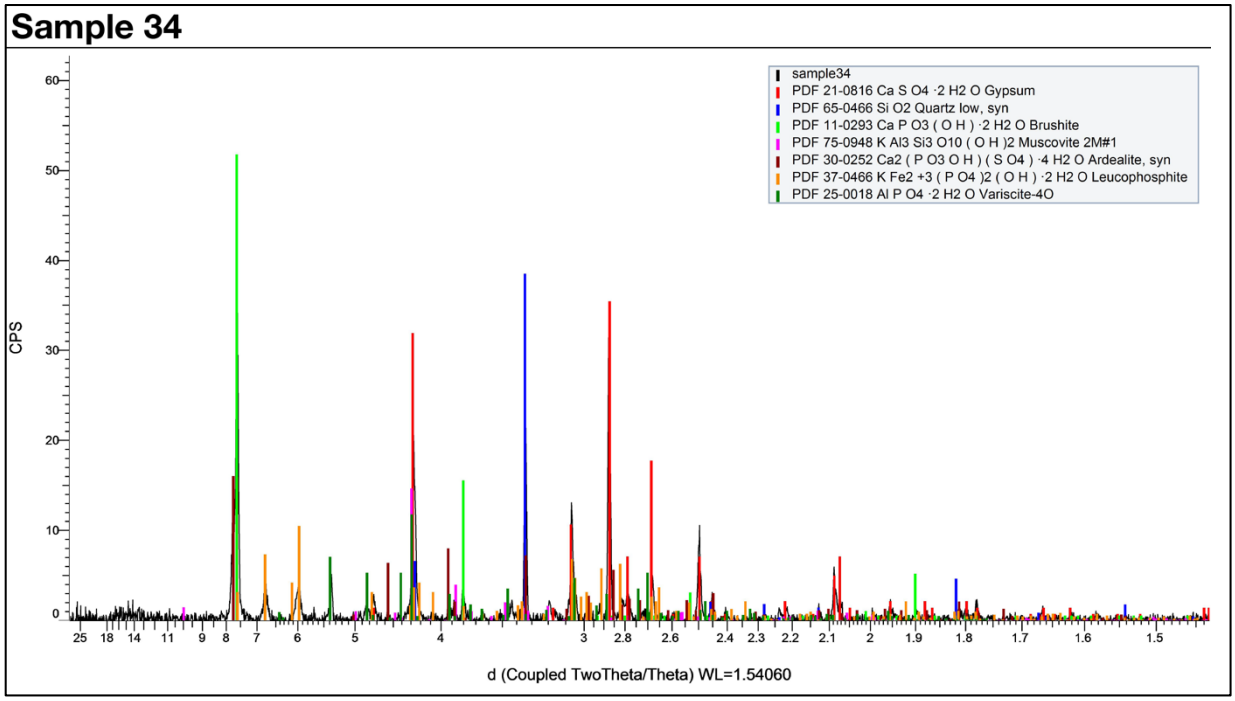

Figure 107. X-ray diffractogram of Sample 34.

Squares S8E3 to S9E3

Table 19 presents the results for Squares S8E3 to S9E3, situated in the eastern part of the Central Zone.

Table 19. Summary of mineralogical characterization results for Squares S8E3 to S9E3.

Square	Sample	Depth (cm DP)	Sulphates		Phosphates								Silicates			
			Ca							Al	K	Fe	Al			
			H_2O		PO_3OH	CO_3	PO_4	Mg					Mg	H_2O	SiO_2	
			GY	*AR*	*BR*	*MN*	*CHAP*	*HAP*	*MG*	*VR*	*TK*	*LC*	*MM*	*OP*	*QZ*	*CH*
S9E3	36	-125	xxx		xx		xx			x			xx		xxx	
S9E3	37	-144		x	xx		xx			x			xx		xxx	
S9E3	38	-157		xx	xx	xx	xx		xx	x	xx			xx	xx	
S9E3	39	-167		xxx	xx	x	xx			x	xx			xx		xx
S9E3	39.5	-213			x			xx		xxx				x	xx	
S9E3	40	-231						xx		xxx				xxx	xx	
S9E3	41	-259						xx		xxx				xxx	xx	
S9E3	42	-276						xx		xxx				xx	xx	
S9E3	43	-299						xx		xxx				x	xx	
S8E3	44	-305					xxx			x					x	
S8E3	45	-325						xx		x / xx		xxx		xx	x / xx	

Figure 108 presents the vertical profile for Square S9E3. No profile is available for S8E3, so its samples were projected here.

The mineralogical profile can generally be divided into lower and upper halves, with the midpoint represented by Sample 39.5 (Layer 6).

In the lower half of the profile, no sulphates were detected. The dominant phase is crystalline variscite (VR; mainly identifiable through the FTIR peak at 1151 cm^{-1}), accompanied by simple hydroxylapatite (HAP) in an advanced state of crystallization, as in Sample 42 (Figure 109). Quartz (QZ) is present, but it is often accompanied and influenced by opal (OP).

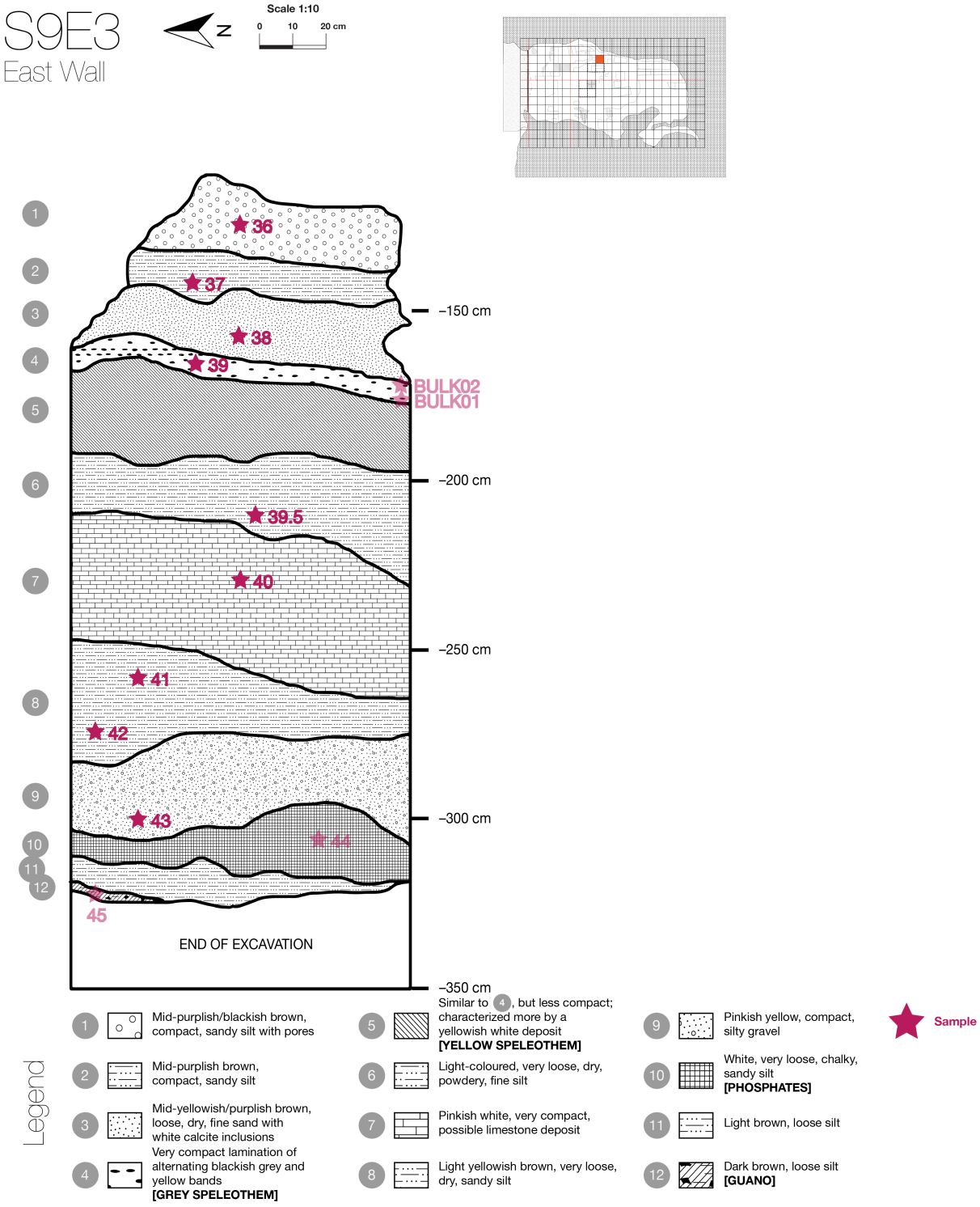

Figure 108. East Wall vertical profile for Square S9E3, with the location of Samples 36 to 45 indicated. Samples projected from Square S8E3 are rendered translucent.

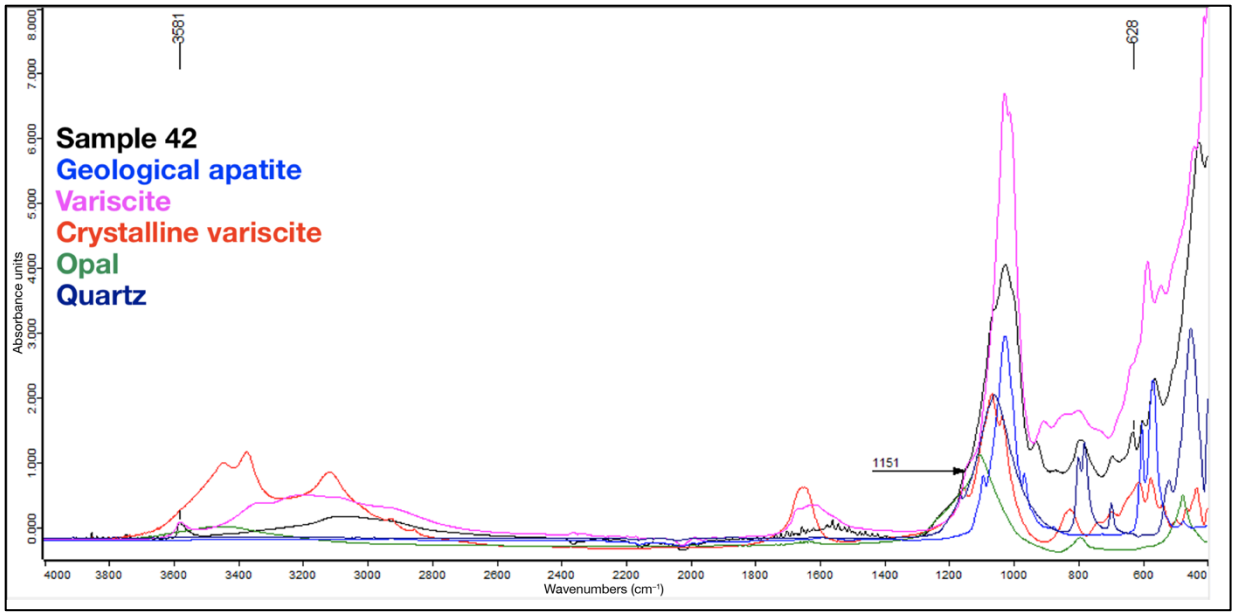

Figure 109. ATR-FTIR spectrum of Sample 42 in absorbance mode.

In the guano deposit at the bottom, Layer 12, Sample 45 is composed of simple hydroxylapatite (HAP), variscite (VR), opal (OP), and quartz (QZ). A strongly present mineral component of this sample that was identified in XRD but not in FTIR, however, was leucophosphite (LC) (Figure 110).

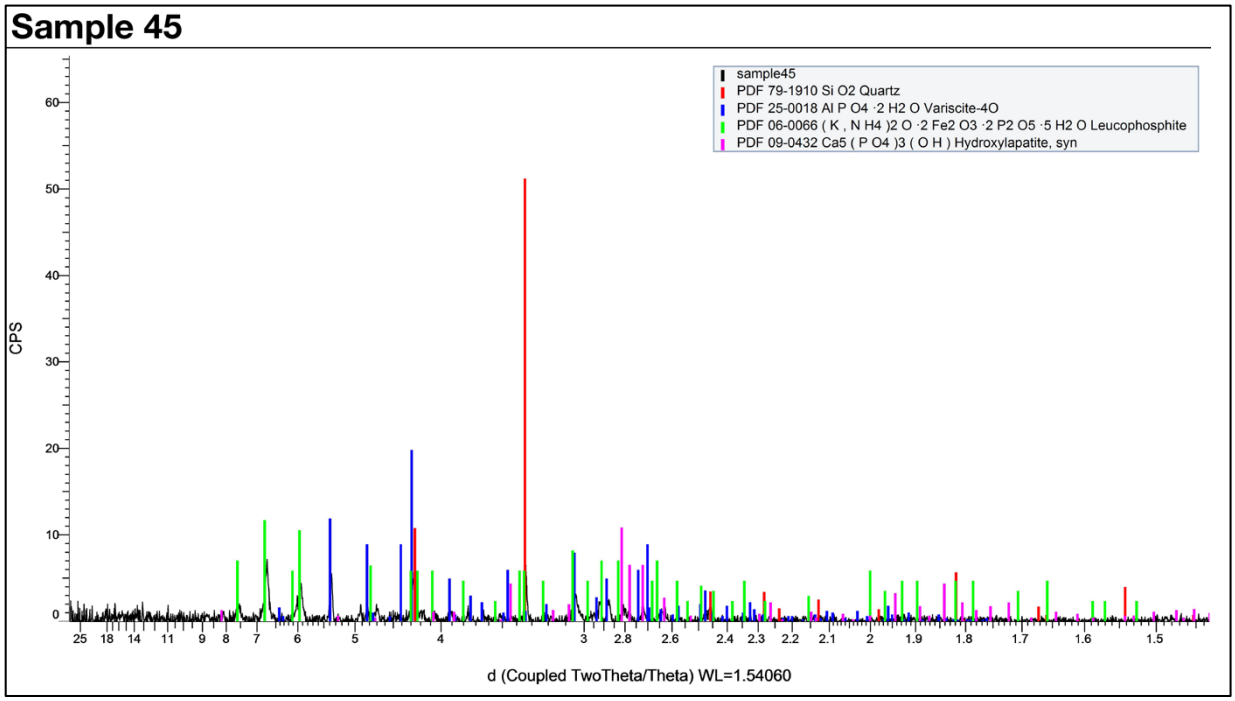

Figure 110. X-ray diffractogram of Sample 45.

Just above, carbonate-rich hydroxylapatite (CHAP) has a very strong presence in Sample 44, collected from the white sandy silts of Layer 10. Variscite (VR) and quartz (QZ) are present in trace amounts in this sample.

In the upper half, brushite (BR), carbonate-rich hydroxylapatite (CHAP), and most importantly, sulphates, constitute the characteristic minerals. Brushite (BR) is dehydrated in certain instances to produce monetite (MN), while the presence of the carbonate anion CO_3^{2-} and a lower degree of crystallinity differentiate the hydroxylapatite here from that below. Ardealite (AR) is the main sulphate in this part of the profile, although the topmost sample is marked by the very strong presence of gypsum (GY) instead (absence of the phosphate anion $[PO_3(OH)]^{2-}$ and additional water molecules present in ardealite). Among aluminium phosphates, variscite (VR) is only faintly present, but montgomeryite (MG, containing calcium and magnesium) and taranakite (TK, containing potassium) were identified in Samples 39 and 38 (Layers 4 and 3) (Figure 111). These samples also contain transforming opal (OP) and chert (CH) as silicates, while montmorillonite (MM) and well-expressed quartz (QZ) dominate instead at the top.

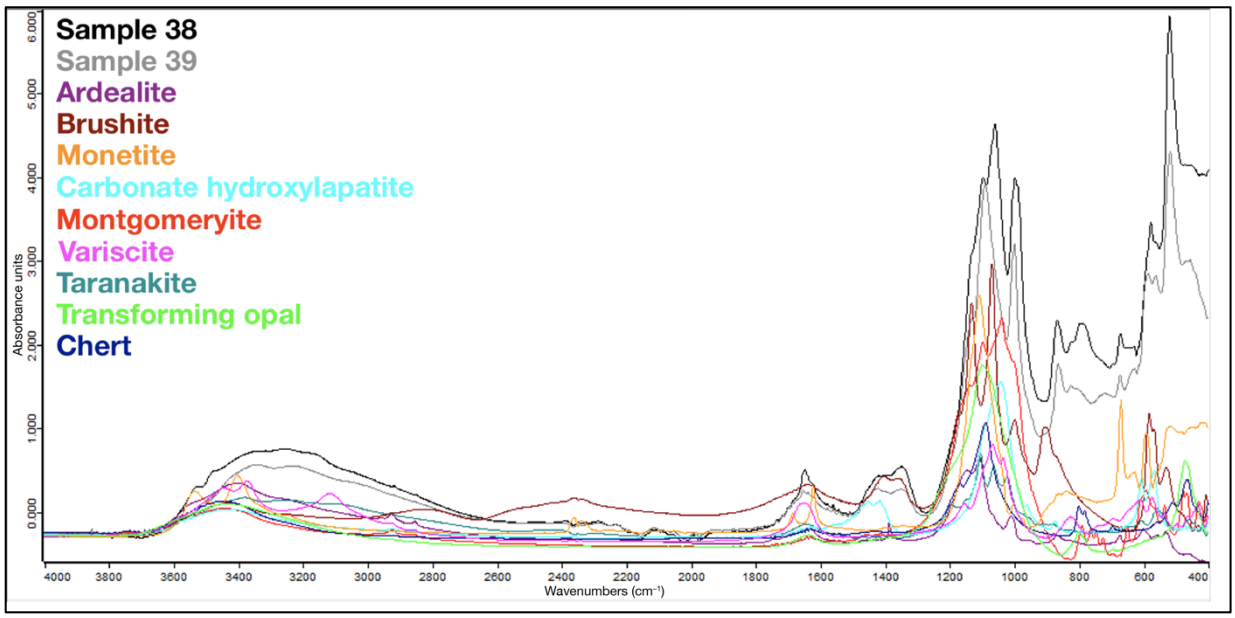

Figure 111. ATR-FTIR spectra of Samples 38 and 39 in absorbance mode.

Squares S6E2 to S7E2

Table 20 presents the results for Squares S6E2 to S7E2, situated in the eastern part of the Central Zone.

Table 20. Summary of mineralogical characterization results for Squares S6E2 to S7E2.

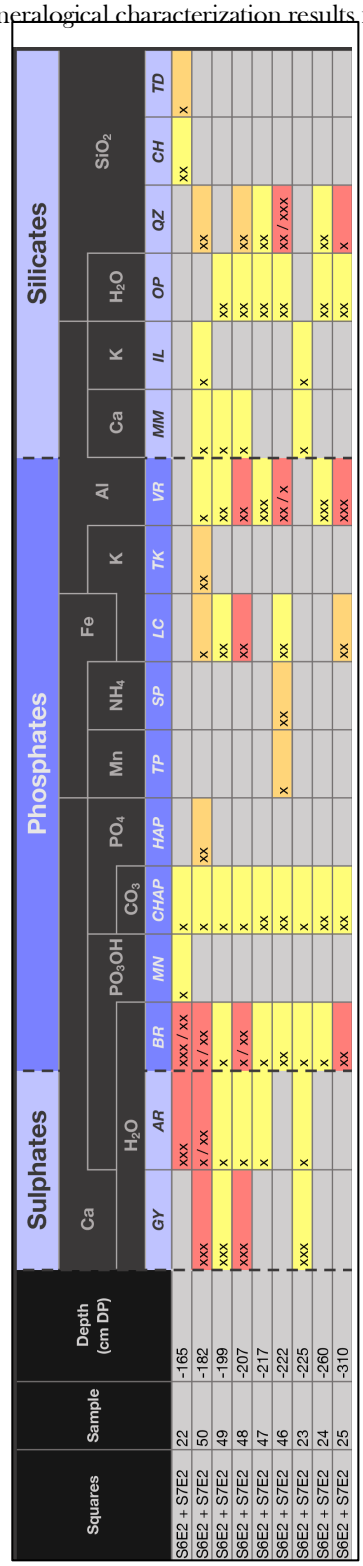

Figure 112 presents the vertical profile for Squares S6E2 to S7E2.

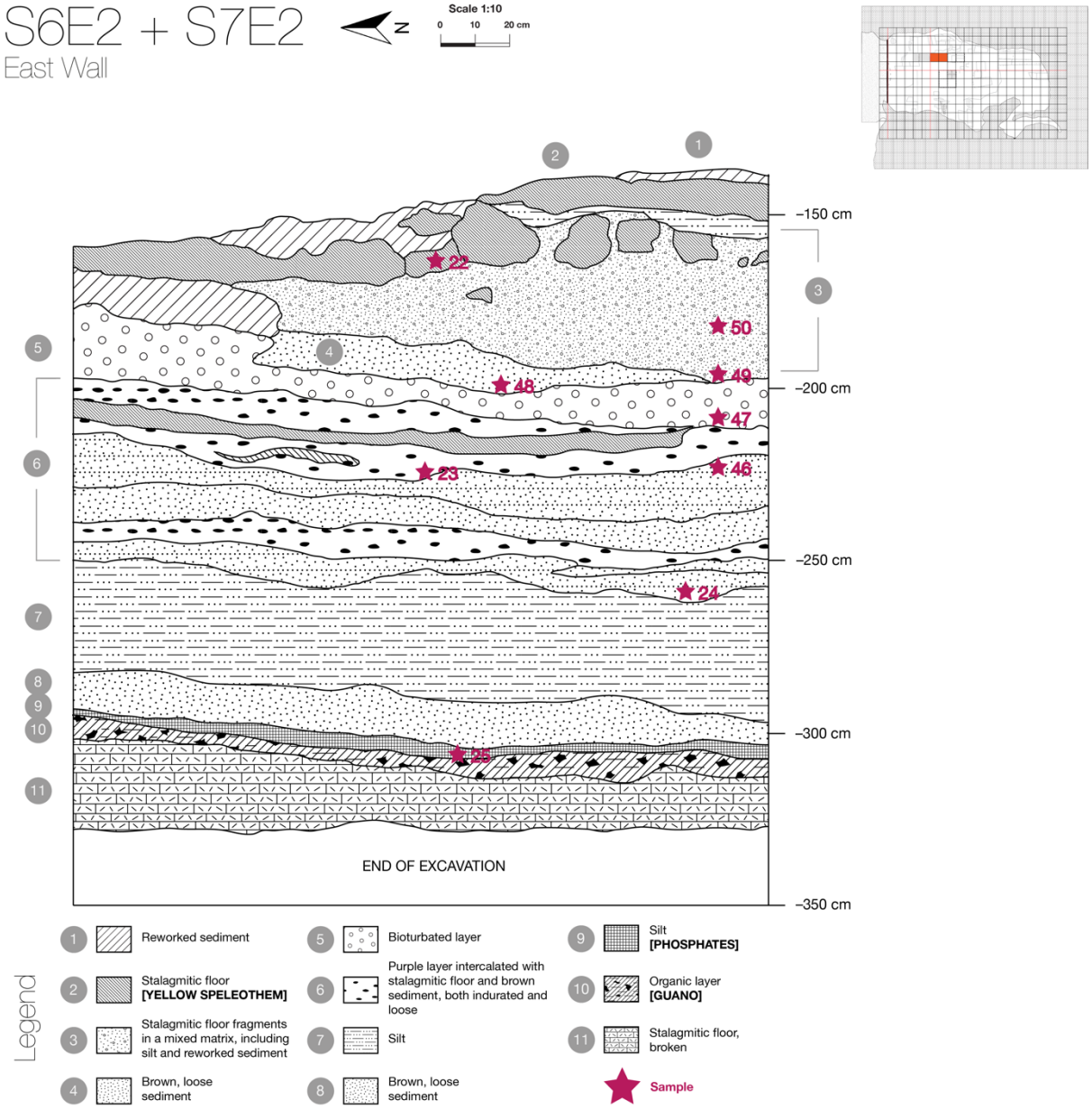

Figure 112. East Wall vertical profile for Squares S6E2 to S7E2, with the location of Samples 22 to 25 and 46 to 50 indicated.

Sulphates have a generally strong presence in this sequence. Collected from the purple deposit (Layer 6; Figure 113), gypsum (GY) is the major phase in Sample 23 (Figure 114), as well as in Samples 48, 49, and 50 (Layers 4 and 3).

Figure 113. Layer 6, consisting of intercalated purple and yellow deposits. Photo by Florent Détroit.

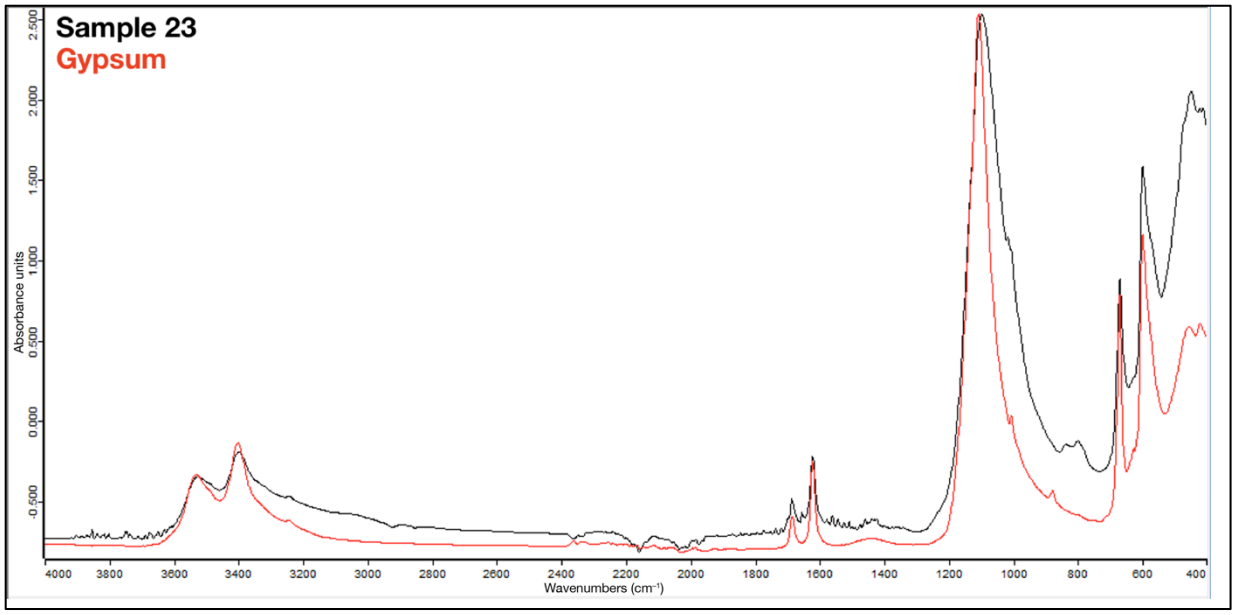

Figure 114. ATR-FTIR spectrum of Sample 23 in absorbance mode.

Ardealite (AR) was also identified in these samples, but is best represented by Sample 22, collected from the 'stalagmitic floor' near the top of the sequence (Layer 2; Figure 115). It is accompanied by strongly-expressed brushite (BR), some monetite (MN), and some carbonate-rich hydroxylapatite (CHAP) in early crystallization (Figure 116).

Figure 115. Layer 2, the 'stalagmitic floor' in Squares S6E2 to S7E2. Photo by Florent Détroit.

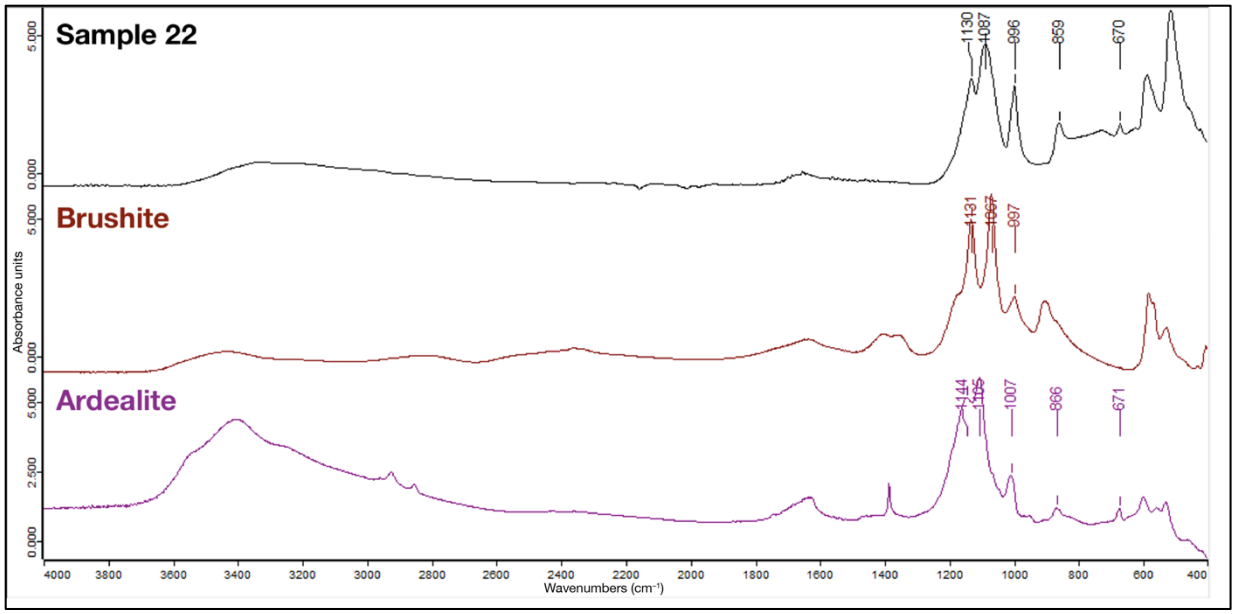

Figure 116. ATR-FTIR spectrum of Sample 22 in absorbance mode.

Brushite (BR) and carbonate-rich hydroxylapatite (CHAP) are present in varying degrees elsewhere throughout the sequence, although the former is more prominent in the upper layers, and the latter more crystalline in the lower ones. In Sample 50, XRD identifies the hydroxylapatite (HAP) phase as fluorian, but this is not corroborated by FTIR (Figure 117).

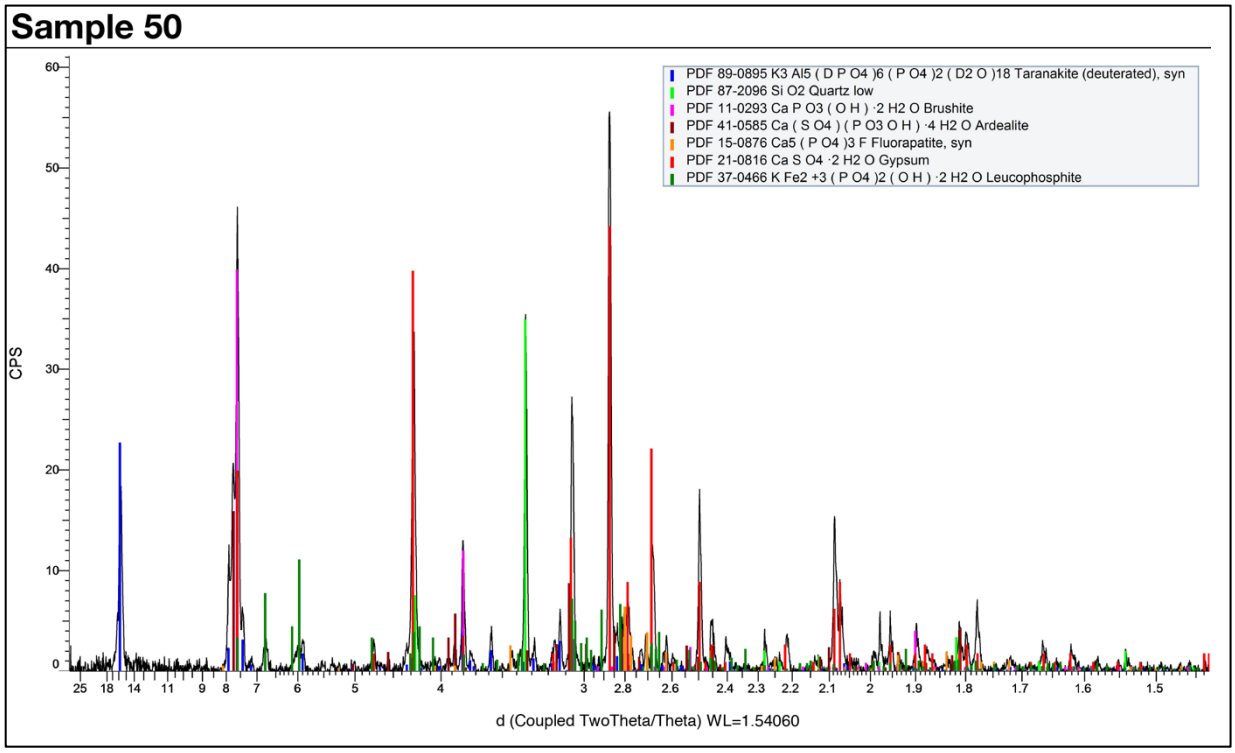

Figure 117. X-ray diffractogram of Sample 50.

Various iron and aluminium phosphates were also identified in the sequence. Chief among these are leucophosphite (LC) and variscite (VR), whose presence is more pronounced at deeper levels. Variscite (VR) also appears to be more crystalline in the lower part of the profile (Figure 118). Leucophosphite (LC) was not always detected in FTIR, and in Sample 46, where it *was* detected in FTIR, XRD proposes its ammonium version, spheniscidite (SP, where the potassium cation K^+ is replaced by the ammonium cation NH_4^+) (Figure 119). Additional XRD-only identifications include the iron phosphate triplite (TP, containing manganese) for Sample 46, and taranakite (TK) for Sample 50.

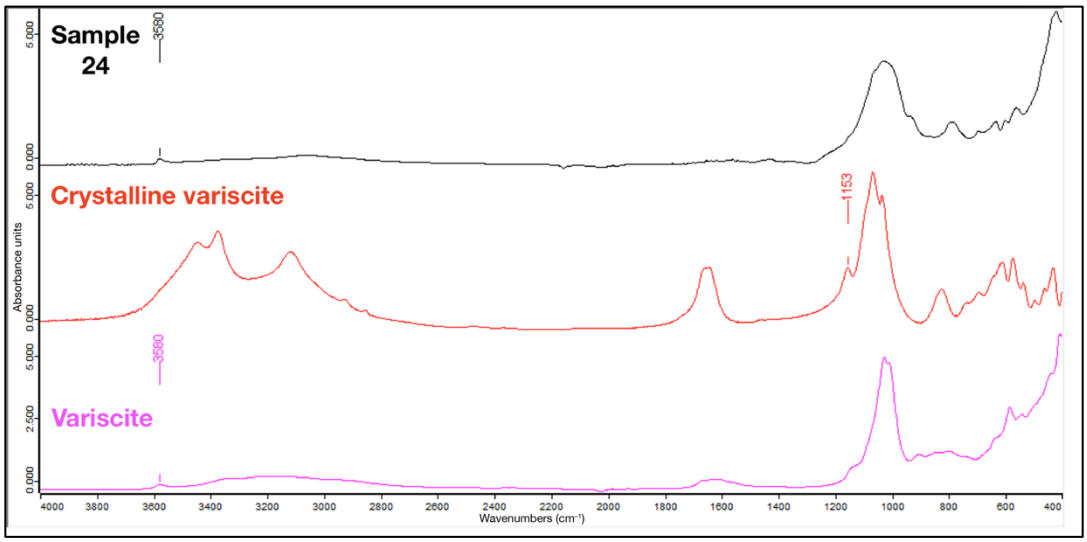

Figure 118. ATR-FTIR spectrum of Sample 24 in absorbance mode.

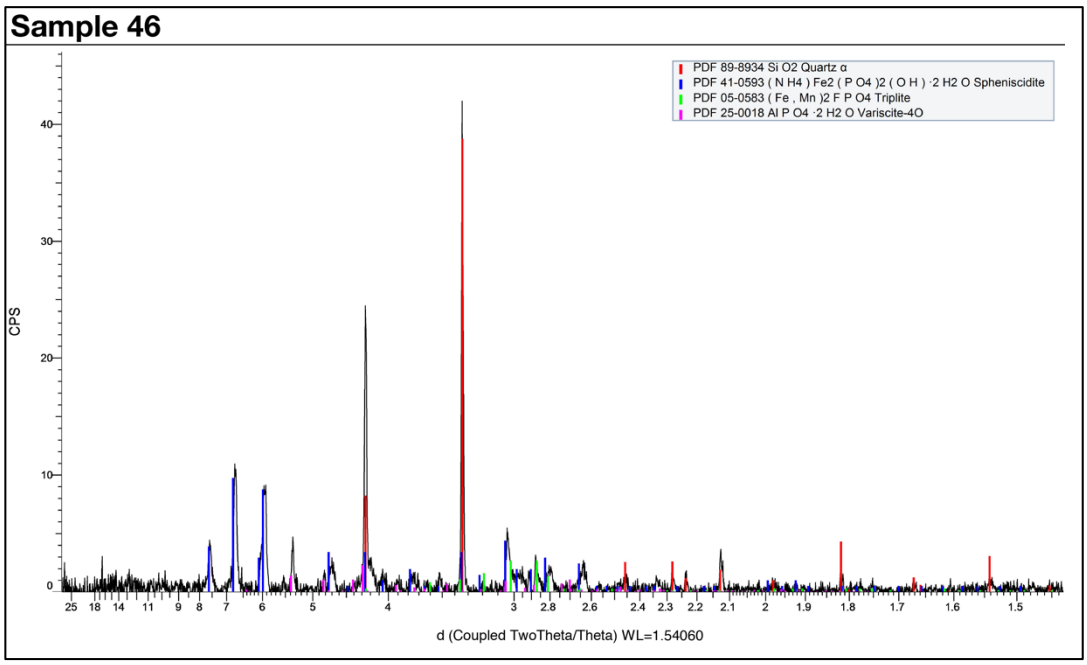

Figure 119. X-ray diffractogram of Sample 46.

The silicates are mainly composed of quartz (QZ) and opal (OP). In the deeper samples, quartz (QZ) was identified in both FTIR and XRD, but the silicate doublet peaks at around 800 and 780 cm^{-1} in FTIR are almost fused or barely visible. This is probably due to the influence of transforming opal (OP), present throughout the sequence but particularly crystalline in Sample 25 at the bottom as geological opal (OP) (Figure 120). In the higher samples, where montmorillonite (MM) and sometimes illite (IL) are faintly present, quartz (QZ) was only identified in XRD.

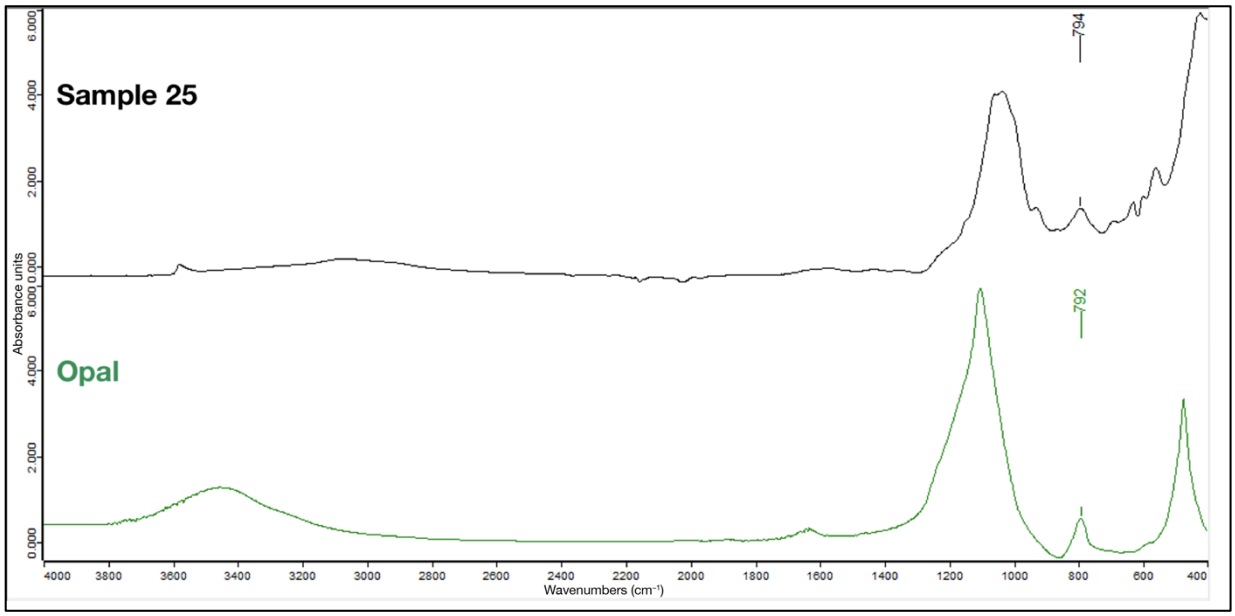

Figure 120. ATR-FTIR spectrum of Sample 25 in absorbance mode.

Montmorillonite (MM) and illite (IL) are also present in Sample 23, while Sample 22 of the 'stalagmitic floor' at the top has chert (CH; identified in FTIR) and tridymite (TD; identified in XRD) instead of quartz (QZ) (Figures 121 and 122).

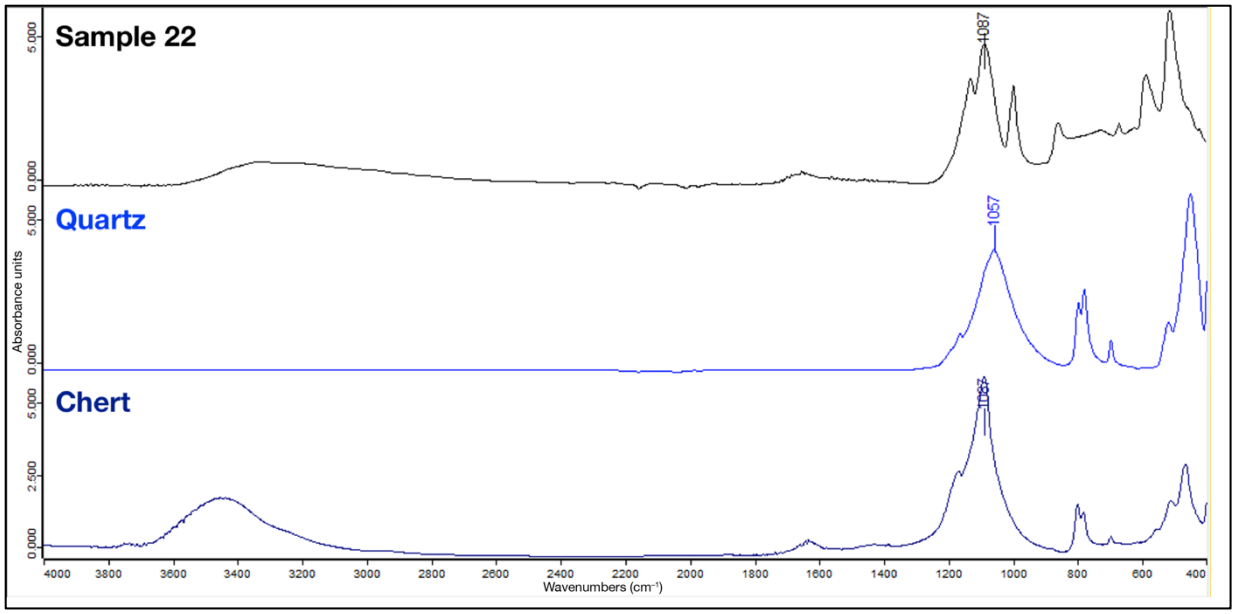

Figure 121. ATR-FTIR spectrum of Sample 22 in absorbance mode.

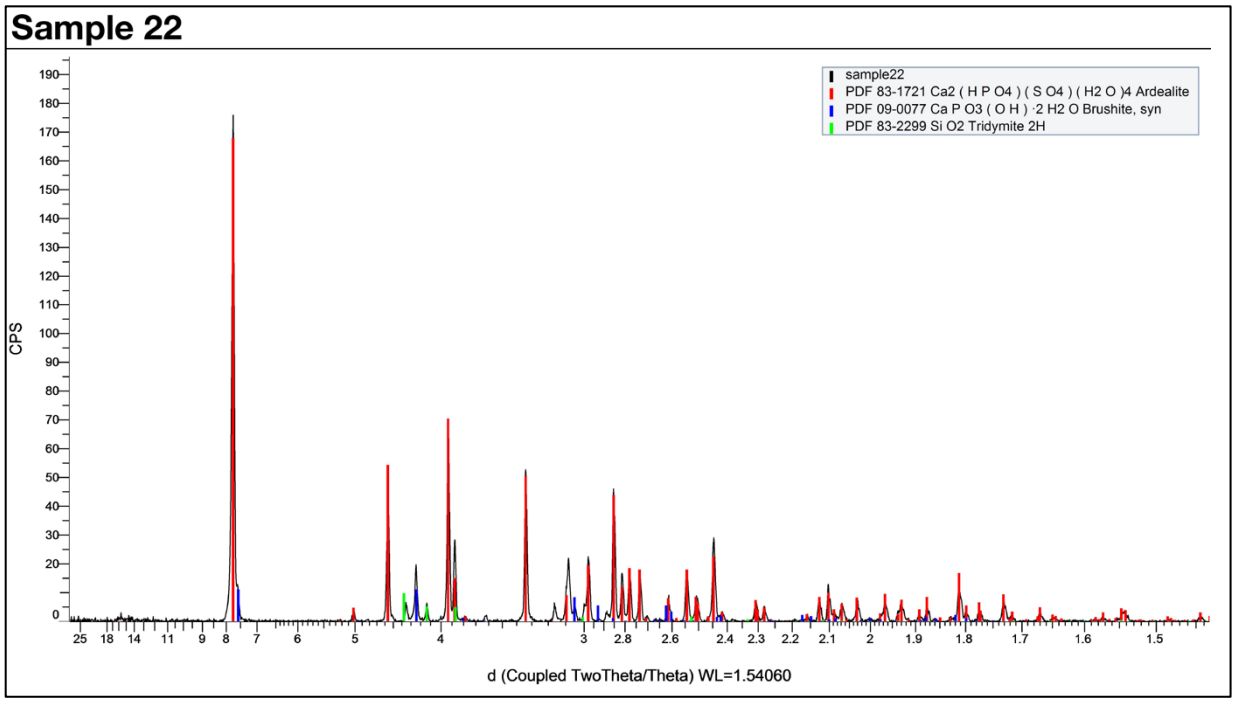

Figure 122. X-ray diffractogram of Sample 22.

Squares S8E1 to S8W1

Table 21 presents the results for Squares S8E1 to S8W1, situated in the central part of the Central Zone.

Table 21. Summary of mineralogical characterization results for Squares S8E1 to S8W1.

Square	Sample	Depth (cm DP)	Sulphates	Carbonates			Phosphates								Silicates					
			Ca	CO_3			H_2O	PO_3OH	Fe			K		Al	Ca	K			H_2O	SiO_2
			GY	CC	CHAP	BR	MN	VV	ST	LC	TK	VR	MM	IL	MC	OP	QZ
S8E1	16	-212	xxx			x / xx		x	x		x	xx	x	x			x
S8W1	29	-249			x	x						xxx				xx	xx
S8E1	17	-260			x	x / xx	x	xx		xx / xxx		x / xx				xx		
S8E1	18	-280		xx	x	x						xxx			xx	xx	xx
S8E1	19	-300			xx	xx				xx		xxx					xx
S8E1	20	-318			xxx	x					xx	x					x
S8E1	21	-326			xxx	xx					xx	x					
S8E1	26	-350			xxx	xx					xx	x					

Figure 123 presents the vertical profile for Squares S8E1 to S9E1. No profile is available for S8W1, so its samples were projected here.

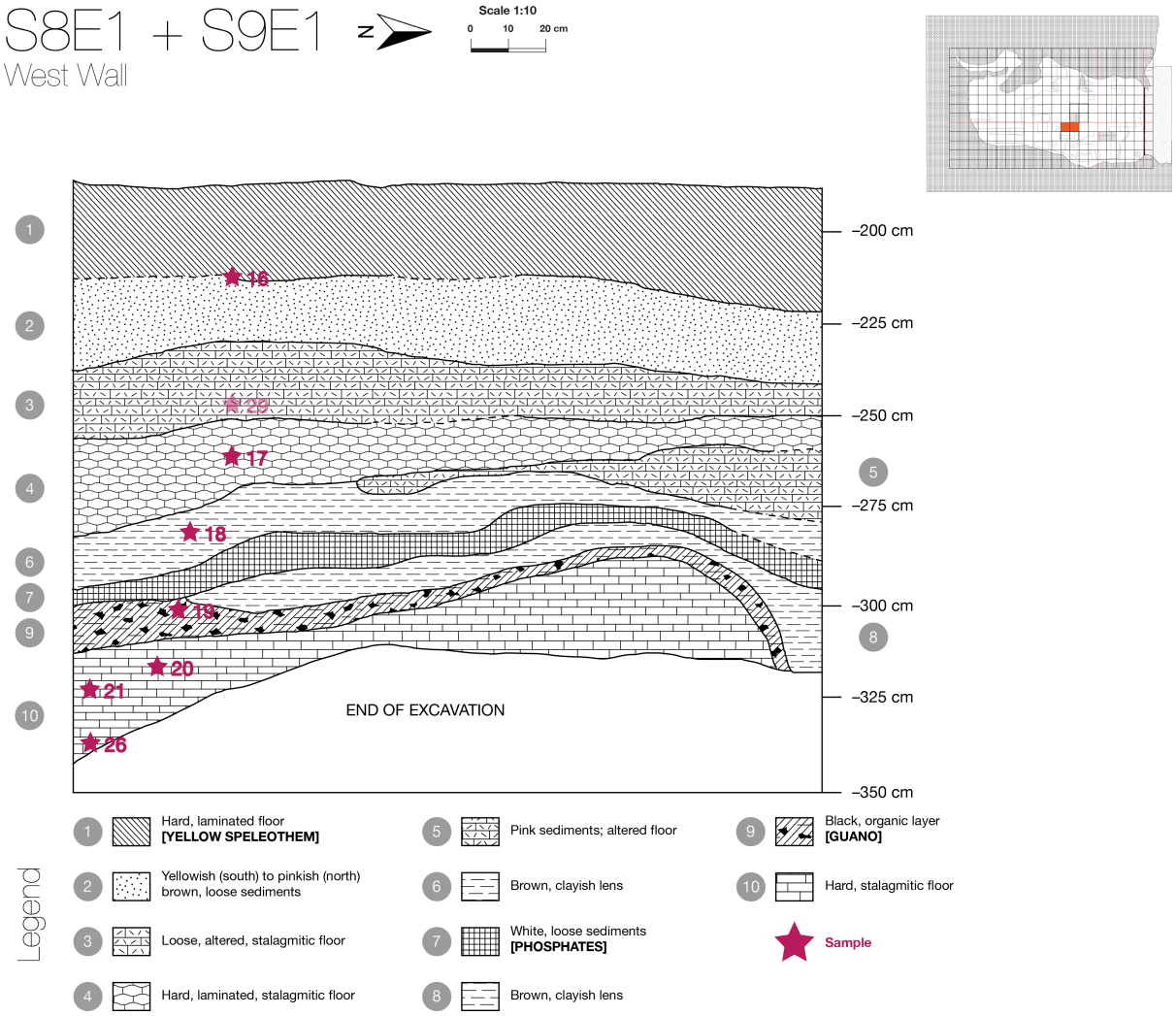

Figure 123. West Wall vertical profile for Squares S8E1 to S9E1, with the location of Samples 16 to 21, 26, and 29 indicated. Sample 29, projected from Square S8W1, is rendered translucent.

Only Sample 16, collected from what remains of the hard, laminated floor corresponding to Layer 1, was found to contain sulphates—it is very strongly dominated by gypsum (GY) (Figures 124 and 125). This is accompanied to a smaller extent by the phosphates brushite (BR), vivianite (VV), strengite (ST), taranakite (TK), and variscite (VR). Traces of the silicates montmorillonite (MM), illite (IL), and quartz (QZ) were also identified.

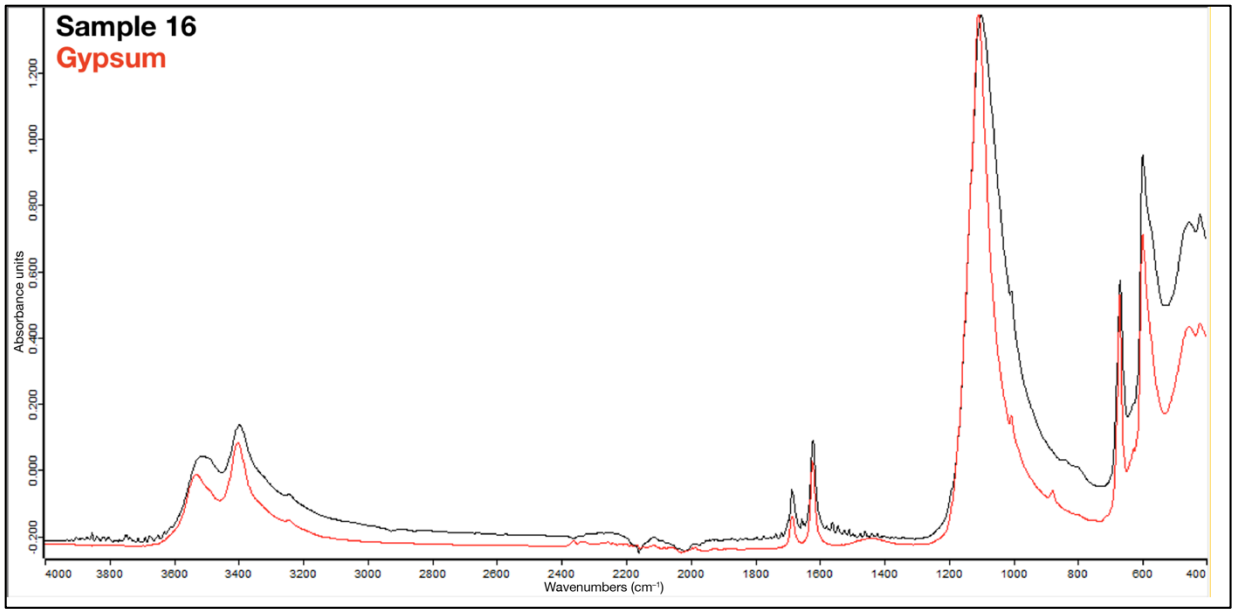

Figure 124. ATR-FTIR spectrum of Sample 16 in absorbance mode.

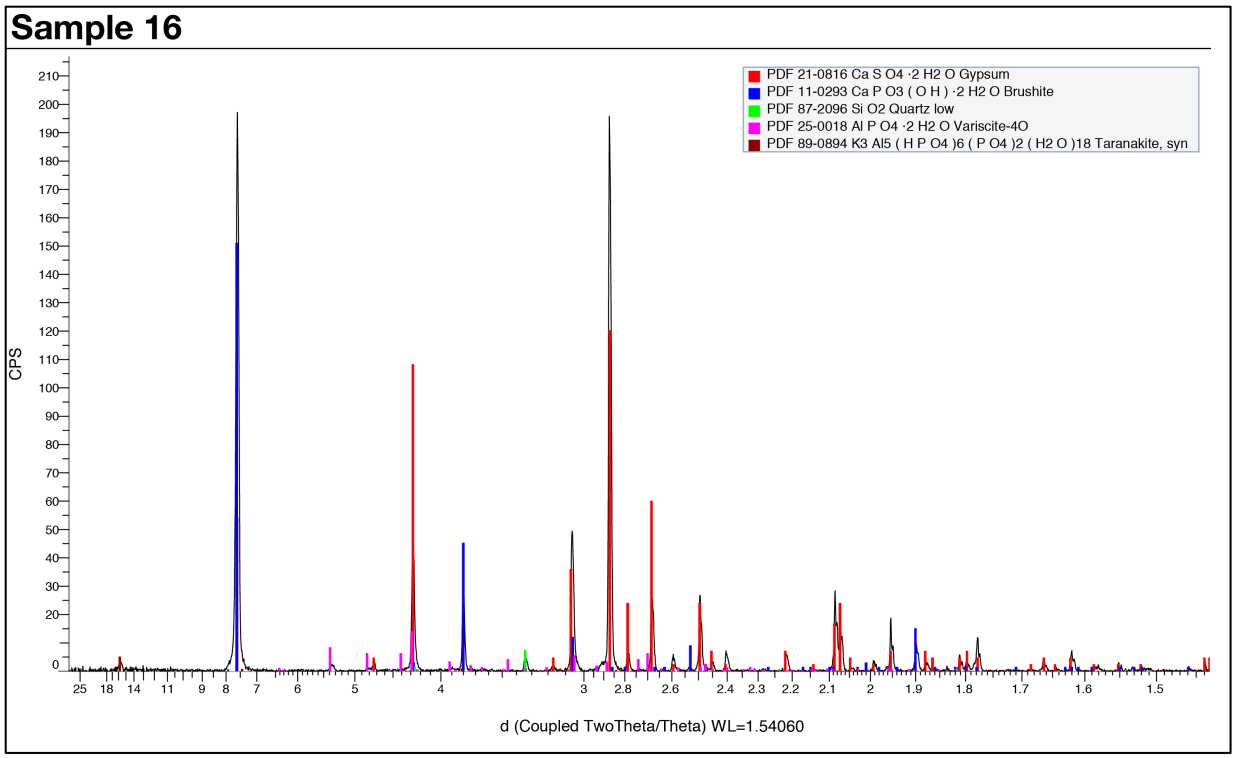

Figure 125. X-ray diffractogram of Sample 16.

Calcium phosphates have a strong presence at the bottom of the sequence, mainly in the form of highly crystalline carbonate-rich hydroxylapatite (CHAP) in Samples 26, 21, and 20 (collected from Layer 10, one of the numerous 'stalagmitic floors' that constitute the profile) (Figure 126). The degree of crystallization varies elsewhere in the sequence. Brushite (BR)

is also present in varying quantities throughout but is more prominent toward the top, while traces of monetite (MN) were noted in Sample 17.

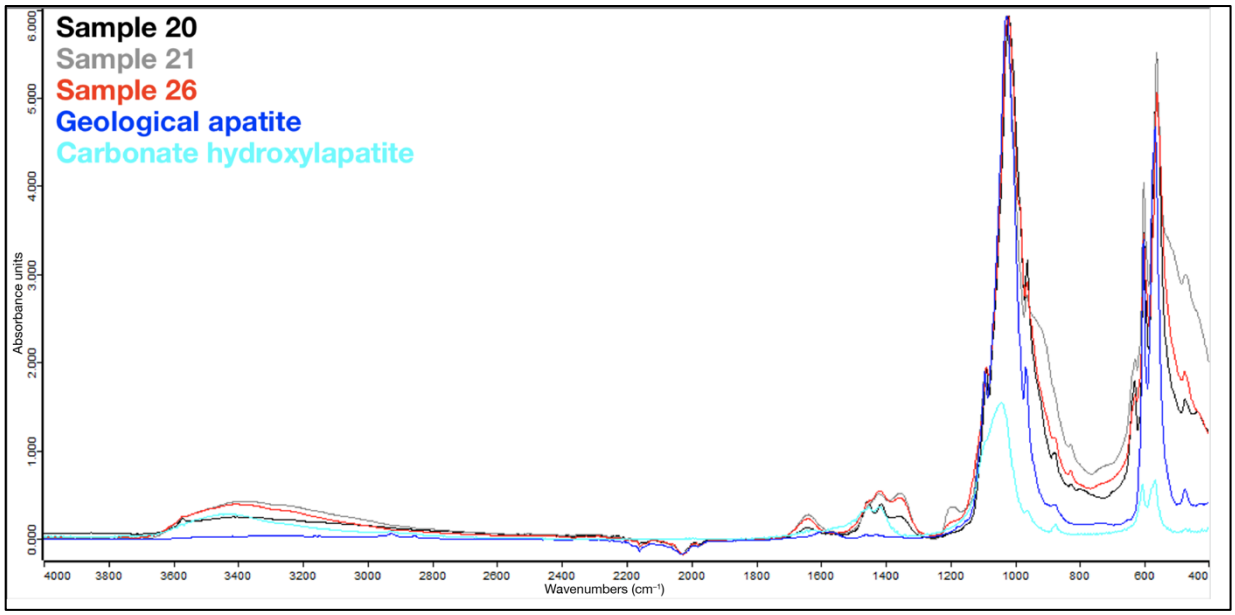

Figure 126. ATR-FTIR spectra of Samples 20, 21, and 26 in absorbance mode.

Iron phosphate species were also identified in the profile. Leucophosphite (LC) has a strong presence in Samples 19 (collected from Layer 9, composed of guano) and especially 17 (collected from Layer 4, an apparent 'stalagmitic floor'); it was identified in both FTIR and XRD in this latter sample (Figures 127 and 128). Vivianite (VV) and strengite (ST) are the other iron phosphate minerals that were detected, with a particularly confident characterization for vivianite (VV) in Sample 17 via XRD.

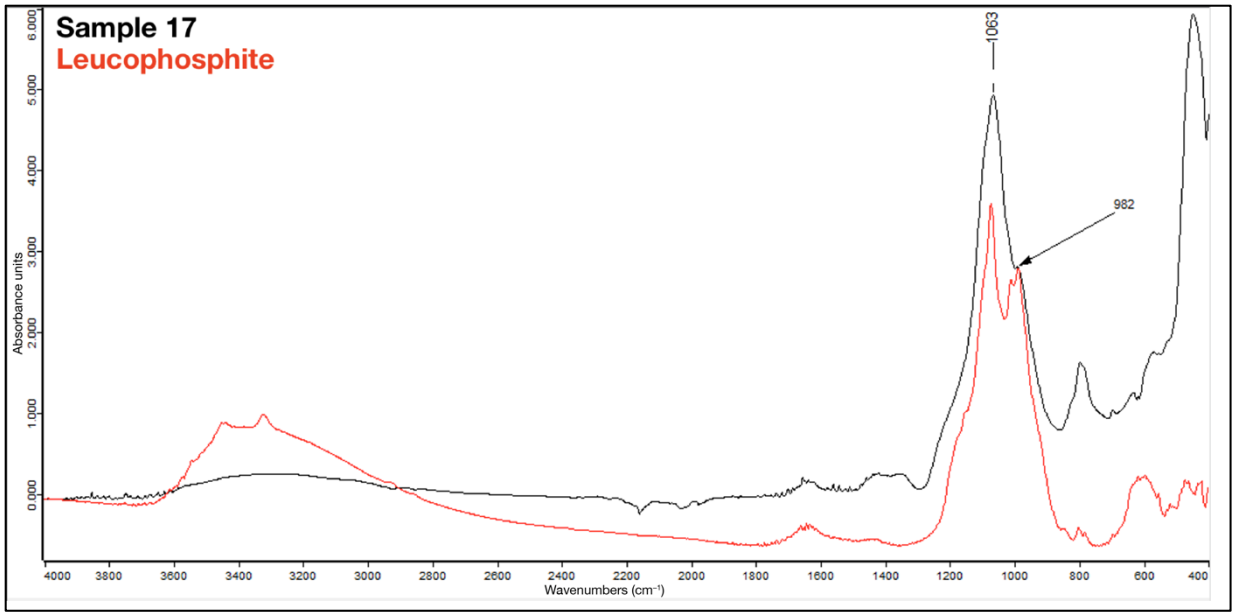

Figure 127. ATR-FTIR spectrum of Sample 17 in absorbance mode.

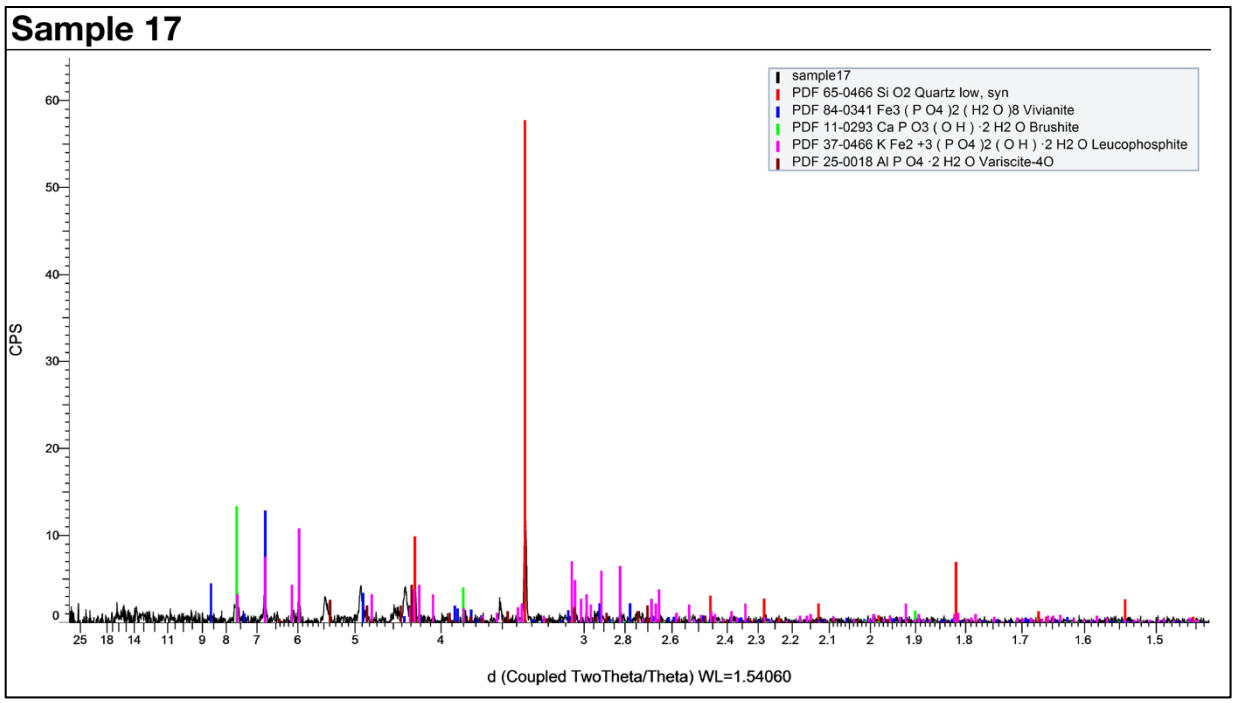

Figure 128. X-ray diffractogram of Sample 17.

Aluminium phosphates compose another major group of minerals that populate the sequence. The lower part of the profile contains taranakite (TK), accompanied by some variscite (VR). However, the upper part is almost entirely dominated by variscite (VR), consistently detected here in XRD and appearing to be particularly crystalline in Layer 9. Taranakite (TK) was identified again in Sample 16, at the top.

Quartz (QZ) and occasionally opal (OP) are the silicates that characterize most of the sequence, although quartz (QZ) is not particularly strongly expressed. In Sample 18, however, XRD suggests the presence of muscovite (MC). Calcite (CC) was also identified in this sample, one of the rare instances in the entire cave (Figure 129).

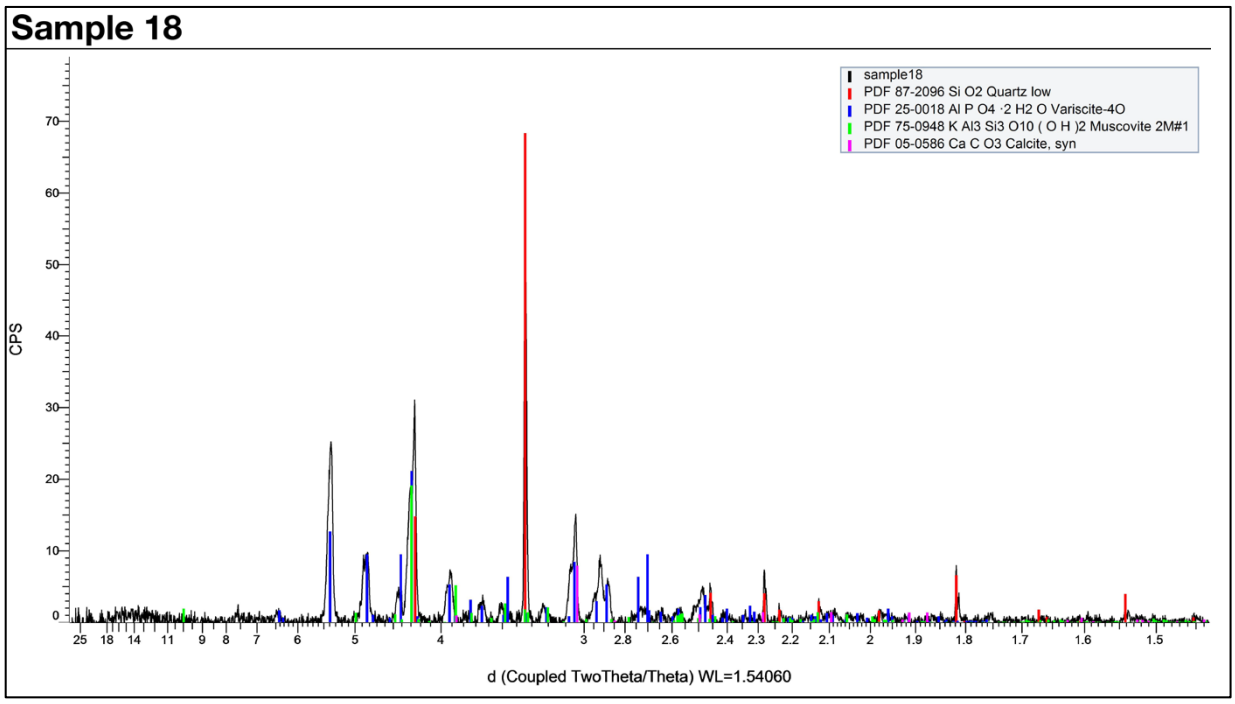

Figure 129. X-ray diffractogram of Sample 18.

Square S10E1: the deepest excavation pit

Table 22 presents the results for Square S10E1, situated in the central part of the Central Zone.

Table 22. Summary of mineralogical characterization results for Square S10E1.

Square	Sample	Depth (cm DP)	Sulphates	Phosphates													Silicates					Others	
							Ca	Al	K			Fe	Ca	Al	K				SiO_2				
			AR	PO_3OH	BR	CO_3 CHAP	PO_4 HAP	CR	VR	TK	LC	NH_4 SP	VV	MT	MM	IL	H_2O OP	QZ	CH	CT	NU
S10E1	X20	-177			x		xx		xxx								x	xx			
S10E1	X19	-182			xx	xx			xxx								x	xx		x	
S10E1	X18	-203			xx	xx			xxx								x	xx		x	
S10E1	X17	-218			xx	xx			xxx								x	xx		x	
S10E1	X16	-225	xx		xx	xx			xxx									xx			
S10E1	X15	-240			x		xx	x	xx	xx					x				x		
S10E1	X14	-246			x	x		x	x		xx				x	x	x				
S10E1	X13	-247			xx	xx			xxx									xx			
S10E1	X12	-270			x	x			x									xxx			
S10E1	X11	-280			xx	xx		x / xx	xx			xx			x	x		x / xxx			
S10E1	X10	-290			xx	xx		xxx	x		x							x / xxx			
S10E1	X9	-300				x	x	xxx	xx		x			xxx				x			
S10E1	X8	-320			x	xxx	xxx							xx							x
S10E1	X7	-345			x	xx	xx	x / xx	x	xx			xx	xxx	x			x			
S10E1	X6	-377			x	x			x						xx			xxx			
S10E1	X5	(not available)					x		x						xx			xxx			
S10E1	X4	-400			x	x			x						xxx			xxx			
S10E1	X3	-415			x	x			x						xxx			xxx			
S10E1	X2	-440							x						xxx			xxx			
S10E1	X1	-460					x		x							xx		xxx			

Figure 130 presents the vertical profile for Square S10E1.

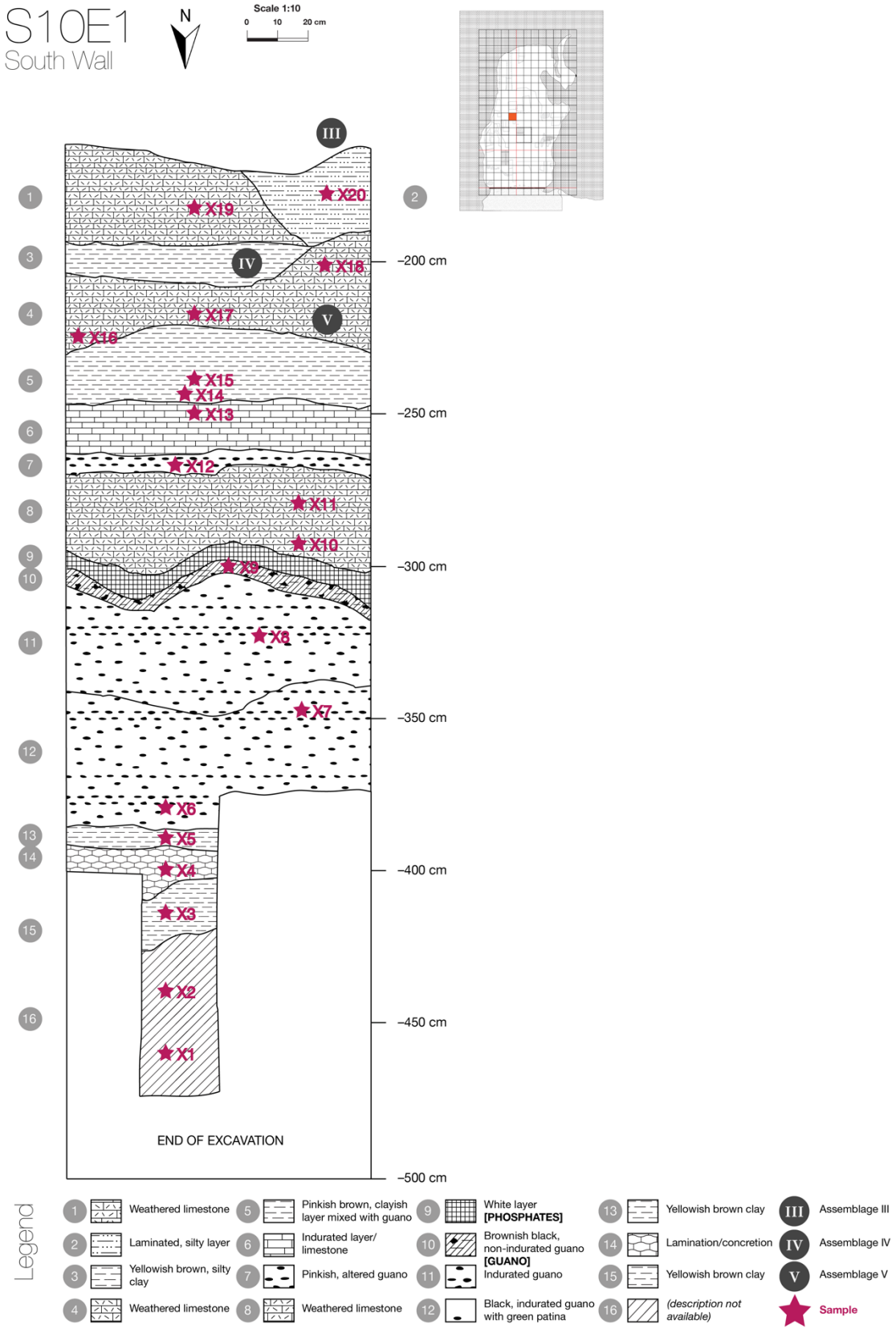

Figure 130. South Wall vertical profile for Square S10E1, with the location of Samples X1 to X20 indicated.

The mineralogical profile for this square divides its stratigraphic sequence into two parts: Layers 16 to 12 (Samples X1 to X7), and Layers 11 to 1 (Samples X8 to X20).

In the deeper part of the sequence, from Layers 16 to 12, the mineralogical profile is dominated by montmorillonite (MM) (illite/IL at the very bottom) and quartz (QZ)—this is best seen in Sample X4 (Figure 131). A few phosphates were identified (brushite, BR; hydroxylapatite, HAP; variscite, VR), but they are only faintly present. Quartz (QZ) is extremely well-expressed here, with the silicate doublet in FTIR exhibiting very sharp peaks at around 800 and 780 cm^{-1}.

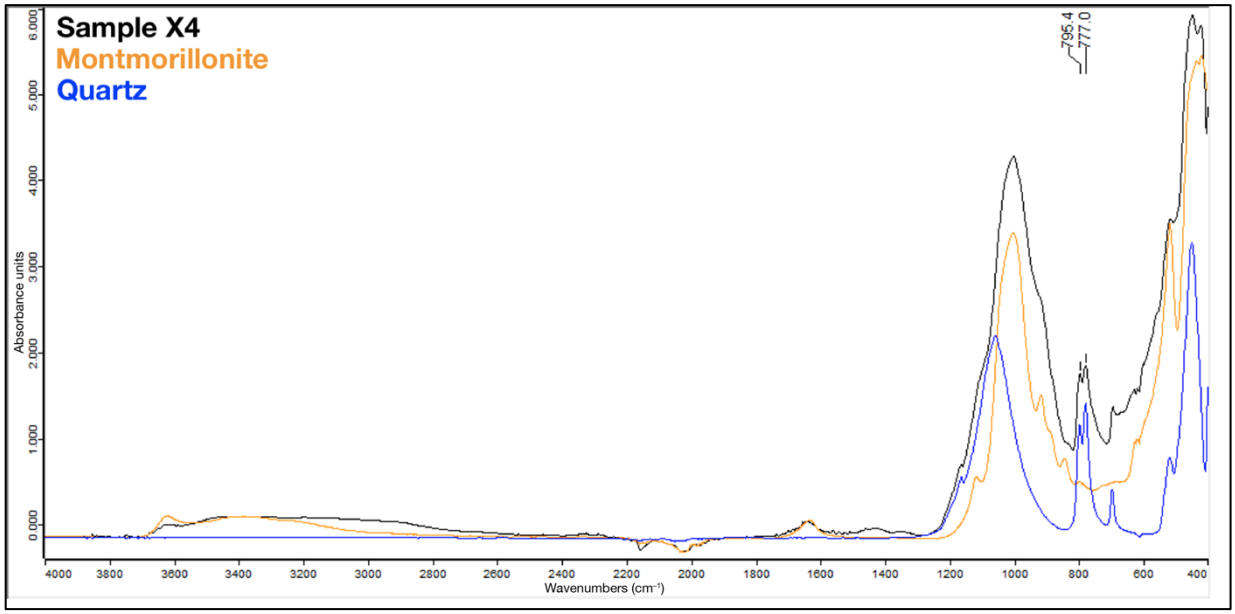

Figure 131. ATR-FTIR spectrum of Sample X4 in absorbance mode.

In Layers 11 to 1, the focus shifts from silicates to phosphates. This part of the sequence is largely dominated by variscite (VR), especially in the upper layers, followed by a host of calcium phosphates: brushite (BR), hydroxylapatite (both the carbonate-rich and simple forms—CHAP and HAP—with varying degrees of crystallization), and crandallite (CR) (Figures 132 and 133). Occasional identifications include taranakite (TK), leucophosphite (LC), spheniscidite (SP), and mitridatite (MT).

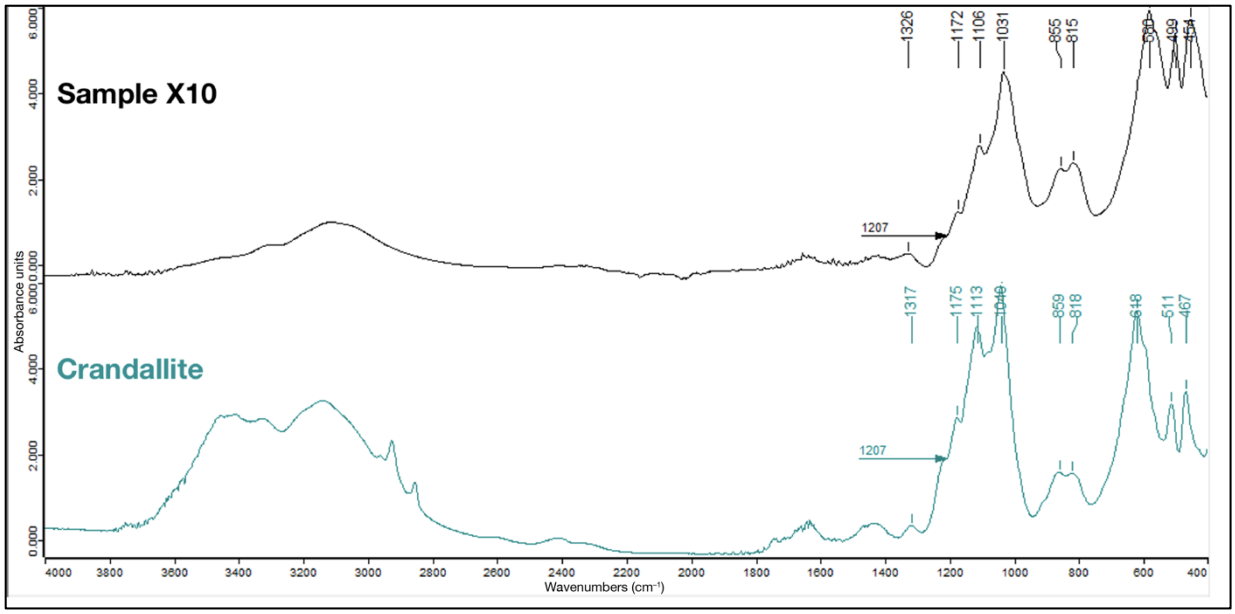

Figure 132. ATR-FTIR spectrum of Sample X10 in absorbance mode.

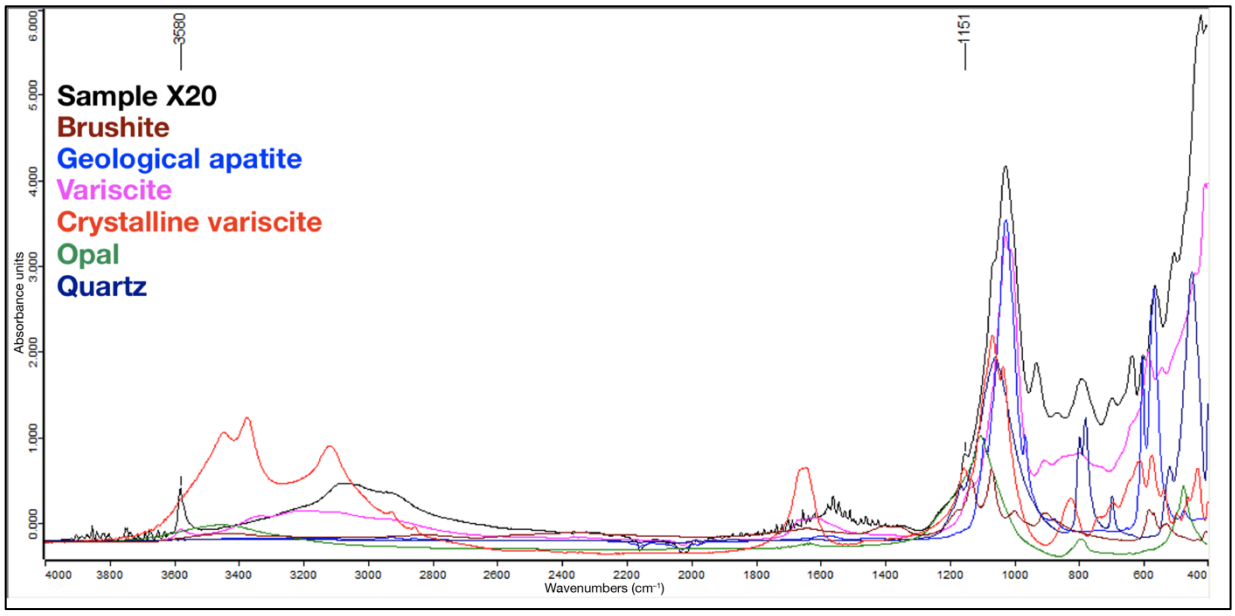

Figure 133. ATR-FTIR spectrum of Sample X20 in absorbance mode.

Quartz (QZ) is the main silicate species in this part of the profile. It is occasionally accompanied by montmorillonite (MM) and illite (IL) halfway up. However, the detection of opal (OP) in the topmost layers (4 to 1) makes the presence of quartz (QZ) here more difficult to affirm with certainty. In general, it remains surprisingly complicated to identify in this part of the sequence compared with the lower layers, at least in FTIR.

Finally, Samples X17, X18, and X19 (Layers 4 and 1) also exhibit some peaks attributable to chitin (CT), notably between 1800 and 1200 cm^{-1} (Figure 134).

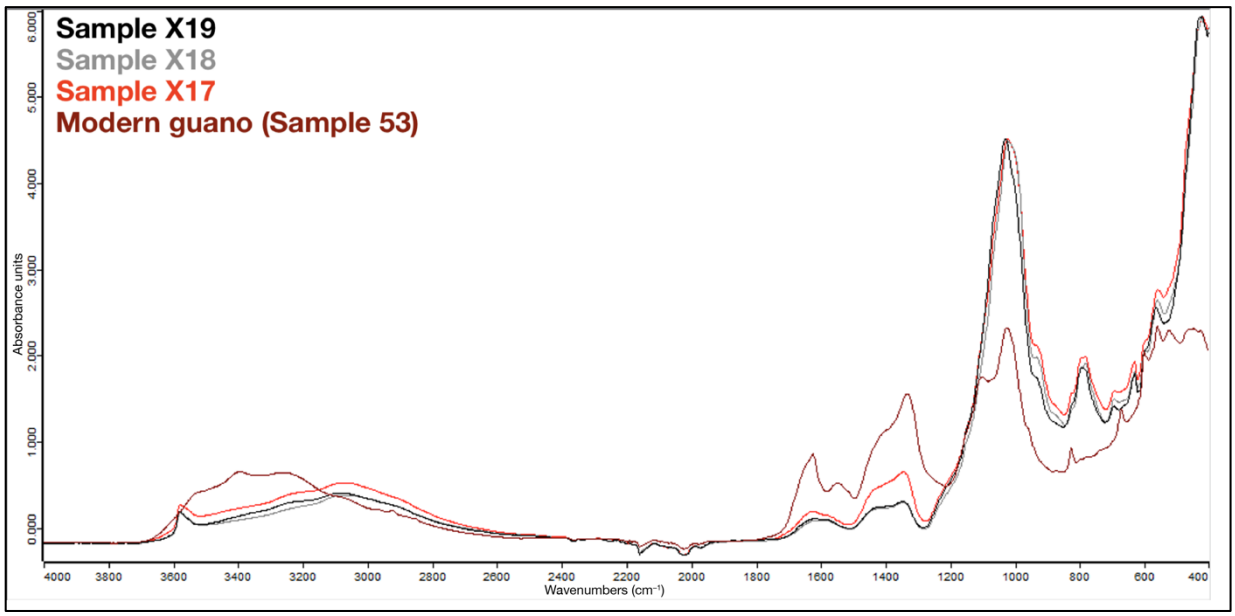

Figure 134. ATR-FTIR spectra of Samples X19, X18, and X17 in absorbance mode.

A unique identification is natrouranospinite (NU; $Na_2(UO_2)_2(AsO_4)_2 \cdot 5H_2O$) in Sample X8, not found anywhere else in the cave (Figure 135).

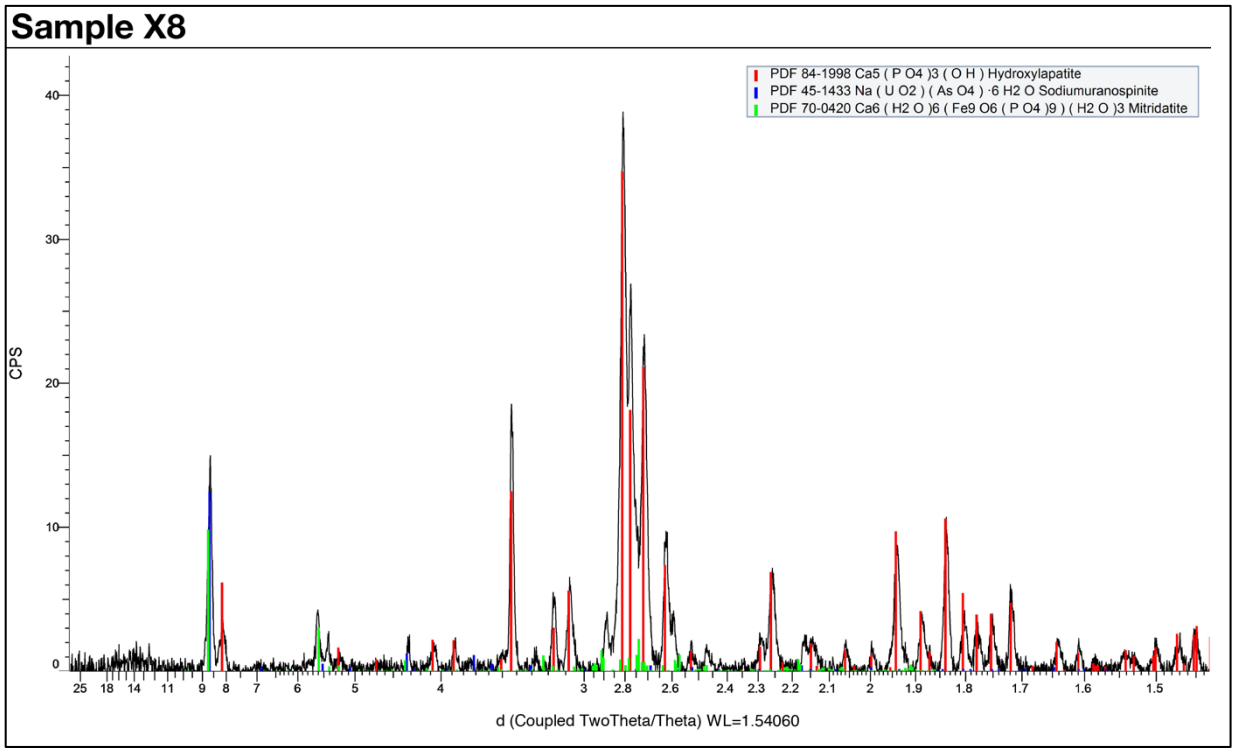

Figure 135. X-ray diffractogram of Sample X8.

4.2.3. The South Zone: transects S14 to S18

Table 23 presents the results for the South Trench (Squares S16E1 to S18E1), situated in the central part of the South Zone, and the diverticulum (Square S16W7), situated in the west part.

Table 23. Summary of mineralogical characterization results for the South Trench and the diverticulum.

Squares	Sample	Depth (cm DP)	Sulphates	Phosphates														Silicates													
			Al	Ca				Mg	Al			K		Ca			Al	K				SiO_2									
				PO_4		CO_3	PO_3OH					OH	PO_3OH	Fe	Mg					H_2O											
			RS	HAP		CHAP	BR	WL	MG	CR	VR	TL	TK	MT	MM	IL	MC	KL	OP	QZ	TD										
South Trench	G	-113	xx																												
South Trench	MM4	-135 to -140				x	x				x	x			xx					x / xxx	xx										
South Trench	F	-142				x	x				x	x			xx					xx / xxx											
South Trench	E	-162				x	x				x	x				xx				xx / xxx											
South Trench	D	-220				x					xx							xx		xx / xxx											
South Trench	MM3	-223 to -228		xx		x					xx / xxx	xx			xx					xx / xxx											
South Trench	C	-238				x				x	xx	x			x					xx / xxx											
South Trench	MM2	-265 to -270		xx		x					xx / xxx	xxx			xx					xx / xxx											
South Trench	B	-285		xx		xx		xx			x		x	x		x			x	x / xx											
South Trench	MM1	-316 to -321		xxx		xx		xxx	xx		x	x	x	xx		xx				x / xx											
South Trench	A	-333		xx		xx				xx	x		x			xx			x	x / xxx											
Diverticulum	30	Surface		xxx		xxx		x			x					xx				x											

Figure 136 presents the vertical profile for the South Trench. No stratigraphical profiles are available for the diverticulum.

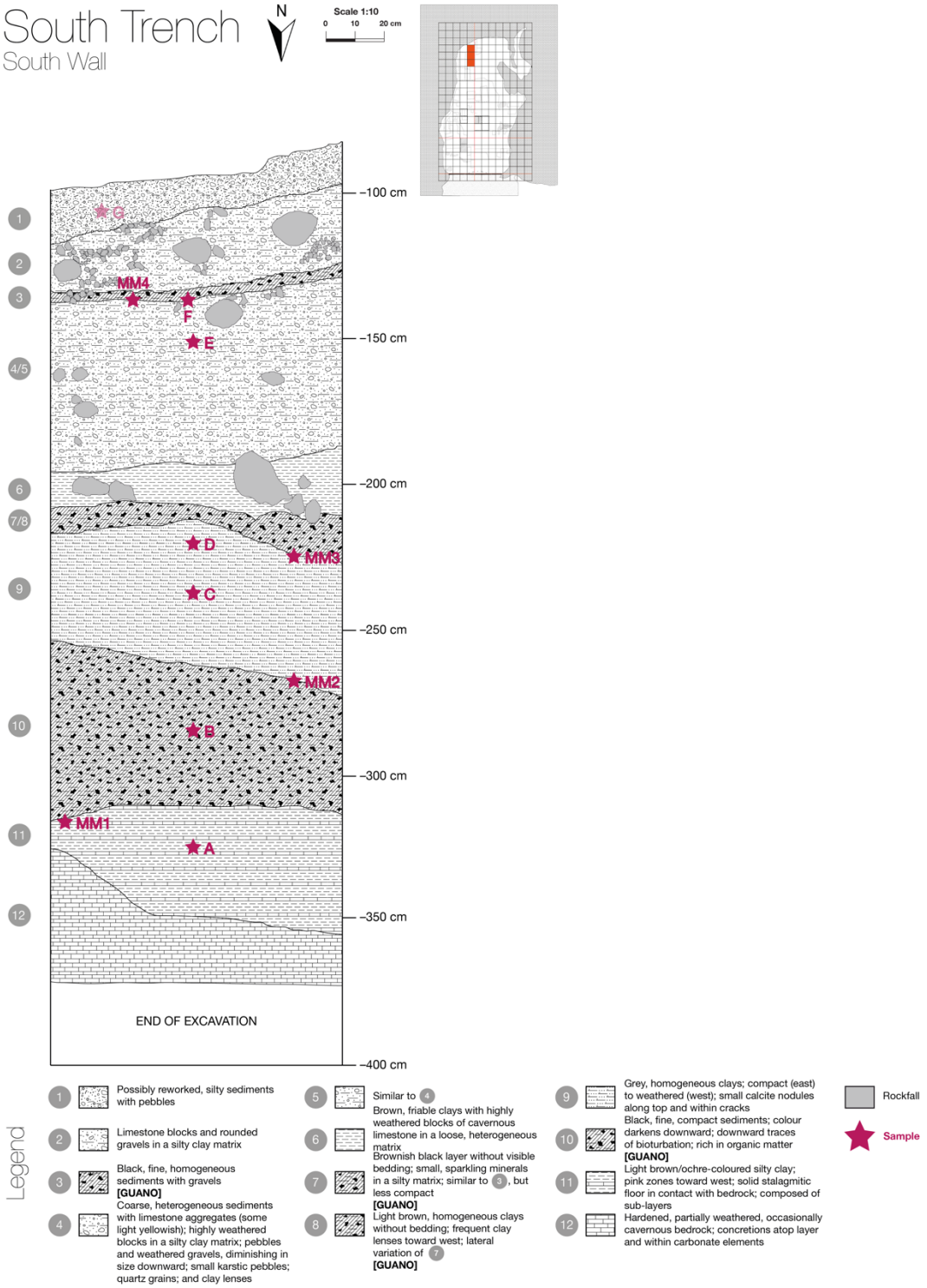

Figure 136. South Wall vertical profile for the South Trench, with the location of Samples A to G and MM1 to MM4 indicated. Sample G, projected from the East Wall, is rendered translucent.

All the samples in this zone were analysed in both FTIR and XRD.

Three minerals are present all throughout the sequence: hydroxylapatite (HAP) (except in Sample G, at the very top), variscite (VR), and quartz (QZ). Hydroxylapatite (HAP) is consistently in an advanced state of crystallization (peak at around 630 cm^{-1}), although XRD was unable to detect it in the upper half of the profile. Variscite (VR) went undetected in XRD at the bottom of the sequence (perhaps a sign of poor crystallinity); however, it has a strong presence in Samples MM2 (between Layers 10 and 9) and MM3 (between Layers 9 and 7/8), as well as in Sample G (Layer 1). Quartz (QZ) was easily identifiable and largely prominent in XRD, but slightly less so in FTIR.

A number of other phosphate minerals were identified. FTIR detected traces of taranakite (TK) in Samples A, MM1, and B at the bottom of the profile (Layers 11 to 10), as well as traces of brushite (BR) in Samples E, F, and MM4 around the topmost guano level (Layer 3). However, most of the phosphates were identified in XRD: these include whitlockite (WL), montgomeryite (MG), crandallite (CR), and mitridatite (MT) in the lower half of the sequence (Figures 137 and 138), while tinsleyite (TL) is strongly represented in Sample MM2 but less so in the upper half of the profile (Figure 139).

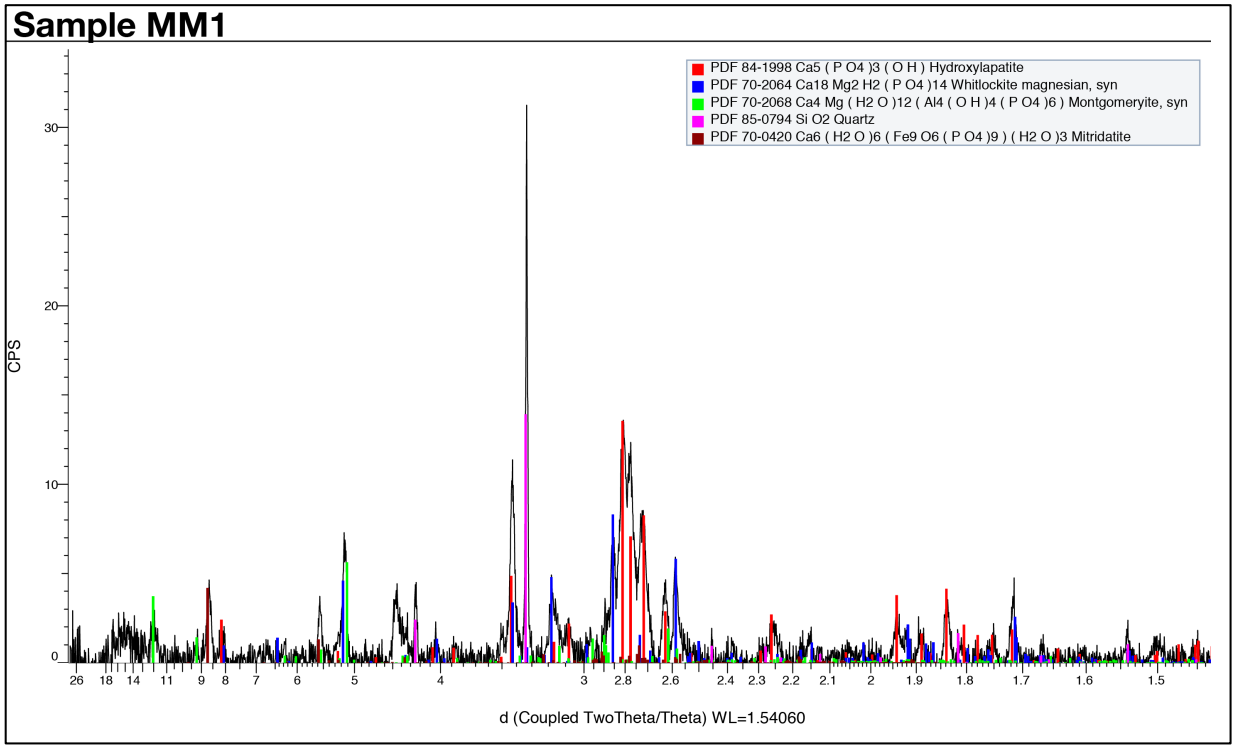

Figure 137. X-ray diffractogram of Sample MM1.

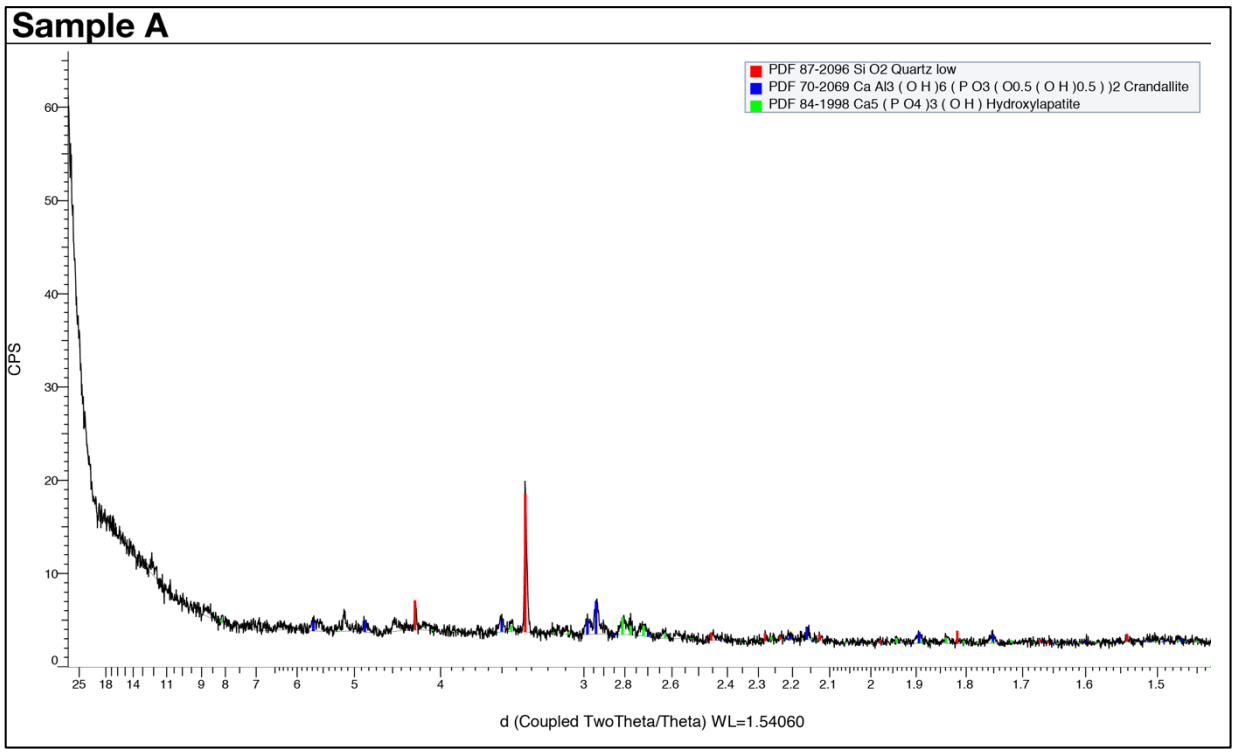

Figure 138. X-ray diffractogram of Sample A.

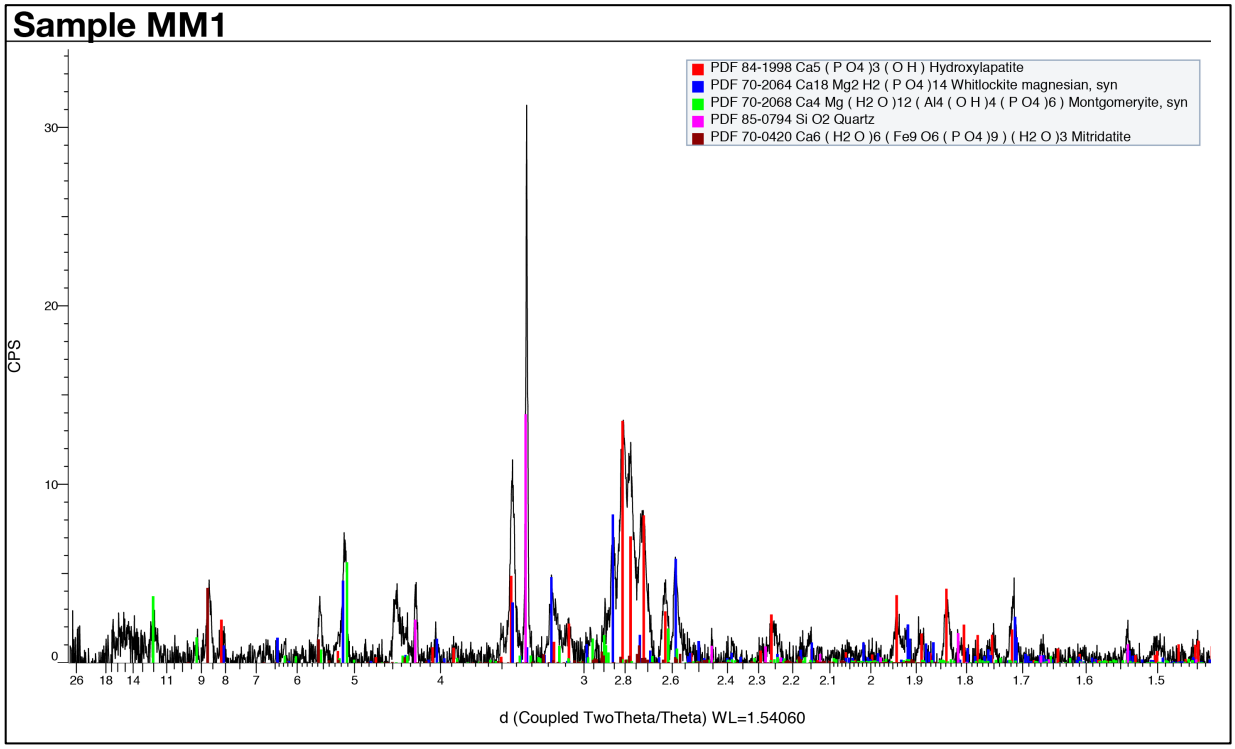

Figure 139. X-ray diffractogram of Sample MM2.

The South Trench also contains a more diverse range of clay minerals than other areas of the cave. Aside from montmorillonite (MM) and illite (IL), previously identified in other squares, muscovite (MC) and kaolinite (KL) were also detected here (Figures 140, 141, and 142).

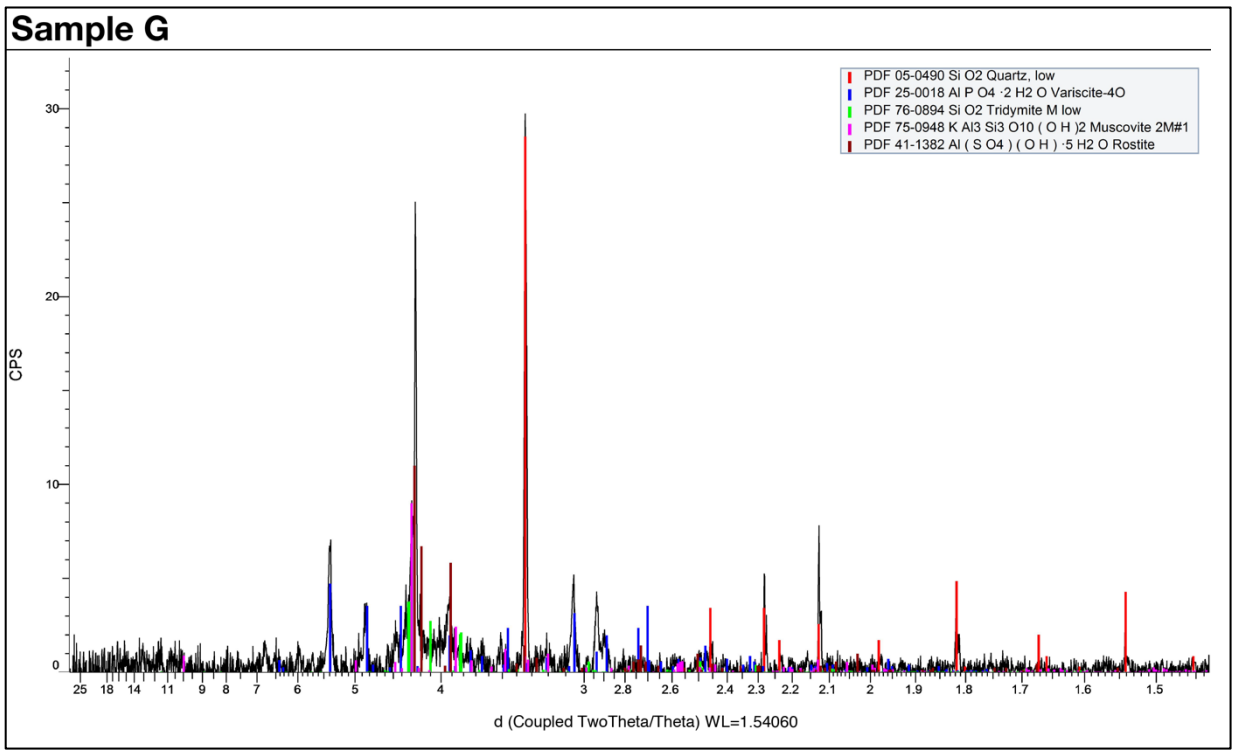

Figure 140. X-ray diffractogram of Sample G.

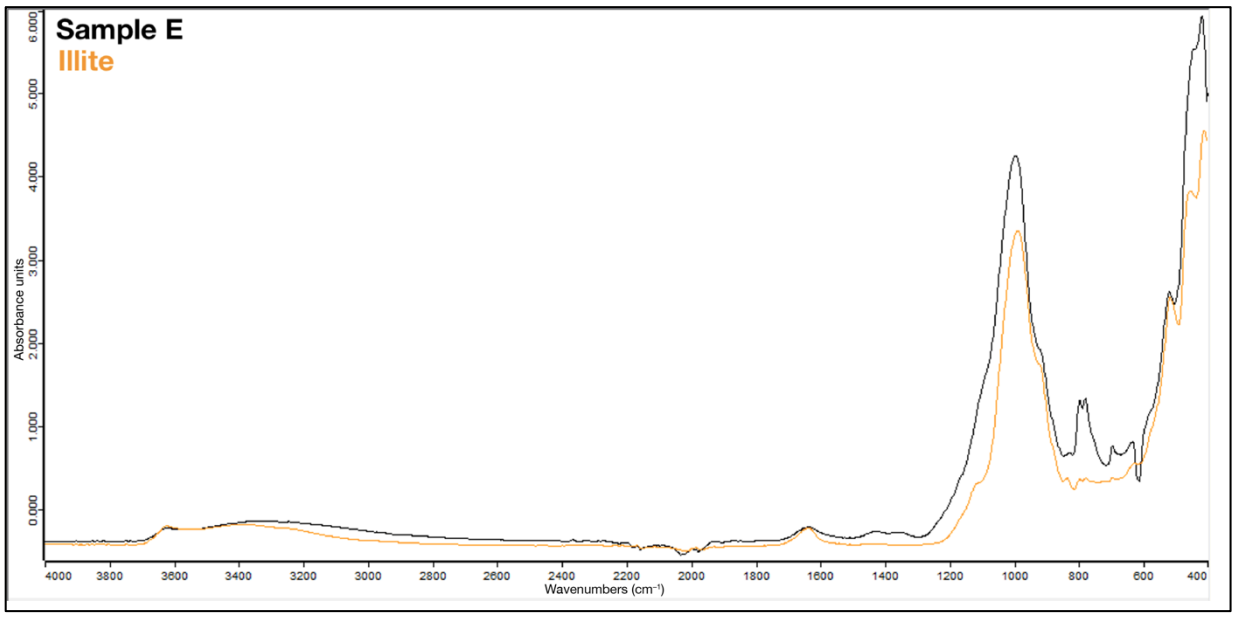

Figure 141. ATR-FTIR spectrum of Sample E in absorbance mode.

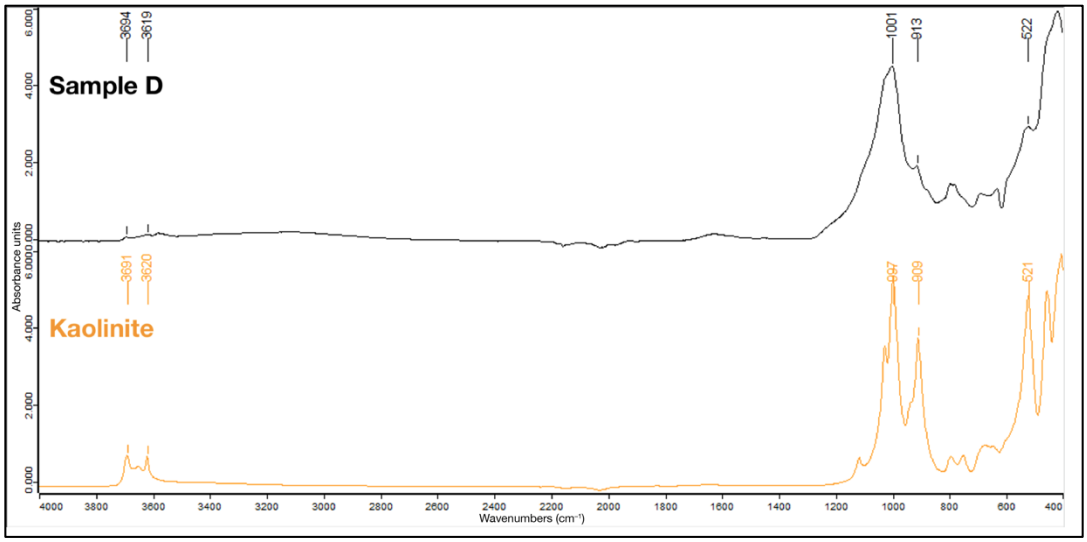

Figure 142. ATR-FTIR spectrum of Sample D in absorbance mode.

Opal (OP) is only occasionally present. In Sample G, at the top of the sequence, tridymite (TD) was also identified in XRD. None of the usual sulphates previously identified in the cave (gypsum, GY; ardealite, AR) were found here. Instead, an aluminium sulphate called rostite (RS) was detected via XRD in Sample G.

Going west into the diverticulum, Sample 30 shows a mineralogical profile that is very similar to samples from the bottom of the South Trench (Figure 143). Carbonate-rich hydroxylapatite (CHAP) is the dominant phase (with a particularly prominent carbonate doublet just left of 1400 cm^{-1} in FTIR), accompanied by traces of whitlockite (WL) and variscite (VR) in XRD, plus some illite (IL) and quartz (QZ).

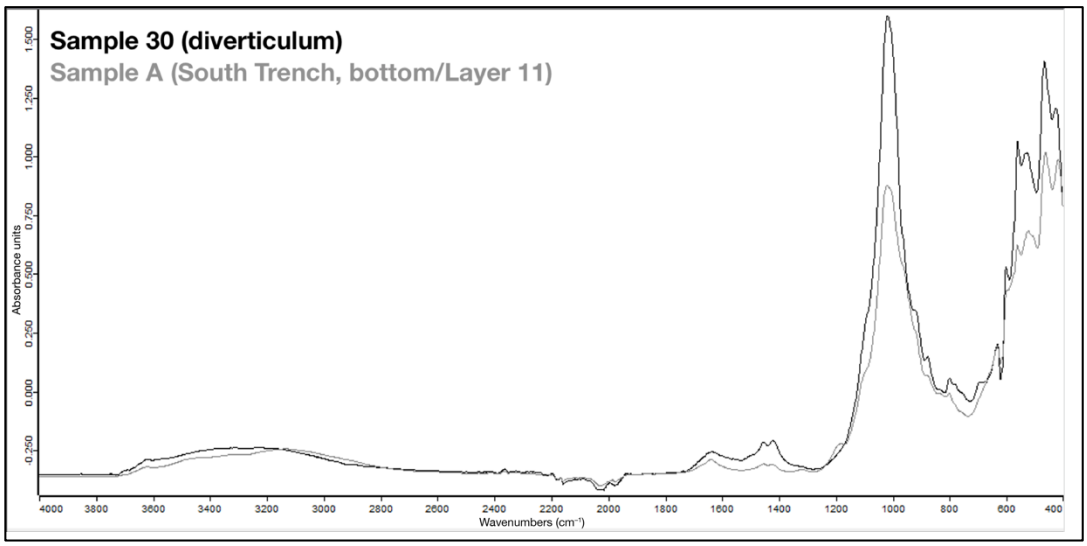

Figure 143. ATR-FTIR spectra of Samples 30 and A in absorbance mode.

4.2.4. Modern guano mounds

Table 24 presents the results for Square S9W6, situated in the western part of the Central Zone, and Square S14E2, situated in the eastern part of the South Zone.

Table 24. Summary of mineralogical characterization results for Squares S9W6 and S14E2.

Square	Sample	Depth (cm DP)	Sulphates		Phosphates				Silicates			Others	
			Ca	PO_3OH		CO_3	PO_4	Al	Ca	K	SiO_2		
			GY	AR	BR	CHAP	HAP	VR	MM	IL	QZ	CT	RK
S9W6	53	Surface	xxx	xx	x	xxx		xx	xx		x / xx	xx	
S14E2	52	Surface	x	xx		x	xx	xx		x		xx	xxx

The samples were collected from modern guano mounds in their respective squares.

Being guano samples, the first component that was expected is chitin (CT). Surprisingly, however, some sulphate and phosphate minerals were also found (Figures 144, 145, and 146). Both samples contain gypsum (GY), particularly dominant in Sample 53, and ardealite (AR). Brushite (BR) and hydroxylapatite (HAP) were also detected, with the carbonate-rich form of the latter (CHAP) exhibiting a particularly strong presence in Sample 53. Crystalline variscite (VR) is also present in both samples. In terms of silicates, Sample 53 was found to contain montmorillonite (MM) and quartz (QZ), while traces of illite (IL) were identified in Sample 52. Finally, a rare mineral called rokühnite (RK; $FeCl_2 \cdot 2H_2O$) was detected in Sample 52 via XRD.

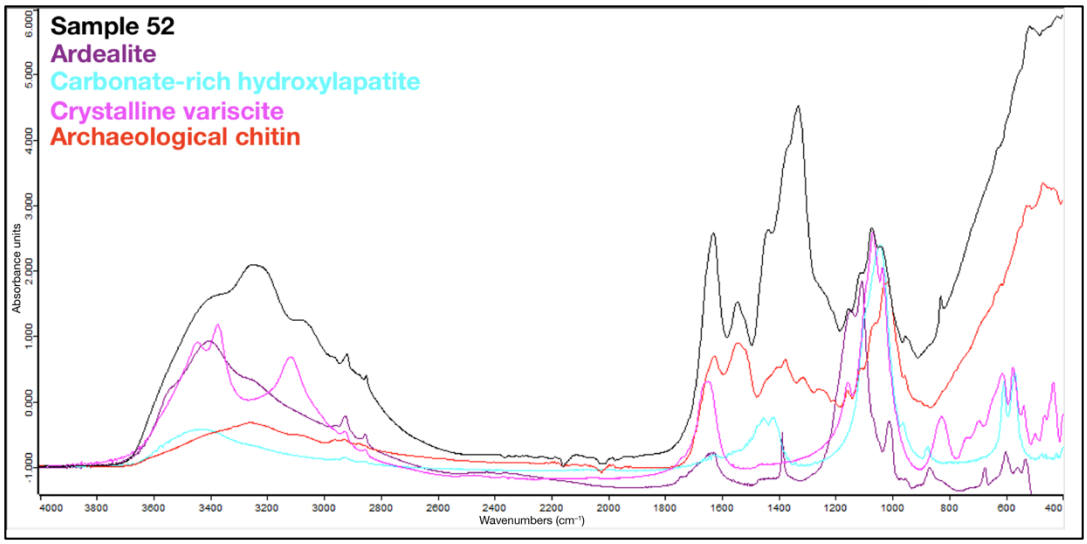

Figure 144. ATR-FTIR spectrum of Sample 52 in absorbance mode.

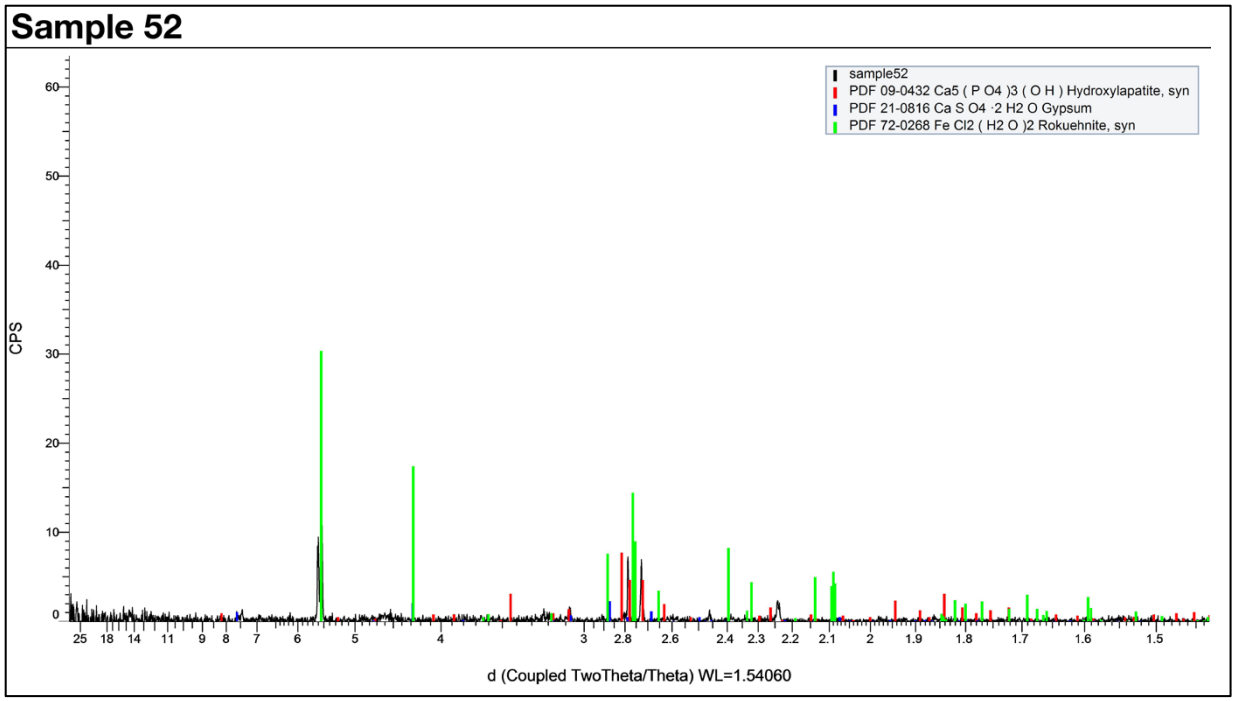

Figure 145. X-ray diffractogram of Sample 52.

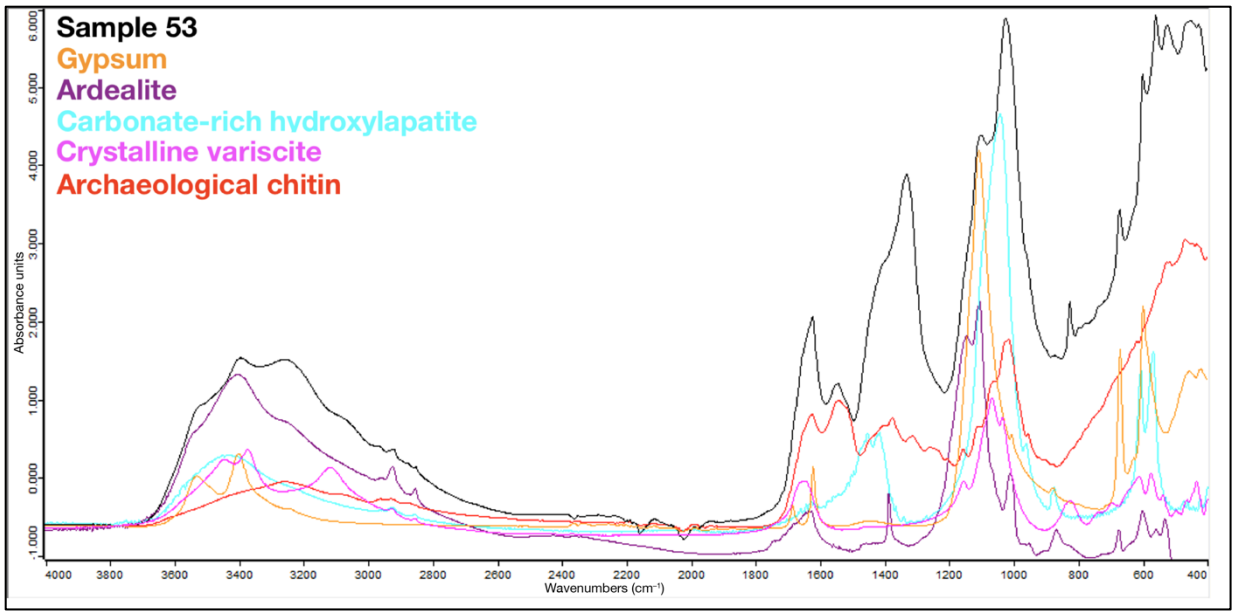

Figure 146. ATR-FTIR spectrum of Sample 53 in absorbance mode.

4.3. Stable isotope analysis

Table 25 summarizes the stable isotope analysis results. The samples are grouped by square, arranged in the table from north to south in order of increasing distance from the cave entrance. For each square, the samples are presented in order of increasing depth.

To facilitate the legibility of this section, the horizontal profile of the cave with the squares sampled for stable isotope analysis highlighted is included just below (Figure 147).

Table 25. Summary of stable isotope results. Samples with blank weight fields did not yield sufficient material for analysis after treatment for insect cuticle isolation.

Square(s)	Sample	Nature	Weight (mg)	%C	%N	C/N	$\delta^{13}C$ (‰)	$\delta^{15}N$ (‰)
S2E1	2	Altered guano	0.071	5.07	–	–	-26.051	–
S2E1	3	Fossil guano	0.771	6.09	1.71	4.14	-25.185	18.049
S2E1	7	Fossil guano	0.763	11.84	3.98	3.48	-23.901	17.719
S4W1	BULK03	Fossil guano	–	–	–	–	–	–
S4W1	BULK04	Fossil guano	–	–	–	–	–	–
S4W1	BULK05 + BULK06	Fossil guano	0.764	26.57	10.95	2.83	-23.482	17.161
S4W4	13	Fossil guano	0.729	10.09	1.18	9.97	-25.537	9.508
S4W4	8	Fossil guano	0.767	8.27	2.06	4.69	-25.180	5.978
S4W4	9	Fossil guano	0.737	6.70	1.39	5.62	-25.482	5.687
S4W4	10	Fossil guano	0.771	7.94	1.52	6.09	-25.199	5.532
S4W4	11	Fossil guano	0.756	12.99	2.18	6.95	-25.618	5.930
S4W4	12	Fossil guano	0.734	8.64	1.21	8.32	-26.372	6.294
S8E1	21	Fossil guano	–	–	–	–	–	–
S8E3	45	Fossil guano	0.748	5.25	0.59	10.46	-27.719	15.831
S9W6	Sample 53-1	Modern guano	0.359	43.82	10.16	5.03	-25.423	5.345
S9W6	Sample 53-2	Modern guano	0.335	41.58	9.64	5.03	-25.325	6.263
S10E1	X17	Fossil guano	0.758	3.65	0.79	5.37	-26.145	6.462

Square(s)	Sample	Nature	Weight (mg)	%C	%N	C/N	$\delta^{13}C$ (‰)	$\delta^{15}N$ (‰)
S14E2	Sample 52-1	Modern guano	0.338	45.27	10.11	5.22	-26.062	6.409
S14E2	Sample 52-2	Modern guano	0.355	45.44	10.41	5.09	-26.581	4.733
S16E1 to S18E1 (South Trench)	G	Gravels in silty matrix	0.737	6.36	1.20	6.19	-25.425	8.017
S16E1 to S18E1 (South Trench)	BULK07	Fossil guano	0.715	23.56	7.03	3.91	-24.513	10.120
S16E1 to S18E1 (South Trench)	BULK08	Fossil guano	0.762	26.84	8.16	3.84	-24.597	9.989
S16E1 to S18E1 (South Trench)	BULK09	Fossil guano	0.785	28.90	8.53	3.95	-24.885	9.901
S16E1 to S18E1 (South Trench)	BULK10	Fossil guano	–	–	–	–	–	–
S16E1 to S18E1 (South Trench)	MM4	Fossil guano	0.738	35.00	10.57	3.86	-25.930	10.226
S16E1 to S18E1 (South Trench)	F	Fossil guano	0.759	32.02	9.99	3.74	-25.370	9.709
S16E1 to S18E1 (South Trench)	E	Gravels in silty clay	–	–	–	–	–	–
S16E1 to S18E1 (South Trench)	D	Clay	–	–	–	–	–	–
S16E1 to S18E1 (South Trench)	MM3	Fossil guano	0.747	3.94	0.51	9.07	-30.777	-1.740
S16E1 to S18E1 (South Trench)	C	Clay	–	–	–	–	–	–
S16E1 to S18E1 (South Trench)	MM2	Fossil guano	0.730	4.49	0.75	6.98	-28.918	2.269
S16E1 to S18E1 (South Trench)	B	Fossil guano	–	–	–	–	–	–
S16E1 to S18E1 (South Trench)	MM1	Fossil guano	0.769	9.29	1.38	7.86	-28.160	1.860
S16E1 to S18E1 (South Trench)	A	Silty clay	–	–	–	–	–	–
S16W7 (diverticulum)	30	Modern guano	0.742	40.46	11.24	4.20	-27.260	10.161

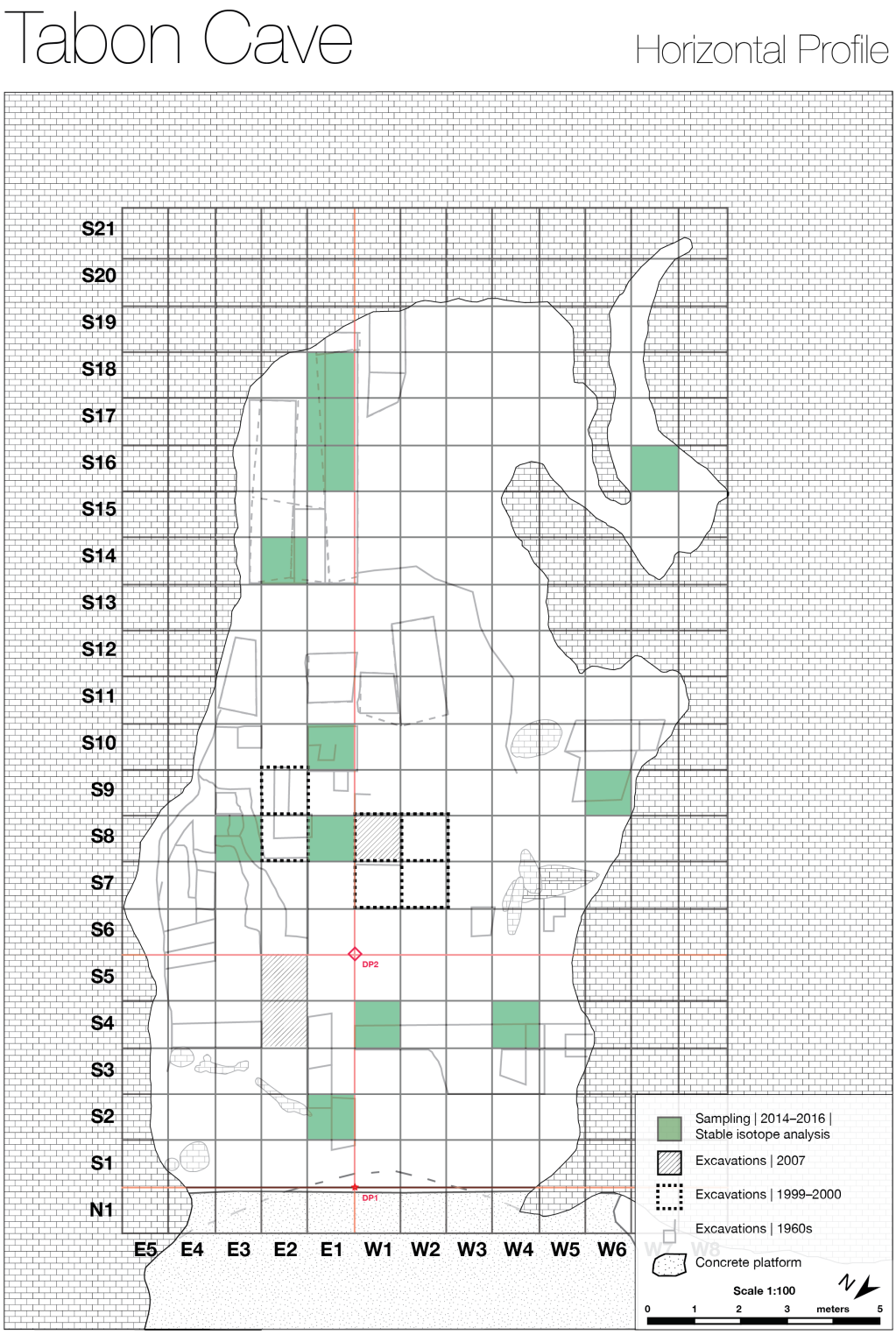

Figure 147. Sampling squares for stable isotope analysis.

4.3.1. Material yield

Based on the carbon content of previously analyzed fossil guano samples from the cave (Choa *et al.*, 2016), between 0.7 and 0.8 mg of material (representing a yield of around 12 to 13%, based on the initial weight of approximately 6 g) was calculated to be necessary for reliable stable isotope results.

Unfortunately, some samples produced insufficient to no material after pre-treatment. They have still been included in the table, where their corresponding cells in the results columns contain an en-dash ('–'; Table 25).

Sample 2, from Square S2E1, only yielded 0.071 mg after pre-treatment. This result was partially expected since the sample consists of altered guano. Nevertheless, mass spectrometry was still performed on the specimen. Data were obtained for %C and $\delta^{13}C$, but not for %N nor for $\delta^{15}N$. Due to the extremely low amount of analyzed material, the results for this sample should be considered unreliable, or at best, merely indicative, and will hence be excluded from analysis.

For Samples BULK05 and BULK06, from Square S4W1, remaining material after pre-treatment was again insufficient. Since both samples come from the same layer and were originally collected as duplicates, they were combined into a new sample, BULK05 + BULK06, to attain the 0.7 to 0.8 mg weight bracket.

The South Trench samples were all analyzed, and generally speaking, only the fossil guano yielded results, as expected. In detail, however, fossil guano samples B and BULK10 did not produce sufficient material for mass spectrometry. Somewhat surprisingly, Sample G, from a non-guano layer, gave material that was both sufficient and exploitable for mass spectrometry, probably composed of other organic matter. Nevertheless, this sample will be excluded from analysis because it does not come from an identified guano layer (its data cannot be interpreted using the framework for palaeoenvironmental reconstruction used in this study, applicable only to guano).

For the modern guano samples except Sample 30, quantities were reduced to between 0.3 and 0.4 mg to prevent signal saturation during analysis due to extremely high carbon content. For Sample 30, however, the fossil guano weight bracket of 0.7 to 0.8 mg was used.

4.3.2. Carbon content (%C)

Figure 148 presents the carbon content of the guano samples, arranged from left to right in order of increasing distance from the cave entrance.

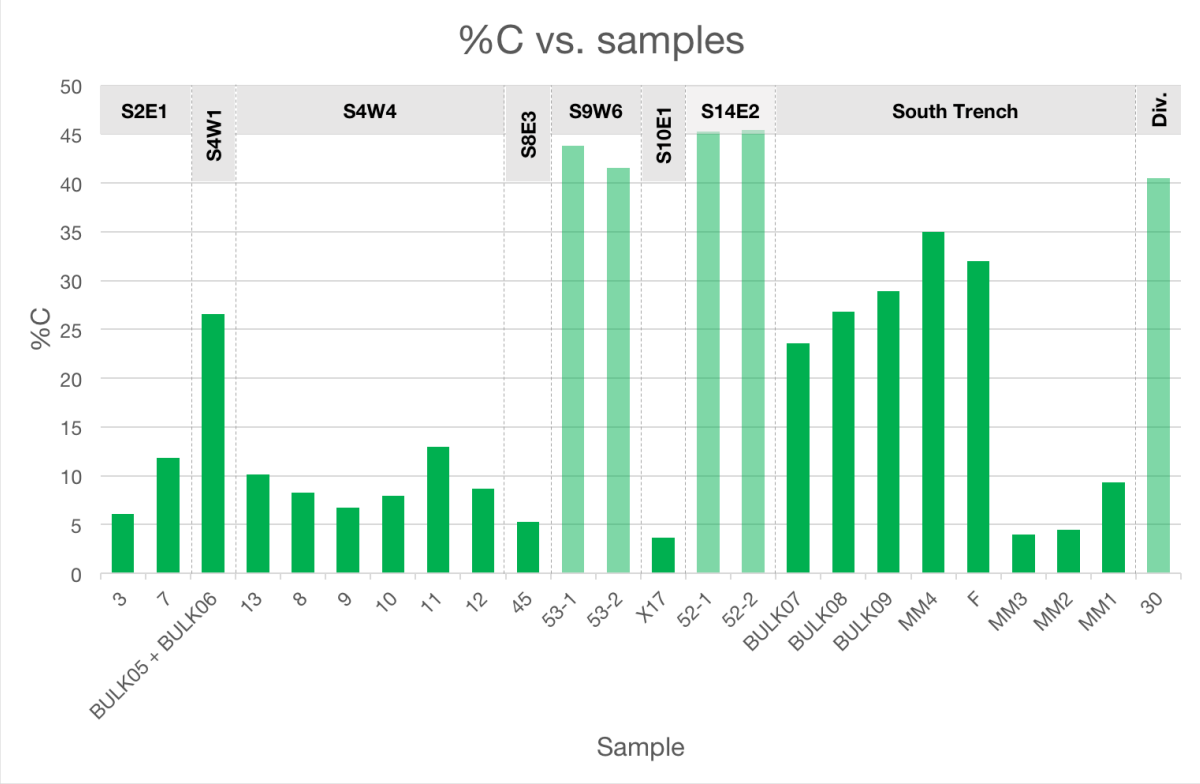

Figure 148. Carbon content of the guano samples. Fossil specimens are indicated in dark green and modern ones in light green.

The modern samples come out very clearly on top, with %C values ranging between approximately 40 and 45%. This may be taken to represent the 'base' carbon content of guano from Tabon Cave, decreasing over time with organic matter decomposition.

The fossil samples all have %C values that are lower than their modern counterparts, but internal variation is wide (from less than 5% to 35% flat—a range of 30%). Two main groups can be distinguished:

- **High carbon content (> 23%).** This group consists primarily of Samples BULK07, BULK08, BULK09, MM4, and F, collected from Layer 3 in the South Trench (at the back of the cave). Sample BULK05 + BULK06, from Layer 5 in Square S4W1 (at the opposite end of the cave, near the entrance) also forms part of this group. The samples are relatively rich in carbon, with %C values running from approximately 24% to 35%.
- **Low carbon content (< 13%).** The remaining samples, including the deeper ones from the South Trench (MM3, MM2, and MM1), all have %C values below 13%.

In Figure 149, carbon content is plotted against depth. In general, both factors decrease in proportion to each other (R^2 = .79). The modern samples, located at the top, have the highest %C values, while the deepest specimens are comparatively depleted in carbon. Nevertheless, two of the 24 samples lie outside the trend: Sample 13 from Square S4W4, and Sample BULK05 + BULK06 from Square S4W1 (both located toward the cave entrance). Their hypothetical exclusion tightens correlation between the remaining samples (R^2 = .90).

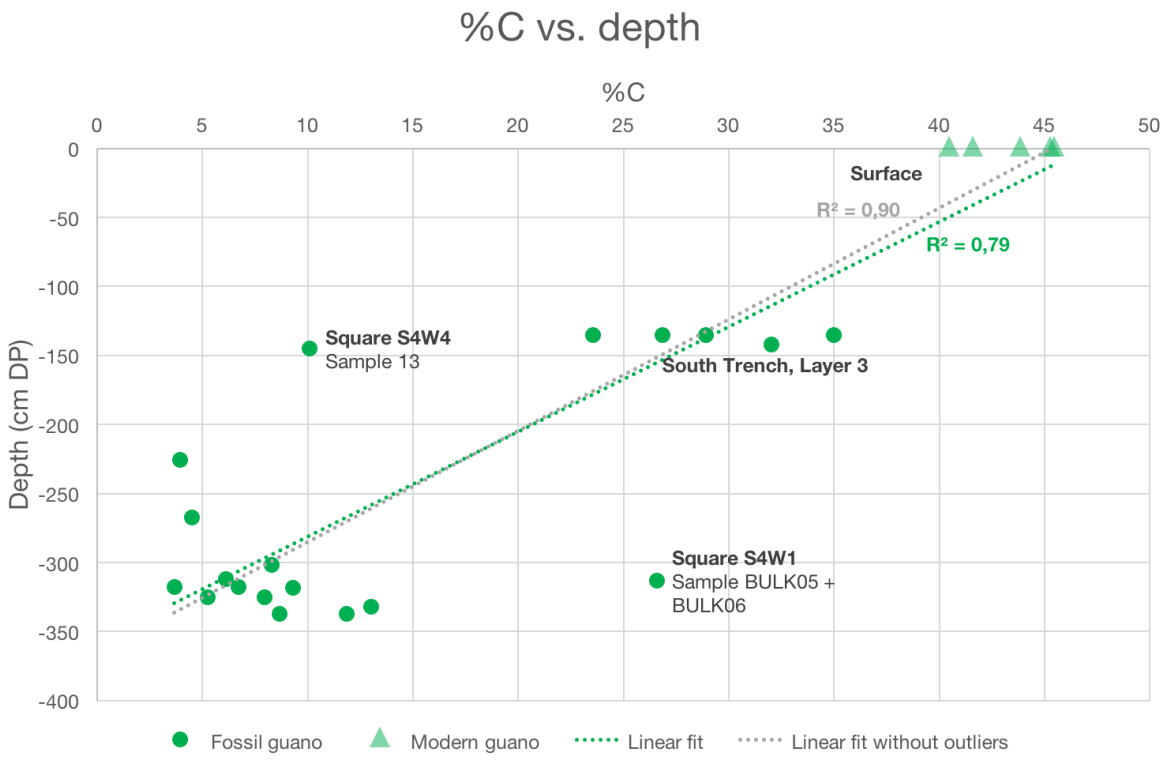

Figure 149. Carbon content against depth. Modern specimens are plotted at 0 cm DP for simplicity (having been collected from the present cave floor surface).

4.3.3. Nitrogen content (%N)

Nitrogen content is presented in Figure 150, again arranged from left to right in order of increasing distance from the cave entrance.

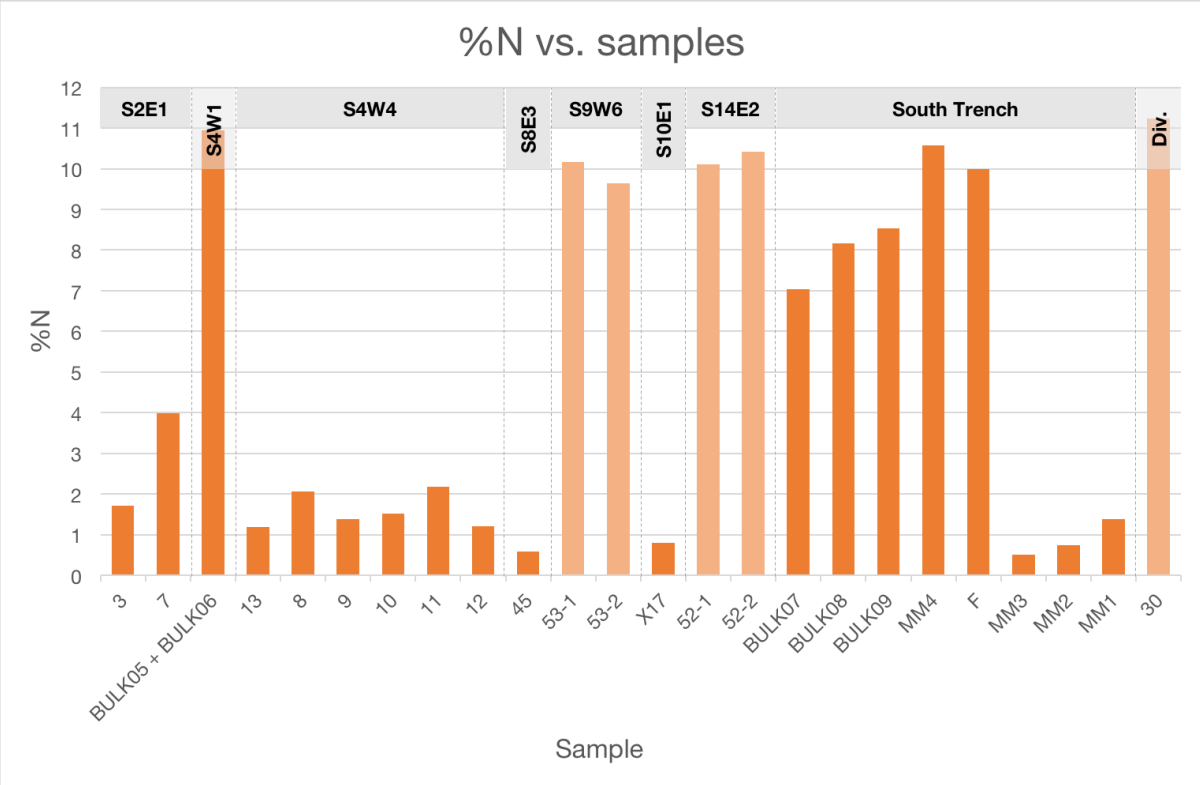

Figure 150. Nitrogen content of the guano samples. Fossil specimens are indicated in dark orange and modern ones in light orange.

This time, the %N values of certain fossil samples are closer to those of the modern ones. This is the case for the samples from Layer 3 in the South Trench (Samples BULK07 to F) as well as the sole specimen from Square S4W1 (Sample BULK 05 + BULK06), comparatively rich in nitrogen: all of them fall between 7 and 12%, while the rest of the samples are below 4%. Incidentally, these are also the fossil samples that have the highest %C values (see Section 4.3.2).

Examining the relationship between nitrogen content and depth, Figure 151 shows a trend similar to that observed for carbon: nitrogen content generally decreases with depth. However, the points are more scattered (R^2 = .61). Removing the same outliers as for carbon (13 from S4W4 and BULK05 + BULK06 from S4W1) improves correlation (R^2 = .84), but the trend remains comparatively less pronounced.

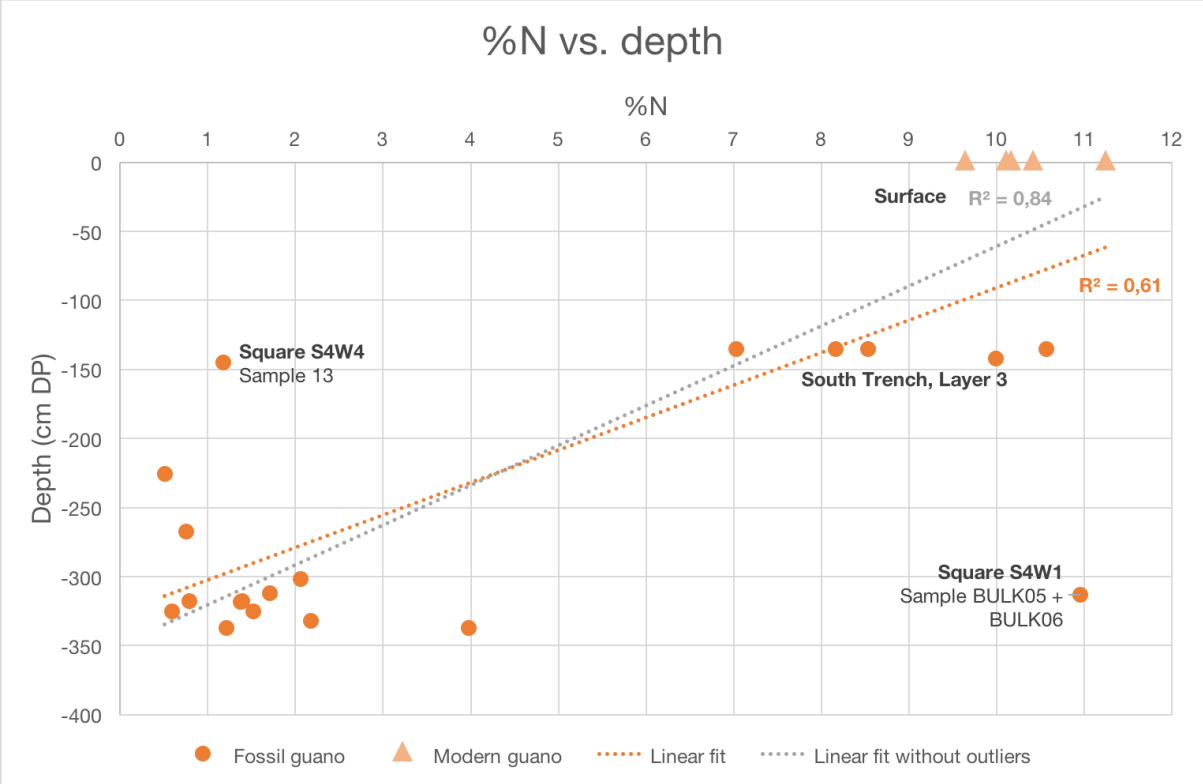

Figure 151. Nitrogen content against depth.

4.3.4. Carbon-nitrogen elemental ratios (C/N)

Looking at carbon-nitrogen elemental ratios, shown in Figure 152, four of the five modern samples have values that hover around 5; the exception, Sample 30 (from the diverticulum), is at 4.20.

Among the fossil samples, those from Layer 3 of the South Trench (Samples BULK07 to F) share similar values with Sample 30, all of which are located in the back part of the cave. Another sample that has a comparable C/N ratio is Sample 3 (4.14), although it is situated at the other end of the cave (toward the entrance), having been collected from Square S2E1.

For the majority of the modern samples, whose C/N ratio is approximately 5, only 2 fossil samples have relatively close values: Samples 8 (C/N = 4.69; Square S4W4), and X17 (C/N = 5.37; Square S10E1).

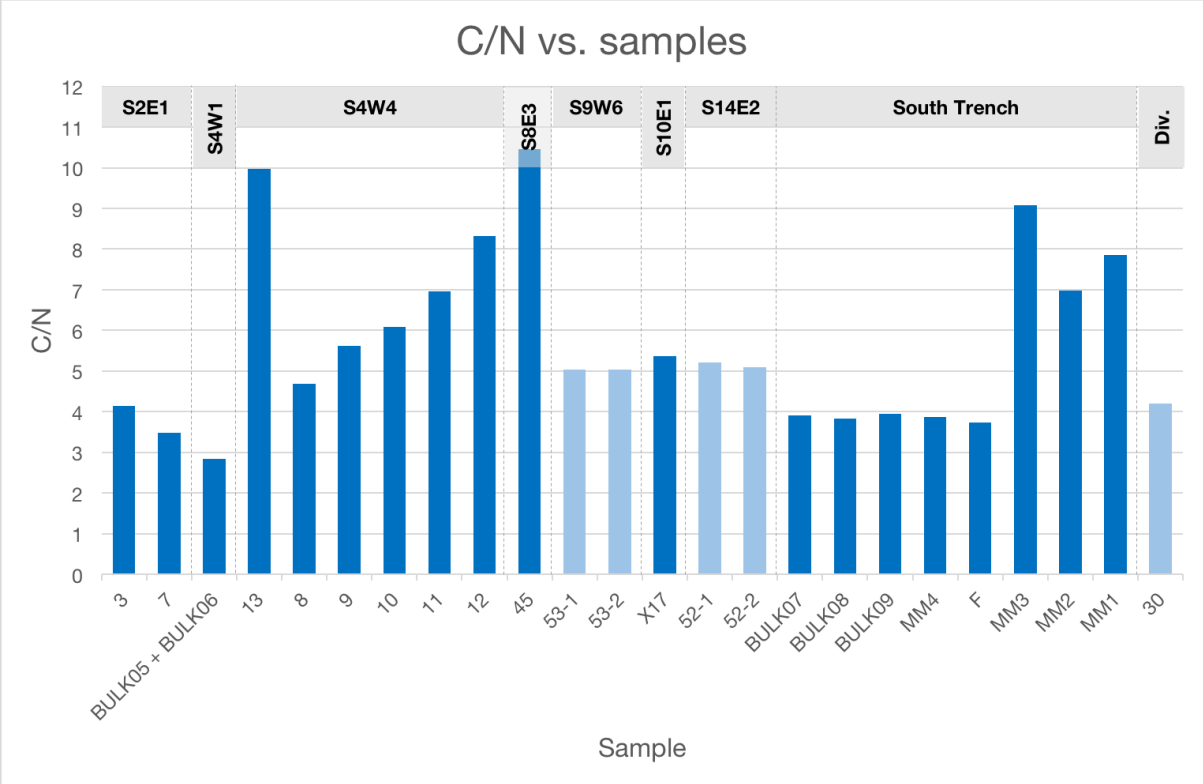

Figure 152. C/N ratios of the guano samples. Fossil specimens are indicated in dark blue and modern ones in light blue.

Plotting the C/N ratios against depth gives Figure 153. The general observation is that, at shallower depths, samples are more tightly clustered together, while deeper samples are more widely distributed. A very stark outlier, however, is Sample 13 (from Square S4W4, toward the cave entrance): it is located at a comparable depth to the South Trench, Layer 3 samples (which are tightly clustered), but characterized by a vastly superior C/N ratio.

To look at how carbon and nitrogen content vary with each other, they are examined in Figure 154. Overall, there is a relatively strong correlation between carbon and nitrogen content among all samples (R^2 = .91). The South Trench, Layer 3 samples, in particular, can almost be connected by a line, suggesting straightforward covariation between carbon and nitrogen. Supposing the exclusion of the modern samples, however, makes the fit even tighter (R^2 = .95).

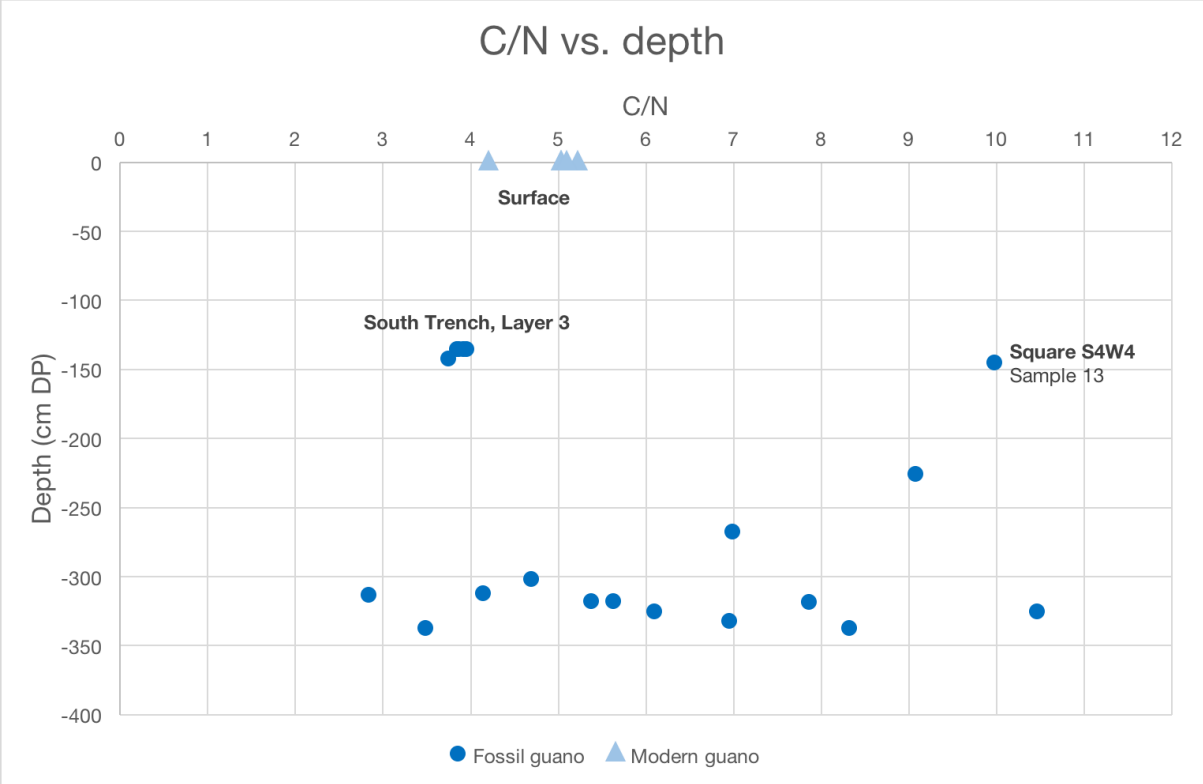

Figure 153. C/N ratio against depth.

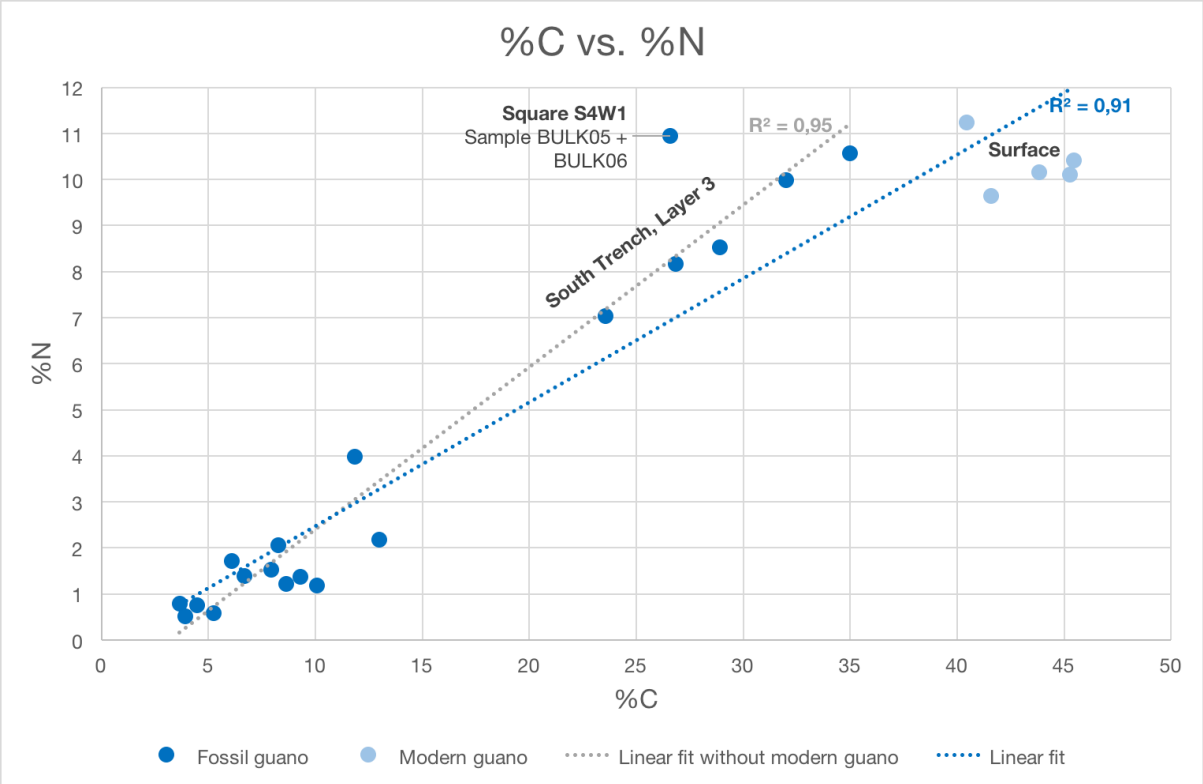

Figure 154. Carbon and nitrogen content plotted against each other.

4.3.5. Carbon-13 isotopic signatures ($\delta^{13}C$)

Figure 155 presents the $\delta^{13}C$ values of the samples. The modern specimens run from slightly below –27‰ to slightly below –25‰. The fossil specimens are quite widely spread out—some are more positive than the modern guano samples, while others are more negative.

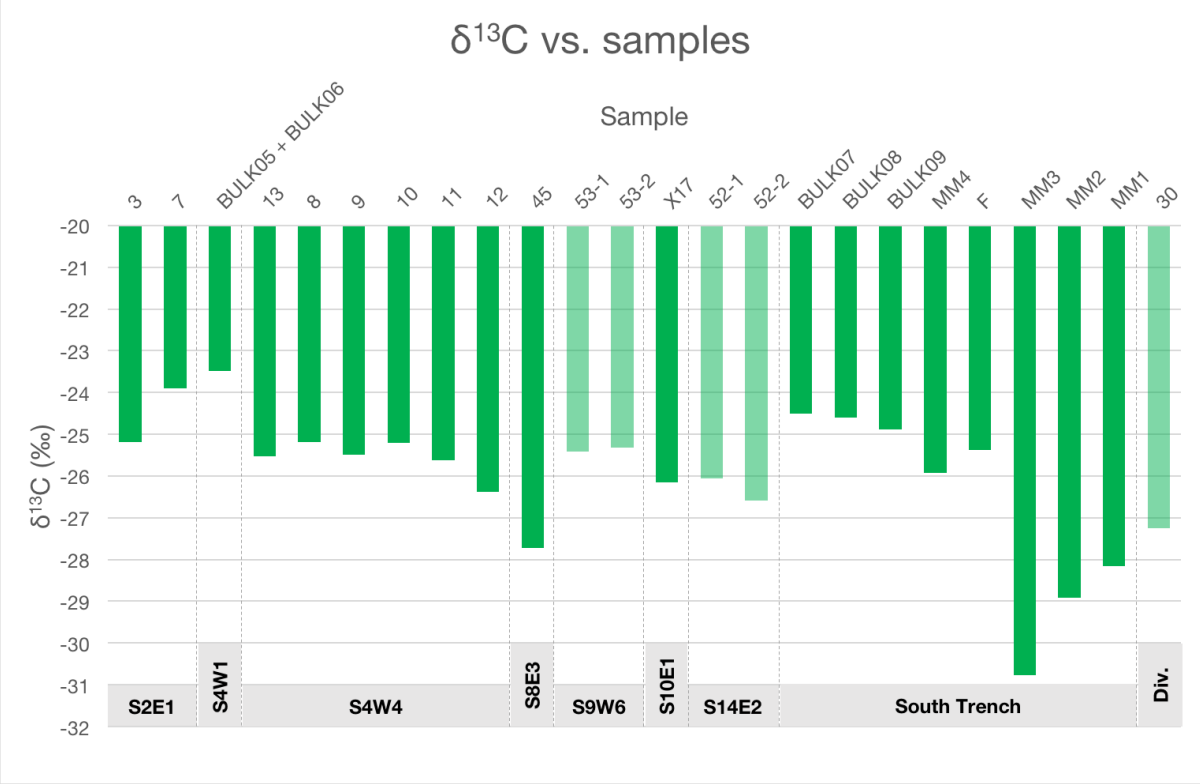

Figure 155. $\delta^{13}C$ values of the guano samples. Fossil specimens are indicated in dark green and modern ones in light green.

Figure 156 plots the $\delta^{13}C$ values according to depth. No particular patterns stand out, but it can be noted that the fossil samples situated at around 150 cm below DP are more positive than the modern samples. At lower depths, $\delta^{13}C$ varies much more broadly, between –31 and –23‰. No trends are visible either when comparing $\delta^{13}C$ with carbon content, as shown in Figure 157.

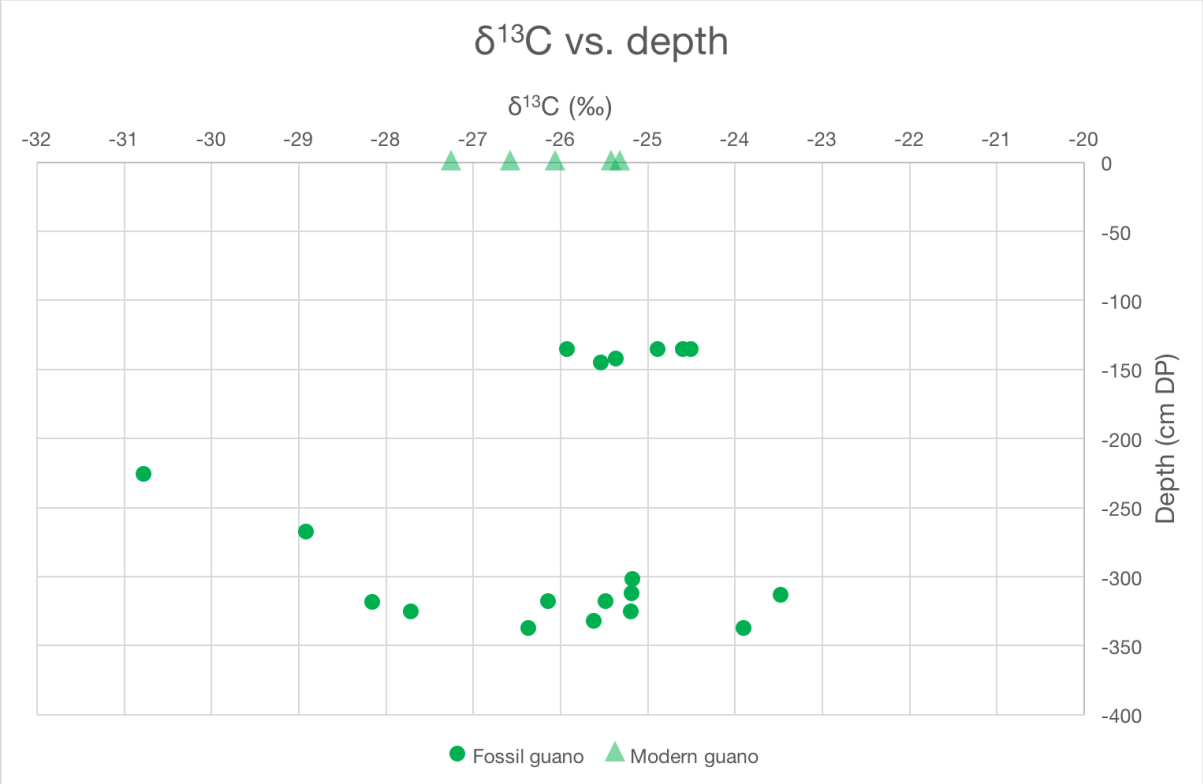

Figure 156. $\delta^{13}C$ against depth.

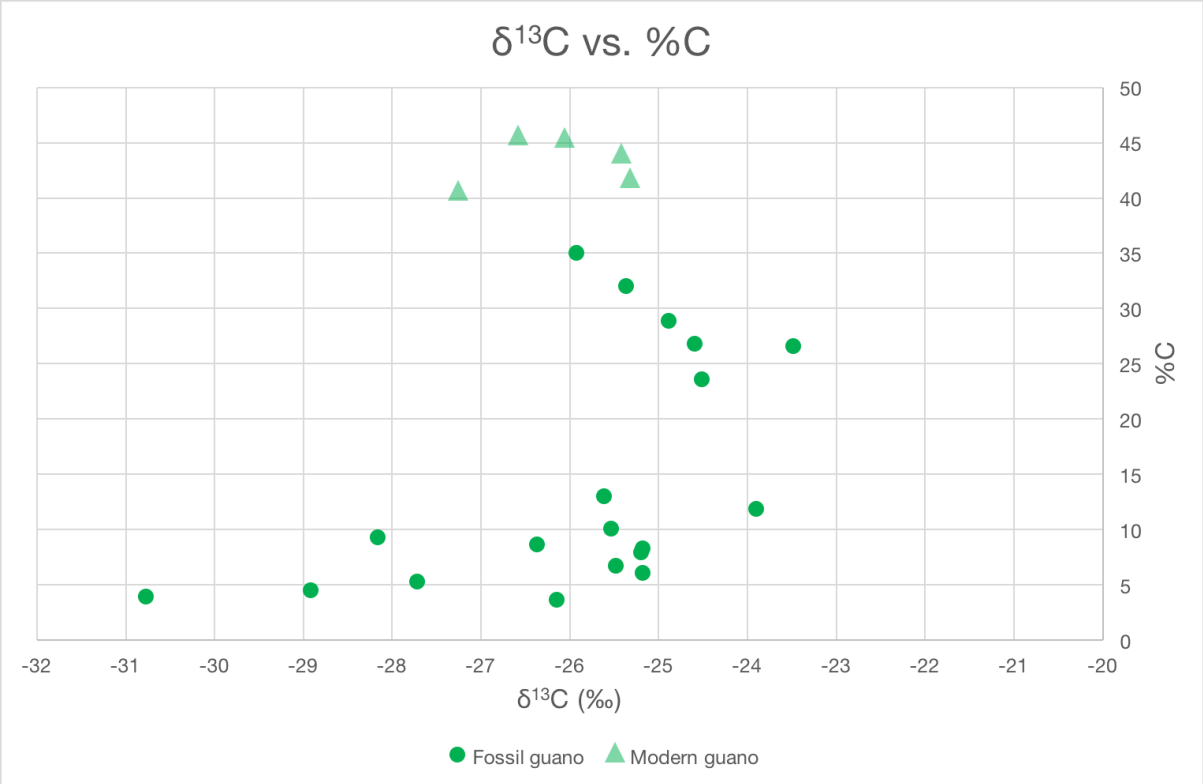

Figure 157. $\delta^{13}C$ against carbon content.

Comparing $\delta^{13}C$ with C/N, Figure 158 does not suggest any strong linear correlations, whether modern samples are taken into account ($R^2 = .42$; $p = .0006$) or not ($R^2 = .49$; $p = .0008$). By eliminating supposed outliers (Samples 45 and 13), the correlation improves ($R^2 = .60$; $p = .00003$), but it remains inconclusive. However, the scattered points at least seem to converge toward more positive $\delta^{13}C$ values and lower C/N ratios.

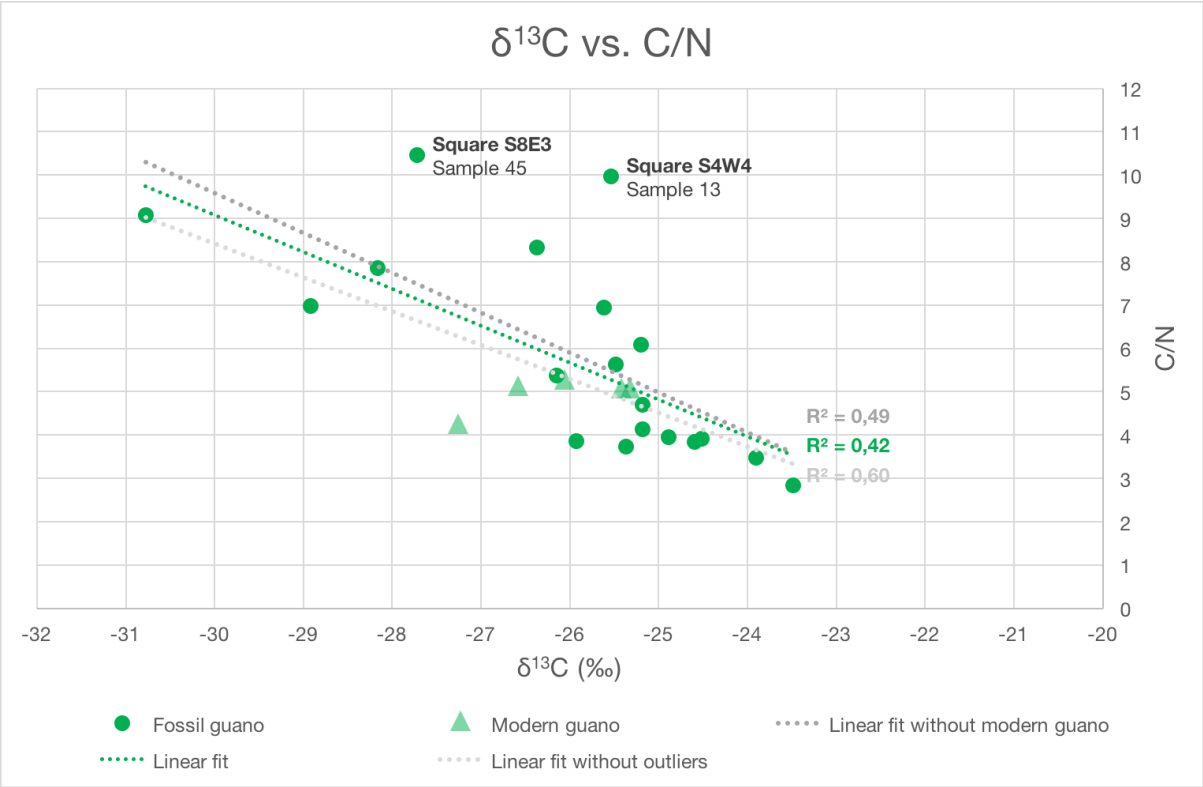

Figure 158. $\delta^{13}C$ against C/N. Labelled points are considered outliers (Samples 45 and 13).

4.3.6. Nitrogen-15 isotopic signatures ($\delta^{15}N$)

The $\delta^{15}N$ values are shown in Figure 159. The modern samples can be divided into 2 groups:

- **Group M1:** This contains a lone member, Sample 30 (from the diverticulum), with a $\delta^{15}N$ of +10‰.
- **Group M2:** The other modern specimens have more in common with each other, ranging roughly from +4 to +6‰.

The fossil samples, in turn, can be divided into 4 groups:

- **Group F1:** These specimens have the highest $\delta^{15}N$ values, spanning approximately +16 to +18‰. They come from Squares S2E1, S4W1, and S8E3.
- **Group F2:** This lot is characterized by a $\delta^{15}N$ value of approximately +10‰. Members include Sample 13 (from Square S4W4, in the front part of the cave) and all the South Trench, Layer 3 samples (BULK07 to F, from the back).
- **Group F3:** Members of this group have $\delta^{15}N$ values that oscillate around +6‰. They include the rest of the S4W4 samples, as well as X17 from S10E1.
- **Group F4:** The last set is composed of the deeper South Trench samples, MM3 to MM1. They fall in the range –2 to +2‰.

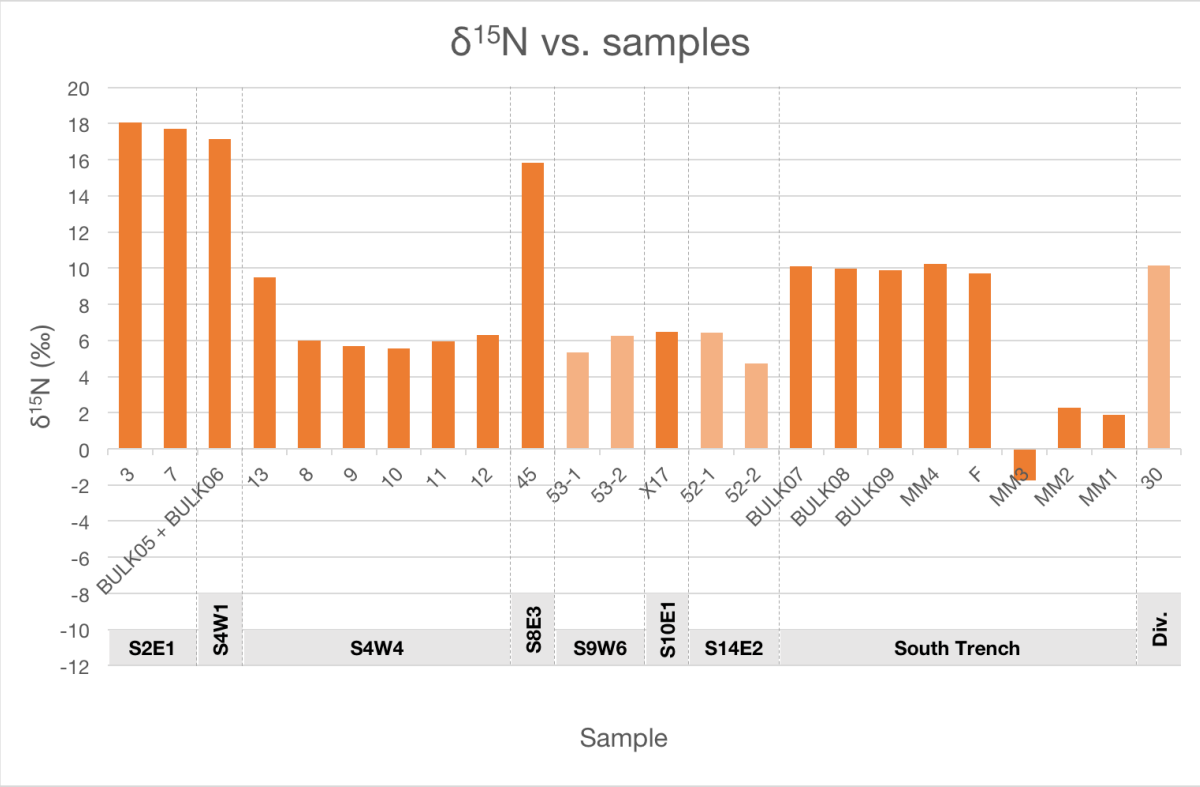

Figure 159. $\delta^{15}N$ values of the guano samples. Fossil specimens are indicated in dark orange and modern ones in light orange.

These groupings are very clearly exposed when $\delta^{15}N$ is plotted against depth, as seen in Figure 160. Additionally, the graph associates modern and fossil sample groups by placing them along common axes: Group M1 with Group F2, and Group M2 with Group F3.

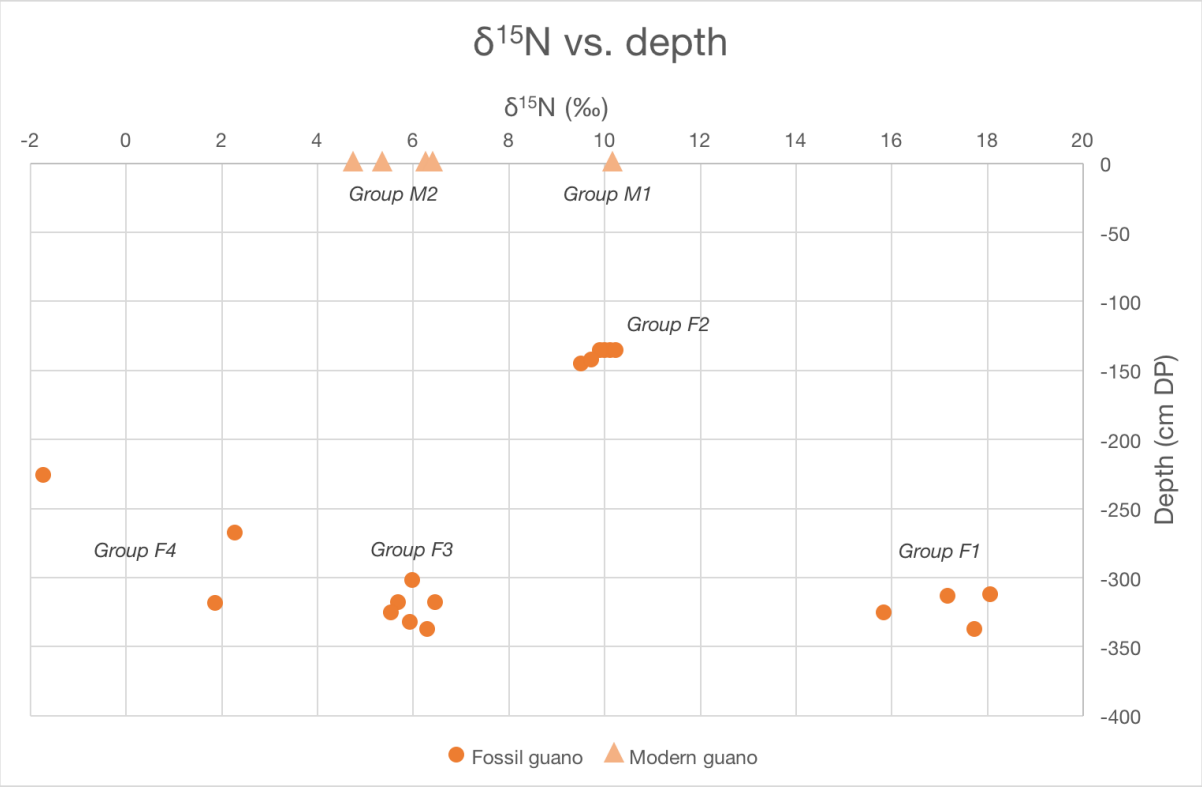

Figure 160. $\delta^{15}N$ against depth.

In contrast, there does not seem to be any relationship between $\delta^{15}N$ and nitrogen content, much as none was observed between $\delta^{13}C$ and carbon content (Figure 161). The majority of the fossil samples, with low nitrogen content (≤ 4%), have $\delta^{15}N$ values that run across nearly the entire range presented in the graph, indicating no particular dependencies between the 2 factors.

Plotting $\delta^{15}N$ against C/N, no patterns are immediately visible (Figure 162). As with $\delta^{13}C$ against C/N, linear correlation is extremely weak, regardless of whether modern samples are included ($R^2 = .15$; $p = .065$) or not ($R^2 = .18$; $p = .070$). Interestingly, by excluding the same supposed outliers as with $\delta^{13}C$ against C/N (Samples 13 and 45), R^2 jumps to .63 ($p = .00001$). Nevertheless, these results are insufficient for establishing covariation between $\delta^{15}N$ and C/N.

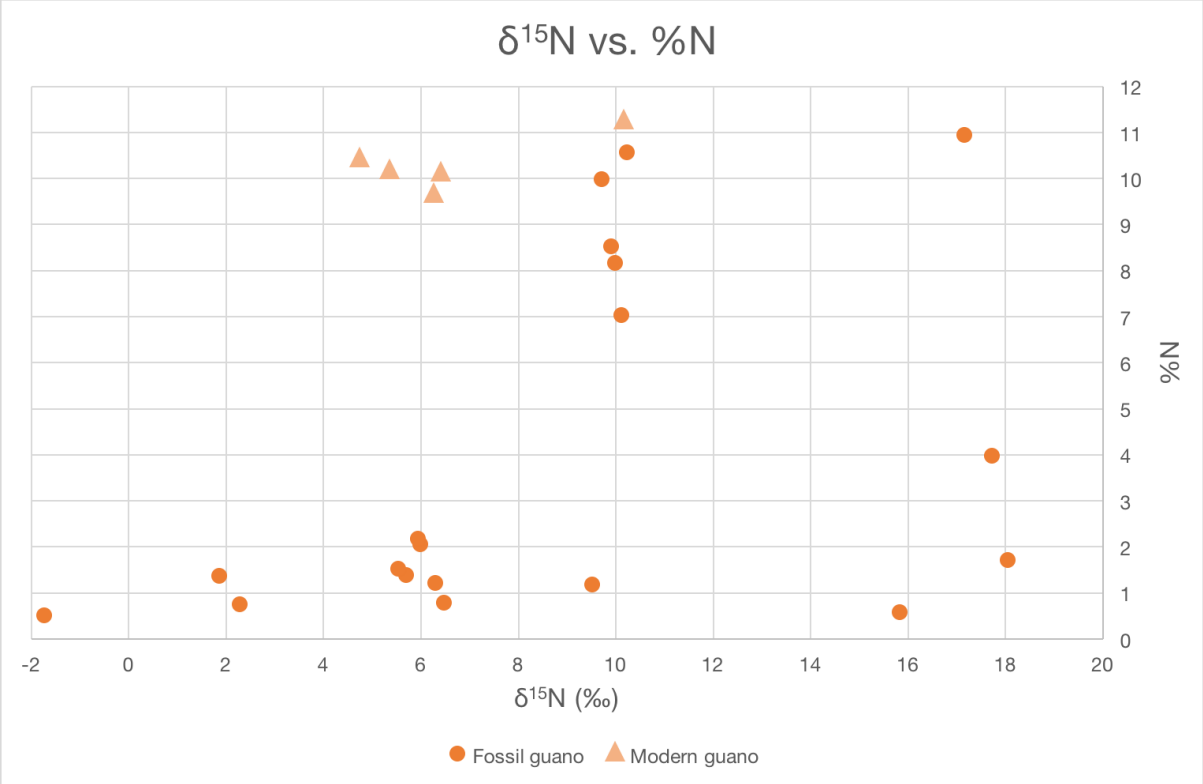

Figure 161. $\delta^{15}N$ against nitrogen content.

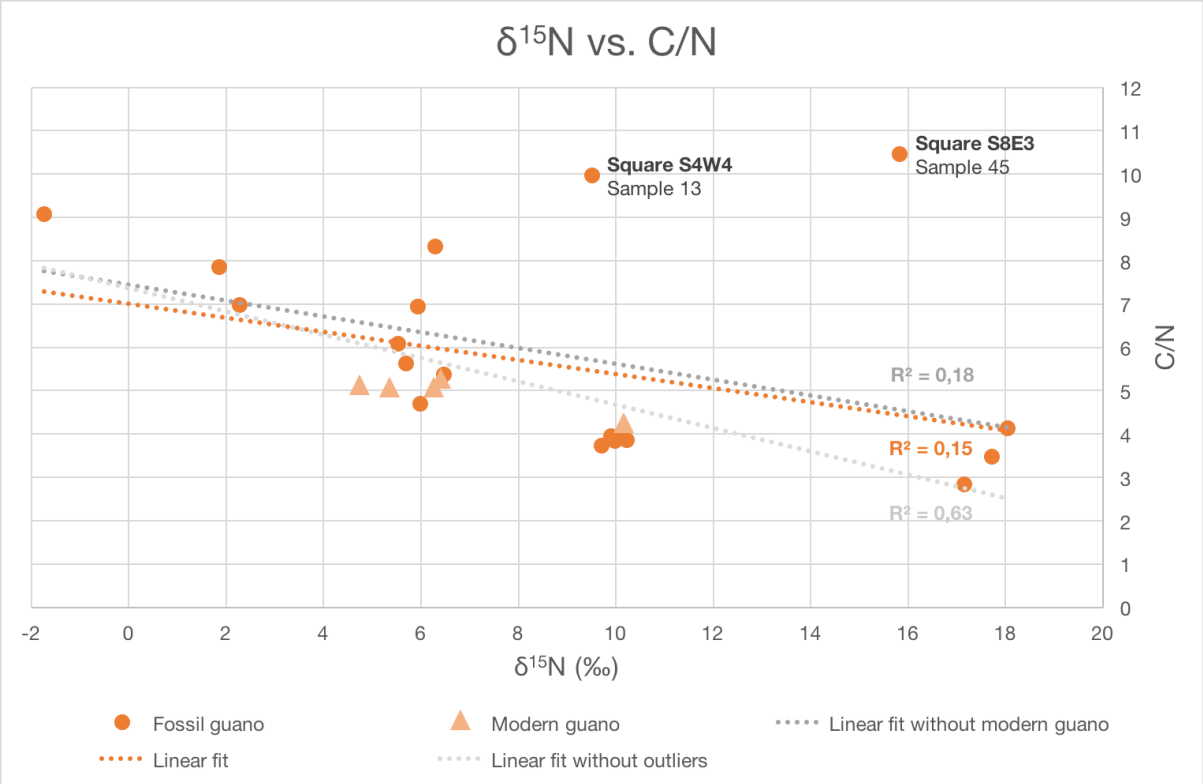

Figure 162. $\delta^{15}N$ against C/N. Labelled points are considered outliers (Samples 13 and 45).

Finally, looking at how $\delta^{13}C$ and $\delta^{15}N$ behave with respect to each other, Figure 163 does not initially reveal any trends ($R^2 = .38$; $p = .001$). By excluding several outliers (Samples 45, 7, and BULK05 + BULK06), a very loose relationship may be drawn between the rest of the samples ($R^2 = .47$; $p = .0007$) that is not sufficiently robust to draw any interpretations about covariation between the 2 isotopic signatures.

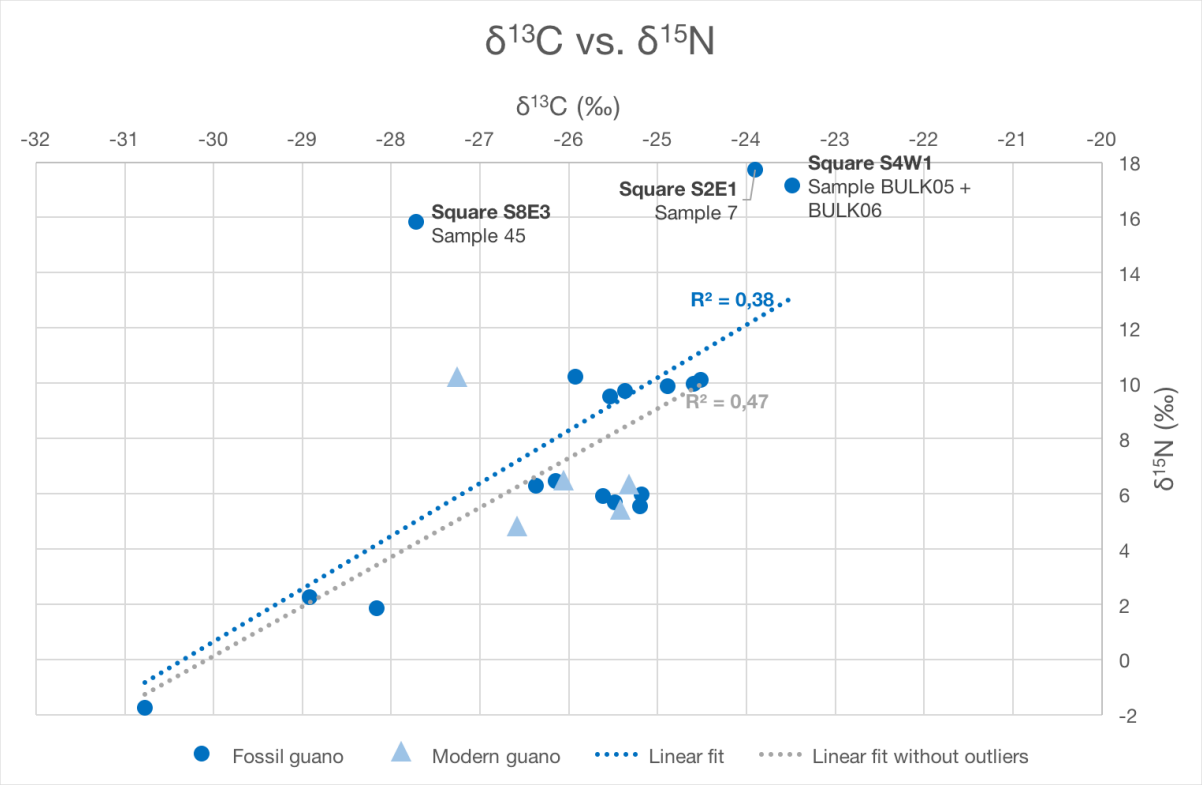

Figure 163. $\delta^{13}C$ against $\delta^{15}N$. Labelled points are considered outliers (Samples 45, 7, and BULK05 + BULK06).

4.4. Radioisotope dating

4.4.1. Guano

The radiocarbon dating results for the guano samples are presented in Table 26. Ages were calculated following Mook and van der Plicht (1999). Fractionation was corrected using the carbon-13 isotope signature ($\delta^{13}C$) calculated from the carbon-13 to carbon-12 ratio ($^{13}C/^{12}C$) measured on the carbon-14 accelerated mass spectrometer (AMS) ARTEMIS.

Measurement uncertainty takes into account both statistical error and measurement variability for samples and background. Age results are presented without reservoir corrections.

Table 26. List of radiocarbon results for the guano samples.

Sample	mg C	$\delta^{13}C$	pMC	Error pMC	Age BP	Error age BP
F	1.20	-14.8	0.87871	0.13019	38000	1200
MM4	1.32	-16.8	0.93513	0.12679	37500	1100
45	0.98	-23.7	3.07625	0.13398	27970	350

Samples F and MM4, both collected from Layer 3 (at approximately 140 cm below DP) of the South Trench (in the back of the cave), exhibit relatively close ages and limited error margins at 38 ± 1.2 and 37.5 ± 1.1 ka BP, respectively. Their carbon-13 isotope signatures ($\delta^{13}C$; not comparable to the quantity measured in mass spectrometry for stable isotope analysis), as well as their carbon-14 activities (expressed in pMC or percent Modern Carbon, normalized to a $\delta^{13}C$ of –25‰), are also relatively comparable, at least with respect to Sample 45. This latter sample, collected from Layer 12 (at 325 cm below DP) of Square S9E3 (in the centre of the cave), has a more negative $\delta^{13}C$ value and three times more carbon-14 activity. The resulting age is 27.97 ± 0.35 ka BP.

4.4.2. The grey speleothem

The uranium-series dating results for the grey speleothem samples are presented in Table 27.

Table 27. List of uranium-series analysis results for the grey speleothem samples.

Sample	[^{238}U] ppm	±	[^{232}Th] ppm	±	(^{234}U / ^{238}U)	±	(^{230}Th / ^{234}U)	±
SG-01	0.5117	0.0014	0.1313	0.0004	1.056	0.005	0.567	0.007
SG-02	0.9847	0.0027	0.1883	0.0006	1.068	0.005	0.455	0.005
SG-03	0.6589	0.0017	0.1973	0.0006	1.056	0.005	0.543	0.006
SG-04	1.6788	0.0046	0.1477	0.0004	1.023	0.004	0.316	0.003
SG-05	1.1570	0.0032	0.2058	0.0006	1.035	0.004	0.414	0.004
SG-06	2.3832	0.0070	0.2979	0.0009	1.038	0.004	0.447	0.003

Sample	(^{230}Th / ^{238}U)	±	(^{230}Th / ^{232}Th)	±	Age (ka)	±
SG-01	0.599	0.007	7.135	0.084	90.5	1.7
SG-02	0.486	0.005	7.772	0.089	65.8	1.1
SG-03	0.574	0.006	5.858	0.064	84.8	1.4
SG-04	0.323	0.003	11.232	0.099	41.4	0.5
SG-05	0.428	0.004	7.358	0.070	58.1	0.7
SG-06	0.464	0.003	11.348	0.090	64.5	0.7

The uranium-238 concentrations [^{238}U] of the six samples run from 0.51 to 2.38 parts per million (ppm).

Figure 164 plots the uranium-238 concentrations of the six samples against their calculated ages. With the exception of Sample SG-06, which does not come from the same solid block as the first five but was collected separately in the field, the samples seem to share a rough relationship with respect to the two variables under consideration (despite the high R^2 value of 0.9976, there are not enough samples to give sufficient weight to the observed trend). Generally speaking, the calculated age of the samples from the solid block has an inverse exponential relationship with the measured uranium-238 concentration. Higher concentrations correspond to younger ages, while lower concentrations correspond to older ages. The variation of concentrations and ages in space while still remaining related to each other suggests

that the same uranium moved around within the system over time. To calculate the true age of the system by capitalizing on this relationship, it would be necessary to determine the uranium-238 concentration before the onset of mobility and to prove that the system stayed closed afterward.

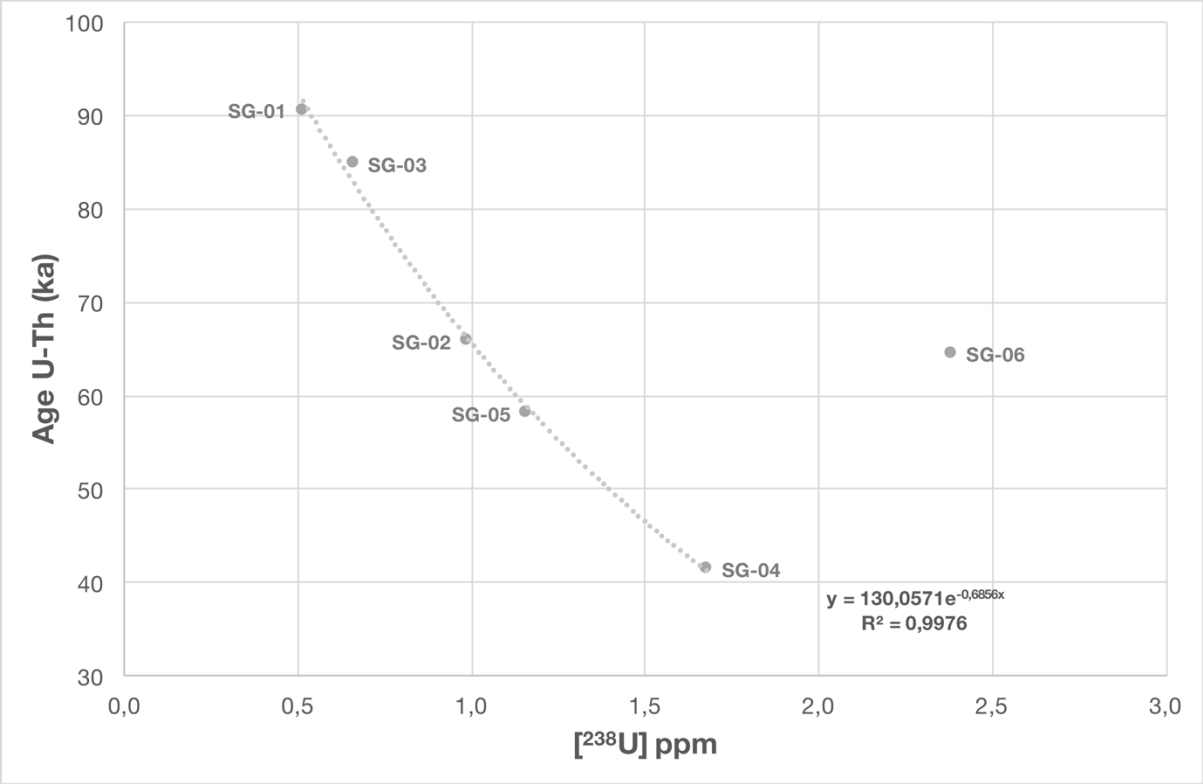

Figure 164. Uranium-238 concentration (in ppm) plotted against age (in ka) for the grey speleothem samples.

$^{234}U/^{238}U$

The uranium-234 to uranium-238 activity ratios ($^{234}U/^{238}U$) go slightly over 1 (from 1.023 to 1.068), a state of relatively weak secular disequilibrium. In a closed system, the activity ratio will tend toward secular equilibrium over time:

$$\lim_{t\to\infty}\left(\frac{^{234}U}{^{238}U}\right) = 1 \text{ . (Equation 18)}$$

At the time of formation ($t = 0$), however, the initial activity ratio $(^{234}U/^{238}U)_0$ and would fall into one of two cases.

Case I

$$\left(\frac{^{234}\mathrm{U}}{^{238}\mathrm{U}}\right)_0 > 1 \text{ (Equation 19)}$$

or

$$(^{234}\mathrm{U})_0 > (^{238}\mathrm{U})_0 \text{ (Equation 20)}$$

where $(^{234}\mathrm{U})_0$ and $(^{238}\mathrm{U})_0$ are the respective initial activities of uranium-234 and uranium-238.

This would correspond to a depositional environment similar to seawater, preferentially enriched in uranium-234. The daughter isotope uranium-234 is more easily leached from rocks, being situated in crystal lattice sites damaged by recoil from the decay of its parent isotope uranium-238. The formation conditions of the grey speleothem in Tabon Cave could be analogous, replacing seawater with cave waters enriched in phosphates from guano. If the system remained closed over time and was left to achieve secular equilibrium, then the age of the deposit could be calculated by solving the following equation for t (assuming that the initial activity ratio is known, measured, or inferred):

$$\left(\frac{^{234}\mathrm{U}}{^{238}\mathrm{U}}\right) = 1 + \left[\left(\frac{^{234}\mathrm{U}}{^{238}\mathrm{U}}\right)_0 - 1\right] e^{-\lambda_{234} t} \text{ (Equation 21)}$$

where λ_{234} represents the decay constant of uranium-234.

This equation applies exclusively to closed systems. Its derivation requires simplifications based on the assumption that uranium-238 activity at both the time of formation and at present remains relatively unchanged:

$$(^{238}\mathrm{U})_0 \approx (^{238}\mathrm{U}) \text{ . (Equation 22)}$$

The terms represent, respectively, the initial and current activities of uranium-238.

This assumption is taken to hold true on the scale of uranium-234's half-life of 2.455 x 10^5 years, several orders of magnitude smaller than uranium-238's half-life of 4.468 x 10^9 years. It also implies that all uranium-238 activity is dedicated to uranium-234 production.

However, if the system was perturbed at any given moment subsequent to its formation (for example, via uranium uptake or loss), then the assumption no longer holds true, and the age calculations become more complex. Beyond a simple exponential decay function that depends in part on the initial activity ratio, new factors will have to be taken into account: specifically, the divergence between the uranium-234 and uranium-238 activities after formation, as well as the time-dependence of the uranium-238 activity. The resulting equation becomes

$$\left(\frac{^{234}\mathrm{U}}{^{238}\mathrm{U}}\right) = 1 + \left\{\left[\frac{\left(^{234}\mathrm{U}\right)_0}{^{238}\mathrm{U}}\right] - 1\right\} e^{-\lambda_{234} t} \text{ . (Equation 23)}$$

Case 2

$$\left(\frac{^{234}\mathrm{U}}{^{238}\mathrm{U}}\right)_0 < 1 \text{ (Equation 24)}$$

or

$$\left(^{234}\mathrm{U}\right)_0 < \left(^{238}\mathrm{U}\right)_0 \text{ . (Equation 25)}$$

In this scenario, there is initially more uranium-238 activity. Uranium-234 activity is either just picking up, as in early systems, or decreased through loss of the isotope, as in rocks having undergone leaching. The age of the deposit can be calculated following the same equations cited in Case 1, and the same constraints apply.

^{230}Th/^{234}U

The thorium-230 to uranium-234 activity ratios (^{230}Th/^{234}U) are far from 1 (between 0.316 and 0.567), indicating a certain degree of fractionation and secular disequilibrium between this parent-daughter isotope pair.

In a closed system, ($^{230}Th/^{234}U$) would fall below 1 if:

1. thorium-230 activity is overshadowed by uranium-234 activity;
2. thorium-230 activity decreased; or
3. uranium-234 activity increased.

The first situation would indicate that thorium-230 activity just began, and therefore, that the system is in its early history.

In the second situation, a decrease in thorium-230 activity implies a decrease in the activity of its parent isotope uranium-234, and by extension, a decrease in the 'grandparent' isotope uranium-238's activity. This hypothesis is incompatible with the closed system assumption, because in the absence of external stimuli, uranium-238 activity will not move away from equilibrium with uranium-234 activity.

Finally, in the third situation, an increase in uranium-234 activity implies an increase in the activity of its parent isotope uranium-238, which is again impossible in a closed system.

Thus, ($^{230}Th/^{234}U$) values below 1 would correspond to a system in its early history, assuming it is closed.

In an open system, however, the activity ratios could fall below 1 in case of uranium uptake, which would cause an increase in uranium activity. Changes in the activity of thorium-230 are much less likely, if not improbable, as it is insoluble.

$^{230}Th/^{232}Th$

The thorium-230 to thorium-232 activity ratios ($^{230}Th/^{232}Th$) run between 5 and 12, which are extremely low. In order to be viable, the ratios need to reach at least 20.

Ages

The ages obtained are highly variable, running from 41.4 ± 0.5 to 90.5 ± 1.7 ka with a difference of almost 50 ka between the oldest and the youngest samples.

Looking at just the first five samples SG-01 to SG-05, which were prepared from the same solid block, the horizontal and especially vertical variability is significant—the difference of 50 ka spans just 2 cm (Figure 165).

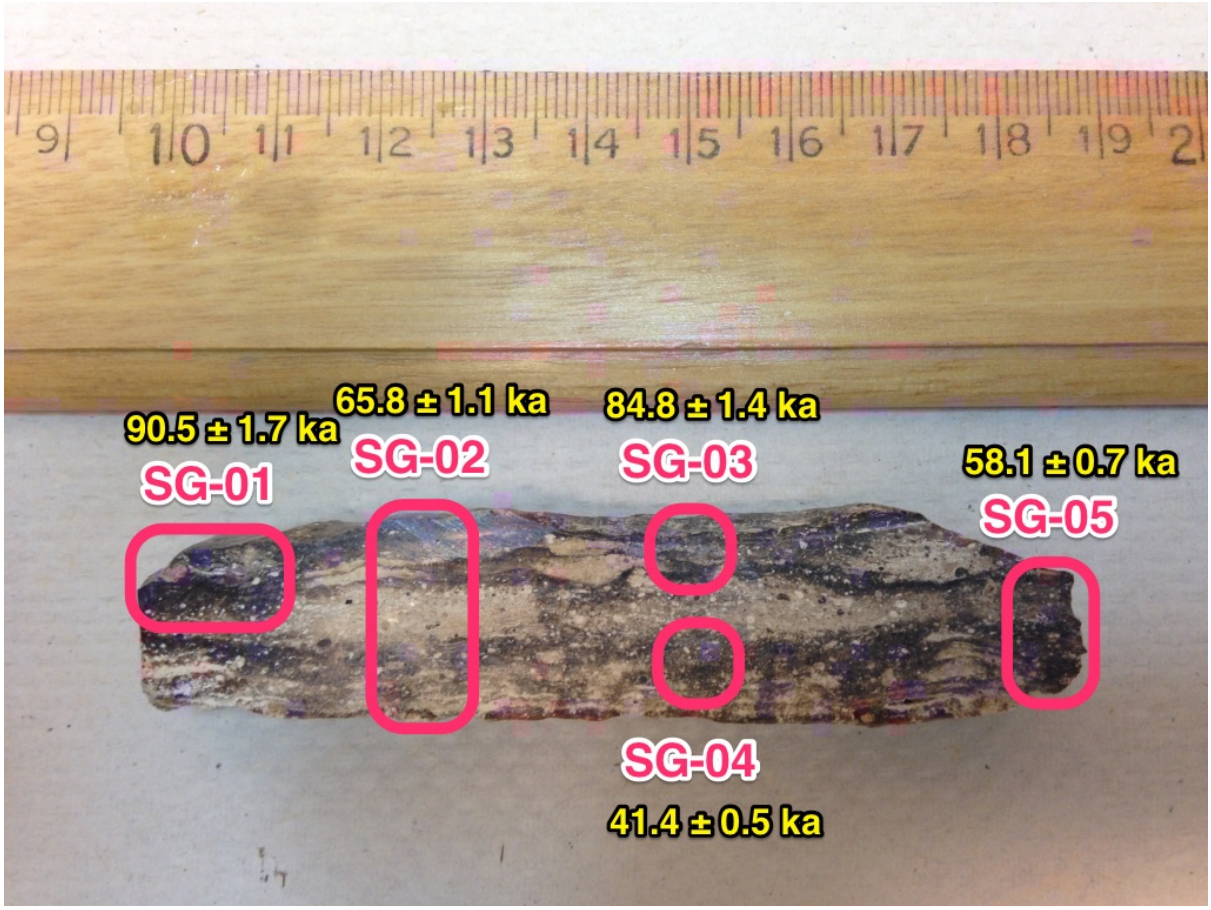

Figure 165. The subsampling locations and calculated ages of Samples SG-01 to SG-05 on the bar sampled from the original grey speleothem block.

4.4.3. Hydroxylapatite

The uranium-series dating results for the hydroxylapatite samples are presented in Table 28.

Table 28. List of uranium-series analysis results for the hydroxylapatite samples.

Sample	[^{238}U] ppm	±	[^{232}Th] ppm	±	(^{234}U / ^{238}U)	±	(^{230}Th / ^{234}U)	±
Sample 06	4.3453	0.0191	0.3842	0.0070	1.029	0.007	0.810	0.011
Sample 15	11.1702	0.0553	0.9012	0.0049	0.980	0.008	0.970	0.008
Sample 20	10.2187	0.0495	1.7574	0.0147	1.064	0.010	1.106	0.014
Sample 28	13.7473	0.0602	2.5081	0.0268	1.038	0.009	1.061	0.012
Sample 44	9.6902	0.0278	1.9942	0.0213	1.059	0.005	1.124	0.011

Sample	(^{230}Th / ^{238}U)	±	(^{230}Th / ^{232}Th)	±	Age (ka)	±
Sample 06	0.834	0.011	28.812	0.635	178.8	6.1
Sample 15	0.952	0.008	36.046	0.313	415.4	47.8
Sample 20	1.177	0.013	20.911	0.274	2290.6	798.1
Sample 28	1.101	0.011	18.444	0.260	949.3	192.7
Sample 44	1.190	0.012	17.678	0.253	2987.3	847.9

Compared to the grey speleothem samples. the hydroxylapatite ones are much richer in uranium-238. The poorest hydroxylapatite specimen, Sample 06, has a concentration that is still almost twice as much that of the richest grey speleothem specimen, Sample SG-06 (4.35 ppm for the former versus 2.40 ppm for the latter).

The closest points of comparison for the hydroxylapatite samples would be D6, a hydroxylapatite sample previously tested in (Ghaleb *et al.*, 2012) that is also of authigenic origin, as well as a number of human fossils from the cave, consisting of biogenic hydroxylapatite and dated via uranium-series in (Détroit *et al.*, 2004).

The uranium-238 concentrations in the human fossils range from 0.56 to 2.88 ppm, which are lower than the hydroxylapatite samples (Figure 166). This difference in scale may be due to the structure of the hydroxylapatite samples, essentially sedimentary, as opposed to that of the fossils, consisting of bone. With its more compact structure, bone may be less susceptible

to exchanges with its environment than sediment (although they do not always represent closed systems—bone is known to undergo uranium uptake).

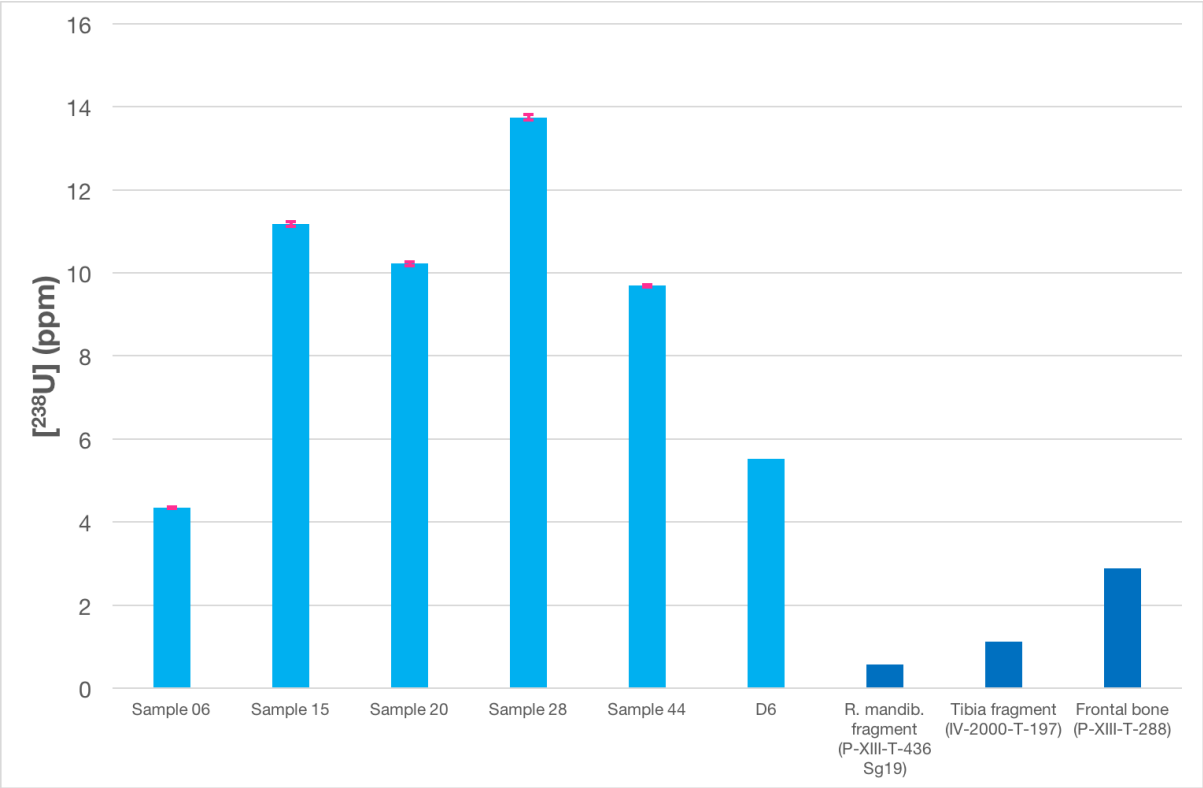

Figure 166. Uranium-238 concentrations (in ppm) in the hydroxylapatite samples (authigenic hydroxylapatite; in light blue) compared with those in the human fossils (biogenic hydroxylapatite; in dark blue). Data for the human fossils come from (Détroit *et al.*, 2004), while data for D6 come from (Ghaleb *et al.*, 2012).

$^{234}U/^{238}U$

Figure 167 presents the activity ratios of uranium-234 to uranium-238 in the hydroxylapatite samples and in the human fossils. The former are closer to secular equilibrium (($^{234}U/^{238}U$) = 1) than the latter, but given their sedimentary nature and their mineralogical history, it is difficult to justify this state as being the natural product of undisturbed radioactive behaviour; rather, it is more likely to be the result of continuous enrichment and leaching.

Sample 15 is exceptional in that its activity ratio falls below 1—this could be a stark example of enrichment in uranium-238, thereby driving the activity ratio down.

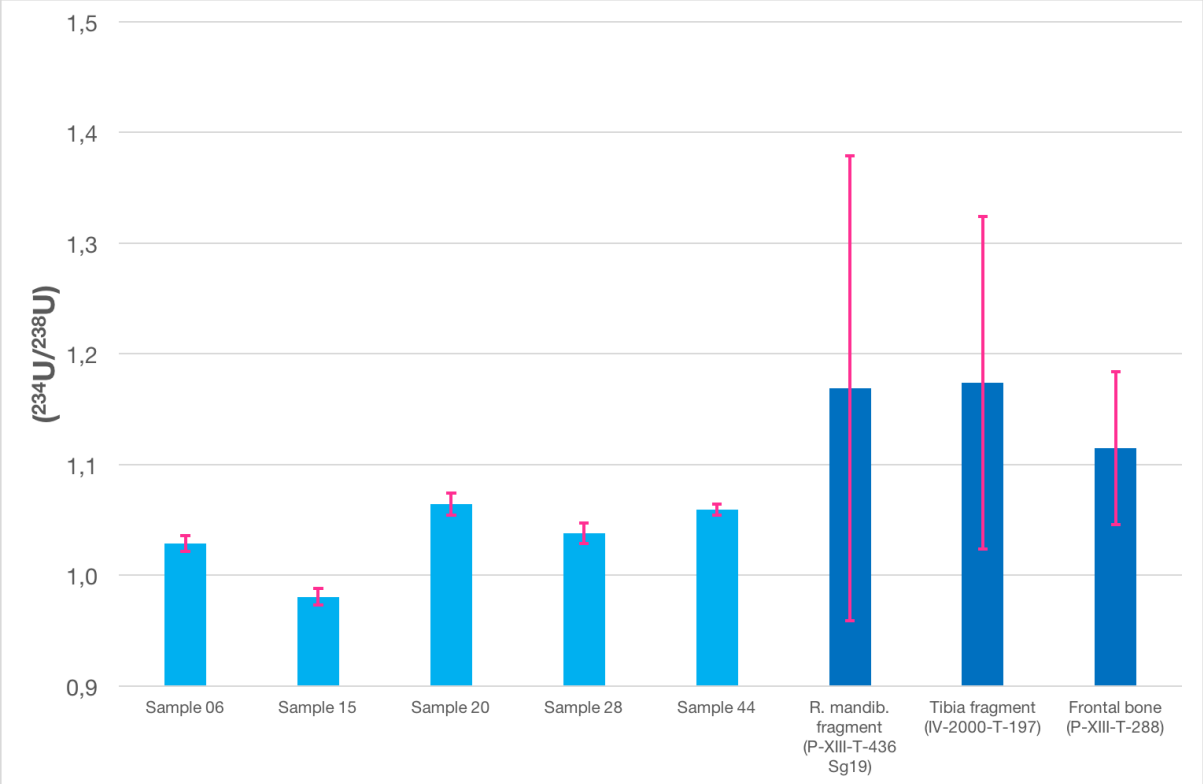

Figure 167. Uranium-234 to uranium-238 activity ratios of the hydroxylapatite samples (in light blue) compared with those of the human fossils (in dark blue).

$^{230}Th/^{234}U$

In terms of the thorium-230 to uranium-234 activity ratios this time, the hydroxylapatite samples again hover around secular equilibrium ($(^{230}Th/^{234}U) = 1$) whereas the fossils have more pronounced uranium-234 activity, pulling the ratios down (Figure 168).

It is possible that the thorium-230 activity in the hydroxylapatite samples is due to contamination by detrital thorium, composed of thorium-232, thorium-230, and other isotopes. This would be supported by the high concentrations in thorium-232 (Figure 169).

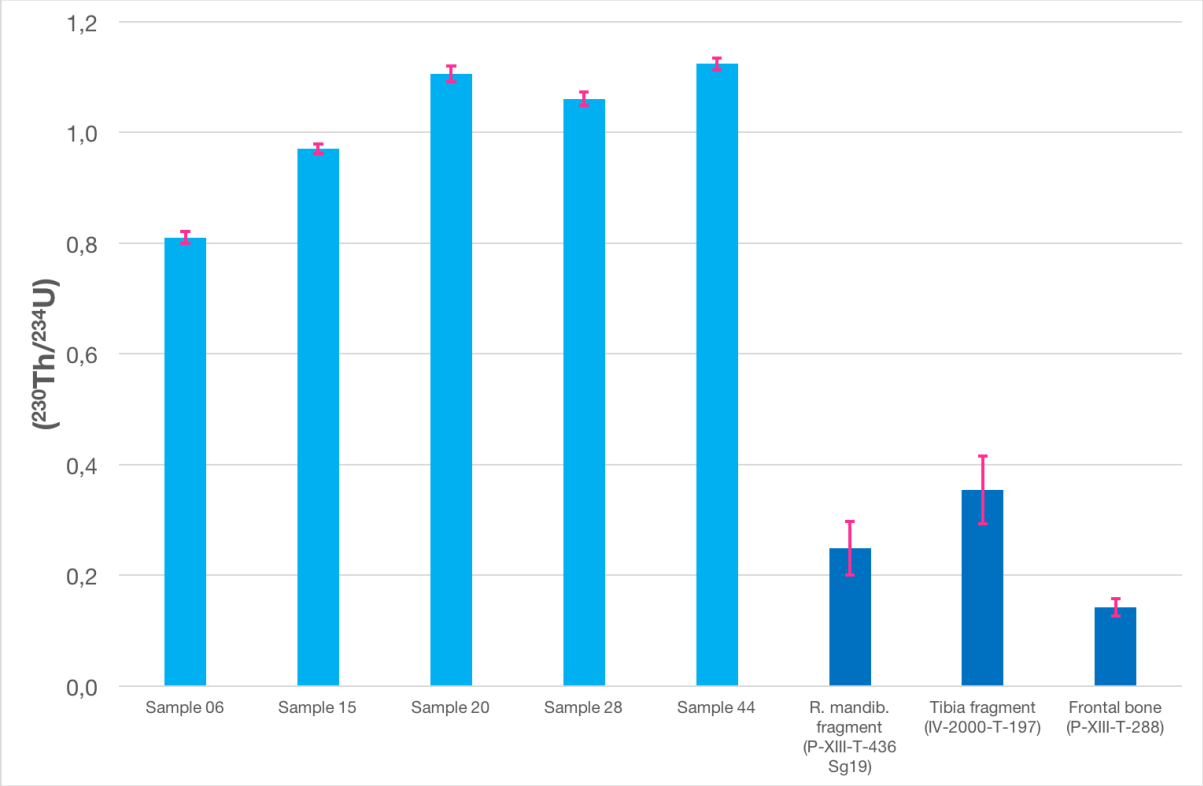

Figure 168. Thorium-230 to uranium-234 activity ratios of the hydroxylapatite samples (in light blue) compared with those of the human fossils (in dark blue).

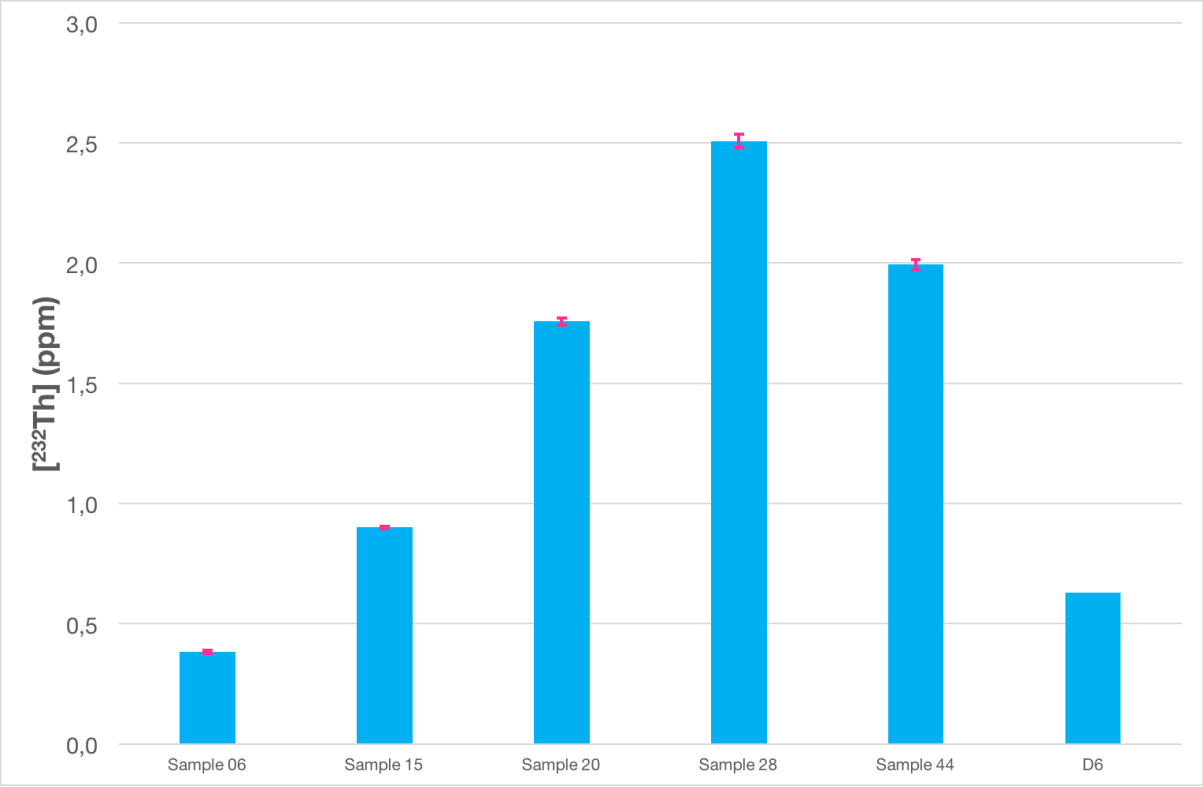

Figure 169. Thorium-232 concentrations (in ppm) in the hydroxylapatite samples.

$^{230}Th/^{232}Th$

The thorium-230 to thorium-232 activity ratios in the hydroxylapatite samples are quite low, and two of them barely make the minimum viable value of 20 (Figure 170). For comparison, the fossils have ratios of at least around 50. The best-dated fossil, the frontal bone, has a ratio of more than 100 (Dizon *et al.*, 2002). The data strongly suggest the introduction of detrital thorium after formation, which is again not surprising given the porous, sedimentary nature of the hydroxylapatite samples as well as their mineralogical evolution.

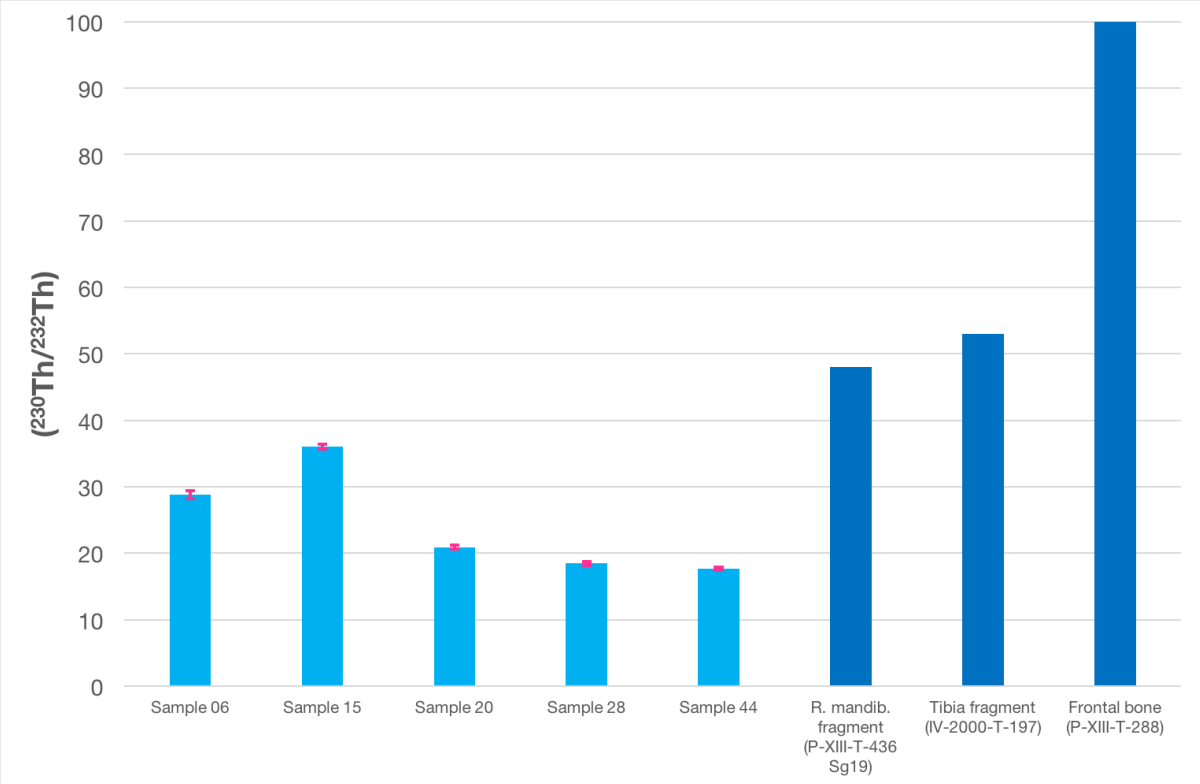

Figure 170. Thorium-230 to thorium-232 activity ratios of the hydroxylapatite samples (in light blue) compared with those of the human fossils (in dark blue).

Ages

The ages for Samples 20, 28, and 44 are purely theoretical and should be rejected outright, since they exceed the technical limits of the method (500 ka). It is worth noting that these same three samples have the highest thorium-232 concentrations. As for Samples 06 and 15, the respective calculated ages of 178.8 +6.1/–5.8 and 415.4 +47.8/–33.0 ka are very far apart (a difference of around 240 ka), but the lower thorium-232 concentration of Sample 06 suggests that it is less contaminated and may therefore be closer to the true age of the layer. Including the previously studied sample D6 in the analysis shows that Sample 06 is the closest specimen

to it in terms of both uranium-238 and thorium-232 concentration (Figure 171). Their calculated ages are also closer to each other than to any of the other samples (Figure 172).

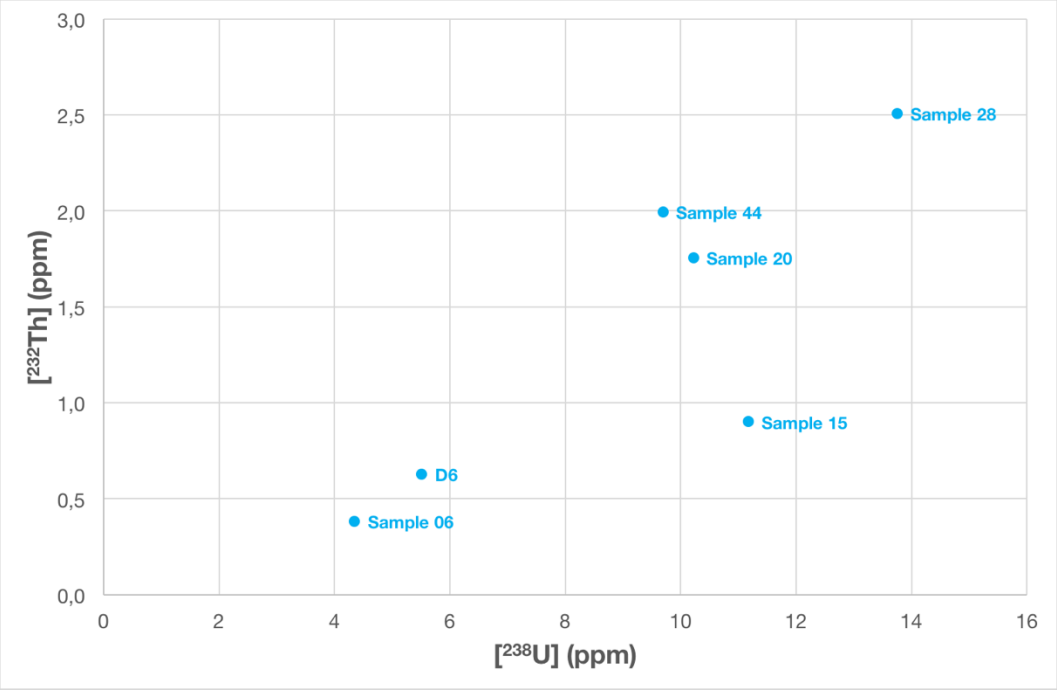

Figure 171. Uranium-238 versus thorium-232 concentrations in the hydroxylapatite samples.

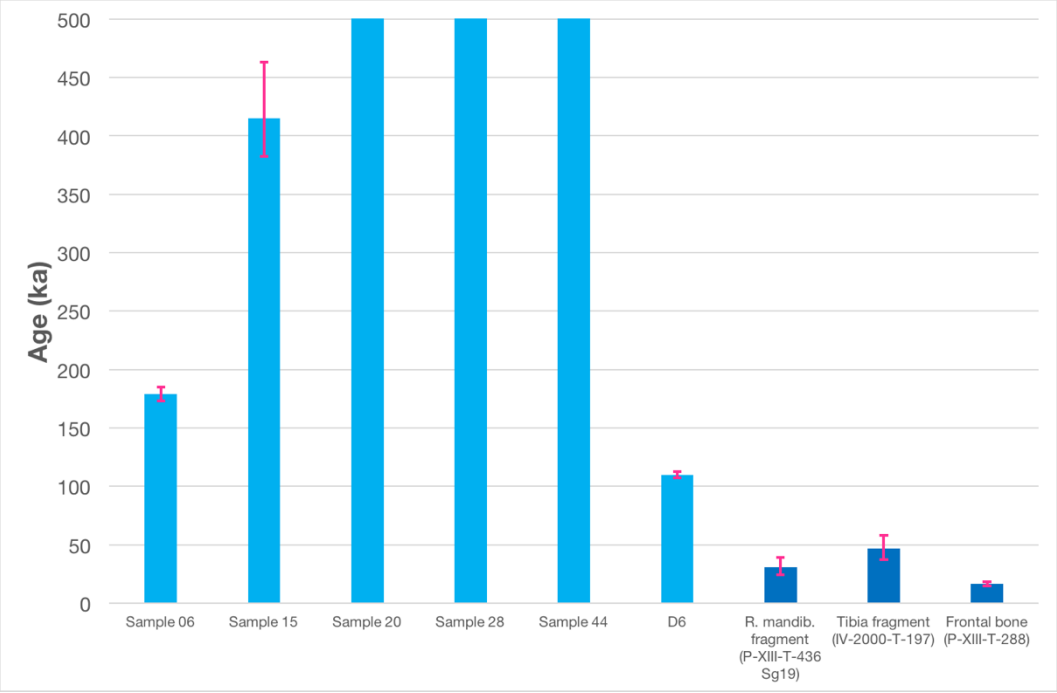

Figure 172. Calculated uranium-series ages of the hydroxylapatite samples (in light blue) compared with those of the human fossils (in dark blue).

4.4.4. The yellow speleothem

Compared to the other sample types, gypsiferous Sample 16 from the yellow speleothem is very poor in uranium-238 (0.17 ppm). Nevertheless, this is still higher than the values obtained by Lewis *et al.* (2008) on U-Th1 and U-Th2, two other gypsum samples from the cave (Figure 173).

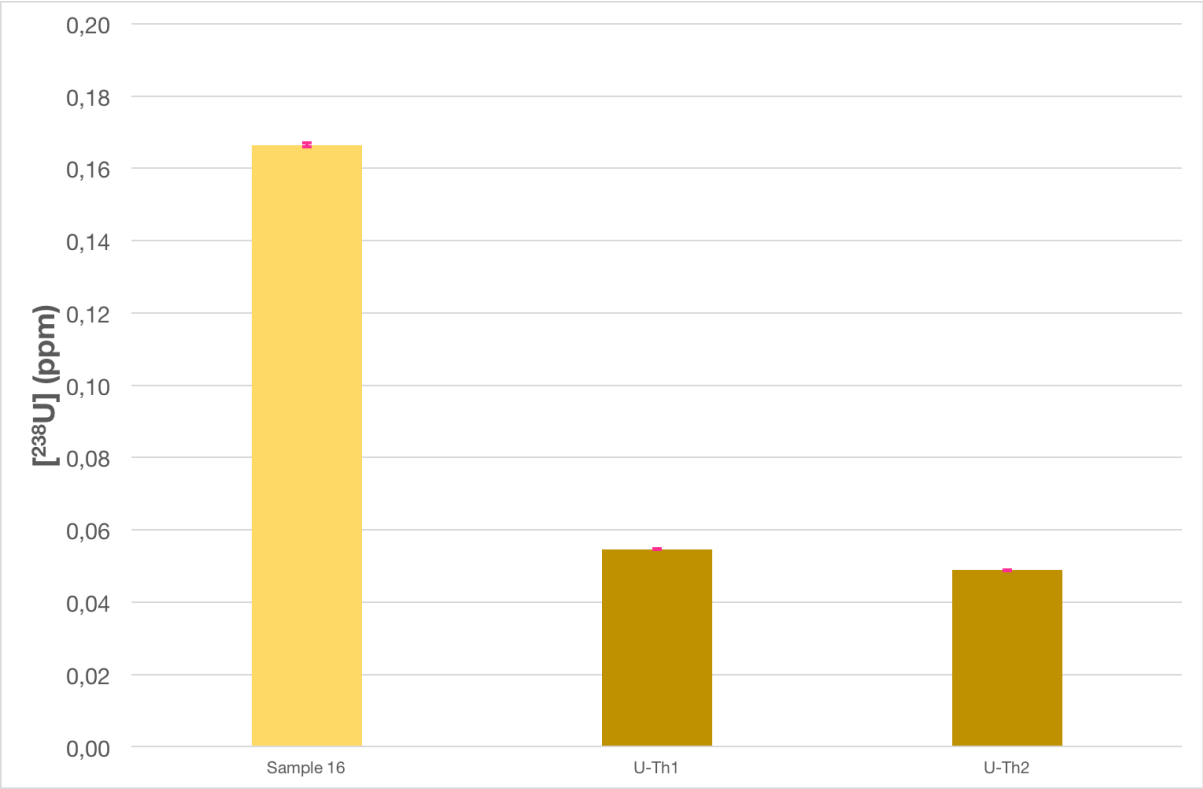

Figure 173. Uranium-238 concentration (in ppm) in the gypsum sample analyzed for this study (Sample 16; in light yellow), compared with those in the gypsum samples analyzed by Lewis *et al.* (2008) (U-Th1 and U-Th2; in dark yellow).

There is also a vast difference in the thorium-232 concentrations. The Lewis samples are about three orders of magnitude smaller, necessitating the use of a logarithmic scale for plotting (Figure 174).

The thorium-230 to uranium-238 activity ratios show that fractionation is relatively weak in Sample 16. In U-Th1 and U-Th2, however, the very low values indicate high fractionation and high uranium activity (Figure 175).

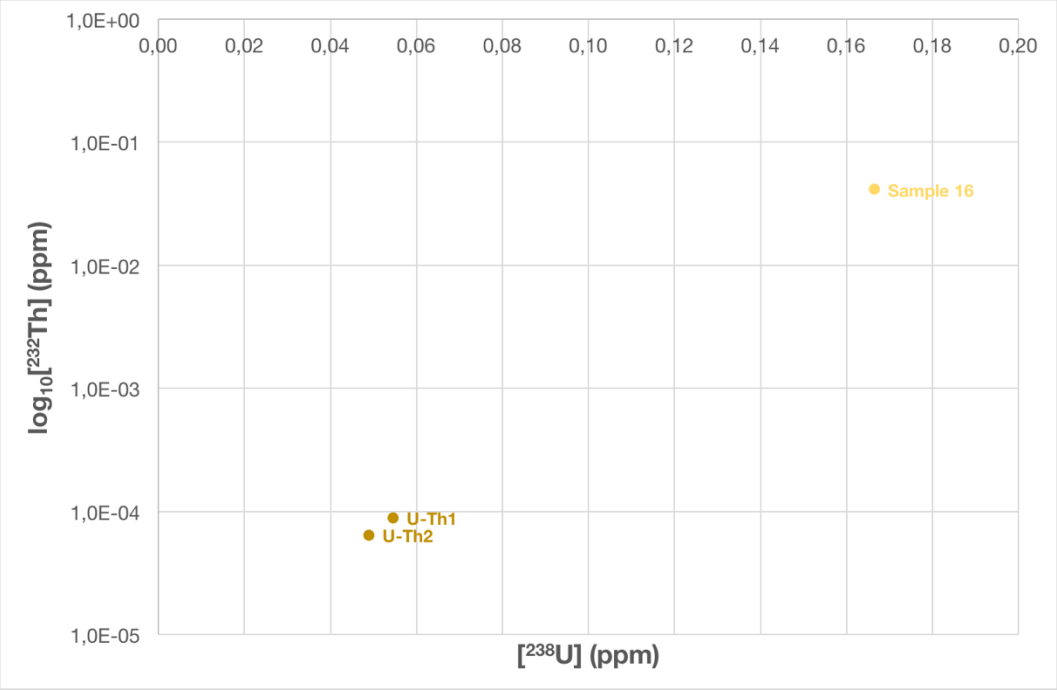

Figure 174. Uranium-238 versus thorium-232 concentrations in the gypsum sample analyzed for this study (Sample 16; in light yellow), compared with those in the gypsum samples analyzed by Lewis *et al.* (2008) (U-Th1 and U-Th2; in dark yellow).

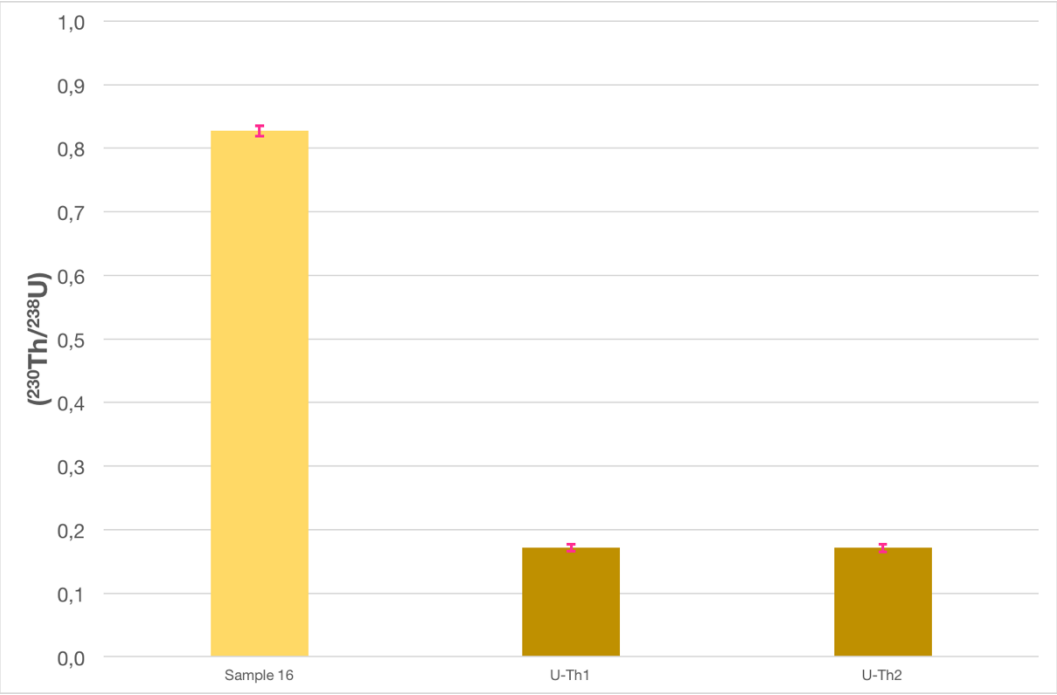

Figure 175. Thorium-230 to uranium-238 activity ratios of the gypsum sample analyzed for this study (Sample 16; in light yellow), compared with those in the gypsum samples analyzed by Lewis *et al.* (2008) (U-Th1 and U-Th2; in dark yellow).

Looking at the thorium-230 to thorium-232 activity ratios, the very low value for Sample 16 (< 20) suggests a strong influence from thorium-232, whereas U-Th1 and U-Th2 have very high values that suggest that the samples may be viable for dating in this regard (Figure 176).

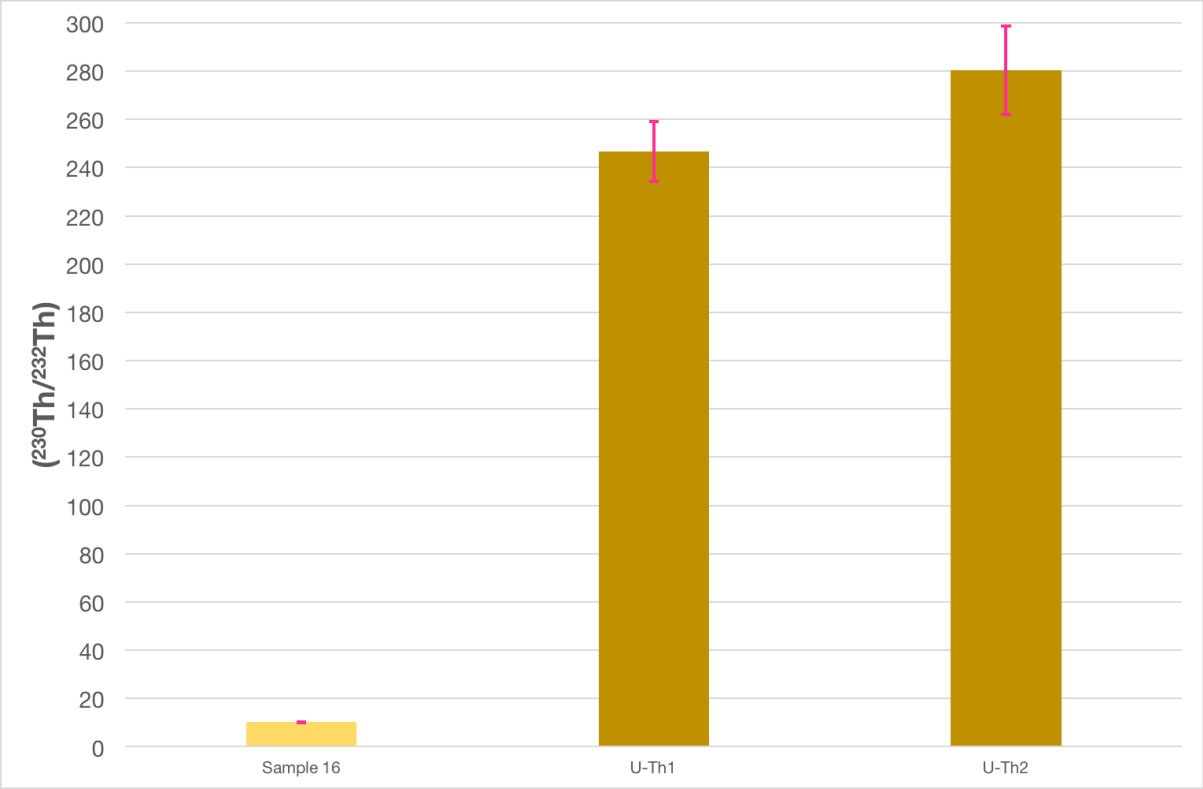

Figure 176. Thorium-230 to thorium-232 activity ratios of the gypsum sample analyzed for this study (Sample 16; in light yellow), compared with those in the gypsum samples analyzed by Lewis *et al.* (2008) (U-Th1 and U-Th2; in dark yellow).

Finally, the calculated ages are very far apart. Sample 16 returned a value of 188.2 +5.5/–5.2 ka, while U-Th1 and U-Th2 are around 20 ka (Figure 177).

The uranium-series dating results for Sample 16 and the two reference samples U-Th1 and U-Th2 are presented in Table 29.

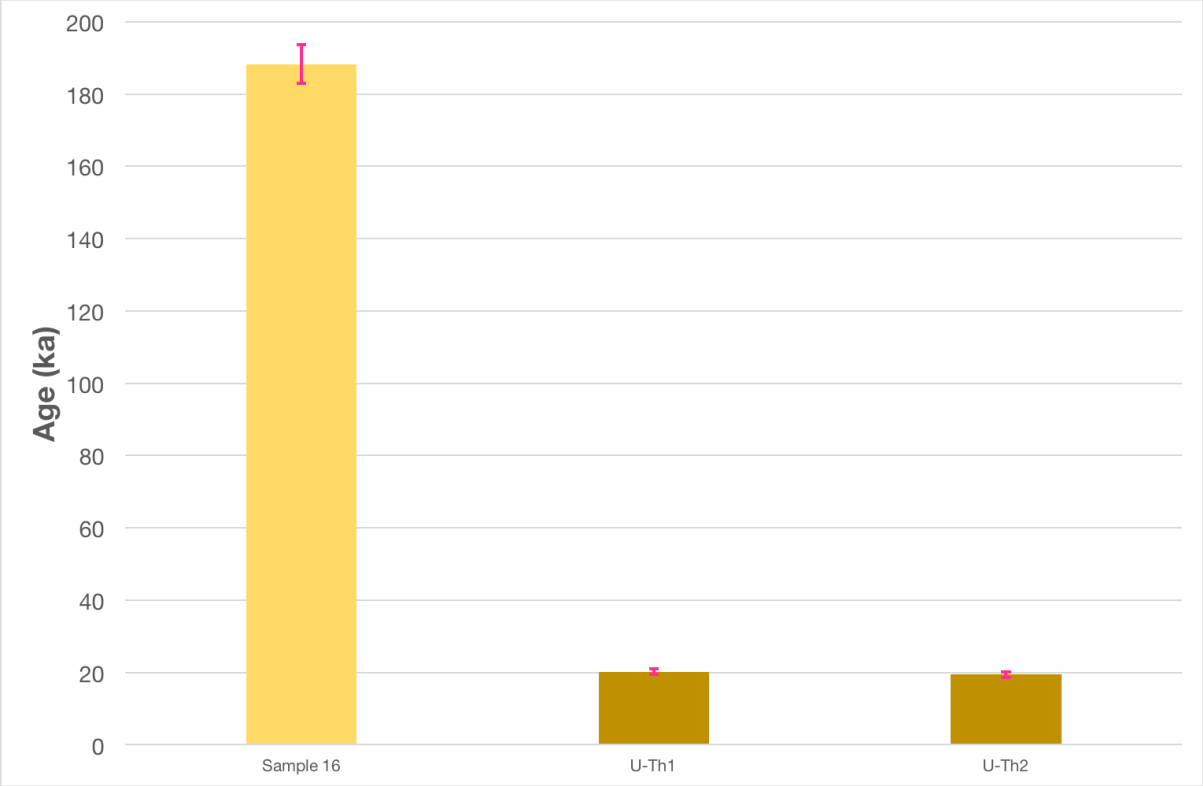

Figure 177. Calculated uranium-series ages of the gypsum sample analyzed for this study (Sample 16; in light yellow), compared with those in the gypsum samples analyzed by Lewis *et al.* (2008) (U-Th1 and U-Th2; in dark yellow).

Table 29. List of uranium-series analysis results for Sample 16 and the two reference samples from Lewis *et al.* (2008), U-Th1 and U-Th2.

Sample	[^{238}U] ppm	±	[^{232}Th] ppm	±	(^{234}U / ^{238}U)	±	(^{230}Th / ^{234}U)	±
Sample 16	0.1665	0.0005	0.0411	0.0003	1.031	0.005	0.802	0.008
U-Th1	0.0546	0.0001	0.000089	0.000003	-	-	-	-
U-Th2	0.0489	0.0001	0.000064	0.000004	-	-	-	-

Sample	(^{230}Th / ^{238}U)	±	(^{230}Th / ^{232}Th)	±	Age (ka)	±
Sample 16	0.827	0.008	10.234	0.123	188.2	5.5
U-Th1	0.1715	0.0055	246.7	12.4	20.2	0.8
U-Th2	0.1711	0.0057	280.3	18.2	19.4	0.8

Chapter V

Discussion

5.1. Stratigraphy and deposit formation

Based on re-evaluation of the stratigraphic profiles presented in this study and concurrent review of the different analytical results obtained, broad patterns in the stratigraphy of Tabon Cave can be drawn, based in particular on the formation and evolution of its diverse deposits.

In Section 2.2.2, the following threefold division of the cave was presented:

- the North Zone, covering transects S1 to S4;
- the Central Zone, covering transects S6 to S10; and
- the South Zone, covering transects S14 to S18.

These zones are once again shown in Figure 178. The North and Central Zones together form the front half of the cave, while the South Zone represents the back half.

The back half is characterized by a relatively straightforward and apparently intact sequence of original deposition, making it the best area for understanding the physical formation of the cave deposits. The stratigraphy of the front half, however, remains difficult to define despite the number of available vertical profiles: highly heterogeneous changes in all three dimensions due to a complex geochemical history as well as reworking make the profiles perplexing to stitch together. Their unification remains a key research goal for the site due to the significant archaeological importance of this part of the cave. However, through identification of common, characteristic layers, connections can be established across the different squares. These 'flags' are a useful tool for guiding the presentation and discussion of the complex deposits in Tabon Cave.

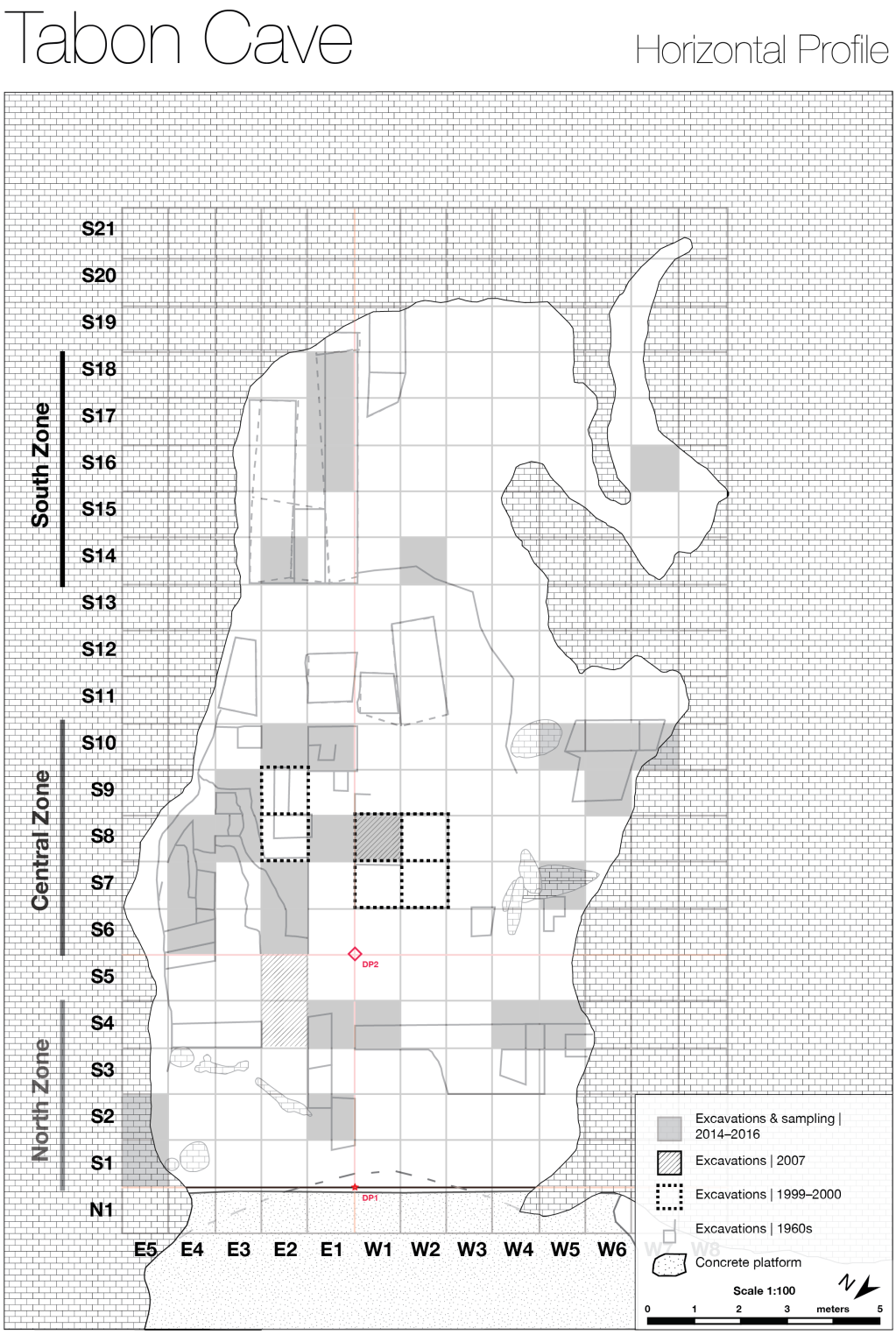

Figure 178. The three zones of Tabon Cave, previously defined in Section 2.2.2.

5.1.1. Back half (South Zone)

The South Trench vertical profile is once again presented in Figure 179.

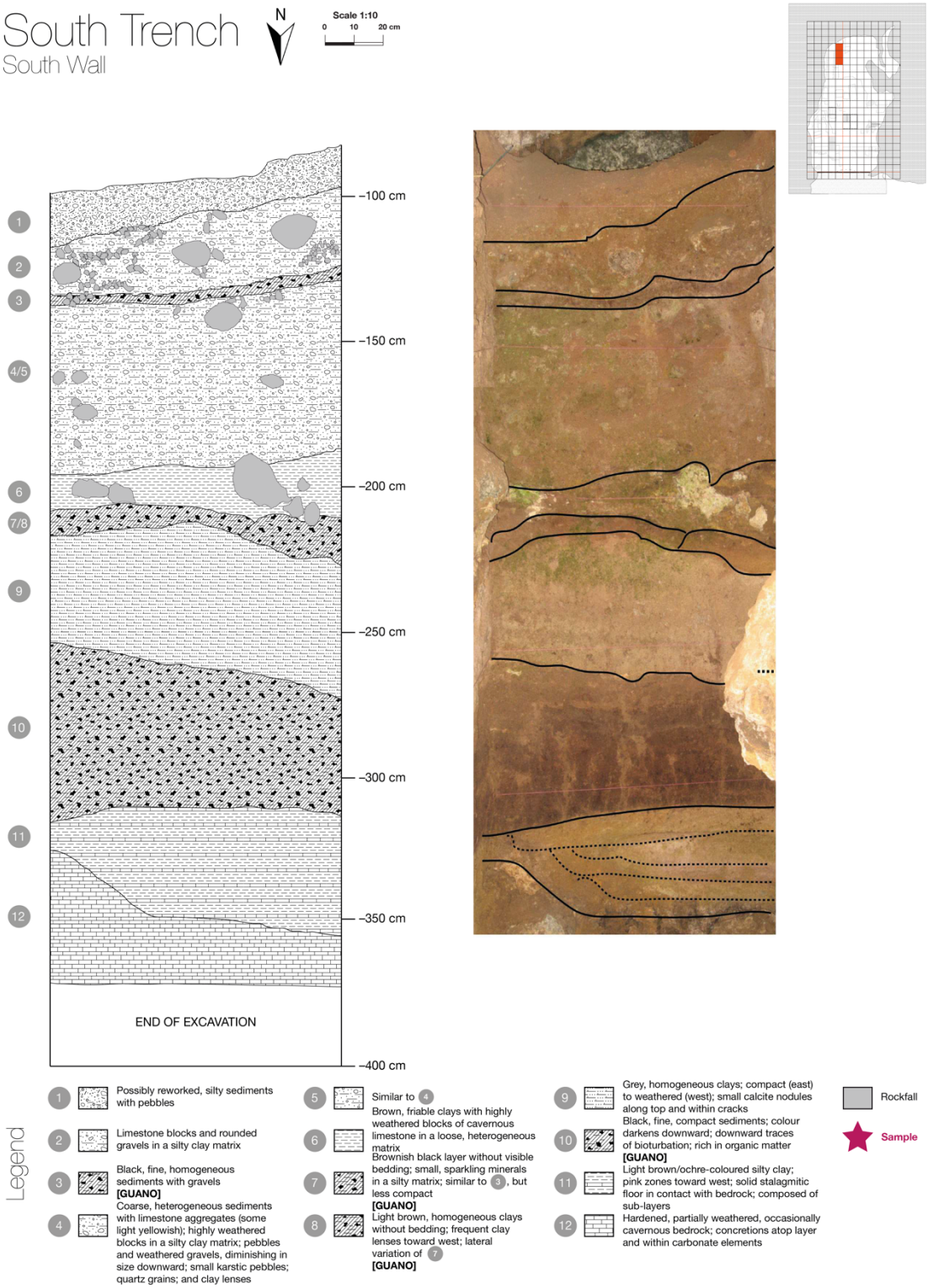

Figure 179. The vertical profile of the South Trench, previously presented in Section 2.2.2.

Five characteristic deposits can be identified in the profile:

- Layer 2: limestone blocks/rockfall
- Layer 3: guano
- Layer 6: limestone blocks/rockfall
- Layers 7/8: guano
- Layer 10: guano

The three guano deposits would have formed during periods when bats/birds occupied the cave, with the thick 40 to 60 cm of Layer 10 representing the oldest and longest period of continuous occupation. Each guano deposit stops accumulating at a given point in time to be overlain by the next deposit. For Layers 7/8 and 3 (the two upper guano deposits), the limestone blocks that constitute their overlying layers 6 and 2 could hold the explanation: these may correspond to natural rockfall events that occurred during phases of karstic activity, possibly triggered by increased precipitation. This would be coherent with the documented presence of karstic pebbles in a sedimentary layer at around 220 cm below DP in nearby Square S14W2, roughly equivalent to Layer 6 in the South Trench after accounting for a slight downward slope toward the cave entrance (Figure 180).

For Layer 9, which overlies the guano of Layer 10, the cave was abandoned for reasons that are less evident. This almost equally thick deposit (40 to 50 cm) has a fine grain-size composition (roughly 80% silt and 20% clay) and is very well sorted). Its mineralogical profile consists primarily of quartz, accompanied by some aluminium and potassium phosphates (variscite, tinsleyite, crandallite). The dominance of quartz suggests a physical origin (as opposed to chemical), while the high proportion of silt-sized grains points to deposition by wind or water transport at moderate current speeds (Miskovsky and Debard, 2002: 498)—consistent with the overall parabolic nature of the grain-size cumulative distribution curve. After deposition, Layer 9 likely experienced auxiliary chemical influence from the underlying guano of Layer 10, as evidenced by the weak presence of authigenic phosphate minerals.

Figure 180. The karstic pebbles from the sedimentary layer (highlighted) in Square S14W2.

Moving west, the neighbouring diverticulum was initially investigated to uncover potential links with the South Trench deposits, notably as a source of material for their formation. Sample 30, collected from the surface of this small chamber, has visual and textural similarities to clayey sediment that was thought to be permeate the South Trench profile. While it does contain illite (a clay mineral, identified in FTIR but not in XRD), it is overwhelmingly characterized by [carbonate-rich] hydroxylapatite, as well as some whitlockite (bearing calcium and magnesium) and variscite (bearing aluminium)—all authigenic phosphate minerals. The assemblage also suggests influence from guano, which is confirmed by the current presence of a bat colony in this small chamber.

The mineralogical characterization results presented in Section 4.2.3 showed that Sample 30 shares similarities with the samples from the base of the South Trench—namely, A, MM1, and

B, from Layers 10 (guano) and 11 (stalagmitic floor in contact with bedrock). The assemblages correspond to the interaction of guano with the host rock of the cave (Wurster *et al.*, 2015). The calcium-magnesium phosphate mineral whitlockite ($Ca_9Mg(PO_3OH)(PO_4)_6$) in particular seems to be concentrated in zones where this interaction occurs: it is present in the diverticulum (Sample 30), in Layer 10 (Sample B), and at the interface of Layers 10 and 11 (Sample MM1), but was never identified elsewhere in the cave.

While the deposits in the diverticulum and those at the bottom of the South Trench have much in common, they are also marked by two major differences: their age gap (the diverticulum deposits having been constituted by the present-day bat colony inside), and the presence of iron and potassium phosphate minerals (mitridatite, taranakite) in the South Trench deposits. These are products of increased acidity due to a more active hydrological regime, facilitating the leaching of phosphate ions from guano into the cave environment. The higher pH causes the breakdown of clay minerals, releasing iron, aluminium, and other elements into the cave environment, where they interact with the guano phosphate ions to form new authigenic minerals (Weiner *et al.*, 2002; Shahack-Gross *et al.*, 2004). The diverticulum can thus be considered a 'laboratory' for studying the early geochemical evolution that took place at the base of the South Trench, prior to the advent of more acidic conditions.

5.1.2. Front half (North and Central Zones)

In the front half of the cave, two main stratigraphic markers distributed across various squares can be established:

- the 'light-on-dark' sequence, and
- the yellow speleothem.

The 'light-on-dark' sequence

In Square S6E2, a characteristic weathering sequence generally composed of two bands (with occasional variations) has previously been studied (Choa *et al.*, 2016). The lower band corresponds to a fossil guano layer of dark, brownish/reddish black colour, while the upper band is a light, greyish/bluish white phosphate layer. In the vertical profile for Squares S6E2 to S7E2, this 'light-on-dark' sequence corresponds to Layers 9 and 10 (Figure 181).

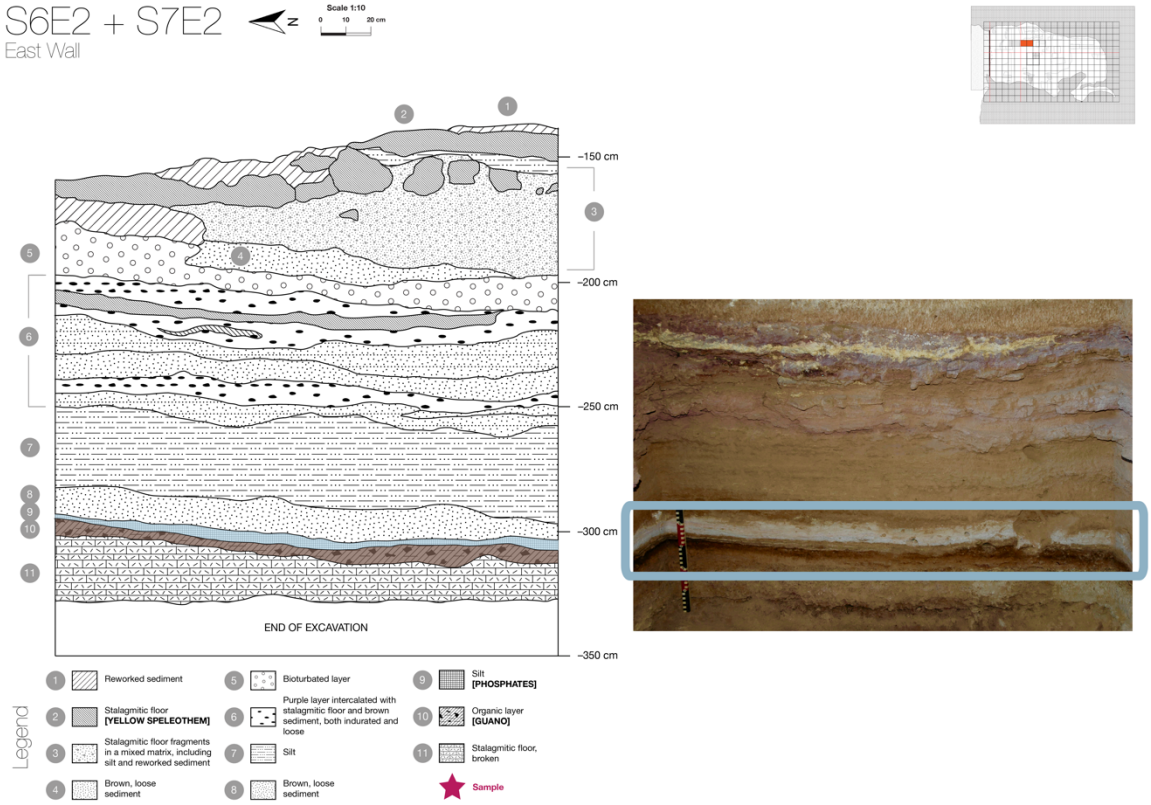

Figure 181. The East Wall vertical profile for Squares S6E2 to S7E2. The 'light-on-dark' weathering sequence (highlighted) corresponds to Layers 9 and 10.

The sequence can be found in several neighbouring squares. Figure 182 shows the proposed correspondences between the light and dark layers across these squares. The squares are plotted in Figure 183 and appear to be concentrated in the eastern part of the cave.

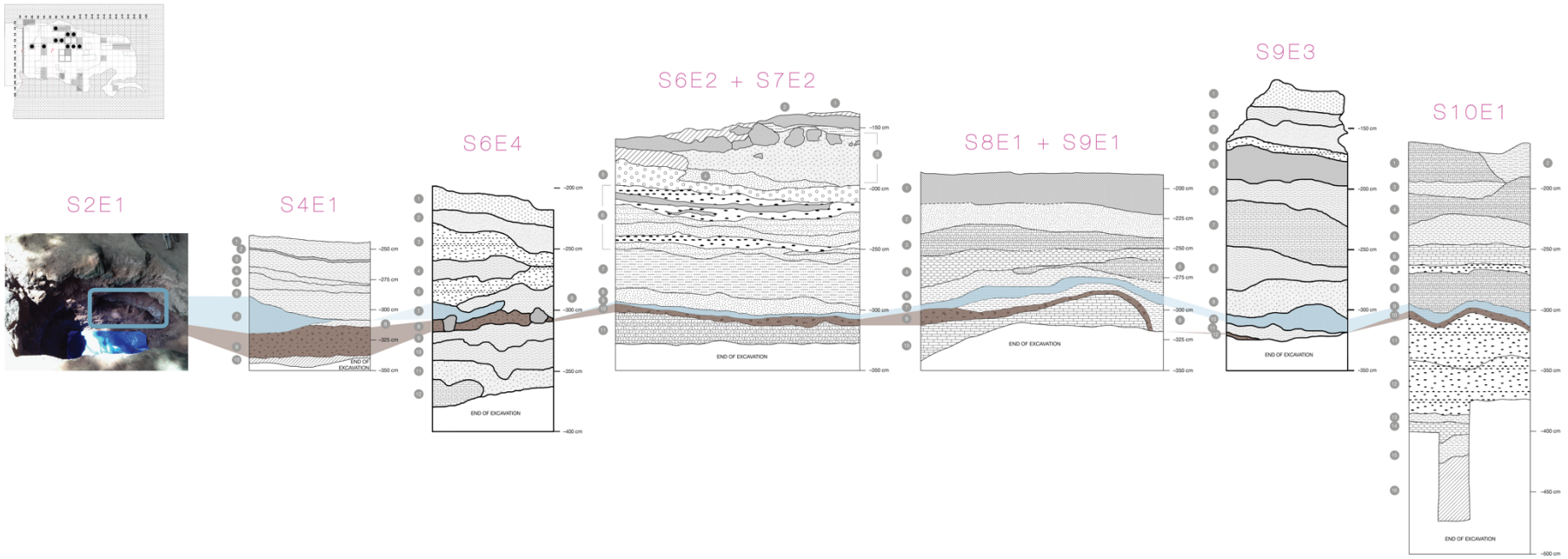

Figure 182. Proposed correspondences between the two layers of the 'light-on-dark' sequence across different squares. For detailed profile descriptions, please refer to Section 2.2.2.

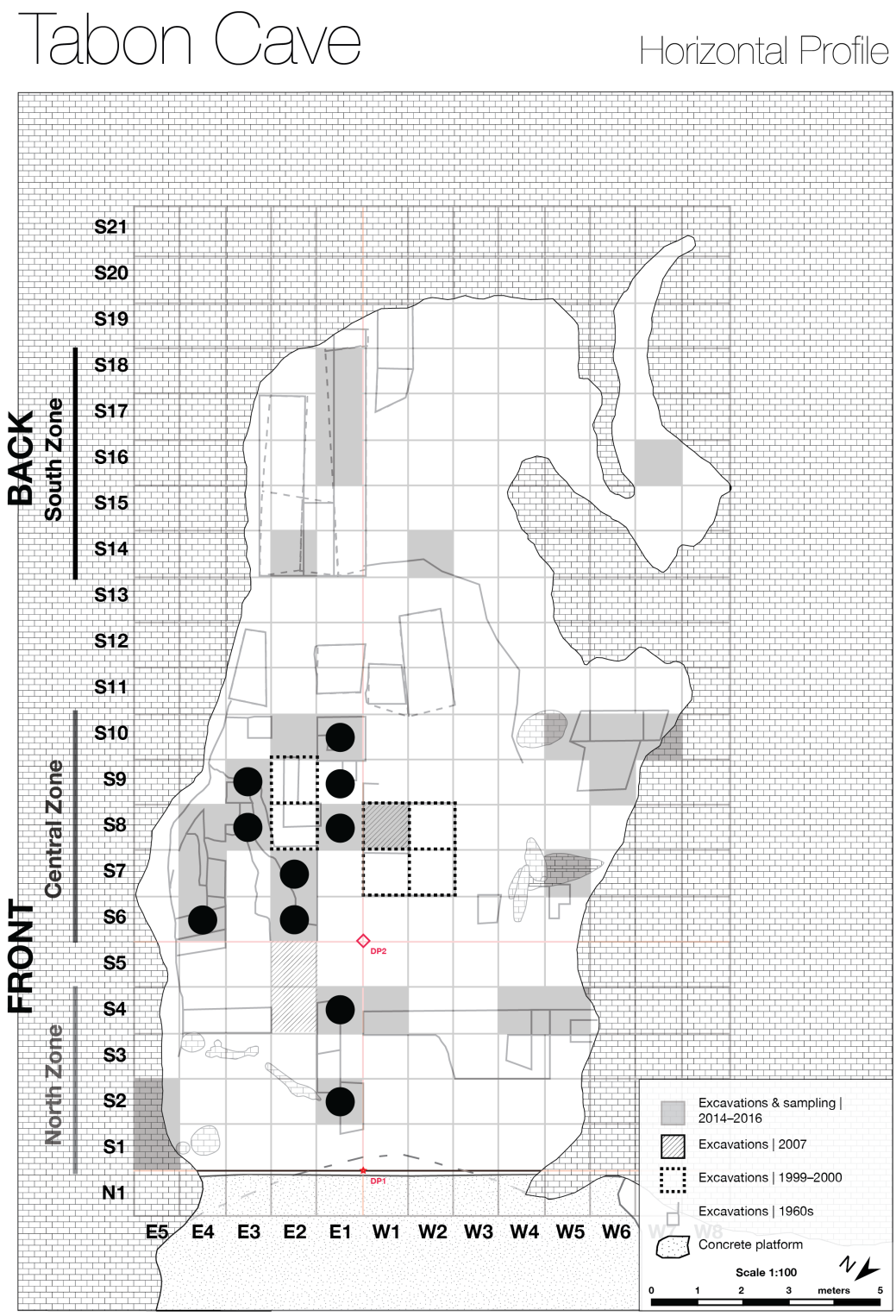

Figure 183. The Tabon Cave horizontal profile. The black circles indicate the identified presence of the 'light-on-dark' weathering sequence.

Table 30 recapitulates the proposed equivalencies between the light and dark layers across the relevant squares. Based on the layer depths, the sequence seems to have its peak at the centre of the cave and slopes down in all directions at varying angles except to the west, where its presence was not recorded and its behaviour unknown.

Table 30. Proposed correspondences between the two layers of the 'light-on-dark' sequence across different squares in the front half of the cave. For Square S2E1, since no vertical profiles are available, the layer depths are instead represented by those of the samples collected from them.

Square(s)	Light layer	Min. depth (cm DP)	Max. depth (cm DP)	Dark layer	Min. depth (cm DP)	Max. depth (cm DP)
S10E1	9	–290	–315	10	–298	–318
S8E1 to S9E1	7	–275	–300	9	–285	–318
S9E3	10	–295	–320	12	–320	–325
S6E2 to S7E2	9	–292	–318	10	–295	–315
S6E4	7	–292	–310	8	–300	–318
S4E1	7	–288	–320	9	–312	–340
S2E1	-	(–337)	(–337)	-	(–367)	(–367)

From a mineralogical perspective, the light and dark layers have relatively distinct profiles, even if they share many minerals in common (Table 31). Looking at the light layers first, with the notable exception of Sample 25, the samples are very strongly dominated by carbonate-rich hydroxylapatite. Traces of other phosphates are also present (brushite, variscite, vivianite), as well as some quartz. The dark layers are much more diverse: dominant minerals include crandallite, mitridatite, variscite, and leucophosphite, and Sample 7 even has chitin. Sample 25, collected from the light layer in Squares S6E2 to S7E2, is notable in that its mineralogical profile is actually much closer to those found in the dark layers, in particular that of Sample 19 from Squares S8E1 to S9E1.

Table 31. Mineralogical profiles of samples from the 'light-on-dark' sequence. The mineral nomenclature follows the one used in Section 4.2: CHAP (carbonate-rich hydroxylapatite), HAP (hydroxylapatite), BR (brushite), CR (crandallite), VR (variscite), LC (leucophosphite), VV (vivianite), MT (mitridatite), SC (sarcolite), MM (montmorillonite), OP (opal), QZ (quartz), and CT (chitin). The estimated concentrations also follow the same convention defined in Section 4.2: xxx (strong), xx (average), and x (weak).

Square(s)	Light layer sample	Depth (cm DP)	Mineralogy	Dark layer sample	Depth (cm DP)	Mineralogy
S10E1	-	-	-	X9	–300	CR (xxx), MT (xxx), VR (xx), CHAP (x), LC (x), QZ (x)
S8E1 to S9E1	-	-	-	19	–300	VR (xxx), CHAP (xx), BR (xx), LC (xx), QZ (xx)
S8E3	44 (projected onto S9E3)	–305	CHAP (xxx), VR (x), QZ (x)	45 (projected onto S9E3)	–325	LC (xxx), HAP(xx), OP (xx), VR (x / xx), QZ (x / xx)
S6E2 to S7E2	25	–310	VR (xxx), CHAP (xx), BR (xx), LC (xx), OP (xx), QZ (x)	-	-	-
S6E4	28	–307	CHAP (xxx), VR (x), QZ (x)	-	-	-
S4E1	15	–300	CHAP (xxx), BR (x), VR (x), VV (x)	-	-	-
S2E1	6	–337	CHAP (xxx), BR (x), VR (x), VV (x), SC (x), QZ (x)	7	–367	CT (xxx), CHAP (xx), BR (xx), VR (xx), QZ (xx), MM (x)

The light layers are consistently characterized by the ascendancy of carbonate-rich hydroxylapatite ($Ca_5(PO_4,CO_3)_3(OH,O)$). Hydroxylapatite ($Ca_5(PO_4)_3(OH)$) is one of the first phosphate minerals to form during guano diagenesis (Karkanas and Goldberg, 2010; Weiner, 2010). In karst contexts, it is due directly to the reaction of phosphates in bat guano with calcium in limestone (Onac and Veres, 2003). However, it can also result from the dissolution of bone or ash (Schiegl *et al.*, 1996; Karkanas *et al.*, 1999; Forbes and Bestland, 2006).

In archaeological caves, calcium and carbonate ions may be attributed to one or several of the following origins:

- **geogenic** – limestone (calcite/aragonite: $CaCO_3$) or dolomite (dolomite: $CaMg(CO_3)_2$), common constituents of karst structures;
- **biogenic** – shells (calcite/aragonite: $CaCO_3$) or bone (hydroxylapatite: $Ca_5(PO_4)_3(OH)$), transported via natural or anthropic means; and
- **pyrogenic** – ash (calcite: $CaCO_3$), due primarily to anthropic activities.

For the calcium carbonate polymorphs (calcite and aragonite), dissolution in water confers a pH of 8 on the resulting aqueous solution. Upon contact with large amounts of organic matter (e.g. food or excrement), the solution pH decreases from 8 to 7. The phosphate ions from the organic matter react with the calcium and are fixed in place, forming authigenic hydroxylapatite ($Ca_5(PO_4)_3(OH)$) (Weiner, 2010). In the case of bone, composed of biogenic hydroxylapatite, certain changes in environmental chemistry (including a decrease in pH, but generally not below 7) may provoke dissolution. This is followed by precipitation as authigenic hydroxylapatite in chemical equilibrium with geogenic hydroxylapatite, which has a more ordered crystal structure and a different stability field (Berna *et al.*, 2004; Weiner, 2010).

In contrast with the relative simplicity of the light layers, the dark layers host a complex interplay of aluminium, iron, potassium, calcium, and phosphate ions, representing an advanced state of diagenesis. The strong presence of crandallite in Square S10E1 is indicative of low phosphate concentrations (Weiner, 2010). This could be due to more significant leaching in this square compared to its neighbours. The intermediate-stage authigenic mineral had also begun losing calcium to give way to variscite and leucophosphite. Variscite, particularly dominant in Squares S8E1 to S9E1 and S6E2 to S7E2, is generally formed through

the interaction of phosphate-rich guano leachates with aluminium-rich clays or rock in an acidic environment (Onac and White, 2003; Onac *et al.*, 2004). However, it can also follow crandallite in a diagenetic sequence moving toward higher acidity (Weiner, 2010). Leucophosphite, another crandallite successor, is indicative of particularly severe diagenesis, and its association with opal in Square S8E3 is interesting as a possible indicator of the past presence of wood ash (Karkanas *et al.*, 2000). Leucophosphite forms with the onset of reducing conditions (exclusion of oxygen), allowing iron to enter the ferrous state and dissolve before combining with potassium and phosphate ions. However, iron switches to the ferric state upon the formation of leucophosphite, reversing conditions from reducing to oxidizing and consequently facilitating organic matter destruction (Karkanas *et al.*, 2000). Siliceous aggregates in ash are rich in iron and potassium and could be a source of these elements for the formation of leucophosphite. Other potential sources include bone and clays or rock.

The yellow speleothem

Aside from the 'light-on-dark' guano weathering sequence, horizontal speleothems are another key stratigraphic feature in the front half of the cave. They have previously been called 'stalagmitic floors' (e.g. in the vertical profiles established from field descriptions).

One of them in particular has been described by Fox as "a thick calcareous floor laminated with layers of hard travertine", and "which elsewhere in the cave may be traced as an ivory-colored layer" (Fox, 1970: 26–27). He describes the layer as being particularly compact, necessitating the use of crowbars and picks for removal. The indurated nature of the layer was confirmed during the 2007 excavations, when intact portions were removed; however, by the 2014 excavations, remaining outcrops in certain areas were observed to be friable, disintegrating into a fine powder (X. Gallet, *pers. comm.*). Lewis *et al.* (2008) were the first to pay closer attention to this speleothem: in the process of conducting uranium-series dating, they found that it was composed of gypsum and not calcite. Gypsum ($CaSO_4 \cdot 2H_2O$) is a sulphate mineral that forms in very acidic environments. In karstic areas, such conditions can be created by the degradation of insectivorous bat (and bird) guano; in this case, the presence of associated authigenic minerals like ardealite ($Ca_2(PO_3OH)(SO_4) \cdot 4H_2O$) and brushite ($Ca(PO_3OH) \cdot 2H_2O$) can be expected (Shahack-Gross *et al.*, 2004). Under oxidizing conditions (for example, during early decomposition of organic matter), microorganisms transform sulphur from organic compounds in guano to sulphate. The subsequent interaction of sulphate with calcium-rich

waters in this acidic environment then favours the crystallization of gypsum (Rinaudo and Abbona, 1988; Bird *et al.*, 2007; Dumitraş *et al.*, 2008). An alternative formation pathway would be cave water leaching of sulphuric acid, again produced by microbial action; the interaction of these acidic waters with limestone/dolomite in the form of bedrock or fallen stalactites could then also lead to the precipitation of gypsum (Onac and Forti, 2011).

The layer has a light yellow colour and is informally called the 'yellow speleothem' (Figure 184). Mineralogical characterization combined with re-evaluation of stratigraphic profiles in this study have enabled clearer horizontal and vertical delimitation of this important layer. It is spread over nearly the same area as the 'light-on-dark' sequence, although at higher altitudes (Figure 185 and Figure 186). The additional squares where its presence was recorded are S7E4 to S8E4 and S4W1, while it was not observed in S6E4 unlike the 'light-on-dark' sequence.

Figure 184. The yellow speleothem as seen on the North Wall of Square S7W1. Photo by Florent Détroit.

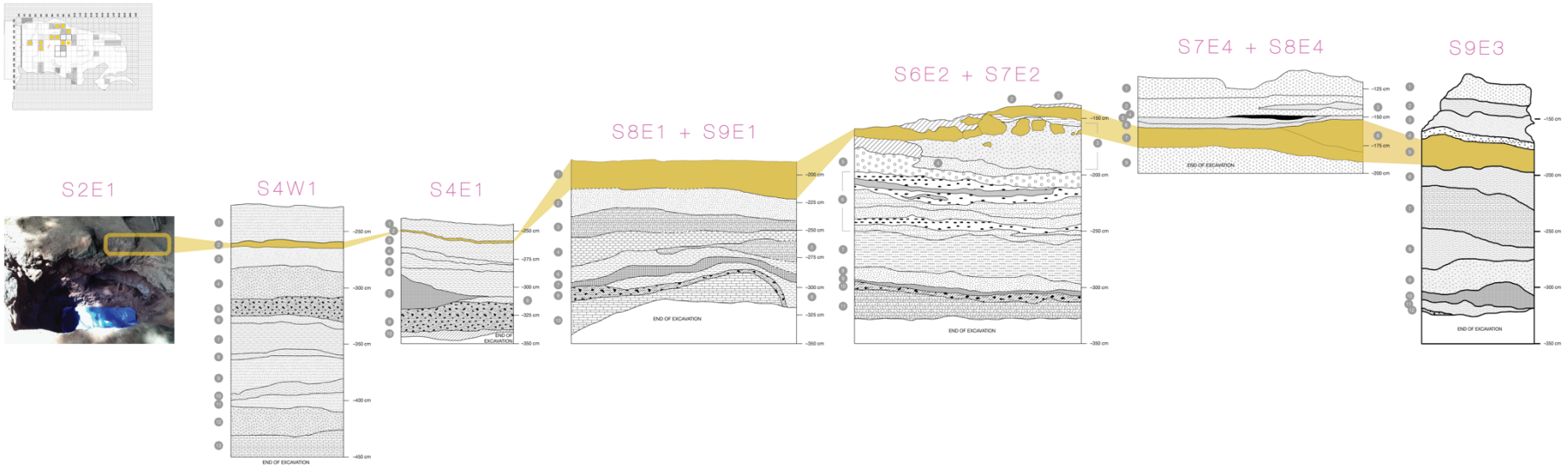

Figure 185. Proposed correspondences between the yellow speleothem layers across different squares. For detailed profile descriptions, please refer to Section 2.2.2.

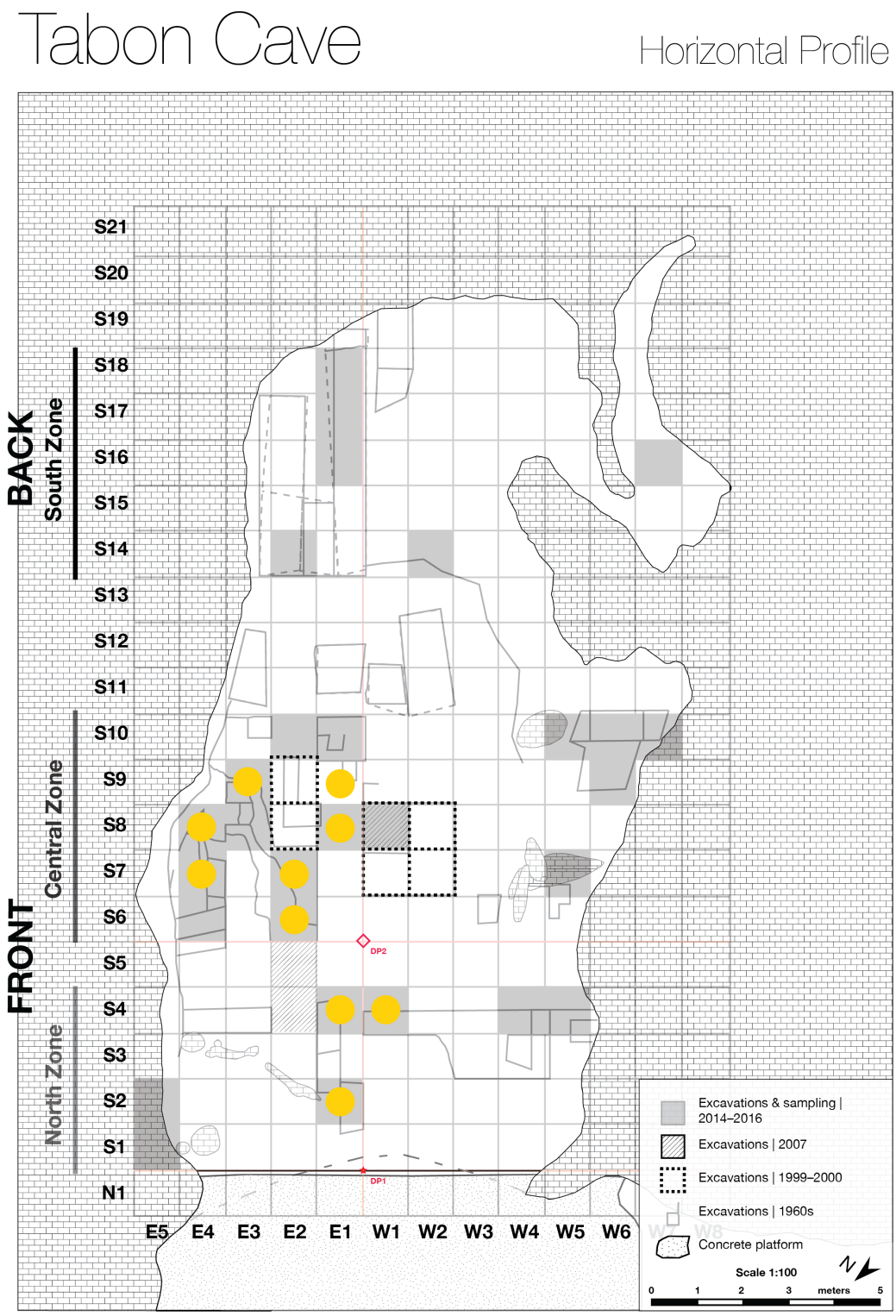

Figure 186. The Tabon Cave horizontal profile. The yellow circles indicate the identified presence of the yellow speleothem.

Table 32 shows the proposed correspondences between the yellow speleothem layers across the cited squares.

Table 32. Proposed correspondences between the yellow speleothem layers across different squares in the front half of the cave. For Square S2E1, since no vertical profiles are available, the layer depth is instead represented by that of the collected sample.

Square(s)	Layer(s)	Min. depth (cm DP)	Max. depth (cm DP)
S8E1 to S9E1	1	–185	–222
S9E3	5	–163	–197
S7E4 to S8E4	7, 8	–152	–190
S6E2 to S7E2	2	–140	–170
S4E1	2	–248	–262
S4W1	2	–257	–265
S2E1	-	(–260)	(–260)

In agreement with previous findings by Lewis *et al.* (2008), the layer has a mineralogical signature that is strongly dominated by gypsum. It is accompanied by ardealite and brushite, as well as phosphates that correspond to advanced diagenesis (e.g. variscite, leucophosphite) and clay minerals (e.g. montmorillonite, illite). These results are summarized in Table 33.

After their formation, gypsum and its associated minerals are not expected to persist in a wet environment, being highly soluble in water (Shahack-Gross *et al.*, 2004). Their surprising presence here likely indicates the prevalence of dry conditions in (and perhaps around) the cave after their precipitation: this would be coherent with the presence of monetite ($Ca(PO_3OH)$) in Squares S6E2 to S7E2, the dehydrated form of brushite ($Ca(PO_3OH) \cdot 2H_2O$). Another possibility is an exceptional degree of preservation in the layer (for example, incorporation into the fossil guano matrix; see Wurster *et al.*, 2015). This would imply a drastic difference in temperature between the guano deposit and the cave itself: in Măgurici Cave (Romania), the persistence of highly soluble phosphammite in a moist environment was found to be due to the [dry] guano matrix having a temperature that was twice the annual average in the cave (Onac and Veres, 2003).

Table 33. Mineralogical profiles of samples from the yellow speleothem. The mineral nomenclature follows the one used in Section 4.2: GY (gypsum), AR (ardealite), BR (brushite), MN (monetite), CHAP (carbonate-rich hydroxylapatite), VR (variscite), LC (leucophosphite), TK (taranakite), VV (vivianite), ST (strengite), MM (montmorillonite), IL (illite), muscovite (MC), OP (opal), QZ (quartz), CH (chert), TD (tridymite). The estimated concentrations also follow the same convention defined in Section 4.2: xxx (strong), xx (average), and x (weak).

Square(s)	Sample	Depth (cm DP)	Mineralogy
S8E1 to S9E1	16	–212	GY (xxx), BR (x / xx), VR (xx), TK (x), VV (x), ST (x), MM (x), IL (x), QZ (x)
S9E3	-	-	-
S7E4 to S8E4	34	–168	GY (xxx), AR (xx), CHAP (xx), LC (xx), VR (xx), QZ (x / xx), BR (x), MM (x), MC (x), OP (x), CH (x)
S6E2 to S7E2	22	–165	AR (xxx), BR (xxx / xx), CH (xx), MN (x), CHAP (x), TD (x)
S4E1	-	-	-
S4W1	-	-	-
S2E1	1	–260	GY (xxx), CHAP (x), BR (x), VR (x), MM (x), IL (x)

The advanced diagenesis phosphates identified are likely to be due to influence from the lower layers, where they have a strong presence, while the clay minerals may have been brought in by wind or water transport due to the proximity of the cave mouth.

Traces of chert were also detected in Squares S6E2 to S7E2 and S7E4 to S8E4, near the fireplace. This could correspond to very fine debris from Flake Assemblage II (located in this area; Corny, 2008)) that was incorporated into the speleothem.

In more remote areas of the cave, visually similar encrustations (primarily in terms of colour) were observed, but these are unlikely to correspond to the same stratigraphic unit as the yellow speleothem. In the South Trench, for example, a sample collected from the top of the profile described in the field as a 'capping speleothem' (Sample G, Layer 1) is actually more strongly characterized by the authigenic phosphate mineral variscite, as well as some silicate minerals (muscovite, opal, quartz, tridymite). While the sample was found to contain a sulphate mineral (rostite, $Al(SO_4)(OH) \cdot 5H_2O$), the overall differences with the yellow speleothem specimens in terms of mineralogy (i.e. absence of gypsum, ardealite, brushite) and texture suggest that

the two layers are stratigraphically distinct. In the western part of the cave, a similar 'speleothem' was noted just under the current cave floor surface in Squares S10W5 to S10W7 (informally called the 'West Trench'). The potsherds found underneath the layer suggest that it is much younger than the hypothetical minimum age of ca. 20 ka assigned to the yellow speleothem, and therefore, that the two are likely to be different.

5.1.3. Deep guano: bridging the front and back of the cave

In the west part of the cave, a thick (up to 45 cm) layer of guano is visible in the lower part of the profile for Squares S4W3 to S4W4 (Layer 6; Figure 187).

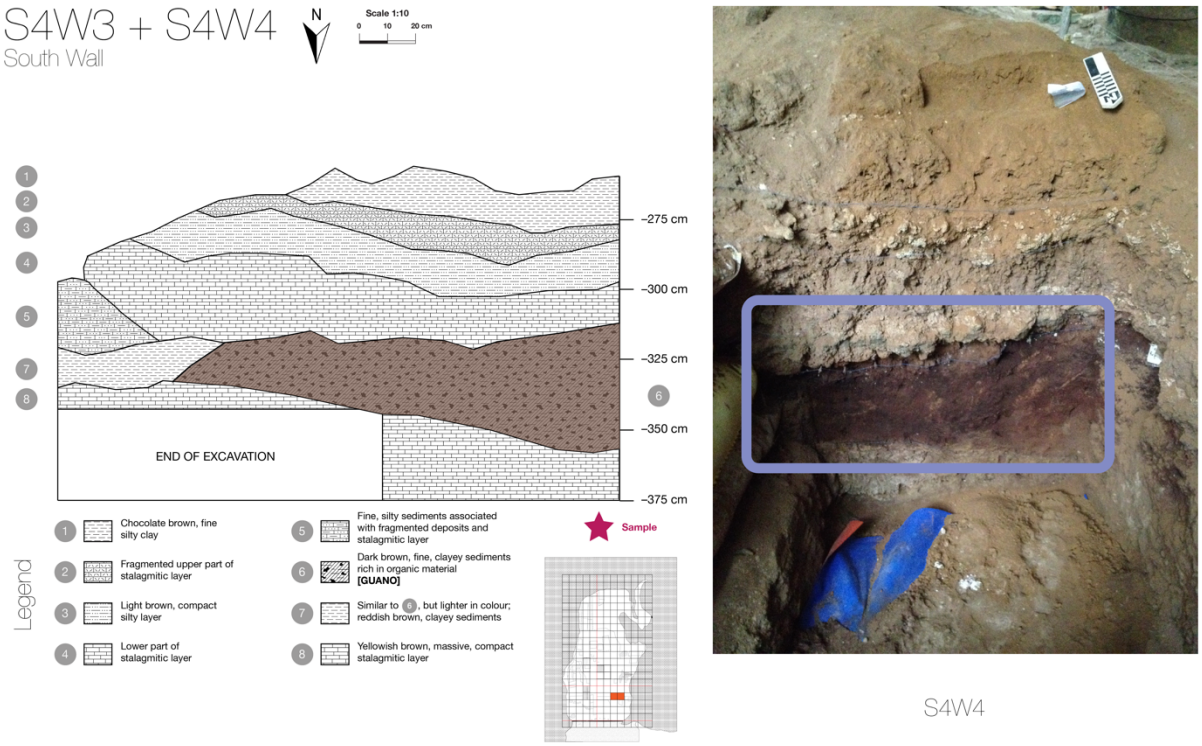

Figure 187. The South Wall vertical profile for Squares S4W3 to S4W4. The guano layer (highlighted) corresponds to Layer 6.

Moving further into the cave while staying along the western edge, a similar-looking guano layer is also visible in Square S7W5, as well as near the base in Squares S10W5 to S10W7 (the West Trench) (Figure 188 and Figure 189).

Figure 188. The South Wall of Square S7W5. The guano layer (highlighted) is the dark deposit in the lower part of the profile.

Figure 189. The South Wall of Squares S10W5 to S10W7 (the West Trench). The guano layer (highlighted) is the dark deposit in the lower part of the profile.

Zooming out of the western edge and considering the entire front half of the cave, nearly every recorded profile features one guano layer (corresponding to the dark band in the 'light-on-dark' sequence), generally located in its lower half. Meanwhile, in the South Trench (back), three guano levels were identified. The existence of these seemingly omnipresent guano layers at more or less the same depth raises the interesting possibility of a link between them.
To obtain a rough idea of how these various 'deep guano' layers relate to each other in space and help test the above hypothesis, their minimum, maximum, and average depths were plotted. Figure 190 shows the resulting graphs.

The graphs indicate that the depths are not radically divergent, assuming that the variations can be attributed to the naturally heterogeneous topography of the underlying deposits, as well as deposition rates that are functions of space. The north-south view suggests the presence of a downward slope from the back of the cave to the front, which confirms field observations. In the east-west view, the layers seem to be more compact in the east than in the west.

Figure 191 shows the proposed correspondences between the 'deep guano' layers across the relevant squares, while Figure 192 shows the horizontal profile of the cave indicating these squares.

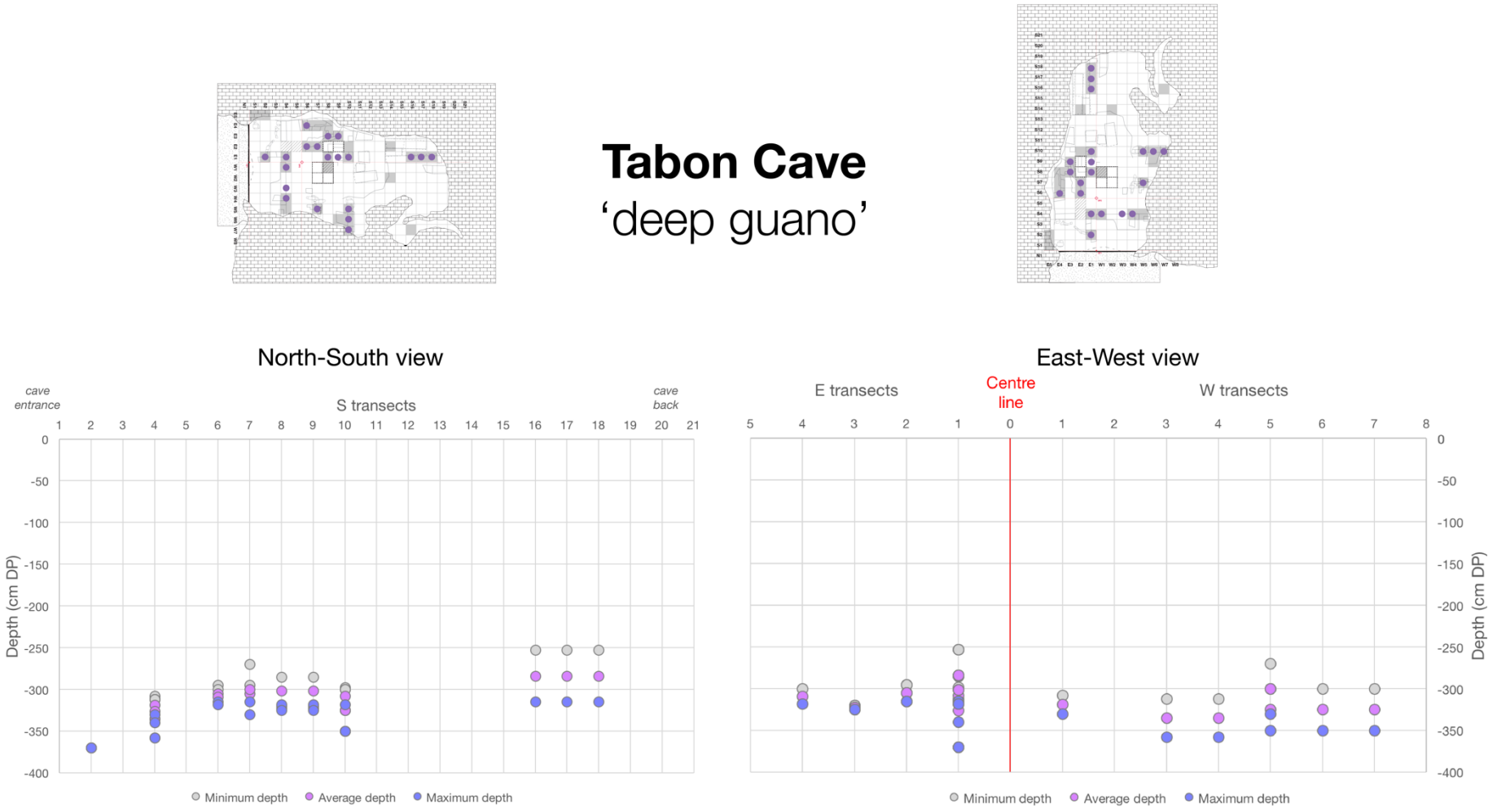

Figure 190. Depth plots of the 'deep guano' layers.

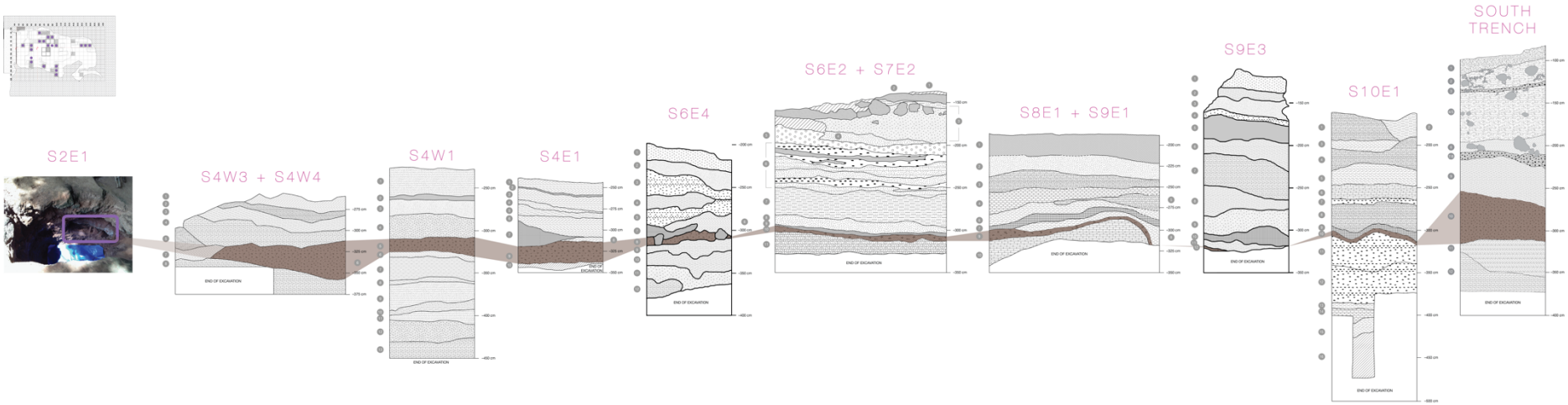

Figure 191. Proposed correspondences between the ‘deep guano’ layers across different squares. For detailed profile descriptions, please refer to Section 2.2.2.

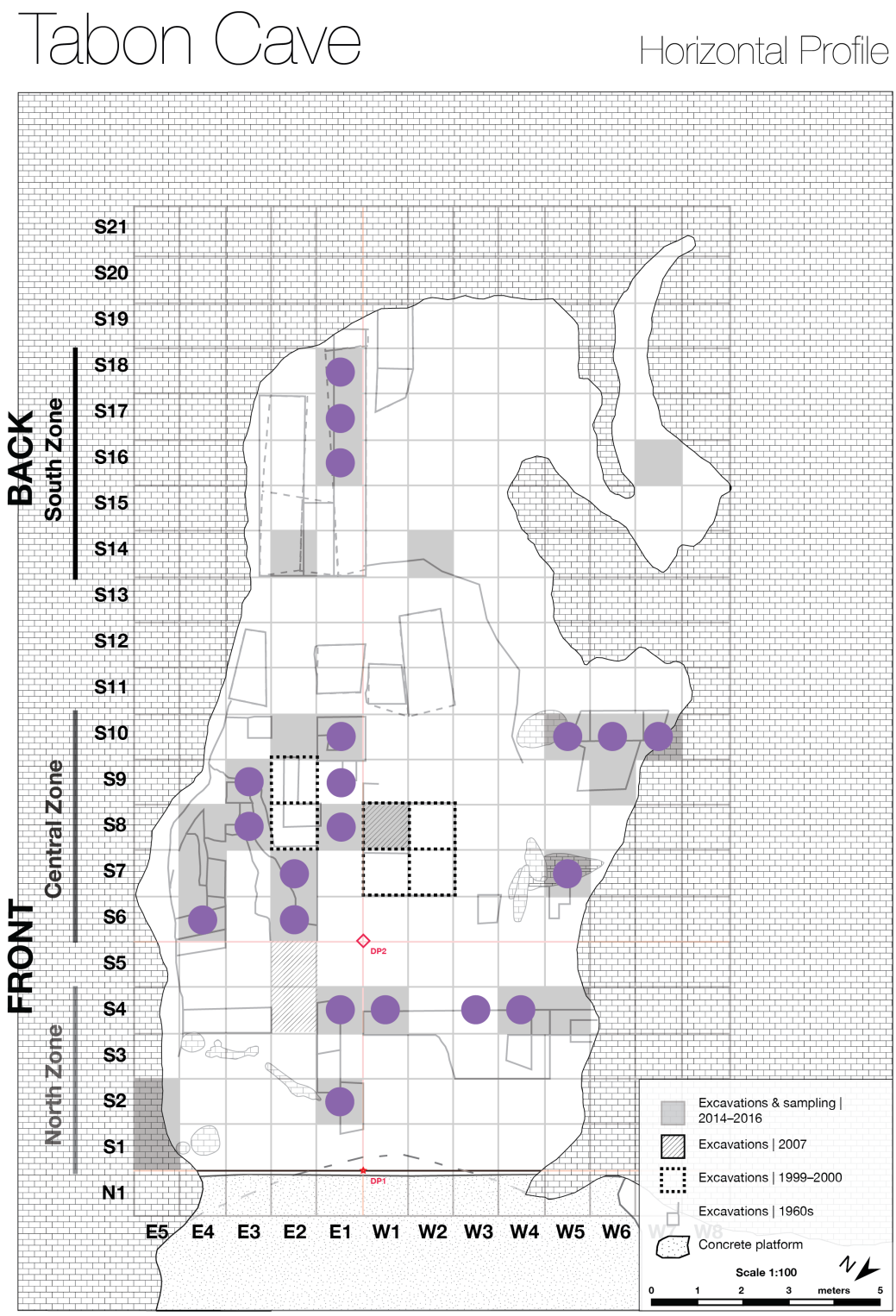

Figure 192. The Tabon Cave horizontal profile. The purple circles indicate the identified presence of 'deep guano' layers.

The mineralogy is broadly homogeneous, with a core signature dominated by minerals characteristic of early-stage diagenesis (e.g. carbonate-rich hydroxylapatite, brushite), although some aluminium phosphates (e.g. crandallite, variscite) that are certainly linked to the associated clay minerals (e.g. montmorillonite) are also present. Diagenesis seems to be more advanced in certain areas than in others, however—this is particularly the case in the east part of the cave, where minerals like leucophosphite were found. (This area of the cave has a particularly rich and complex geochemical history as seen in the upper layers, which include the yellow speleothem.) However, at the cave mouth, where exposure to the elements was expected to result in severe diagenesis, preservation conditions are somewhat better than expected—the fossil guano samples here have chitin peaks left in their infrared spectra without needing to undergo insect cuticle extraction.

The presence of 'deep guano' layers in practically every square excavated to a sufficient depth, as well as the relative comparability of these depths, point to the possible unity of all these layers as one stratigraphical unit, tying the heretofore irreconcilable parts of the cave together. The cave floor may conceivably have been covered entirely in guano over a given period in the past. Today, modern guano mounds can only be found along the cave walls, where natural cavities host swiftlet nests. The cave ceiling configuration could have been different in the past, with more stalactites serving as bat roosts, and subsequently modified by periods of landscape instability.

5.2. Palaeoenvironment and palaeoclimate

5.2.1. Quality of stable isotope data

Given the varying degrees of stratigraphic preservation and diagenetic variability observed in Tabon Cave, it is worth examining the reliability of the stable isotope data before proceeding with palaeoenvironmental interpretations.

The first key index to consider is the carbon content (%C). This only refers to organic carbon, as samples were decarbonated with HCl during preparation. The modern specimens (52-1, 52-2, 53-1, 53-2) show the expected rate of carbon content for fresh guano that has undergone little to no diagenesis, which is upwards of 40%. Over time, this rate decreases due to organic matter breakdown by micro-organisms, which release enzymes to oxidize organic compounds and recover the resulting energy and carbon—the carbon content may thus be considered a rough proxy of organic matter content.

As discussed in Section 4.3.2, the samples can be divided into two groups based on their %C values:

- **High carbon content (> 23%).** This group includes the samples collected from Layer 3 in the South Trench (at the back of the cave) as well as Layer 5 in Square S4W1 (near the cave entrance), with %C values running from roughly 24% to 35%.
- **Low carbon content (< 13%).** The rest of the samples, including the deeper ones from the South Trench, which all have %C values below 13%.

Accordingly, the first two groups may be considered to have better organic matter preservation than the last group. However, this cannot be attributed to spatial proximity, as they are situated at opposite ends of the cave. A more plausible explanation is the development of reducing conditions in these layers shortly after the onset of organic matter breakdown, effectively 'freezing' the process of decomposition. Nevertheless, as a general rule of thumb based on the carbon content depth plot (Figure 149), deeper samples can be expected to have lower carbon content (and less organic matter).

The carbon-nitrogen elemental ratio (C/N) is another index that has been used to determine chitin preservation quality for reliability of stable isotope signatures. Theoretical chitin, through its component monomer *n*-acetyl-*d*-glucosamine, has a C/N ratio of 6.9 (Wurster *et al.*, 2010b). However, protein-binding and partial de-acetylation of natural chitin in sclerotized insect cuticles cause the C/N ratio to decrease from the theoretical value (Schimmelmann and DeNiro, 1986). In Wurster *et al.*'s paper, they obtained C/N ratios of between 6 and 8 on a portion of their solvent-extracted guano samples (using the same protocol as the present study). While the proximity to theoretical chitin seems reassuring, the ratios are higher than expected for natural chitin, so they were interpreted as having largely degraded protein.

The tight covariation (R^2 = .91) between carbon and nitrogen content (%C and %N) among the samples in this study suggests that there was minimal to no preferential enrichment in, or depletion of, either carbon or nitrogen. The 'baseline' C/N ratio for Tabon Cave guano can be established from the modern samples, which give an average value of around 5. The samples with the closest values to this average are those of Layer 3 in the South Trench. Thus, if the C/N ratio were to be used as a criterion of stable isotope signature reliability, then these samples would be the ones that could be most confidently used for palaeoenvironmental reconstruction. Apart from them, only a handful of spatially scattered fossil specimens have comparable values. The rest fluctuate significantly, especially at lower depths where most have high C/N ratios—this reflects degradation of protein bonds and is likely due to diagenetic action.

Concerning isotopic signatures, Schimmelmann and DeNiro (1986) suggest that $\delta^{13}C$ values in chitin are related to C/N ratios, again because of protein binding and partial de-acetylation. Consequently, chemical changes are expected to result in strong correlations between the two indices (Wurster *et al.*, 2010b). The relatively moderate correlation observed for the Tabon Cave samples, combined with the presence of at least early-stage authigenic minerals, point to restrained diagenetic alteration. Bird *et al.* (2007) estimate the associated isotopic fractionation to decrease $\delta^{13}C$ values by less than 2‰, which has an arguably mitigated impact on palaeoenvironmental interpretation considering the scale used (–32‰ to –9‰). Additionally, the noticeable impact of diagenesis on organic matter preservation does not seem to be reflected in $\delta^{13}C$ values. The five samples collected from Layer 6 in Square S4W4 (near the cave entrance) have much lower carbon content (< 15%) than modern guano (> 40%);

however, they still have remarkably similar $\delta^{13}C$ values (σ = 0.486‰) that are comparable to the other samples.

The story is somewhat different for $\delta^{15}N$, as post-depositional fractionation related to microbial production of ammonia can increase values by up to 7‰ (Bird *et al.*, 2007; Wurster *et al.*, 2010b). This is quite significant considering that the usefulness of $\delta^{15}N$ for identifying the trophic level of guano producers relies on a scale that is of the same order of magnitude as the shift due to fractionation (from around +5‰ to over +10‰). Isolation of the original $\delta^{15}N$ signal has been a longstanding problem in stable isotope analysis of fossil guano for palaeoenvironmental reconstruction (Royer *et al.* 2017). Its interpretation continues to remain fraught with difficulty and uncertainty, and its use is generally restricted to affirming the occurrence of post-depositional isotopic fractionation (although Bird *et al.* (2007) propose that 'high' values of beyond +10‰ are indicative of an insectivorous diet).

In summary, the Tabon Cave guano samples can be used for palaeoenvironmental reconstruction. While diagenesis is present and affects the preservation of chitin in particular and organic matter in general, it has nevertheless a minimal impact on $\delta^{13}C$, the key isotopic index for understanding past vegetation around the site.

5.2.2. Outside the cave: vegetation and ecology

The $\delta^{13}C$ values obtained on the guano samples in this study run from –31‰ to –23‰, which place them squarely within the bracket for C_3 plants (–32‰ to –20‰; Cerling *et al.*, 1997; Bowsher *et al.*, 2008). However, the values exhibit significant internal variation.

The modern samples (–27‰ to –25‰) occupy a relatively central position within both the sample set and the entire C_3 range. Their $\delta^{13}C$ values are closely comparable to those of other present-day guano specimens from Palawan (Bird *et al.*, 2007; Wurster *et al.*, 2010a). However, they may have undergone positive-shift due to C_4 contributions from present-day agriculture (E. Robles, *pers. comm.*). It is not possible to quantify this shift for Tabon Cave since none of the fossil guano deposits are vertically contiguous with the modern ones, but Bird *et al.* (2007) estimate a difference of 2‰ in Makangit Cave, northern Palawan. Assuming a similar value for Tabon Cave, this would make the 'corrected' $\delta^{13}C$ value range more negative (–29‰ to –27‰).

The fossil samples are more widely distributed. The ones from the youngest phase of guano deposition, corresponding to Layer 3 in the South Trench, are clustered between –26‰ and –24‰. In comparison with the modern samples, they incorporate a more significant C_4 component, but still correspond to vegetation dominated by C_3 plants. The overall landscape surrounding the cave at this time was still likely to have been characterized by closed forest, although influence from C_4 plants suggests drier conditions than today that were either more frequent or more pronounced.

The intermediate phase, corresponding to Layers 7/8 in the South Trench, has the most negative $\delta^{13}C$ value of all the samples analyzed in this study (–30.777‰). This points to an extremely wet period that may be related to the overlying rockfall (in Layers 6 and 4/5) through increased karstic activity. Lipuun Point was likely covered in dense tropical forest during this time.

Finally, the oldest phase ('deep guano'), corresponding to Layer 10 in the South Trench and just about every other guano layer in the front half of the cave (as suggested in Section 5.1.3/Deep guano: bridging the front and back of the cave), is characterized by a broad range of values from –29‰ to –23‰. This represents a substantially varied palette of vegetation types, from generally closed environments to more open ones. Building on the hypothesis that the entire cave was populated by guano producers during this time, the variability in $\delta^{13}C$ values might be explained by the cohabitation of bat and/or bird populations with varying foraging strategies. In this situation, each colony can be expected to occupy a specific part of the cave, which would result in spatial clustering of $\delta^{13}C$ values. Figure 193, which maps $\delta^{13}C$ averages for the 'deep guano' layers across the cave, suggests that this may have been the case. Similar, strongly negative values can be found along the east wall and the back of the cave: the deep guano deposits in these areas were possibly deposited by either the same colony, or by multiple colonies that have similar foraging habits (whether they belong to the same species or not). The cave entrance features a more diverse range of values and could correspond to either a single colony with diverse foraging habits, or to altogether different colonies.

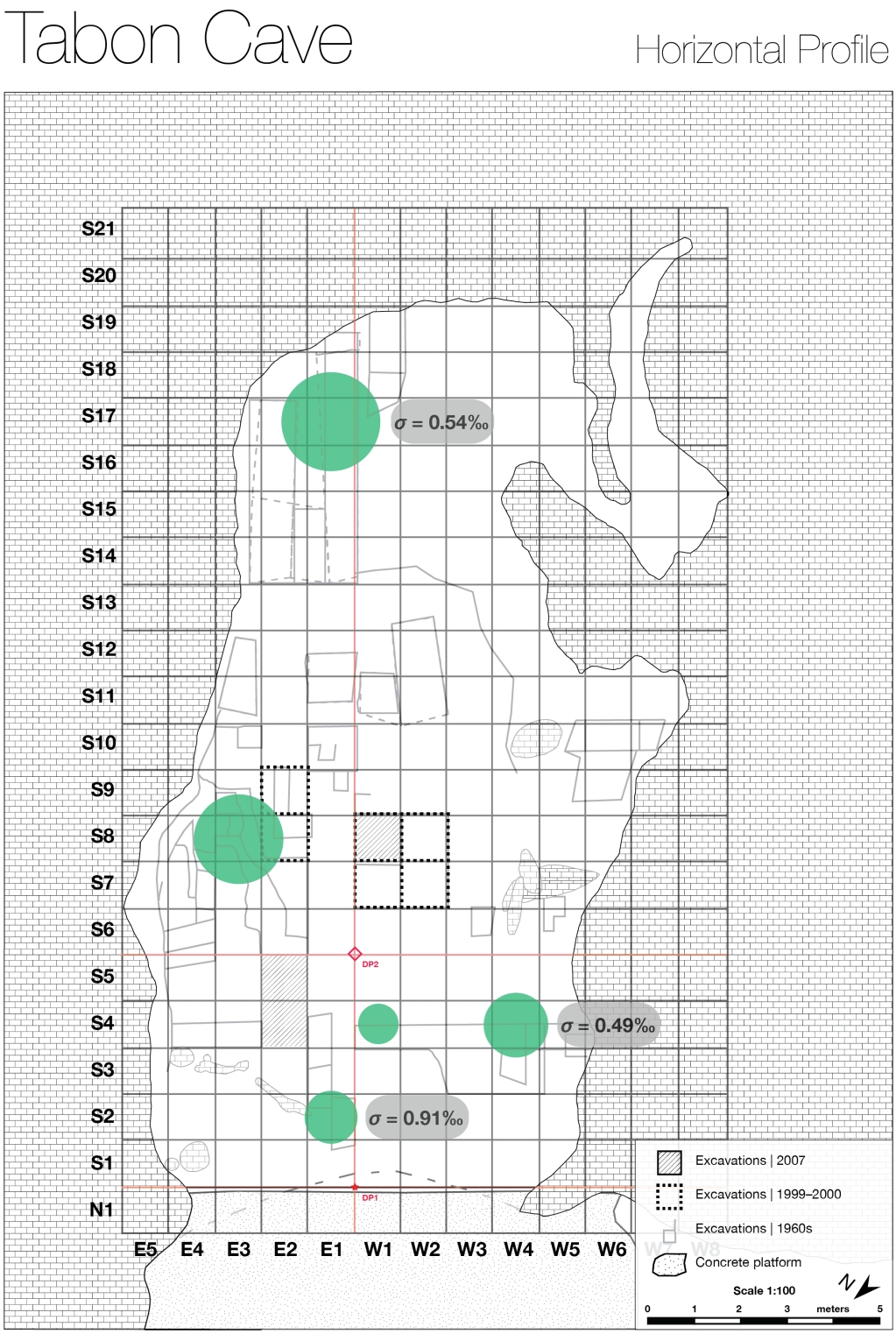

Figure 193. Comparative spatial visualization of average $\delta^{13}C$ values for 'deep guano' layers. Bigger circles indicate more negative (stronger C_3) values. Squares with multiple samples are accompanied by the standard deviation (σ) to give an idea of spread.

Another possible explanation for the spatial variability in $\delta^{13}C$ values within what is currently hypothesized to be a single guano layer is space-dependent diagenetic alteration, as suggested by the mineralogy. However, as mentioned in Section 5.2.1, this effect is unlikely to exceed 2‰ and cannot entirely account for the variability observed.

In order to be accurate, interpretation of $\delta^{13}C$ values from guano must take ecological factors into account. In the transfer of carbon from plants to guano producers (with or without insects), differences in foraging behaviour combined with landscape variability complicate reconstruction of original environments, but they cannot be ignored. A general understanding of foraging behaviour in Palaeotropical bat communities is proposed by McKenzie *et al.* (1995), who divide them into five groups called 'Strategies' based on wing morphology and foraging habitat.

- Strategy I: slow flyers that forage insects close to their roost; adapted to forest understorey and other cluttered habitats
- Strategy II: aerial foragers that hunt flying insects in partially open areas below or near the canopy
- Strategy III: strong flyers that range far from their roost and hunt insects in open spaces or high above vegetation
- Strategy IV: frugivorous and nectarivorous bats that forage at short distances underneath the canopy
- Strategy V: frugivorous and nectarivorous bats that cross open spaces and cover large distances while foraging

Stimpson (2012) summarized the relationship between Strategies and foraging habitat in Figure 194.

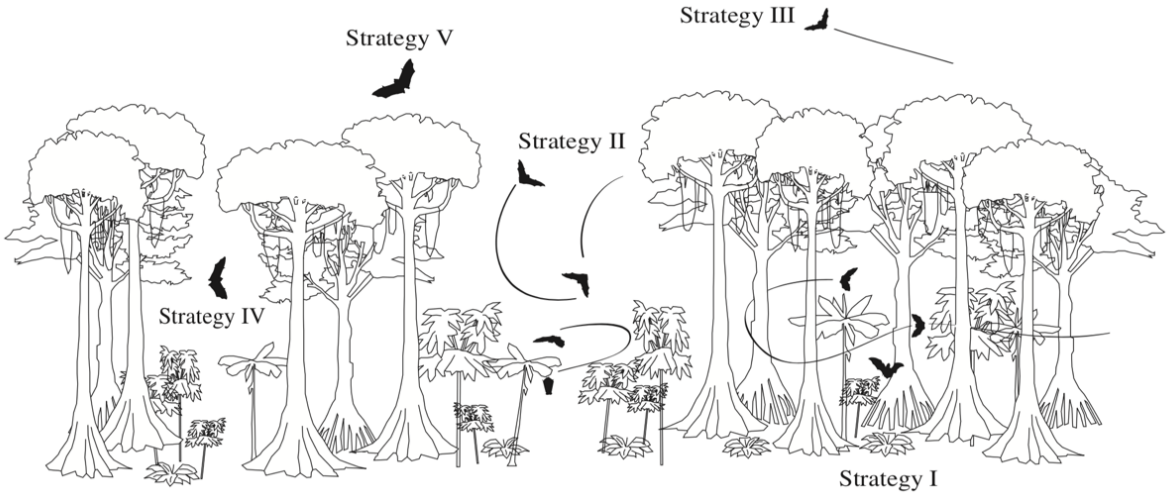

Figure 194. Strategies and foraging habitat as proposed by McKenzie *et al.* (1995). Diagram from Stimpson (2012).

From the diagram, it can be surmised that the palaeoenvironmental signal recorded in guano and deciphered through $\delta^{13}C$ values will depend on bat foraging behaviour. To obtain an accurate picture of the local environment from a given guano deposit, the deposit should ideally be from Strategy I, II, or IV bats; for regional validity, deposits should ideally have been constituted by Strategy III or V bats.

Unfortunately, for Tabon Cave, no formal microfaunal studies are available that might help determine the geographical range of the stable isotope data. Corny (2008) points out the notable discrepancy between the excavation of numerous (and mainly small) animal remains in the Fox reports and their near-absence in the collections, concluding that they were most probably discarded. However, examination of current bat species in the area may give an idea of past populations. In September 2013, a team from the Zoology Division of the National Museum of the Philippines did a survey of the mammalian and herpetofauna in the Tabon Caves Complex (M.J.S. Veluz, *pers. comm.*). Table 34 presents the bat species that were recorded, along with some basic information on their diet, foraging habits, Strategy type, and roost companions.

Table 34. List of bat species recorded from the September 2013 faunal survey of the Tabon Caves Complex conducted by the National Museum of the Philippines – Zoology Division. Accompanying data compiled primarily from the IUCN Red List of Threatened Species 2008 and the Field Museum Synopsis of Philippine Mammals.

Latin name	English common name	Diet	Foraging habits	Strategy	Roost companions
Emballonura alecto	Small Asian Sheath-tailed Bat	Insects; sometimes fruit	High above canopy in secondary forest & lowland disturbed forest; open spaces; mixed agro-forestry areas; long distances	III	
Eonycteris robusta	Philippine Dawn Bat	Nectar; pollen; soft fruit	Lowland forest adjacent to limestone caves (undisturbed; sometimes in secondary, disturbed, mixed forest & clearings)	IV	*Eonycteris spelaea; Rousettus amplexicaudatus*
Hipposideros diadema	Diadem Leaf-nosed Bat	Insects (especially [large] beetles)	Low flier in gallery forests and over water pools (Nicobar subspecies); primary and disturbed lowland forest; agri. areas	II	Other *Hipposideros* spp. (Nicobar subspecies); swiftlets
Miniopterus australis	Little Long-fingered Bat	Insects	Above canopy in primary and secondary lowland forest; rainforest; *Meleleuca* swamps; dry sclerophyll forests; montane forest; agricultural areas	II/III	*Miniopterus schreibersii*
Miniopterus schreibersii	Schreiber's Bent-winged Bat	Insects (moths; sometimes flies)	Old and second-growth lowland forest (and occasionally montane forest) near caves; open and semi-open natural and artificial habitats, including agricultural areas	II	*Miniopterus australis*; other cave bats (forming large, mixed colonies)
Myotis macrotarsus	Pallid Large-footed Myotis	Insects	Freshwater; rivers; small streams; primary lowland forest; agricultural areas	II	
Pteropus vampyrus	Large Flying-fox	Fruit (wild and cultivated, esp. *Ficus* spp.); flowers; leaves	Above canopy of primary/undisturbed/riparian and secondary lowland forest; adjacent agricultural areas; range of 17 km or more	V	*Acerodon jubatus*
Taphozous melanopogon	Black-bearded Tomb Bat	Insects (flying); sometimes small fruit	Above canopy over large areas of diverse forested and secondary habitats	III	

The list shows that the Tabon Caves Complex is currently inhabited by a mix of pure, semi-, and non-insectivorous species with diverse foraging strategies: some hunt above the forest canopy while others hunt close to water sources at ground level, some cover broad distances while others stay near their roost. Combining this with possible landscape variability gives an idea of just how delicate and challenging the precise interpretation of $\delta^{13}C$ values from guano can become. Additionally, many of the species cited above also forage in or near agricultural areas, which confirms the necessity of accounting for an anthropic C_4 contribution to $\delta^{13}C$ values from modern guano. While this effect can be discounted for the fossil guano deposits as they are at least 30,000 years old, it remains difficult to produce more precise interpretations of their $\delta^{13}C$ values without specific data on past microfauna in the cave. Remains of *Hipposideros diadema* recovered during the 2014 field campaign initially offered a sliver of hope, but they were unfortunately devoid of stratigraphical context, and none of them could be directly correlated with any of the fossil guano deposits (N. Amano, *pers. comm.*). Nevertheless, the current chiropteran biodiversity of the area gives an idea of its capacity to host varying species, information which will be vital to refining palaeoenvironmental inferences from stable isotope analysis.

Unfortunately, detailed data was not obtained for current bird populations in the Tabon Caves Complex, but Tabon Cave itself is currently inhabited by swiftlet colonies (Collocaliini), which are exclusively insectivorous.

Given that stable isotope data is limited to general validity, it needs to be complemented with other palaeoenvironmental markers as much as possible. Unfortunately, previous attempts at pollen isolation in Tabon Cave have not always been very fruitful—this has often been attributed to poor preservation conditions for organic matter due to guano diagenesis. Recently, however, a sample collected for palynology in the guano deposit from Square S4W1 (near the cave entrance), Layer 5, yielded pollen in good condition (A.-M. Sémah, *pers. comm.*). The preliminary results ($n > 50$) are presented in Figure 195.

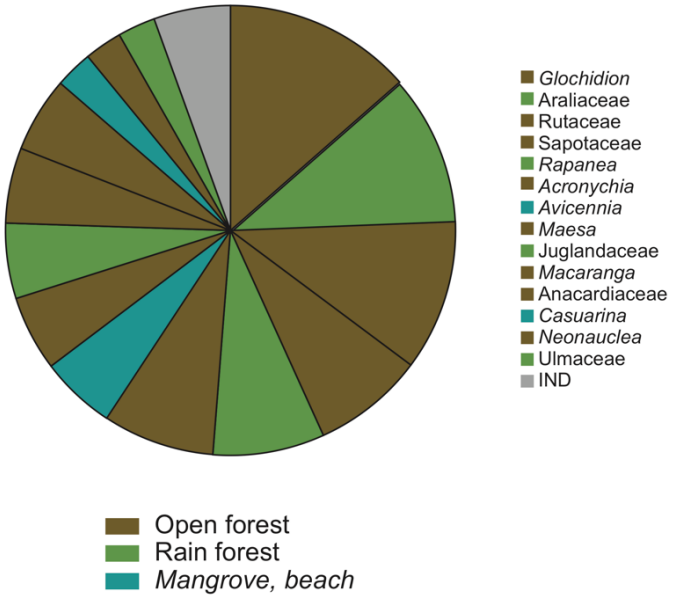

Figure 195. Pollen distribution and corresponding environmental attributions from a sample in the guano deposit Layer 5 of Square S4W1 (near the cave entrance) (A.-M. Sémah, *pers. comm.*).

It is interesting to note that, while the results are to be considered with caution at this stage owing to an insufficient number of pollen grains, they are in agreement with available geochemical data for this layer. The relatively high organic carbon content (26.57%) may explain the good preservation state of the pollen. Additionally, most of the identified taxa correspond to an open forest environment, which rhymes with the $\delta^{13}C$ value (–23.482‰) that points to a stronger influence from C_4 plants than recorded elsewhere in the cave. This opens up interesting future perspectives for possible correlation of pollen and stable isotope data in Tabon Cave, assuming that pollen can be successfully recovered from the other guano layers.

5.2.3. Inside the cave: palaeochemistry and microclimate

Whereas the environment and climate outside of the cave can be studied through stable isotopes, the effects inside the cave are reflected in the mineralogy of its deposits. Additionally, information from stable isotopes concerns parameters before guano deposition, while mineralogy describes what happens after as the deposits evolve in time.

Authigenic minerals form over short periods of time following matrix deposition, requiring only several tens of years and rapidly attaining a steady state (Karkanas *et al.*, 2000; Shahack-Gross *et al.*, 2003, 2004; Forbes and Bestland, 2006). On archaeological time scales, they can thus be considered practically contemporaneous with their associated matrix. Additionally, diagenesis occurs primarily in near-surface environments, implying that authigenic minerals record palaeochemical conditions at the time of their formation (Karkanas *et al.*, 2000; Shahack-Gross *et al.*, 2003). This information can be correlated with stable isotope signatures from the associated fossil guano and other palaeoenvironmental markers (e.g. pollen). In conjunction with chronological data, this would provide a more detailed picture of the environment around the cave that can be correlated to specific palaeoclimatic periods.

While the formation of authigenic minerals requires the presence of water, the persistence of certain soluble ones in Tabon Cave is somewhat surprising. In particular, the preservation of the extensive gypsum speleothem is interesting given that this highly soluble mineral is not expected in mature deposits. Its presence indicates either exceptional conditions of preservation, or that Tabon Cave somehow managed to stay dry after its deposition. This makes it an ideal shelter, as suggested by traces of human presence (flake tools and a fireplace) just above the gypsum speleothem. The presence of gypsum and other dry minerals in other Southeast Asian caves has been recorded, although their paradoxal persistence in these wet environments remains curious and unexplained (Wurster *et al.*, 2015). In any case, the gypsum speleothem in Tabon Cave certainly did form during a period of increased moisture, as proposed by Lewis *et al.* (2008); however, this was followed by a dry period in the cave, leading to preservation of the highly soluble constituent mineral assemblage.

5.3. Chronology and archaeology

5.3.1. Uranium-series dating of authigenic mineral deposits

Among the three authigenic mineral deposits analyzed for dating in this study, the grey speleothem seems to present the most promise because of the apparent relationship between uranium-238 concentration and calculated age in the samples. Although it is not possible at this stage to determine the true age of the layer as evidenced by the wide range of calculated ages, some hypotheses can be proposed.

In the best-case scenario, the system would have become closed shortly after formation and would have stayed closed like a traditional carbonate speleothem. Internal uranium mobility could then explain the differences in uranium content observed among the samples and the apparent relationship with calculated age. In this case, the oldest sample, SG-01 (90.5 ± 1.7 ka), would represent the minimum age of deposition, while the maximum age of deposition is given by the *y*-intercept of the fitted exponential curve in Figure 164,

$$y = 130.0571e^{-0.6856x}, \quad \text{(Equation 26)}$$

which corresponds to 130.1 ka and exhaustion of initial uranium-238. Assuming that the system can be shown to have stayed closed, the true age of the layer is to be found somewhere in this wide interval between 90 and 130 ka. A more realistic possibility, however, is that the system remained partially or completely permeable after its formation. In this case, recent uranium uptake would upset system movement toward radioactive equilibrium, increasing fractionation (through the $^{230}Th/^{238}U$ ratios) and causing the layer to appear younger.

Concerning the hydroxylapatite samples, out of the five that were analyzed, three were unfortunately undateable (Samples 20, 28, and 44), while the other two have calculated ages that are far from both each other (Sample 06: 178.8 +6.1/–5.8 ka, Sample 15: 415.4 +47.8/–33.0 ka) and from the first sample test-dated in this layer (Sample D6: 109.8 ± 2.6 ka, (Ghaleb *et al.* 2012)). The samples are very rich in uranium, and the proximity of their activity ratios to secular equilibrium points to continuous enrichment and leaching that balance each other out. In addition to the continuous circulation of uranium in and out of the layer, high thorium-232 concentrations coupled with low thorium-230 to thorium-232 activity ratios contribute detrital contamination to the complex geochemical dynamics of this layer.

The close association with the underlying guano layer that represents a rich source of organic matter has many implications on the behaviour of uranium. Microbes in organic matter influence uranium oxidation state and stability through a variety of mechanisms, such as enzymatic reduction and biomineralization (Cumberland *et al.*, 2016). Enzymatic reduction immobilizes uranium by transforming it from its hexavalent oxidation state U(VI), in which it is soluble in water, to its tetravalent oxidation state U(IV), in which it is insoluble. This phenomenon is thought to dominate under ambient conditions and is a growing subject of research in nuclear site remediation (Bargar *et al.*, 2013; Newsome *et al.*, 2014). However, enzymatic reduction and other forms of microbial processing of uranium are conditioned by the the presence of certain ions, like PO_4^{3-} (present in guano), CO_3^{2-}, and Ca^{2+} (both present in [carbonate-rich] hydroxylapatite). On one hand, carbonates and calcium interfere with microbial processing of uranium and promote its mobility because of their strong affinity for the actinide (Ulrich *et al.*, 2011). On the other hand, phosphates increase uranium reduction (thereby trapping it) as phosphatase enzymes produced by microorganisms liberate phosphate ions from their organic bonds, and under low pH (acidic conditions), they may form new bonds with available uranium to create uranyl phosphate minerals (Salome *et al.*, 2013). Phosphate chemistry has a considerable effect on uranium mobility and is still poorly understood, despite advances in research on specific uranyl phosphate complexes (Vazquez *et al.*, 2007; OECD-NEA, 2012). However, in the case of this specific layer, the simultaneous presence of calcium, carbonate, and phosphate ions in the form of carbonate-rich hydroxylapatite could be exerting opposing effects on uranium mobility, reflecting the continuous enrichment and leaching that the uranium activity ratios close to unity seem to suggest. In any case, within the specific perimeter of Tabon Cave, chemical transformations and the ensuing diagenetic manifestations that may be linked to climatic changes have had complex effects on uranium behaviour that are not particularly easy to retrace. Due to the complex interaction of these various factors, it is difficult to get even indicative uranium-series ages for the hydroxylapatite layer as things stand.

Finally, as regards the yellow speleothem, the extremely high thorium-232 content of Sample 16 suggests that its calculated age is also unusable. Lewis *et al.* (2008) encountered the same problem with two of the four samples that they analyzed, U-Th3 and U-Th4; only the data for U-Th1 and U-Th2, the samples considered to have admissible ages, were included in their paper. This is most likely due to contamination from clay minerals (onto which thorium is

most commonly adsorbed) in incorporated detrital components like aeolian dust, despite efforts to target only the 'clean' parts of the sample (Frechen *et al.*, 2007; Sanna *et al.*, 2010). External elements may also explain the more than threefold difference in uranium content between Sample 16 and the Lewis samples. Gypsum is expected to have little uranium because of the low ion pairing affinity between UO_2^{2+} and SO_4^{2-}, generally leaving UO_2^{2+} in solution rather than favouring adsorption onto growing gypsum surfaces (Sanna *et al.*, 2010). As such, high uranium content is suspicious and likely points to an exogenous source. Future dating efforts, if undertaken, should include multiple samples and conserve only the ones that are 'clean', i.e. with thorium-232 content below 0.1 ppb.

5.3.2. Radiocarbon dating of organic matter

While uranium-series dating efforts in Tabon Cave have been constantly hampered by recurring issues, mainly radioactive system porosity and uranium mobility, results are much more promising for radiocarbon dating and, at the moment, seem to hold the most potential for advancing understanding of ancient human occupations in the cave. Figure 196 presents the spatial distribution of the recent radiocarbon results.

Firstly, in Squares S7E4 to S8E4, the fireplace (Layer 4) that is one of the most important traces of human presence in the cave has undergone a series of dating attempts from 2009 to 2015. The results are now officially presented here for the first time, in Table 35.

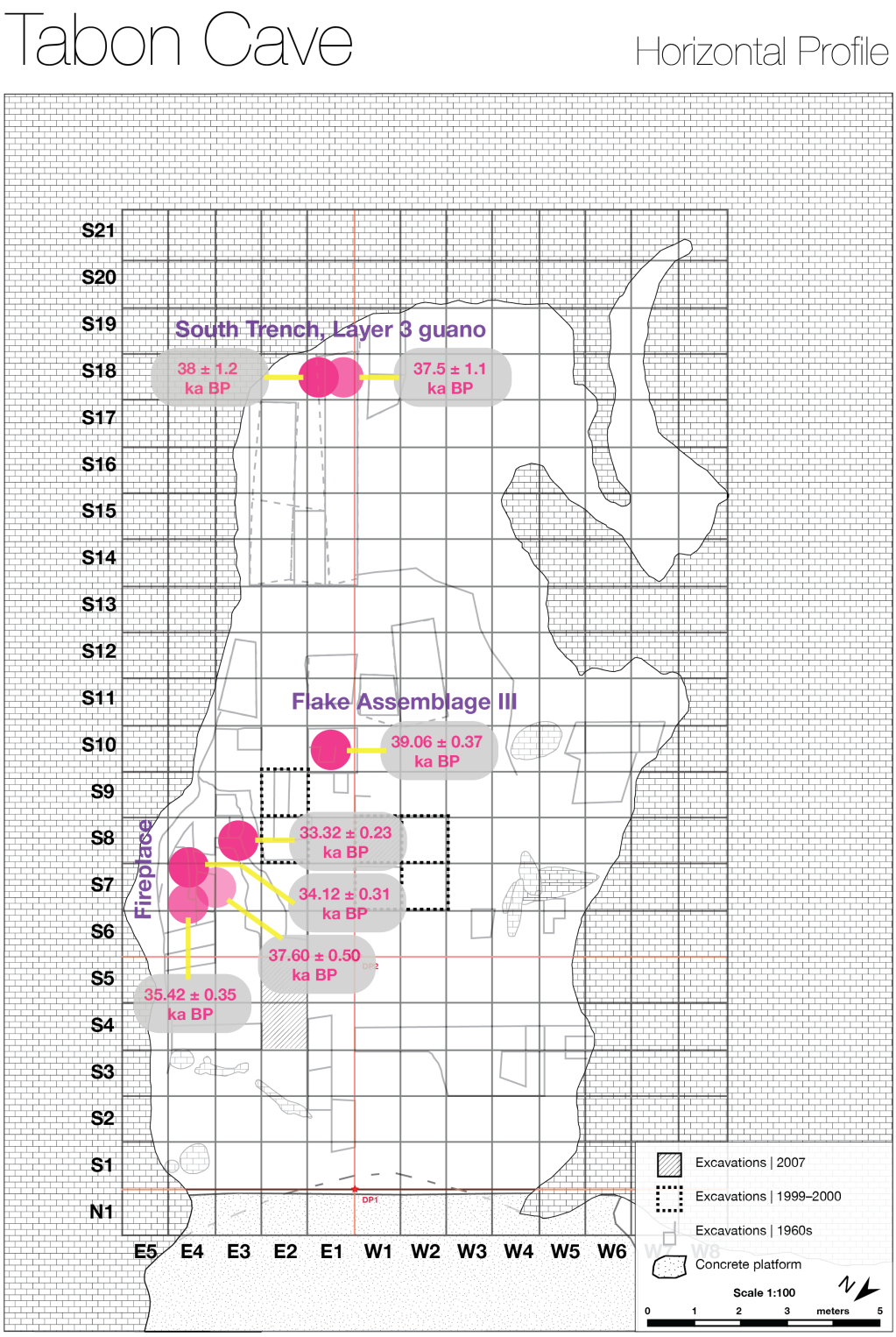

Figure 196. Spatial distribution of recent radiocarbon results in Tabon Cave.

Table 35. Radiocarbon ages for the fireplace.

Sample name	^{14}C age (ka BP)	Lab code
TCS707CHARC3	35.42 ± 0.35	BETA-259326
Tcs7E4CHARC1	34.12 ± 0.31	BETA-261802
Ta12_D15	37.60 ± 0.50	Oxford
Ta14_Ch2	33.32 ± 0.23	BETA-423462

The ages obtained show a relatively restrained spread from ca. 33 to 38 ka BP. However, despite considerable efforts devoted to stratigraphic analysis, these results are impossible to reconcile with the uranium-series ages obtained by Lewis *et al.* (2008) on the yellow speleothem situated just underneath, which was dated to 20.2 ± 0.8 ka and 19.4 ± 0.8 ka. These uranium-series ages previously seemed consistent with what little is understood of the cave's chronostratigraphy, as the yellow speleothem is sandwiched between charcoal samples associated with Flake Assemblages II (above) and III (below), respectively dated to > 21 ka BP (max.) and 23.2 ± 1 ka BP (Fox, 1970: 27). However, the stratigraphic position of Flake Assemblage III below the fireplace, whose dates seem reliable, warrants a re-examination of its age.

Recently, a charcoal sample found in the reserves of the National Museum of the Philippines (accession code P-XIII-T-4072) and contextually associated with Flake Assemblage III in the centre of the cave yielded an age of 39.06 ± 0.37 ka BP (J. Corny, *pers. comm.*). This is stratigraphically coherent with the radiocarbon ages for the fireplace, but it differs from the Fox radiocarbon age for Flake Assemblage III by more than 15 ka. It is conceivable that the age for Flake Assemblage II, with which the fireplace is most likely associated, is also off by roughly a similar amount and will have to be re-evaluated if associated charcoal samples can be recovered and dated in the future.

Finally, as already mentioned in Section 5.3.1, the age of the yellow speleothem needs to be re-examined. While it is possible that the layer underwent a recent episode of uranium uptake, hence the young age, a more likely explanation is heterogeneity in the spatial distribution of uranium and thorium within the layer, causing age to vary strongly with sampling and subsampling location.

Figure 197 summarizes the stratigraphic relationships between the fireplace, the yellow speleothem, and Flake Assemblages II and III.

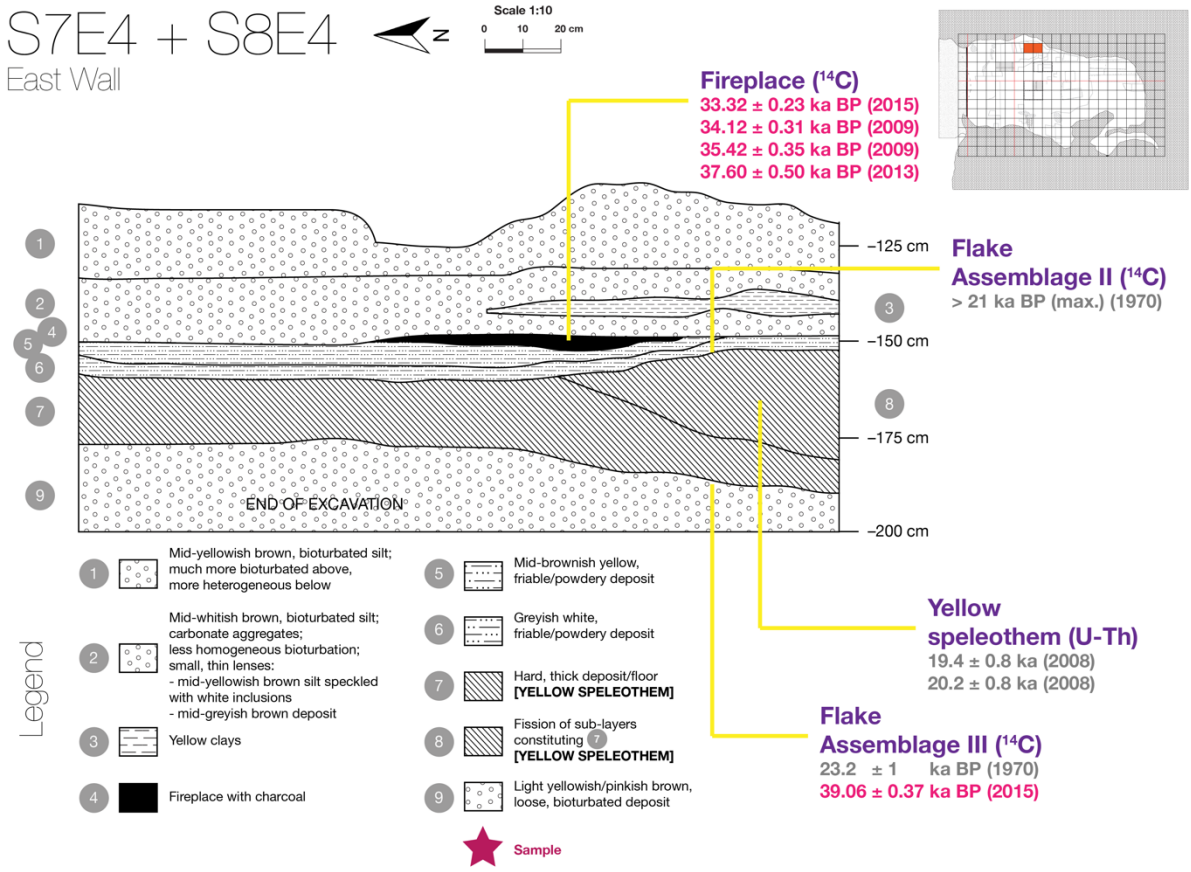

Figure 197. Projected stratigraphic relationships between the fireplace, the yellow speleothem, and Flake Assemblages II and III. Stratigraphically coherent ages are indicated in pink, and incoherent ones in grey.

Aside from the fireplace, another significant layer that was successfully dated via radiocarbon is the topmost guano deposit in the South Trench, Layer 3. The closely similar ages obtained (38 ± 1.2 ka BP, 37.5 ± 1.1 ka BP) seem to be reliable in light of good organic matter preservation in this layer (see Section 5.2.1).

This layer has considerable added value to the study of the cave for two reasons:

- it is the only layer in the entire cave for which reliable chronological *and* palaeoenvironmental data were both obtained; and
- the chronological data tie it to the recent radiocarbon result for Flake Assemblage III, bridging palaeoenvironment and archaeology.

The other guano layer that was dated, Layer 12 in Square S9E3 (in the centre of the cave), unfortunately gave a radiocarbon age of 27.97 ± 0.35 ka BP that is inconsistent with its stratigraphic position below the fireplace—this is possibly due to contamination with younger organic matter.

5.3.3. Human occupations in Tabon Cave between 30,000 and 40,000 years ago

There are three human fossils from the cave that have been directly dated (via uranium-series):

- the frontal bone (P-XIII-T-288), dated to 16.5 ± 2 ka;
- a right mandibular fragment (P-XIII-T-436 Sg19), dated to 31 +8/–7 ka; and
- a right tibia fragment (IV-2000-T-197), dated to 47 +11/–10 ka.

(The parentheses indicate the National Museum of the Philippines accession code for each specimen.)

Of these three fossils, the right mandibular fragment has the best chronological proximity with the radiocarbon ages for the fireplace. While its stratigraphic context is unknown as it was recovered from sieving, its horizontal location in the cave was reconstructed to be in Fox's Square 19; in the current grid system, this approximately corresponds to the area covered by Squares S8E3 to S10E4 (Corny, 2008). This places it just south of the fireplace.

A total of 19 other bones were recovered by Fox from sieving in this area and bear the same accession code prefix (P-XIII-T-436), suggesting possible contextual association with the right mandibular fragment (Corny, 2008). Of the 19 bones, Corny identified seven that are likely to be of considerable age and that resemble the mandible in physical appearance, although none of them have been directly dated so far. The MNI is 1 and several of the bones were noted to be gracile.

The spatial and chronological proximity of the right mandibular fragment to the fireplace could indicate a link between them, but this is difficult to establish with certainty; the association is indirect at best, and missing stratigraphical information concerning the fossil complicates matters. Nevertheless, what *can* be put forward with relative certainty is that the fireplace confirms human presence in the cave between ca. 33 and 38 ka BP, during MIS 3, and thus

represents the earliest evidence for use of fire in the Philippine archipelago. The fireplace is very likely associated with Flake Assemblage II, also situated right atop the yellow speleothem. Based on Corny's (2008) spatial reconstruction, Flake Assemblage II is in the exact same area as the fireplace. Furthermore, Fox (1970: 26) describes the context of Flake Assemblage II as distinctive, being characterized by wasp nests—these very likely refer to the bioturbated deposits (Layers 1 and 2) just above the fireplace in Squares S7E4 to S8E4. Flake Assemblage II consists of hundreds of chert pieces representing all the stages of the lithic *chaîne opératoire*. Biological remains include small fragments of animal bones, human and animal teeth, and charcoal.

Flake Assemblage III, situated this time below the yellow speleothem, is described as being situated within an archaeological horizon (Fox, 1970: 27). This level yielded charcoal fragments from scattered cooking fires, numerous microfaunal remains (birds, bats, small mammals; much, if not all, of these were unfortunately discarded by Fox), and some human fossils. The main feature of this level is an extensive lithic assemblage (so much so that Fox devotes an entire section to discussing it in his monograph with a degree of detail not accorded to the other lithic assemblages), composed of "... hundreds of lumps and nodules of chert, cores, waste flakes, primary flakes, as well as utilized flake" and, like Flake Assemblage II, also represents various stages of the *chaîne opératoire* (Fox, 1970: 29). Fox interpreted the spatial distribution of the lithic remains as corresponding to workshop areas in the cave.

Figure 198 summarizes the spatial relationships between available chronological data immediately below and above the yellow speleothem.

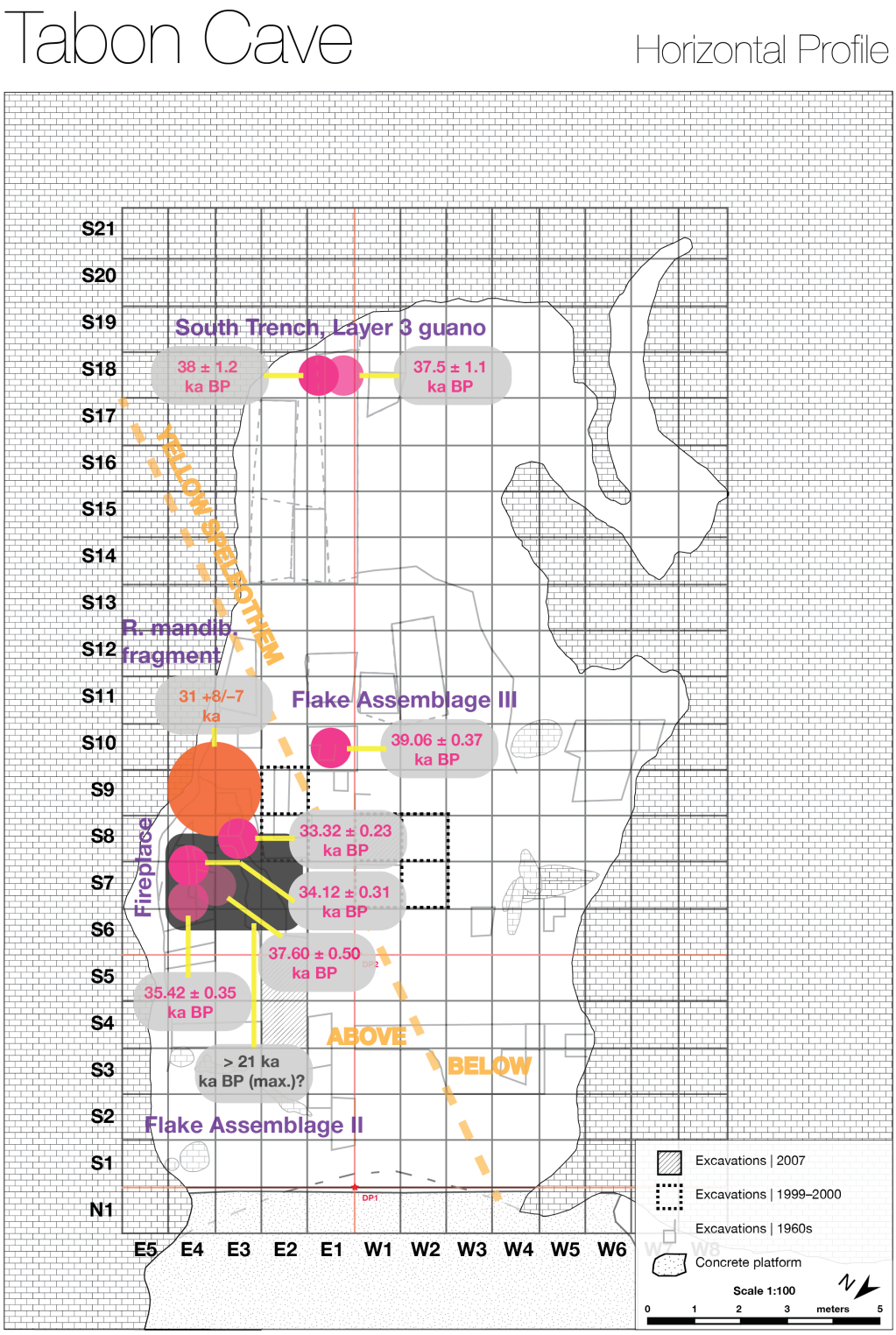

Figure 198. Spatial distribution of available chronological data from dated materials stratigraphically situated immediately below and above the yellow speleothem. Below (right), Flake Assemblage III is practically contemporaneous with the Layer 3 guano deposit in the South Trench. Above (left), Flake Assemblage II (black rounded rectangle), the right mandibular fragment (orange circle), and the fireplace (pink circles) share close associations.

The abundance of lithic artefacts composing Flake Assemblages II and III may suggest relatively easy access to raw material. Schmidt (2008) concludes in his comparative and experimental study of lithic artefacts from Tabon Cave (which were unfortunately recovered in reworked contexts and impossible to attribute to any of the Fox flake assemblages) that the cave occupants would have travelled 7 to 8 km inland to the southwest to collect raw material from the beds of the Panitian and Malatgao rivers. However, lower sea levels at this time (fluctuating between 40 and 80 m below current sea level; Chappell *et al.*, 1996; Yokoyama *et al.*, 2001; Chappell, 2002;) would have revealed other rivers that are submerged today by the South China Sea to the northeast (Robles *et al.*, 2015). These could also have served as sources of lithic raw material, as well as food.

The palaeoenvironmental data from the guano of Layer 3 in the South Trench, dated to around the same period as the human occupation corresponding to Flake Assemblage III, suggest a landscape that was overall characterized by closed forest but nevertheless included occasional clearings and other open areas. The climate was drier than present-day conditions. The human occupants that were responsible for Flake Assemblage III then abandoned the cave, upon which bats/birds took over and started the formation of the Layer 3 guano; however, they did not stay long as evidenced by the thinness of the layer compared to other guano deposits in the cave. This is possibly due to landscape instability leading to a short but intense peak of hydrological activity inside the cave between ca. 38 and 39 ka BP, marked by the formation of the yellow speleothem that separates Flake Assemblages II and III and supported by the second rockfall episode Layer 2 in the South Trench sequence, just above the thin guano deposit of Layer 3. At the end of this climatic interruption, conditions went back to being partly dry and thus favourable to the preservation of the yellow speleothem. The cave was then reoccupied by humans, leading to the formation of the fireplace and of Flake Assemblage II.

Figure 199 presents a schematic synthesis of the cave's stratigraphy accompanied by the corresponding climatic, environmental, and chronological data.

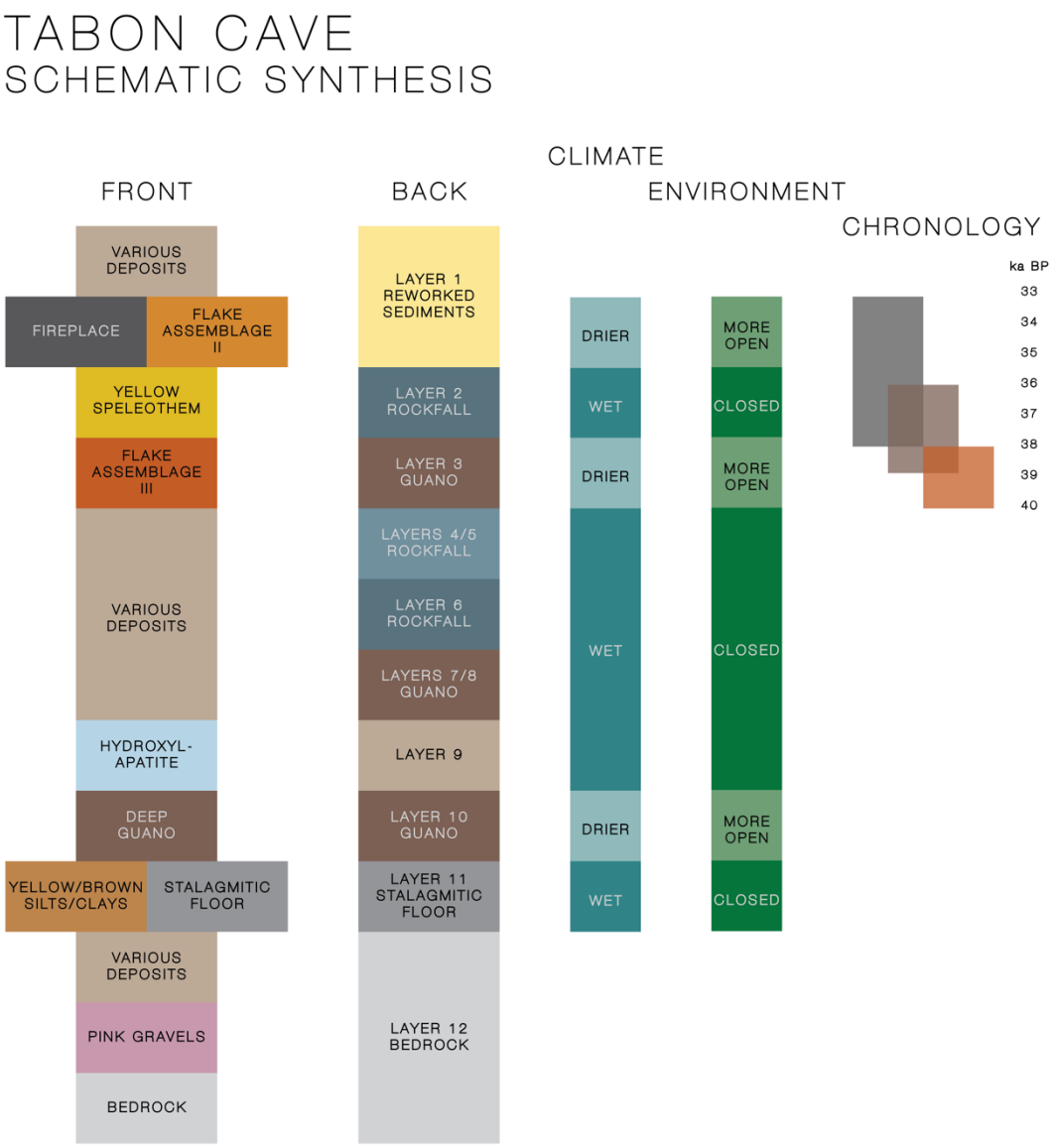

Figure 199. Schematic synthesis of Tabon Cave stratigraphy (for both the front and back halves of the cave), climate, environment, and chronology.

5.4. Methodological issues

While the approach of the present study was developed as a tailored response to the specific challenges posed by the site, it has also unexpectedly shed light on a number of issues that have more far-reaching implications.

5.4.1. Specific technical contributions

As regards the use of spectroscopic methods for mineralogical characterization, it was observed the study that X-ray diffraction was more effective than Fourier-transform infrared spectroscopy in identifying authigenic minerals. This finding is rather paradoxical, as authigenic minerals generally consist of small, poorly-formed crystals, whereas XRD is better adapted to highly crystalline materials. While identification through XRD was relatively straightforward (with occasional exceptions in the form of a few, unidentified peaks), the task was much more arduous with FTIR. Peaks were not always located where references indicated they should be; this variability could reflect an 'elastic' reaction by the underlying molecular structures in response to external chemical stimuli, such as those that characterize diagenesis.

However, XRD alone would not have been sufficient provide a complete picture of the mineralogical diversity of the Tabon Cave deposits. Amorphous phases, like opal, can only be detected in FTIR. Furthermore, FTIR peak shapes often reflect degree of crystallinity, which is related to diagenetic advancement; the technique thus provides insight into phase transitions and paints more detailed pictures of diagenetic states. FTIR is also better adapted to the identification and analysis of the very specific organic material treated in this work, chitin. Finally, another surprising result was how clay species were identified and distinguished in FTIR while going almost undetected in XRD—this could be due to the strong diagenesis undergone by clay minerals in Tabon Cave, making their crystal structure more amorphous.

These findings concerning mineralogical characterization techniques could have interesting implications for guano-rich sites in general, whether around the Mediterranean, in the Caribbean, in Southeast Asia, or in Oceania. In the Mediterranean and in Southeast Asia, there is strong emphasis on optical methods like soil micromorphology and back-scattered electron imaging in scanning electron microscopy; however, optical methods alone are insufficient for mineral identification, so spectroscopy has a complementary but nevertheless important function (Shahack-Gross *et al.*, 2004; Stephens *et al.*, 2017). In the Caribbean and in Oceania,

though, more comprehensive mineralogical characterization remains to be integrated into guano-based palaeoenvironmental studies, remaining relatively basic at this stage (Royer *et al.*, 2017; Wirrmann *et al.*, 2017).

Another subset of methodological contributions from this study concerns the guano pre-treatment protocol for stable isotope analysis. In particular, static dense medium separation needs to be optimized, as minerals like silicates were still left in the extracted organic matter. While silicates do not contain carbon, their presence may affect sample weighing for isotope analysis and is a potential source of error. Other contaminants may also be present—Wurster *et al.* (2010b) note that factors such as mineral orientation and size may call for additional purification steps, and in their study, dense medium separation was not able to remove all mineral matter. This particular step may need to be adapted to each study in terms of density adjustment, depending on the specific mineral content of the samples being analyzed.

5.4.2. Data quality

More generally, data quality in stable isotope analysis of guano is an important issue highlighted in this study that, so far, has not been sufficiently addressed in the literature. In many cases, this did not appear to be a problem, as guano deposits were successfully corroborated with other proxies (particularly palynological ones; see Forray *et al.*, 2015 and Campbell *et al.*, 2017). However, cross-validation by other proxies is not necessarily conclusive and can, in fact, be argued to be insufficient. Whenever possible, independent means of establishing data reliability should be employed as a form of 'internal' quality assurance testing before proceeding with cross-validation. Some disciplines, like palynology, rely on statistics to establish this. While similar tools are not necessarily applicable to other fields because of the nature of the material that they work with, it remains important to be aware of the limitations of one's data.

In certain contexts, the quality of guano stable isotope data warrants more than careful examination: this is the case at greater time depths and in humid, tropical environments. Aside from being risk factors for the destruction and reworking of organic matter (through decomposition and bioturbation; Cleary *et al.*, 2016), these two conditions are also often associated with guano diagenesis: they nurture complex chains of geochemical processes, embodied by authigenic mineral formations, that may impact stable isotope data and the resulting interpretations. In sites like Tabon Cave, where 'traditional' proxies like pollen

and fauna are rare and where guano is one of the few rare sources of palaeoenvironmental information, data quality is thus a crucial component of an integrated research strategy. Morley (2017:5) notes that, "at present[,] we have generated insufficient geoarchaeological data from the humid tropics to be confident in the recognition of biological and chemical signatures specific to these exceptional environments."

5.4.3. Dating methods

Geochemical dynamics are also important to take into account in geochronological research. This is already the case with uranium-series dating of open-system calcareous materials, including bones and teeth: uptake models (e.g. linear uptake, diffusion-adsorption-decay) are applied to minimize the gap between calculated and true ages by approximating real-world conditions—notably uranium exchanges with the outside environment—as closely as possible (Grün and Taylor, 1996; Thompson *et al.*, 2003; Villemant and Feuillet, 2003; Scholz *et al.*, 2004; Sambridge *et al.*, 2012). However, in sites that are rich in organic matter, the highly complex interaction between uranium compounds and organic matter on the molecular level, combined with the biochemical intervention of microorganisms, mean that much more care should be taken in interpreting uranium-series data in these contexts (Cumberland *et al.*, 2016). For Tabon Cave, a concrete consequence is the potential necessity of re-examining and nuancing the uranium-series ages obtained on the human fossils (although this is frustratingly complicated by the fact that the original sedimentary contexts of the fossils are unknown).

The radiocarbon ages published in this study are another unexpected surprise (the fireplace was, in particular, dated multiple times over several years): they challenge the orthodox cultural chronology of Tabon Cave that has been in place since the 1970s, especially by pushing back the age of Flake Assemblage III by around 15 ka. It is possible that other radiocarbon ages produced during the early days of the method may need to be re-evaluated today, especially given advances in radiocarbon research over the past several decades.

5.4.4. Regional climate models

The regional climatic significance of the extensive, gypsiferous yellow speleothem in Tabon Cave needs to be reviewed. Up to this point, it has been considered to represent a peak in humidity just before the Last Glacial Maximum around 20 ka ago (Bird *et al.*, 2007; Lewis *et al.*, 2008). However, the results of this study push its potential age back by 16 to 18 ka.

This would put it in MIS 3 and line it up with Dansgaard-Oeschger cycles 8 to 5, situated between Heinrich events 4 and 3, as recorded in $\delta^{18}O$ data from the northern South China Sea (Figure 200; Oppo and Sun, 2005). Growing evidence points to a link between Dansgaard-Oeschger cycles, and fast and strong hydrological responses in tropical and subtropical zones (Medina-Elizalde *et al.* 2017); this speleothem could be the result of such a response, corresponding to a relatively short but extremely intense period of precipitation. These patterns extend further south into the Sulu Sea (immediately southeast of Palawan) and demonstrate the significant influence of the East Asian monsoon on the region's climate (Figure 201; Dannenmann, 2003).

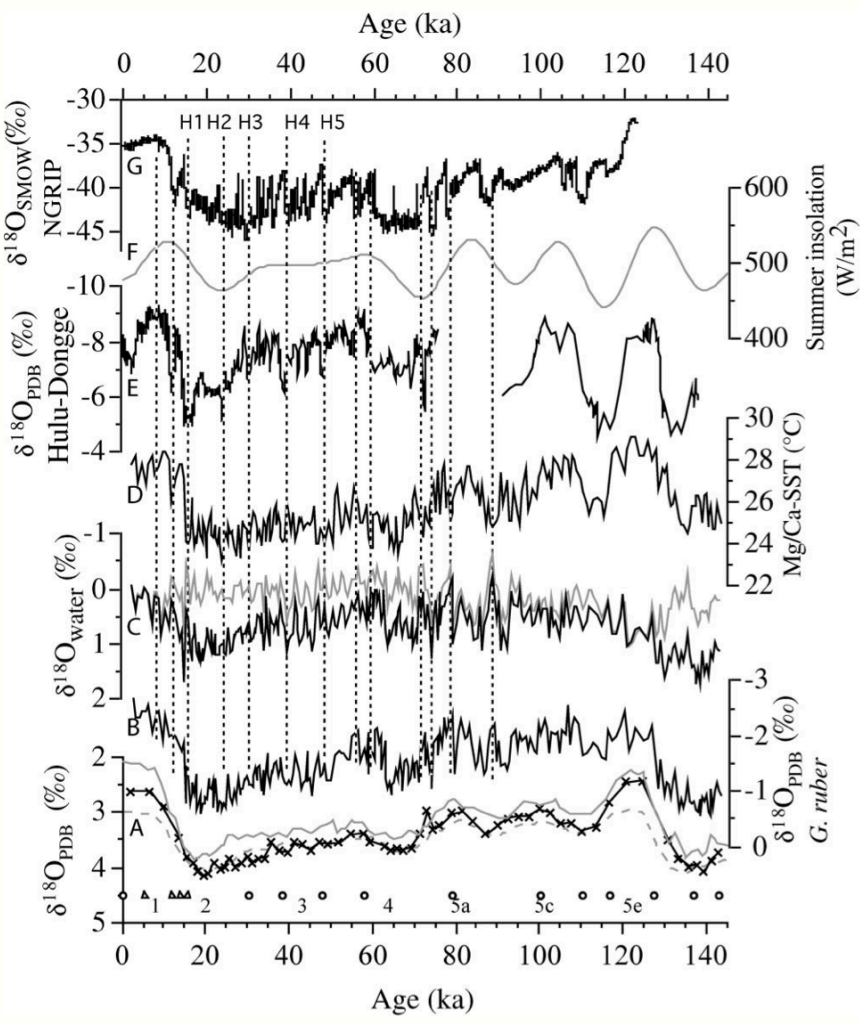

Figure 200. $\delta^{18}O$ curves from Site 1145 in the northern South China Sea (A, B, C, D), Hulu Cave in China (E), and Greenland ice (G) (Oppo and Sun, 2005). The yellow speleothem is estimated to have developed between Heinrich events 4 and 3 (H4 and H3).

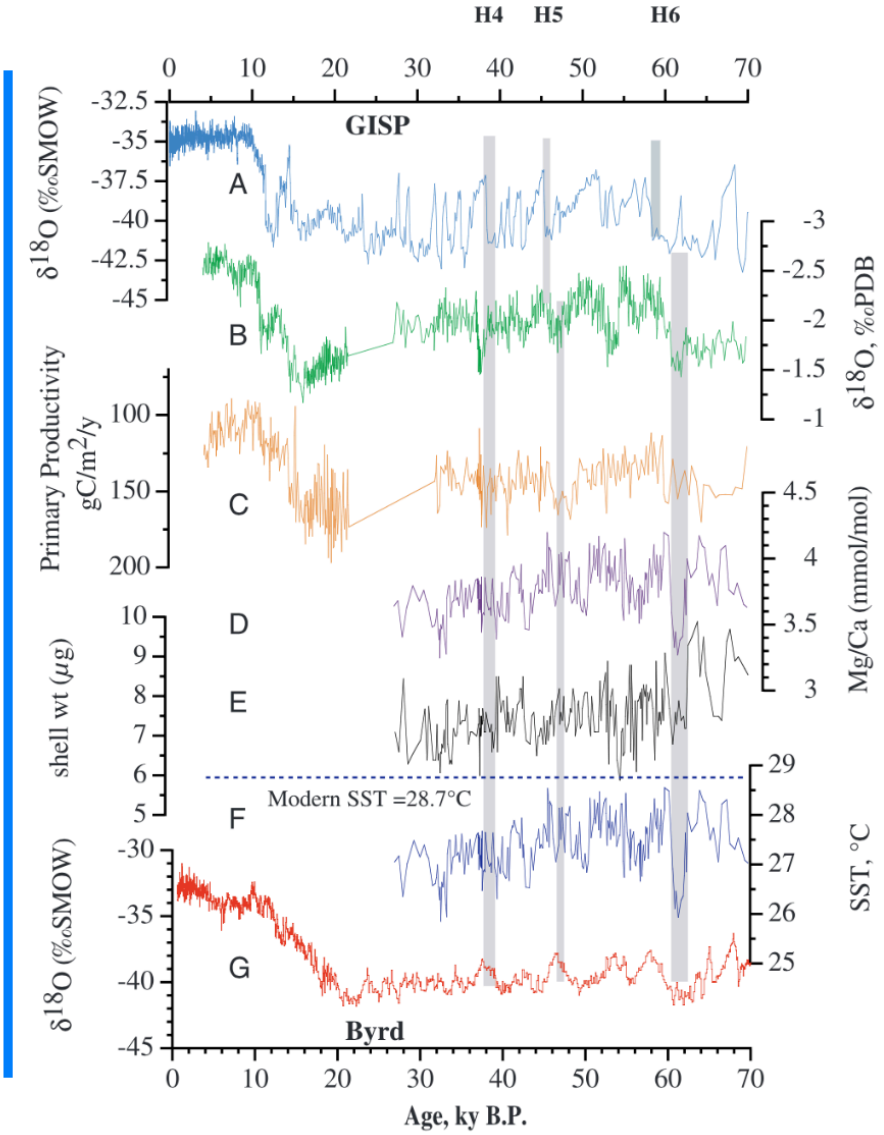

Figure 201. $\delta^{18}O$ curves from Greenland ice (A), Hulu Cave in China (B), Sulu Sea (C, D, E), and Antartica ice (F) (Dannenmann, 2003).

Regional climate models, including the Sundaland 'savanna corridor' proposed by Heaney (1991) and later expanded by Bird *et al.* (2005), as well as the concept of 'rainforest refugia' (Gathorne-Hardy *et al.*, 2002; Wurster *et al.*, 2010a), deal primarily with biogeographical developments around the Last Glacial Maximum, at the start of MIS 2. Data from terrestrial records have been lacking on MIS 3, despite its significance as the period during which *Homo sapiens* arrived in Island Southeast Asia, and the present study contributes to this gap.

5.4.5. The study of complex cave sediments

On a more positive note, Tabon Cave is an example of how complex sedimentary sequences, which are actually quite widespread in caves, can still yield useful information when studied using targeted, innovative approaches. This is important as many caves are of archaeological importance, and proper interpretation of their deposits is crucial to understanding human occupation and use. It is important to adjust expectations when dealing with complex sequences, to be realistic about the kinds of data that they can provide and the kinds of research questions that they can address, and to adapt one's strategy accordingly. Caves are extremely complex and dynamic environments, where sedimentation and geology are intertwined with biological activity, and where localized processes lead to heterogeneous facies. Hunt *et al.* (2015) point out that reassessment of existing cave sequences in light of modern techniques, as has been done in this study, will inevitably lead to the realization of previously unsuspected complexity (notably in terms of chronology), and that the proper consideration of this complexity is necessary to draw sound archaeological interpretations. This is even more true in tropical environments, where specific challenges await the unprepared geoarchaeologist: increased biological dynamism, monsoon effects, taphonomic processes, and soil formation (Morley and Goldberg, 2017).

While this work has delved primarily into chemical phenomena underpinning the formation of certain deposits, the complementary perspective provided by the understanding of physical processes through approaches such as soil micromorphology would certainly have helped complete the picture, especially given strong evidence of phenomena such as bioturbation and reworking in Tabon Cave. Various models have been proposed for understanding authigenic mineral formation in caves based on chemical data, including stability fields (Karkanas *et al.*, 2000) and reaction cascades (Weiner *et al.*, 2002), but they have not been able to explain why 'early-stage' minerals coexist with 'advanced-stage' minerals in many of the deposits in Tabon Cave. Rather than a linear process, authigenic mineral formation in tropical cave deposits is probably more similar to a web, with numerous physical and chemical factors criss-crossing in complex interplay. It is relatively straightforward to discuss the formation of individual minerals, usually by identifying sources for their component atoms or molecules, or by predicting the conditions of their genesis; what is extremely intricate is how *entire assemblages* evolve in time in reaction to changes in their environment.

5.4.6. Stratigraphical specificities

In archaeology, the site is the macroscopic unit that serves as the framework for the disciplinary studies that are essential components of modern research projects, and stratigraphy is the central pillar of this framework. Poor understanding of this element handicaps disciplinary studies and limits how far they can go in their interpretations. While it is at some point necessary to undertake simplifications in order to obtain an overall perspective, spatial variability must not be ignored; embracing specificities paves the way for more accurate interpretations, especially in sites with complex depositional histories like caves. Far from being a static entity that merely serves as a stage for biological activity, cave sites themselves can almost be considered 'living', transforming and evolving over time. Every modern archaeological research project should thus incorporate a basic understanding of site formation processes, and even though much work remains to be done, it is reassuring that the future of geoarchaeology seems to be headed in this direction, especially in Southeast Asia (Canti and Huisman, 2015; Morley and Goldberg, 2017).

Chapter VI

Conclusion

In recent years, considerable efforts and resources have been dedicated to advancing research on Southeast Asian prehistory. Old sites are being re-examined from fresh angles using modern methods, while new sites of key importance continue to surface. However, many basic interrogations remain surrounding the arrival, dispersions, and lifeways of anatomically modern humans in the region during the Late Pleistocene. Who were the first true *Homo sapiens* to set foot on the Philippine archipelago? How did they navigate and adapt to their new island landscapes? What was their world like in terms of environment and climate? These big questions remain surprisingly difficult to answer in a clear and straightforward manner in 2018, but it is hoped that the present study has shone some light on them.

Tabon Cave is a particularly challenging archaeological site to study due to the highly complex interplay between natural and human factors, but its unquestionable role in the story of our species in this part of the world make it an essential star in the constellation of Island Southeast Asian prehistory. This work initially set out to explore the geochemical history of the cave in the hope of understanding the environments—and, by extension, the lifeways and adaptations—of the first humans in Palawan. While resolving some pre-existing questions, the study also confirms the immense complexity of the site as seen in its intricate, interrelated physical and chemical dynamics. While further work needs to be done to acquire a detailed and truly complete understanding of the stratigraphy, the present study has shed light on certain aspects of it that are meaningful for understanding the environmental, climatic, and archaeological history of the site.

The back half of the cave is characterized by an apparently straightforward sequence, of which the most important features are three distinct guano deposits and two rockfall episodes. However, the simple appearance of the sequence belies the presence of authigenic minerals all throughout it. The deposits in the neighbouring diverticulum, thought to be a source of

clay material for the cave sequence (F. Sémah, *pers. comm.*), actually consist of guano and mirror the early stages of diagenesis that took place at the base of the South Trench.

In the front half of the cave, most of the complex, spatially variable sequences can be correlated with the help of two stratigraphic markers, the 'light-on-dark' guano weathering sequence and the yellow speleothem. The 'light-on-dark' sequence, composed of hydroxylapatite on variably altered fossil guano, and the yellow speleothem, composed of gypsum and other soluble minerals that are also products of guano diagenesis, reflect changes in cave chemistry (pH, oxidation conditions, humidity) related to cave environments, and possibly the larger environment. The ancient guano is interesting from a stratigraphical point of view as it appears to cover the entire cave area, thus linking the front and back halves of the site, heretofore seemingly unrelated. Meanwhile, the yellow speleothem is crucial from an archaeological perspective as it is sandwiched between Flake Assemblages III and II. A new radiocarbon date for Flake Assemblage III pushes the age of this archaeological context back by more than 15 ka to ca. 39 ka BP, while the fireplace that is very likely associated with Flake Assemblage II has been dated to between ca. 33 and 38 ka BP, older by at least 10 ka. These chronological constraints would actually place the yellow speleothem in MIS 3 rather than the Last Glacial Maximum. Since its formation presupposes an active hydrological regime inside the cave, and given the new chronological constraints on its possible age, its presence would point to a short but extremely wet period between ca. 36 and 38 ka BP. This interrupts an important phase of active human use of the cave, represented by Flake Assemblage III. However, following this short, wet period, dry conditions prevailed inside the cave, as suggested by the formation through evaporation, then subsequent preservation, of the yellow speleothem and its soluble constituent authigenic minerals (mainly gypsum). These conditions made the cave an ideal shelter at this time, and human presence reappears in the archaeological record through Flake Assemblage II and the fireplace.

Stable isotope analysis of the three phases of guano deposition reveals changing environments that are, for the most part, dominated by closed forest. The oldest phase, corresponding to the 'deep guano' layer covering the entire cave, is characterized by a broad variety of vegetation types that may be a result of cohabitation between guano producers with different foraging strategies. The intermediate phase of guano deposition paints a picture of a very wet environment that likely corresponded to thick tropical forest. Finally, during the phase

dated via radiocarbon to ca. 38 ka BP, conditions were drier than today and may indicate the presence of clearings and other open areas, although the environment was still relatively closed overall (in comparison with 'savannas' recorded in northern Palawan guano during the Last Glacial Maximum; Bird *et al.*, 2007; Wurster *et al.*, 2010a). Beyond the production of new palaeoenvironmental data that will be of value to future local and regional research, the uniqueness of the current study lies in the successful application of stable isotope analysis on guano in extracting palaeoenvironmental information from an important archaeological site—one that is not only poor in conventional markers like pollen and microfauna, but also subject to strong diagenetic changes. This could open up new perspectives for palaeoenvironmental research in similar guano-rich cave sites across the globe, notably in the Mediterranean, in the Caribbean, in Oceania, and elsewhere in Southeast Asia (Shahack-Gross *et al.*, 2004; Royer *et al.*, 2017; Stephens *et al.*, 2017; Wirrmann *et al.*, 2017).

An important and feasible avenue for future studies is classic analysis of carbonate speleothems, whether from Tabon Cave itself or from neighbouring caves in Lipuun Point. The application of uranium-series dating and ^{18}O isotope analysis on this material for chronological and palaeoclimatic reconstruction is a relatively mature field (McDermott, 2004; Fairchild *et al.*, 2006; McDermott *et al.*, 2006). This makes it less risky (although also less innovative) than direct study of phosphate/sulphate speleothems; microbial processing of phosphate sources, in particular, facilitates oxygen isotope exchange with water in the environment and makes it difficult to trace ^{18}O sources in these authigenic mineral speleothems (Chang *et al.*, 2010). This approach may enable discussion of the periodicity of environmental wetness in Lipuun Point during MIS 3 and possibly later, represented by the yellow speleothem and the rockfall episode that followed the youngest phase of guano deposition. The said period is of particular archeological interest for Palawan because of the sustained human presence in, and extensive use of, Tabon Cave, as evidenced by the richness of both Flake Assemblages III and II (Fox, 1970). Additionally, on a broader scale, this corresponds to the earliest arrivals and dispersals of anatomically modern humans in Island Southeast Asia. Palaeoclimatic and palaeoenvironmental data for MIS 3 in the region from terrestrial proxies are still sorely lacking, and future contributions would certainly help elucidate the conditions surrounding the colonization of the archipelagos by *Homo sapiens*.

Direct uranium-series dating of fossil guano and related phosphate and sulphate minerals is currently fraught with numerous problems. Changing hydrological regimes and ensuing transformations in cave chemistry have complex ties to guano diagenesis and uranium mobility that make it difficult to obtain reliable ages (B. Ghaleb, *pers. comm.*). The attempts performed on various materials in this study—the grey speleothem phosphates, hydroxylapatite, and the yellow speleothem gypsum—did not yield usable results. The age of the yellow speleothem gypsum sample was calculated to be 188.2 +5.5/–5.2 ka, which does not fit within the constraining radiocarbon ages of ca. 36 and 38 ka BP. This is attributed to strong influence from detrital thorium, most likely due to contamination from clay minerals, which may also have contributed excess uranium. Meanwhile, out of the five hydroxylapatite samples analyzed, three were technically undateable (beyond method limits), while the other two had calculated ages that are far from both each other (178.8 +6.1/–5.8 ka and 415.4 +47.8/–33.0 ka) and from the first sample test-dated in this layer (109.8 ± 2.6 ka). The high uranium content and the proximity of the activity ratios to secular equilibrium suggest continuous enrichment and leaching, part of which could be due to the underlying guano layer, as organic matter microbiology and diagenetic chemistry influence uranium behaviour in complex ways (Cumberland *et al.*, 2016). Finally, the 'grey speleothem' samples would have been the most promising ones because of an apparent relationship between uranium concentration and calculated age. A best-case scenario analysis in which the system would have become closed shortly after the formation of the deposit suggests that the uranium mobility, while still present, would have been confined within the deposit; this hypothesis puts the true age of the layer between 90 and 130 ka. However, without the use of models based on a more complete understanding of open radioactive system dynamics, the general approach of applying direct uranium-series dating to fossil guano and related phosphate and sulphate minerals currently does not seem to be viable for chronological studies. Other dating methods—for example, luminescence techniques—should be explored to place the stable isotope data from the older guano deposits in Tabon Cave within a chronological framework and thus maximize their value. Nevertheless, the analyses conducted in this study shine light on the complex geochemical dynamics behind the diagenetic processes at work in the cave and complement understanding of the mineralogical changes observed.

Concerning the human remains, the ones associated with the right mandibular fragment (the P-XIII-T-436 series) and corresponding to criteria for ancient fossils of probable Pleistocene age as defined by Corny (2008) merit evaluation through the combination of dating tests and contextual reconstruction. Assuming that their contextual association can be supported by their ages, palaeoanthropological analysis of these remains could be tied to lithic analysis (of either Flake Assemblage II or III), the fireplace ages, palaeoenvironmental data from stable isotopes on guano, and palaeoclimatic data as inferred from the yellow speleothem to give a more complete picture of human presence in the cave between 30,000 and 40,000 years ago. This is a key period for human evolution and dispersals in Island Southeast Asia, still poorly understood due to the paucity of Late Pleistocene hominin fossils in the region, but undoubtedly crucial in bridging the earliest human arrivals in the region and the transition into the Holocene and beyond.

Appendix A

Complete list of samples

The complete list of samples analyzed in the present study is presented in the following table.

Sample	Square	Wall	Depth (cm below DP)	Description
1	S2E1	N	260	Cream-coloured white concretions with green patina. Very compact; mineralised? Extends from surface to 283 cm below DP.
2	S2E1	N	292	Cream-coloured white sediment in light greyish brown sediment matrix; guano weathering horizon?
3	S2E1	N	312	Dark reddish brown sediment; guano? Loose.
4	S2E1	N	343	Dark greyish yellow sediment. Compact; mineralised?
5	S2E1	W	300-320	Localised white zones in loose dark reddish brown matrix; mineral formations in guano?
6	S2E1	S	367	White sediment above black sediment; early guano weathering horizon?
7	S2E1	S	337	Black sediment; guano?
8	S4W4	S	302	Dark reddish brown sediment; guano?
9	S4W4	S	318	Dark reddish brown sediment; guano?
10	S4W4	S	325	Dark reddish brown sediment; guano?
11	S4W4	S	332	Dark reddish brown sediment; guano?
12	S4W4	S	337	Dark reddish brown sediment; guano?
13	S4W4	S	145	Dark reddish brown; clay?
14	S4W5	S	140	Dark reddish brown; clay?
15	S4E1	S	300	Light greyish white
16	S8E1	W	212	Light whitish yellow

17	S8E1	W	260	Light brownish white; concretions
18	S8E1	W	280	Light brownish white; tabular layer?
19	S8E1	W	300	Mid-reddish brown
20	S8E1	W	318	Light brownish white
21	S8E1	W	326	Dark purplish black
22	S6E2	E	165	Light yellowish white; compact block
23	S6E2	E	233	Purple mineral with powdery yellow coating
24	S6E2	E	260	Pink concretions
25	S6E2	E	305	Light brownish white
26	S8E1	W	350	Dark brownish purple
27	S2E1	S	266	Indurated pink concretion; x = 50, y = 0
28	S6E4	N	307	From Layer 7 on profile
29	S8W1	S	249	From orange layer under yellow speleothem in longitudinal section/Layer 3 on S8E1 profile
30	Diverticulum	-	Surface	Deposit from small chamber
31	S8E4	E	121	Fox baulk; bioturbated layer? Dark greyish brown
32	S8E4	E	136	Mid-greyish brown
33	S7E4	E	157	Light brownish white
34	S8E4	E	168	Pink bedding
35	S8E4	E	182	Mid-brownish white
36	S9E3	E	125	Dark blackish brown; bioturbated?
37	S9E3	E	144	Dark purplish brown
38	S9E3	E	157	Mid-greyish white
39	S9E3	E	167	Light brownish white; indurated plaques
39.5	S9E3	E	213	Light brownish white; loose
40	S9E3	E	231	Light brownish white; indurated plaques
41	S9E3	E	259	Light brownish white; loose
42	S9E3	E	276	Light brownish white; loose
43	S9E3	E	299	Light brownish white; round aggregates
44	S8E3	E	305	Light brownish white; loose

45	S8E3	E	325	Dark reddish brown; loose
46	S6E2	E	222	Mid-greyish brown; round aggregates
47	S6E2	E	217	Light reddish brown; bioturbated?
48	S6E2	E	207	Light reddish brown; loose
49	S6E2	E	199	Light brownish white; loose
50	S6E2	E	182	Light brownish white; loose
52	S14E2	-	Surface	Modern guano
53	S9W6	-	Surface	Modern guano
A	South Trench	S	333	Dark yellowish brown; clayey
B	South Trench	S	285	Dark reddish black; from Layer 10 on profile
C	South Trench	S	238	Mid-greyish brown
D	South Trench	S	220	Mid-reddish brown; from Layer 7/8 on profile
E	South Trench	S	162	Mid-yellowish brown
F	South Trench	S	142	Dark reddish brown; from Layer 3 on profile
G	South Trench	E	113	From capping speleothem/Layer 1 on profile
MM1	South Trench	S	316-321	
MM2	South Trench	S	265-270	
MM3	South Trench	S	223-228	
MM4	South Trench	S	135-140	
TABON2016BULK03	S4W1	E	313	Bulk sample from Layer 5 on profile (fossil guano?)

TABON2016BULK04	S4W1	E	313	Bulk sample from Layer 5 on profile (fossil guano?)
TABON2016BULK05	S4W1	E	313	Bulk sample from Layer 5 on profile (fossil guano?)
TABON2016BULK06	S4W1	E	313	Bulk sample from Layer 5 on profile (fossil guano?)
TABON2016BULK07	S Trench	S	135	Bulk sample from Layer 3 on profile (fossil guano?)
TABON2016BULK08	S Trench	S	135	Bulk sample from Layer 3 on profile (fossil guano?)
TABON2016BULK09	S Trench	S	135	Bulk sample from Layer 3 on profile (fossil guano?)
TABON2016BULK10	S Trench	S	130	Bulk sample from Layer 3 on profile (fossil guano?)
X1	S10E1	S	560	Mid-greenish yellow
X2	S10E1	S	540	Dark greenish grey
X3	S10E1	S	515	Dark yellowish brown
X4	S10E1	S	500	Dark greyish brown; laminated white concretions
X5	S10E1	S	?	Dark yellowish brown; indurated lumps
X6	S10E1	S	477	Dark greyish brown; dry; assorted particle sizes
X7	S10E1	S	445	Dark yellowish black; very hard indurated rocks with sharp angles
X8	S10E1	S	420	Dark brownish black; white grains
X9	S10E1	S	400	Dark reddish brown; pink inclusions; white alterations on indurated fragments
X10	S10E1	S	390	Mid-yellowish brown; assorted grain size
X11	S10E1	S	380	Mid-yellowish brown; assorted
X12	S10E1	S	370	Mid-reddish brown; uric acid
X13	S10E1	S	347	Dark reddish brown; indurated chunks
X14	S10E1	S	346	Mid-greyish brown; loose; aggregate inclusions
X15	S10E1	S	340	Dark reddish brown; loose
X16	S10E1	S	325	Mid-yellowish brown; concretions

X17	S10E1	S	318	Dark reddish brown; loose
X18	S10E1	S	303	Dark greyish brown; loose
X19	S10E1	S	282	Light greyish brown; loose
X20	S10E1	S	277	Light greyish brown; indurated plaques
X21	S2E5	*	140	Dark yellowish brown; indurated chunks; *under stalagmitic pillar
X22	S1E5	*	180	Dark yellowish brown; round aggregates; *surface sediment

Appendix B

Sample preparation protocol for stable isotope analysis

This appendix details the implementation of the sample preparation protocol for stable isotope analysis developed and applied in this study.

B.1. Delipidation

Delipidation was performed via solvent extraction.

Approximately 6 g of each sample was weighed into a corresponding 50-ml Erlenmeyer flask. The flasks were placed in a drying oven set to 40 °C and left to sit overnight to eliminate moisture.

The next day, the samples were taken out and placed under a fume hood. A 2:1 solution by volume of chloroform/methanol was prepared as solvent, and 40 ml was poured into each flask. The flasks were agitated manually to homogenize the contents, then covered with aluminium foil to minimize evaporation. After 2 hours, the flasks underwent sonication for 5 minutes, with occasional manual agitation. After another 2 hours, the flasks were sonicated again. Finally, after 2 more hours (6 hours after solvent introduction), the samples were transferred to 100-ml round-bottom glass centrifuge tubes and centrifuged at 2000 rpm. The liquid phase, containing dissolved lipids, was then transferred into 250-ml glass beakers. The beakers and the centrifuge tubes, loosely capped, were left under a fume hood for evaporation.

The solvent bath and double sonication were repeated the following day. For the sonication, custom foam moulds were fabricated to hold the centrifuge tubes upright. Centrifugation and

collection of dissolved lipids in the same beakers were repeated, after which the beakers and the loosely capped centrifuge tubes were left to sit for evaporation, as was previously done.

On the fourth day, the samples received a last solvent bath and again underwent double sonication. They were not agitated this time before centrifugation. Dissolved lipids were transferred into the corresponding, existing beakers and allowed to evaporate as before together with the centrifuge tubes, which were now left uncapped.

Upon drying, the beaker contents were scraped and transferred into glass vials for storage.

B.2. Static dense medium separation

A sodium polytungstate (SPT) solution was prepared and adjusted to obtain a density of 1.87 g/cm^3. (A special formulation with very low carbon and nitrogen concentration was used to minimize exogenous contributions to geochemical data: SPT0 by TC-Tungsten Compounds, Grub am Forst, Germany). A volume of 25 ml was added to each sample in its centrifuge tube. The tubes were then agitated manually and sonicated for 20 minutes, followed by centrifugation for 12 minutes at 1800 rpm to separate the light and heavy fractions, with the SPT in between. Afterward, the samples were transferred to a tube rack and left to settle overnight to complete the separation.

The following day, the tube rack was placed in a freezer for at least 3 hours to solidify the samples and enable recovery of the light fraction on top while keeping the heavy fraction at the bottom in place. The tubes were taken out one at a time and allowed to thaw slightly, upon which the light fraction was scraped into 50-ml beakers. The beakers were then covered with aluminium foil to protect the samples from contamination, whereas the tubes were set aside for SPT recovery later.

B.3. Recovery of insect cuticles

A filtration system was set up by connecting a polysulfone filtration unit (Thermo Scientific™ Nalgene™), fitted with glass fibre filters of 0.7 µm-retention capacity (Grade 698; VWR, Pennsylvania, USA), to a vacuum pump.

Each sample was filtered with distilled H_2O to eliminate the associated SPT. The filter was then recovered and placed in the original 50-ml beaker corresponding to the sample. The aluminium foil covers were put back on the beakers.

The tubes were centrifuged for 12 minutes at 1800 rpm to re-separate the SPT from the solid phase. The resulting liquid fraction, concentrating the SPT in solution, was transferred to a 1-L beaker, filtered, and stored in a tightly sealed bottle for reuse.

The filters were transferred from their 50-ml beakers to 250-ml ones. Sample material was then rinsed from the filters with 2N HCl. The samples were left to sit in the acid bath for 3 hours.

After the bath, the samples were filtered with distilled H_2O to rinse off the HCl. The new filters carrying the samples were then transferred into the original 50-ml beakers.

Next, the samples were rinsed off their filters into 100-ml round-bottom centrifuge tubes using distilled H_2O. Centrifugation was done for 12 minutes at 1800 rpm. Afterward, excess H_2O was poured off, with just a few millilitres left to keep the samples immersed. The tubes were then agitated to dislodge solid sample particles stuck to the bottom. Now in suspension, the samples were poured into glass vials, the tubes rinsed with distilled H_2O to minimize sample loss.

Water content in the vials was reduced by approximately three-quarters using a pipette. The vials were covered with aluminium foil, in which 6 holes were pierced. The samples were then placed in a freezer for 3 hours.

Next, the samples were transferred into a freeze dryer (Alpha 2-4 LD; Martin Christ Gefriertrocknungsanlagen GmbH, Osterode am Harz, Germany), pre-chilled to –80 °C. Once the samples were in place, the pressure was gradually reduced to 100 mbar to bring the temperature down to an ideal –90 °C. Freeze-drying was left to continue overnight.

The following day, the samples were transferred into a dessicator for storage until analysis.

B.4. Verification

Finally, select samples were verified for chitin content. Given the extremely small amount of material left after application of the protocol, as well as the presence of characteristic infrared spectrum peaks in chitin that facilitate its identification, *Fourier-transform infrared microspectroscopy* was deemed to be the most suitable technique for this step.

Samples were mounted on a diamond cell for analysis via an infrared microspectroscope. Spectra were acquired in transmission mode and converted to absorbance mode for results presentation. Scanning was performed at a resolution of 4 cm^{-1} with 256 scans for samples and 512 scans for the background.

References

Bargar, J.R., Williams, K.H., Campbell, K.M., Long, P.E., Stubbs, J.E., Suvorova, E.I., Lezama-Pacheco, J.S., Alessi, D.S., Stylo, M., Webb, S.M., Davis, J.A., Giammar, D.E., Blue, L.Y., Bernier-Latmani, R., 2013. Uranium redox transition pathways in acetate-amended sediments. *Proceedings of the National Academy of Sciences of the USA* 110, pp. 4506–4511.

Barker, G. (ed.), 2013. *Rainforest Foraging and Farming in Island Southeast Asia*, Cambridge: McDonald Institute for Archaeological Research, University of Cambridge.

Barker, G., Barton, H., Bird, M., Daly, P., Datan, I., Dykes, A., Farr, L., Gilbertson, D., Harrisson, B., Hunt, C.O., Higham, T., Kealhofer, L., Krigbaum, J., Lewis, H., McLaren, S.J., Paz, V., Pike, A., Piper, P., Pyatt, B., Rabett, R., Reynolds, T., Rose, J., Rushworth, G., Stephens, M., Stringer, C., Thompson, J., Turney, C., 2007. The "human revolution" in lowland tropical Southeast Asia. *Journal of Human Evolution* 52, pp. 243–261.

Barker, G., Farr, L. (eds.), 2016. *Archaeological Investigations in the Niah Caves, Sarawak*. Cambridge: McDonald Institute for Archaeological Research, University of Cambridge.

Bautista, A., 2000. *Archaeological assessment of the area in front of Tabon Cave, Lipuun Point, Quezon, Palawan.* Manila: National Museum of the Philippines. Unpublished report.

Berger, R., Libby, W.F., 1966. UCLA Radiocarbon Dates V. *Radiocarbon* 8, pp. 467–497.

Berna, F., Matthews, A., Weiner, S., 2004. Solubilities of bone mineral from archaeological sites: the recrystallization window. *Journal of Archaeological Science* 31, pp. 867–882.

Bird, M., Taylor, D., Hunt, C.O., 2005. Palaeoenvironments of insular Southeast Asia during the Last Glacial Period: a savanna corridor in Sundaland? *Quaternary Science Reviews* 24, pp. 2228–2242.

Bird, M., Boobyer, E.M., Bryant, C., Lewis, H., Paz, V., Stephens, W.E., 2007. A long record of environmental change from bat guano deposits in Makangit Cave, Palawan, Philippines. *Earth and Environmental Science Transactions of the Royal Society of Edinburgh* 98, pp. 59–69.

Bowler, J.M., Johnston, H., Olley, J.M., Prescott, J.R., Roberts, R.G., Shawcross, W., Spooner, N.A., 2003. New ages for human occupation and climatic change at Lake Mungo, Australia. *Nature* 421, pp. 837–840.

Bowsher, C., Steer, M., Tobin, A., 2008. *Plant Biochemistry*. New York/Abingdon: Garland Science.

Brown, T., Brown, K., 2011. *Biomolecular Archaeology: an Introduction.* Wiley-Blackwell.

Brown, R.M., Diesmos, A.C., 2009. Philippines, Biology, in: Gillespie, R.G., Clague, D.A. (eds.), *Encyclopedia of Islands*. Berkeley/Los Angeles/London: University of California Press, pp. 723–731.

Campbell, J.W., Waters, M.N., Rich, F., 2017. Guano core evidence of palaeoenvironmental change and Woodland Indian inhabitance in Fern Cave, Alabama, USA, from the mid-Holocene to present. *Boreas* 46, pp. 462–469.

Cárdenas, G., Cabrera, G., Taboada, E., Miranda, S.P., 2004. Chitin characterization by SEM, FTIR, XRD, and ^{13}C cross polarization/mass angle spinning NMR. *Journal of Applied Polymer Science* 93, pp. 1876–1885.

Cerling, T.E., Harris, J.M., MacFadden, B.J., Leakey, M.G., Quade, J., Eisenmann, V., Ehleringer, J.R., 1997. Global vegetation change through the Miocene/Pliocene boundary. *Nature* 389, pp. 153–158.

Chappell, J., 2002. Sea level changes forced ice breakouts in the Last Glacial cycle: new results from coral terraces. *Quaternary Science Reviews* 21, pp. 1229–1240.

Chappell, J., Omura, A., Esat, T., McCulloch, M., Pandolfi, J., Ota, Y., Pillans, B., 1996. Reconciliaion of late Quaternary sea levels derived from coral terraces at Huon Peninsula with deep sea oxygen isotope records. *Earth and Planetary Science Letters* 141, pp. 227–236.

Choa, O., 2014. *Diagenesis in a guano-rich tropical cave site: palaeoenvironments and archaeological record preservation of Tabon Cave, Palawan, the Philippines.* Paris: Muséum national d'histoire naturelle. Master's thesis.

Choa, O., Lebon, M., Gallet, X., Dizon, E., Ronquillo, W., Jago-on, S.C., Détroit, F., Falguères, C., Ghaleb, B., Sémah, F., 2016. Stable isotopes in guano: Potential contributions towards palaeoenvironmental reconstruction in Tabon Cave, Palawan, Philippines. *Quaternary International* 416, pp. 27–37.

Clarkson, C., Jacobs, Z., Ben Marwick, Fullagar, R., Wallis, L., Smith, M., Roberts, R.G., Hayes, E., Lowe, K., Carah, X., Florin, S.A., McNeil, J., Cox, D., Arnold, L.J., Hua, Q.,

Huntley, J., Brand, H.E.A., Manne, T., Fairbairn, A., Shulmeister, J., Lyle, L., Salinas, M., Page, M., Connell, K., Park, G., Norman, K., Murphy, T., Pardoe, C., 2017. Human occupation of northern Australia by 65,000 years ago. *Nature* 547, pp. 306–310.

Cleary, D.M., Onac, B.P., Forray, F.L., Wynn, J.G., 2016. Effect of diet, anthropogenic activity, and climate on $\delta^{15}N$ values of cave bat guano. *Palaeogeography, Palaeoclimatology, Palaeoecology* 461, pp. 87–97.

Corlett, R., 2014. Biogeography, in: *The Ecology of Tropical East Asia*. Oxford: Oxford University Press, pp. 62–85.

Corny, J., 2008. *Les restes humains de la grotte de Tabon (Palawan, Philippines) : répartition spatiale et étude d'une collection d'ossements inédite.* Paris: Muséum national d'histoire naturelle. Master's thesis.

Corny, J., Détroit, F., 2010. Les ossements humains de la grotte de Tabon (Palawan, Philippines) : répartition spatiale et étude d'une collection d'ossements inédite. *Annali dell'Università di Ferrara, Museologia Scientifica e Naturalistica* 6, pp. 77–84.

Cumberland, S.A., Douglas, G., Grice, K., Moreau, J.W., 2016. Uranium mobility in organic matter-rich sediments: a review of geological and geochemical processes. *Earth Science Reviews* 159, pp. 160–185.

Demeter, F., Shackelford, L., Westaway, K.E., Barnes, L., Duringer, P., Ponche, J.-L., Dumoncel, J., Sénégas, F., Sayavongkhamdy, T., Zhao, J., Sichanthongtip, P., Patole-Édoumba, E., Dunn, T., Zachwieja, A., Coppens, Y., Willerslev, E., Bacon, A.-M., 2017. Early modern humans from Tam Pà Ling, Laos: fossil review and perspectives. *Current Anthropology* 58, pp. S527–S538.

Des Marais, D.J., Mitchell, J.M., Meinschein, W.G., Hayes, J.M., 1980. The carbon isotope biogeochemistry of the individual hydrocarbons in bat guano and the ecology of the insectivorous bats in the region of Carlsbad, New Mexico. *Geochimica et Cosmochimica Acta* 44, pp. 2075–2086.

Détroit, F., Dizon, E., Falguères, C., Hameau, S., Ronquillo, W., Sémah, F., 2004. Upper Pleistocene *Homo sapiens* from Tabon Cave (Palawan, Philippines): description and dating of new discoveries. *Comptes Rendus Palevol* 3, pp. 705–712.

Dizon, E., 2000. *A brief report on the Tabon fossils research in France.* Unpublished report.

Dizon, E., Détroit, F., Sémah, F., Falguères, C., Hameau, S., Ronquillo, W., Cabanis, E., 2002. Notes on the morphology and age of the Tabon Cave fossil *Homo sapiens*. *Current Anthropology* 43, pp. 660–666.

Dizon, E., 2003. New direct dating of the human fossils from Tabon Cave, Palawan, Philippines, in: *Proceedings of the Society of Philippine Archaeologists Volume I*, pp. 63–67.

Dumitraş, D.-G., Marincea, Ş., Bilal, E., Hatert, F., 2008. Apatite-(CaOH) in the fossil bat guano deposit from the "dry" Cioclovina Cave, Şureanu Mountains, Romania. *The Canadian Mineralogist* 46, pp. 431–445.

Dykes, A.P., 2007. Mass movements in cave sediments: investigation of a ~40,000-year-old guano mudflow inside the entrance of the Great Cave of Niah, Sarawak, Borneo. *Landslides* 4, pp. 279–290.

Fairchild, I.J., Smith, C.L., Baker, A., Fuller, L., Spötl, C., Mattey, D., McDermott, F., EIMF, 2006. Modification and preservation of environmental signals in speleothems. *Earth Science Reviews* 75, pp. 105–153.

Ferguson, G.J., Libby, W.F., 1963. *UCLA Radiocarbon Dates III.* California: Institute of Geophysics, University of California, Los Angeles. Mimeo.

Folk, R.L., Ward, W.C., 1957. Brazos River bar: a study in the significance of grain size parameters. *Journal of Sedimentary Petrology* 27, pp. 3–26.

Forbes, M.S., Bestland, E.A., 2006. Guano-derived deposits within the sandy cave fills of Naracoorte, South Australia. *Alcheringa: an Australasian Journal of Palaeontology* 30, pp. 129–146.

Forray, F.L., Onac, B.P., Tanţău, I., Wynn, J.G., Tămaş, T., Coroiu, I., Giurgiu, A.M., 2015. A Late Holocene environmental history of a bat guano deposit from Romania: an isotopic, pollen and microcharcoal study. *Quaternary Science Reviews* 127, pp. 141–154.

Fox, R.B., 1969. *Tabon Cave vertical profiles.* Unpublished data.

Fox, R.B., 1970. *The Tabon Caves: Archaeological Explorations and Excavations on Palawan Island, Philippines.* Manila: National Museum of the Philippines.

Frechen, M., Sierralta, M., Oezen, D., Urban, B., 2007. Uranium-series dating of peat from central and northern Europe, in: Sirocko, F., Claussen, M., Goñi, M.F.S., Litt, T. (eds.), *The Climate of Past Interglacials.* Amsterdam/Oxford, pp. 93–117.

Fröhlich, F. 1981. L' analyse minéralogique des sédiments pélagiques associés aux nodule polymétalliques par la spectrométrie d' adsorption infrarouge. *Bulletin du Muséum national d' histoire naturelle de Paris* 3, pp. 159-181.

Fröhlich, F., 1989. Deep-sea biogenic silica: new structural and analytical data from infrared analysis – geological implications. *Terra Nova* 1, pp. 267–273.

Gallet, X., 2012. *Données stratigraphiques, sédimentologiques et géochronologiques du site de Tabon Cave (Palawan, Philippines).* Paris. Unpublished report.

Garrison, E.G., 2016. Instrumental analytical techniques for archaeological geology, in: *Techniques in Archaeological Geology*. Berlin/Heidelberg, pp. 209–246.

Gathorne-Hardy, F.J., Syaukani, Davies, R.G., Eggleton, P., Jones, D.T., 2002. Quaternary rainforest refugia in south-east Asia: using termites (Isoptera) as indicators. *Biological Journal of the Linnean Society* 75, pp. 453–466.

Ghaleb, B., Falguères, C., Sémah, A.-M., Sémah, F., 2012. *Progress report abstract: follow-up of the Tabon field trip (March 2012).* Unpublished report.

Gilbertson, D., Bird, M., Hunt, C.O., McLaren, S.J., Banda, R.M., Pyatt, B., Rose, J., Stephens, M., 2005. Past human activity and geomorphological change in a guano-rich tropical cave mouth: initial interpretations of the Late Quaternary succession in the Great Cave of Niah, Sarawak. *Asian Perspectives* 44, pp. 16–41.

Gross, J.H., 2017. *Mass Spectrometry: a Textbook.* Springer.

Grün, R., Taylor, L., 1996. Uranium and thorium in the constituents of fossil teeth. *Ancient TL* 14, pp. 21–25.

Harris, D., Horwath, W.R., van Kessel, C., 2001. Acid fumigation of soils to remove carbonates prior to total organic carbon or carbon-13 isotopic analysis. *Soil Science Society of America Journal* 65, pp. 1853–1856.

Harrison, T., Krigbaum, J., Manser, J., 2006. Primate biogeography and ecology on the Sunda Shelf islands: a paleontological and zooarchaeological perspective, in: Lehman, S.M., Fleagle, J.G. (eds.), *Primate Biogeography*. New York: Springer, pp. 331–372.

Heaney, L.R., 1991. A synopsis of climatic and vegetational change in Southeast Asia. *Climatic Change* 19, pp. 53–61.

Hoefs, J., 2015. Theoretical and experimental principles, in: *Stable Isotope Geochemistry*. Cham/Heidelberg/New York/Dordrecht/London: Springer, pp. 1–46.

Inman, D.L., 1952. Measures for describing the size distribution of sediments. *Journal of Sedimentary Research* 22, pp. 125–145.

Jago-on, S.C., 2006. *Analysis of the lithic materials recovered during the 2000–2001 archaeological excavations of Tabon Cave, Palawan Island, Philippines.* Paris: Muséum national d'histoire naturelle. Master's thesis.

Jones, H.G., 2009. *Plants and Microclimate*, 3rd ed. Cambridge: Cambridge University Press.

Karkanas, P., Kyparissi-Apostolika, N., Bar-Yosef, O., Weiner, S., 1999. Mineral assemblages in Theopetra, Greece: a framework for understanding diagenesis in a prehistoric cave. *Journal of Archaeological Science* 26, pp. 1171–1180.

Karkanas, P., Bar-Yosef, O., Goldberg, P., Weiner, S., 2000. Diagenesis in prehistoric caves: the use of minerals that form *in situ* to assess the completeness of the archaeological record. *Journal of Archaeological Science* 27, pp. 915–929.

Karkanas, P., Goldberg, P., 2010. Phosphatic features, in: Stoops, G., Marcelino, V., Mees, F. (eds.), *Interpretation of Micromorphological Features of Soils and Regoliths.* Amsterdam/Oxford: Elsevier, pp. 521–541.

Kaya, M., Seyyar, O., Baran, T., Turkes, T., 2014. Bat guano as new and attractive chitin and chitosan source. *Frontiers in Zoology* 11, pp. 59–10.

Kienitz, H., 1968. Einführung, in: Kienitz, H. (ed.), *Massenspektrometrie*. Weinheim: Verlag Chemie.

Krumbein, W.C., Aberdeen, E., 1937. The sediments of Barataria Bay. *Journal of Sedimentary Research* 7, pp. 3–17.

Lewis, H., 2005. *Thin sections from Tabon Cave, Palawan, Philippines: landscape and occupation history under the microscope.* British Academy Committee for South East Asian Studies and the Evans Fund. Unpublished manuscript.

Lewis, H., 2007. Preliminary soil micromorphology studies of landscape and occupation history at Tabon Cave, Palawan, Philippines. *Geoarchaeology* 22, pp. 685–708.

Lewis, H., Johnson, K., Ronquillo, W., 2008. Preliminary results of speleothem dating from Tabon Cave, Palawan, Philippines: moisture increase at the Last Glacial Maximum. *Hukay* 12, pp. 35–50.

Liu, W., Martinón-Torres, M., Cai, Y.-J., Xing, S., Tong, H.-W., Pei, S.-W., Sier, M.J., Wu, X.-H., Edwards, R.L., Cheng, H., Li, Y.-Y., Yang, X.-X., de Castro, J.M.B., Wu, X.-J., 2015. The earliest unequivocally modern humans in southern China. *Nature* 526, pp. 696–699.

Macintosh, N.W.G., Barker, B.C.W., Larnach, S.L., 1978. The Tabon Cave mandible. *Archaeology and Physical Anthropology in Oceania* 13, pp. 143–159.

Malainey, M.E., 2011. Isotope analysis, in: *A Consumer's Guide to Archaeological Science: Analytical Techniques.* New York: Springer, pp. 177–200.

Marwick, B., Van Vlack, H.G., Conrad, C., Shoocongdej, R., Thongcharoenchaikit, C., Kwak, S., 2017. Adaptations to sea level change and transitions to agriculture at Khao Toh

Chong rockshelter, Peninsular Thailand. *Journal of Archaeological Science* 77, pp. 94–108.

McDermott, F., 2004. Palaeo-climate reconstruction from stable isotope variations in speleothems: a review. *Quaternary Science Reviews* 23, pp. 901–918.

McDermott, F., Schwarcz, H., Rowe, P.J., 2006. Isotopes in Speleothems, in: *Isotopes in Palaeoenvironmental Research, Developments in Paleoenvironmental Research.* Dordrecht; Springer, pp. 185–225.

McFarlane, D.A., Lundberg, J., 2018. New records of guano-associated minerals from caves in northwestern Borneo. *International Journal of Speleology* 47, 119–126.

McSween, H.Y., Jr., Richardson, S.M., Uhle, M.E., 2003. *Geochemistry: Pathways and Processes*, 2nd ed. New York: Columbia University Press.

Medina-Elizalde, M., Burns, S.J., Polanco-Martinez, J., Lases-Hernández, F., Bradley, R., Wang, H.-C., Shen, C.-C., 2017. Synchronous precipitation reduction in the American Tropics associated with Heinrich 2. *Scientific Reports* 7: 11216, pp. 1–12.

Meier-Augenstein, W., 2010. *Stable Isotope Forensics: An Introduction to the Forensic Application of Stable Isotope Analysis.* Chichester: John Wiley & Sons, Ltd.

Mijares, A.S.B., Détroit, F., Piper, P., Grün, R., Bellwood, P., Aubert, M., Champion, G., Cuevas, N., de Leon, A., Dizon, E., 2010. New evidence for a 67,000-year-old human presence at Callao Cave, Luzon, Philippines. *Journal of Human Evolution* 59, pp. 123–132.

Milosevic, M., 2012. Applications of ATR spectroscopy, in: *Internal Reflection and ATR Spectroscopy.* Hoboken: John Wiley & Sons, Inc.

Miskovsky, J.-C., Debard, E., 2002. Granulométrie et morphoscopie des pierres, in: Miskovsky, J.-C. (ed.), *Géologie de la préhistoire*. Paris: presses universitaires de Perpignan, pp. 479–502.

Mizutani, H., McFarlane, D.A., Kabaya, Y., 1992a. Carbon and nitrogen isotopic signatures of bat guanos as a record of past environments. *Mass Spectroscopy* 40, pp. 67–82.

Mizutani, H., McFarlane, D.A., Kabaya, Y., 1992b. Nitrogen and carbon isotope study of bat guano core from Eagle Creek Cave, Arizona, U.S.A. *Mass Spectroscopy* 40, pp. 57–65.

Mook, W.G., van der Plicht, J., 1999. Reporting ^{14}C activities and concentrations. *Radiocarbon* 41, pp. 227–239.

Morley, M.W., 2017. The geoarchaeology of hominin dispersals to and from tropical Southeast Asia: a review and prognosis. *Journal of Archaeological Science* 77, pp. 78–93.

Morley, M.W., Goldberg, P., 2017. Geoarchaeological research in the humid tropics: a global perspective. *Journal of Archaeological Science* 77, pp.1–9.

Morley, M.W., Goldberg, P., Sutikna, T., Tocheri, M.W., Prinsloo, L.C., Jatmiko, Saptomo, E.W., Wasisto, S., Roberts, R.G., 2017. Initial micromorphological results from Liang Bua, Flores (Indonesia): Site formation processes and hominin activities at the type locality of *Homo floresiensis*. *Journal of Archaeological Science* 77, pp. 125–142.

National Museum of the Philippines, 2014. *Tabon Cave Complex* [web article]. Available at: http://www.nationalmuseum.gov.ph/nationalmuseumbeta/ASBMD/Tabon.html [accessed 29 December 2017].

Newsome, L., Morris, K., Lloyd, J.R., 2014. The biogeochemistry and bioremediation of uranium and other priority radionuclides. *Chemical Geology* 363, pp. 164–184.

O'Connor, S., Barham, A., Aplin, K.P., Maloney, T., 2017. Cave stratigraphies and cave breccias: implications for sediment accumulation and removal models and interpreting the record of human occupation. *Journal of Archaeological Science* 77, pp. 143–159.

OECD-NEA, 2012. *Uranium 2011: Resources, Production and Demand.* Organisation for Economic Co-operation and Development (OECD) Nuclear Energy Agency (NEA) and the International Atomic Energy Agency (IAEA).

Office of the President of the Philippines, 1972. *Proclamation No. 996 declaring the Tabon Cave Complex and all of Lipuun Point in Quezon, Palawan, as a Site Museum Reservation.* Manila: Official Gazette of the Republic of the Philippines.

Onac, B.P., Forray, F.L., Wynn, J.G., Giurgiu, A.M., 2014. Guano-derived $\delta^{13}C$-based paleo-hydroclimate record from Gaura cu Muscă Cave, SW Romania. *Environmental Earth Sciences* 71, pp. 4061–4069.

Onac, B.P., Forti, P., 2011. Minerogenetic mechanisms occurring in the cave environment: an overview. *International Journal of Speleology* 40, pp. 1-20.

Onac, B.P., Kearns, J., Breban, R.C., Cîntă Pânzaru, S., 2004. Variscite ($AlPO_4 \cdot 2H_2O$) from Cioclovina Cave (Şureanu Mountains, Romania): a tale of a missing phosphate. *Studia Universitatis Babeş-Bolyai, Geologia* 49, pp. 3–14.

Onac, B.P., Vereş, D.Ş., 2003. Sequence of secondary phosphates deposition in a karst environment: evidence from Măgurici Cave (Romania). *European Journal of Mineralogy* 15, pp. 741–745.

Onac, B.P., White, W.B., 2003. First reported sedimentary occurrence of berlinite ($AlPO_4$) in phosphate-bearing sediments from Cioclovina Cave, Romania. *American Mineralogist* 88, pp. 1395–1397.

OpenStax, 2017. *Atomic Structure and Symbolism* [web article]. Available at: http://cnx.org/contents/655f88b2-7a90-4e30-9547-68a423e8f606@10 [accessed 10 February 2017].

Oppo, D.W., Sun, Y., 2005. Amplitude and timing of sea-surface temperature change in the northern South China Sea: dynamic link to the East Asian monsoon. *Geology* 33, pp. 785–788.

Orogo, A.B., 2000a. *Progress report: result of the archaeological re-investigation and re-excavation of Tabon Cave at the Municipality of Quezon, Palawan Province, May 4 to June 2, 2000.* Manila: National Museum of the Philippines. Unpublished report.

Orogo, A.B., 2000b. *Second progress report: archaeological re-investigation and re-excavation of Tabon Cave, Municipality of Quezon, Palawan Province, August 24 to September 23, 2000.* Manila: National Museum of the Philippines. Unpublished report.

Orogo, A.B., 2001a. *Progress report: result of the archaeological re-investigation and re-excavation of Tabon Cave, Municipality of Quezon, Palawan, March 1 to 31, 2001.* Manila: National Museum of the Philippines. Unpublished report.

Orogo, A.B., 2001b. *Progress report: results of the fourth phase of archaeological re-excavation of Tabon Cave, Lipuun Point, Quezon, Palawan, September 12 to October 11, 2001.* Manila: National Museum of the Philippines. Unpublished report.

Patole-Édoumba, E., 2002. *L'industrie lithique préhistorique de débitage des Philippines de la fin du Pléistocène à l'Holocène moyen.* Aix-en-Provence/Marseille: Aix-Marseille Université. PhD thesis.

Pavia, D.L., Lampman, G.M., Kriz, G.S., Vyvyan, J.R., 2015. Infrared spectroscopy, in: *Introduction to Spectroscopy.* Stamford: Brooks/Cole Cengage Learning, pp. 14–106.

Pearson, F.G., Marchessault, R.H., Liang, C.Y., 1960. Infrared spectra of crystalline polysaccharides. V. Chitin. *Journal of Polymer Science Part A: Polymer Chemistry* 43, pp. 101–116.

Pettijohn, F.J., 1957. *Sedimentary Rocks*, 2nd ed. New York: Harper and Brothers.

Pollard, A.M., Batt, C.M., Stern, B., Young, S.M.M., 2007a. Molecular analysis by absorption and Raman spectroscopy, in: *Analytical Chemistry in Archaeology.* Cambridge: Cambridge University Press, pp. 70–92.

Pollard, A.M., Batt, C.M., Stern, B., Young, S.M.M., 2007b. X-ray techniques and electron beam microanalysis, in: *Analytical Chemistry in Archaeology.* Cambridge: Cambridge University Press, pp. 93–122.

Pollard, A.M., Heron, C., 2008. Analytical techniques applied to archaeology, in: *Archaeological Chemistry*. Cambridge: The Royal Society of Chemistry.

Provincial Government of Palawan, 2017. Physical features and climate [web article]. Available at: http://www.palawan.gov.ph/climate.php [accessed 31 December 2017].

Quattropani, L., Charlet, L., de Lumley, H., Menu, M., 1999. Early Palaeolithic bone diagenesis in the Arago Cave at Tautavel, France. Mineralogical Magazine 63, pp. 801–812.

Ramnarine, R., Voroney, R.P., Wagner-Riddle, C., Dunfield, K.E., 2011. Carbonate removal by acid fumigation for measuring the $\delta^{13}C$ of soil organic carbon. *Canadian Journal of Soil Science* 91, pp. 247–250.

Rawle, A., 2000. *Basic principles of particle size analysis.* Worcestershire: Malvern Instruments.

Reitz, E.J., Shackley, M., 2012. Introduction to environmental archaeology, in: *Environmental Archaeology, Manuals in Archaeological Method, Theory and Technique*. Boston: Springer, pp. 1–39.

Rinaudo, C., Abbona, F., 1988. A contribution to the study of the crystal chemistry of calcium sulfate phosphate hydrate. *Mineralogica et Petrographica Acta* 31, pp. 95-105.

Robinson, I.K., Ferrer, S., Torrellas, X., Alvarez, J., Silfhout, R.V., Schuster, R., Kuhnke, K., Kern, K., 1995. Vibrational anisotropy of a CO monolayer on Ni(110). Europhysics Letters 32, pp. 37–42.

Robles, E., Piper, P., Ochoa, J., Lewis, H., Paz, V., Ronquillo, W., 2015. Late Quaternary sea-level changes and the palaeohistory of Palawan Island, Philippines. *Journal of Island and Coastal Archaeology* 10, pp. 76–96.

Ronquillo, W., 1985. Archaeological research in the Philippines, 1951–1983. *Bulletin of the Indo-Pacific Prehistory Association* 6, pp. 74–88.

Ronquillo, W., 1995. Anthropological and cultural values of caves. *Philippine Quarterly of Culture and Society* 23, pp. 138–150.

Royer, A., Queffelec, A., Charlier, K., Puech, E., Malaizé, B., Lenoble, A., 2015. Seasonal changes in stable carbon and nitrogen isotope compositions of bat guano (Guadeloupe). *Palaeogeography, Palaeoclimatology, Palaeoecology* 440, pp. 524–532.

Royer, A., Malaizé, B., Lécuyer, C., Queffelec, A., Charlier, K., Caley, T., Lenoble, A., 2017. A high-resolution temporal record of environmental changes in the Eastern Caribbean (Guadeloupe) from 40 to 10 ka BP. *Quaternary Science Reviews* 155, pp. 198–212.

Salome, K.R., Green, S.J., Beazley, M.J., Webb, S.M., Kostka, J.E., Taillefert, M., 2013. The role of anaerobic respiration in the immobilization of uranium through biomineralization of phosphate minerals. *Geochimica et Cosmochimica Acta* 106, pp. 344–363.

Sambridge, M., Grün, R., Eggins, S., 2012. U-series dating of bone in an open system: the diffusion-adsorption-decay model. *Quaternary Geochronology* 9, pp. 42–53.

Sanna, L., Saez, F., Simonsen, S., Constantin, S., Calaforra, J.-M., Forti, P., Lauritzen, S.-E., 2010. Uranium-series dating of gypsum speleothems: methodology and examples. *International Journal of Speleology* 39, pp. 35–46.

Schiegl, S., Goldberg, P., Bar-Yosef, O., Weiner, S., 1996. Ash deposits in Hayonim and Kebara Caves, Israel: macroscopic, microscopic and mineralogical observations, and their archaeological implications. *Journal of Archaeological Science* 23, pp. 763–781.

Schimmelmann, A., DeNiro, M.J., 1986. Stable isotopic studies on chitin, measurements on chitin/chitosan isolates and d-glucosamine hydrochloride from chitin, in Muzzarelli, R., Jeuniauz, C., Gooday, G. (eds.), *Chitin in Nature and Technology*. New York: Plenum, pp. 357–364.

Schmidt, P., 2008. *Caractérisation et provenance géologique de la matière première en jaspe utilisée pour les débitages lithiques à Tabon Cave, Philippines.* Paris: Muséum national d'histoire naturelle. Master's thesis.

Scholz, D., Mangini, A., Felis, T., 2004. U-series dating of diagenetically altered fossil reef corals. *Earth and Planetary Science Letters* 218, pp. 163–178.

Seagrave, S., Seagrave, P., 2003. *Gold Warriors: America's Secret Recovery of Yamashita's Gold*. London/New York: Verso.

Shahack-Gross, R., Marshall, F., Weiner, S., 2003. Geo-ethnoarchaeology of pastoral sites: the identification of livestock enclosures in abandoned Maasai settlements. *Journal of Archaeological Science* 30, pp. 439–459.

Shahack-Gross, R., Berna, F., Karkanas, P., Weiner, S., 2004. Bat guano and preservation of archaeological remains in cave sites. *Journal of Archaeological Science* 31, pp. 1259–1272.

Stephens, M., Rose, J., Gilbertson, D., 2017. Post-depositional alteration of humid tropical cave sediments: micromorphological research in the Great Cave of Niah, Sarawak, Borneo. *Journal of Archaeological Science* 77, pp. 109–124.

Stephens, M., Rose, J., Gilbertson, D., Canti, M., 2005. Micromorphology of cave sediments in the humid tropics: Niah Cave, Sarawak. *Asian Perspectives* 44, pp. 42–55.

Stiner, M.C., Kuhn, S.L., Surovell, T.A., Goldberg, P., Meignen, L., Weiner, S., Bar-Yosef, O., 2001. Bone preservation in Hayonim Cave (Israel): a macroscopic and mineralogical study. *Journal of Archaeological Science* 28, pp. 643–659.

Stuart, B.H., 2002. *Polymer Analysis*. Chichester: John Wiley & Sons, Ltd.

Subcommission on Quaternary Stratigraphy, 2016. *Major divisions* [web article]. Available at: http://quaternary.stratigraphy.org/majordivisions/ [accessed 24 March 2017].

Syvitski, J.P.M. (ed.), 2007. *Principles, Methods, and Application of Particle Size Analysis.* Cambridge: Cambridge University Press.

Thompson, W.G., Spiegelman, M.W., Goldstein, S.L., Speed, R.C., 2003. An open-system model for U-series age determinations of fossil corals. *Earth and Planetary Science Letters* 210, pp. 365–381.

Ulrich, K.-U., Veeramani, H., Bernier-Latmani, R., Giammar, D.E., 2011. Speciation-dependent kinetics of uranium(VI) bioreduction. *Geomicrobiology Journal* 28, pp. 396–409.

UNESCO World Heritage Centre, 2018. *The Tabon Cave Complex and all of Lipuun* [web article]. Available at: http://whc.unesco.org/en/tentativelists/1860/ [accessed 25 March 2018].

UNESCO, 2013. Palawan [web article]. Available at: http://www.unesco.org/new/en/natural-sciences/environment/ecological-sciences/biosphere-reserves/asia-and-the-pacific/philippines/palawan [accessed 31 December 2017].

Vazquez, G.J., Dodge, C.J., Francis, A.J., 2007. Interactions of uranium with polyphosphate. *Chemosphere* 70, pp. 263–269.

Villemant, B., Feuillet, N., 2003. Dating open systems by the ^{238}U–^{234}U–^{230}Th method: application to Quaternary reef terraces. *Earth and Planetary Science Letters*, 210, pp. 105–118.

Wang, Y., Cheng, H., Edwards, R.L., Kong, X., Shao, X., Chen, S., Wu, J., Jiang, X., Wang, X., An, Z., 2008. Millennial- and orbital-scale changes in the East Asian monsoon over the past 224,000 years. *Nature* 451, pp. 1090–1093.

Weiner, S., Karkanas, P., Rigaud, J.-P., Simek, J.F., Albert, R.M., 2002. Ash bones and guano: a study of the minerals and phytoliths in the sediments of Grotte XVI, Dordogne, France. *Journal of Archaeological Science* 29, pp. 721–732.

Weiner, S., Goldberg, P. & Bar-Yosef, O., 2002. Three-dimensional distribution of minerals in the sediments of Hayonim Cave, Israel: diagenetic processes and archaeological implications. *Journal of Archaeological Science* 29, pp. 1289–1308.

Weiner, S., 2010. Common mineral components of the archaeological record, in: *Microarchaeology, Beyond the Visible Archaeological Record*. New York: Cambridge University Press, pp. 87–117.

van Welzen, P.C., Parnell, J.A.N., Ferry Slik, J.W., 2011. Wallace's Line and plant distributions: two or three phytogeographical areas and where to group Java? *Biological Journal of the Linnean Society* 103, pp. 531–545.

Westaway, K.E., Louys, J., Awe, R.D., Morwood, M.J., Price, G.J., Zhao, J.-X., Aubert, M., Joannes-Boyau, R., Smith, T.M., Skinner, M.M., Compton, T., Bailey, R.M., van den Bergh, G.D., de Vos, J., Pike, A., Stringer, C., Saptomo, E.W., Rizal, Y., Zaim, J., Santoso, W.D., Trihascaryo, A., Kinsley, L., Sulistyanto, B., 2017. An early modern human presence in Sumatra 73,000–63,000 years ago. *Nature* 548, pp. 322–325.

Widga, C., Colburn, M., 2015. Paleontology and paleoecology of guano deposits in Mammoth Cave, Kentucky, USA. *Quaternary Research* 83, pp. 427–436.

Wikramanayake, E., Dinerstein, E., Loucks, C.J., Olson, D.M., Morrison, J., Lamoreux, J., McKnight, M., Hedao, P., 2002. *Terrestrial Ecoregions of the Indo-Pacific: a Conservation Assessment.* Washington/Covelo/London: Island Press.

Wirrmann, D., Sémah, A.-M., Mendez-Millan, M., Schmidt, S., Boissenin, M., Boucher, H., Bouloubassi, I., Brescia, F., Cetin, F., Djouraev, I., Klein, V., 2017. Signification environnementale du guano de salanganes et de chiroptères de Nouvelle-Calédonie : premiers résultats. *Quaternaire* 28, pp. 315–326.

Wurster, C.M., Bird, M., Bull, I., Bryant, C., Ascough, P., 2009. A protocol for radiocarbon dating tropical subfossil cave guano. *Radiocarbon* 51, pp. 977–986.

Wurster, C.M., Bird, M., Bull, I., Creed, F., Bryant, C., Dungait, J., Paz, V., 2010a. Forest contraction in north equatorial Southeast Asia during the Last Glacial Period. *Proceedings of the National Academy of Sciences of the USA* 107, pp. 15508–15511.

Wurster, C.M., McFarlane, D.A., Bird, M., 2007. Spatial and temporal expression of vegetation and atmospheric variability from stable carbon and nitrogen isotope analysis of

bat guano in the southern United States. *Geochimica et Cosmochimica Acta* 71, pp. 3302–3310.

Wurster, C.M., McFarlane, D.A., Bird, M., Ascough, P., Beavan Athfield, N., 2010b. Stable isotopes of subfossil bat guano as a long-term environmental archive: insights from a Grand Canyon cave deposit. *Journal of Cave and Karst Studies* 72, pp. 111–121.

Wurster, C.M., Munksgaard, N., Zwart, C., Bird, M., 2015. The biogeochemistry of insectivorous cave guano: a case study from insular Southeast Asia. *Biogeochemistry* 124, pp. 163–175.

Wurster, C.M., Patterson, W.P., McFarlane, D.A., Wassenaar, L.I., Hobson, K.A., Athfield, N.B., Bird, M., 2008. Stable carbon and hydrogen isotopes from bat guano in the Grand Canyon, USA, reveal Younger Dryas and 8.2 ka events. *Geology* 36, pp. 683–686.

Wurster, C.M., Rifai, H., Haig, J., Titin, J., Jacobsen, G., Bird, M., 2017. Stable isotope composition of cave guano from eastern Borneo reveals tropical environments over the past 15,000 cal yr BP. *Palaeogeography, Palaeoclimatology, Palaeoecology* 473, pp. 73–81

Wurster, C.M., Saiz, G., Calder, A., Bird, M., 2010c. Recovery of organic matter from mineral-rich sediment and soils for stable isotope analyses using static dense media. *Rapid Communications in Mass Spectrometry* 24, pp. 165–168.

Xhauflair, H., 2009. *Analyse tracéologique et recherche de résidus : contribution à l'étude de l'industrie lithique de Tabon Cave, Palawan, Philippines*. Paris: Muséum national d'histoire naturelle. Master's thesis.

Xhauflair, H., Revel, N., Vitales, T.J., Callado, J.R., Tandang, D., Gaillard, C., Forestier, H., Dizon, E., Pawlik, A., 2017. What plants might potentially have been used in the forests of prehistoric Southeast Asia? An insight from the resources used nowadays by local communities in the forested highlands of Palawan Island. *Quaternary International* 448, pp. 169–189.

Yokoyama, Y., Esat, T.M., Lambeck, K., 2001. Last glacial sea-level change deduced from uplifted coral terraces of Huon Peninsula, Papua New Guinea. Quaternary International 83–85, pp. 275–283.